Instabilities and modeling of falling film flows

Christian Ruyer-Quil

Université Pierre et Marie Curie (UPMC)
laboratoire FAST UMR 7608

Synthèse des travaux

présentée en première version en vu d'obtenir le diplôme
d'Habilitation à Diriger des Recherches, spécialité "mécanique"

par

Christian Ruyer-Quil

De la modélisation et des instabilités des films liquides tombants

Instabilities and modeling of falling film flows

HDR soutenue le 26 octobre 2012 devant le jury composé de :

M.	Pierre-Yves Lagrée	UPMC	(Président)
M.	Patrice Laure	Université de Nice	(Rapporteur)
M.	Ranga Narayanan	University of Florida	(Rapporteur)
M.	Jean-Paul Vila	INSA Toulouse	(Rapporteur)
M.	Paul Manneville	École polytechnique	(Examinateur)
M.	Serafim Kalliadasis	Imperial College London	(Examinateur)

À Géraldine, Matthieu, Axel et Joël…

Acknowledgments

First of all, I would like to thank Neil Ribe, director of the FAST laboratory. Without his impulse I would never have come to the idea that my work would be worthy of being assembled and presented. He has put me under a certain strain whose result is the present memoir.

I am very much indebted to my own PhD supervisor, Paul Manneville. He trained me, encouraged me, shaped me into the researcher I am. All I know comes from his training. The time I have spent under his guidance at LadHyX is a golden age that I wish to live again.

Above all, I am indebted to the colleagues and students I had the opportunity to work with and/or to supervise: Pierre Carlès, Symphony Chakraborty, Didier Chasseur, Camille Duprat, Frédérique Giorgiutti-Dauphiné, Philippe Gondret, Benoit Goyeau, Serafim Kalliadasis, Nicolas Kofman, Sophie Mergui, Marc Rabaud, Arghya Samanta, Benoit Scheid, Manuel G. Velarde, R. Kh. Zeytounian. Without their help, there would have been much less to be presented in this memoir.

I would like to thank Patrice Laure, Jean-Paul Vila and Ranga Narayanan for having accepted to referee this manuscript.

I would like to thank Pierre-Yves Lagrée, Paul Manneville and Serafim Kalliadasis for having wholeheartedly accepted to be part of the examining committee.

Finally, I would like to thank my wife Géraldine, whose support in the writing of this memoir was paramount.

Orsay, October 29, 2012.

Contents

Introduction

Celui qui sait s'arrêter ne périclite jamais.
(proverbe chinois)

Since my arrival at FAST laboratory in December 1999, I have conducted some numerical and theoretical researches in fluid mechanics.

The aim of this memoir is to present a synthesis of this work. This task looks to me quite difficult. My principal concern is a persistent feeling of vanity and failure. I feel sorry for those attempting a perusal of this document.

I have worked on the field of interfacial "long wave" instabilities using an asymptotic approach that I have initially developed during my PhD [1]. I have improved this approach and made use of it to study (a little) (i) Kelvin-Helmholtz instability in a Hele-Shaw cell, and to study (a lot) falling film instabilities: (ii) Kapitza (or "roll wave"), (iii) Marangoni and (iv) Rayleigh-Plateau instabilities.

Today my research activities are devoted to the dynamics of falling films in the presence (v) of non-Newtonian fluids (pseudoplastic, shearthinning, viscoplatic fluids) (vi) of a porous substrate (vii) and finally when sheared by a gas flow.

I only present in this memoir the main lines of these works gathered in five chapters. Each of this chapter is followed by some selected publications (in bold faces in the lists below). However, each chapter is written so as to preserve its self-consistency. The appended publications are only there to invite the reader to deepen his knowledge of the subject and their perusal is not required for an understanding of the matter at hand.

The *first chapter* presents in an exhaustive way some low-dimensional modeling approaches: long-wave expansion, weighted residual methods and center manifold analysis applied to inertial flows in a Hele-Shaw cell. Below are listed some publications I have co-authored on this subject:

- C. Ruyer-Quil, Inertial corrections to the Darcy law in a Hele-Shaw cell, C. R. Acad. Sci. Paris, **329**, Série IIb, pp. 337-342 (2001)
- L. Meignin, P. Gondret, C. Ruyer-Quil and M. Rabaud, Subcritical Kelvin-Helmholtz instability in a Hele-Shaw cell, Phys. Rev. Lett. **90**, pp. 234502 (2003)

The *second chapter* presents a review of the Kapitza instability or "roll-wave" instability of a Newtonian film down an inclined plane.

[1] "Dynamique d'un film mince s'écoulant le long d'un plan incliné" under the guidance of Paul Manneville (LadHyX, 1996–1999)

- C. Ruyer-Quil and P. Manneville, Further accuracy and convergence results on the modeling of flows down inclined planes by weighted-residual approximations, Phys. of Fluids **14**, pp. 170-183 (2002)
- C. Ruyer-Quil and P. Manneville, Comment on "Low-dimensional models for vertically falling viscous films", Phys. Rev. Lett. **93**, pp. 199401 (2004)
- **C. Ruyer-Quil and P. Manneville, On the speed of solitary waves running down a vertical wall. J. Fluid Mech. 531, pp. 181-190 (2005)**
- **B. Scheid, C. Ruyer-Quil and P. Manneville, Wave patterns in film flows: Modelling and three-dimensional waves, J. Fluid Mech. 562, pp. 183-222 (2006)**

The *third chapter* is devoted to the influence of a temperature gradient on a falling liquid film (Marangoni effect).

- S. Kailladasis, E.A. Demekhin, C. Ruyer-Quil and M.G. Velarde, Thermocapillary instability and wave formation on a film falling down a uniformly heated plane, J. Fluid Mech. **492**, pp. 303-338 (2003)
- B. Scheid, C. Ruyer-Quil, U. Thiele, O.A. Kabov, J.-C. Legros and P. Colinet, Validity domain of the Benney equation including the Marangoni effect for closed and open flows, J. Fluid Mech. **527**, pp. 303-335 (2005)
- C. Ruyer-Quil, B. Scheid, S. Kailladasis, M.G. Velarde, R. Kh. Zeytounian, Thermocapillary long waves in a liquid film flow. Part I. Low-dimensional formulation, J. Fluid Mech. **538**, pp. 199-222 (2005)
- **B. Scheid, C. Ruyer-Quil, S. Kailladasis, M.G. Velarde, R. Kh. Zeytounian, Thermocapillary long waves in a liquid film flow. Part II. Linear and nonlinear waves, J. Fluid Mech. 538, pp. 223-244 (2005)**
- P. Trevelyan, B. Scheid, S. Kalliadasis and C. Ruyer-Quil, Heated Falling Films, J. Fluid Mech. **592**, 295-334 (2007)
- B. Scheid, S. Kalliadasis,C. Ruyer-Quil and P. Colinet, Spontaneous channeling of solitary pulses in heated film flows, Europhys. Lett. **84**, 64002 (2008)
- B. Scheid, S. Kalliadasis, C. Ruyer-Quil and P. Colinet, Interaction of three-dimensional hydrodynamic and thermocapillary instabilities in film flows, Phys. Rev. E **78**, 066311 (2008)

The *fourth chapter* presents my work on the dynamics of an axisymmetrical film down a fiber where the Kapitza and Rayleigh plateau instabilities interplay.

- C. Duprat, C. Ruyer-Quil, S. Kalliadasis and F. Giorgiutti-Dauphiné, Absolute and convective instabilities of a film flowing down a vertical fiber, Phys. Rev. Lett. **98**, 244502 (2007)

- **C. Ruyer-Quil, P. Treveleyan, F. Giorgiutti-Dauphiné, C. Duprat and S. Kalliadasis, Modelling film flows down a fibre, J. Fluid Mech. 603, 431-462 (2008)**
- C. Duprat, C. Ruyer-Quil and F. Giorgiutti-Dauphiné, Spatial evolution of a film flowing down a fiber, Phys. Fluids **21**, 042109 (2009)
- C. Ruyer-Quil and S. Kalliadasis, Wavy regimes of film flow down a fiber, Pys. Rev E, **85** 046302 (2012)

The *fifth chapter* presents my recent work on the influence of a non-Newtonian rheology, of a porous substrate and of a gas flow. (2008–up to now).

- A. Samanta, C. Ruyer-Quil and B. Goyeau, A falling film down a slippery inclined plane. J. Fluid Mech. **684**, 353-383 (2011)
- A. Samanta, B. Goyeau and C. Ruyer-Quil, Falling film on a porous medium. *submitted to J. Fluid Mech.*
- **C. Ruyer-Quil, S. Chakraborty and B.S. Dandapat, Wavy regime of a power-law film flow. J. Fluid Mech. 692, 220-256 (2012)**
- G.F. Dietze and C. Ruyer-Quil, Wavy liquid films interacting with a confined laminar gas flow. *submitted to J. Fluid Mech.*

There is no "Conclusion" chapter in this memoir: Let the reader draw his own conclusions. Each chapter contains a "Perspectives" section suggesting some possible follow-ups. In chapter 5, some more perspectives can be found. However, an exhaustive list of suggestions for future studies is offered at chapter 10 of the recent monograph I have co-authored with S. Kalliadasis, B. Scheid and M. G. Velarde (Kalliadasis et al. 2012).

1 Low-dimensional modeling of a flow in a Hele-Shaw cell

This chapter is based on the work I have done during my ATER one-year non-permanent teaching position in the academic year 2000-2001 corresponding to my arrival at FAST laboratory within the Paris Sud university.

At that time Philippe Gondret and Marc Rabaud were running an experiment where a liquid was sheared by a co-current gas flow in a Hele-Shaw cell. They thus observed the development of surface waves as a result of the classical Kelvin-Helmholtz instability induced by the shear exerted by the gas flow onto the liquid one.

Their motivation (as far as I can say) was the study of a well-defined one-dimensional open flow in presence of an instability. Figure 1.1 presents a sketch of the experiment by Gondret and Rabaud. The Hele-Shaw cell consisted of two glass plates separated by a constant sub-millimetric gap. A silicon oil and a nitrogen gas were introduced at inlet at the same pressure and exited the cell at the atmospheric pressure.

This experiment is probably one of the best controlled and rich open-flow system. First of all, the base flow is perfectly parallel, which promises a good agreement between the classical stability analysis and the experiments. (Yet this prospect has later been unconfirmed because of the presence of meniscus regions which singularly complexes the treatment of this

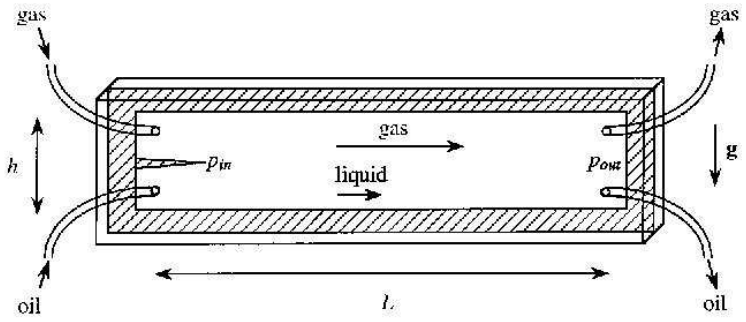

Figure 1.1 – *Sketch of the experiment by Gondret and Rabaud (reproduced from Gondret and Rabaud (1997)). The liquid consists of silicon oil and the gas is nitrogen.*

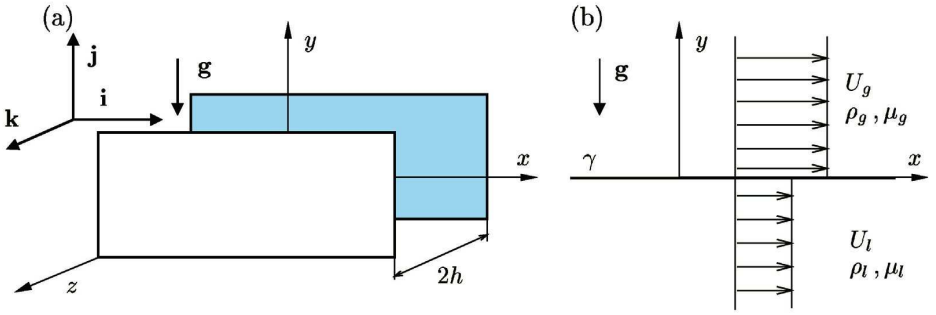

Figure 1.2 – *(a) Geometry of the Hele–Shaw cell; (b) the shear flow studied by Gondret and Rabaud [from Ruyer-Quil (2001)].*

problem.) Secondly, a transition from a convective to an absolute instabilities was easily observed (Gondret et al. 1999). Thirdly, this system also exhibits a conditional stability with a subcritical onset of the instability *(Meignin et al. 2003)* [1] .

In this chapter, I present my contribution to this problem which consists in a mere modification of the averaged equations which govern the evolution of the velocity field averaged across the cell. The material of Ruyer-Quil (2001) is presented somewhat differently than it was initially. The exposure of the weighted residual method benefits from the later development over the years. The emphasis is put here on a description of the gradient expansion and weighted residual averaging techniques which I have applied in the context of long-wave instabilities of falling films and that are discussed in the subsequent chapters.

I contrast these low-dimensional modeling techniques with the center manifold analysis introduced by Roberts (1997). The exposure of the different methods is as thorough as possible. My hope is that this chapter may benefit interested readers in the low-dimensional modeling techniques. However, this chapter might be skipped without impediment, and readers which are uninterested by technicalities might be willing to move directly to the next chapter.

1.1 Gradient expansion approach (lubrication theory)

Let us consider a cell made of two plates separated by a constant gap $2h$ (cf. figure 1.2). Here $\mathbf{g}$ is the gravitational acceleration; the horizontal, vertical and cross-stream coordinates are respectively denoted by x, y and z, and accordingly the unit vectors are $\mathbf{i}$, $\mathbf{j}$ and $\mathbf{k}$. The viscosity is denoted by μ. p is the pressure, ρ is the density. $\mathbf{u} == u\mathbf{i} + v\mathbf{j} + w\mathbf{k}$ is the velocity field. I further denote by $\mathbf{u}_{xy} = u\mathbf{i} + v\mathbf{j}$ the in-plane velocity projection. The symbol $\nabla_{xy} \equiv \mathbf{i}\partial_x + \mathbf{j}\partial_y$ corresponds to the two-dimensional gradient operator. For convenience, let us introduce length and time scales based on the half gap h and the characteristic speed U so that inertia effects are measured by the Reynolds number $Re = \rho U h/\mu$ and gravitational forces by the Froude number $Fr = U/(gh)^{1/2}$.

This configuration has been studied at length leading to the derivation

[1] Throughout this memoir I have emphasized publications that I have co-authored whenever my participation to the said publications is not conspicuous.

of the well known Darcy law (Darcy 1856) which reads

$$\langle \mathbf{u}_{xy} \rangle (x,y) = -\frac{Re}{3} \left(\nabla_{xy} p(x,y) + \frac{1}{Fr^2} \right) , \tag{1.1}$$

where $\langle \mathbf{u}_{xy} \rangle = \frac{1}{2} \int_{-1}^{1} \mathbf{u}_{xy} dz$ is the averaged velocity. Since inertia plays a crucial role in the Kelvin-Helmholtz instability, Gondret and Rabaud (1997) proposed the following extension which reads in its dimensional form

$$\partial_t \langle \mathbf{u}_{xy} \rangle + \frac{6}{5} \langle \mathbf{u}_{xy} \rangle \cdot \nabla_{xy} \langle \mathbf{u}_{xy} \rangle = -\nabla_{xy} p - \frac{1}{F^2} \mathbf{j} - \frac{3}{Re} \langle \mathbf{u}_{xy} \rangle . \tag{1.2}$$

Gondret and Rabaud heuristically derived (1.2) assuming a parabolic velocity profile and averaging the momentum balance across the cell. My (very small) contribution to this problem is the consistent derivation of an averaged momentum equation similar to (1.2). The approach is based on a classical perturbative technique lying on the existence of a basic state to which small deviations are applied. This basic state corresponds to a stationary two-dimensional flow which is uniform in the x and y directions, so that the velocity field is a function of z only and $w = 0$. Thus I simply consider the usual Poiseuille flow with a constant pressure gradient $\nabla_{xy} p$.

$$p \equiv p^{(0)}(x,y) , \qquad \mathbf{u}_{xy} \equiv \mathbf{u}_{xy}^{(0)} = -\frac{Re}{2} \left(\nabla_{xy} p^{(0)} + \frac{1}{Fr^2} \mathbf{j} \right) (1 - z^2) \tag{1.3}$$

In the following, I consider slow space and time evolutions of the velocity field, that is on space and time scales much longer than the gap $2h$ and the viscous relaxation time $\rho h^2 / \mu$. Therefore, I introduce a small formal parameter $\epsilon \sim h/L$ where L refers to the typical length scale of the in-plane spatial modulations. The continuity equation reads

$$\partial_x u + \partial_y v + \partial_z w = 0 , \tag{1.4}$$

so that the cross-stream velocity w is formally $\propto \epsilon$ and can be written as a function of u and v

$$w = -\int_{-1}^{z} \nabla_{xy} \cdot \mathbf{u}_{xy} \, dz , \tag{1.5}$$

since the no-slip boundary condition implies $w(z = \pm 1) = 0$.

Neglecting terms formally of order ϵ^2 and higher in the Navier–Stokes equation I obtain

$$\partial_t \mathbf{u}_{xy} + \mathbf{u}_{xy} \cdot \nabla_{xy} \mathbf{u}_{xy} + w \partial_z \mathbf{u}_{xy} = -\nabla_{xy} p - \frac{1}{Fr^2} \mathbf{j} + \frac{1}{Re} \partial_{zz} \mathbf{u}_{xy} , \tag{1.6}$$

$$0 = -\partial_z p + \frac{1}{Re} \partial_{zz} w , \tag{1.7}$$

which is completed by (1.5) and the boundary conditions at the plates

$$u = v = w = 0 \quad \text{at } z = \pm 1 . \tag{1.8}$$

Integration of Eq. (1.7) between -1 and z gives $p = p\big|_{z=-1} + (1/Re)(\partial_z w - \partial_z w\big|_{z=-1})$. Moreover, $\partial_z w\big|_{-1} = -\partial_x u\big|_{-1} - \partial_y v\big|_{-1}$ which can be seen to be zero with the help of the no-slip condition (1.8). Then, $\nabla_{xy} \partial_z w$ is a second order term so that $\nabla_{xy} p = \nabla_{xy} p\big|_{-1} + O(\epsilon) = \nabla_{xy} p^{(0)}$ at first order

and is uniform along the z-direction. The system to solve thus reduces to (1.6), where w is given by (1.5), completed by the no-slip boundary conditions. Note that this set of equations is similar to the Prandtl equations in boundary layer theory (Schlichting 1979) with the difference that there is no outer flow but boundary conditions at the edges of the Hele-Shaw cell.

The solution to (1.6) can be sought by expanding the velocity profile into

$$\mathbf{u}_{xy} = \mathbf{u}_{xy}^{(0)}(x,y,z,t) + \mathbf{u}_{xy}^{(1)}(x,y,z,t) \tag{1.9}$$

where the $O(\epsilon^0)$) terms corresponds to the base flow

$$\mathbf{u}_{xy}^{(0)}(x,y,z,t) = \mathbf{a}_0(x,y,t)(1-z^2) \tag{1.10}$$

and the $O(\epsilon)$ corrections $\mathbf{u}^{(1)}$ are induced by the inertia of the flow.

Substitution of the ansatz (1.9) and (1.10) into (1.5) gives

$$w = \frac{1}{3}(z-2)(1+z)^2 \nabla_{xy}\cdot\mathbf{a_0} + O(\epsilon^2)\,, \tag{1.11}$$

so that the no-slip boundary condition at $z=1$ yields

$$\nabla_{xy}\cdot\mathbf{a_0} = 0\,. \tag{1.12}$$

and $w = O(\epsilon^2)$. Next, substitution (1.9) and (1.10) in the momentum balance (1.6), truncation at order ϵ and integration with respect to z using the boundary conditions (1.8) straightforwardly gives

$$\begin{aligned}\mathbf{u}_{xy}^{(1)} &= -\left(\frac{Re}{2}\nabla_{xy}p^{(0)} + \frac{Re}{2Fr^2}\mathbf{j} + \mathbf{a_0}\right)(1-z^2)\\ &\quad + Re\frac{1}{12}\left(-5+6z^2-z^4\right)\partial_t\mathbf{a_0}\\ &\quad + Re\frac{1}{30}\left(-1+z^2\right)\left(11-4z^2+z^4\right)\mathbf{a_0}\cdot\nabla_{xy}\mathbf{a_0}\,.\end{aligned} \tag{1.13}$$

However a *gauge condition* must be introduced to make unique the decomposition (1.9). The introduction of such a condition enables also to give a physical meaning to the amplitude vector $\mathbf{a_0}$. The simplest choice is to demand that the average of $\mathbf{u}_{xy}^{(1)}$ is zero, i.e. $\int_{-1}^{1}\mathbf{u}_{xy}^{(1)}dz = 0$. As a result, the mass flux within the cell is all contained in $u^{(0)}$ and $\mathbf{a}_0$ can be identified with the average velocity $\langle\mathbf{u}_{xy}\rangle = \frac{1}{2}\int_{-1}^{1}\mathbf{u}dz = \frac{2}{3}\mathbf{a}_0$. From (1.13) the gauge condition reads

$$\frac{6}{5}\partial_t\langle\mathbf{u}_{xy}\rangle + \frac{54}{35}\langle\mathbf{u}_{xy}\rangle\cdot\nabla_{xy}\langle\mathbf{u}_{xy}\rangle = -\nabla_{xy}p - \frac{1}{Fr^2}\mathbf{j} - \frac{3}{Re}\langle\mathbf{u}_{xy}\rangle\,, \tag{1.14}$$

which is an averaged momentum equation completed by the averaged continuity equation

$$\nabla_{xy}\cdot\langle\mathbf{u}_{xy}\rangle = 0\,. \tag{1.15}$$

Equation (1.14) is thus a compatibility condition for the decomposition (1.9) of the velocity field into the zeroth order base state and a perturbation which results from the specific choice of the ansatz (1.10) with the request that the amplitude vector is the averaged velocity field. In Ruyer-Quil (2001), I derived (1.14) starting with a projection of the velocity field on polynomial functions. The above discussion shows that it is not necessary and that the procedure is not hampered by some necessity to employ polynomials.

1.2 Weighted residual approach

In this section, I introduce the weighted residual approach that I have extensively employed to solve falling film long-wave stability problems as summarized in the rest of this memoir.

Written formally, primitive governing equations read $\mathcal{E}(\mathcal{U}) = 0$ for some set of variables $\mathcal{U}$, typically the pressure and the velocity field. Solution is looked after in the form of a series expansion $\mathcal{U} = \sum_{j=0}^{N} \mathcal{A}_j \mathcal{F}_j$ on test functions $\mathcal{F}_j$. Weight functions, $\mathcal{W}_j$, are next chosen as ingredients of a projection rule defining $N+1$*residuals*: $\mathcal{R}j = \langle \mathcal{W}_j | \mathcal{E}(\mathcal{A}_j \mathcal{F}_j) \rangle$. Canceling the residuals $\mathcal{R}_j$ thus yields a system to be solved for the amplitudes $\mathcal{A}_j$. Weighted residual methods (WRMs) differ generally by the definition of the weights $\mathcal{W}_j$. Dirac functions are used in the collocation, whereas hat functions identify the method of subdomains. The most popular weighted residual method is the Galerkin method because of its equivalence with variational methods once variational principle holds (Finlayson 1972). In essence, weighted residual methods belong to the general class of spectral methods and benefit from the quick convergence properties of such methods. For instance, the application of WRMs to boundary layers has shown that increasing the number of functions and adding boundary conditions at the plate to the averaging condition improves the accuracy of the computed solution (Schlichting 1979).

Here, the projection rule is simply the integration across the gap $\langle \cdot | \cdot \rangle = \int_{-1}^{1} (\cdot) dz$. The primitive equations are the boundary-layer-like momentum balance (1.6) where w is given by (1.5) completed by the continuity equation (1.4) and the no-slip boundary conditions (1.8). The set of variables $\mathcal{U} = \mathbf{u_{xy}}$ consist in the in-plane velocity vector.

The fact that (i) the basic Poiseuille flow is a parabola, (ii) polynomials constitute a close set of functions with respect to the differentiations and products, make the choice of polynomial test functions appropriate. The test functions $\mathcal{F}_j = f_j(z)$ fulfill the no-slip boundary conditions and are defined as

$$f_j(z) = z^j (1 - z^2) \tag{1.16}$$

The velocity field is thus expanded as

$$\mathbf{u}_{xy} = \sum_{j=0}^{N} f_j(z) \mathbf{a}_j(x, y, t) \,. \tag{1.17}$$

From now on, I take advantage of the decomposition (1.9) of the velocity field into a zeroth order term –the Poiseuille flow– and a $O(\epsilon)$ correction induced by long modulations. As a consequence $\mathbf{a}_0 = O(1)$ and $\mathbf{a}_j = O(\epsilon)$ for $j \geq 1$. Time and space derivatives of the corrective variables $\partial_{x,t} \mathbf{a}_j$, $j \geq 1$, are second order terms that can be dropped out. The residuals thus read

$$\mathcal{R}_j = \int_{-1}^{1} \left(\partial_t \mathbf{u}_{xy}^{(0)} + \mathbf{u}_{xy}^{(0)} \cdot \nabla_{xy} \mathbf{u}_{xy}^{(0)} + \nabla_{xy} p + \frac{1}{Fr^2} \mathbf{j} - \frac{1}{Re} \partial_{zz} \mathbf{u}_{xy} \right) w_j(z) \, dz \,. \tag{1.18}$$

One thus obtains a linear system of $N+1$ equations for the unknowns $\mathbf{a}_j$, $j \geq 1$ whose inversion yields the N correction velocities as functions of $\mathbf{a}_0$

and its time and space derivatives, plus one compatibility condition which can be recast as an evolution equation for $\mathbf{a}_0$. Next, the averaged velocities $\langle \mathbf{u}_{xy} \rangle$ can substituted for $\mathbf{a}_0$ using their definition

$$\mathbf{a}_0 \int_{-1}^{1} f_0 \, dz = 2\langle \mathbf{u}_{xy} \rangle - \sum_{1}^{N} \mathbf{a}_j \int_{-1}^{1} f_j \, dz \tag{1.19}$$

The result is an averaged momentum equation which is similar to (1.14)

$$\frac{6}{5} K_1 \, \partial_t \langle \mathbf{u}_{xy} \rangle + \frac{54}{35} K_2 \, \langle \mathbf{u}_{xy} \rangle \cdot \nabla_{xy} \langle \mathbf{u}_{xy} \rangle = -\nabla_{xy} p - \frac{1}{Fr^2} \mathbf{j} - \frac{3}{Re} \langle \mathbf{u}_{xy} \rangle \, . \tag{1.20}$$

As shown in Ruyer-Quil (2001), if the number of test functions N is sufficient (that is $N \geq 4$), the process must necessarily converge to the solution (1.14) with $K_1 = K_2 = 1$. Indeed, substitution of (1.17) in (1.6) and truncation at $O(\epsilon)$ yields

$$\frac{1}{Re} \sum_{j=1}^{N} \mathbf{a}_j \partial_{yy} f_j = \partial_t \mathbf{u}_{xy}^{(0)} + \mathbf{u}_{xy}^{(0)} \cdot \nabla_{xy} \mathbf{u}_{xy}^{(0)} + \nabla_{xy} p + \frac{1}{Fr^2} \mathbf{j} \equiv \mathcal{P}(z) \tag{1.21}$$

where $\mathcal{P}$ is a polynomial in z of degree 4 since $\mathbf{u}_{xy}^{(0)}$ is of degree 2. Equating the two sides of (1.21) monomial after monomial yield $N+1$ relations that are similar to the residuals $\mathcal{R}_j$. Since the l.h.s. of (1.21) is of degree N and the r.h.s of degree 4, I get $\mathbf{a}_j = 0$ for $j \geq 5$. The residuals $\mathcal{R}_j$ and the $N+1$ relations from (1.21) form equivalent systems of equations for $N \geq 4$.

As an example, table 1.1 illustrates the convergence of (1.21) to (1.14) in the case of the collocation method.

Table 1.1 – *Convergence of the collocation method to Eq. (1.14). The weight functions are* $\mathcal{W}_j = \delta(z_j)$ *where* $z_j = (2j - N)/(N + 2)$.

N	0	1	2	3	4
K_1	$\frac{3}{2}\frac{5}{6} = 1.25$	$\frac{4}{3}\frac{5}{6} \simeq 1.11$	1	1	1
K_2	$\frac{9}{4}\frac{35}{54} \simeq 1.46$	$\frac{16}{9}\frac{35}{54} \simeq 1.15$	$\frac{117}{80}\frac{35}{54} \simeq 0.95$	$\frac{936}{625}\frac{35}{54} \simeq 0.97$	1

Every WRM ultimately leading to (1.14), it is interesting to find the one which is the most efficient, i.e. bringing the result with the least algebra. In any residual $\mathcal{R}$ the only place where the corrections $\mathbf{u}_{xy}^{(1)}$ are involved is the viscous drag term.

$$\langle \mathcal{L}\mathbf{u}_{xy}^{(1)} | w \rangle \equiv \int_{-1}^{1} -\frac{1}{Re} \partial_{zz} \mathbf{u}_{xy}^{(1)} w \, dz = \langle \mathbf{u}_{xy}^{(1)} | \mathcal{L}^{\dagger} w \rangle \tag{1.22}$$

where the adjoint operator $\mathcal{L}^{\dagger}$ is obtained by two integrations by part. One finds $\mathcal{L}^{\dagger} = \mathcal{L}$ with w fulfilling the no-slip boundary conditions $w(\pm 1) = 0$ and the linear operator $\mathcal{L}$ is self-adjoint. The viscous drag term (1.22) can thus be easily canceled out using the gauge condition $\langle \mathbf{u}_{xy}^{(1)} | 1 \rangle = 0$ and looking for the solution to

$$\mathcal{L}^{\dagger} w = cst \tag{1.23}$$

The operator $\mathcal{L}$ being self-adjoint and the Poiseuille flow being solution to $\mathcal{L}\mathbf{u}_{xy}^{(0)} = Re(\nabla_{xy} p + Fr^{-2}\mathbf{j}$ where the r.h.s. is independent of z, one gets $w \propto f_0$.

As a consequence choosing $w = f_0$ brings the looked-after averaged momentum equation (1.14) with the computation of only one residual ($N = 0$) ! Selecting the weights equal to the test functions defines the Galerkin method. It is then clear that the Galerkin method is the most efficient WRM. The efficiency of the Galerkin method is here directly related to the self-adjoint property of the linear operator $\mathcal{L}$.

1.3 Center manifold analysis

Both the gradient expansion (§ 1.1) and the weighted residual approach (§ 1.2) assume a slow time evolution, i.e. $\partial_t = O(\epsilon)$. This assumption holds in the case of the Kelvin-Helmholtz instability studied by Gondret and Rabaud. Indeed experimental observations show that waves travel at a speed which is close to two times the speed of the liquid velocity. Since the pressure drop in the two phases is equal, $U_g/U_l = \mu_l/\mu_g$. The gas flow sees a quasi-static interface and is quasi-stationary whereas the relevant time scale in the liquid is the advection time $t_a = L/U_l$ where L refers here to the typical length of the waves. The ratio of the typical advection time and viscous relaxation time thus reads $t_a/t_\nu = \mu L/(\rho h^2) = 1/(\epsilon Re)$. The slow evolution assumption $t_a \gg t_\nu$ thus holds whenever Re is $O(1)$ or smaller and the long-wave assumption $L \gg h$ holds.

However, such an argument cannot be generalized and the reliability of the averaged momentum equation (1.14) can be argued in other situations. Indeed, considering slow spatial modulations ($L \gg h$), the advection terms present in the momentum balance (1.6) are small $O(\epsilon)$ terms and the relevant timescale is a priori prescribed by the viscous relaxation.

I will show in that section that (1.14) is still acceptable even if the slow evolution assumption does not hold. The idea of the argument developed below is to apply a low-dimensional modeling method, which does not assume $\partial_t = O(\epsilon)$, and to show that this method yields an averaged momentum equation which is almost identical to (1.14).

The center manifold analysis has been employed by A.J. Roberts to model the long space and time evolutions of solutions to partial differential equations (Roberts 1997) [2]. The idea comes from the center manifold analysis of dynamical systems of finite dimension (Carr 1981, Guckenheimer and Holmes 1983) which is useful in order to consider the dynamics around equilibria. A center manifold is an invariant manifold that is tangent to the subspace of the linearized dynamical system corresponding to the eigenvalues of zero real part. When the corresponding eigenvalue is exactly zero, the center manifold is called a slow manifold. Further, if the equilibrium is a center (every eigenvalue has a negative or zero real part), all orbits arriving in the vicinity of the equilibrium is attracted to the slow manifold, in which case the long-time dynamics is governed by the slow manifold.

[2] A detailed description of the method can be found at `http://www.maths.adelaide.edu.au/anthony.roberts/modelling.php`.

Center manifold analysis may be sketched as follows. Consider the evolution of a set of physical variables $\mathbf{u}$ governed by a dynamical system of finite dimension:

$$\frac{d}{dt}\mathbf{u} = \boldsymbol{\mathcal{L}}\mathbf{u} + \mathbf{N}(\mathbf{u}, \boldsymbol{\epsilon}), \tag{1.24}$$

where $\boldsymbol{\epsilon}$ is a vector of parameters, $\boldsymbol{\mathcal{L}}$ is a linear operator that describes the flow dynamics close to the origin, $(\mathbf{u}, \boldsymbol{\epsilon}) = (\mathbf{0}, \mathbf{0})$, and $\mathbf{N}$ is a nonlinear functional of $\mathbf{u}$ and $\boldsymbol{\epsilon}$.

Let us assume that the linear operator $\boldsymbol{\mathcal{L}}$ has n eigenvalues with zero real part and all other eigenvalues have negative real parts. $\mathbf{u}$ can be projected onto the eigenmodes of $\boldsymbol{\mathcal{L}}$. If $\mathbf{a}$ is the vector of the amplitudes of the eigenfunctions of $\boldsymbol{\mathcal{L}}$ with zero real part in the projection for $\mathbf{u}$, the dynamics of the "flow" in a small neighborhood of the origin in the $(\mathbf{u}, \boldsymbol{\epsilon})$-space is governed by the n modes, i.e. by $\mathbf{a}$. This means that the n-dimensional vector $\mathbf{a} = (a_j)$ of the associated amplitudes satisfies in the small neighborhood of the origin

$$\frac{d}{dt}\mathbf{a} = \mathbf{G}(\mathbf{a}, \boldsymbol{\epsilon}) \quad \text{such that} \quad \mathbf{u} = \mathbf{U}(\mathbf{a}, \boldsymbol{\epsilon})\,, \tag{1.25}$$

where the"hypersurface" $\mathcal{C}$ of equation $\mathbf{u} = \mathbf{U}(\mathbf{a})$ is the center manifold and $\frac{d}{dt}\mathbf{a} = \mathbf{G}$ is the n-dimensional model of the dynamics. The existence of the center manifold is then assured by the convergence of the solution to $\mathcal{C}$: suppose a solution $\mathbf{u}(t_0)$ of (1.24) lies at time t_0 in a small neighborhood at the origin in the $(\mathbf{u}, \boldsymbol{\epsilon})$ space. Then there exists a trajectory $\mathbf{U}(\mathbf{a})$ on the center manifold that verifies

$$\|\mathbf{u}(t_0 + t) - \mathbf{U}(\mathbf{a}(t_0 + t))\| = O(\exp(-\alpha t))\,, \quad \text{for} \quad t > 0 \tag{1.26}$$

where $\|\cdot\|$ is an appropriately chosen norm and $-\alpha$ is some upper bound on the negative real part of the eigenvalues of $\boldsymbol{\mathcal{L}}$.

Using the chain rule $\partial_t \mathbf{U} = (\partial \mathbf{U}/\partial \mathbf{a})\partial_t \mathbf{a}$, one gets

$$\boldsymbol{\mathcal{L}}\mathbf{U} = \frac{\partial \mathbf{U}}{\partial \mathbf{a}}\mathbf{G} - \mathcal{N}(\mathbf{U})\,. \tag{1.27}$$

Solving (1.27) defines the center manifold. Yet, (1.27) is ill-posed since $\boldsymbol{\mathcal{L}}$ is a singular operator whose kernel is not empty. A crucial compatibility condition is that the r.h.s. of (1.27) lies within the range of $\boldsymbol{\mathcal{L}}$. This condition can be transposed mathematically by introducing a scalar product $\langle\cdot|\cdot\rangle$ and the adjoint operator defined by :

$$\langle \boldsymbol{\mathcal{L}}\mathbf{u}|\mathbf{w}\rangle = \langle \mathbf{u}|\boldsymbol{\mathcal{L}}^{\dagger}\mathbf{w}\rangle \tag{1.28}$$

$\boldsymbol{\mathcal{L}}$ and $\boldsymbol{\mathcal{L}}^{\dagger}$ have the same rank and therefore their kernels have the same dimension n. Let us denote by $\mathbf{v}_j$ and $\mathbf{v}_j^{\dagger}$ the $2n$ eigenvectors of the direct and adjoint operators. The compatibility condition thus read:

$$\langle \boldsymbol{\mathcal{L}}\mathbf{U}|{\mathbf{v}_\mathbf{j}}^{\dagger}\rangle = \langle \mathbf{U}|\boldsymbol{\mathcal{L}}^{\dagger}{\mathbf{v}_\mathbf{j}}^{\dagger}\rangle = 0 \tag{1.29}$$

which defines the n dimension $\mathbf{G}$ vector and yields (1.25).

The center manifold $\mathcal{C}$ can be constructed iteratively by means of an expansion in powers of the parameters. A parametrization is initially chosen to define the amplitudes $\mathbf{a}$. The process starts by imposing that the center manifold is tangent to the kernel of $\boldsymbol{\mathcal{L}}^\dagger$

$$\mathbf{U} = \sum a_j \mathbf{v}_j \qquad \frac{d}{dt}\mathbf{a} = 0\,. \tag{1.30}$$

Extending this procedure to dynamical system of infinite dimension provides a powerful tool to derive low-dimensional models in a variety of situations. For instance, A.J. Roberts applied this method in the context of falling films (Roberts 1996), of thin film flows (Roberts and Li 2006, Roberts 2006), turbulent geophysical floods and roll waves (Mei et al. 2002). In this section, I apply this method to the problem at hand and derive an averaged momentum equation, similar to (1.14), which governs the flow dynamics on the slow manifold. To my knowledge, this is the first time this approach is used in the context of the modeling of a flow in a Hele-Shaw cell. Though the adopted procedure is very similar to the one developed in Roberts (1996) in the context of falling films (see chapter 2), I will use a slightly different formulation and check that the result is not modified.

Let us consider each point on the (x,y) plane of the Hele-Shaw cell as a dynamical system in time t of infinite dimension parametrized by the z coordinate (discretizing the problem in the z coordinate generates a series of phase coordinates, say z_j, with associated variables $\mathbf{u}(x,y,z_j,t)$, which form a countable infinite set). Each dynamical system is coupled to its neighbors through long-range spatial modulations (the order $O(\epsilon)$ terms in the momentum balance (1.6)). The Poiseuille flow (1.3) is an equilibrium of the considered dynamical system and I look after the long-time dynamics in the vicinity of this equilibrium and an associated invariant manifold on which the dynamics of the flow is one-dimensional (elimination of the dependence on the coordinate z).

Linearizing around this equilibrium gives

$$\partial_t \mathbf{u}_{xy} = \mathcal{L}_1 \mathbf{u}_{xy} \equiv \partial_{yy}\mathbf{u}_{xy}\,, \qquad \mathbf{u}_{xy}(z=\pm 1) = 0 \tag{1.31}$$

The linear operator $\mathcal{L}_1$ (the reasons for the introduction of the subscript 1 will be given in a moment) admits a spectrum whose eigenvectors $v_1^n(z)$ and eigenvalues λ_1^n are given by

$$v_1^n(z) = \sin(l_1^n(z+1))\,, \quad \lambda_1^n = -\left(l_1^n\right)^2 \quad \text{and} \quad l_1^n = \frac{(2n+1)\Pi}{2}\,, \quad \text{for} \quad n \in \mathbb{N}\,. \tag{1.32}$$

All eigenvalues are negative and there is no center manifold in the vicinity of the Poiseuille flow. However, there exists a large spectral gap between the first eigenvalue $\lambda_1^0 = -\pi^2/4 \approx -2.47$ and the next ones $\lambda_1^1 = -9\pi^2/4 \approx -22.2$, $\lambda_1^2 = -25\pi^2/4 \approx -61.7$. The eigenmodes are therefore rapidly damped except for the first one. One therefore expects that any perturbation around the equilibrium (Poiseuille flow) is quickly aligned with the first eigenmode. This very idea can be mathematically expressed by slightly modifying the momentum balance (1.6):

$$\begin{aligned}\partial_t \mathbf{u}_{xy} \;=\; & -\mathbf{u}_{xy}\cdot\nabla_{xy}\mathbf{u}_{xy} - w\partial_z\mathbf{u}_{xy} - \gamma^2\left(\nabla_{xy}p - \frac{1}{Fr^2}\mathbf{j}\right) \\ & + \frac{1}{Re}\left(\partial_{zz}\mathbf{u}_{xy} + (1-\gamma)\partial_z\mathbf{u}_{xy}|_{z=-1}\right)\,,\end{aligned} \tag{1.33}$$

A new parameter γ is introduced, the primitive equation being retrieved at $\gamma = 1$. In the limit $\gamma = 0$, the modified dynamical system admits an equilibrium at the origin $\mathbf{u}_{xy} = 0$ (bringing the equilibrium at the origin greatly simplifies the required algebra). The corresponding linearized dynamical system at the origin thus reads

$$\partial_t \mathbf{u}_{xy} = \mathcal{L}_0 \mathbf{u}_{xy} \equiv \frac{1}{Re} \left(\partial_{zz} \mathbf{u}_{xy} + \partial_z \mathbf{u}_{xy}|_{z=-1} \right) , \qquad \mathbf{u}_{xy}(z = \pm 1) = 0 \quad (1.34)$$

(where the subscript 0 refers to the value of γ, which also justifies the introduction of the notation $\mathcal{L}_1$ above). The operator $\mathcal{L}_0$ has a nonzero kernel:

$$v_0^0 = 1 - z^2 , \quad \lambda_0^0 = 0 . \quad (1.35)$$

The other eigenmodes of $\mathcal{L}_0$ have been numerically computed by varying γ starting from $\gamma = 1$ using the continuation software AUTO07P (Doedel 2008). The first eigenvalues are graphically depicted in figure 1.3 as functions of γ showing the gradual deformation of the spectrum of $\mathcal{L}_1$ to the spectrum of $\mathcal{L}_0$.

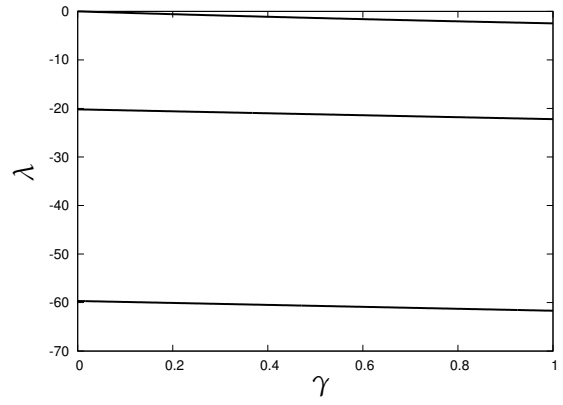

Figure 1.3 – *Discrete eigenvalues of the linear operator $\mathcal{L}_\gamma$ as function of γ*

We are then in a position to construct the slow manifold around the equilibrium at the origin ($\mathbf{u}_{xy} = 0$) with a linearized dynamics governed by $\mathcal{L}_0$ as perturbed by the small long-range spatial modulations ($\epsilon \ll 1$) and by the small adjustable terms (the dummy parameter is supposed small, i.e. $\gamma \ll 1$). A double expansion in ϵ and γ is thus introduced with the hope that the obtained series in γ have radii of convergence that are greater than 1, in which case the slow manifold tangent to v_1^0 is obtained.

The kernel of $\mathcal{L}_0$ is one-dimensional and therefore the slow manifold is a hyper-surface with an equation of the type $\mathbf{u}_{xy}(x, y, z) = \mathcal{U}(\mathbf{f}(x, y), z)$. We can then introduce the averaged velocity field $\langle \mathbf{u}_{xy} \rangle$ as a parametrization of the slow manifold, which leads to the ansatz:

$$\mathbf{u}_{xy}(x, y, z, t) = \mathbf{V}(\langle \mathbf{u}_{xy} \rangle, \gamma, z) \sim \sum_{m=0}^{1} \sum_{n=1}^{\infty} \epsilon^m \gamma^n \mathbf{V}^{m,n}(\langle \mathbf{u}_{xy} \rangle, z) . \quad (1.36)$$

The evolution in time along the slow manifold is thus given by an evolution equation for $\langle \mathbf{u}_{xy} \rangle$ that can also be expanded in powers of ϵ and γ.

$$\partial_t \langle \mathbf{u}_{xy} \rangle = \mathbf{G}(\langle \mathbf{u}_{xy} \rangle, \gamma, z) \sim \sum_{m=0}^{1} \sum_{n=1}^{\infty} \epsilon^m \gamma^n \mathbf{G}^{m,n}(\langle \mathbf{u}_{xy} \rangle, z) , \quad (1.37)$$

and which I rewrite formally as $\partial_t \mathbf{u}_{xy} = \mathcal{L}_0 \mathbf{u}_{xy} + \mathcal{N}(\mathbf{u}_{xy})$. Defining a scalar product (here again $\langle f|g\rangle = \int_{-1}^{1} f\, g dz$), and the adjoint operator $\mathcal{L}_0^\dagger$ reads

$$\mathcal{L}_0^\dagger g = \frac{1}{Re} g'' \,, \tag{1.38}$$

where the adjoint space is spanned by the integrable real functions on the interval $z \in [-1,1]$ verifying the boundary conditions

$$\int_{-1}^{1} g dz - g(-1) = 0 \qquad \text{and} \qquad g(1) = 0 \,. \tag{1.39}$$

The kernel of $\mathcal{L}_0^\dagger$ is spanned by $g_0 = 1 - z$.

Multiplying (1.27) with the scalar real function g_0, integrating across the cell thus gives the looked-after scalar compatibility condition

$$\langle \frac{\partial \mathbf{V}}{\partial \langle \mathbf{u}_{xy} \rangle} \mathbf{G} - \mathcal{N}(\mathbf{V}) | g_0 \rangle = 0 \,. \tag{1.40}$$

In practice, solving equation (1.40) gives $\mathbf{G}$ and defines the evolution along the slow manifold ($\partial_t \langle \mathbf{u}_{xy} \rangle$). The first term of the series (1.36) must belong to the kernel of the linear operator $\mathcal{L}_0$ which corresponds to a Poiseuille flow

$$\mathbf{V}^{0,1} = \frac{3}{2} \langle \mathbf{u}_{xy} \rangle (1 - z^2) \tag{1.41}$$

Equation (1.27) is solved iteratively, order after order in ϵ and γ. The shear rate at the boundary $\partial_z \mathbf{u}_{xy}|_{z=-1}$ is determined with the help of the choice of the parametrization by the averaged velocities $\langle \mathbf{u}_{xy} \rangle$ which provides the constraint $\langle \mathbf{V}^{m,n} | 1 \rangle = 2\delta_{m,1}\delta_{n,0} \langle \mathbf{u}_{xy} \rangle$ where $\delta_{i,j}$ stands for the Kronecker symbol. Since polynomials constitute a closed set with respect to products and differentiations, the terms $\mathbf{V}^{m,n}$ of the series are necessarily polynomials. One gets for instance

$$\mathbf{V}^{0,2} = \frac{1}{40}(1 - 6z^2 + 5z^4)(3\langle \mathbf{u}_{xy} \rangle + Re \nabla_{xy} p + \frac{Re}{Fr^2} \mathbf{j}) \,, \tag{1.42}$$

$$\mathbf{V}^{1,2} = \frac{3}{1400}(z^2 - 1)[11 + 35z^2(z^2 - 2)] Re \langle \mathbf{u}_{xy} \rangle \cdot \nabla_{xy} \langle \mathbf{u}_{xy} \rangle \,. \tag{1.43}$$

The convergence of the series at $\gamma = 1$ has been checked bringing an approximation of the looked-after invariant slow manifold.

Truncating (1.33) at the lowest order ϵ^0 gives an affine equation. As a consequence, the slow manifold is not different from the eigenspace spanned by the sinus function $v_1^0(z)$ which gives

$$\sum_{n=1}^{\infty} \mathbf{V}^{0,n}(\langle \mathbf{u}_{xy} \rangle, z) = \mathbf{u}_{xy}^{(0)} + \frac{l_1^0}{3} v_1^0(z) \left(3\langle \mathbf{u}_{xy} \rangle + Re \nabla_{xy} p + \frac{Re}{Fr^2} \mathbf{j} \right) \tag{1.44}$$

where $\mathbf{u}_{xy}^{(0)}$ is the Poiseuille flow defined in (1.3). (Note that $\frac{l_1^0}{2} \int_{-1}^{1} l_1 v_1^0 dz = 1$ as requested by the definition of the averaged velocity $\langle \mathbf{u}_{xy} \rangle$.) At the lowest order ϵ^0, the center manifold analysis thus reduces to a mere projection on the sine function $v_1^0(z)$ of the deviations from the Poiseuille flow solution.

At order ϵ, the dynamics along the slow manifold is given by

$$\begin{aligned}\partial_t\langle \mathbf{u}_{xy}\rangle \;\approx\; & \frac{\pi^2}{12}\left(-\nabla_{xy}p-\frac{1}{Fr^2}\mathbf{j}-\frac{3}{Re}\langle \mathbf{u}_{xy}\rangle\right)-1.346\langle \mathbf{u}_{xy}\rangle\cdot\nabla_{xy}\langle \mathbf{u}_{xy}\rangle\\ & -10^{-3}\times\Big[14.1Re\left((\langle \mathbf{u}_{xy}\rangle\cdot\nabla_{xy})\nabla_{xy}p+\nabla_{xy}p\cdot\nabla_{xy}\langle \mathbf{u}_{xy}\rangle\right)\\ & -4.90Re\nabla^2_{xy}p\langle \mathbf{u}_{xy}\rangle-0.80Re^2(\nabla_{xy}p\cdot\nabla_{xy})\nabla_{xy}p\\ & -0.18Re^2\nabla^2_{xy}p\nabla_{xy}p\Big] \end{aligned} \tag{1.45}$$

Coefficient $\pi^2/12\approx 0.822$ is dictated by the first eigenvalue $\lambda_1^0=-\pi^2/4$. Equation (1.45) should be contrasted to (1.14) which reads

$$\partial_t\langle \mathbf{u}_{xy}\rangle\approx 0.833\left(-\nabla_{xy}p-\frac{1}{Fr^2}\mathbf{j}-\frac{3}{Re}\langle \mathbf{u}_{xy}\rangle\right)-1.286\langle \mathbf{u}_{xy}\rangle\cdot\nabla_{xy}\langle \mathbf{u}_{xy}\rangle \tag{1.46}$$

The most important terms, namely the advection by the flow and the viscous drag appear with very close coefficients (0.822 as compared to 0.833 and 1.346 as compared to 1.286). The difference between the two equations lies in the inertia terms in the second to fourth lines of (1.45). All these terms are associated to small coefficients and should not influence significantly the result. (This is still to be verified though.)

I conclude that the center manifold approach leads to a result that is in fact very similar to the gradient expansion approach. Yet (1.45) contains complex terms that are not present in (1.14), and, though I suspect that the two equations should bring close results, the former is much more difficult to handle than the latter.

The closeness of the coefficients in the two averaged equations results from the closeness of the Poiseuille parabolic velocity profile $f_0=1-z^2$ and of the sine first eigenmode $v_1^0=\sin(\pi(z+1)/2)$ tangent to the slow manifold. Indeed the ratio of the coefficients of the viscous drag terms in the two averaged equation corresponds to

$$\frac{\langle f_0|v_1^0\rangle}{\langle f_0|f_0\rangle}=\frac{\pi^2/12}{5/6}\approx 1.013\,. \tag{1.47}$$

The normalized Poiseuille parabolic profile and the first sine eigenmode are compared in figure 1.4.

The unexpected agreement between the weighted residual approach and the center manifold analysis is fortunate. However, as compared to the former, the latter does not bring a "better" result. In other words, equation (1.45) cannot be assumed to behave any better than (1.14) when the long-time assumption ($\partial_t\sim\epsilon$) holds.

Indeed, the center manifold analysis relies on the assumption of a dynamics that is essentially governed by the first viscous relaxation mode. This assumption cannot hold at times that are much longer than the viscous time $t_\nu=h^2/\nu$, all viscous modes having relaxed to the Poiseuille equilibrium. In other words, the assumption of small perturbations of the advection terms on the first viscous eigenmode is unacceptable at $t\gg t_\nu$. The dynamics of the flow is then governed by inertia which perturbs this equilibrium (the mathematical transposition of this very idea is the decomposition (1.9)).

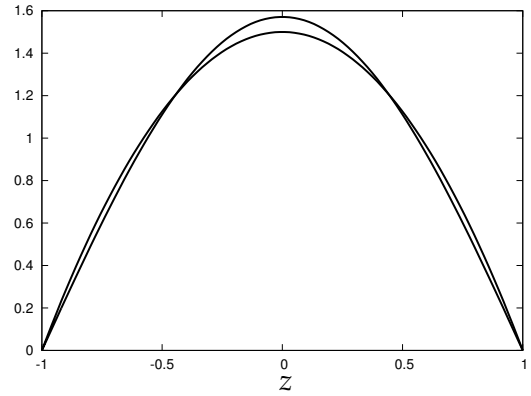

Figure 1.4 – *Comparison of the normalized first sine eigenmode* $v_1^0/\langle v_1^0|1\rangle$ *with the normalized parabola* $f_0/\langle f_0|1\rangle$.

Stated still otherwise, the approach of the Poiseuille equilibrium flow along the first viscous relaxation mode is meaningful only when the inertial time, $t_a = L/U$ gets close to the viscous time t_ν. Yet, $t_a = O(t_\nu)$ yields $\epsilon Re = O(1)$ so that inertia and viscous diffusion have the same order of magnitude and the whole idea of small perturbations induced by long spatial modulations becomes meaningless.

Some remarks

In this chapter, I have considered a laminar flow in a Hele-Shaw cell and and the consistent extension (1.14) of the classical Darcy law (1.1) to account for inertia effects.

Because of its straightforwardness for this specific problem, I have described at length the methodology that I have developed and applied on long-wave instabilities (falling film flows essentially). The methodology relies on the assumption of slow evolutions in time and space ($\partial_t = O(\epsilon)$ and $\partial_{x,y} = O(\epsilon)$ which enables to eliminate the dependence on the 'fast' variable (here the normal coordinate z). I have tried to be as clear as possible in order to help interested readers to apply this method to other (more difficult) problems. For that purpose, the presentation of the approach is here limited to a required consistency at $O(\epsilon)$ only. However, extension to second order is possible (and was the subject of a short paper I wrote and which was rejected for publication in *Phys. Fluids* as "uninteresting".)

The approach combines a gradient expansion (§ 1.1) —lubrication theory— to the classical methods of weighted residuals (§ 1.2). A proper choice of the weight functions enables to dramatically reduce the necessary algebra and, in the present case, the Galerkin method is the most straightforward method. (This is not always the case though.) In the next chapters, I shall not go to that level of description of the methodology any more. A thorough description of the gradient expansion and weighted residual approach in the context of falling film flows can be found in the chapters 5 and 6 of the monograph by *Kalliadasis et al. (2012)*.

The weighted residual approach is compared to the center manifold analysis developed by A.J. Roberts, where the evolution of the flow is con-

sidered to be driven by the first viscous relaxation mode. Fortunately, the two approaches bring very similar results, which is a consequence of the closeness of the Poiseuille flow and the sine eigenfunction of the viscous relaxation mode with the largest eigenvalue. This demonstrates that the assumption of slow time evolution ($\partial_t = O(\epsilon)$) is not very stringent. However, the center manifold analysis cannot be said to be any "better" than the weighted residual method. As stressed in § 1.3, the two approaches should bring noticeably different results only when $\epsilon Re = O(1)$, in which case the long-wave approximation of small spatial modulations is no more sustainable anyway.

Finally, the usefulness of a low-dimensional modeling strategy can be measured not only by the accuracy of the results it yields, but also by the straightforwardness of its application and the simplicity of the models it brings. The weighted residual approach is much more straightforward than the center manifold analysis, which always requires the help of symbolic mathematics and computer algebra software. The former approach also brings more manageable systems of equations than the latter. As a matter of fact, the center manifold analysis does not seem to have been much employed by the thin film community, A.J. Roberts and his group apart. The weighted residual approach has somewhat more diffused, being used for instance by Amaouche and coworkers in Algeria (Amaouche et al. 2004; 2009; 2012), by J.-P. Pascal and his group in Canada (D'Alesio et al. 2010) , Häcker and Uecker in Germany (Haecker and Uecker 2009) and recently by Alba et al. (2011) (Canada and France).

Kapitza instability of a falling liquid film

2

After my arrival at FAST, I have gone on working on the problem of a falling film on an inclined plane with Paul Manneville and later on with Benoit Scheid and Serafim Kalliadasis. This chapter is an attempt to summarize my work with them, to put it in perspective and to address the challenges and numerous issues that still require answers. Most of the material presented in this chapter is detailed in the chapters 5, 6 and 7 of a recent monograph (Kalliadasis et al. 2012). However, I have endeavored to update the presentation of the phenomenology (§ 2.1) and of the different low-dimensional modeling attempts (§ 2.3). Methodologies have been introduced and detailed in chapter 1 on the more simpler (but not less interesting) problem of the modeling of a flow in a Hele-Shaw cell. They are simply sketched in this chapter.

2.1 Phenomenology

Several experimental studies have been devoted to the wavy regime of film flows since the seminal work by Kapitza (1948) and Kapitza and Kapitza (1949). They have been reviewed by Alekseenko et al. (1994), Chang et al. (1994), Chang and Demekhin (2002) and more recently by Craster and Matar (2009) and *Kalliadasis et al. (2012)*. Gollub and coworkers have performed an extensive study of water-glycerin mixtures flowing down weakly inclined planes, see Liu et al. (1993), Liu and Gollub (1993; 1994), Liu et al. (1995). The relatively small inclination of the plane had several advantages: (i) for a given flow rate, the film is thicker and moves more slowly. As a consequence, the waves are more easily detectable. (ii) On an inclined plane, the film primary instability presents a threshold $Fr^{-2} = \cot\beta/(3Re) = 2/5$ (Benjamin 1961), which enables to control easily the wave regime by varying the distance of the control parameter to the threshold (either Reynolds or Froude number). In any case, the wave dynamics reported by Liu and Gollub does not seem to present significantly different features from what is observed on a vertical wall by e.g. Alekseenko et al. (1985; 2005).

Controlling the entrance flow rate, Liu and Gollub applied a periodic forcing at the inlet and observed the response of the film at given frequency. Their experiments give the clearest picture of the phenomenology of interacting waves on film flows (see figure 2.1). Four stages corresponding each to a different region on the plane can be identified by following

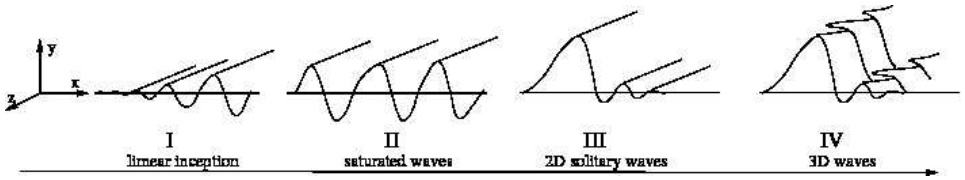

(a) *low frequency*

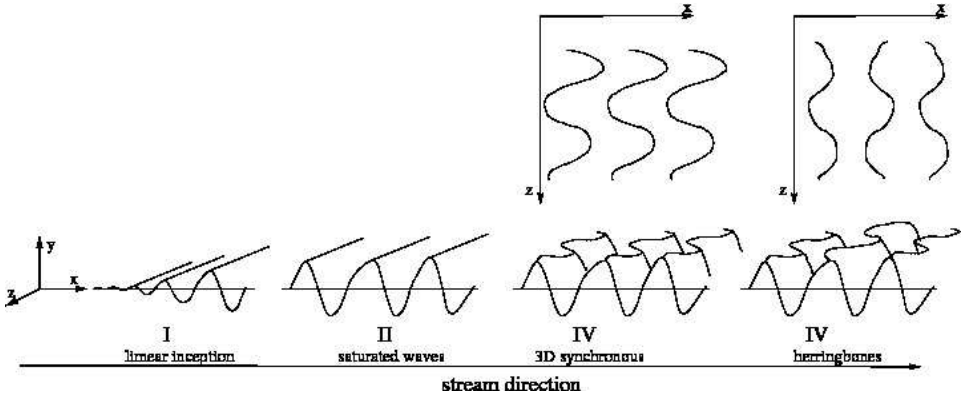

(b) *high frequency*

Figure 2.1 – *Phenomenological sketch of the spatial evolution of film flows, after Chang et al. (1994), Liu et al. (1995), reproduced from Kalliadasis et al. (2012)*

the flow along the inclined plane.These four stages correspond to the same number of symmetry breaking, or bifurcations, all new solutions branching from the previous ones supercritcally The inception region is the domain close to the inlet where the primary linear instability of the flat film develops in space. Squire's theorem stipulating that the most dangerous perturbations are spanwise-independent has been shown to apply to free surface flows by Yih (1955), which theoretically backs the fact that observed primary waves are two-dimensional (2D).

The amplitude of the waves next saturates and their shape remains unchanged over distances corresponding to a few wavelengths (Region II). These waves are slow and present wide bumpy crests and deep thin troughs. They belong to the γ_1 family in the terminology introduced by Chang et al. (1993a). The rest of the story depends on the forcing frequency f as compared to the cut-off frequency $f_c$and the frequency f_m of maximum spatial growth rate.

At low frequency, $f_c/2 \lessapprox f \ll f_c$, (figure 2.1, top) the slow γ_1 waves experience a secondary instability which, close to the threshold, remains 2D ending in large amplitude solitary waves in the form of fast humps preceded by small capillary ripples (Region III). Such waves belong to the γ_2 family. They are generally unstable against transverse perturbations which leads to the last stage of secondary three-dimensional instabilities (Region IV). Figure 2.2 displays an example of modulated γ_2 waves.

At larger frequencies, $f_c/2 \ll f \lessapprox f_c$, (figure 2.1, bottom), the slow γ_1 2D waves undergo a secondary 3D instability. Liu *et al.* reported two different scenarios that are strongly reminiscent of what happens in boundary layers (Schmid and Henningson 2001). The first one, referred to as a *synchronous* mode, is characterized by wave crests deformed in phase

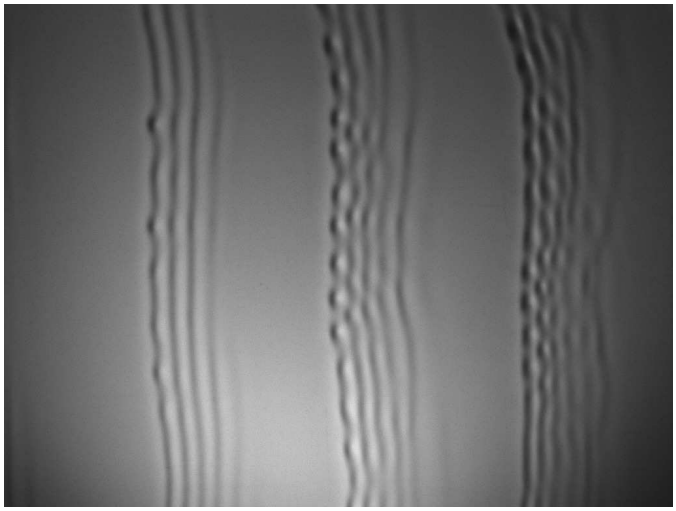

Figure 2.2 – *Secondary 3D instability of a fast γ_2 wavetrain. $Re = 70$, $\beta = 5^\circ$ ($Re/Re_c = 7.4$), $f = 3.1$ Hz, $\Gamma = 4978$. Aqueous solution of butanol, 1.0 % by weight, at 19.4° C. The real size of the image is 29.4×22.0 cm. Courtesy of Nicolas Kofman and Sophie Mergui.*

in the spanwise direction. The second one, less commonly observed, appears when two successive crests are deformed with a phase shift of π. This leads to checkerboard (or herringbone) patterns characteristic of a streamwise subharmonic instability combined to a spanwise modulation. At high enough forcing frequency, the flow becomes disordered before the 2D solitary waves have a chance to appear because 3D instabilities are stronger than the 2D mode, which explains the absence of Region III in the corresponding picture. Both 3D secondary instability modes of the slow γ_1 waves generate modulations of the troughs of the waves. The modulations tend to form trains of isolated depressions which detached from the back of the γ_1 waves and interact with the next γ_1 front (cf. figure 2.3). At the end of the process, γ_1 slow wavetrains are removed and replaced with γ_2 quasi-2D waves that are strongly modulated and disordered in the transverse direction.

Finally, at very low forcing frequencies, $f_m \lessapprox f < f_c/2$, saturated γ_1 waves(Region II) do not show up while solitary waves of the γ_2 family emerge directly. At still lower frequency, $f \ll f_m$, the film does not respond any more to the inlet forcing and the film dynamics is said to be natural, that is triggered by the ambient noise which is sufficient to generate the wavy regime of the film.

When the wall is vertical, Liu and Gollub's portrait of successive primary and secondary 2D and 3D instabilities is somewhat more difficult to discern even in the presence of inlet forcing. Indeed, hydrostatic pressure stabilizing mechanism is absent and the Kapitza instability is always triggered. Because at low flow rates, waves have an amplitude that is nearly unnoticeable (which thus wrongly induced Kapitza to think that the instability presented a threshold (Kapitza and Kapitza 1949)), experiments are conducted at Reynolds numbers equal to a few decades at least, a situation that is already far from threshold ($Re = 0$). The experiments of Park and Nosoko (2003), consisting of water films running down a vertical wall,

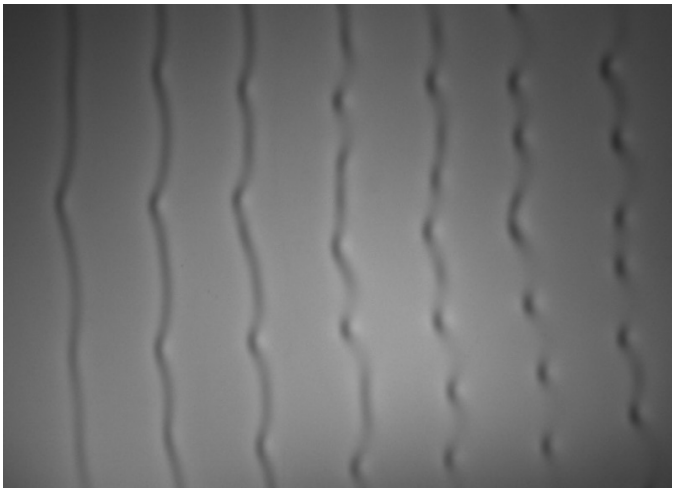

Figure 2.3 – *Secondary 3D instability of a slow γ_1 wavetrain. $Re = 70$, $\beta = 5^\circ$ ($Re/Re_c = 7.4$), $f = 8.7$ Hz, $\Gamma = 2239$. Aqueous solution of glycerin, 29.1 % by weight, at 19.3° C. The real size of the image is 23.7×17.1 cm. Courtesy of Nicolas Kofman and Sophie Mergui.*

give a detailed account of the 3D instability of the quasi-solitary fast γ_2 waves. Park and Nosoko generate controlled perturbations in the transverse direction by means of regularly dispatched needles. They observe two types of structures. At low Reynolds number quasi-2D fronts presenting rugged modulations (cf. figure 2.4), made of nearly flat backs and rounded fronts, are observed. At higher Reynolds number, they reported arrays of quasi-3D solitary waves presenting a horseshoe-like shape (see figure 2.5).

In the absence of inlet forcing, the observed flow pattern is very noisy as the primary instability of the flow is always convective (Brevdo et al. 1999) and amplifies all frequencies below the cut-off frequency f_c. Noise driven falling films are thus an example of active, dissipative and dispersive non-linear media displaying the onset of spatio-temporal disordered chaos, characterized by particle-like structures in interaction, a state referred to as *weak turbulence* by Manneville (1990). The instability (activity) of the film promotes structures (either slow γ_1 or fast γ_2 waves) which result from the balance of inertia, non-linearity and surface tension, the latter being the dissipative (or damping) mechanism which enables to turn back to the primary flow at short length scale, the energy supplied by the Kapitza instability at long length scale and transferred from short to long scales by the nonlinearities. The essential role of dissipation —again, dissipation is here synonymous to surface tension— explains the christening *dissipative structures* that has been introduced by Paul Manneville (though it was in the context of Rayleigh–Bénard convection) (Manneville 1990).

It is useful to stress that the spatio-temporal disordered state that characterizes the noise-driven evolution of the film is in fact always observed even if a well-controlled signal applied at inlet is able to synchronize the flow at the forcing frequency f. The synchronization of the wave pattern is always lost at some distance sufficiently far from the inlet, leading way to a disordered state organized around quasi-2D solitary waves presenting noisy modulations, or 3D horseshoe-like solitary waves in interaction. For

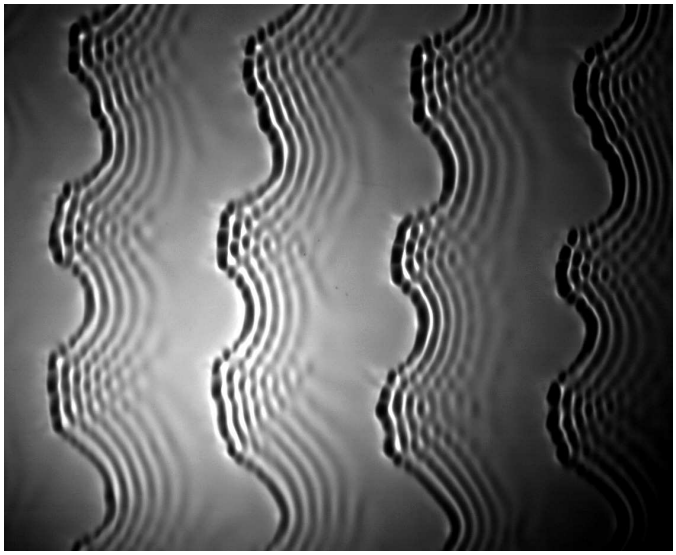

Figure 2.4 – *Quasi-2D fronts presenting rugged modulations.* $Re = 70$, $\beta = 17.9°$ ($Re/Re_c = 260$), $f = 7.5$ *Hz*, $\Gamma = 4962$. *Water at* 20.3° *C* , 1.0 % *by weight. Courtesy of Nicolas Kofman and Sophie Mergui.*

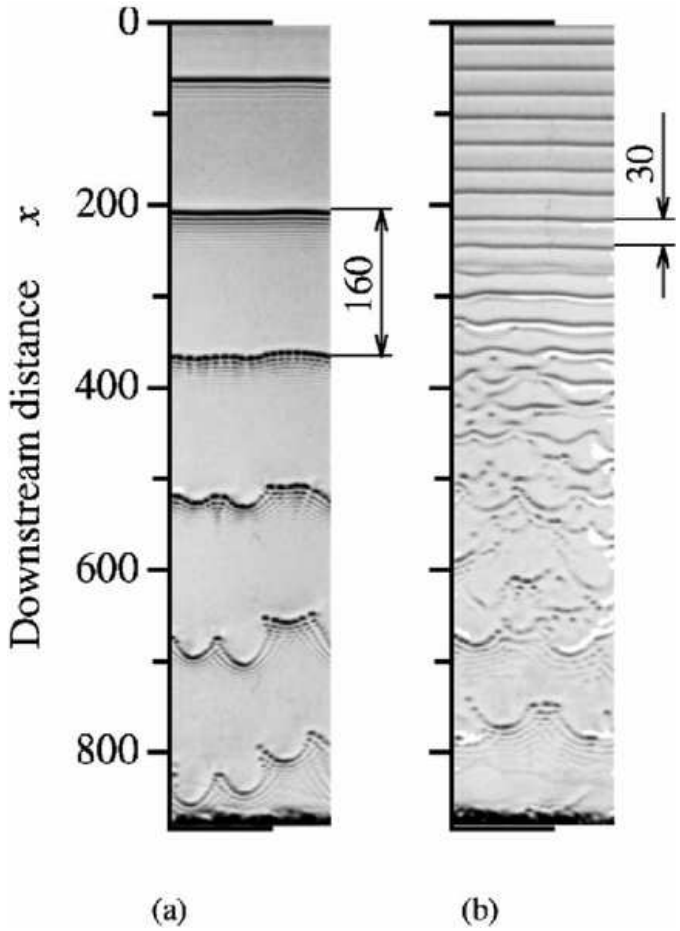

Figure 2.5 – *Wave patterns on a water film at* 23° *C running down a vertical plane; (a) forcing at* $f = 13$ *Hz and (b)* $f = 45$ *Hz.* $Re = 69$, $\rho = 994.3$ *kg*/m^3, $\nu = 0.93 \times 10^{-6}$ m^2/*s*, $\sigma = 69$ *mN/m* ($\Gamma = 3650$). *Reproduced from Miyara (2000), Nosoko et al. (1996).*

instance, the regularity of the 2D solitary waves that are generated by the inlet forcing in the experiment by Nosoko reported in figure2.5 is rapidly lost through secondary instability leading way to 3D horseshoe-like waves whose pattern is not different from the one triggered by the excitation of the ambient noise.

The selection between a pattern made of noisy quasi-2D solitary waves, and a gas of 3D horseshoe-like waves seems to strongly depend on the inclination angle, or perhaps more adequately on the distance Re/Re_c to the threshold. The former quasi-2D disordered state has been observed by Liu et al. (1995) for a moderately inclined plane, whereas the later, organized around isolated 3D structures, and sometimes referred to as "surface turbulence" has been reported in film flows over vertical walls (Tailby and Portalski 1960, Demekhin et al. 2007a;b).

2.2 Geometry and parameters

Let us consider the flow of a Newtonian liquid down a plane making an angle β with the horizontal. Coordinate x defines the streamwise direction, y denotes the direction normal to the plane, and z is along the spanwise direction. $u \equiv u\mathbf{i} + v\mathbf{j} + w\mathbf{k}$ is the velocity field, p is the pressure and $\mathbf{i}$, $\mathbf{j}$ and $\mathbf{k}$ are the unit vectors. Surface tension σ, viscosity μ, and density ρ, are assumed to remain constant. $\nu = \mu/\rho$ is the kinematic viscosity, and g refers to the gravity acceleration.

Two reference length scales can be defined by balancing viscosity, surface tension and the streamwise gravity acceleration $g\sin\beta$, the capillary length $l_c = \sqrt{\sigma/(\rho g \sin\beta)}$, and $l_\nu = \nu^{2/3}(g\sin\beta)^{-1/3}$ referred hereinater as the viscous-gravity scale. A first set of pertinent dimensionless groups arises from these scales and the thickness $\bar{h}_\mathrm{N}$ of the Nusselt flat-film solution, namely the dimensionless thickness $h_\mathrm{N} = \bar{h}_\mathrm{N}/l_\nu$ and the Kapitza number $\Gamma = (l_c/l_\nu)^2$ completed with the inclination anagle β. The dimensionless thickness h_N is related to the Reynolds number, defined as the ratio of the inlet flow rate per unit length $\bar{q}_\mathrm{N}$ and the kinematic viscosity, through $Re = \bar{q}_\mathrm{N}/\nu = h_\mathrm{N}^3/3$. The advantage of the set of parameters Re, Γ and β is that when the geometry and the working fluid are fixed, the inclination angle β and the Kapitza number Γ are constant and the only free control parameter is the Reynolds number Re.

The Kapitza number compares the capillary length, that is the length below which surface tension is effective on the gravity-driven flow, and the viscous gravity length, below which viscosity becomes also effective. As a consequence, at large Kapitza numbers, short waves are efficiently damped by surface tension before the elongational, or streamwise viscosity, may act. In practice, usual fluids such as water or alcohol correspond to high Kapitza numbers. Neglecting the damping action of the elongational viscosity on the waves —an effect that is dispersive and can be referred to as viscous dispersion— at high Kapitza numbers, the set of parametrs should be reduced from three to only two by a rescaling. This idea was introduced by Shkadov (1977) who made apparent the separation of scales in the streamwise and spanwise directions with respect to the cross-stream one by introducing a scaling ratio κ that is adjusted by

balancing the gravitational acceleration $\rho g \sin\beta$ with the capillary pressure gradient $\propto \sigma \partial_{xxx} h$ which gives $\kappa = [\sigma/(\rho g \sin\beta \bar{h}_{\mathrm{N}}^2)]^{1/3} = (l_c/\bar{h}_{\mathrm{N}})^{2/3}$. The length scale in the cross-stream direction is thus the Nusselt thickness $\bar{h}_{\mathrm{N}}$, whereas the length scale in the streamwise and spanwise directions is chosen as $\kappa \bar{h}_{\mathrm{N}}$.

Shkadov's scales introduce three new dimensionless groups: a 'reduced Reynolds number' (Chang 1994),

$$\delta \equiv 3Re/\kappa \tag{2.1a}$$

which compares inertia and the viscous drag at the scale $\kappa \bar{h}_{\mathrm{N}}$ introduced by the balance of gravity and capillarity, a streamwise 'viscous dispersion parameter',

$$\eta \equiv 1/\kappa^2 = (\bar{h}_{\mathrm{N}}/l_c)^{4/3} \tag{2.1b}$$

and a reduced slope

$$\zeta = \cot\beta/\kappa \tag{2.1c}$$

Shkadov's approximation of neglecting the damping of the waves by viscosity corresponds to setting η to zero, in which case one is left with only two parameters. It is also seful to introduce the Froude number $Fr^2 = 3Re/\cot\beta = \delta/\zeta$ ad the threshold of the primary instability corresponds to a constant value of the Froude number $Fr_c^2 = 5/2$ (Benjamin 1961, Kalliadasis et al. 2012).

2.3 Low dimensional modeling

The Kapitza instability of a falling liquid film is a long-wave instability, i.e. the linear instability threshold corresponds to a zero wavenumber and frequency. This peculiarity introduces a separation of scales between the cross-stream y coordinate and the in-plane coordinates (x and z) similar to the one we have encountered in chapter 1 in the context of the modeling of a flow in a Hele-Shaw cell.

This separation of scales is expressed by the introduction of a *film parameter* $\epsilon \sim \partial_{x,z,t}$. In the linear regime, it is easily related to the wavenumber k of an infinitesimal harmonic perturbation as $\epsilon \sim kh/(2\pi)$. When the wave is nonlinear, the film parameter is a measure of the local slope of the film elevation $\epsilon \sim |\partial_x h|$ which can vary significantly along the wave. As a consequence, it is generally difficult to give a value to ϵ and we think of it a s a *formal* parameter which expresses an ordering in terms of the derivatives in space and time.

Every modeling strategy applied to falling liquid film flows is based on the assumption of a separation of scales with the aim at an elimination of the dependence on the 'fast' cross-stream variable y. Low-dimensional models thus consist in sets of evolution equations for carefully chosen variables, or *degrees of freedom*, which characterize locally the flow at a given location on the (x,z) plane. The in-depth coherence of the flow, which is ensured by the viscosity of the fluid, enables to turn from a flow description in terms of the motion of fluid particles of infinitesimal size at any location in the fluid, to a description in terms of the motion of an entire fluid column of infinitesimal cross-section which extends from the wall to the upper interface.

In the remainder of this section, the different modeling strategies are presented and discussed for spanwise-independent two-dimensional flows ($\partial_z = 0$, $w = 0$), their extension to three-dimensional flows being generally straightforward.

2.3.1 Gradient expansion: the long-wave theory

The gradient expansion approach —or long-wave expansion in the context of falling films— was first applied by Benney (1966) who derived an evolution equation for the film thickness h. Considering slow evolutions in time en space $\partial_{x,t} \sim \epsilon$, Benney introduced an expansion of the flow variables (velocity field and pressure) with respect to the film parameter ϵ. Benney showed that the velocity field u can be written as a series of polynomials in y, *i.e.* $u = \sum_n A_n(h) P_n(\bar{y})$, where $\bar{y} = y/h(x,t)$ is a reduced normal coordinate, and the coefficients A_n are functions of the thickness h and its space-time derivatives, meaning that, in this limit, the velocity field is completely enslaved to the dynamics of h. The film elevation h is thus the sole degree of freedom retained by the long-wave theory. Benney's work was followed by several others (Lin 1974, Nakaya 1975, Roskes 1970, Gjevik 1970; 1971, Panga and Balakotaiah 2003; 2005) which mostly differ one from the other by their degree of consistency, the order of magnitude of the surface tension or viscous terms and the 2D or 3D nature of the flow. In all cases, an evolution equation for the film thickness h is obtained which can be recast in the form

$$\partial_t h + \partial_x q = 0\,, \tag{2.2a}$$

$$q = \mathcal{Q}(h)\,, \tag{2.2b}$$

where $\mathcal{Q}(h)$ is a function of the film thickness and its derivatives. Equation (2.2a) is the (exact) mass balance of a liquid column obtained after the integration of the continuity equation over the film thickness (for details see for instance Ruyer-Quil and Manneville (1998)). This equation is equivalent to the kinematic boundary condition stated that the interface is a material line, and relates the mass (h) of a liquid column to the flux of liquid $q = \int_0^h u dy$ entering that column. For that reason, (2.2) is the generic format of *kinematic wave equations* (Whitham 1974).

The so-called Benney equation (Gjevik 1970; 1971)

$$\partial_t h + \frac{1}{3}\partial_x \left\{ h^3 + \frac{2}{15}\delta h^6 \partial_x h - \zeta h^3 \partial_x h + h^3 \partial_{xxx} h \right\} = 0\,. \tag{2.3}$$

is the prototype of the evolution equations for the film height h, or *surface equation*, that have been derived within the long-wave gradient expansion. This equation is consistent at first order, meaning that all dropped-out terms are of $O(\epsilon^2)$ or higher. The Benney equation (BE) is well known for the singular behavior of its solutions when the reduced Reynolds number δ becomes large enough. Pumir et al. (1983) showed that the finite-time blow-up of time-dependent solutions closely corresponds to the loss of one-hump solitary waves, *i.e. homoclinic* orbits in the terminology of the dynamical systems theory. The occurrence of the finite-time blow-ups of the time-dependent solutions depend on the flow conditions and especially on the range of frequencies of the inlet excitation *(Scheid et al. 2005b)*.

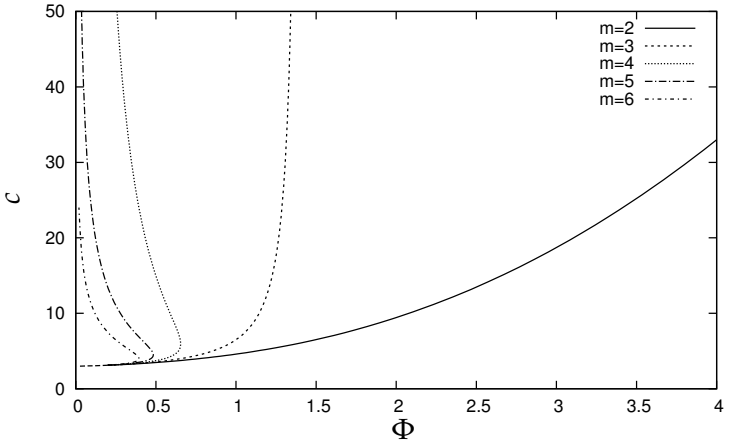

Figure 2.6 – *Branches of single-hump solutions to (2.4) in the plane speed c versus parameter Φ for different values of the index m*

However, it is clear that the Benney equation becomes useless when δ is above a few units.

The occurrence of spurious finite-time blow-up is a direct consequence of the high-nonlinearities that are contained in (2.3) and especially in the inertial term $\partial_x(\delta h^6 \partial_x h)$. In fact, (2.3) is a specific case of a general evolution euation of the form

$$\partial_t h + \partial_x \left(h^3 + \Phi\, h^m \partial_x h + h^3 \partial_{xxx} h \right) = 0 \,, \tag{2.4}$$

where m is a positive integer and Φ a positive parameter. Figure 2.6 shows that the solitary-wave branch exhibits a turning point, say at $\Phi = \Phi^\star$, and branch multiplicity (with two branches, a lower branch and an upper one) for $m > 3$. It means that for $\Phi > \Phi^\star$, (2.4) does not allow for solitary wave solutions. Numerical evidence suggests that the deviant finite blow-up behavior of BE occurs in the region where solitary waves do not exist. Bertozzi and Pugh (1998) showed that nonlinearities with powers $m < 5$ can allow for bounded solutions under certain conditions. With $m = 2$, (2.4) is encountered when the thermocapillary instability of a thin film is considered [equation (3.18) and chapter 3]. This equation admits solitary-wave solutions for all values of Φ and time-dependent simulations do not present any unphyscial finite-time blow-up beavior.

With $m = 3$, equation (2.4) is equivalent to the Frenkel equation (4.12) and applies to the problem of thin film flowing down a vertical fiber (Frenkel 1992, Kalliadasis and Chang 1994) (see. chapter 4). The solitary-wave branch of solution presents a limiting point $\Phi^\star \approx 1.4$ which is pushed to infinity ($c \to \infty$). Numerical simulations at $m = 3$ do show an accelerated growth of the amplitude of solitary waves that was associated with the drop-formation process on the film (Kalliadasis and Chang 1994, Chang and Demekhin 1999), but not a true finite-time blow-up.

Unfortunately, raising the consistency of the models does not improve the situation as the order of the nonlinearities also rapidly increases. In their study of the second-order Benney equation, Oron and Gottlieb (2004) even found the occurrence of a spurious subcritical Hopf bifurcation ! The gradient expansion has poor convergence properties indeed.

A brilliant attempt to remedy to the drawbacks of the Benney expansion has been proposed by Ooshida (1999). His approach is inspired from the use of Padé approximant technique to improve the radius of convergence of a power series $Q = \sum_k Q_k x^k$ by expressing Q as a ratio F/G of two series F and G where the zeros of G are supposed to capture the causes of the divergence. Adjusting the coefficients introduced in $F = F_0 + F_1 x + F_2 x^2 \dots$ and $G = 1 + G_1 x + G_2 x^2 + \dots$ so that the terms in the series Q are reproduced exactly up to some given degree is the essence of the approximation, the ratio F/G being used in place of Q. Ooshida translated this idea by introducing a regularization operator $\mathcal{G} = \mathcal{I} + \mathcal{G}^{(1)} + \mathcal{G}^{(2)}$, where $\mathcal{I}$ is the identity, $\mathcal{G}^{(1)} = G^{(1)}(h)\partial_x$, and $\mathcal{G}^{(2)} = G^{(2)}(h)\partial_{xx}$, so that the expansion of q as a function of h and its derivatives from the long wave expansion, formally written as $q \equiv \mathcal{Q}(h)$, is rewritten as $\mathcal{G}^{-1}\mathcal{F}$. He obtained

$$\partial_t h + \frac{1}{3}\partial_x \left\{ h^3 - 3\eta\, h^2 \partial_{xt} h - \frac{2}{7}\delta\, \partial_t(h^5) - \frac{36}{245}\delta \partial_x(h^7) - \frac{1}{4}\zeta \partial_x(h^4) + h^3 \partial_{xxx} h \right\} = 0\,, \tag{2.5}$$

which is consistent up to $O(\epsilon^2)$. No loss of the one-humped solitary wave branch of solutions to (2.5) can be found and time-dependent computations do not lead to spurious finite-time blow-ups. However, Ooshida's regularization of Benney's long-wave expansion is not sufficient to obtain quantitative agreement with experiments and DNS results. As already recognized by Ooshida (1999), the amplitudes of solitary waves are indeed grossly underestimated by (2.5).

The Ooshida equation (2.5) allows for some flexibility in the slaving of the velocity field to the kinematics of the free surface by introducing time derivatives in the expression of the flow rate $q = \mathcal{Q}(h)$. This gives the idea that some freedom should be given back to the velocity field. As a matter of fact, the Benney long-wave approach is now practically abandoned and there is now a widespread agreement that low-dimensional modeling of film flows should be based on two or more degrees of freedom and other variables than the film thickness must be considered, *e.g.* the local flow rate q, the stress at the wall, *etc.*

Since the mass balance (2.2a) is *exact*, a natural step forward is to construct two-equation models for the film thickness h and the flow rate q. This can be introduced by the decomposition

$$u = u^{(0)} + u^{(1)}\,, \tag{2.6a}$$

$$u^{(0)} \equiv \frac{3q}{h}\left(\bar{y} - \frac{1}{2}\bar{y}^2\right) \qquad \text{with} \qquad \bar{y} = y/h\,, \tag{2.6b}$$

$u^{(1)}$ stands for the $O(\epsilon)$ corrections to the parabolic profile $u^{(0)}$. The Nusselt flat film solution is recovered when $u^{(1)} = 0$ and $q = h^3/3$. Notice that $u^{(0)}$ therefore also contains $O(\epsilon)$ deviations from the Nusselt flow by allowing q to differ from $h^3/3$, thus relaxing the strict slaving of the velocity field to the film thickness in the long-wave limit $\partial_x \to 0$. The definition of the flow rate $q = \int_0^h u dy$ is retained and yields a *gauge condition* $\int_0^h u^{(1)} dy = 0$ which singles out the decomposition (2.6) among all possible ones. Inserting the ansatz (2.6) into the streamwise momentum balance truncated at $O(\epsilon)$ yields after integration

$u^{(1)} = U^{(1)}(q(x,t), h(x,t), \bar{y}) + O(\epsilon^2)$ as a polynomial in $\bar{y}$ of degree six plus second order terms. The gauge condition $\int_0^h U^{(1)} dy = 0$ then gives

$$\delta\, \partial_t q = \frac{5}{6} h - \frac{5}{2}\frac{q}{h^2} + \delta \left[\frac{9}{7}\frac{q^2}{h^2}\partial_x h - \frac{17}{7}\frac{q}{h}\partial_x q \right] - \frac{5}{6}\zeta h \partial_x h + \frac{5}{6} h \partial_{xxx} h \qquad (2.7)$$

which is an averaged momentum equation consistent at $O(\epsilon)$. Coupled with the mass balance (2.2a), (2.7) constitutes an alternative to the Benney equation (2.3) which does not present spurious blow-up behaviors. The consistency at first order ensures that the instability threshold $Fr^{-2} = \zeta/\delta = 2/5$ is correctly recovered. This procedure can be repeated at the next orders to determine $u^{(1)} = \sum_n U^{(n)}(q(x,t), h(x,t), \bar{y})$. Finally, let us emphasize that (2.7) being derived within the long-wave approximation, the flow rate remains formally slaved to the film thickness as $q = h^3/3 + O(\epsilon)$. Making use of this zeroth order equivalence in (2.7) thus immediately leads back to the Benney equation (2.3).

2.3.2 Weighted residual methods

During my PhD thesis under the supervision of Paul Manneville, I have applied the weighted residual methods (WRMs) to obtain consistent models at $O(\epsilon)$ and $O(\epsilon^2)$. Weighted residual methods are presented in § 1.2.

The velocity field is expanded on $N+1$ polynomial test functions (Ruyer-Quil and Manneville 2000).

$$\begin{aligned} u(x,y,t) &= \tilde{u}^{(0)} + \tilde{u}^{(1)} = \sum_{j=0}^{N} a_j(x,t) g_j(\bar{y}) \qquad \text{with} \quad \bar{y} = y/h(x,t) \\ a_0 &= O(1) \quad \text{and} \quad a_j = O(\epsilon) \quad \text{for} \quad j > 0 \end{aligned} \qquad (2.8)$$

The choice of polynomial test functions is motivated by the fact that the Benney expansion leads to a representation of the velocity field as a sum of polynomials. The first term of this expansion is necessarily $g_0(\bar{y}) = \bar{y} - \frac{1}{2}\bar{y}^2$, the flat film parabolic velocity profile so that a_0 is an order one quantity and the a_j, $j > 0$ are small corrections induced by the deformations of the free surface. A Galerkin projection follows for which the weights w_j are chosen equal to the test functions g_j. Writing formally the streamwise momentum balance as $BL(u) = 0$, the residuals read $\mathcal{R}_i(u) = \langle BL(u) | g_i(\bar{y}) \rangle$, where $\langle f | g \rangle = \int_0^h f\, g \, \mathrm{d}y$ refers to the scalar product.

Derivation at $O(\epsilon)$

Truncated at first order, the first residual $\mathcal{R}_0(u)$ readily yields an $O(\epsilon)$ evolution equation for a_0. Substituting the flow rate q for a_0 using its definition $q = \int_0^h u dy$, so that

$$a_0 = 3q/h - \sum_{j=1}^{N} a_j \int_0^1 g_j d\bar{y} \qquad (2.9)$$

next leads to the averaged momentum equation (2.7). Indeed, assuming that the velocity field can be projected on a series of polynomials (which

is asymptotically true), the ansatz (2.8) is equivalent to (2.6) provided the relation (2.9) holds. As detailed in § 1.2, substituting (2.6) for (2.8) and computing $\mathcal{R}_0$, the only place where the corrections $u^{(1)}$ are involved is the viscous drag term. This term can be dropped out using the gauge condition $\langle u^{(1)} dy|1\rangle = 0$ if the weight $w(y)$ verifies

$$\mathcal{L}^\dagger w = cst \tag{2.10}$$

where $\mathcal{L} = \partial_{yy}$ and $\mathcal{L}^\dagger$ is the adjoint operator. One readily gets $w = g_0$ which justifies that the Galerkin method is the most appropriate. It can be shown indeed that, if the number $N+1$ of test functions is sufficiently large ($N \geq 4$), every weighted residual method yields (2.7) (Ruyer-Quil and Manneville 2002). Thus selecting $w_0 = g_0$, the derivation of (2.7) does not necessitate the determination of the first order corrections $u^{(1)}$ as realized by Amaouche et al. (2009), Luchini and Charru (2010a;b).

Derivation at $O(\epsilon^2)$

First-order corrections to the parabolic velocity distribution can be described entirely with the help of only two more polynomials of degree four and six, g_1 and g_2. The polynomials g_1 and g_2 are constructed using a Gram-Schmidt orthogonalization procedure in order to ensure an orthogonality $\int_0^1 g_i g_j d\bar{y} = \delta_{i,j}$ of the polynomials and to reduce the required algebra. Setting the three residuals $\mathcal{R}_i(u)$ to zero formed a system of three evolution equations for the three unknowns q, r and s. This system is completed with the mass balance (2.2a) yielding a four-equation model. Again, as shown in Ruyer-Quil and Manneville (2002), the use of the Galerkin method is not necessary, the use of different weight (and thus WR methods) leading to the answer if the number of test functions is sufficiently large.

The theoretical analysis and the numerical integration of models such as four-equation models are indeed simpler than the corresponding study of the full Navier–Stokes problem, or even of the boundary-layer formulation. Handling the four fields still remains a difficult task, and a reliable two-field formulation consistent at order ϵ^2 would be welcome. At this stage setting r and s to zero in $\mathcal{R}_0$ lowers the order of the approximation. This procedure leads to a simplified averaged momentum equation

$$\begin{aligned}\delta\,\partial_t q &= \frac{5}{6}h - \frac{5}{2}\frac{q}{h^2} + \delta\left[\frac{9}{7}\frac{q^2}{h^2}\partial_x h - \frac{17}{7}\frac{q}{h}\partial_x q\right] - \frac{5}{6}\zeta h\partial_x h + \frac{5}{6}h\partial_{xxx}h \\ &\quad +\eta\left[4\frac{q}{h^2}(\partial_x h)^2 - \frac{9}{2h}\partial_x q\partial_x h - 6\frac{q}{h}\partial_{xx}h + \frac{9}{2}\partial_{xx}q\right].\end{aligned} \tag{2.11}$$

The set of equations to be solved is next closed by the mass conservation equation (2.2a). The two-equation simplified model is consistent up to $O(\epsilon)$ and $O(\epsilon^2)$ for the viscous terms. This consistency ensures a correct prediction of the linear stability threshold and cut-off wavenumber.

A consistent elimination of the $O(\epsilon)$ corrective fields r and s leads from the four-equation model to a consistent two-equation model. Since the WRM approach is consistent, this model is identical to the one obtained by determining the $O(\epsilon^2)$ corrections $U^{(2)}(q(x,t), h(x,t), \bar{y})$ within

the long-wave expansion with the ansatz (2.6) (see above § 2.3.1). However, this model is of no practical use since its solutions are not exempt of the spurious finite-time blow-up behavior encountered with the Benney equation (2.3). In order to solve this problem, *(Scheid et al. 2006)* introduce a a algebraic Padé-like regularization approach The first residual $\mathcal{R}_0$, obtained after averaging the momentum equation with the parabolic weight g_0, is searched in the form $\mathcal{G}^{-1}\mathcal{F}$ where $\mathcal{G}$ is now simply a function of h, q and their derivatives, and $\mathcal{F} = \mathcal{R}_0 - \mathcal{R}_0^{(2),\delta}$ is the residual bereft of the second-order inertial terms. The factor $\mathcal{G}$ is next adjusted to achieved consistency with the long-wave expansion at second-order with the nonlinearities of lowest possible order making use of the zeroth-order equivalence between the flow rate and the film thickness $q = h^3/3 + O(\epsilon)$, which yields:

$$\begin{aligned}\delta\,\partial_t q &= \delta\left[\frac{9}{7}\frac{q^2}{h^2}\partial_x h - \frac{17}{7}\frac{q}{h}\partial_x q\right] \\ &\quad + \left\{\frac{5}{6}h - \frac{5}{2}\frac{q}{h^2} + \eta\left[4\frac{q}{h^2}(\partial_x h)^2 - \frac{9}{2h}\partial_x q\partial_x h - 6\frac{q}{h}\partial_{xx}h + \frac{9}{2}\partial_{xx}q\right]\right. \\ &\quad \left. -\frac{5}{6}\zeta h\partial_x h + \frac{5}{6}h\partial_{xxx}h\right\} \times \left[1 - \frac{\delta}{70}q\partial_x h\right]^{-1}, \qquad (2.12)\end{aligned}$$

(2.12) differs from (2.11) by the factor $\mathcal{G} = (1 - \frac{\delta}{70}q\partial_x h)^{-1}$. Completed with (2.2a), (2.12) forms a two-equation model consistent at $O(\epsilon^2)$.

2.3.3 Center manifold analysis

A possible alternative to the gradient expansion approach is the center manifold analysis (CMA) introduced by Roberts (1996; 1997). Roberts'idea is to extend to partial differential equations, the center manifold analysis of solutions to an ordinary differential equation in the vicinity of an equilibrium state (Carr 1981, Guckenheimer and Holmes 1983). The framework of the center manifold analysis is developed in § 1.3 in the context of the modeling of the flow in a Hele-Shaw cell.

Each column of fluid at a given location x in the plane is modeled as a dynamical system of infinite dimension parametrized by the vertical coordinate y, the long scale modulations of the film interface introducing some coupling between neighboring fluid columns. The long time evolution of the film is then governed by the dynamics on the invariant manifold, or slow manifold, which is tangent to the eigenspace of zero eigenvalue.

In the long-wave limit ($\epsilon \sim \partial_x \to 0$), the linearized set of equations reads

$$\delta\partial_t\tilde{u} = \partial_{\bar{y}\bar{y}}\tilde{u} + 2\tilde{h} \equiv \mathcal{L}_1\tilde{u} \quad \text{with} \quad \tilde{u}(0) = 0 \quad \text{and} \quad \partial_{\bar{y}}\tilde{u}(1) = 0 \qquad (2.13)$$

where $\bar{y} = y/h$, and where $\tilde{u}$ and $\tilde{h}$ are small perturbations to the velocity field and free surface elevation. The operator $\mathcal{L}_1$ admits only one eigenmode with a zero eigenvalue, $\tilde{u} = 2\tilde{h}g_0(\bar{y})$ which is made possible by the elasticity of the free surface. Indeed, from (2.2a) it is clear that the displacement of the interface from h to $h + \tilde{h}$ is a neutral mode as $\partial_x \to 0$. The slow manifold is one-dimensional, parametrized by the free surface

elevation, i.e. $\theta(x,y,t) = \Theta(h(x,t),\bar{y})$ where θ refers to the unknowns either velocity or pressure. In fact, one can readily see that the long-wave expansion is equivalent to the center manifold analysis, the evolution on the slow manifold being governed by (2.2) with $u = \sum_n A_n(h)P_n(\bar{y})$.

In order to relax the strict slaving of the film dynamics to the kinematics of the free surface, Roberts (1996) assumed that the flow dynamics is determined by the kinematic eigenmode associated to the zero eigenvalue $\lambda_1^1 = 0$ *and* by the viscous relaxation mode associated with the largest eigenvalue $\lambda_1^1 = -\pi^2/4$ (all of them being negative, this is the one that is closest to zero). These two eigenmodes are associated to the eigenvectors $v_1^0 \propto g_0(\bar{y})$ and $v_1^1 \propto \sin(\pi\bar{y}/2)$ respectively. The invariant manifold, say $\mathcal{C}_1$, that is tangent to the subspace spanned by the Poiseuille semi-parabola g_0 and by the sine function $\sin(\pi\bar{y}/2)$. In order to proceed to the construction of $\mathcal{C}_1$, Roberts introduced a perturbation parameter γ which associate the initial linear problem (2.13) (recovered at $\gamma = 1$) to a subsidiary one whose spectrum admits a double zero eigenvalue (at $\gamma = 0$). The looked-after invariant manifold is thus constructed as a double series in the long wave parameter ϵ and in the dummy parameter γ. $\mathcal{C}_1$ is two-dimensional defined as $\theta(x,y,t) = \Theta(h(x,t),q(x,t),\bar{y})$, the long-wave dynamics on $\mathcal{C}_1$ being governed by a two couple evolution equations for h and q.[1]

In the long-wave limit $\epsilon \sim \partial_x \to 0$, the system of equations to be solved is affine, and therefore, in that limit, the invariant manifold coincides with the linear subspace spanned by g_0 and by the sine function $\sin(\pi\bar{y}/2)$:

$$u(x,y,t) \approx h^2 g_0\left(\frac{y}{h}\right) + \frac{\pi}{6}\left(\frac{3q}{h} - h^2\right)\sin\left(\frac{\pi y}{2h}\right) + O(\epsilon)\,. \tag{2.14}$$

The long-time dynamics being driven by the neutral kinematic mode and the first viscous relaxation mode

$$\partial_t h = O(\epsilon) \qquad \text{and} \qquad \delta\partial_t q = -\frac{\pi^2}{4}\left(\frac{q}{h^2} - \frac{h}{3}\right) + O(\epsilon) \tag{2.15}$$

At $O(\epsilon^2)$, the center manifold analysis of Roberts gives the following con-

[1] In fact Roberts (1996) used another equivalent parametrization based on h and the averaged velocity $\bar{u} = q/h$. I chose to recast his results using h and q instead in order to help the comparisons with the other modeling attempts.

sistent averaged momentum balance

$$\begin{aligned}
\delta\partial_t q \approx{}& \frac{\pi^2}{12}\left(h-\zeta h\partial_x h+h\partial_{xxx}h-3\,\frac{q}{h^2}\right)+\delta\left[-2.504\,\frac{q}{h}\partial_x q+1.356\,\frac{q^2}{h^2}\partial_x h\right]\\
&+\eta\left[3.459\,\frac{q}{h^2}(\partial_x h)^2-3.353\,\frac{\partial_x h\partial_x q}{h}-4.676\,\frac{q}{h}\partial_{xx}h+4.093\,\partial_{xx}q\right]\\
&+\frac{1}{100}\left(\delta\left[1.727\,hq\partial_x h+0.7983\,h^2\partial_x q\right]+\delta^2\left[-0.1961\,\frac{q^3}{h^2}(\partial_x h)^2\right.\right.\\
&\left.\left.-1.78\,\frac{q^2}{h}\partial_x h\partial_x q+0.1226\,q(\partial_x q)^2-1.792\,\frac{q^3}{h}\partial_{xx}h+0.7778\,q^2\partial_{xx}q\right]\right)\\
&+\frac{\zeta\,\delta}{100}\left(-1.357\,hq(\partial_x h)^2-1.012\,h^2\partial_x h\partial_x q-1.713\,h^2q\partial_{xx}h\right.\\
&\left.+0.4821\,h^3\partial_{xx}q\right)+\frac{\delta}{100}\left(-10.98\,\frac{q}{h}(\partial_x h)^4+7.12\,(\partial_x h)^3\partial_x q\right.\\
&\quad+10.68\,q(\partial_x h)^2\partial_{xx}h-4.451\,h\partial_x h\partial_x q\partial_{xx}h-1.113\,hq(\partial_{xx}h)^2\\
&-2.225\,h(\partial_x h)^2\partial_{xx}q+0.6404\,h^2\partial_{xx}h\partial_{xx}q+0.244\,hq\partial_x h\partial_{xxx}h\\
&+1.225\,h^2\partial_x q\partial_{xxx}h+0.4269\,h^2\partial_x h\partial_{xxx}q+1.713\,h^2q\partial_{xxxx}h\\
&\left.-0.4821\,h^3\partial_{xxxx}q\right)\,, \qquad (2.16)
\end{aligned}$$

which forms a consistent second-order model with the mass balance (2.2a). Roberts averaged momentum equation (2.16) must be contrasted with the results of the gradient expansion. The simplified averaged momentum equation (2.11) must be compared to (2.16) truncated to its two first lines. The remaining terms are second-order terms of inertia origin, except for the two terms $\frac{1}{100}\delta\left[1.727\,hq\partial_x h+0.7983\,h^2\partial_x q\right]$ at the third line which are $O(\epsilon)$ terms. On can easily recognize in the first two lines of (2.16) all terms present (2.11) but with slightly different coefficients. As detailed in § 1.3, this is an effect of the closeness between the parabola $g_0(\bar{y})$ and the sine function $\frac{\pi}{6}\sin(\pi\bar{y}/2)$, which has been illustrated in figure 1.4. The ansatz (2.6) is therefore very close to the projection (2.14).

The principal difference between CMA and WRM consists in the projection of the deviations from the Nusselt semi-Poiseuille solution on the first sine viscous relaxation mode (2.14). As stressed in § 1.3, this decomposition is meaningful only when the inertial time is comparable to the viscous time (all viscous modes, including the first one, having relaxed otherwise), i.e. when $\epsilon Re = O(1)$, in which case the perturbations to the balance of gravity and viscosity induced by inertia cannot be supposed weak. Simply stated, Roberts CMA would be useful only if the gradient expansion converges at ϵRe of order unity, which is far from being the case.

2.3.4 Shallow-water approach

The study of the dynamics of waves that are long in comparison to the thickness of the fluid layer has a long history in hydraulics and constitutes the shallow-water theory (see e.g. Whitham (1974)). As early as 1871, A.-J.-C. Barré de Saint-Venant formulated a set of evolution equations for the free surface elevation h and the averaged velocity $\bar{u} = q/h$ by depth-wise

integrating the governing equations (Saint-Venant 1871). These shallow-water equations are still commonly used for instance in oceanography.

The same idea has been applied to viscous fluids by Kapitza (1948) in his seminal work and later on by Shkadov (1967). Depth-wise integration of the momentum balance leads to the momentum balance of an associated column of liquid which reads at $O(\epsilon)$

$$\delta\left[\partial_t q + \frac{\partial}{\partial x}\left(\frac{\Upsilon q^2}{h}\right)\right] = h - \zeta h\partial_x h + h\partial_{xxx}h - \tau_w\,, \tag{2.17a}$$

where $\tau_w = \partial_y u|_0$ is the shear at the wall and Y is a shape factor defined as Prokopiou et al. (1991),

$$\Upsilon = \frac{h}{q^2}\int_0^h u^2\,dy\,, \tag{2.17b}$$

which relates the "first moment" of u, $\int_0^h u\,dy$, to its "second moment", $\int_0^h u^2\,dy$. The set of two equations (2.2a) and (2.17a) is closed provided that expressions of the shape factor Y and the wall shear τ_w as functions of h and q are known.

Kapitza and Shkadov proposed a closure based on the assumption that the velocity profile remains parabolic and self-similar:

$$u = u^{(0)} \equiv \frac{3q}{h}\left(\bar{y} - \frac{1}{2}\bar{y}^2\right) \qquad \text{with} \qquad \bar{y} = y/h \tag{2.18}$$

so that q still verifies $q = \int_0^h u dy$. The ansatz (2.18) ensures that the Nusselt flat film solution is correctly recovered by the model leading back to the zeroth-order equivalence $q = h^3/3 + O(\epsilon)$ between the flow rate and the film thickness. However the Kapitza–Shkadov model does not captures adequately the threshold of instability, $Fr_c^{-2} = \zeta/\delta = 1/3$ instead of the correct answer 2/5 (a 20 % discrepancy). As a consequence, the Kapitza–Shkadov model is generally used only in the vertical configuration. A large number of studies have been devoted to falling film flows based on (2.17) (see Chang et al. (1994) for a review and the most recent works by Sisoev and Shkadov (1999), Shkadov and Sisoev (2004), Sisoev et al. (2006), Demekhin et al. (2007a;b)). Some attemps have been made to cure the deficiencies of the Kapitza–Shkadov model, most of them being inconsistent (Prokopiou et al. 1991, Yu et al. 1995, Nguyen and Balakotaiah 2000). Because of the inability of (2.2a), (2.17a) to capture properly the onset of the Kapitza instability, the in-depth integration of a the momentum equation with a uniform weight is now practically a thing of the past, a more careful choice of the weight yielding far better results as shown in the previous subsection.

Yet, the shallow-water equations (2.17) admit a conservative form

$$\delta\left(\partial_t \mathbf{X} + \partial_x \mathbf{Q}\right) = \mathbf{R} \tag{2.19a}$$

where $\mathbf{X} = (h, q)$ is the vector of unknowns, $\mathbf{Q} = (h, \Upsilon q^2/h + \zeta h^2/2)$ is the vector of associated flux, and $\mathbf{R} = (0, h + h\partial_{xxx}h - \tau_w)$ are source terms (gravity acceleration, capillary forces and wall friction). The conservative

form (2.19a) is particularly useful in the analytical treatment of shocks and roll waves that arise when surface tension forces are too weak to prevent the breaking of the waves (Dressler 1949, Brock 1970, Chang and Demekhin 2000, Liu et al. 2005). Unfortunately, the $O(\epsilon)$ consistent averaged momentum equation (2.7) does not admit a conservative form. Such deficiencies motivated Vila, Noble and others to reconsider the long-wave asymptotics and to formulate consistent models that retain the conservative form (2.19a) (Vila, Fernández-Nieto et al. 2010, Boutounet et al. 2008). Vila's approach is based on the asymptotic expression $u = \sum_n A_n(h)P_n(\bar{y})$ of the velocity field that is provided by the Benney long-wave expansion, followed by a quest for admissible consistent expressions $\mathbf{Q}$ and $\mathbf{R}$ as functions of q and h obtained by using the equivalence $q = h^3/3 + O(\epsilon)$. Boutounet (2011) in his PhD thesis thus proposed

$$\mathbf{Q} = \left(h, C_1\frac{q^2}{h} + \left(\frac{1}{5} - \frac{C_1}{9} - \frac{2C_2}{75}\right)h^5 + \frac{C_2}{6}\zeta h^2\right), \tag{2.19b}$$

$$\mathbf{R} = \left(0, \frac{C_2}{3}\left(h + h\partial_{xxx}h - 3\frac{q}{h^2}\right)\right). \tag{2.19c}$$

Boutounet proved that, if the conditions $C_1 = 1$ and $0 < C_2 \leq 10/3$ are verified, then the flux $\mathbf{Q}$ is hyperbolic and a quadratic entropy in q can be found. The $O(\epsilon)$ model derived by Vila corresponds to $C_1 = 6/5$ and $C_2 = 3$. Boutounet performed numerical simulations of an horizontal film sheared by a co-current gas flow modeled by a Blasius boundary layer taking $C_1 = 1$ and $C_2 = 3$. The film was modeled by an extension of (2.19) accounting for the shear stress exerted by the gas. His simulations show a great sensitivity on the coefficient C_1, a mere variation of 6 % of C_1 yielding a 20 % variation of the wavelength of the observed waves !

2.3.5 Energy integral approach

To complete this short review of the different modeling attempts, let us signal some modeling strategies based on the kinetic energy balance that is obtained by a scalar product of the momentum equation with the velocity field (Usha and Uma 2004, Novbari and Oron 2009, Luchini and Charru 2010a). Multiplying $BL(u)$ by u and integrating it with a uniform weight across the film depth yields at first order in ϵ

$$\delta\left[\partial_t\int_0^h \frac{{u^{(0)}}^2}{2}dy + \frac{\partial}{\partial x}\int_0^h \frac{{u^{(0)}}^3}{2}dy\right] - q\left(1 - \zeta h\partial_x h + \partial_{xxx}h\right) + \int_0^h (\partial_y(u^{(0)} + u^{(1)})^2 dy \equiv EK(u) = 0\,. \tag{2.20}$$

Using $\int_0^h u^{(1)}dy = 0$ and the boundary condition $u|_0 = 0$, $\partial_y u|_h = O(\epsilon)$, we have

$$\int_0^h (\partial_y(u^{(0)} + u^{(1)})^2 dy = \int_0^h u^{(0)}\partial_{yy}\left(u^{(0)} + 2u^{(1)}\right)dy \tag{2.21}$$

and it is then easy to show that

$$\mathcal{R}_0 = \langle BL(u^{(0)})|g_0\rangle = \frac{3h}{q}EK(u) + O(\epsilon^2) \tag{2.22}$$

As a consequence, the WRM approach and the energy integral approach are equivalent at $O(\epsilon)$.

2.4 Discussion

The modeling strategies sketched in the previous section are all based on the long-wave approximation of small spatial variations. Consistent models at a given order of approximation (generally $O(\epsilon)$ or $O(\epsilon^2)$) are therefore all asymptotically equivalent. In the limit $\epsilon \to 0$, their solutions must converge. Indeed, making use of the slaving of the velocity field to the film thickness expressed by e.g. $q = h^3/3 + O(\epsilon)$, one is led back from every $O(\epsilon)$ consistent two-equation models to the Benney equation (2.3).

Inertia enters the gradient expansion at $O(\epsilon)$, as a perturbation of the Nusselt flat-film equilibrium achieved as a balance between the gravity acceleration and the viscous drag. Every modeling approach relies on the cross-stream coherence enforced by the viscosity which makes possible an elimination of the cross-stream variable y. Whenever inertia overcomes viscous relaxation, the cross-stream coherence of the flow is lost and with it any hope to reduce the dimensionality of the problem at hand. Yet, the Kapitza instability mechanism has an inertial origin: it is precisely because the velocity field adjusts with a delay to a deformation of the free surface that energy can be pumped from the base state to the perturbations. Therefore, the very idea of small inertia effects is sustained only when the instability mechanism is weak, that is whenever the amplitude of the waves is small. As a matter of fact, Benney-like surface equations are useful only in that case, yielding unrealistic or unphysical results for large-amplitude waves (My personal experience with the Benney equation is that unphysical finite-time blow-ups are observed when the amplitude of the waves is larger than 20 % of the Nusselt film thickness.)

The difficulty lies precisely in the fact that, in the wavy regimes of interest, the wave amplitude is not small (For solitary waves, the ratio $h_{\max}/h_s$ of the maximum height to substrate thickness can be as large as seven !) and the assumption of small inertia effects is certainly not well established. The different modeling strategies are thus attempts to extend as far as possible in the parameter space the convergence properties of the gradient expansion, that are valid only close to the instability threshold. The ability of the models to capture the dynamics of the flow must therefore be tested in the linear and nonlinear regime which demands to establish a validation procedure with identified milestones, the question being which features to be captured by the model and what is the required degree of precision. For instance, it is clear that the instability threshold must be retrieved with full precision, which is achieved whenever a model is consistent at $O(\epsilon)$ due to the long-wave nature of the instability. A reasonable reckoning of the range of unstable wavenumber and the maximum growth rate of the instability cannot be achieved without taking into account the streamwise viscous dispersion effects —elongational viscosity, or Trouton viscosity (Ribe 2001). Close to the instability threshold, this requires to extend the consistency of the models up to $O(\epsilon^2)$ for viscous terms (Ruyer-Quil and Manneville 1998; 2002). A good agreement in the linear regime is important not only to capture correctly the incep-

tion of the waves but also to properly account for the interaction between solitary waves which is governed by the linear superposition of their tails. Among others, Ruyer-Quil and Manneville (2000; 2002) have shown that the spatial stability of the film can be well approached by low-dimensional models for a quite extended range of parameters (typically for Reynolds numbers up to a few hundreds).

A much more demanding requirement is the reproduction of the nonlinear regime which is structured by solitary-like waves. It is particularly important that low-dimensional models admit solitary wave solutions in the whole parameter range of interest in order to avoid spurious blow-up behaviors. This should be tested in the most severe situation corresponding to negligible streamwise viscous dispersion at high Kapitza number (for water films for instance) and in the vertical geometry where the stabilizing hydrostatic pressure is absent, in which case one is left with only one control parameter: the reduced Reynolds number δ since $\zeta = 0$ and $\eta \approx 0$. Figure 2.7 presents the characteristics (speed and amplitude) of one-hump solitary waves solutions to the WRM model (2.2a,2.7), to Vila's and Boutounet's shallow-water formulations, i.e. (2.2a,2.19) with (C_1, C_2) equal to $(6/5, 3)$ and $(1, 3)$ respectively, and to Roberts model truncated at $O(\epsilon)$ which reads

$$\delta\partial_t q \approx \frac{\pi^2}{12}\left(h - \zeta h\partial_x h + h\partial_{xxx}h - 3\,\frac{q}{h^2}\right) + \delta\left[-2.504\,\frac{q}{h}\partial_x q + 1.356\,\frac{q^2}{h^2}\partial_x h\right] + \frac{1}{100}\delta\left[1.727\,hq\partial_x h + 0.7983\,h^2\partial_x q\right] \tag{2.23}$$

again completed with the mass balance (2.2a). The results of the low-dimensional models must be contrasted with the DNS results obtained by Chasseur (2011) using the Navier-Stokes solver Gerris[2] developed by Popinet (2003; 2009).

As first noticed by Ooshida (1999), two different regimes can be identified. At low values of δ, the amplitude of the waves is small, in which case a weakly nonlinear analysis leads to the Kuramoto-Sivashinky equation, from which the following power laws are derived (Ruyer-Quil et al. 2012)

$$c \approx 1 + 0.102\,\delta^{3/2} \qquad \text{and} \qquad h_{\max} \approx 1 + 0.132\,\delta^{3/2}\,. \tag{2.24}$$

This regime corresponds to the balance of gravity and viscous diffusion, inertia playing only a perturbative role, which justifies the christening *drag-gravity* regime introduced by Ooshida. An elimination of δ from (2.24) provides a linear dependency of the amplitude of the waves to their speed $h_{\max} - 1 \approx 1.29(c-1)$ which must be contrasted with the experimental relation $h_{\max} - 1 \approx 1.67(c-1)$ reported by Tihon et al. (2006) in their study of 2D solitary waves at moderate inclination angle (cf. figure 2.8). Figure 2.7c indicates that the linear relationship between amplitude and speed of the waves extends up to $\delta \approx 2$ and signals the transition to the second regime.

This second regime corresponds to large values of δ. It is characterized by highly non-symmetrical solitary waves with a steep front and a gentle back tail that can be referred to as "capillary roll waves". The formation

[2] `http://gfs.sourceforge.net`

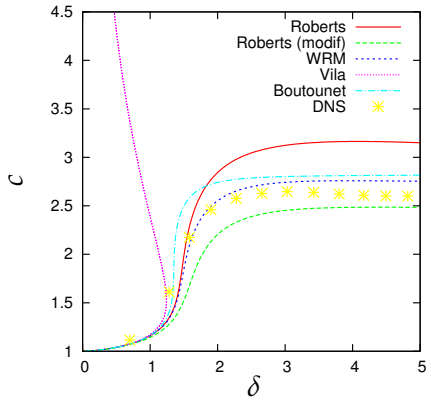

(a) *speed c versus δ*

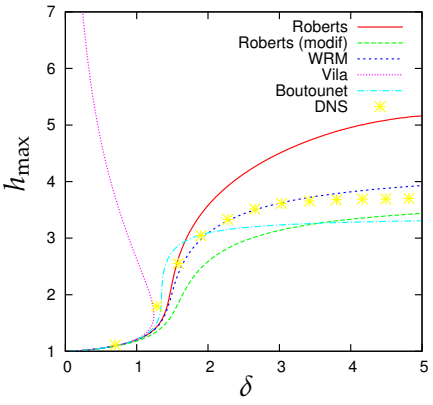

(b) *amplitude $h_{\max}$ versus δ*

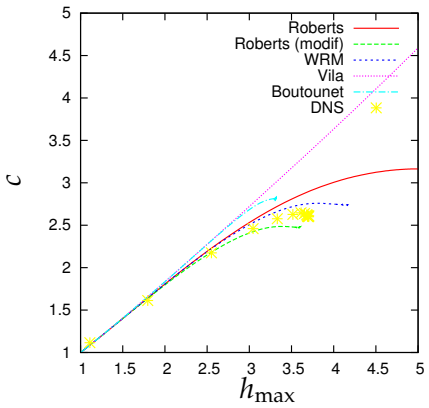

(c) *speed c versus amplitude $h_{\max}$*

Figure 2.7 – *Characteristics (speed and maximum height) of one-hump solitary waves running down a vertical plane. 'Roberts' and 'Roberts (modif)' refer to (2.2a, 2.23) with and without the small inertial terms $\frac{1}{100}\delta\left[1.727\,hq\partial_x h + 0.7983\,h^2\partial_x q\right]$. 'Vila' and 'Boutounet' refer to the shallow-water model (2.2a, 2.19) with (C_1, C_2) equal to $(6/5, 3)$ and $(1, 3)$ respectively.*

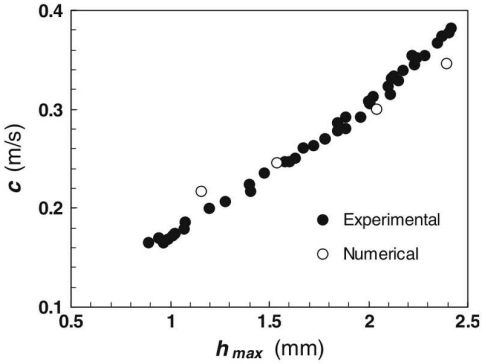

Figure 2.8 – *Reproduction of figure 8 in Tihon et al. (2006) showing the phase velocity as a function of the maximum film height for solitary waves running down an inclined plane. The Reynolds number lies in the range $10 < Re < 60$. The liquid was a 5 % by weight aqueous solution of Emkarox HV45 (polyalkylene glycols) ($\rho = 1007$ kg/m^3, $\nu = 3.9 \times 10^{-6}$ m^2/s. and $\sigma = 60$ mN/m). The inclination angle $\beta = 5°$ and the Kaptiza number is $\Gamma = 1480$.*

of these waves result from the balance of inertia, gravity and viscous drag and Ooshida referred to this regime as the *drag-inertia* one. Ruyer-Quil and Manneville (2005) (this publication is appended to this chapter) showed that the speed of the waves go to an asymptote c_∞ as δ goes to infinity that can be determined using Thomas condition (Thomas 1939). The rate of convergence to the asymptotic result is proportional to δ^{-3} which explains that c is already close to c_∞ at $\delta = 5$.

As expected, all models provide close result in the drag-gravity regime for $\delta \lessapprox 1$. Indeed, the long-wave asymptotic series converges in this regime, and the discrepancies between the different models are $O(\epsilon^2)$ small terms owing to their consistency at first order of the film parameter. At larger values of δ, the differences between the model predictions become important, which suggests that the convergence radius of the long-wave gradient expansion is smaller than one for a vertical wall. The branch of solitary-wave solutions to Vila's model presents a turning point at $\delta \approx 1.2$ and unphysical finite-time blow-ups are expected to occur in time-dependent simulations for δ above that value. In contrast, Boutounet's model does not present a loss of the solitary-wave solutions which emphasizes the great sensitivity of the shallow-water approach on coefficient C_1. Roberts model (2.2a, 2.23) grossly overestimates the speed and amplitude of the solitary waves. Surprisingly, dropping out the 'small' inertial terms at the second line of (2.23), as suggested by Roberts and Li (2006), yields an accurate prediction of the asymptotic speed $c_\infty \approx 2.5$ in good agreement with DNS results. However, this simplification spoils the consistency of the model and brings an erroneous prediction of the instability threshold ($Fr_c^{-2} = 0.384$ instead of $2/5$, a 4 % error). The weighted-residual approach seems to offer the best agreement, the amplitude of the solitary wave being well capture whereas the asymptotic speed $c_\infty \approx 2.738$ is slightly higher than the one predicted by DNS (a roughly 10 % overestimate). Bearing in mind the almost constant effort devoted to the modeling of falling film flows —there is hardly a year without a paper on this subject— this is quite surprising.

As a whole, the sensitivity of the different models to seemingly 'small' terms is appalling. Because of this sensitivity, the algebraic regularization process yielding (2.12) from the four-equation second-order WRM model was designed so that the asymptotic speed c_∞ of solitary-wave solutions to the model would not be different from the one corresponding to the first-order or simplified WRM model.

A second test of the accuracy of low-dimensional models in the nonlinear regime is to evaluate the accuracy of their predictions of the velocity field under the waves in both the laboratory frame or reference and the moving frame of the waves. A large-amplitude solitary wave exhibits a recirculation zone located in its hump which transports the "trapped" fluid mass downstream (and in that respect a solitary pulse carries mass) (Wasden and Duckler 1989). These recirculation zones —which can be located by drawing the streamlines in the moving frame— have a noticeable effect on the transfer of mass at the film-gas interface (Yoshimura et al. 1996).

At the wall, a backflow phenomenon may significantly enhance the the wall to fluid transfer of heat or mass (if the wall is permeable, see for instance Samanta et al. (2012) and chapter 5). The possibility of such

backflow at the thinnest part of the waves have been predicted early by Kapitza and Kapitza (1949) and later on by Portalski (1964) and reported by Dietze et al. (2008; 2009), Malamataris and Balakotaiah (2008). At the front of large waves, where the wave breaking is arrested by surface tension, gradients of capillary pressure push the liquid from the ripple crests to the ripple depressions. These pressure gradients may overcome the gravitational forces, displace the liquid in the upward direction and promote separations of the flow near the wall. Backflow phenomena generate inversion of the shear at the wall which locally affect heat and mass transfers.

Scheid et al. (2006) have questioned the ability of the WRM models to reproduce the velocity distribution computed by Malamataris et al. (2002) in their DNSs of a solitary wave observed by Liu and Gollub (1994). Figure 2.9 is a reproduction of figure 4 in Scheid et al. (2006) showing the velocity distribution at regularly spaced locations around the minimum of thickness [panels (a) to (d)], the streamlines in the moving frame [panels (e) and (f)]. The figure is completed with panels (g) and (h) where the streamlines in the laboratory frame have been drawn. The streamwise velocity distributions is computed using the three first polynomials g_0 , g_1 and g_2 (see Appendix A in Scheid et al. (2006) reproduced at the end of this chapter for details). The left part of figure 2.9 presents the results from the two-equation regularized model (2.2a,2.12), which are contrasted with the results of the four-equation second-order WRM model in the right part of the said figure. The similarity with the DNS by Malamataris et al. (2002) (not shown) is particularly convincing for the four-equation model both at behind the first ripple and in front of the main hump (the reader is invited to compare figure 2.9 to figure 7 in Malamataris et al. (2002); even the two inflection points they observed are recovered). For the two-equation regularized model, comparisons remain satisfactory everywhere except at the front of the main hump where the gradients are the largest. A reconstruction of the velocity field based on the two-equation model is no longer sufficient there. Panels (g) and (h) evince eddy-like loops referred to as capillary separation eddies by Dietze et al. (2008; 2009). The flow reversal extends from the wall up to the free surface and the streamlines remain opened in the liquid phase in agreement with Dietze's observations for a vertical non slippery wall. The inaccuracy in the reconstruction of the velocity by the two-equation model yields an exaggeration of the intensity of the capillary separation eddies and an overestimation of the heat and mass transfers at the wall. However, the streamlines in the moving frame of the waves show little differences whether a four-equation or a two-equation WRM model is employed. Indeed, at the thickness minimum where the relative deviations away from the parabolic profile are noticeable, the streamwise velocity u is also small, so that in the moving frame at the speed c of the wave, the relative velocity $u - c$ remains accurately estimated by a single parabolic profile.

The accuracy of the WRM models is further put to the test in figures 2.10 and 2.11 corresponding to the simulation of the 2D solitary waves of large amplitude reported by Nosoko et al. (1996) and reproduced in figure 2.5(a). The results from the WRM models are contrasted with the DNS by Miyara (2000).

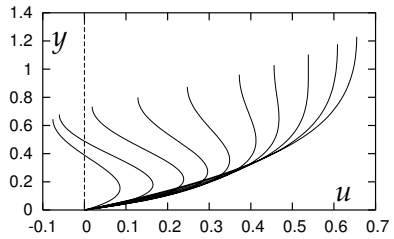

(a) *front of the main hump*

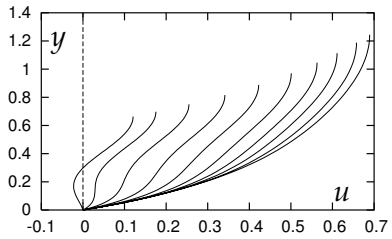

(b) *front of the main hump*

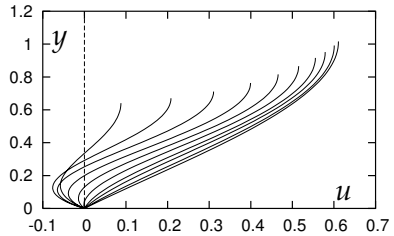

(c) *back of the first ripple*

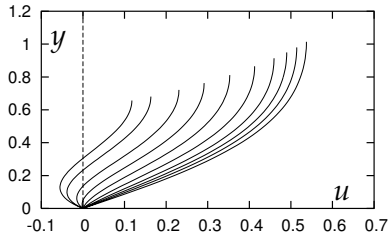

(d) *back of the first ripple*

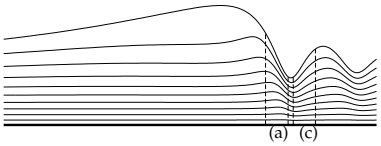

(e) *streamlines in moving frame*

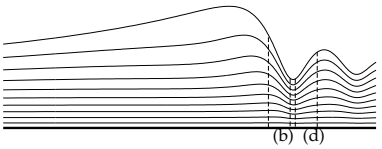

(f) *streamlines in moving frame*

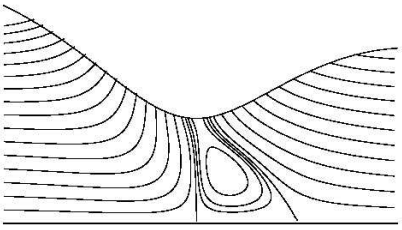

(g) *streamlines in laboratory frame*

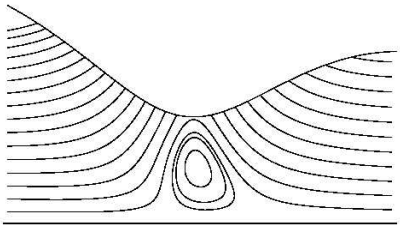

(h) *streamlines in laboratory frame*

Figure 2.9 – *(a-d) Streamwise velocity profile at regularly spaced locations from the front of the solitary hump to the back of the first capillary ripple. (e) and (f) Streamlines in the moving frame; (g) and (h) streamlines in the laboratory frame. The left column, i.e. (a), (c), (e) and (g) correspond to the solution to the regularized model (2.2a,2.12). The right column, i.e. (b), (d), (f) and (h) correspond to the solution to the four-equation second-order model. Extremal positions of the given velocity profiles are indicated by dashed lines in panels (e) and (f). Panels (a) to (f) are taken from Scheid et al. (2006).*

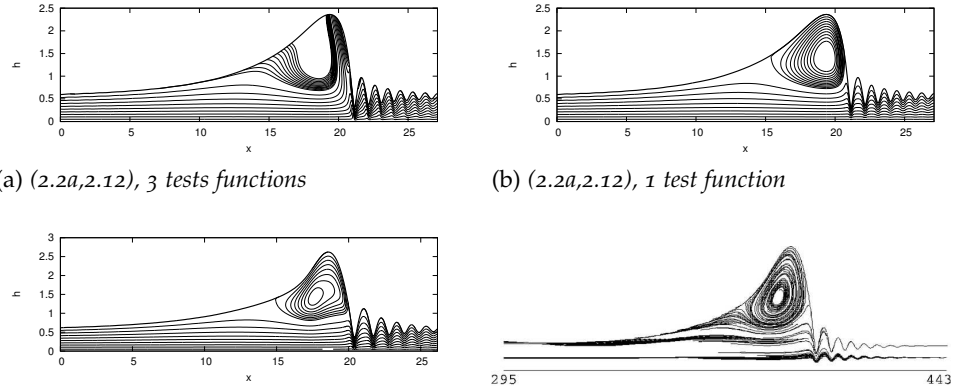

(a) *(2.2a,2.12), 3 tests functions* (b) *(2.2a,2.12), 1 test function*

(c) *4-equation model* (d) *DNS (Miyara 2000)*

Figure 2.10 – *Streamlines in the moving frame. (a) and (b) regularized two-equation model (2.2a,2.12). (a) velocity profile computed with three polynomials; (b) velocity represented by a single test function (g_0). (c) four-equation WRM model. (d) DNS from Miyara (2000).*

This test is a severe one: the wall is vertical, the Kapitza number is high ($\Gamma = 3650$) and the Reynolds number is already quite large ($Re = 69$). The solitary wave has a large amplitude ($h_{\max} \approx 4.5$ times the thickness h_s of the substrate liquid layer on which the wave sits). The reduced Reynolds number based on the substrate thickness $\delta_s = \delta h_s^{11/3} \approx 6$ and the flow conditions clearly correspond to the drag-inertia regime. The solitary wave reported by Nosoko et al. (1996) is therefore an example of capillary roll wave.

Figure 2.11 reveals the wave profiles and streamlines in the moving frame computed with the two-equation model (2.2a,2.12) and with the four-equation WRM model. The results from the low-dimensional models are compared to the DNS by Miyara (2000). The four-equation model gives a representation of the flow pattern in good agreement with DNS. The intensity and location of the recirculation zone in the main hump are both well captured even though the presence of small distortions of the streamlines at the front of the wave suggest that the number of polynomials used to reconstruct the velocity field becomes insufficient there. The two-equation model (panel a) grossly overestimate the intensity of the recirculation phenomenon when the velocity field is computed with the three polynomials g_0, g_1 and g_2. The flow pattern is better reproduced assuming a parabolic velocity profile (only one test function g_0).

The flow pattern in the laboratory frame is presented in figure 2.11 focusing on the accumulation of capillary ripples at the foot of the solitary wave. A sequence of capillary separation eddies are revealed at each local minimum of the film thickness suggesting an important effect on the heat and mass transfers by alternatively sweeping back and forth the fluid at the wall. The flow pattern predicted by the four-equation model is very similar to the observations by Dietze et al. (2008; 2009), whereas the corresponding result from the two-equation model with a reconstruction of the velocity field using three polynomials looks rather doubtful. Again, a

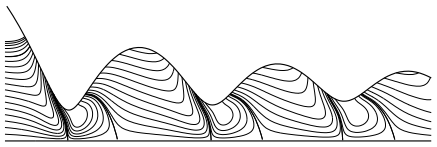

(a) *(2.2a,2.12), 3 tests functions*

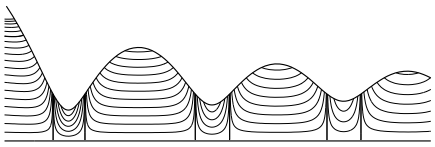

(b) *(2.2a,2.12), 1 test function*

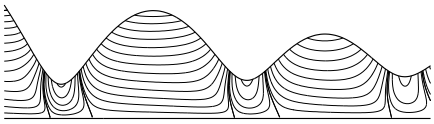

(c) *4-equation model*

Figure 2.11 – *Streamlines in the laboratory frame. (a) and (b) regularized two-equation model (2.2a,2.12). (a) velocity represented by a single test function (g_0); (b) velocity profile computed with three polynomials. (c) four-equation WRM model.*

reconstruction assuming a parabolic velocity profile yields a better result in that case.

Some perspectives

It is by now generally well established that the *qualitative* features of the falling film dynamics are well captured by one-equation models such as the Benney equation (2.3) or by weakly-nonlinear equations such as the Kuramoto-Sivashinsky (KS) equation or the Kawaharah equation

$$\partial_T H + H\partial_X H + \partial_{XX} H + \delta_K \partial_{XXX} H + \partial_{XXXX} H\,, \tag{2.25}$$

which can be obtained by means of an amplitude expansion considering small deviations of the film height from the reference state, i.e. $h = 1 + H$ with $H \ll 1$. The weakly nonlinear Kawaharah equation, also known as the generalized Kuramoto-Sivashinsky (gKS) equation (since the later is obtained when dispersion is absent, i.e. at $\delta_k = 0$), is the prototype of active, dissipative and dispersive media presenting a long-wave instability. Because of its generality and simplicity the KS and gKS equations have received a considerable interest in the recent past (Kawahara 1983, Kawahara and Toh 1988, Toh et al. 1989, Chang 1986, Chang et al. 1993b; 1994; 1998, Tseluiko et al. 2010b).

Because of the identified drawbacks of surface equations, there is a widespread consensus that any representative simulation of the dynamics of a falling film requires a modeling in terms of several evolution equations. However, the number of equations and the complexity of a satisfying low-dimensional model is still a matter of debate. Comparisons of the results from available models to DNSs suggest that a reliable description of the nonlinear wave dynamics can be achieved even at already large values of the Reynolds number far in the drag-inertia regime. This last point is particularly important for industrial applications, where the film is generally three-dimensional, evolves on a non-planar substrate over extended domains, and where full DNS simulations are much too costly.

The needed degree of complexity of the low-dimensional models is determined by the required accuracy. Results from the two and four-equation WRM models suggest that the speed, shape and dynamics of the waves can be reasonably captured by two-equation models. However, a faithful account of the heat and mass transfers from the fluid to the surrounding gas or at the wall probably require a greater complexity. As a consequence, it is probably desirable to design hierarchies of models, the selection of one of them for a particular application being found on a compromise between several factors, for instance the numerical cost, the phenomenon to capture, the required accuracy etc. In that respect, the shallow-water asymptotic approach introduced by Vila must be underlined as the conservative format is appropriate for numerical schemes adapted to hyperbolic systems presenting shocks, e.g. finite volume methods, Godunov methods etc.

Besides offering convenient substitutions to cumbersome DNS numerical experiments, low-dimensional modelings set up convenient mathematical frames for the analytical study of the physical phenomena at hand. Considering this, the derivation of reliable two-equation models represent an important step forward. For instance, they offer a proper account of the mechanisms of the primary instability in terms of Whitham wave hierarchy (Ruyer-Quil et al. 2008, Kalliadasis et al. 2012). The coherent structure theory that has been imitated by (Kawahara 1983, Kawahara and Toh 1988), and recently amended by Tseluiko et al. (2010b) in the context of the Kawaharah equation (2.25), is now extended to two-equation models (Chang and Demekhin 2002, Pradas et al. 2011). Pradas and coworkers showed that the inclusion of the streamwise viscous effects —the elongational viscosity or Trouton viscosity— is paramount for the wave-to-wave interaction processes.

As a rule of thumb, successful modeling strategies must be as simple as possible but not more simple. One can thus enunciate a kind of 'least-degeneracy principle' stating that all relevant physical effects must be accounted for at least at leading order. For instance, this justifies that surface tension effects must be kept (though they formally enter the gradient expansion at $O(\epsilon^3)$), and that second-order streamwise viscous effects are kept, e.g. in (2.11), since they govern the dispersion of the waves. The fact that the center manifold analysis has been less employed than the weighted residual methods does not stem from the fact that the latter may bring better result than the former, the two leading to somewhat close equations, but rather because the CMA is very cumbersome to apply as compared to the WRMs.

It is my hope that low-dimensional modeling may bring some insights into the open questions that are still offered by the complex dynamics of falling films. In particular, the 3D secondary instabilities of 2D flows are not well understood though a Rayleigh mechanism has been suggested by Demekhin et al. (2007a;b). Benoit Scheid, Paul Manneville and myself tried to investigate the mechanisms leading to the selection of the synchronous or subharmonic 3D instabilities of the slow γ_1 waves (see *Scheid et al. (2006)* reproduced at the end of this chapter). Our Floquet analysis showed that the 3D secondary instability is not very selective. The stabil-

ity analysis of the γ_2 waves is currently under study (Nicolas Kofman's PhD).

In particular, the effect of the channel width on the 2D waves require some further understanding. In Liu and Gollub's experiments, 2D solitary waves present curved fronts due to the presence of sidewalls (cf. figure 2.12). This effect can be significant on the primary stability of the film though the Nusselt flat film solution is only locally affected by the presence of the sidewalls (Vlachogiannis et al. 2010). I conjecture that this effect is also paramount when the stability of γ_2 solitary waves is considered.

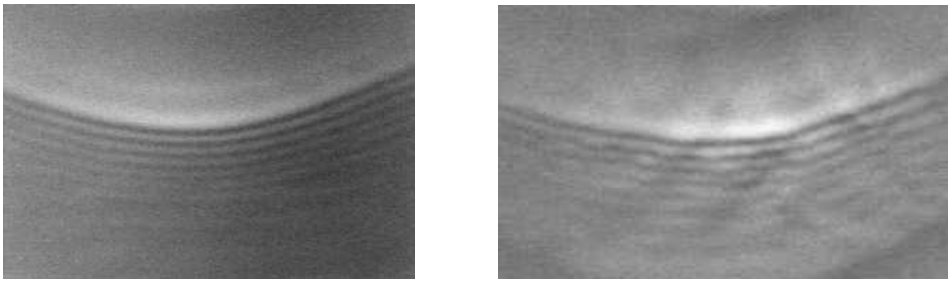

(a) (b)

Figure 2.12 – *(a) curved 2D solitary wave; (b) spanwise instability of a 2D solitary wave (from Émery & Brosse Émery and Brosse (1995), courtesy of Paul Manneville, reproduced from Kalliadasis et al. (2012)).*

But the most challenging problem probably consists in the long-time evolution of three-dimensional flows, this spatio-temporal disordered state that is characterized by the presence of three-dimensional coherent structures, the horseshoe-like waves, which interact continuously with each other as quasi-particles. The precise details of this weakly turbulent regime still escape understanding. Open questions include the number per area, or "density", of the structures that organize the flow.

I have purposely put aside most of the difficulties which arise in practical applications, where heat and mass transfers are paramount, where the geometry of the wall is never simple, where the fluid itself is scarcely Newtonian and shear-thinning, viscoelastic or viscoplatic effects have to be accounted for as well as the permeability of the substrate. Some of these complex situations are further considered in the next chapters.

2.5 C. Ruyer-Quil & P. Manneville, J. Fluid Mech. (2005)

J. Fluid Mech. (2005), *vol.* 531, *pp.* 181–190.
doi:10.1017/S0022112005003885 Printed in the United Kingdom

On the speed of solitary waves running down a vertical wall

By C. RUYER-QUIL[1] AND P. MANNEVILLE[2]

[1]Laboratoire FAST – UMR CNRS 7608, Campus Universitaire, 91405 Orsay, France

[2]LadHyX – UMR CNRS 7646, École Polytechnique, 91128 Palaiseau, France

(Received 5 October 2004 and in revised form 1 February 2005)

Solitary-wave solutions to surface equations or two-equation models of film flows are investigated within the framework of dynamical system theory. The limiting behaviour of one-humped solitary waves (homoclinic orbits) at large Reynolds numbers is considered. Their predicted speed is in good agreement with numerical findings. The theory also explains the absence of solitary-wave solutions to the Benney equation in the same limit.

1. Introduction

Due to the widespread use of film flows in industrial applications, the stability of thin-film flows has received much attention, starting with the seminal work by Kapitza (Kapitza 1948; Kapitza & Kapitza 1949). From a theoretical viewpoint, the interest of this system stems from the fact that the primary instability is spanwise-independent (Yih 1955), of long-wavelength, and supercritical. In most relevant flow regimes, the flow remains close to that of the flat-film solution, called the Nusselt flow, with thickness $h = h_{\mathrm{N}}$ and parabolic velocity profile.

We focus here on liquid films flowing along vertical walls. The usual control parameters are then just the Reynolds number $R = gh_{\mathrm{N}}^3/3\nu^2$ and the Weber number $W = \sigma/\rho g h_{\mathrm{N}}^2$, comparing inertia to viscous effects, and surface tension to gravity, respectively. Here g is the gravity acceleration and ρ, ν and σ are the fluid's density, kinematic viscosity and surface tension. The proximity to the Nusselt flow is measured by the so-called *film parameter* ϵ scaling the typical slope of the film. In flow regimes of interest, the cross-stream coherence of the flow is ensured by viscosity whereas the slope is maintained small enough thanks to surface tension effects. For thickness fluctuations with wavelength ℓ, the order of magnitude of this parameter can be obtained through the estimate $\rho g \sim \sigma \partial_{xxx} h$ as $h_{\mathrm{N}}/\ell \sim W^{-1/3}$. Following Shkadov (1977), it is then advisable to rescale the streamwise and cross-stream directions x and y differently, in order to make this slope of order unity, hence defining the scale ratio $\kappa = W^{-1/3}$. In this process the Reynolds number R is replaced by $\delta = 3R/\kappa$ that compares inertia to surface tension and viscosity directly. (The reduced Reynolds number originally introduced by Shkadov was $\delta/45$ due to different numerical scaling choices.) A second parameter $\eta = W^{-2/3}$ measuring the intensity of the streamwise viscous dispersion is then substituted for the Weber number. When surface tension is strong, the Weber number is large, so that κ and η are small, making typical instability wavelengths long and keeping viscous dispersion negligible.

The film's dynamics is essentially that of isolated large-amplitude solitary waves in the form of a main hump preceded by smaller capillary ripples, which travel much

faster than linear waves (Alekseenko, Nakoryakov & Pokusaev 1994; Liu & Gollub 1994). Direct simulation of Navier–Stokes equations with a free surface remains a formidable task, see e.g. Malamataris *et al.* (2002). This difficulty motivated the search for reliable reduced models. The smallness of parameter ϵ allows a drastic simplification of the primitive equations (Shkadov 1967, 1977) which, after elimination of the pressure, yields the so-called boundary-layer (BL) equations. However this simplification is still not sufficient since these equations retain the same physical dimensionality as the primitive equations, which focuses the attention on even more simplified models where the cross-stream dependence is eliminated through averaging and/or long-wave expansion.

1.1. *Surface equations*

By performing a gradient expansion of the set of primitive equations, Benney (1966) obtained a single evolution equation for the film thickness which, using Shkadov's notations, is

$$\partial_t h + \tfrac{1}{3}\partial_x\left\{h^3 + \tfrac{2}{35}\delta\partial_x(h^7) + h^3\partial_{xxx}h\right\} = 0. \tag{1.1}$$

Benney's equation is the prototype of so-called *surface equations*, solely involving the local film thickness $h(x,t)$ and its derivatives. They are derived by integrating the (exact) continuity equation across the fluid layer:

$$\partial_t h + \partial_x q = 0, \tag{1.2}$$

where $q = \int_0^h u\,\mathrm{d}y$ is the local flow rate. Approximations enter when truncated expressions for q, obtained e.g. through a long-wavelength expansion, are inserted in (1.2).

Numerical simulations of (1.1) demonstrated the occurrence of non-physical blow-ups of unsteady solutions at finite time and sufficiently large δ (Pumir, Manneville & Pomeau 1983; Rosenau, Oron & Hyman 1992). Ooshida (1999) however showed that the long-wavelength expansion could be regularized by applying techniques inspired from the Padé approximation method, which lead him to

$$\partial_t h + \tfrac{1}{3}\partial_x\left\{h^3 - \delta\left[\tfrac{2}{7}\partial_t(h^5) + \tfrac{36}{245}\partial_x(h^7)\right] + h^3\partial_{xxx}h\right\} = 0. \tag{1.3}$$

Comparing inertial terms (with factor δ) of (1.3) with that in (1.1), one can see the introduction of a new term involving a time derivative and a change of the coefficient of the original term from 2/35 to $-36/245$. *Ooshida's equation* does not exhibit finite-time blow-up and solitary-wave solutions can be obtained for all δ but the predicted amplitudes and speeds differ from the observed values by a factor of order 2–3.†

1.2. *Two-equation models*

The validity of the formal expansion leading to (1.1) is restricted to $\delta \ll 1$, as derived from the value of ϵ estimated from the cut-off wavenumber $\propto \sqrt{R/W}$, which yields $\epsilon R \sim R^{3/2}/W^{1/2} \sim \delta^{3/2}$ (Ooshida 1999). That expansion further assumes that the velocity field remains strictly enslaved to the evolution of the thickness of the film. Surface equations are thus not expected to describe wave motions at moderate δ accurately. An alternative to the single-equation approach was proposed in the seminal work by Kapitza (1948) and later by Shkadov (1967). Assuming that the velocity profile across the fluid layer remains parabolic in the wavy regime and averaging the momentum equation across the film, keeping terms up to order ϵ along with the dominant surface

† The equation originally derived by Ooshida contained an extra term $-\eta\partial_x(h^2\partial_{xt}h)$ that accounts for streamwise dissipative effects, but was later shown to have little effect on the amplitude and speed of the solitary waves (Ruyer-Quil & Manneville 2004).

tension term, Shkadov obtained

$$\delta\,\partial_t q = h - 3\frac{q}{h^2} + \delta\left[\frac{6}{5}\frac{q^2}{h^2}\partial_x h - \frac{12}{5}\frac{q}{h}\partial_x q\right] + h\partial_{xxx}h, \tag{1.4}$$

closing the system in h and q by adding the mass conservation equation (1.2). *Shkadov's model* (1.2), (1.4) does not exhibit non-physical blow-ups of its solutions but, whereas it works quite well for vertical walls, when adapted to moderately inclined planes it leads to an incorrect prediction for the instability threshold. A refined derivation based on a systematic weighted-residual expansion of the velocity field on a polynomial basis led us later to overcome this limitation (Ruyer-Quil & Manneville 2000). An equation similar to (1.4) was obtained but with slightly different coefficients

$$\delta\partial_t q = \frac{5}{6}h - \frac{5}{2}\frac{q}{h^2} + \delta\left[\frac{9}{7}\frac{q^2}{h^2}\partial_x h - \frac{17}{7}\frac{q}{h}\partial_x q\right] + \frac{5}{6}h\partial_{xxx}h. \tag{1.5}$$

When compared to equations (1.1) and (1.3), models (1.2), (1.4) and (1.2), (1.5) account for inertial effects in a clearly novel way since the local flow rate $q(x,t)$ now has its own dynamics instead of being enslaved to $h(x,t)$.

1.3. *One-humped solitary waves*

Experimentally observed solitary waves can travel without deformation at constant speed for large distances. Such solutions are computed by changing to a moving frame with coordinate $\xi = x - ct$, which transforms the partial differential problem into an ordinary differential problem. Applying this to (1.1) or (1.3) immediately leads to a single fourth-order differential equation which can be integrated once, yielding a three-dimensional dynamical system. Within the two-equation formulation, the same result is obtained but in two steps. First the mass conservation equation (1.2) becomes $-ch' + q' = 0$, where primes denote derivatives with respect to the moving coordinate ξ. This equation can be integrated to yield

$$q = c\,h + q_0, \tag{1.6}$$

where $q_0 = \int_0^h (u - c)\,\mathrm{d}y$ is an integration constant corresponding to the flow rate in the moving frame. Next the second equation (1.4) or (1.5) is transformed. In all cases, the following equation is obtained:

$$\tfrac{1}{3}h^3h''' + \delta\mathscr{G}(h,c)h' + \tfrac{1}{3}h^3 - ch - q_0 = 0. \tag{1.7}$$

In practice, $\mathscr{G}$ – to be specified below – contains all the inertial effects (with factor δ), while the third-order derivative arises from surface tension effects. The integration constant q_0 can be fixed by imposing $h \equiv 1$ as a solution to (1.7) since $h(\xi) = H$ constant, often taken equal to the unperturbed film thickness h_{N}, is indeed a solution to the problem. Making the changes $h \mapsto Hh$, $c \mapsto Cc$, $q \mapsto Qq$, preserves the structure of the equation provided that ξ is also rescaled as $\xi \mapsto \Xi\xi$ and the control parameter δ as $\delta \mapsto \Delta\delta$. By substitution one is then led to $\Xi = H^{1/3}$ and $\Delta = H^{-11/3}$, whereas $C = H^2$ and $Q = H^3$. Measuring h in units of H, i.e. with the reference unperturbed solution corresponding to $h \equiv 1$, leads to

$$q_0 = 1/3 - c, \tag{1.8}$$

which will be assumed in the following. Our starting point will thus be

$$\tfrac{1}{3}h^3h''' + \delta\mathscr{G}(h,c)h' + \mathscr{H}(h,c) = 0, \tag{1.9}$$

where

$$\mathscr{H}(h,c) \equiv \tfrac{1}{3}h^3 - ch - q_0 = \tfrac{1}{3}(h-1)(h^2 + h + 1 - 3c), \tag{1.10}$$

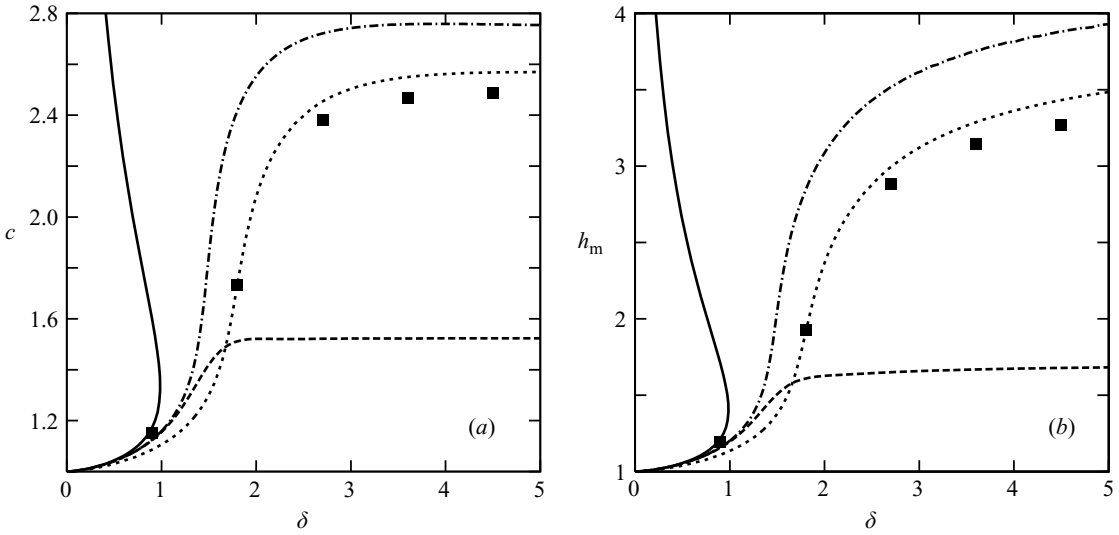

FIGURE 1. (*a*) Speed c and (*b*) maximum height h_m as functions of the reduced Reynolds number δ for the one-hump homoclinic solutions to the Benney equation (solid line), and to the Ooshida equation (dashed line). Dotted and dash-dotted lines correspond to the Shkadov model (1.2), (1.4) and to the modified model (1.2), (1.5), respectively. Filled squares are from simulations of the BL equations (Chang *et al.* 1996).

and the functions $\mathscr{G}(h, c)$ corresponding to the different cases are

$$\begin{aligned}
&\text{Benney equation (1.1):} && \mathscr{G}(h,c) = \tfrac{2}{15}h^6,\\
&\text{Ooshida equation (1.3):} && \mathscr{G}(h,c) = \tfrac{10}{21}ch^4 - \tfrac{12}{35}h^6,\\
&\text{Shkadov model (1.2), (1.4):} && \mathscr{G}(h,c) = \tfrac{2}{5}q^2 - \tfrac{4}{5}cqh + \tfrac{1}{3}c^2h^2\\
&&& \quad = \tfrac{2}{5}c^2 - \tfrac{4}{15}c + \tfrac{2}{45} - \tfrac{2}{15}c^2h^2,\\
&\text{Model (1.2), (1.5):} && \mathscr{G}(h,c) = \tfrac{18}{35}q^2 - \tfrac{34}{35}cqh + \tfrac{2}{5}c^2h^2\\
&&& \quad = \tfrac{1}{35}\left[18c^2 + \tfrac{2}{3}ch - 12c - 2c^2h(h+1) + 2\right].
\end{aligned}$$

The expression for q given by (1.6) using (1.8) has been used to expand $\mathscr{G}$ when needed.

One-humped solitary wave solutions to (1.1), (1.3), (1.2), (1.4) and (1.2), (1.5) have been computed within the dynamical-systems setting described in the next section using the continuation software AUTO97 and its package HOMCONT for the computation of homoclinic orbits (Doedel *et al.* 1997). The speed c and maximum height h_m of such waves are displayed in figure 1 as functions of δ.

The turning point of the branch corresponding to Benney's equation signals the loss of solution for δ greater than $\delta^\star \approx 0.986$, a value that closely corresponds to the occurrence of blow-ups of unsteady solutions mentioned previously. By contrast, Ooshida's equation (1.3) and models (1.2), (1.4) and (1.2), (1.5) possess a one-humped solitary wave solution for all values of δ, in agreement with what was obtained by Chang, Demekhin & Kalaidin (1996) through integration of the much more cumbersome BL equations. While the asymptotic wave speed of order 2.5 reported in Chang *et al.* (1996) should be taken with care† the outcome of Ooshida's regularized

† The apparent good agreement between results from Shkadov's model and BL equations is probably fortuitous owing to limited streamwise resolution of the large-δ BL simulations (only 70 Fourier modes for strongly localized solitary waves).

equation is clearly less satisfactory than the supposedly more reliable results from the two-equation models. Indeed, in the three cases the speeds of the solitary waves saturate but those obtained from (1.3) are a factor of more than 2 smaller than those obtained from models (1.2), (1.4) and (1.2), (1.5) or the BL results. The waves' maximum heights h_{m} also grow rapidly in the transition region around $\delta \sim 1.5$–2 and continue to increase beyond that range for the models and BL solutions, a trend which is not reproduced by Ooshida's solutions, suggesting that the shape of the waves is also not properly approximated by solutions to (1.3) at large δ.

Two different flow regimes were distinguished by Ooshida (1999): the *drag–gravity* regime, which takes place for $\delta \ll 1$ and where the dynamics is governed by a balance between the viscous drag at the wall and gravity and surface tension, with inertia playing the role of a perturbation, and the *drag–inertia* regime at $\delta \gg 1$, when inertia effects are dominant. The rest of this note mainly focuses on the solitary-waves' asymptotic behaviour in the drag–inertia regime, using the tools of dynamical system theory.

2. Solitary waves and dynamical system theory

2.1. *General setting and drag–gravity regime*

Equation (1.9) can be recast as a three-dimensional dynamical system:

$$U_1' = U_2, \quad U_2' = U_3, \quad U_3' = -3[\delta \mathscr{G}(U_1, c)U_2 + \mathscr{H}(U_1, c)]/U_1^3, \tag{2.1}$$

in a phase space spanned by $\boldsymbol{U} = (U_1, U_2, U_3)$ where $U_1 = h$, $U_2 = h'$, $U_3 = h''$, and solutions to (1.9) are trajectories in that phase space.

Solitary wave solutions correspond to *homoclinic orbits* connecting fixed points to themselves. The fixed points of (2.1) are given by $U_2 = U_3 = 0$ and

$$3\mathscr{H}(U_1, c) = (U_1 - 1)\left(U_1^2 + U_1 + 1 - 3c\right) = 0, \tag{2.2}$$

from which it is seen that $U_1 = 1$ is a solution arising from the scaling convention for h. Additional roots are given by

$$U_1^2 + U_1 + 1 - 3c = 0. \tag{2.3}$$

Accordingly, for $c > 1/3$, i.e. for waves travelling faster than the average speed of the Nusselt flow as seen from (1.8), there is one supplementary positive solution:

$$h_{\mathrm{II}} \equiv -1/2 + \sqrt{3(c - 1/4)}, \tag{2.4}$$

so that (2.1) then admits two fixed points $\boldsymbol{U}_{\mathrm{I}} = (1, 0, 0)$ and $\boldsymbol{U}_{\mathrm{II}} = (h_{\mathrm{II}}, 0, 0)$. The study below extends the analysis developed by Pumir *et al.* (1983) for the Benney equation with $\delta \ll 1$ to the models introduced in § 1.1 and § 1.2. The case $\delta \gg 1$ is considered in the next subsection.

Let us first consider fixed point $\boldsymbol{U}_{\mathrm{I}}$. The dispersion relation governing infinitesimal perturbations varying as $\exp(\lambda\xi)$ is

$$\lambda^3 + 3\delta \mathscr{G}(1, c)\lambda - 3(c - 1) = 0. \tag{2.5}$$

Denoting the roots as λ_i, $i = 1, 2, 3$, we have $\lambda_1 + \lambda_2 + \lambda_3 = 0$. Furthermore, one of the roots λ_1 is real and has the sign of the product $\lambda_1\lambda_2\lambda_3 = 3(c - 1)$, thus is positive when $c > 1$ and negative when $c < 1$. The two others roots are complex conjugate (real) when

$$\Delta_{\mathrm{I}} = 4\delta^3 \mathscr{G}(1, c)^3 + 9(c - 1)^2 \tag{2.6}$$

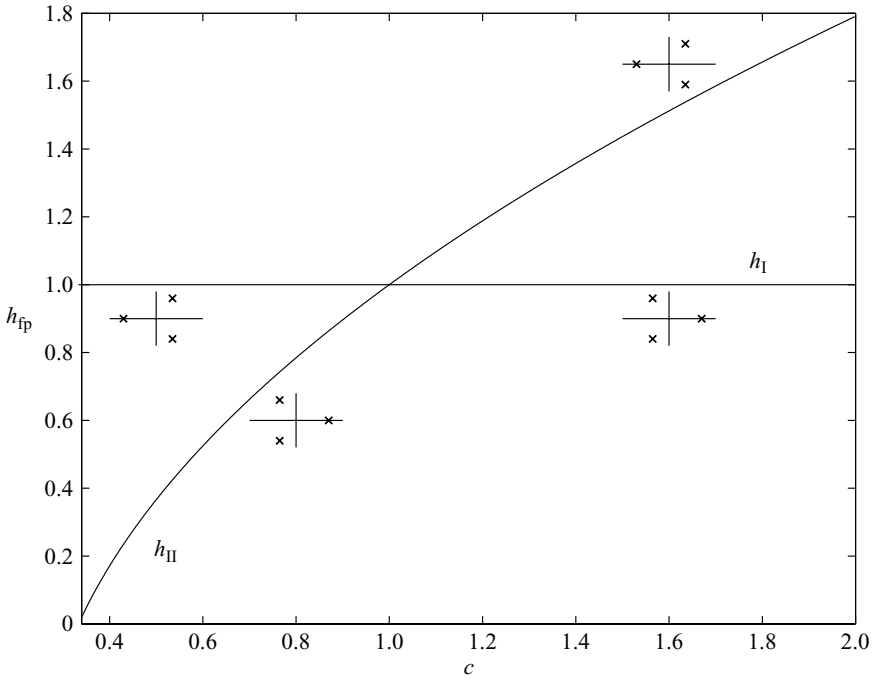

FIGURE 2. Locations of the fixed point height $h_{\rm fp}$ and stability diagram as function of the wave speed c in the case of the Benney equation (1.1).

is positive (negative). In the same way, at the second fixed point $\boldsymbol{U}_{\rm II}$, we obtain

$$h_{\rm II}^3\lambda^3 + 3\delta\mathscr{G}(h_{\rm II}, c)\lambda - 3\big(c - h_{\rm II}^2\big) = 0, \tag{2.7}$$

and the sum of the roots is again zero. One of roots is real and has the sign of $c-h_{\rm II}^2$, hence negative when $c>1$, since $c>h_{\rm II}$ implies $c-h_{\rm II}^2 = c-(3c-1-h_{\rm II}) = (1-c)+(h_{\rm II}-c)<0$. By performing the transformation that allowed us to rescale the equation in order to reset $h_{\rm II}$ to one, it can be seen that the sign of

$$\Delta_{\rm II} = 4\delta^3\mathscr{G}(h_{\rm II}, c)^3 + 9h_{\rm II}^3\big(c - h_{\rm II}^2\big)^2 \tag{2.8}$$

is the same as that of $\Delta_{\rm I}$, which finishes to link the properties of $\boldsymbol{U}_{\rm II}$ to those of $\boldsymbol{U}_{\rm I}$, just exchanging the dimensions of their stable and unstable manifolds.

The case of the Benney equation (Pumir *et al.* 1983) is the easiest one, thanks to the simplicity of the corresponding expression $\mathscr{G}(h, c) = \frac{2}{15}h^6$, independent of c. Since $\mathscr{G}$ is always positive, both fixed points have one real root and one complex pair for all c. As shown in figure 2, they are both saddle-foci. An exchange of properties is seen to take place at $c=1$, which makes the case degenerate with $h_{\rm I}=h_{\rm II}=1$. As proven by Gaspard (1993), the existence of homoclinic trajectories for the Benney equation with $c\approx 1$ when $\delta \ll 1$ stems from the perturbation of conditions $\Delta_{\rm I}=0$ and $c=1$ which define a codimension-two bifurcation at a double stationary-oscillatory instability with eigenvalues 0, and $\pm {\rm i}\omega$. Since $\mathscr{G}(1, c)$ is positive, when $c>1$ we have $\lambda_1>0$ while $\lambda_{2,3}$ are complex conjugate with negative real values. The homoclinic orbit thus starts from $\boldsymbol{U}_{\rm I}$ along the one-dimensional unstable manifold $\mathscr{W}_{\rm I}^u$ in a monotonic way and returns to the fixed point by spiralling along the two-dimensional stable manifold $\mathscr{W}_{\rm I}^s$. At finite but small δ such an orbit can be understood as coming from the homoclinic bifurcation of a limit cycle arising from the Hopf bifurcation of $\boldsymbol{U}_{\rm II}$ for $c>1$, then approaching and finally touching $\boldsymbol{U}_{\rm I}$ as its length is increased. Because $h_{\rm II}>h_{\rm I}=1$, the corresponding wave profile resembles a hump preceded by ripples

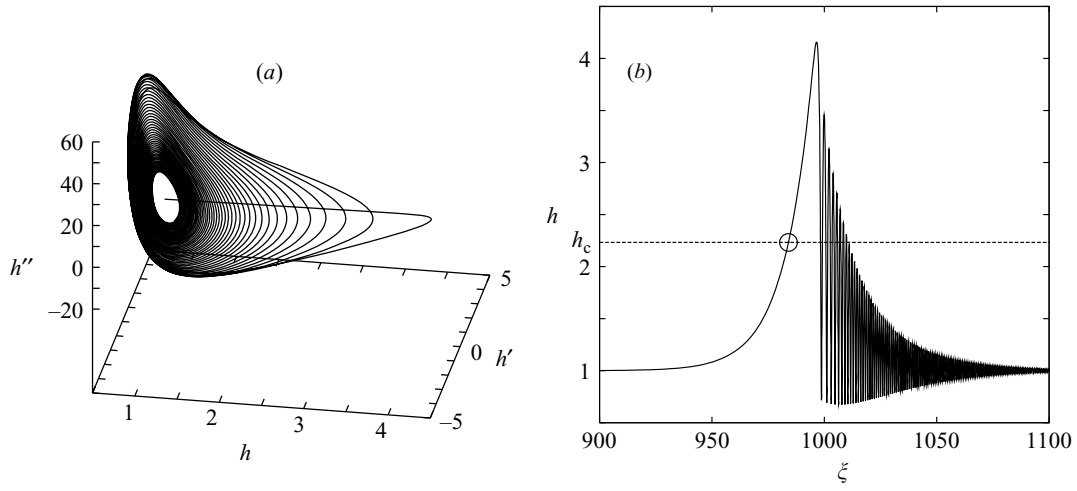

FIGURE 3. Typical solitary wave solution to model (1.2), (1.5) at large δ, here $\delta = 10$. (*a*) Trajectory in the phase space spanned by $\boldsymbol{U} = (U_1, U_2, U_3) \equiv (h, h', h'')$. The spiralling behaviour towards the fixed point $\boldsymbol{U}_{\mathrm{I}}$ has been truncated in order to point out the monotonic starting of the trajectory along $\mathscr{W}^u_{\mathrm{I}}$. (*b*) Profile of the wave $h = h(\xi)$ in the frame moving at speed c, with an indication of the critical level h_{c} to be defined in the text.

corresponding to the spiralling return to $\boldsymbol{U}_{\mathrm{I}}$ but the lack of homoclinic orbit for $\delta \sim 1$ remains unexplained by these considerations.

In the drag–gravity regime, the structure of homoclinic orbits corresponding to solitary waves is easily seen to follow directly from the analysis developed for the Benney equation since one can check that $\mathscr{G}(1, c) > 0$ for the Ooshida equation, as well as for the two-equation models (1.2,1.4) and (1.2,1.5). Accordingly, Δ_{I} is positive and the signatures of the fixed points are the same as for the Benney equation: fixed point $\boldsymbol{U}_{\mathrm{I}}$ is again a saddle-focus with a one-dimensional unstable manifold. Homoclinic orbits are then expected by continuity with the case of the Benney equation since the structure of the latter is recovered from these more elaborate models in the long-wavelength limit.

2.2. *Asymptotic behaviour in the drag–inertia regime*

As can be seen from figure 1, the speeds of the one-humped solitary wave solutions to Ooshida's equation (1.3) and to the two-equation models (1.2), (1.4) and (1.2), (1.5) saturate as δ increases. This is precisely what we wish to predict from a direct analysis of the dynamical system in the drag–inertia regime, $\delta \gg 1$, while attempting to construct the corresponding homoclinic orbits. As seen in figure 3, these trajectories have three different parts: two extend the linearized dynamics around $\boldsymbol{U}_{\mathrm{I}}$ to the weakly nonlinear regime and the third, in-between, accounts for the strongly nonlinear region away from $\boldsymbol{U}_{\mathrm{I}}$ where they bend back. In the course of our derivation, we will need only two empirical results: (i) that apparently smooth one-hump solitary waves do exist in the limit $\delta \to \infty$, with a monotonic rear and an oscillatory front, and (ii) that their speeds are larger than 1.

In the limit $\delta \to \infty$, the linearized dynamics around $\boldsymbol{U}_{\mathrm{I}}$ is controlled by (2.5). Setting $\lambda_1 = 2\sigma$ and $\lambda_{2,3} = -\sigma \pm \omega$, we obtain

$$\omega^2 - 3\sigma^2 = 3\,\delta\,\mathscr{G}(1, c) \qquad \text{and} \qquad 2\sigma(\sigma^2 + \omega^2) = 3(c - 1).$$

Assuming $c > 1$ as suggested by the empirical results, and thus $\mathscr{G}(1, c) > 0$, we have $\omega \sim \delta^{1/2}\sqrt{3\mathscr{G}(1, c)}$ and $\sigma \sim \delta^{-1}(c - 1)/2\mathscr{G}(1, c)$. Accordingly, the escape from $\boldsymbol{U}_{\mathrm{I}}$ along

the one-dimensional unstable manifold $\mathscr{W}_{\mathrm{I}}^{u}$ is slow and monotonic while the convergence toward $\boldsymbol{U}_{\mathrm{I}}$ along its two-dimensional stable manifold $\mathscr{W}_{\mathrm{I}}^{s}$ happens to be a slow relaxation of fast oscillations, in full agreement with empirical results.

When the trajectory has left the immediate vicinity of $\boldsymbol{U}_{\mathrm{I}}$, one must return to the complete system. Focusing on the $\delta \gg 1$ range it may be preferable to rewrite (1.9) as

$$\mathscr{G}(h, c)\, h' = -\frac{1}{\delta}\left[\tfrac{1}{3}h^3 h''' + \mathscr{H}(h, c)\right], \tag{2.9}$$

with $\mathscr{H}(h, c)$ given by (1.10). In the inviscid limit, $\delta = \infty$, one finds $\mathscr{G}(h, c)h' = 0$, so that one can define the 'critical level' as the root in h of

$$\mathscr{G}(h_{\mathrm{c}}, c) = 0, \tag{2.10}$$

at given c. This condition does not select the value of c, so let us return to the complete equation for $\delta < \infty$ in the vicinity of $h = h_{\mathrm{c}}$ whatever its value.

The homoclinic trajectory starts along the one-dimensional unstable manifold of $\boldsymbol{U}_{\mathrm{I}}$, with linear eigenvalue $2\sigma \sim \delta^{-1} \ll 1$. The dynamics along the unstable manifold can be studied by changing to the slow variable $\tilde{\xi} = \xi/\delta$, which leads to (2.9) being rewritten as

$$\mathscr{G}(h, c)h' = -\left[\mathscr{H}(h, c) + \tfrac{1}{3}\delta^{-3}h^3 h'''\right], \tag{2.11}$$

where the prime now denotes differentiation with respect to $\tilde{\xi}$. The last term in (2.11) is negligible along the first part of the trajectory corresponding to ξ (or $\tilde{\xi}$) coming from $-\infty$, i.e. the rear of the wave. So, let us develop the argument at dominant order in δ:

$$\mathscr{G}(h, c)h' = -\mathscr{H}(h, c). \tag{2.12}$$

At given c, $\mathscr{G}(1, c) > 0$ and $\mathscr{G}(h, c)$ decreases as h increases, which is easily seen from the expressions given earlier in the three cases of interest†. The dependent variable h increases with $\tilde{\xi}$ as long as $h' > 0$. Since $\mathscr{H}(h, c) < 0$ for $1 < h < h_{\mathrm{II}}$ where h_{II} is given by (2.4), h' is positive as long as $h < h_{\mathrm{II}}$ and $h < h_{\mathrm{c}}$. If for the considered value of c, $h_{\mathrm{II}} < h_{\mathrm{c}}$, no singularity occurs and h generically goes through a maximum, so that it cannot reach h_{c} at least in the rear part of the trajectory, which contradicts the assumption that we are considering one-hump solitary waves. On the other hand, if h_{c} is reached first, then a singularity takes place with h' diverging at $\tilde{\xi} = \tilde{\xi}_{\mathrm{c}}$, which now contradicts the assumption of smooth solitary waves derived from empirical evidence. The only possibility to remove the singularity is thus that $h_{\mathrm{II}} = h_{\mathrm{c}}$, in which case $\mathscr{G}$ and $\mathscr{H}$ are both zero for the same value of h, which selects the wave speed c at dominant order in δ.

Solving

$$\mathscr{G}(h_{\mathrm{II}}, c) = 0 \tag{2.13}$$

for c with h_{II} given by (2.4) yields the asymptotic values c_∞ reached by c when the limit $\delta \to \infty$ is taken. The values obtained for (1.3), (1.2), (1.4) and (1.2), (1.5) are

Ooshida's equation (1.3):	$c_\infty = \frac{9}{841}(83 + 5\sqrt{141})$	≈ 1.524,
Shkadov's model (1.2), (1.4):	$c_\infty = 1 + 1/\sqrt{6} + \sqrt{1/2 + \sqrt{2/3}}$	≈ 2.556,
Model (1.2), (1.5):	$c_\infty = \frac{1}{6}(9 + \sqrt{43 + 2\sqrt{37}})$	≈ 2.738,

in good agreement with the value obtained from the numerics (figure 1*a*). Considering the Benney equation (1.1), condition (2.13) can never be achieved since c is not present

† The result is immediate for Shkadov's model and straightforward for model (1.2), (1.5) since $c > 1$ is assumed. For the Ooshida equation the decrease only occurs for $h^2 > \frac{25}{27}c$ but this does not change the argument.

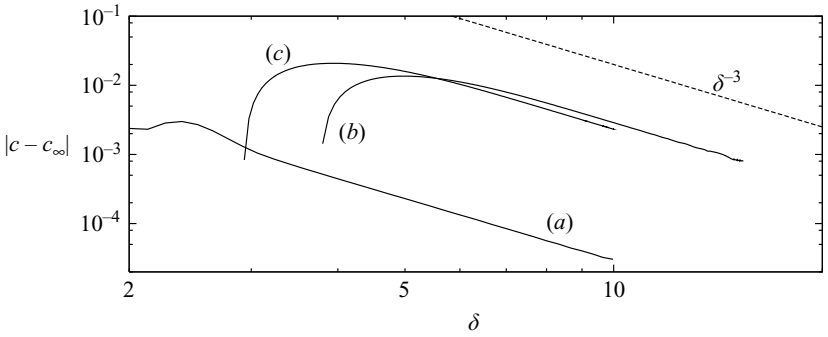

FIGURE 4. Convergence of the speed of solitary waves toward their asymptotic values c_∞ as a function of δ. (*a*) Ooshida's equation (1.3). (*b*) Shkadov's model (1.2), (1.4). (*c*) Model (1.2), (1.5).

in the expression for $\mathscr{G}$, which explains the lack of solitary wave solutions at large Reynolds numbers.

Now, when the limit $\delta \to \infty$ is not taken but δ just assumed to be large, the singularity in (2.11) remains at $h = h_c$ defined by $\mathscr{G}(h, c) = 0$. That singularity will be avoided again provided that the right-hand side is zero when $h = h_c$. In the region $h \sim h_\infty$ where $h_\infty = h_{II}(\delta \to \infty)$ as determined above, the shape of the solution has no reason to change rapidly as δ increases so that one can generically expect $h''' \sim h'''_\infty$, where $h'''_\infty \neq 0$ is the asymptotic value of the third derivative of h in $\tilde{\xi}$ (the slow variable). The condition replacing (2.13) is thus

$$\mathscr{G}(h_c(\delta), c(\delta)) = K\delta^{-3} \tag{2.14}$$

where K is a numerical constant depending on h_∞ and h'''_∞. Looking for the solution to equations (2.10) and (2.14) through their expansion around (h_∞, c_∞) yields

$$c - c_\infty \propto \delta^{-3}, \tag{2.15}$$

a convergence rate which is verified well by the numerics as shown in figure 4.

While explaining the asymptotic behaviour of the speed of one-hump solitary waves, the argument says nothing about how the trajectory bends back towards $\boldsymbol{U}_I$, so it cannot justify their existence that has thus to be taken for granted. This existence property is likely to be more difficult to prove than in the small-δ range where one can make use of Gaspard's result. In this respect, it should be noted that the critical value h_c introduced in the derivation makes sense only on the slow rear part of the wave, i.e. for the value of $\tilde{\xi}$ which achieves the critical condition for the first time when increasing from $-\infty$, since $h = h_c$ also occurs at least once in the fast oscillating front part when h decreases from its maximum value $h_m > h_c$. However the dominant term in the equation is then h''' and to deal with it one has to turn to an expression for the dynamics in terms of a fast variable $\hat{\xi} = \xi\sqrt{\delta}$ and no singularity occurs when $h \sim h_c$. The third derivative term is far from singular as long as h is bounded away from zero. Were this no longer the case, steady-state waves would no longer exist and time-dependent solutions would experience blow-up, but this is irrelevant to the models considered here, as inferred from computational evidence.

3. Summary and conclusion

We have considered one-humped solitary wave solutions to one-equation models (1.1) and (1.3), and depth-averaged two-equation models (1.2), (1.4) and (1.2), (1.5)

using the tools of dynamical system theory. These solutions all derive from similar dynamical systems, differing one from another by the expression for the inertial terms. Analytic expressions for their speed c_∞ have been obtained for the three last models and the expected cubic convergence $c - c_\infty \propto \delta^{-3}$ has been verified. The lack of one-humped solitary waves at large δ for the Benney equation (1.1) has been attributed to the absence of freedom in the expression for $\mathscr{G}$ to match condition (2.13).

In view of comparisons with experiments, the wave profile with fast oscillations preceding the hump shown in figure 3 may seem unrealistic, while such oscillations are known to be strongly damped by viscous dispersion effects. It is thus essential to observe that the result obtained here in the restricted case of films over vertical planes without viscous dispersion extends to the general case, provided that a single equation, of possibly higher order in time, can be obtained through the procedure leading to (1.9). Models derived by us (Ruyer-Quil & Manneville 2000) have been shown to yield results in good agreement with experiments at moderate Reynolds numbers for which two-dimensional solitary waves are indeed observed. This validation is therefore an important supplementary step towards the theoretical understanding of the dynamics of surface waves and the secondary patterning of flows over inclined planes.

REFERENCES

Alekseenko, S. V., Nakoryakov, V. Y. & Pokusaev, B. G. 1994 *Wave Flow of Liquid Films*. Begell House.

Benney, D. J. 1966 Long waves on liquid films. *J. Math. Phys.* **45**, 150–155.

Chang, H.-C., Demekhin, E. & Kalaidin, E. 1996 Simulation of noise-driven wave dynamics on a falling film. *AIChE J.* **42**, 1553–1568.

Doedel, E. J., Champneys, A. R., Fairgrieve, T. F., Kuznetsov, Y. A., Sandstede, B. & Wang, X.-J. 1997 Auto97: Continuation and bifurcation software for ordinary differential equations. *Tech. Rep.*. Department of Computer Science, Concordia University, Montreal, Canada, (Available by FTP from `ftp.cs.concordia.ca` in directory `pub/doedel/auto`).

Gaspard, P. 1993 Local birth of homoclinic chaos. *Physica* D **62**, 94–122.

Kapitza, P. 1948 Wave flow of thin viscous fluid layers. *Zh. Ekper. Teor. Fiz.* **18**, 3–28 (English transl. in *Collected Papers of P. L. Kapitza* (ed. Ter Haar), pp. 662–689, Pergamon, 1965).

Kapitza, P. & Kapitza, S. 1949 Wave flow of thin layers of a viscou fluid. *Zh. Ekper. Teor. Fiz.* **19**, 105–120 (English transl. in *Collected Papers of P. L. Kapitza* (ed. Ter Haar), pp. 690–709, Pergamon, 1965).

Liu, J. & Gollub, J. P. 1994 Solitary wave dynamics of film flows. *Phys. Fluids* **6**, 1702–1712.

Malamataris, N. A., Vlachogiannis, M. & Bontozoglou, V. 2002 Solitary waves on inclined films: Flow structure and binary interactions. *Phys. Fluids* **14**, 1082–1094.

Ooshida, T. 1999 Surface equation of falling film flows which is valid even far beyond the criticality. *Phys. Fluids* **11**, 3247–3269.

Pumir, A., Manneville, P. & Pomeau, Y. 1983 On solitary waves running down an inclined plane. *J. Fluid Mech.* **135**, 27–50.

Rosenau, P., Oron, A. & Hyman, J. 1992 Bounded and unbounded patterns of the Benney equation. *Phys. Fluids* A **4**, 1102–1104.

Ruyer-Quil, C. & Manneville, P. 2000 Improved modeling of flows down inclined planes. *Eur. Phys. J.* B **15**, 357–369.

Ruyer-Quil, C. & Manneville, P. 2004 Comment on "low-dimensional models for vertically falling viscous films". *Phys. Rev. Lett.* **93** (19), 199401.

Shkadov, V. 1967 Wave flow regimes of a thin layer of viscous fluid subject to gravity. *Izv. Ak. Nauk SSSR, Mekh. Zhid. Gaza* **2**, 43–51 (English transl. in *Fluid Dyn.* **2**, 29–34).

Shkadov, V. 1977 Solitary waves in a layer of viscous liquid. *Izv. Ak. Nauk SSSR, Mekh. Zhid. Gaza* **1**, 63–66.

Yih, C. S. 1955 Stability of two-dimensional parallel flows for three-dimensional disturbances. *Q. Appl. Maths* **12**, 434.

2.6 B. Scheid *et al.*, J. Fluid Mech. (2006)

J. Fluid Mech. (2006), *vol.* 562, *pp.* 183–222.
doi:10.1017/S0022112006000978 Printed in the United Kingdom

Wave patterns in film flows: modelling and three-dimensional waves

By BENOIT SCHEID[1], CHRISTIAN RUYER-QUIL[2] AND PAUL MANNEVILLE[3]

[1]Service de Chimie-Physique E.P., Université Libre de Bruxelles, C.P. 165/62, 1050 Brussels, Belgium
[2]Laboratoire FAST – UMR CNRS 7608, Campus universitaire, 91405 Orsay, France
[3]LadHyX – UMR CNRS 7646, École polytechnique, 91128 Palaiseau, France

(Received 17 June 2005 and in revised form 25 January 2006)

In a previous work, two-dimensional film flows were modelled using a weighted-residual approach that led to a four-equation model consistent at order ϵ^2. A two-equation model resulted from a subsequent simplification but at the cost of lowering the degree of the approximation to order ϵ only. A Padé approximant technique is applied here to derive a refined two-equation model consistent at order ϵ^2. This model, formulated in terms of coupled evolution equations for the film thickness h and the flow rate q, accounts for inertia effects due to the deviations of the velocity profile from the parabolic shape, and closely follows the asymptotic long-wave expansion in the appropriate limit. Comparisons of two-dimensional wave properties with experiments and direct numerical simulations show good agreement for the range of parameters in which a two-dimensional wavy motion is reported in experiments.

The stability of two-dimensional travelling waves to three-dimensional perturbations is investigated based on the extension of the models to include spanwise dependence. The secondary instability is found to be not very selective, which explains the widespread presence of the synchronous instability observed in the experiments by Liu *et al.* (1995) whereas Floquet analysis predicts a subharmonic scenario in most cases. Three-dimensional wave patterns are computed next assuming periodic boundary conditions. Transition from two- to three-dimensional flows is shown to be strongly dependent on initial conditions. The herringbone patterns, the synchronously deformed fronts and the three-dimensional solitary waves observed in experiments are recovered using our regularized model, which is found to be an excellent compromise between the complete model, which has seven equations, and the simplified model, which does not include the second-order inertia corrections. Those corrections are found to play a role in the selection of the type of secondary instability as well as of the spanwise wavelength of the emerging pattern.

1. Introduction

Thin films flowing down inclines have a rich dynamics, extensively studied for a long time since Kapitza's experimental and theoretical pioneering work at the end of the 1940s (Kapitza 1948; Kapitza & Kapitza 1949). Most of the experimental studies devoted to this problem are referred to in the book by Alekseenko, Nakoryakov & Pokusaev (1994). More recent experimental results are presented for example in Nosoko *et al.* (1996), Vlachogiannis & Bontozoglou (2001), Park & Nosoko (2003), Nosoko & Miyara (2004), and Argyriadi, Serifi & Bontozoglou (2004). At Haverford,

Gollub and coworkers have performed an extensive study of water–glycerin mixtures flowing down weakly inclined planes, see Liu & Gollub (1993), Liu, Paul & Gollub (1993), Liu & Gollub (1994), and Liu, Schneider & Gollub (1995). Controlling the entrance flow rate, they applied a periodic forcing at the inlet and observed the response of the film at a given frequency. Their experiments give the clearest picture of the phenomenology of waves on film flows. At frequencies close to but below the cut-off frequency f_c, the primary instability gives rise to saturated two-dimensional waves.† These waves are slow and present wide bumpy crests and deep thin troughs. They belong to the γ_1 family in the terminology introduced by Chang, Demekhin & Kopelevitch (1993). At low frequencies, large-amplitude solitary waves in the form of fast humps preceded by small capillary ripples emerge from the inception region. Such waves belong to the γ_2 family. By identifying the different secondary instabilities of the saturated two-dimensional waves leading to disorder, the observations of the Haverford group complete the review by Chang (1994).

The purpose of this paper is to propose an accurate model able to account for the experiments by Liu *et al.* (1995) and ultimately obtain a unified theoretical understanding of the experimental data available in the literature. The separation of scales implied by the long-wave character of the instability allows one to define a small parameter ϵ, called the *film parameter*, basically measuring the slope of the interface in order of magnitude, and to apply Prandtl's simplification of the cross-stream momentum equation, usual in boundary layer theory, which helps one to eliminate the in-depth pressure distribution dominated here by surface tension and gravity. This leads to so-called boundary-layer equations, see Chang *et al.* (1993) for a detailed presentation. These equations can be viewed as the first step of the long-wave expansion performed by Benney (1966). Modulations of the film thickness around the flat-film solution being slow in space and time, the product of the film parameter ϵ and the Reynolds number R is small as in classical lubrication theory. Inertia is thus small and consequently the velocity field stays enslaved to the film thickness. This leads to a single evolution equation for the film thickness h governing the dynamics of the flow at the onset of the instability. Several one-equation models have therefore been proposed to investigate the three-dimensional dynamics of film flows (Roskes 1969; Atherton & Homsy 1976; Roy, Roberts & Simpson 2002; Saprykin, Demekhin & Kalliadasis 2005). However, for the range of Reynolds numbers where three-dimensional wavy regimes have been reported by Liu *et al.* (1995) and Park & Nosoko (2003), one-equation models have been shown to fail, either leading to an underestimation of the wave speeds and heights, or exhibiting unphysical behaviours (Pumir, Manneville & Pomeau 1983; Ooshida 1999; Scheid *et al.* 2005*b*).

An alternative to the gradient expansion approach is to make use of the Kármán–Polhausen averaging technique as in boundary-layer theory (Schlichting 1955). This technique, which was first proposed by Kapitza (1948) and later re-investigated by Shkadov (1967), leads to a two-field model involving the film thickness h and the local flow rate q, for which the velocity field is not taken to be entirely enslaved to the film thickness. In both cases, a reduction of the dimensionality of the basic equations is achieved through the elimination of the cross-stream coordinate. The transition of film flows to three-dimensional dynamics was first theoretically investigated in this

† Two- vs. three-dimensional refers to the fluid velocity dependence. Two-dimensional flow means spanwise independent (coordinates x and y) while the surface elevation is one-dimensionally modulated (along x). On the other hand, full three-dimensional flow (x, y, z) involves two-dimensional thickness modulations (x, z).

context by Trifonov (1989). Starting from two-dimensional solutions to the Kapitza–Shkadov model computed at rest in a moving frame, he analysed their stability to transverse modulations and showed that the subharmonic instability was always the most dangerous one. The stationary three-dimensional waves bifurcating from the two-dimensional waves of the γ_1 family were shown to have transverse modulations with troughs that deepen faster than the peaks grow, which eventually produced trains of isolated depressions, as experimentally observed by Liu *et al.* (1995). Chang *et al.* (1994) attempted to complete Trifonov's study by using the boundary-layer equations. Their stability analysis of the γ_1 family predicted only the subharmonic instability, hence a scenario different from the one reported by Liu & Gollub, i.e. not accounting for the presence of the synchronous mode. Trifonov and Chang *et al.* both only considered vertical walls whereas the experiments at Haverford were performed for an inclined wall where hydrostatic pressure plays a significant role. To our knowledge, there is as yet no thorough theoretical understanding of the full experimental results and especially of the three-dimensional synchronous instability of the slow saturated γ_1 waves.

The basic set of equations and boundary conditions governing the problem is given in § 2.1, followed by a presentation of the boundary layer approximation in § 2.2. From § 3 to § 5, two-dimensional flows are considered, whereas three-dimensional flows are investigated in § 6 to § 8. Section 3 is devoted to a short presentation of the regularization method introduced by Ooshida (1999) to film flows. In § 4, we start discussing our previous extension (Ruyer-Quil & Manneville 2000) of Shkadov's approach (Shkadov 1967) (§ 4.1). An adiabatic elimination of velocity corrections (§ 4.2 and § 4.3) is next followed by an algebraic Padé-like approach (§ 4.4) aiming at a model accurate at order ϵ^2 that does not suffer from the previous limitations. The quantitative validation of the models in the two-dimensional wavy regime is considered in § 5. In § 6, we extend our models to three-dimensional flows. In § 7, we develop a standard Floquet stability analysis of the γ_1 waves corresponding to the experiments by Liu *et al.* (1995). Section 8 is dedicated to the numerical simulations of the models and a comparison with various experimental data existing in the literature. We first concentrate on the selection of the different three-dimensional wave patterns resulting from the streamwise-periodic forcing of γ_1 waves reported by Liu *et al.* (1995) (§ 8.1). The sensitivity to initial conditions is discussed and the results of the different models are compared. We next use the regularized model to study the three-dimensional instability of γ_2 waves corresponding to the experimental work by Park & Nosoko (2003) in § 8.2. Finally, the development of natural (i.e. noise-driven) three-dimensional waves is investigated, from two-dimensional wave trains to three-dimensional solitary waves, and compared to the experimental data by Alekseenko *et al.* (1994) in § 8.3. Concluding remarks and perspectives are presented in § 9.

2. Governing equations

2.1. *Primitive equations*

The flow of a Newtonian liquid down a plane making an angle β with the horizontal is considered. Coordinate x defines the streamwise direction, y denotes the direction normal to the plane, and z is along the spanwise direction (unit vectors $\boldsymbol{i}, \boldsymbol{j}, \boldsymbol{k}$ respectively); $\boldsymbol{u} \equiv u\,\boldsymbol{i} + v\,\boldsymbol{j} + w\,\boldsymbol{k}$ is the velocity field and p is the pressure. Surface tension σ, viscosity μ, and density ρ, are assumed to remain constant. The dimensionless form of the governing equations is obtained with length and time scales based on the kinematic viscosity $\nu = \mu/\rho$ and the streamwise gravitational acceleration

$g \sin\beta$ so that they depend only on the physical properties of the fluid and the inclination angle. They are

$$l_\nu = \nu^{2/3}(g \sin\beta)^{-1/3} \qquad \text{and} \qquad t_\nu = \nu^{1/3}(g \sin\beta)^{-2/3}.$$

This scaling is appropriate provided that $\sin\beta \sim O(1)$, i.e. excluding near-horizontal configurations, for which instabilities that set in are typical of wall flows, involving Tollmien–Schlichting waves of shear-viscous origin, see e.g. Floryan, Davis & Kelly (1987). The flow conditions can further be characterized by the dimensionless thickness of the flat film solution (Nusselt flow), h_N, the inclination $B = \cot\beta$ and the Kapitza number $\Gamma = \sigma/[\rho\nu^{4/3}(g \sin\beta)^{1/3}]$ which compares the surface stress σ/l_ν to the viscous stress μ/t_ν. Using these scales, the Navier–Stokes equation is

$$\partial_t \boldsymbol{u} + \boldsymbol{u}\cdot\nabla\boldsymbol{u} = \boldsymbol{i} - B\,\boldsymbol{j} - \nabla p + \nabla^2\boldsymbol{u}. \tag{2.1}$$

Above and in the following, ∂_α denotes partial differentiation with respect to variable α. The continuity equation for an incompressible flow is

$$\nabla\cdot\boldsymbol{u} = 0. \tag{2.2}$$

The evolution equations need to be supplemented with boundary conditions at the bottom plane, $y = 0$, and at the free surface, $y = h$. A quantity β evaluated at $y = \tilde{y}$ will be denoted by $\beta|_{\tilde{y}}$. The flow is thus subjected to the usual no-slip condition:

$$\boldsymbol{u}|_0 = 0. \tag{2.3}$$

The interface is governed by the kinematic condition expressing that the free surface is a material surface, that is

$$(\partial_t + \boldsymbol{u}\cdot\nabla)(h(x, z, t) - y) = 0,$$

or

$$v|_h = (\partial_t + u|_h\partial_x + w|_h\partial_z)h. \tag{2.4}$$

Finally, the stress balance at the interface is

$$-p\boldsymbol{n} + (\nabla\boldsymbol{u} + \nabla\boldsymbol{u}^T)\cdot\boldsymbol{n} = -\Gamma(\nabla\cdot\boldsymbol{n})\boldsymbol{n}, \tag{2.5}$$

where $\boldsymbol{n}$ is the unit vector normal to the free surface oriented outwards.

Alternatively, Reynolds and Weber numbers based on the entrance flow rate are often preferred though they do not clearly separate flow conditions from the fluid's physical constants. The relations between these dimensionless parameters are easily obtained by noticing that, at the entrance, the interface is flat so that the Reynolds number is related to the dimensionless Nusselt thickness h_N through an integration of the parabolic velocity profile $u \equiv y(h_\mathrm{N} - \frac{1}{2}y^2)$ over the depth. This gives

$$R \equiv q_\mathrm{N} = \tfrac{1}{3}{h_\mathrm{N}}^3, \tag{2.6}$$

where q_N is the dimensionless Nusselt flow rate. Similarly, the Weber number is related to the Kapitza number through

$$W = \Gamma {h_\mathrm{N}}^{-2}. \tag{2.7}$$

2.2. *Lubrication approximation and Shkadov's scaling*

Considering slow space and time variation, the formal parameter ϵ is introduced along with each derivation in space or time $\partial_{x,z,t} \propto \epsilon$. The assumed slow space variation implies that the velocity component normal to the plane v is much smaller than

the streamwise and spanwise components u and w as derived from the continuity equation (2.2). Consequently, the inertia terms in the y-component of the momentum equation are of higher order and can be dropped out. The remaining equation is then linear and can be integrated to give the pressure distribution up to order ϵ. After substitution of the latter and some algebra detailed in Ruyer-Quil & Manneville (1998), approximated streamwise and spanwise momentum equations are obtained.

At this stage it is convenient to proceed to the rescaling of space variables introduced by Shkadov (1977). At a given inlet flow rate, the natural scale for y is the Nusselt flat film thickness h_N, which yields the changes $(y, h) = (h_N\tilde{y}, h_N\tilde{h})$. Then balancing gravity forces and surface tension introduces the scale ratio $\kappa = (\Gamma/h_N^2)^{1/3} \equiv W^{1/3}$. Shkadov proceeded therefore to a compression of the streamwise and spanwise coordinates and took the scale for x and z as κ times the scale for y, hence the changes $x = \kappa h_N\tilde{x}$ and $z = \kappa h_N\tilde{z}$. Scaling time as $t = (\kappa/h_N)\tilde{t}$ and velocity components as $u = h_N^2\tilde{u}$, $w = h_N^2\tilde{w}$ and $v = (h_N^2/\kappa)\tilde{v}$, and dropping tildes, the rescaled streamwise momentum equation is

$$\delta[\partial_t u + \partial_x(u^2) + \partial_y(uv) + \partial_z(uw)] = 1 + \partial_{yy}u - \zeta\,\partial_x h + \partial_{xxx}h + \partial_{xzz}h + \eta[2\partial_{xx}u + \partial_{zz}u + \partial_{xz}w - \partial_x(\partial_y v\big|_h)], \quad (2.8)$$

where

$$\delta = h_N^3/\kappa = 3R\,W^{-1/3} \quad (2.9)$$

is a reduced Reynolds number. The two other reduced parameters

$$\zeta = B/\kappa = \cot\beta\,W^{-1/3} \qquad \text{and} \qquad \eta = \kappa^{-2} = W^{-2/3} \quad (2.10)$$

respectively measure the effect of the gravity component normal to the plane and the viscous second-order effects. The reduced Reynolds number introduced by Shkadov was $\delta/45$; the present choice is preferred since it leaves all numerical coefficients in the equations unchanged.

Except for the presence in (2.8) of the gravity term scaled to unity, the streamwise and spanwise momentum equations are symmetric under the exchange $\{u \leftrightarrow w, x \leftrightarrow z\}$. The rescaling of our set of equations leave the no-slip condition (2.3) and the kinematic condition (2.4) unchanged, whereas the stress balance at the free surface and in the x-direction is now at $O(\epsilon^2)$

$$\partial_y u = \eta\,[\partial_z h(\partial_z u + \partial_x w) + 2\partial_x h(2\partial_x u + \partial_z w) - \partial_x v] \quad \text{at } y = h. \quad (2.11)$$

The set of boundary conditions is then closed by the stress balance in the z-direction obtained from (2.11) through the exchange $\{u \leftrightarrow w, x \leftrightarrow z\}$. The set of equations obtained are usually referred as the second-order boundary-layer equations since the assumptions leading to them are essentially the same as those in the derivation of the Prandtl equation of boundary-layer theory, see Schlichting (1955). Within our basic assumptions, they are consistent at order ϵ^2.

The set of reduced parameters δ, ζ and η is formally equivalent to the set R, B and W (or h_N, B, Γ). An advantage of Shkadov's scaling is that it collects all second-order viscous terms into the sole parameter η. Since these terms are the only physical ones of order ϵ^2 in equations (2.8), (2.11), the truncation of the boundary-layer equations at first order leaves δ as the only parameter, provided that the wall is vertical ($\zeta = 0$), as was the case in many studies.

3. One-equation reduction and Padé-like regularization

Comparisons between existing models and the subsequent discussion about improvements needed can be made simpler if the spanwise dependence of the fields is disregarded. Accordingly, from this section up to § 6, we focus on two-dimensional flows ($\partial_z \equiv 0$, $w \equiv 0$).

A gradient expansion of the basic equations or the boundary-layer equations leads to identical results up to order ϵ^2. Such an expansion of the basic equations was first done by Benney (1966) and next completed by Lin (1974) and Nakaya (1975). Benney showed that the velocity field $\boldsymbol{u}$ can be written as a series of polynomials in y, i.e. $\boldsymbol{u} = \sum_n \boldsymbol{A}_n(h) P_n(y)$, where the coefficients $\boldsymbol{A}_n$ are functions of the thickness h and its space–time derivatives, which means that, in this limit, the velocity field is completely enslaved to the dynamics of h. Integration of the continuity equation across the layer leads to the exact mass balance equation:

$$\partial_t h + \partial_x q = 0, \tag{3.1}$$

where $q = \int_0^h u \, \mathrm{d}y$ is the local flow rate. The gradient expansion of the momentum balance equation next gives an approximate expression for the flow rate as function of h and its derivatives. This expression can be further simplified by using the zeroth-order relation $q^{(0)} = \frac{1}{3}h^3$ to exchange the time derivative of h with its space derivative through

$$\partial_t h = -h^2 \partial_x h, \tag{3.2}$$

which is the equation governing kinematic waves at the interface (Whitham 1974). Gjevik (1970, 1971) thus studied the following equation:

$$\partial_t h + \tfrac{1}{3}\partial_x \left\{ h^3 + \tfrac{2}{35}\delta \partial_x(h^7) - \tfrac{1}{4}\zeta \partial_x(h^4) + h^3 \partial_{xxx} h \right\} = 0, \tag{3.3}$$

generally called the Benney equation.

The relevance of this equation beyond a narrow neighbourhood of the threshold is first limited by the fact that linear stability properties of the flat film solution rapidly depart from those derived from the exact Orr–Sommerfeld (OS) equation, i.e. the range of unstable wavenumbers predicted by (3.3) is much wider than that emerging from the solution of the OS equation. This first limitation seems related to the neglect of the second-order streamwise dissipative terms as shown by Panga & Balakotaiah (2003). Taking only them into account, Panga & Balakotaiah obtained an equation which, within current scalings, is

$$\partial_t h + \tfrac{1}{3}\partial_x \left\{ h^3 - \tfrac{1}{8}\delta \, \partial_t(h^5) - \tfrac{9}{280}\delta \partial_x(h^7) - \tfrac{1}{4}\zeta \partial_x(h^4) + h^3 \partial_{xxx} h + \eta[3h^4 \partial_{xx} h + 7h^3 (\partial_x h)^2] \right\} = 0. \tag{3.4}$$

Panga & Balakotaiah avoided the exchange of the time and space derivatives through (3.2) and showed that the exact OS results are then recovered with better accuracy. Unfortunately, this correction does not cure the second well-known limitation of the Benney equation (3.3), that is, the existence of finite-time blow-up of its solutions beyond some limiting value of the Reynolds number not far beyond threshold (Pumir *et al.* 1983; Scheid *et al.* 2005*b*) since (3.4) also suffers from finite-time blow-up of solutions somewhat beyond threshold (Ruyer-Quil & Manneville 2004). Pumir *et al.* (1983) showed in particular that the finite-time blow-up of time-dependent solutions closely corresponds to the loss of one-hump solitary waves, i.e. *homoclinic* orbits in the terminology of dynamical systems theory. Our experience with similar but more complicated equations (Ruyer-Quil 1999) suggests this that loss of what is called the

'principal homoclinic orbit' by Glendinning & Sparrow (1984) is accompanied by a blow-up of time-dependent solutions.

In order to remedy this deficiency, Ooshida (1999) developed a resummation method inspired by the Padé approximant technique. The latter relies on the idea that the divergence of a power series $Q = \sum_k Q_k x^k$ is due to the hidden presence of poles. This leads one to express Q in an approximate way as a ratio F/G of polynomials F and G where the zeros of G are assumed to capture the causes of the divergence. Adjusting the coefficients introduced in $F = F_0 + F_1 x + F_2 x^2 \ldots$ and $G = 1 + G_1 x + G_2 x^2 + \ldots$ so that the terms in the series Q are reproduced exactly up to some given degree is the essence of the approximation, the ratio F/G being used in place of Q. In this algebraic implementation, the degrees of the polynomials F and G are open to free choice, the number of coefficients to be determined remaining compatible with the number of coefficients available in the series Q.

Ooshida translated this idea to the present case by introducing a regularization operator $\mathscr{G} = \mathscr{I} + \mathscr{G}^{(1)} + \mathscr{G}^{(2)}$, where $\mathscr{I}$ is the identity, $\mathscr{G}^{(1)} = G^{(1)}(h)\partial_x$, and $\mathscr{G}^{(2)} = G^{(2)}(h)\partial_{xx}$, so that the expansion of q as a function of h and its derivatives from the long-wave expansion, formally written as $q \equiv \mathscr{Q}(h)$, is rewritten as $\mathscr{G}^{-1}\mathscr{F}$. Ooshida chose to adjust 'coefficients' $\mathscr{G}^{(1)}$ and $\mathscr{G}^{(2)}$ in $\mathscr{G}$ so that $\mathscr{G}\mathscr{Q} = \mathscr{F}$ could be reduced to $q^{(0)} + \mathscr{F}^{(1)}$, i.e. $\mathscr{F}^{(2)} \equiv 0$, which yielded

$$\mathscr{G} = 1 - \tfrac{10}{21}\delta h^4 \partial_x - \eta h^2 \partial_{xx}.$$

Computation of the regularized identity $\partial_x(\mathscr{G}\mathscr{Q}) \equiv \partial_x \mathscr{F}$ with the replacement of $\partial_x \mathscr{Q}$ by $-\partial_t h$ using (3.1) led him to the equation

$$\partial_t h + \tfrac{1}{3}\partial_x \left\{ h^3 - 3\eta\, h^2 \partial_{xt} h - \tfrac{2}{7}\delta\, \partial_t(h^5) - \tfrac{36}{245}\delta \partial_x(h^7) - \tfrac{1}{4}\zeta\, \partial_x(h^4) + h^3 \partial_{xxx} h \right\} = 0. \quad (3.5)$$

Ooshida's formulation remedies the possible blow-up of time-dependent solutions observed with (3.3) but (3.5) grossly underestimates the amplitudes and speeds of the solitary waves. Panga, Mudunuri & Balakotaiah (2005) attempted to apply Ooshida's idea to regularize equation (3.4) which led them to an expression for q as function of h and $\partial_t q$, which can be recast as an evolution equation for q:

$$\delta\, \partial_t q = \tfrac{8}{5} h - \tfrac{24}{5}\frac{q}{h^2} - \tfrac{9}{25}\delta h^4 \partial_x h - \tfrac{8}{5}\zeta h \partial_x h + \tfrac{8}{5} h \partial_{xxx} h + \eta \left[\tfrac{56}{5} h (\partial_x h)^2 + \tfrac{24}{5} h^2 \partial_{xx} h \right]. \quad (3.6)$$

Equation (3.6) must be completed by the mass conservation equation (3.1) and is referred to hereafter as the PMB model. As a consequence, the flow rate q is no longer slaved to the evolution of the thickness h which indicates that q must be recognized as an independent degree of freedom (Balakotaiah & Mudunuri 2004).

Once it is recognized that some freedom should be given back to the velocity field, this idea should be implemented from the beginning, which calls for a different approach if we require accurate modelling in the largest possible range of Reynolds numbers and not only in the neighbourhood of the instability threshold, i.e. also in what Ooshida called the 'drag–inertia' regime that takes place when inertia plays a more significant role at large δ, as opposed to the 'drag–gravity' regime taking place at small δ and corresponding to a balance between viscous drag on the wall and gravitational acceleration, for which the classical long-wave expansion is expected to be valid.

4. Weighted residual modelling

4.1. *General formulation*

The difficulty with modelling in terms of a single equation is that keeping a single dependent variable, namely h, is not sufficient to account for the dynamics of the film, though the perturbations may well remain long wave. At every step of the asymptotic expansion, the velocity profile is assumed to have no dynamics of its own but to be strictly enslaved to h by equations where the time dependence only comes through that of h. This is justified only as long as the evolution rate of velocity modes, of order unity due to the viscous damping over the thickness, can be considered as large when compared to the evolution rate of h, of order ϵ. Beyond threshold (ϵ finite) this assumption fails, which can be interpreted as a sign of a revolt of enslaved degrees of freedom. The dynamics of the flow can then no longer be described through the evolution of a single field for the film thickness and other variables must be considered, e.g. the local flow rate q, the stress at the wall, etc.

This discrepancy motivated two of us to re-investigate Shkadov's approach (Shkadov 1967) and pursue his original suggestion of expanding the velocity field on a polynomial basis (Ruyer-Quil & Manneville 2000). The first term of this expansion was taken to be $g_0(y) = y - \frac{1}{2}y^2$, the flat-film parabolic velocity profile. We showed that first-order corrections to the parabolic velocity distribution could be described entirely with the help of only two more polynomials of degree four and six, g_1 and g_2, the definition of which are given in Appendix A. We next proceeded to a Galerkin projection retaining terms up to order ϵ^2. Writing the streamwise momentum balance formally as $BL(u) = 0$, the residuals are $\mathscr{R}_i(u) = \langle BL(u),\ g_i(y)\rangle$, where $\langle f,\ g\rangle = \int_0^h f\,g\,\mathrm{d}y$ refers to the scalar product derived from the plain $\mathscr{L}^2$ norm. Setting the three residuals $\mathscr{R}_i(u)$ to zero formed a system of three evolution equations for the three unknowns q, r and s, whose extension to the three-dimensional case is given in Appendix C as (C 1 *a–c*). System (C 1) is completed with the mass balance (3.1), and referred hereafter as the *complete second-order model*.

The theoretical analysis and the numerical integration of models such as the complete model are indeed simpler than the corresponding study of the full Navier–Stokes problem, or even of the boundary-layer formulation. Handling the four fields of (3.1), (C 1) still remains a difficult task, and a reliable two-field formulation consistent at order ϵ^2 would be welcome. At this stage setting r and s to zero in $\mathscr{R}_0$ lowers the order of the approximation. This procedure leads to a simplified averaged momentum equation

$$\delta\,\partial_t q = \frac{5}{6}h - \frac{5}{2}\frac{q}{h^2} + \delta\left[\frac{9}{7}\frac{q^2}{h^2}\partial_x h - \frac{17}{7}\frac{q}{h}\partial_x q\right] - \frac{5}{6}\zeta h\partial_x h + \frac{5}{6}h\partial_{xxx}h + \eta\left[4\frac{q}{h^2}(\partial_x h)^2 - \frac{9}{2h}\partial_x q\,\partial_x h - 6\frac{q}{h}\partial_{xx}h + \frac{9}{2}\partial_{xx}q\right]. \tag{4.1}$$

The set of equations to be solved is next closed by the mass conservation equation (3.1). Our simplified model was shown to predict the correct linear stability threshold. However, contrary to the gradient expansion of the complete model, the gradient expansion of (4.1) failed to reproduce the exact expression of the flow rate q as function of h at order ϵ^2. As a matter of fact, results differ only through the coefficient of the first inertia term, which is $\frac{212}{525}$ instead of the exact value $\frac{127}{315}$ (Ruyer-Quil & Manneville 2000). One should not be fooled by the apparent smallness of the differences between these coefficients. As shown in the next subsection, if small

numerical coefficients are associated with the second-order inertia terms, they contain nonlinearities of high order, the effects of which become noticeable for δ of order unity or higher.

We develop below a consistent elimination strategy for r and s aimed at a two-equation model taking an exact account of the gradient expansion up to order ϵ^2.

4.2. *Reduction of the full second-order model*

A simple argument can be given here to justify the pertinence of the elimination of the corrections to the parabolic velocity distribution, r and s. Since viscosity acts so as to ensure the in-depth coherence of the flow, fluctuations of the flow field varying rapidly in the wall-normal direction are efficiently damped by viscosity, so that r and s corresponding to high-degree polynomials should relax rapidly towards the values forced by the evolution of h and q. This can be observed simply by linearizing system (C 1) around the Nusselt flow in the zero-wavenumber limit, that is, assuming no spatial variations. The mass balance (3.1) thus implies a constant thickness. Writing $q = 1/3 + \varepsilon\tilde{q}$, $r = \varepsilon\tilde{r}$ and $s = \varepsilon\tilde{s}$ where $\varepsilon \ll 1$, we obtain

$$\delta \frac{\mathrm{d}\tilde{\boldsymbol{V}}}{\mathrm{d}t} = \boldsymbol{M}\,\tilde{\boldsymbol{V}}, \tag{4.2}$$

where $\tilde{\boldsymbol{V}} = (\tilde{q},\ \tilde{r},\ \tilde{s})^t$ and $\boldsymbol{M}$ is a 3×3 matrix whose eigenvalues λ_i are respectively -2.47, -22.3, and -87.7. Because of the large gap between λ_1 and $(\lambda_2,\ \lambda_3)$, it is obvious that, at low Reynolds number and provided that the long-wave assumption is valid, the dynamics of the flow is governed by the neutral mode associated with the free-surface elevation and the eigenmode corresponding to λ_1, with eigenvector $(\tilde{q},\ \tilde{r},\ \tilde{s})^t = (1.00, -1.33\,10^{-2}, 1.38\,10^{-4})^t$. Consequently and given that the associated eigenvector is nearly aligned with the first vector of the natural basis, r and s are truly slaved to the dynamics of the thickness h and the flow rate q, at least close to the threshold.

Having justified the elimination of r and s, let us go back to its practical implementation. Fields r and s are corrections to the flat-film parabolic profile corresponding to g_0. So, they are at least first-order terms produced by the deformation of the free surface. In the first residual $\mathscr{R}_0$ associated with the weight g_0, r and s appear through inertia terms involving their space and time derivatives or through products with derivatives of h and q, which are terms of order ϵ^2. Indeed, the corrections to the velocity field cannot appear in $\mathscr{R}_0$ at lowest order since the evaluation of the viscous term $\int_0^h g_0(y/h)\partial_{yy}u\,\mathrm{d}y$ yields $\frac{1}{2}\partial_y u|_{y=h} - q/h^2$, owing to the definition of $q = \int_0^h u\,\mathrm{d}y$, and that $\frac{1}{2}\partial_y u|_{y=h}$ is already of order ϵ^2, as seen from (2.11) that expresses the stress balance at the free surface.

At this stage, it remains to determine the expression for r and s as functions of h, q and their derivatives truncated at order ϵ. Such relations can easily be obtained by dropping all second-order terms from the two last residuals $\mathscr{R}_1$ and $\mathscr{R}_2$ and then solving for r and s.

$$r = \delta\left[\frac{1}{210}h^2\partial_t q - \frac{19}{1925}q^2\partial_x h + \frac{74}{5775}hq\partial_x q\right] + O(\epsilon^2), \tag{4.3a}$$

$$s = \delta\left[\frac{2}{5775}q^2\partial_x h - \frac{2}{17325}hq\partial_x q\right] + O(\epsilon^2). \tag{4.3b}$$

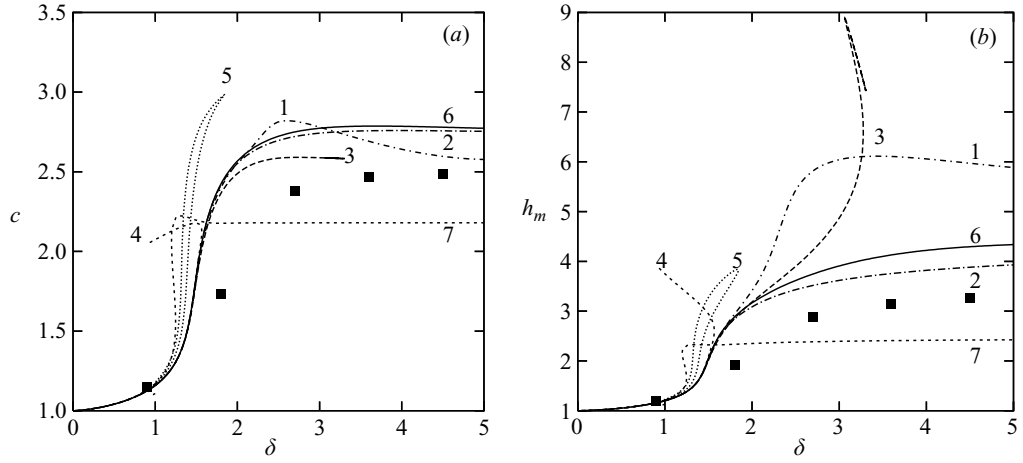

FIGURE 1. (*a*) Speed c and (*b*) amplitude h_{m} of the principal homoclinic orbits as functions of the reduced Reynolds number δ. The wall is vertical and streamwise viscous dissipation is omitted ($\zeta = \eta = 0$). Curve 1: complete second-order model (3.1), (C 1); 2: simplified model (3.1), (4.1); 3: (3.1), (4.4) with $\mathscr{K}$ given by (4.5); 4: with $\mathscr{K}$ given by (4.7); 5: with $\mathscr{K}$ given by (4.8); 6: regularized model (3.1), (4.15); 7: PMB model (3.1), (3.6); filled squares: solutions to the first-order boundary-layer equations after Chang *et al.* (1996).

Substitution of (4.3) into $\mathscr{R}_0$ finally gives

$$\delta\,\partial_t q = \frac{5}{6}h - \frac{5}{2}\frac{q}{h^2} + \delta\left[\frac{9}{7}\frac{q^2}{h^2}\partial_x h - \frac{17}{7}\frac{q}{h}\partial_x q\right] + \delta^2\mathscr{K}(h,\,q) + \eta\left[4\frac{q}{h^2}(\partial_x h)^2 - \frac{9}{2h}\partial_x q\,\partial_x h - 6\frac{q}{h}\partial_{xx}h + \frac{9}{2}\partial_{xx}q\right] - \frac{5}{6}\zeta h\partial_x h + \frac{5}{6}h\partial_{xxx}h, \quad (4.4)$$

where the additional terms arising from the elimination of r and s are second-order inertia terms all collected in $\mathscr{K}$:

$$\mathscr{K} = \frac{1}{210}h^2\partial_{tt}q - \frac{1}{105}q\,\partial_x h\partial_t q + \frac{1}{42}h\partial_x q\,\partial_t q + \frac{17}{630}hq\,\partial_{xt}q + \frac{653}{8085}q(\partial_x q)^2 - \frac{78}{2695}\frac{q^3}{h}\partial_{xx}h - \frac{26}{231}\frac{q^2}{h}\partial_x h\partial_x q + \frac{386}{8085}q^2\partial_{xx}q + \frac{104}{2695}\frac{q^3}{h^2}(\partial_x h)^2. \quad (4.5)$$

4.3. *Effective inertial correction terms*

Obviously, these corrections are highly nonlinear. They also contain time derivatives that are difficult to handle, at least in numerical simulations. Fortunately, the zeroth-order relation between q and h

$$q = \tfrac{1}{3}h^3, \quad (4.6)$$

allows us to simplify the expression for $\mathscr{K}$. Using also $\partial_t h = -h^2\partial_x h + O(\epsilon^2)$, we obtain the more compact expression

$$\mathscr{K} = -\tfrac{1}{630}h^7(\partial_x h)^2. \quad (4.7)$$

The behaviour of the solutions to equation (4.4) where the inertia corrections $\mathscr{K}$ are given by (4.5) or (4.7) have been tested in the drag–inertia regime by computing the one-hump solitary-wave solutions for a vertical wall and neglecting second-order viscous effects ($\eta = 0$) as explained at the beginning of § 5. Figure 1 displays the speed and amplitude of the solitary waves as a function of the reduced Reynolds number δ. They are compared to the solutions to the complete second-order model (3.1), (C 1)

as curves 1, to the simplified model (3.1), (4.1) as curves 2, to the PMB model (3.1), (3.6) as curves 7, and to the results obtained by Chang, Demekhin & Kalaidin (1996) with the first-order boundary-layer equations as filled squares.

The simplified model and the complete second-order model both exhibit unique one-hump solitary-wave solutions at given δ and have speed in reasonable agreement with the results of Chang *et al.* On the contrary, the branch of principal homoclinic solutions is seen to turn back in the transition region between the drag–gravity and the drag–inertia regimes ($\delta \sim 1$) with both expressions (4.5) and (4.7) for $\mathscr{K}$ (curves 3 and 4 in figure 1). This unphysical behaviour is similar to the one encountered with the Benney equation (3.3) and is likely to be related to the high-degree nonlinearities present in (4.5) and (4.7). The same difficulty as in the case of surface equations arises and calls for a formulation in which inertia effects are accurately accounted for in the widest possible range of reduced Reynolds numbers δ.

Other forms of the second-order inertia corrections $\mathscr{K}$ can be obtained by using the flat-film relation (4.6). For example, Roberts (1996) has applied a centre manifold analysis to the problem of a falling film and derived a second-order model in terms of the film thickness h and the depth-averaged velocity equivalent to the flow rate q. His approach relied on the linear viscous dissipating modes of the streamwise-uniform film in the zero-wavenumber limit, which is basically a reduction of the slow time and space evolution of the film to the two first eigenmodes $(h,\ u) \propto (1,\ 0)$ and $(h,\ u) \propto (0, \sin(\pi y/(2h)))$. His model is similar to those obtained using the classical depth-averaged method with coefficients close to those appearing in (4.4). As noticed by Ooshida (1999), this agreement can be understood from the fact that the velocity profile $u_{\rm rob} \propto \sin(\pi y/(2h))$ is very close to the parabolic profile since $\langle u_{\rm rob}, g_0\rangle/\sqrt{\langle u_{\rm rob}, u_{\rm rob}\rangle\langle g_0, g_0\rangle} \approx 0.999$. Inertia corrections obtained by Roberts are

$$\mathscr{K} = \frac{1}{100}\left(-0.1961\,\frac{q^3}{h^2}(\partial_x h)^2 - 1.78\,\frac{q^2}{h}\partial_x h\partial_x q + 0.1226\,q(\partial_x q)^2 \right.$$
$$\left. - 1.792\,\frac{q^3}{h}\partial_{xx} h + 0.7778\,q^2\partial_{xx} q \right). \tag{4.8}$$

The results obtained with this expression for $\mathscr{K}$ are also displayed in figure 1 as curves 5. A loss of solutions is once more observed at $\delta \approx 2$, a failure due to the fact that $\mathscr{K}$ is obtained from a perturbation method which is strictly valid only in the drag–gravity regime where inertia has a perturbative role only. Our derivations of (4.4) with $\mathscr{K}$ given by (4.5) or (4.7) are also based on perturbative techniques applied to the Nusselt flat-film solution. However, the presence of the principal homoclinic solutions to the simplified model (3.1), (4.1) for all δ shows that it should be possible to describe the drag–inertia regime at low cost in terms of a model including the second-order inertial effects and involving h and q only.

4.4. *Padé-like regularization*

Here, we follow a procedure more closely inspired by the Padé approximant technique than Ooshida's, by looking for a kind of algebraic preconditioner able to remove the dangerous second-order terms of inertia origin (in δ^2). Instead of thinking in terms of an expansion of the flow rate q, we consider the residual $\mathscr{R}_0$ obtained by averaging the momentum equation (2.8) with weight g_0, which can be written as a series in ϵ, $\mathscr{R}_0^{(0)} + \mathscr{R}_0^{(1)} + \mathscr{R}_0^{(2),\eta} + \mathscr{R}_0^{(2),\delta}$. In the second-order terms of this expansion, we have isolated those having a viscous origin (superscript η) from those accounting for the convective acceleration induced by the deviations of the velocity profile from the

parabolic shape (superscript δ). The simplified equation (4.1) is recovered just by neglecting $\mathscr{R}_0^{(2),\delta}$. So $\mathscr{R}_0$ is sought in the form $\mathscr{G}^{-1}\mathscr{F}$ where $\mathscr{G}$ is now simply a function of h, q and their derivatives, and $\mathscr{F}$ is reduced to $\mathscr{R}_0^{(0)}+\mathscr{R}_0^{(1)}+\mathscr{R}_0^{(2),\eta}$, i.e. the residual that was obtained assuming a parabolic velocity profile. Setting $\mathscr{F}=\mathscr{G}\mathscr{R}_0$ to zero gives

$$\delta\,\mathscr{G}(h,q)\int_0^h g_0(y/h)[\partial_t u+u\partial_x u+v\partial_y u]\,\mathrm{d}y$$
$$=\mathscr{G}(h,q)\int_0^h g_0(y/h)\{1+\partial_{yy}u-\zeta\,\partial_x h+\partial_{xxx}h+\eta(2\partial_{xx}u-\partial_x[\partial_y v|_h])\}\,\mathrm{d}y, \qquad (4.9)$$

where inertia terms isolated on the left-hand side are

$$\delta\mathscr{G}\int_0^h g_0(y/h)[\partial_t u+u\partial_x u+v\partial_y u]\,\mathrm{d}y$$
$$=\delta\mathscr{G}\left\{\left[\frac{2}{5}\partial_t q-\frac{18}{35}\frac{q^2}{h^2}\partial_x h+\frac{34}{35}\frac{q}{h}\partial_x q\right]-\frac{2}{5}\delta\mathscr{K}\right\}\equiv\mathscr{G}\left\{\mathscr{R}_0^{(1),\delta}+\mathscr{R}_0^{(2),\delta}\right\}, \qquad (4.10)$$

which we want to identify with

$$\delta\left[\frac{2}{5}\partial_t q-\frac{18}{35}\frac{q^2}{h^2}\partial_x h+\frac{34}{35}\frac{q}{h}\partial_x q\right]\equiv\mathscr{R}_0^{(1),\delta}. \qquad (4.11)$$

This leads to taking the regularization factor as

$$\mathscr{G}=\left[1+\frac{\mathscr{R}_0^{(2),\delta}}{\mathscr{R}_0^{(1),\delta}}\right]^{-1}. \qquad (4.12)$$

An asymptotically equivalent expression for $\mathscr{G}$ can be found using $q=h^3/3+O(\epsilon)$, and $\partial_t h=-h^2\partial_x h+O(\epsilon^2)$. We then obtain

$$\mathscr{R}_0^{(1),\delta}=-\frac{2}{15}\delta h^4\partial_x h+O(\epsilon^2)\qquad\text{and}\qquad\mathscr{R}_0^{(2),\delta}=\frac{\delta^2}{1575}h^7(\partial_x h)^2+O(\epsilon^3),$$

which, when substituted in (4.12), yields

$$\mathscr{G}=\left[1-\frac{\delta}{210}h^3\partial_x h\right]^{-1}+O(\epsilon^2). \qquad (4.13)$$

In order to lower the degree of nonlinearity as much as possible, $\mathscr{G}$ is finally rewritten in terms of the local slope $\partial_x h$ and the local Reynolds number $\delta\,q$:

$$\mathscr{G}=\left[1-\frac{\delta}{70}q\,\partial_x h\right]^{-1}. \qquad (4.14)$$

The resulting set of equations is

$$\delta\,\partial_t q=\delta\left[\frac{9}{7}\frac{q^2}{h^2}\partial_x h-\frac{17}{7}\frac{q}{h}\partial_x q\right]$$
$$+\left\{\frac{5}{6}h-\frac{5}{2}\frac{q}{h^2}+\eta\left[4\frac{q}{h^2}(\partial_x h)^2-\frac{9}{2h}\partial_x q\,\partial_x h-6\frac{q}{h}\partial_{xx}h+\frac{9}{2}\partial_{xx}q\right]\right.$$
$$\left.-\frac{5}{6}\zeta h\partial_x h+\frac{5}{6}h\partial_{xxx}h\right\}\left[1-\frac{\delta}{70}q\,\partial_x h\right]^{-1}, \qquad (4.15)$$

along with the mass balance equation (3.1).

Hereafter, the system (3.1), (4.15) will be referred to as the *regularized model*. Homoclinic orbits corresponding to one-hump solitary-wave solutions to (3.1), (4.15) have been computed and are displayed as curves 6 in figure 1. Non-physical turning back of the curves has never been observed for all the values of δ studied. Moreover, system (3.1), (4.15) is fully consistent at second order with the Benney expansion and takes into account modifications of the momentum balance of the film induced by the deviations of the velocity profile from the parabolic Nusselt solution.

5. Validation

Periodic waves at rest in their moving frame $\xi = x - c\,t$, where c is the wave speed, have been computed by continuation using AUTO97, which, together with its package HOMCONT (Doedel *et al.* 1997) has been used extensively to obtain numerical results. Their characteristics are then compared to available DNS results (Salamon, Armstrong & Brown 1994; Ramaswamy, Chippada & Joo 1996; Malamataris, Vlachogiannis & Bontozoglou 2002) and laboratory experiments (Liu & Gollub 1994). For stationary waves, the mass conservation equation (3.1) can be integrated once to give

$$q = c\,h + q_0, \tag{5.1}$$

where q_0 is an integration constant corresponding to the conservation of the flow rate in the moving frame. Denoting by $\langle\cdot\rangle = \Lambda^{-1}\int_0^{\Lambda}(\cdot)\,\mathrm{d}\xi$ the average operator over a wavelength Λ in the moving frame, the constant q_0 is adjusted at every step of the continuation procedure to ensure either $\langle h\rangle = 1$ or $\langle q\rangle = 1/3$. The constant-thickness formulation corresponds to the periodic-boundary conditions often used in numerical simulations, whereas the constant-flux formulation is encountered when the spatial development of a time-periodic signal is considered (Scheid *et al.* 2005*b*).

5.1. *Comparisons to direct numerical simulations*

Salamon *et al.* (1994) have performed a systematic analysis of the two travelling-wave branches of slow γ_1 and fast γ_2 solutions observed experimentally. Their numerical scheme enforces a constant averaged thickness $\langle h\rangle = 1$. In figure 2, we reproduce the bifurcation diagrams in the parameter space (speed c, wavenumber k) for the largest value of the reduced Reynolds number δ tested by these authors, $\delta = 2.79$ (Salamon *et al.* 1994, figures 15 and 17). For weak viscous diffusion $\eta = 0.015$, the γ_1 family emerges from a Hopf bifurcation of the Nusselt flat-film solution at the marginal wavenumber $k_c \approx 1.02$, whereas the γ_2 family bifurcates from the γ_1 branch by period doubling at a wavenumber close to $k_c/2$. At a larger viscous diffusion $\eta = 0.075$, the situation is reversed. Computations with our regularized model (3.1), (4.15) are compared to findings by Salamon *et al.* in figure 2, showing excellent agreement. Wave profiles and streamlines in the moving frame of reference are also displayed. As can be observed from the DNS by Salamon *et al.* the capillary oscillations following the γ_1 waves or preceding the γ_2 waves are damped by viscous diffusion (Salamon *et al.* 1994, figures 16 and 18).

Travelling waves obtained by DNS when a periodical forcing is simulated at inlet correspond to the constant-flux formulation $\langle q\rangle = 1/3$. Our results are displayed in figure 3 together with the corresponding numerical solution obtained by Malamataris *et al.* (2002) and the results from the PMB model. Parameters are those of the experiment by Liu & Gollub (1994) with $\beta = 6.4^\circ$, $R = 19.33$, $\Gamma = 526$, and forcing

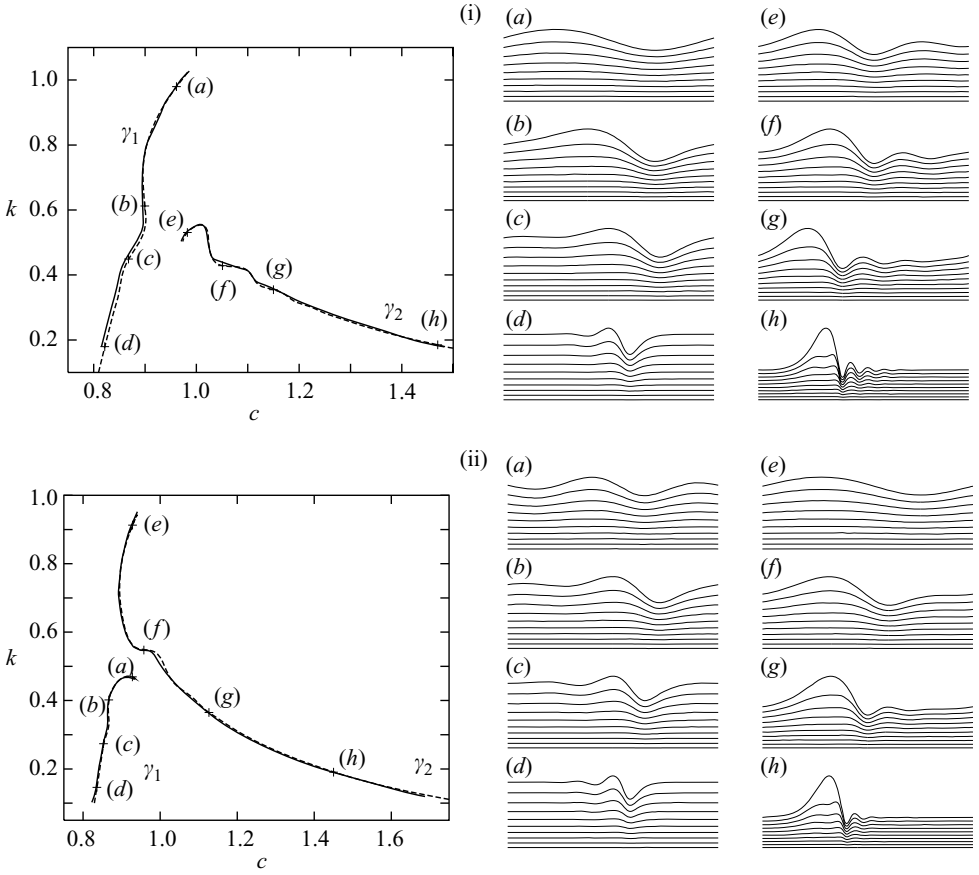

FIGURE 2. Travelling-wave families γ_1 and γ_2. Dashed lines refer to solutions to the regularized model (3.1), (4.15), whereas solid lines refer to the results from DNS (after Salamon *et al.* 1994). Left: speed c as function of the wavenumber k; right: wave profiles and streamlines in the moving frame of reference for wave families γ_1 (labels a to d) and γ_2 (labels e to h). (i) $\delta = 2.79$, $\zeta = 0$ and $\eta = 0.015$ ($R = 7.59$ and $\Gamma = 4374$); (ii) $\delta = 2.79$, $\zeta = 0$ and $\eta = 0.075$ ($R = 3.40$ and $\Gamma = 228.8$).

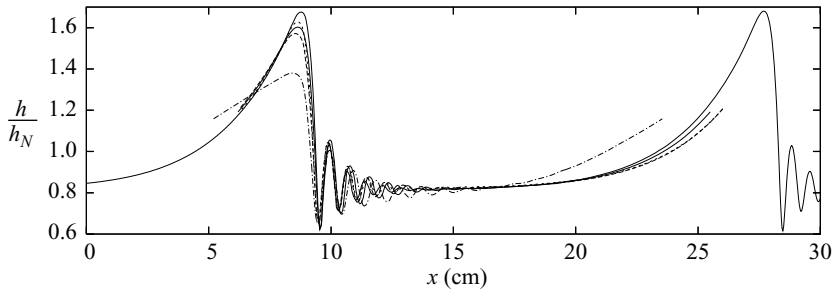

FIGURE 3. Travelling wave train approaching solitary waves corresponding to an experiment by Liu & Gollub (1994). The forcing frequency is $f = 1.5$ Hz. Parameters are $\beta = 6.4°$, $R = 19.33$ and $\Gamma = 526$ ($\delta = 17.7$, $\zeta = 2.72$ and $\eta = 0.093$). The thin solid line shows the numerical computation by Malamataris *et al.* (2002). Results of the regularized (simplified) model correspond to the thick solid (dashed) line. The solution to the complete second-order model is the dotted line and the solution to the PMB model is the dashed-dotted line.

frequency $f = 1.5$ Hz. Results of our models are in excellent agreement with the DNS results, predicting a wave amplitude that is slightly smaller than the one given by the Navier–Stokes equations. The complete model gives the closest answer whereas the amplitude of the solution to the simplified model is significantly lower. As could be expected, the prediction of the regularized model lies somewhere in between. Regarding wavelengths, the regularized model gives a value closer to that given by Malamataris' computation than the simplified and the complete second-order models. Sharing the main characteristics of the solitary waves obtained by Ooshida, unsurprisingly the solutions to the PMB model (3.1), (3.6) capture their properties much less faithfully than those obtained from our regularization procedure.

Malamataris *et al.* (2002) questioned the similarity assumption of a parabolic velocity profile. They showed that significant differences could be found in the case of large solitary waves. Deviations from the parabolic profile were mostly located in front of the main hump and behind the first capillary ripple, where gradients of the film thickness are the largest. They also proved the occurrence of a counterflow ($u < 0$) in the region bracketing the thickness minimum. This feature, confirmed in the experiments by Tihon *et al.* (2003), is reproduced well in our models. We have reconstructed the streamwise velocity distributions based on expansions truncated beyond the three first polynomials g_0, g_1 and g_2 (see Appendix A for details) at regularly spaced locations around that minimum and for the wave train shown in figure 3. Corresponding profiles are displayed in figure 4 for the complete second-order model (*b*, *d*) and the regularized model (*a*, *c*). The presence of a counterflow is recovered in both cases. The similarity with DNS results is particularly convincing for the complete second-order model both at behind the first ripple and in front of the main hump (figure 4 compared to figure 7 in Malamataris *et al.* (2002); even the two inflection points they observed are recovered). For the regularized model, comparisons remain satisfactory everywhere except at the front of the main hump where the gradients are the largest. This implies that a reconstruction of the velocity field based on the expressions at first order for r and s given by (4.3) is no longer sufficient there, whereas the agreement is re-obtained once the slope of the interface is less steep.

The streamlines in the moving frame of reference, i.e. the isocontours of the streamfunction $\int_0^y (u - c)\,\mathrm{d}y$, show little difference whether the complete or the regularized model is considered (the streamlines computed with the regularized model are shown in figure 4*e*). The reason is that, at the thickness minimum where the relative deviations away from the parabolic profile are noticeable, the streamwise velocity u is also small, so that in a reference frame moving at the speed of the wave, the velocity $u - c$ remains everywhere close to that corresponding to a parabolic profile.

5.2. *Comparisons to experiments*

To complete the validation of our models, we present results for the speeds and amplitudes of solitary waves corresponding to experimental conditions considered by Liu & Gollub (1994) for an inclined plane at a fixed angle $\beta = 8^\circ$ using a glycerin–water mixture ($\Gamma = 488$), and at different Reynolds numbers. The experimental findings are compared to the corresponding travelling-wave results in figure 5. Solutions to (4.1), (4.15), and (C 1) completed with (3.1) were obtained by varying the wavelength and imposing a constant average flow rate $\langle q \rangle = 1/3$. In order to obtain the γ_2 branch, we proceeded by starting from the linear threshold for a vertical film and high viscous second-order diffusion η (or low Γ) since it is known that the γ_2 waves then emerge

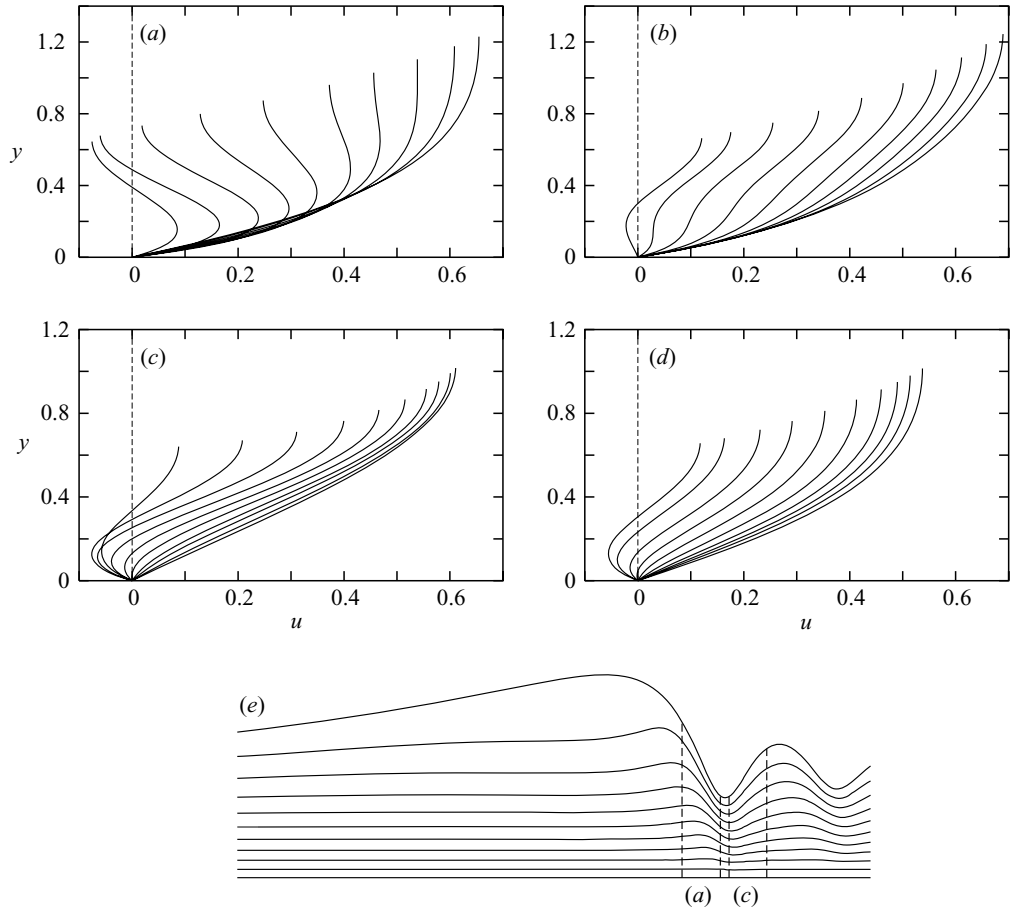

FIGURE 4. Streamwise velocity profile at regularly spaced locations from the front of the solitary hump (*a*, *b*) to the back of the first capillary ripple (*c*, *d*). (*a*, *c*) Solutions to the regularized model (3.1), (4.15); (*b*, *d*) solutions to the complete second-order model (3.1), (C 1); (*e*) wave profile and streamlines corresponding to the regularized model. Extremal positions of the given velocity profiles are indicated by dashed lines.

from the flat-film solution through a Hopf bifurcation. We next adjusted the slope (β) and surface tension (Γ) to the desired values. The γ_2 branch of solutions is found to extend from high speed to low speed, where it terminates as a negative solitary pulse. The curves globally have a linear shape in agreement with the linear relation between maximum height and wave speed obtained by Chang (1986) for solitary waves through a normal form analysis of the Kuramoto–Sivasinsky equation. Both the regularized model and the complete second-order model predict maximum heights larger than the experimental findings, which is in agreement with the DNS of the primitive equations that also predicted larger amplitudes than the experimental wave profiles observed by Liu & Gollub, see Ramaswamy *et al.* (1996); Malamataris *et al.* (2002). This peculiarity could be a consequence of the neglect of the transverse curvature of the humps, or else a slight smoothing of the wave crests linked to the experimental measurement of the thickness. The near-perfect agreement between experiments and the results from the simplified model (4.1) is therefore accidental. For comparison, the results from the PMB model (3.1), (3.6) are also reported in figure 5(*a*) showing again less convincing agreement than with our models.

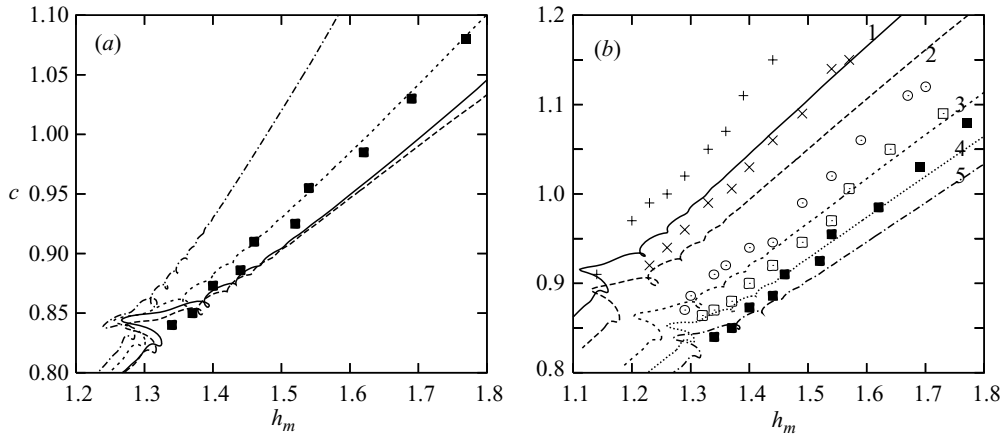

FIGURE 5. Phase speed of solitary-like wave trains as a function of their peak height compared to the experimental data provided by Liu & Gollub (1994) (shown as symbols) at $\beta = 8°$, $\Gamma = 488$. (*a*) $R = 20.1$, comparison to the corresponding travelling wave families computed with the complete second-order model (3.1), (C 1) (solid line), the regularized model (3.1), (4.15) (dashed line), the simplified model (3.1), (4.1) (dotted line) and the PMB model (3.1), (3.6) (dashed-dotted line); (*b*) comparison to the solutions of the regularized model for different Reynolds numbers, $R = 11.9$ (1, +), 13.6 (2, $\times$), 16.8 (3, $\odot$), 18.7 (4, $\boxdot$) and 20.1 (5, $\blacksquare$).

From the above comparisons, it can be concluded with some confidence that our models predict correctly the shape, speed and maximum height of the solitary waves at least in the range of parameters explored by Liu & Gollub.

6. Two-dimensional modelling of three-dimensional film flows

We now turn to the three-dimensional formulation of the problem, and look for two-dimensional equations in the streamwise (x) and spanwise (z) coordinates that mimic the full three-dimensional motion of the fluid. The flat-film solution is a parallel flow with no spanwise component, i.e. $w = 0$. A valid approach is therefore to consider w of order ϵ, with the meaning that spanwise flows are triggered by the modulations of the free surface. Ruyer-Quil & Manneville (2000) used this assumption to simplify the cumbersome system of equations which models the three-dimensional flow dynamics. However, considering the continuity equation (2.2), the least-degeneracy principle suggests w be taken as an $O(1)$ quantity like u and this is the approach we will take below.

Following the same procedure as for the two-dimensional case, one finds that six fields are needed to account for the velocity components at second order: q, r, s, the spanwise flow rate $q_z = \int_0^h w \, \mathrm{d}y$, and the corrections r_z and s_z. For symmetry, the streamwise flow rate and the corrections to the streamwise parabolic velocity profile are hereafter denoted by $q_x \equiv q$, $r_x \equiv r$ and $s_x \equiv s$. The boundary-layer equations are then averaged using the Galerkin method by writing residuals $\langle E_\alpha, g_i \rangle$ where $\langle f, g \rangle = \int_0^h f \, g \, \mathrm{d}y$, while $\alpha = x$ and $\alpha = z$ refer to the streamwise and spanwise momentum balances, respectively. These residuals yield a system of six evolution equations for h, q_α, r_α and s_α completed with the mass balance obtained through integration of (2.2) across the layer depth $\partial_t h + \partial_x q_x + \partial_z q_z = 0$. The full expression of the complete model is very cumbersome and is provided in Appendix C as equations (C 1). First-order expressions for the four fields r_α, s_α are readily obtained from the truncation at order ϵ of the residuals corresponding to the weights g_1 and

g_2. Substitution of these expressions in the first two residuals $\mathscr{R}_{0,\alpha} = \langle E_\alpha, g_0 \rangle$ produces second-order inertia terms, formally written as $\mathscr{R}^{(2),\delta}_{0,\alpha}$. These terms contain high-order nonlinearities that we next eliminate by adjusting algebraic preconditioners. So residuals $\mathscr{R}_{0,\alpha}$ are sought in the form $\mathscr{G}_\alpha^{-1}\mathscr{F}_\alpha$ where the $\mathscr{F}_\alpha$ correspond to the expressions for the residuals $\mathscr{R}_{0,\alpha}$ when a parabolic velocity profile is assumed, i.e. when corrections r_α and s_α are neglected. Isolating inertia terms, we thus set

$$\mathscr{G}_\alpha\left(\mathscr{R}^{(1),\delta}_{0,\alpha} + \mathscr{R}^{(2),\delta}_{0,\alpha}\right) = \mathscr{R}^{(1),\delta}_{0,\alpha}, \tag{6.1}$$

where superscripts refer to first-order and second-order inertia terms. Zeroth-order expressions for the flow rates $q_x = h^3/3 + O(\epsilon)$ and $q_z = O(\epsilon)$, i.e. the gravity-oriented (base) flow, are next invoked to reduce the degree of nonlinearity of the regularization factors $\mathscr{G}_\alpha$. Consequently, the inertia terms $\mathscr{R}^{(2),\delta}_{0,z}$ induced by deviations of the spanwise velocity field from the parabolic profile appear asymptotically at order ϵ^3. So that we merely obtain $\mathscr{G}_z = 1 + O(\epsilon^2)$. Similarly, the asymptotic expression for $\mathscr{R}^{(2),\delta}_{0,x}$ corresponds exactly to the one obtained for a spanwise-independent flow. Hence we have $\mathscr{G}_z \equiv 1$ and $\mathscr{G}_x \equiv \mathscr{G}$ given in (4.14). The three-dimensional extension of the regularized model, whose explicit expression is given in Appendix B, is formally written:

$$\partial_t h = -\partial_x q_x - \partial_z q_z, \tag{6.2a}$$

$$\delta\,\partial_t q_x = \delta\,\mathscr{I}_x^{2D} + \mathscr{G}_x\left\{\frac{5}{6}h - \frac{5}{2}\frac{q_x}{h^2} + \delta\,\mathscr{I}_x^{3D} + \eta\left[\mathscr{D}_x^{2D} + \mathscr{D}_x^{3D}\right] + \frac{5}{6}h\partial_x\mathscr{P}\right\}, \tag{6.2b}$$

$$\delta\,\partial_t q_z = \delta\,\mathscr{I}_z^{2D} - \frac{5}{2}\frac{q_z}{h^2} + \delta\,\mathscr{I}_z^{3D} + \eta\left[\mathscr{D}_z^{2D} + \mathscr{D}_z^{3D}\right] + \frac{5}{6}h\partial_z\mathscr{P}, \tag{6.2c}$$

where $\mathscr{I}$ and $\mathscr{D}$ stand for terms of inertia and viscous diffusion origin, easily identified in (B 1b) and (B 1c). The two terms $\mathscr{P} = -\zeta h + (\partial_{xx} + \partial_{zz})h$ stem from the gravitational and capillary contributions to the pressure respectively. In (6.2b), we have also isolated terms already present in the two-dimensional model (superscript $2D$) from those arising from the spanwise dependence (superscript $3D$). Expressions collected into terms with subscripts x are obtained from those with subscripts x by making the exchanges $\{x \leftrightarrow z\}$.

Equations (6.2a), (6.2b), (6.2c) express mass conservation, and the averaged momentum balance in directions x and z, respectively. The viscous drag corresponds to the terms $\frac{5}{2}q_x/h^2$ in (6.2b) and $\frac{5}{2}q_z/h^2$ in (6.2c). In the boundary-layer equations, gravity contributes only to the streamwise momentum balance through the term $\frac{5}{6}h$ in (6.2b).

The regularized model (6.2) is fully consistent with the Benney expansion at second order, whereas the three-dimensional *simplified model*, corresponding to the averaging of the momentum balance equations across the layer depth assuming both parabolic velocity profiles and weights, is not. The latter can be recovered from the former by replacing the factor $\mathscr{G}_x$ by 1.†

† Notice that the simplified model formulated by Ruyer-Quil & Manneville (2000) contains two typing mistakes in their equation (54): terms $-\frac{97}{56}q_x\partial_z q_z/h$ and $\frac{129}{56}q_x q_z\partial_z h/h^2$ should be corrected to read $-\frac{8}{7}q_x\partial_z q_z/h$ and $\frac{9}{7}q_x q_z\partial_z h/h^2$.

7. Floquet analysis

In this section, the stability of two-dimensional waves to transverse perturbations is investigated in the experimental conditions considered by Liu *et al.* (1995). Experimental profiles indicate that the waves selected by the linear inception are of type γ_1, slow waves with deep troughs and bumped crests. Our efforts have accordingly been concentrated on the stability analysis of the γ_1 travelling waves. These waves were computed using AUTO97 (Doedel *et al.* 1997) by continuation. The constant flux condition $\langle q_x \rangle = 1/3$ was enforced (see § 5). We started from infinitesimal sinusoidal waves at linear threshold, and increased the period. A standard Floquet stability analysis of the wave to both streamwise and spanwise modulations was performed next. Each unknown field X in the frame moving with the wave $\xi = x - c\,t$ was expressed as $X(\xi, z, t) = X_0(\xi) + \varepsilon X_1(\xi, z, t)$ where $\varepsilon \ll 1$ and X_0 is the basic two-dimensional travelling wave. The perturbation X_1 was expanded as $\sum_{\varphi,k_z} \tilde{X}_{\varphi,k_z}(\xi) \exp\{\mathrm{i}\varphi k_x \xi + \mathrm{i}k_z z + s\,t\}$ where $\tilde{X}_{\varphi,k_z}$ is periodic in ξ with period $2\pi/k_x$, k_x is the wavenumber of the two-dimensional basic stationary wave, and k_z is the wavenumber of the transverse perturbation. The detuning parameter, φ, is the ratio of the streamwise wavenumber of the perturbation to that of the base state, hence $\varphi \in [0, 1[$. $\varphi \in \mathbb{Q}$ signals a subharmonic mode, especially $\varphi = 1/2$, and $\varphi \notin \mathbb{Q}$ an incommensurate modulated mode. Denoting $\boldsymbol{X}_0(\xi)$ the vector formed by the different components of the base state, and $\tilde{\boldsymbol{X}}$ the vector formed by the amplitudes of the perturbations, the linearized set of equations can be formally written as

$$\varsigma \tilde{\boldsymbol{X}} = \mathscr{L}(\boldsymbol{X}_0; c, q_0, \delta, \zeta, \eta, \varphi, k_z)\, \tilde{\boldsymbol{X}}, \tag{7.1}$$

where $\mathscr{L}$ is a linear operator and ς is the complex growth rate. The maximum real part denoted ς_r^M corresponds to the fastest growing perturbation of interest from the experimental point of view. The parameter space $\varphi \times k_z$ can be reduced by invoking two symmetries: (i) reflection in the spanwise direction, which allows us to consider only positive k_z; (ii) invariance of (7.1) under the transformation $(\varphi, k_z, \varsigma, \tilde{\boldsymbol{X}}) \rightarrow (-\varphi, -k_z, \varsigma^\star, \tilde{\boldsymbol{X}}^\star)$, the star denoting complex conjugation. The parameter space $\varphi \times k_z$ can thus be limited to $[0, \frac{1}{2}] \times [0, \infty[$. The eigenvalue problem (7.1) was solved in Fourier space where 256 real modes have been used to represent the computed two-dimensional waves and 128 complex modes to represent the perturbation (limited to 32 for the complete model owing to its complexity). Eigenvalues and eigenvectors were computed using a QR algorithm implemented on an RS/6000 IBM workstation.

Liu *et al.* (1995) considered a falling film of a glycerol–water mixture ($\rho = 1070\,\mathrm{kg\,m^{-3}}$, $\nu = 2.3 \times 10^{-6}$ m^2 s^{-1} and $\sigma = 67 \times 10^{-3}$ N m^{-1}), with $\beta = 6.4^\circ$ and $R = 56$. They measured the wavelength of the two-dimensional base state λ_x as well as the wavelength of the transverse modulations λ_z, obtained by varying the frequency of the periodic forcing. Results of Floquet analysis using the complete, regularized and simplified models are presented in figure 6 using dimensional units. In line with the results discussed in § 5, the computed wavelengths λ_x of γ_1 waves are of the same order of magnitude as found experimentally, see figure 6(*a*). Our computations also indicate relatively small variations of λ_z with the frequency, which is in agreement with the results reported by Liu *et al.* (see figure 6*b*). The transverse wavelengths of the most amplified perturbations for the regularized and the complete models agree with each other, whereas the simplified model predicts larger wavelengths. This shows the role of the second-order inertia terms arising from corrections to the velocity profile in the mechanism of the three-dimensional secondary instability. At low frequency, λ_z goes to infinity so that the most amplified perturbation is spanwise-uniform, while the

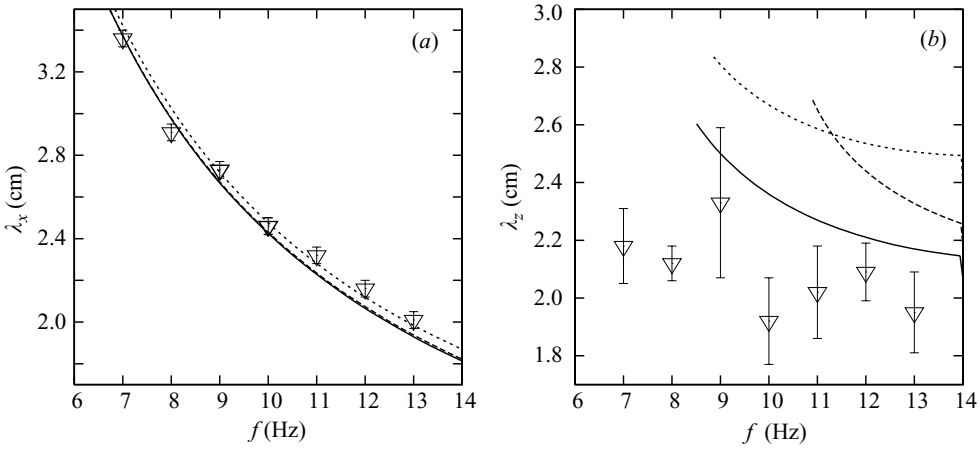

FIGURE 6. (*a*) Streamwise wavelengths λ_x of two-dimensional waves and (*b*) spanwise wavelengths λ_z of the fastest growing three-dimensional perturbations versus the forcing frequency f, with $\beta = 6.4°$, $R = 56$ and $\Gamma = 2002$. Down triangles are experimental findings by Liu *et al.* (1995). Solid, dashed and dotted lines correspond to the complete model, the regularized model (6.2) and the simplified model, respectively. In panel (*a*), solid and dashed lines are nearly superimposed.

experimental λ_z remains finite. Another difference is that Floquet analysis predicts that the detuning parameter for the fastest growing perturbation (not shown) corresponds to a subharmonic secondary instability ($\varphi = \frac{1}{2}$, chequerboard pattern) rather than to the synchronous transition ($\varphi \approx 0$) reported by Liu *et al.*

Figure 7(*a*) summarizes the experimental findings by Liu *et al.* in the (R, f)-plane for the same glycerol–water mixture and with $\beta = 4°$. Liu *et al.* reported two different scenarios that are strongly reminiscent of what happens in boundary layers (Schmid & Henningson 2001). The first one, referred to as a *synchronous* mode, is characterized by wave crests deformed in phase in the spanwise direction. The second one, less commonly observed, appears when two successive crests are deformed with a phase shift of π. This leads to chequerboard (or herringbone) patterns characteristic of a streamwise subharmonic instability combined with a spanwise modulation. These two modes are reminiscent of aligned and staggered Λ-vortices developing in transitional boundary layers, thus analogous to the type-K and type-H transitions, respectively (Herbert 1988). Corresponding results for the stability of γ_1 waves are presented in figure 7(*b–d*), as obtained from the regularized model. The results for the solutions to the complete and simplified models are very similar to those obtained with the regularized model and thus not shown. We have computed the detuning parameter (figure 7*b*) and the spanwise wavenumber (figure 7*c, d*) of the fastest growing perturbation, with a Reynolds step of 1 and a frequency step of 1 Hz (the lowest frequency considered is 4 Hz owing to the large number of modes necessary to represent the solution in that case). Computations show that k_z decreases steadily as R is reduced and goes to zero in a region close to the neutral stability curve (see figure 7*d*). This rapid decrease of k_z corresponds to the boundary separating two- and three-dimensional secondary instabilities, which agrees well with the results of Liu *et al.* who reported two-dimensional flows mainly close to the threshold of the primary instability (see figure 7*a*). In this small region, the γ_1 waves undergo a subharmonic two-dimensional instability ($\varphi = \frac{1}{2}$). At low frequency and large Reynolds number, the instability is also found to be two-dimensional ($k_z = 0$) but corresponds to an incommensurate mode ($\varphi \in]0, \frac{1}{2}[$). This provides an indication that the boundary

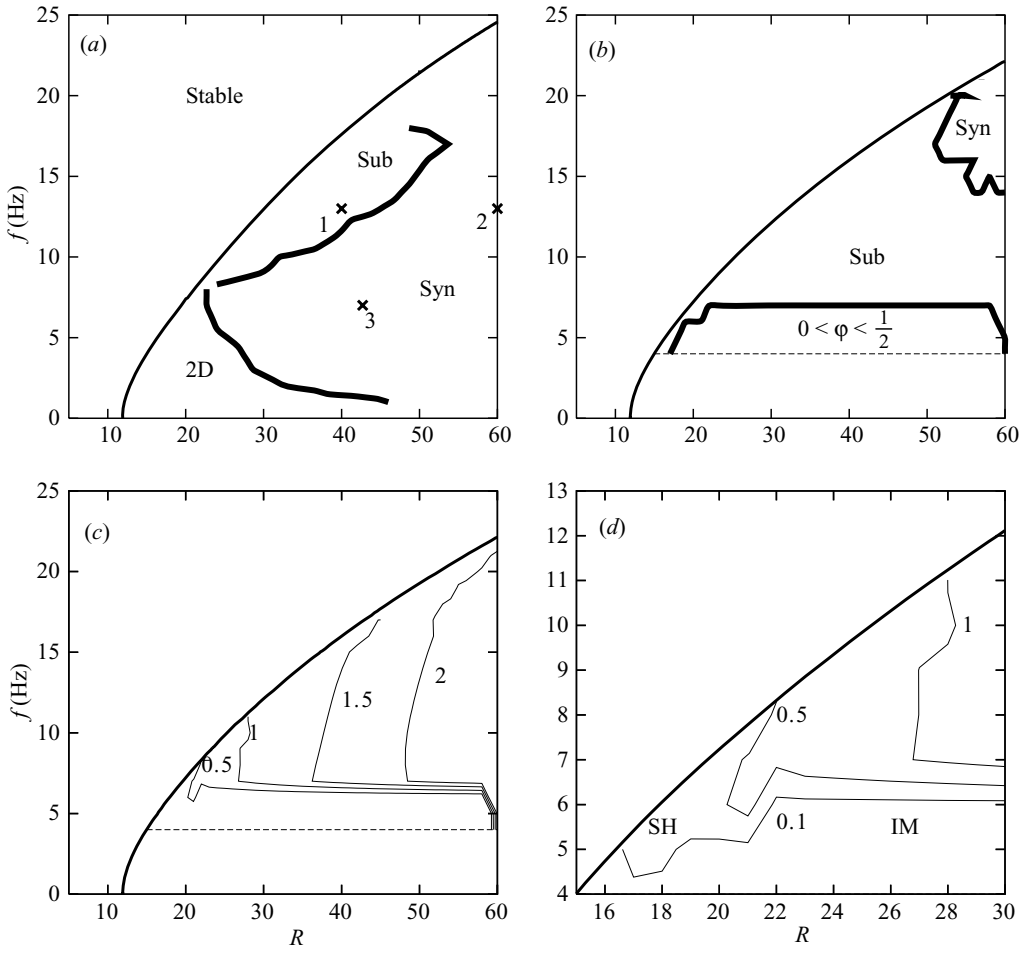

FIGURE 7. Stability of the γ_1 waves to three-dimensional modes as a function of the Reynolds number R and the frequency f for $\beta = 4°$ and $\Gamma = 2340$ (Liu *et al.* 1995, figure 6). (*a*) Experimental stability chart. Stability zones are bounded by thick lines: 'two-dimensional' where no three-dimensional instability was observed, 'Sub' for three-dimensional subharmonic instability and 'Syn' for three-dimensional synchronous instability. The neutral stability curve is represented by a thin solid line (Orr–Sommerfeld analysis). Crosses refer to parameter sets reported in table 1. (*b*) Detuning parameter, where the synchronous (Syn) and subharmonic (Sub) instability regions correspond to $\varphi = 0$ and 0.5, respectively. (*c*) Wavenumber k_z of the fastest growing transverse modulation (in cm^{-1}). (*d*) Enlargement of (*c*): 'SH' subharmonic two-dimensional instability ($\varphi = \frac{1}{2}$), 'IM' incommensurate modulated two-dimensional mode ($0 < \varphi < \frac{1}{2}$). Dashed lines in (*b*, *c*) indicate the limit (4 Hz) of the computations. Results presented in (*b–d*) have been obtained using the regularized model.

between two- and three-dimensional flows may exist and is not an experimental artifact due to finite-size effects. At low frequency and large Reynolds number, Floquet stability analysis of γ_1 waves predicts a two-dimensional region wider than reported in experiments, which can be understood if one keeps in mind that γ_2 waves are likely to develop in that region of the parameter plane in place of γ_1 waves, the stability of which is considered in this section.

As already mentioned, computations predict an overwhelming presence of the subharmonic scenario ($\varphi = \frac{1}{2}$) whereas Liu *et al.* observed it only close to the neutral stability curve at large frequencies and large Reynolds numbers. In fact, our computations predict a region of synchronous three-dimensional instability at

Set	R	β (deg.)	Γ	f (Hz)	k	c	$\langle h \rangle$
1	40.0	4.0	2340	13	1.565	0.824	0.987
2	60.0	4.0	2340	13	1.494	0.689	0.970
3	42.7	4.0	2340	7	0.953	0.703	0.975
4	48.0	6.4	2002	10	0.980	0.628	0.965

TABLE 1. Dimensionless wavenumber k, phase speed c and averaged thickness $\langle h \rangle$ of the computed γ_1 waves corresponding to experimental conditions by Liu *et al.* (1995). Figures 7 and 11 in that reference correspond to sets 3 and 4, respectively. The constant mean flow rate condition $\langle q \rangle = 1/3$ was enforced. Parameters are the Reynolds number R, the inclination β, the Kapitza number Γ and the forcing frequency f.

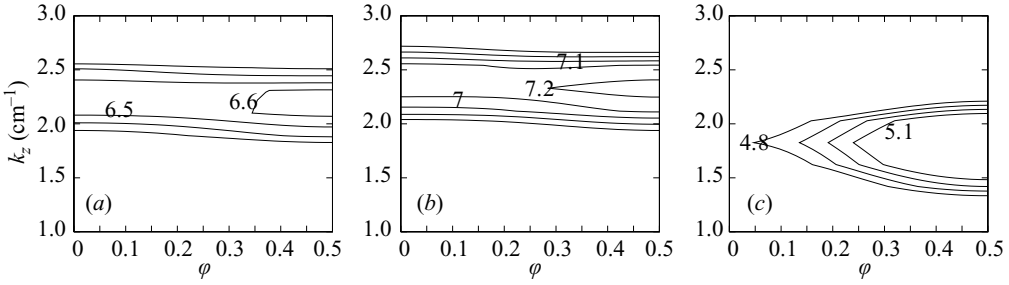

FIGURE 8. Maximum growth rate in s^{-1} as function of the detuning parameter φ and the transverse wavenumber k_z in cm^{-1}, computed with the different models for set 2 ($k_x = 3.2\,\mathrm{cm}^{-1}$): (*a*) complete, (*b*) regularized, (*c*) simplified.

large Reynolds numbers only when using the regularized model. Figure 8 shows the isocontours of the growth rate ς_r of the fastest growing perturbation in the (φ, k_z)-plane for the three models, corresponding to the set 2 of table 1. Similar results (not shown) have been obtained with parameter set 3. Again, the simplified model predicts longer spanwise wavelengths than both the complete and the regularized models. Moreover, figure 8(*a, b*) shows that ς_r varies very little with the detuning parameter φ. Indeed, for the complete and the regularized models, the growth rates for $\varphi = 0$ and $\varphi = \frac{1}{2}$ are close to each other so that the instability is not selective. On the other hand, the simplified model is more selective (see figure 8*c*) and clearly predicts a subharmonic instability. This result again shows the subtle role of the second-order inertia terms in the pattern selection.

The direct correspondence between results from Floquet analysis and the experiments is based on three assumptions. First, the γ_1 waves emerge from the primary instability. Second, a broadband white noise is assumed. As indicated by Liu *et al.*, the irregularities at the entrance section are time-independent and preferentially trigger in-phase modulations of the evolving three-dimensional patterns. Therefore experimental noise may contain a large amount of in-phase perturbation, which may trigger the synchronous instability instead of the subharmonic mode, given that they have growth rates close to each other. Third, Floquet analysis assumes that two-dimensional waves saturate before the onset of the three-dimensional instability. Precisely because inlet noise may contain significant spanwise perturbations, three-dimensional instabilities may arise before the saturation of the two-dimensional waves is achieved. Such a sensitivity to inlet conditions can only be checked by direct numerical simulations of the models.

8. Two-dimensional simulations of three-dimensional flows

In this section we perform time integrations of the complete model, the regularized model (6.2) and the simplified model ((6.2) with $\mathscr{G}_x = 1$). Periodic boundary conditions in both x- and z- directions are imposed. This allows us to take advantage of the good convergence properties of spectral methods. A pseudo-spectral scheme has been developed, with derivatives evaluated in Fourier space and nonlinearities in physical space. The time dependence is accounted for by a fifth-order Runge–Kutta scheme, which allows control of truncation errors by difference with an embedded fourth-order scheme (Press *et al.* 1992). In practice, the time step is adapted to limit the relative error on each variable to 10^{-4}. The explicit character of the algorithm makes it easy to implement the different models. The computational domain of size $L_x \times L_z$ is discretized as a lattice of $M \times N$ regularly spaced grid points with coordinates $x_i = iL_x/M$ and $z_j = jL_z/N$. The three-dimensionality of the waves is evaluated through

$$E_x(t) \equiv \frac{1}{MN} \sum_{j=1}^{N} \left(\sum_{m=1}^{M/2-1} |a_m(z_j, t)|^2 \right)^{1/2}, \tag{8.1a}$$

$$E_z(t) \equiv \frac{1}{MN} \sum_{i=1}^{M} \left(\sum_{n=1}^{N/2-1} |b_n(x_i, t)|^2 \right)^{1/2}, \tag{8.1b}$$

where the spatial Fourier coefficients a_m and b_n are defined by

$$a_m(z, t) = \sum_{i=0}^{M/2-1} [h(x_{2i}, z, t) + \mathrm{i}\, h(x_{2i+1}, z, t)] \exp [2\pi \mathrm{i}\, mi/(M/2)], \tag{8.1c}$$

$$b_n(x, t) = \sum_{j=0}^{N/2-1} [h(x, z_{2j}, t) + \mathrm{i}\, h(x, z_{2j+1}, t)] \exp [2\pi \mathrm{i}\, nj/(N/2)], \tag{8.1d}$$

and where i stands for the imaginary unit. E_x and E_z are the streamwise and the spanwise energy of deformations (Joo & Davis 1992; Press *et al.* 1992).

Owing to the spatial periodicity in the streamwise direction, our simulations physically correspond to a closed flow for which the fluid leaving the downstream border of the computational domain is reinjected at the upstream boundary. The mass is therefore conserved in the domain so that the space-averaged film thickness remains constant and is equal to the initial flat-film thickness. In experiments, the fluid accelerates and film thinning is observed so that the time average of the thickness decreases downstream, whereas the time average of the flow rate is conserved and is equal to its value at the inlet, 1/3. Therefore in order to account for the acceleration of the flow observed in experiments, in our simulations the uniform thickness at the initial time is set to the mean thickness $\langle h \rangle < 1$ of the two-dimensional travelling waves at the forcing frequency, which are obtained using AUTO97 when a constant averaged flow rate $\langle q \rangle = 1/3$ is enforced, which ensures that the amount of liquid in our computational domain lying under the corresponding travelling waves is appropriate. Since the local flow rate varies as the cube of the local film thickness, this requirement can be crucial in recovering experimental results. The development of two-dimensional waves undergoing three-dimensional instabilities is simulated by enforcing the initial condition

$$h(x, z, 0) = \langle h \rangle + A_x \cos(2\pi n_x x/L_x) + A_z \cos(2\pi n_z z/L_z) + A_{\mathrm{noise}} \tilde{r}(x, z), \tag{8.2}$$

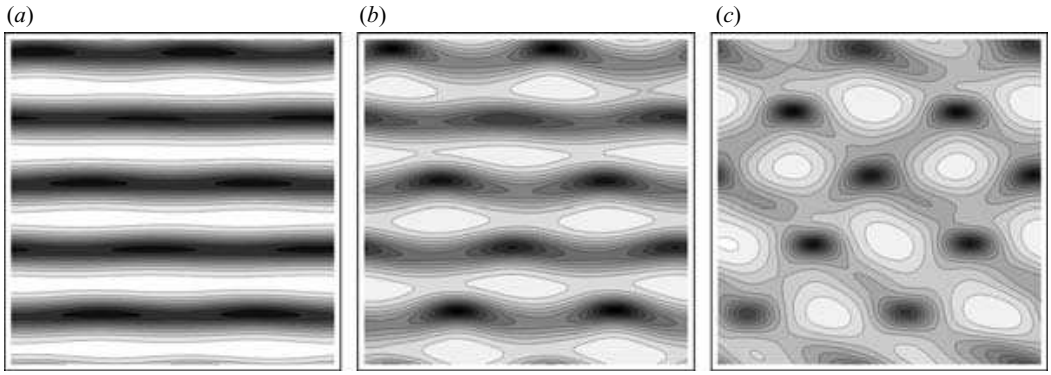

FIGURE 9. Snapshots of free-surface deformations giving rise to a herringbone pattern, computed for the parameter set 1 (see table 1) with the regularized model at different times: (*a*) $t = 150$, (*b*) $t = 175$, (*c*) $t = 195$. Isothickness contours are separated by an elevation step of 0.06. The numbers of grid points are $M \times N = 128 \times 64$ and $L = 2n_x\pi/k$. Amplitudes of the initial periodic forcing are $A_x = 0.1$, $A_z = 0$ and $A_{\text{noise}} = 10^{-3}$, with $n_x = 5$. Dark and bright zones stand for depressions and elevations, respectively.

where $A_x, A_z, A_{\text{noise}}$ are small amplitudes, $n_x, n_z \in \mathbb{N}$ represent the number of sinusoidal waves in each direction, and $\tilde{r}$ is a random function with values in the interval $[-1, 1]$. The last term of (8.2) accounts for ambient white noise. In the following we take $A_{\text{noise}} = 10^{-3}$. In most cases, the aspect ratio of the computational domain is set to unity and $L_x = L_z \equiv L$. The value of L must be taken large enough to allow complex flow dynamics. The general form of (8.2) enables us to explore a wide range of experimental results on three-dimensional waves emerging from two-dimensional waves. In the following, we consider three-dimensional modulations of γ_1 waves, γ_2 waves, and natural waves.

8.1. *Three-dimensional modulations of γ_1 waves*

We first consider the transition from two-dimensional γ_1 waves to three-dimensional patterns, which corresponds to the experimental results by Liu *et al.* (1995). Their well-controlled experiments will also serve as a benchmark for a systematic evaluation of the accuracy and usefulness of the different models.

Liu *et al.* have imposed a spanwise-uniform time-periodic forcing at the inlet. In order to mimic their experiments, we choose initial conditions corresponding to sinusoidal two-dimensional waves plus small white noise ($A_z = 0$ and $A_{\text{noise}} \ll A_x$). L is set equal to five times the wavelength $2\pi/k$ of the precursor two-dimensional travelling wave, i.e. $n_x = 5$. The values of the parameters for the different numerical experiments are indicated in table 1. We start by considering flow conditions for an inclination angle $\beta = 4^\circ$ and Kapitza number $\Gamma = 2340$ (sets 1–3 in table 1 and in figure 7*a*). Each chosen couple (frequency, Reynolds number) is indicated by a cross in figure 7(*a*). Set 1 corresponds to the region of the plane (f, R) where herringbone patterns were observed experimentally, i.e. subharmonic instability. Simulations of the complete, regularized and simplified models agree with both the Floquet analysis and the experimental data by showing the presence of staggered crests and troughs. Isothickness contours of the wave patterns are shown at different times in figure 9 for the regularized model: at the final stage (figure 9*c*), the film evolves towards a staggered arrangement of smooth and large bumps, and thin and deep depressions, which agrees qualitatively with the experimental observations.

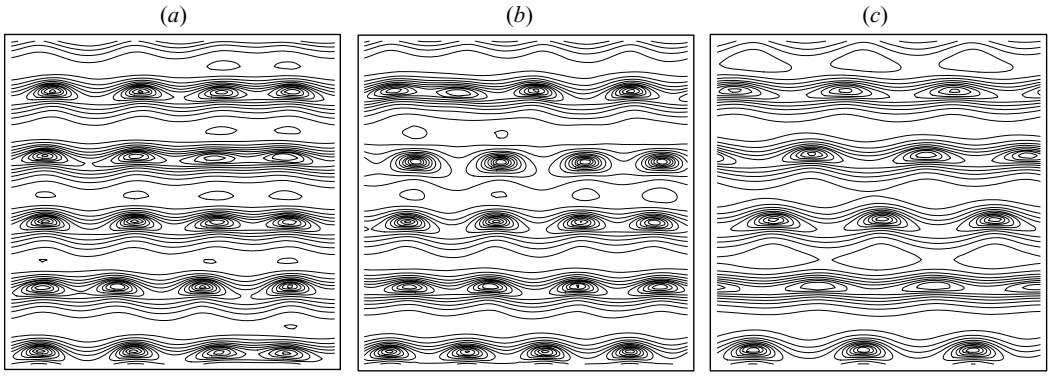

FIGURE 10. Snapshots of free-surface deformations computed for parameter set 2 at $E_z \approx 0.05$ for the three models: (*a*) complete, $t = 125$; (*b*) regularized, $t = 125$; (*c*) simplified, $t = 155$. Isothickness contours are separated by a level difference of 0.08. See also the caption of figure 9. The size of the computational domain is 9.8×9.8 cm. Note that the shading have been removed for clarity.

Using parameter set 2, we move to the region in figure 7(*a*) where synchronous secondary instability has been reported by Liu *et al.* (1995) whereas the Floquet analysis predicts a subharmonic instability (compare figure 7*a* to figure 7*b*). Time integrations of the different models, given in figure 10 for the same spanwise deformation energy E_z, disagree: the complete model (panel *a*) shows a sideband instability, $\varphi \ll 1$, leading to a synchronous pattern while the simplified model (panel *c*) gives staggered troughs and more deformed crests indicating a subharmonic instability, $\varphi = \frac{1}{2}$. Solution to the regularized model (figure 10*b*) corresponds to a combination of synchronous and staggered modulations, while appearing closer to the complete model's solution (and experimental observations) than to that of the simplified model: spanwise and streamwise wavelengths have values close to each other (four spanwise modulations for the complete and regularized model, in contrast with three for the simplified one). This is in line with the fact that, as seen in figure 8(*a, b*), the secondary instability is not selective for parameter set 2. On the other hand, as expected from the linear prediction (figure 8*c*), the simplified model clearly selects the subharmonic instability, ending in a staggered pattern (figure 10*c*). Similar behaviours of the three models (not shown here) have been also found for parameter set 3.

Parameter set 4 of table 1 corresponds to a more pronounced inclination angle ($\beta = 6.4^\circ$) and thus to a smaller Kapitza number ($\Gamma = 2002$). Our simulations indicate that, if the initial excitation is spanwise uniform ($A_z = A_{\text{noise}} = 0$), the two-dimensional steady state corresponds to an oscillatory mode instead of a travelling wave. This is illustrated in figure 11 by plotting in (*a*) the time evolution of the streamwise deformation energy E_x and in (*b*) the wave profiles at two different times corresponding to a maximum (label '1') and a minimum (label '2') of E_x during one oscillating period. Such an oscillatory mode has been numerically observed by Ramaswamy *et al.* (1996) who called this regime *quasi-periodic*. The direct numerical simulations of the Navier–Stokes equations indicate that the quasi-periodic regime is widely present in the case of a vertical plane when the Reynolds number becomes large. This behaviour is generated by the destabilization of the existing limit cycle and can be predicted by looking at the maximum growth rate of Floquet perturbations, the imaginary part of which was also found to be positive.

The wave patterns for the different models are shown in figure 12. We see that both the complete and the simplified models yield staggered patterns whereas the

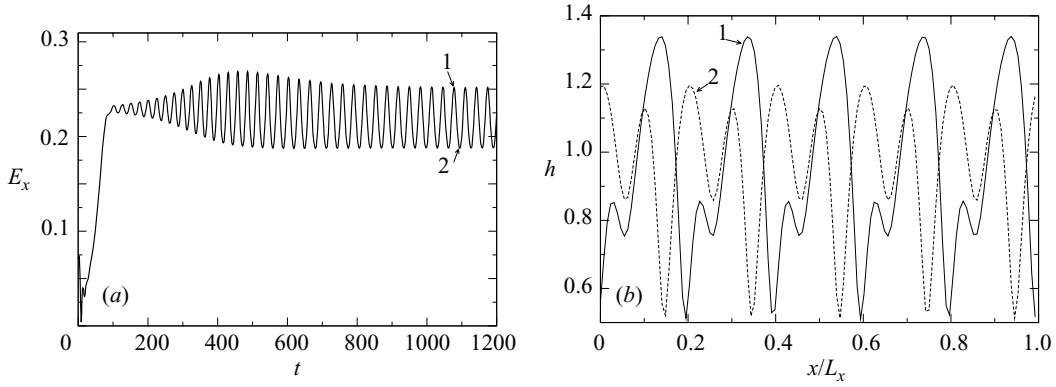

FIGURE 11. (*a*) Energy of streamwise deformations E_x computed for parameter set 4 as a function of time; (*b*) corresponding two-dimensional wave profiles. The complete model has been used for computations and $A_x = 0.1$, $A_z = 0$, $A_{\text{noise}} = 0$, $n_x = 5$, $L = 2n_x\pi/k$ for the initial conditions.

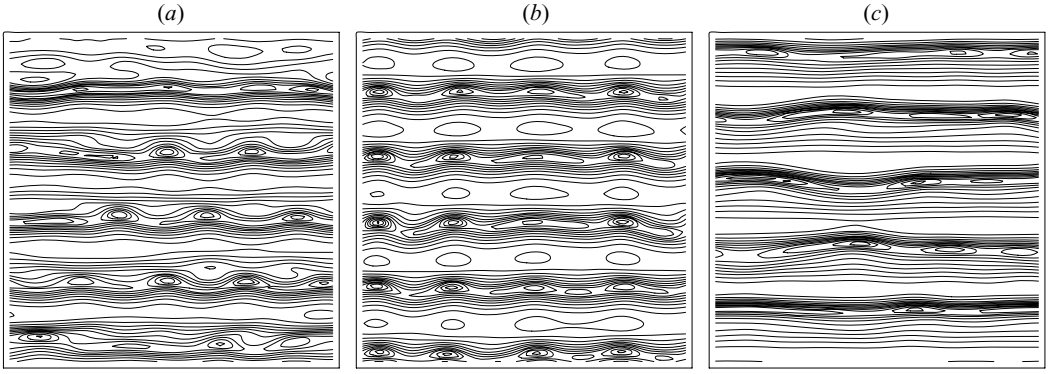

FIGURE 12. Free-surface deformations computed for parameter set 4 at $E_z \approx 0.05$ for the three models: (*a*) complete, $t = 345$; (*b*) regularized, $t = 305$; (*c*) simplified, $t = 295$. Isothickness contours are separated by an elevation step of 0.06. Amplitudes of the initial forcing are $A_x = 0.2$, $A_z = 0$ and $A_{\text{noise}} = 10^{-3}$.

regularized model yields a synchronous pattern, in agreement with experimental observations. In fact, it appears that the onset of the three-dimensional pattern is strongly influenced by the presence of the two-dimensional oscillatory mode and then by the exchange of energy between this mode and the three-dimensional instability mode. This exchange depends on the initial conditions and in particular on the amplitude A_x of the initial streamwise modulations. Figure 13 shows three-dimensional wave patterns computed with the regularized model for two different values of A_x. Significant qualitative differences can be noted when comparing them to figure 12(*b*): at low initial amplitude $A_x = 0.1$, the final transverse modulations seem to have longer wavelengths than at the larger values of $A_x = 0.2$ and $A_x = 0.3$. In addition, crests display out-of-phase modulations whereas modulations are more in-phase when the initial amplitude A_x is increased. Time evolution of the energies E_x and E_z is displayed in figure 14. When $A_x = 0.1$, the system approaches the unstable stationary wave solution and remains close to it for a long time. Therefore, the Floquet analysis still applies and the staggered pattern obtained corresponds to the predicted subharmonic instability. This is no longer the case for larger values of A_x where the modulation of the two-dimensional wave train occurs prior to the

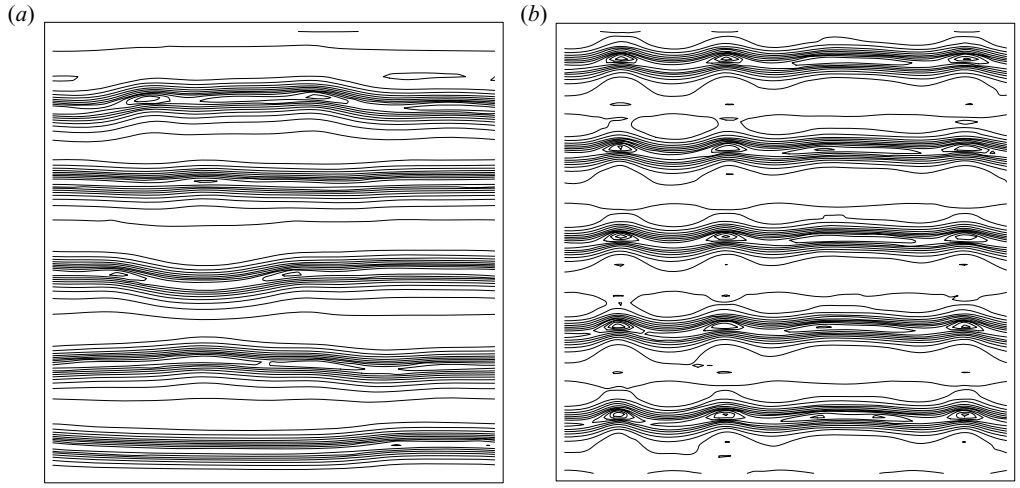

FIGURE 13. Free-surface deformations computed for parameter set 4 (regularized model) at $E_z \approx 0.05$ ($A_z = 0$ and $A_{\text{noise}} = 10^{-3}$): (*a*) $A_x = 0.1$ and $t = 300$, (*b*) $A_x = 0.3$ and $t = 220$.

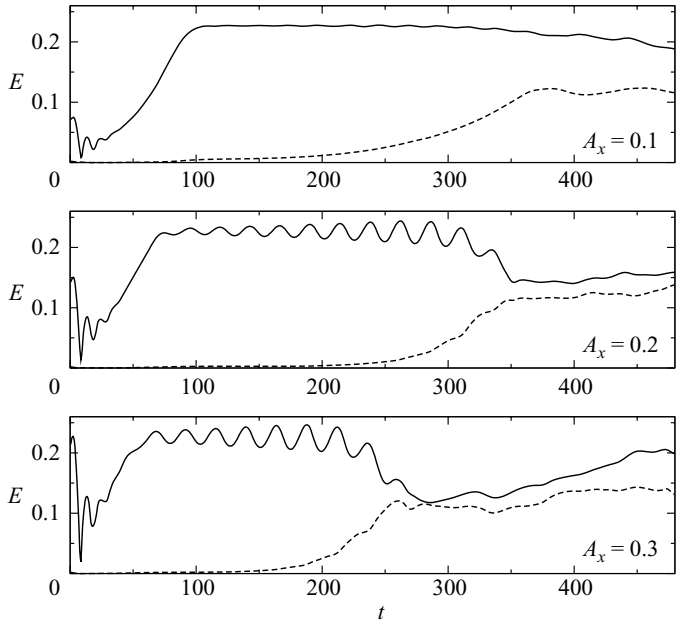

FIGURE 14. Deformation energies computed for parameter set 4 using the regularized model (6.2) and various values of A_x. Solid and dashed lines correspond to E_x and E_z, respectively. Figures 13(*a*), 12(*b*) and 13(*b*) correspond to pictures taken at times when E_z crosses the level 0.05.

development of the three-dimensional instability. The observed synchronous pattern is thus the complex result of two ingredients: the growth of two-dimensional oscillations and the three-dimensional instability.

We have already noticed how pattern formation is sensitive to the initial conditions, due to the poor selectivity of the secondary instability. In order to mimic the effect of possible inlet inhomogeneities in our simulations, we have added an x-independent noise $\tilde{r}'(z)$ to the initial condition (8.2), whose amplitude A'_{noise} represents the inlet roughness. A realistic estimate of about 1 μm roughness gives an amplitude of $A'_{\text{noise}} = 0.01$ for a typical film thickness of 100 μm. Figures 15 and 16 display results

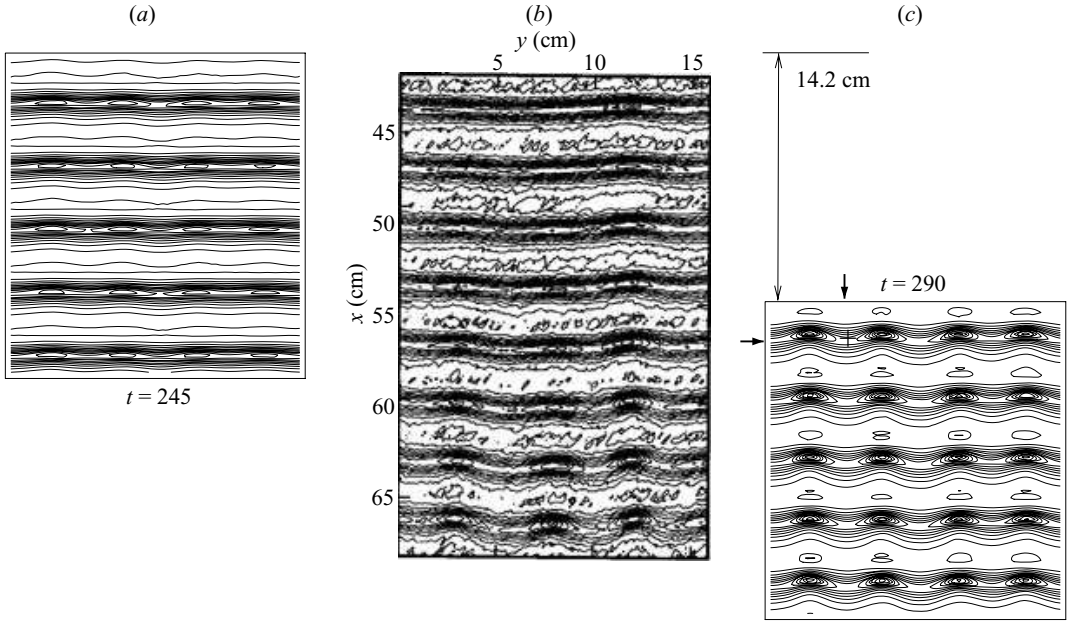

FIGURE 15. (*a*, *c*) Snapshots of the film free surface obtained using the regularized model (6.2) at two different times, along with (*b*) the experimental picture reused with permission from Jun Liu, *Physics of Fluids*, vol. 7, p. 55 (1995). Copyright 1995, American Institute of Physics. Parameters correspond to set 3 in table 1. $A_x = 0.2$, $n_x = 5$, $A_z = 0$, $L = 2n_x\pi/k$, $A_{\text{noise}} = 10^{-3}$: an x-independent noise with amplitude $A'_{\text{noise}} = 10^{-2}$ is added to mimic the effect of wall roughness. The size of the computational domain is 148×148 mm. Isothickness contours are separated by an elevation step of 0.06. The location of a saddle point in (*c*) (see text) is indicated by a cross and two arrows.

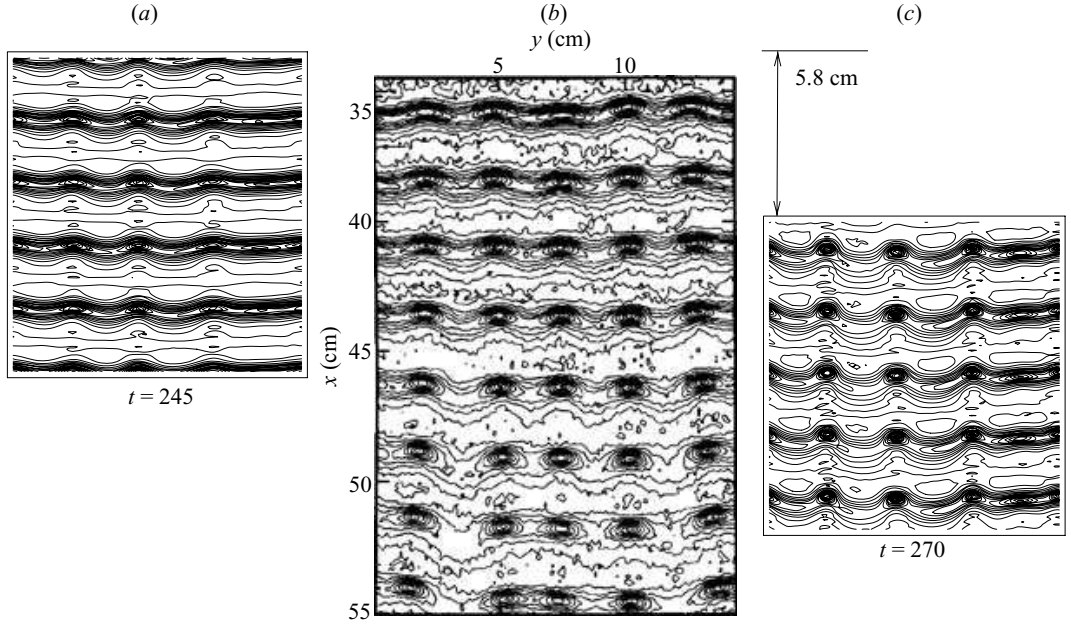

FIGURE 16. As figure 15 but with parameter set 4. The experimental picture in panel (*b*) is reused with permission from Jun Liu, *Physics of Fluids*, vol. 7, p. 55 (1995). Copyright 1995, American Institute of Physics. The size of the computational domain is 118×118 mm. Isothickness contours are separated by an elevation step of 0.08.

obtained with the regularized model, compared to those obtained experimentally (Liu *et al.* 1995, figures 7 and 11). They show the influence of such a perturbation, which effectively biases the evolution in favour of the synchronous instability. To facilitate comparisons with the experimental results, numerical snapshots are separated in the vertical direction by the distance covered by the waves between the two times at which the snapshots have been taken (roughly 14.2 cm and 5.8 cm in the case of figures 15 and 16 respectively). The agreement with experiments is now reasonable even though, mostly because of the choice of periodic boundary conditions, some differences can still be noticed. The spanwise wavelength selected in the simulation shown in figure 15 seems to be a little smaller than in the experiment (37 mm in comparison to roughly 46 mm), whereas in the case of figure 16, the simulation and the experiment give essentially the same answer (28 mm compared to 26 mm). However, experiments and simulations share common qualitative features. Isothickness contours agree well with each other, and strong modulations of the troughs are observed, whereas the crests remain nearly undeformed, which leads to the formation of isolated depressions. In particular, as experimentally observed by Liu *et al.*, our numerical simulations indicate the formation of local saddle points on the wave pattern corresponding to minima in the spanwise direction and maxima in the streamwise direction (see figure 15(*c*) where one such saddle point is indicated by a cross). Liu *et al.* have measured the difference in height between the minima of the thickness at a trough and the height of the nearby saddle point. They called it 'trough transverse modulation amplitude', denoted $\Delta h_{\min}(x)$. From the measurement of $\Delta h_{\min}(x)$ at different locations for the experimental data corresponding to parameter set 3, i.e. their figure 7 and our figure 15, they computed a spatial growth rate of approximately $0.11\,\mathrm{cm}^{-1}$. Following a similar procedure, we define $\Delta h_{\min}(t)$ as the height difference between the minimum of the thickness in the entire computational domain and the closest saddle point at a given time t. From the measurement of $\Delta h_{\min}(t)$ in our simulation, we found a temporal growth rate of approximately $2.6\,\mathrm{s}^{-1}$, which is converted into a spatial growth rate, $0.125\,\mathrm{cm}^{-1}$, hence of the correct order of magnitude, with the help of the speed of the corresponding two-dimensional γ_1 waves, $20.8\,\mathrm{cm\,s}^{-1}$.

Despite differences between our numerical simulations and experimental conditions, both the synchronous instability and the herringbone patterns observed by Liu *et al.* (1995) were qualitatively recovered with the complete and the regularized models, whereas the synchronous instability cannot be obtained using the simplified one. This indicates the necessity of taking into account the second-order inertia corrections to reproduce satisfactorily the experimental findings. The regularized model (6.2) therefore seems to be a good compromise between accuracy and simplicity and will be the only one used from now on to compare numerical simulations with experimental findings.

8.2. *Three-dimensional modulations of γ_2 waves*

In this section, we investigate the experimental conditions of Park & Nosoko (2003) who observed three-dimensional wave patterns emerging from two-dimensional waves of γ_2-type for films of water on a vertical wall. Parameter sets corresponding to the different numerical experiments are given in table 2. Controlling inlet perturbations, Park & Nosoko (2003) have imposed a spanwise-uniform forcing at a given frequency f and periodic modulations in the spanwise direction by means of regularly spaced needles with period $\lambda_{z,\mathrm{ndl}}$. At R below approximately 40, regular spanwise forcing

Set	R	β (deg.)	Γ	f (Hz)	$\lambda_{z,\mathrm{ndl}}$ (mm)	k	c	$\langle h \rangle$	k_z
5	20.7	90	3375	15.0	10	0.3461	0.900	0.899	0.699
6	40.8	90	3375	19.1	20	0.3845	0.714	0.912	0.377
7	59.3	90	3375	17	20	0.3126	0.630	0.955	0.393

TABLE 2. Parameters of the simulations corresponding to experiments on a vertical plane and with pure water at 25°C (Park & Nosoko 2003, figure 7). $\lambda_{z,\mathrm{ndl}}$ is the spanwise intervals of the needle array and k_z is the corresponding dimensionless wavenumber. The dimensionless wavenumber k, phase speed c and averaged thickness $\langle h \rangle$ of the corresponding two-dimensional γ_2 waves are also given.

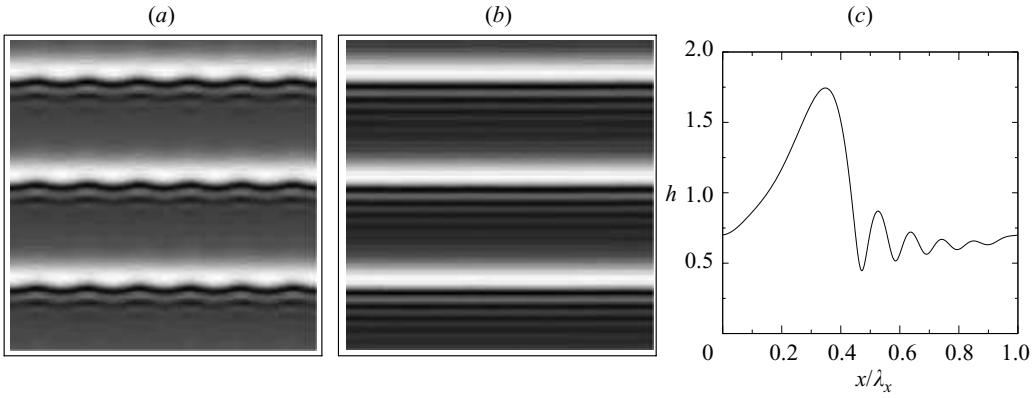

FIGURE 17. (a, b) Snapshots of the film free surface at times $t = 27$ and $t = 172$ computed with the regularized model and for set 5 in table 2 ($R = 20.7$). $n_x = 3$, $n_z = 6$ and $L = 2n_x\pi/k$. The computational domain is 60×60 mm with 128×128 grid points. Bright (resp. dark) zones correspond to elevations (resp. depressions). (c) two-dimensional wave profile of (b).

of the waves led to low-level spanwise modulations whereas at R above 40, the waves broke into horseshoe-like solitary waves having curved fronts and long oblique legs. The existence of stationary horseshoe-like waves has been demonstrated experimentally by Alekseenko *et al.* (2005). The initial conditions (8.2) corresponding to the inlet conditions imposed by Park & Nosoko and adapted to our simulations are taken as: $A_x = 0.2$, $A_z = 0.05$ and $A_{\mathrm{noise}} = 0$.

Figure 17 shows snapshots for parameter set 5 with $R = 20.7$. Initial spanwise modulations of length $\lambda_{z,\mathrm{ndl}} = 10$ mm ($n_z = 6$) are quickly damped, i.e. $E_z \to 0$, and the pattern evolves to two-dimensional travelling waves, i.e. $E_x \to$ const, the profile of which is given in figure 17(c). This corresponds to a γ_2 wave with a large hump preceded by capillary ripples, in accordance with the fact that when the forcing frequency is small, the γ_1 slow waves are not observed. The linear inception region is thus immediately followed by the formation of fast γ_2 waves, that are stable for a while. This is in agreement with the experimental observations, where the inlet forcing is quickly damped. Park & Nosoko then observed the downstream growth of another mode leading to spanwise-modulated waves with a wavelength roughly equal to 3 cm. Similar modulated γ_2 waves (not shown here) are recovered by increasing the length of the initial spanwise modulations $\lambda_{z,\mathrm{ndl}}$ to 30 mm ($n_z = 2$). They also decay (with $E_z \to 0$) but at a much smaller rate indicating that the wavelength $\lambda_z = 3$ cm is close to (but still below) the cut-off wavelength for spanwise instability with our regularized model.

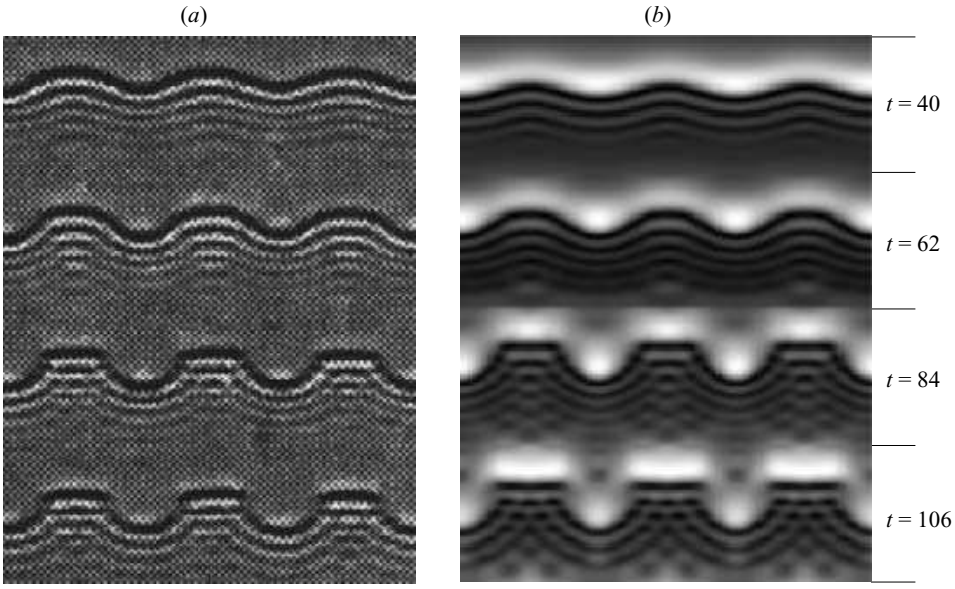

FIGURE 18. (*a*) Experimental picture (real size 60×80 mm) for set 6 ($R = 40.8$) (Park & Nosoko 2003, figure 7*c*, with permission from John Wiley & Sons, Inc.) (*b*) Simulations with $n_x = 3$, $n_z = 3$ and $L = 2n_x\pi/k$. The domain size is 60×60 mm with 256×256 grid points. Each of the six wave fronts has been obtained at a different dimensionless time, in an interval of 22.

Simulation results for a larger Reynolds number $R = 40.8$ are presented in figure 18 (parameter set 6) and compared to experimental findings (Park & Nosoko 2003, figure 7*c*). Like for $R = 20.7$, we first observe sinusoidal spanwise modulations of the two-dimensional waves. However, they rapidly evolve into rugged modulations, made of nearly flat backs and rounded fronts. To facilitate qualitative comparisons to the spatial evolution observed in experiments, snapshots of only a third of the numerical domain, corresponding to one streamwise wavelength, are displayed in figure 18 at increasing times. The interval of time separating each pair of snapshots roughly corresponds to the travelling of the fronts over a distance equal to one wavelength. Despite our use of periodic boundary conditions, the resemblance with the experimental findings (Park & Nosoko 2003, figure 7*c*) is convincing. For instance the chequerboard interference pattern of the capillary waves preceding the flat zones is recovered.

Above $R \approx 40$, Park & Nosoko (2003) observed a breaking of the modulated fronts leading to horseshoe-like waves. Simulation results for $R = 59.3$ are presented in figure 19 (parameter set 7) and compared to the experimental findings (Park & Nosoko 2003, figure 7*d*). Owing to computational limitations, the computational domain was limited to only one and two wavelengths in the streamwise and spanwise directions respectively ($n_x = 1$ and $n_z = 2$). Compared to $R = 40.8$, the rugged modulations develop faster and do not saturate. Instead, the bulges of the wave front continuously expand into horseshoe shapes, reducing the span of the flat parts at the back. As time proceeds, the legs of the horseshoes extend and split off into dimples, in qualitative agreement with experimental observations. The growth of the spanwise perturbations in our simulation is however faster than in the experiment.

8.3. *Three-dimensional natural waves*

In this section, we study the formation of noise-driven three-dimensional waves in the absence of periodic forcing. To match with the experiments by Alekseenko

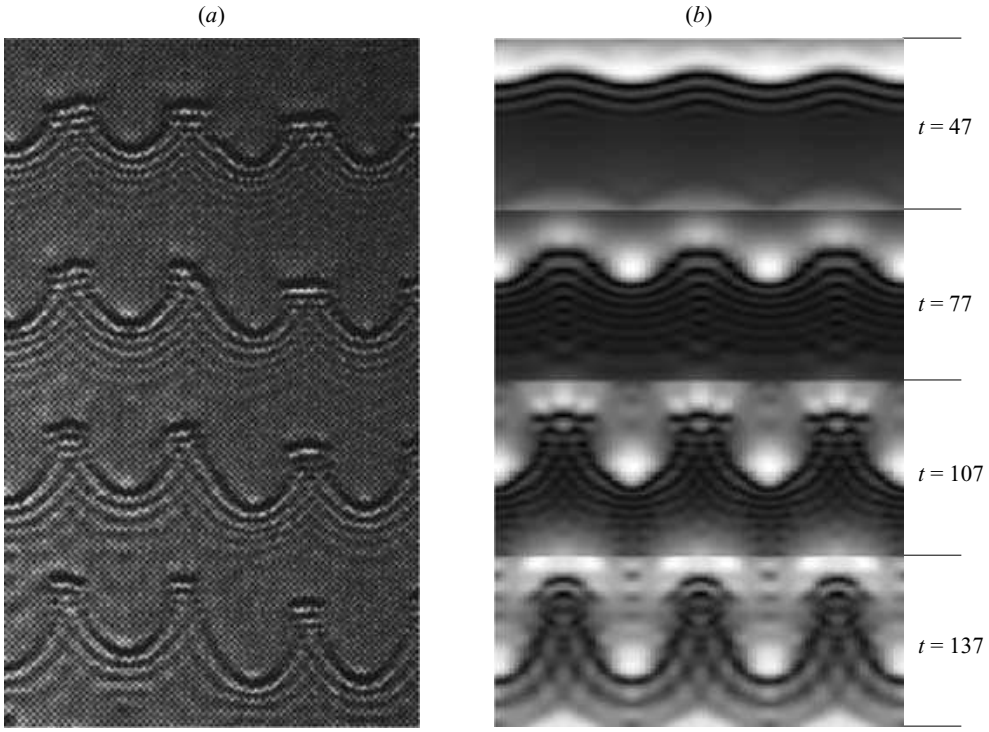

FIGURE 19. (*a*) Experimental picture (real size 60×100 mm) for set 7 ($R = 59.3$) (Park & Nosoko 2003, figure 7*d*, with permission from John Wiley & Sons, Inc.) (*b*) Snapshots of the simulated free surface. The domain size is 40×25 mm with 256×256 grid points. Each of the five wave fronts has been obtained at increasing dimensionless times, by interval of 30.

Set	R	β (deg.)	Γ	λ_x (mm)	k	c	$\langle h \rangle$
8	8	75	1106	40	0.15	1.322	0.906
9	16	75	1106	30	0.21	1.062	0.876
10	45	75	1106	25	0.28	0.749	0.904

TABLE 3. Parameters of the simulations corresponding to experiments on an inclined plane and with a 16% water–ethanol solution at 25°C ($\rho = 972$ kg m^{-3}, $\nu = 1.55 \times 10^{-6}$ m^2 s^{-1} and $\sigma = 40.8 \times 10^{-3}$ N m^{-1}) (Alekseenko *et al.* 1994, figure 1.6). The two-dimensional wave characteristics k, c and $\langle h \rangle$ have been computed from the wavelength λ_x, which has been estimated by the average streamwise separation of the three-dimensional waves observed in the experimental pictures. See also the caption of table 1.

et al. (1994), the initial conditions (8.2) need to be chosen with white noise of amplitude $A_{\text{noise}} = 10^{-3}$ and $A_x = A_z = 0$. Parameter values for the different numerical experiments are given in table 3. Snapshots of the free-surface deformation are reported in figure 21 where the three columns correspond to different Reynolds numbers (sets 8–10 of table 3). The experimental pictures obtained by Alekseenko *et al.* (1994) are shown for reference in figure 20. Each row in figure 21 corresponds to a particular transient regime: first, mostly two-dimensional waves; second, coalescence processes, and finally three-dimensional solitary waves. Both the dimensionless time t and the approximate location of the numerical domain on the experimental plane are given in figure 21. The distance being again estimated from the phase speed c of the two-dimensional waves (see table 3).

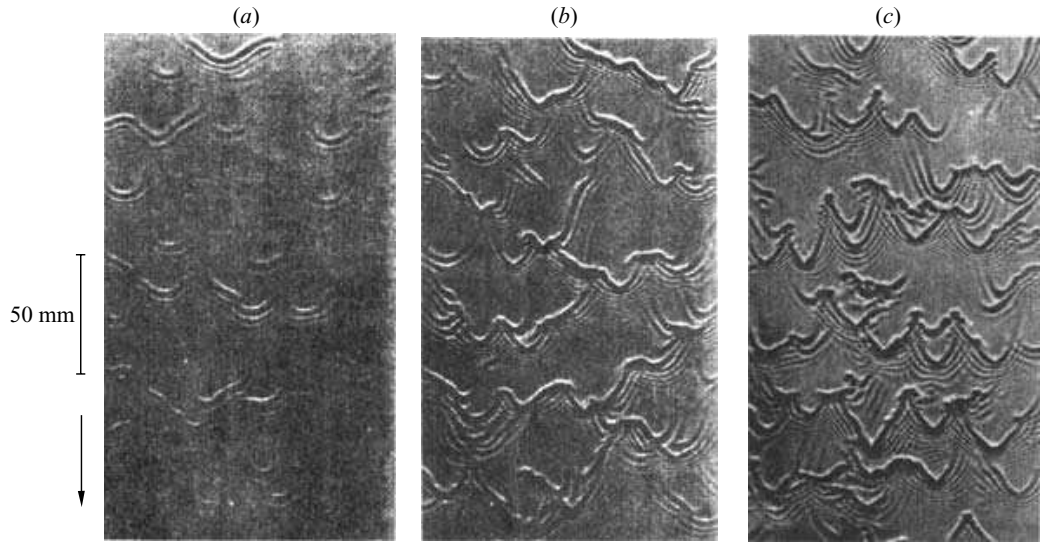

FIGURE 20. Wave patterns obtained experimentally by Alekseenko *et al.* (1994) (see table 3), courtesy of S. V. Alekseenko.

The large-amplitude waves travel faster, catch up the preceding slower ones and finally absorb them, which explains the coarsening process leading to an increase of the size of the flat zones that separate the waves. The development of capillary ripples in front of the humps is observed and the waves therefore resemble the two-dimensional γ_2 waves. Panels (*g, j*) and (*h, k*) of figure 21 share features similar to the experimental wave patterns. (For comparison, one should keep in mind that the grey levels represent surface elevation in simulations but surface slope in experiments.) The unsteady experimental pattern is characterized by interacting quasi-steady three-dimensional solitary waves separated by portions of constant thickness of length 10 to 50 cm. For $R = 8$, the average distance between the solitary waves tends to saturate for $t > 890$, which indicates either that solitary waves have reached a fully developed regime, or that the streamwise-periodic conditions are felt. For $R = 16$, no fully developed regime has been reached at the end of the simulation, which was run for 1500 time units. In that case, the final stage corresponds to interacting oblique fronts rather than three-dimensional horseshoe-like waves. For $R = 45$, the three-dimensional waves tend to form localized structures rather than extended wave fronts as observed for smaller values of R. This is in agreement with the results of Alekseenko *et al.* (1994) and Park & Nosoko (2003) who observed V-shaped or horseshoe-like solitary waves with a sharp curved front and long backwards tails under similar conditions (see panels *i* and *l*).

9. Concluding remarks

In most cases, asymptotic expansions are poorly converging and the Benney expansion is no exception to this rule (Oron & Gottlieb 2004). If an improvement of the accuracy is achieved by increasing the order of the approximation, this is at the cost of an increased complexity and a reduction of the range of parameters for which comparisons with DNS and experiments are satisfactory. Padé approximant techniques are well known for their ability to extend the radius of convergence of algebraic series.

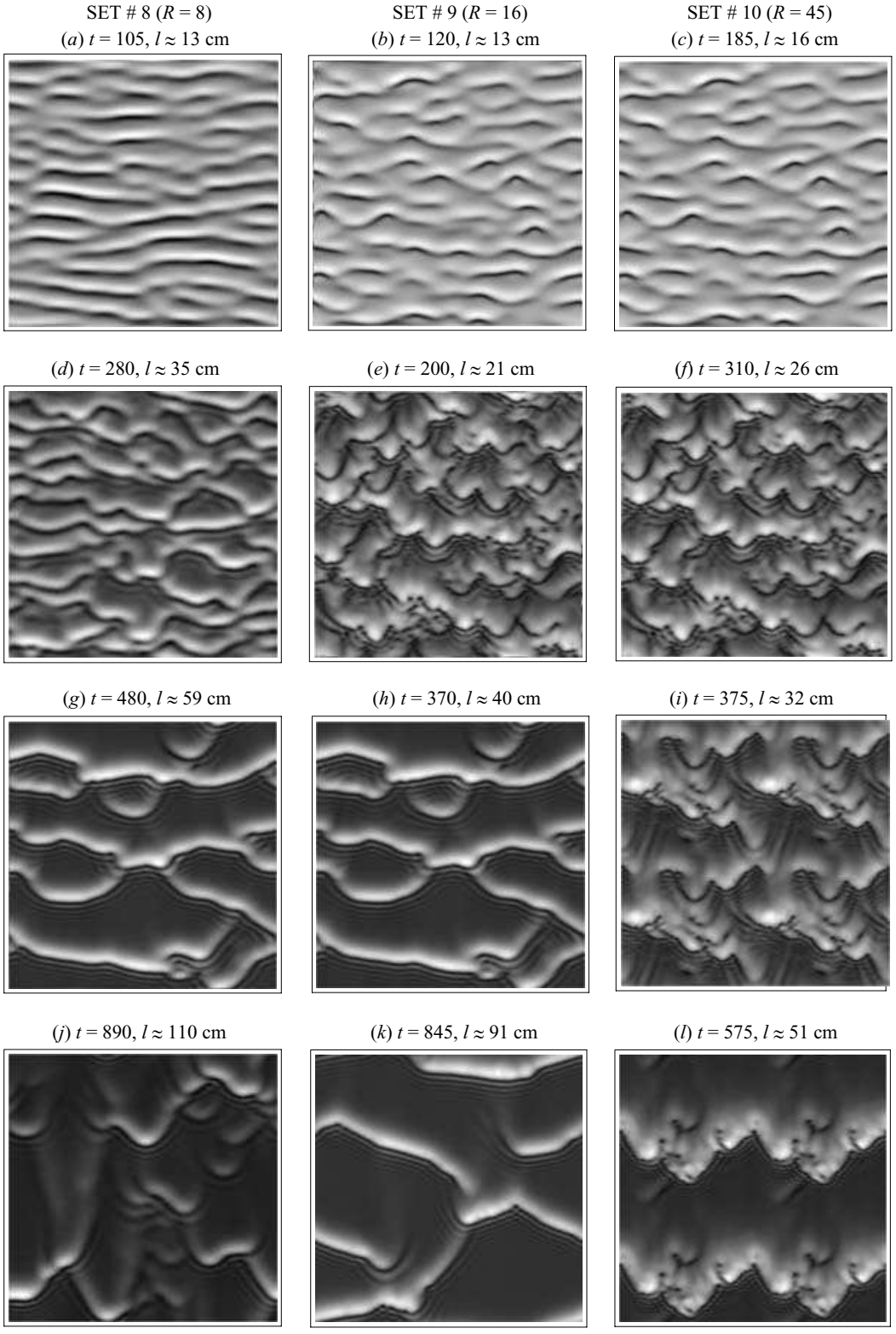

FIGURE 21. Simulations of natural (noise-driven) three-dimensional wave patterns corresponding to the experiments by Alekseenko *et al.* (1994) (see figure 20). The computational domain is $100 \times 100\,\mathrm{mm}^2$ with 256×256 grid points for set 8 and 9 and 512×256 for set 10 except for (i,l) where it corresponds to $50 \times 50\,\mathrm{mm}^2$ and 256×256 grid points: the snapshot obtained is repeated four times. l is the estimated distance from the inlet. The bright (dark) zones correspond to elevations (depressions).

In the case of two-dimensional flows, Ooshida's application of this idea to the Benney expansion remedies the unphysical occurrence of finite-time blow-up of solutions to (3.3) but a quantitative agreement cannot be achieved with experiments for δ of order unity or larger. We have shown elsewhere that a weighted residual procedure based on a polynomial expansion of the velocity field leads to a two-equation model at order ϵ in terms of the film thickness h and the flow rate q (Ruyer-Quil & Manneville 2000). Augmenting the order of the approximation to ϵ^2 again leads to a dramatic increase of the complexity yielding a four-equation model in the two-dimensional case and seven equations in the three-dimensional case. A way out can be found by dropping second-order inertial terms while retaining streamwise viscous diffusion effects, thus leading to the simplified model (3.1), (4.1). However, this simplification is done at the cost of a lowering of the order of the approximation. Based on the Padé approximant approach, the first part of this study has been devoted to the derivation of a two-equation model consistent at order ϵ^2, aiming at an agreement with DNS and experiments in the largest possible range of parameters.

Focusing on the treatment of inertia terms, our algebraic regularization procedure enabled us to obtain a two-equation model (3.1), (4.15) which is fully consistent with the Benney expansion up to second order. The approach developed here remedies the lack of systemization of the derivations presented in Ruyer-Quil *et al.* (2005) and Scheid *et al.* (2005*a*) where *ad-hoc* arguments were invoked to treat the case of a film uniformly heated from below. The use of a kind of algebraic preconditioner makes its application much simpler than Ooshida's approach based on differential operators. Our hope is that this Padé-like strategy might be useful for different related problems in lubrication theory for which a careful treatment of inertial effects are of importance, e.g. film flows where mass and heat transfer are involved, films down fibres, and roll waves (Balmforth & Liu 2004).

Computations of the two-dimensional solitary wave branches of solutions and two-dimensional periodic travelling waves agree quantitatively with laboratory and DNS experiments for the whole range of parameters for which two-dimensional wavy motion is observed. In particular, our models are able to capture the near-wall counterflow observed in the DNS by Malamataris *et al.* (2002) and in the experiments by Tihon *et al.* (2003), an effect that might be important when transfer of heat or mass from the substrate are considered.

We have extended our models to include the spanwise dependence in order to study the transition from two-dimensional to three-dimensional flows. A systematic Floquet analysis of the stability of the two-dimensional slow γ_1 waves has been performed, followed by numerical simulations using periodic boundary conditions. Our focus is the description of the three-dimensional wave patterns observed experimentally, with three main objectives: (i) using experimental results as benchmarks for a validation of our models; (ii) reproducing the synchronous and subharmonic transitions from γ_1 waves to three-dimensional patterns found by Liu *et al.* (1995); (iii) recovering the wave dynamics observed by Park & Nosoko (2003) in the case of well-controlled spanwise perturbations of fast γ_2 waves, and by Alekseenko *et al.* (1994) in the case of noise-driven instabilities.

Floquet analysis shows that the secondary three-dimensional instability is not selective, since the maximum growth rate remains nearly unchanged over the whole range $0 \leqslant \varphi \leqslant 1/2$ of the detuning parameter. This property makes the three-dimensional instability strongly dependent on the initial conditions, and thus prevents one relating unequivocally the results of Floquet analysis to experimental findings. By contrast, numerical simulations have shown good agreement with experimental results by Liu *et al.* (1995), provided that initial conditions are appropriately tuned. The

widespread observation of the synchronous instability in experiments could then be attributed to the presence of spanwise non-uniformities at the inlet, favouring in-phase modulations of the wave fronts. In some cases, the three-dimensional patterns emerge from a two-dimensional oscillatory mode rather than from saturated travelling waves, as also observed in direct numerical simulations by Ramaswamy *et al.* (1996). The competition between the growing two-dimensional modulation and the secondary three-dimensional instability makes the evolution of the film more sensitive to initial conditions. Complex three-dimensional dynamics deep in the nonlinear regime, in particular isolated synchronous depressions (figure 16), rugged-modulated waves (figure 18) as well as horseshoe-like three-dimensional solitary waves (figures 19 and 21*i,l*) and oblique solitary waves (figure 21*k*) found in our simulations were observed in experiments.

The application of a systematic strategy to the problem of film flows is shown here to lead to systems of equations of reduced dimensionality that capture the physical mechanisms quite faithfully, helping us to highlight the observed dynamics by isolating the important physical effects. Having reliable low-dimensional models at our disposal allows us to attack many questions still open for plain film flows over inclined planes, but also in more difficult cases, for example when heat or mass transfer are involved.

The authors wish to express their gratitude to N. A. Malamataris, M. Vlachogiannis and V. Bontozoglou for providing them with the wave profile corresponding to the full-scale numerical computation of the basic equations and shown in figure 3. C.R.-Q. and B.S. would like to thank Serafim Kalliadasis for stimulating discussions during his stay in Orsay. This study was partly funded by a grant from both French and Belgium research agencies (CNRS/CGRI-FNRS cooperation agreement). B.S. acknowledges funding from the European Commission through the Marie-Curie Training Centre.

Appendix A. Reconstruction of the velocity profile

Expressions for the polynomials g_0, g_1 and g_2 used to expand the velocity field are (Ruyer-Quil & Manneville 2000)

$$g_0(\bar{y}) = \bar{y} - \tfrac{1}{2}\bar{y}^2,$$
$$g_1(\bar{y}) = \bar{y} - \tfrac{17}{6}\bar{y}^2 + \tfrac{7}{3}\bar{y}^3 - \tfrac{7}{12}\bar{y}^4,$$
$$g_2(\bar{y}) = \bar{y} - \tfrac{13}{2}\bar{y}^2 + \tfrac{57}{4}\bar{y}^3 - \tfrac{111}{8}\bar{y}^4 + \tfrac{99}{16}\bar{y}^5 - \tfrac{33}{32}\bar{y}^6.$$

Streamlines and velocity profiles displayed in figure 4 were reconstructed from the solutions to the complete and the regularized models using the projection of the streamwise velocity on $g_0 = \bar{y} - \frac{1}{2}\bar{y}^2$, g_1 and g_2:

$$u = 3\frac{q-r-s}{h} g_0\left(\frac{y}{h}\right) + 45\, r\, g_1\left(\frac{y}{h}\right) + 210\, s\, g_2\left(\frac{y}{h}\right). \tag{A 1}$$

In the case of the regularized model (3.1), (4.15), expressions for the corrections r and s were given by their first-order approximation (4.3).

Appendix B. Three-dimensional regularized model

$$\partial_t h = -\partial_x q_x - \partial_z q_z, \tag{B 1a}$$

$$\delta\, \partial_t q_x = \delta\left[\frac{9}{7}\frac{q_x^2}{h^2}\partial_x h - \frac{17}{7}\frac{q_x}{h}\partial_x q_x\right] + \left\{\frac{5}{6}h - \frac{5}{2}\frac{q_x}{h^2} + \delta\left[-\frac{8}{7}\frac{q_x \partial_z q_z}{h} - \frac{9}{7}\frac{q_z \partial_z q_x}{h}\right.\right.$$

$$+\frac{9}{7}\frac{q_x q_z \partial_z h}{h^2}\Big] + \eta\Big[4\frac{q_x(\partial_x h)^2}{h^2} - \frac{9}{2}\frac{\partial_x q_x \partial_x h}{h} - 6\frac{q_x \partial_{xx} h}{h} + \frac{9}{2}\partial_{xx} q_x + \frac{13}{4}\frac{q_z \partial_x h \partial_z h}{h^2}$$
$$-\frac{\partial_z q_x \partial_z h}{h} - \frac{43}{16}\frac{\partial_x q_z \partial_z h}{h} - \frac{13}{16}\frac{\partial_z q_z \partial_x h}{h} + \frac{3}{4}\frac{q_x(\partial_z h)^2}{h^2} - \frac{23}{16}\frac{q_x \partial_{zz} h}{h} - \frac{73}{16}\frac{q_z \partial_{xz} h}{h}$$
$$+\partial_{zz} q_x + \frac{7}{2}\partial_{xz} q_z\Big] - \frac{5}{6}\zeta h\,\partial_x h + \frac{5}{6}h(\partial_{xxx} + \partial_{xzz})h\Big\}\left(1 - \frac{\delta}{70}q_x \partial_x h\right)^{-1}, \quad \text{(B 1}b\text{)}$$

$$\delta\,\partial_t q_z = \delta\Big[\frac{9}{7}\frac{q_z^2}{h^2}\partial_z h - \frac{17}{7}\frac{q_z}{h}\partial_z q_z\Big] - \frac{5}{2}\frac{q_z}{h^2} + \delta\Big[-\frac{8}{7}\frac{q_z \partial_x q_x}{h} - \frac{9}{7}\frac{q_x \partial_x q_z}{h} + \frac{9}{7}\frac{q_x q_z \partial_x h}{h^2}\Big]$$
$$+\eta\Big[4\frac{q_z(\partial_z h)^2}{h^2} - \frac{9}{2}\frac{\partial_z q_z \partial_z h}{h} - 6\frac{q_z \partial_{zz} h}{h} + \frac{9}{2}\partial_{zz} q_z + \frac{13}{4}\frac{q_x \partial_x h \partial_z h}{h^2} - \frac{\partial_x q_z \partial_x h}{h}$$
$$-\frac{43}{16}\frac{\partial_z q_x \partial_x h}{h} - \frac{13}{16}\frac{\partial_x q_x \partial_z h}{h} + \frac{3}{4}\frac{q_z(\partial_x h)^2}{h^2} - \frac{23}{16}\frac{q_z \partial_{xx} h}{h} - \frac{73}{16}\frac{q_x \partial_{xz} h}{h} + \partial_{xx} q_z$$
$$+\frac{7}{2}\partial_{xz} q_x\Big] - \frac{5}{6}\zeta h\,\partial_z h + \frac{5}{6}h(\partial_{xxz} + \partial_{zzz})h. \quad \text{(B 1}c\text{)}$$

Appendix C. Complete second-order model

Writing $\varepsilon_x = 1$ and $\varepsilon_z = 0$, the complete second-order model consists of the evolution equations for q_x, r_x and s_x:

$$\delta\,\partial_t q_x = \varepsilon_x\frac{27}{28}h - \frac{81}{28}\frac{q_x}{h^2} - 33\frac{r_x}{h^2} - \frac{3069}{28}\frac{s_x}{h^2} + \delta\Big[-\frac{12}{5}\frac{q_x r_x \partial_x h}{h^2} - \frac{126}{65}\frac{q_x s_x \partial_x h}{h^2} + \frac{12}{5}\frac{r_x \partial_x q_x}{h}$$
$$+\frac{171}{65}\frac{s_x \partial_x q_x}{h} + \frac{12}{5}\frac{q_x \partial_x r_x}{h} + \frac{1017}{455}\frac{q_x \partial_x s_x}{h} + \frac{6}{5}\frac{q_x^2 \partial_x h}{h^2} - \frac{12}{5}\frac{q_x \partial_x q_x}{h} - \frac{6}{5}\frac{q_x \partial_z q_z}{h}$$
$$-\frac{6}{5}\frac{q_z \partial_z q_x}{h} + \frac{6}{5}\frac{q_x q_z \partial_z h}{h^2} - \frac{6}{5}\frac{q_x r_z \partial_z h}{h^2} - \frac{63}{65}\frac{q_x s_z \partial_z h}{h^2} - \frac{6}{5}\frac{q_z r_x \partial_z h}{h^2} - \frac{63}{65}\frac{q_z s_x \partial_z h}{h^2}$$
$$+\frac{6}{5}\frac{r_x \partial_z q_z}{h} + \frac{108}{65}\frac{s_x \partial_z q_z}{h} + \frac{6}{5}\frac{r_z \partial_z q_x}{h} + \frac{63}{65}\frac{s_z \partial_z q_x}{h} + \frac{6}{5}\frac{q_x \partial_z r_z}{h} + \frac{576}{455}\frac{q_x \partial_z s_z}{h}$$
$$+\frac{6}{5}\frac{q_z \partial_z r_x}{h} + \frac{63}{65}\frac{q_z \partial_z s_x}{h}\Big] + \eta\Big[\frac{5025}{896}\frac{q_x(\partial_x h)^2}{h^2} - \frac{5055}{896}\frac{\partial_x q_x \partial_x h}{h} - \frac{10851}{1792}\frac{q_x \partial_{xx} h}{h}$$
$$+\frac{2027}{448}\partial_{xx} q_x + \partial_{zz} q_x - \frac{2463}{1792}\frac{\partial_z q_x \partial_z h}{h} + \frac{2433}{1792}\frac{q_x(\partial_z h)^2}{h^2} - \frac{5361}{3584}\frac{q_x \partial_{zz} h}{h}$$
$$+\frac{7617}{1792}\frac{q_z \partial_x h \partial_z h}{h^2} - \frac{4749}{3584}\frac{\partial_z q_z \partial_x h}{h} - \frac{10545}{3584}\frac{\partial_x q_z \partial_z h}{h} - \frac{16341}{3584}\frac{q_z \partial_{xz} h}{h}$$
$$+\frac{1579}{448}\partial_{xz} q_z\Big] - \frac{27}{28}\zeta h\,\partial_x h + \frac{27}{28}h(\partial_{xxx} + \partial_{xzz})h, \quad \text{(C 1}a\text{)}$$

$$\delta\,\partial_t r_x = \varepsilon_x\frac{1}{10}h - \frac{3}{10}\frac{q_x}{h^2} - \frac{126}{5}\frac{r_x}{h^2} - \frac{126}{5}\frac{s_x}{h^2} + \delta\Big[\frac{1}{35}\frac{q_x \partial_x q_x}{h} - \frac{3}{35}\frac{q_x^2 \partial_x h}{h^2} + \frac{108}{55}\frac{q_x r_x \partial_x h}{h^2}$$
$$-\frac{5022}{5005}\frac{q_x s_x \partial_x h}{h^2} - \frac{103}{55}\frac{r_x \partial_x q_x}{h} + \frac{9657}{5005}\frac{s_x \partial_x q_x}{h} - \frac{39}{55}\frac{q_x \partial_x r_x}{h} + \frac{10557}{10010}\frac{q_x \partial_x s_x}{h}$$
$$-\frac{2}{35}\frac{q_x \partial_z q_z}{h} + \frac{3}{35}\frac{q_z \partial_z q_x}{h} - \frac{3}{35}\frac{q_x q_z \partial_z h}{h^2} + \frac{54}{55}\frac{q_x r_z \partial_z h}{h^2} + \frac{54}{55}\frac{q_z r_x \partial_z h}{h^2} - \frac{54}{55}\frac{r_z \partial_z q_x}{h}$$
$$-\frac{54}{55}\frac{q_z \partial_z r_x}{h} - \frac{2511}{5005}\frac{q_z s_x \partial_z h}{h^2} - \frac{2511}{5005}\frac{q_x s_z \partial_z h}{h^2} + \frac{2511}{5005}\frac{s_z \partial_z q_x}{h} + \frac{2511}{5005}\frac{q_z \partial_z s_x}{h}$$

$$-\frac{49}{55}\frac{r_x\partial_z q_z}{h}+\frac{7146}{5005}\frac{s_x\partial_z q_z}{h}+\frac{3}{11}\frac{q_x\partial_z r_z}{h}+\frac{1107}{2002}\frac{q_x\partial_z s_z}{h}\Big]+\eta\Big[\frac{93}{40}\frac{q_x(\partial_x h)^2}{h^2}$$
$$-\frac{69}{40}\frac{\partial_x h\partial_x q_x}{h}+\frac{21}{80}\frac{q_x\partial_{xx}h}{h}-\frac{9}{40}\partial_{xx}q_x-\frac{57}{80}\frac{\partial_z q_x\partial_z h}{h}+\frac{81}{80}\frac{q_x(\partial_z h)^2}{h^2}-\frac{3}{40}\frac{q_x\partial_{zz}h}{h}$$
$$+\frac{27}{80}\frac{q_z\partial_{xz}h}{h}+\frac{21}{16}\frac{q_z\partial_x h\partial_z h}{h^2}-\frac{63}{80}\frac{\partial_z q_z\partial_x h}{h}-\frac{9}{40}\frac{\partial_z h\partial_x q_z}{h}-\frac{9}{40}\partial_{xz}q_z\Big]$$
$$-\frac{1}{10}\zeta h\partial_x h+\frac{1}{10}h(\partial_{xxx}+\partial_{xzz})h, \qquad (C\,1b)$$

$$\delta\,\partial_t s_x=\varepsilon_x\frac{13}{420}h-\frac{13}{140}\frac{q_x}{h^2}-\frac{39}{5}\frac{r_x}{h^2}-\frac{11817}{140}\frac{s_x}{h^2}+\delta\Big[-\frac{4}{11}\frac{q_x r_x\partial_x h}{h^2}+\frac{18}{11}\frac{q_x s_x\partial_x h}{h^2}$$
$$-\frac{2}{33}\frac{r_x\partial_x q_x}{h}-\frac{19}{11}\frac{s_x\partial_x q_x}{h}+\frac{6}{55}\frac{q_x\partial_x r_x}{h}-\frac{288}{385}\frac{q_x\partial_x s_x}{h}-\frac{2}{11}\frac{q_x r_z\partial_z h}{h^2}-\frac{2}{11}\frac{q_z r_x\partial_z h}{h^2}$$
$$+\frac{2}{11}\frac{r_z\partial_z q_x}{h}+\frac{2}{11}\frac{q_z\partial_z r_x}{h}+\frac{9}{11}\frac{q_x s_z\partial_z h}{h^2}+\frac{9}{11}\frac{q_z s_x\partial_z h}{h^2}-\frac{9}{11}\frac{s_z\partial_z q_x}{h}-\frac{9}{11}\frac{q_z\partial_z s_x}{h}$$
$$-\frac{8}{33}\frac{r_x\partial_z q_z}{h}-\frac{10}{11}\frac{s_x\partial_z q_z}{h}-\frac{4}{55}\frac{q_x\partial_z r_z}{h}+\frac{27}{385}\frac{q_x\partial_z s_z}{h}\Big]$$
$$+\eta\Big[-\frac{3211}{4480}\frac{q_x(\partial_x h)^2}{h^2}+\frac{2613}{4480}\frac{\partial_x h\partial_x q_x}{h}-\frac{2847}{8960}\frac{q_x\partial_{xx}h}{h}+\frac{559}{2240}\partial_{xx}q_x+\frac{3029}{8960}\frac{\partial_z q_x\partial_z h}{h}$$
$$-\frac{3627}{8960}\frac{q_x(\partial_z h)^2}{h^2}+\frac{299}{17920}\frac{q_x\partial_{zz}h}{h}-\frac{559}{1792}\frac{q_z\partial_x h\partial_z h}{h^2}+\frac{4927}{17920}\frac{\partial_z q_z\partial_x h}{h}$$
$$-\frac{533}{17920}\frac{\partial_x q_z\partial_z h}{h}-\frac{5993}{17920}\frac{q_z\partial_{xz}h}{h}+\frac{559}{2240}\partial_{xz}q_z\Big]$$
$$-\frac{13}{420}\zeta h\partial_x h+\frac{13}{420}h(\partial_{xxx}+\partial_{xzz})h, \qquad (C\,1c)$$

along with a symmetrical set of equations for q_z, r_z and s_z, obtained from equations (C 1) through the exchanges $\{x\leftrightarrow z\}$. The set of equations is then completed by the mass conservation $\partial_t h=-\partial_x q_x-\partial_z q_z$. The complete two-dimensional model is obtained by setting $\partial_z\equiv 0$ and $q_z=r_z=s_z\equiv 0$ in these equations.

REFERENCES

Alekseenko, S. V., Antipin, V. A., Guzanov, V. V., Kharlamov, S. M. & Markovich, D. M. 2005 Three-dimensional solitary waves on falling liquid film at low Reynolds numbers. *Phys. Fluids* **17**, 121704.

Alekseenko, S. V., Nakoryakov, V. Y. & Pokusaev, B. G. 1994 *Wave Flow of Liquid Films.* Begell House.

Argyriadi, K., Serifi, K. & Bontozoglou, V. 2004 Nonlinear dynamics of inclined films under low-frequency forcing. *Phys. Fluids* **16**, 2457–2468.

Atherton, R. W. & Homsy, G. M. 1976 On the derivation of evolution equations for interfacial waves. *Chem. Engng Commun.* **2**, 57–77.

Balakotaiah, V. & Mudunuri, R. R. 2004 Reply to comment on "Low-dimensional models for vertically falling viscous films". *Phys. Rev. Lett.* **93**, 199402.

Balmforth, N. J. & Liu, J. J. 2004 Roll waves in mud. *J. Fluid Mech.* **519**, 33–54.

Benney, D. J. 1966 Long waves on liquid film. *J. Math Phys.* **45**, 150–155.

Chang, H.-C. 1986 Traveling waves on fluid interfaces: Normal form analysis of the Kuramoto-Sivashinsky equation. *Phys. Fluids* **29**, 3142–3147.

Chang, H.-C. 1994 Wave evolution on a falling film. *Annu. Rev. Fluid Mech.* **26**, 103–136.

Chang, H.-C., Cheng, M., Demekhin, E. A. & Kopelevitch, D. I. 1994 Secondary and tertiary excitation of three-dimensional patterns on a falling film. *J. Fluid Mech.* **270**, 251–275.

Chang, H.-C., Demekhin, E. & Kalaidin, E. 1996 Simulation of noise-driven wave dynamics on a falling film. *AIChE J.* **42**, 1553–1568.

Chang, H.-C., Demekhin, E. A. & Kopelevitch, D. I. 1993 Nonlinear evolution of waves on a vertically falling film. *J. Fluid Mech.* **250**, 433–480.

Doedel, E. J., Champneys, A. R., Fairgrieve, T. F., Kuznetsov, Y. A., Sandstede, B. & Wang, X.-J. 1997 Auto97: Continuation and bifurcation software for ordinary differential equations. *Tech. Rep.* Department of Computer Science, Concordia University, Montreal, Canada (available by FTP from `ftp.cs.concordia.ca` in directory `pub/doedel/auto`).

Floryan, J., Davis, S. & Kelly, R. 1987 Instabilities of a liquid film flowing down a slightly inclined plane. *Phys. Fluids* **30**, 983–989.

Gjevik, B. 1970 Occurence of finite-amplitude surface waves on falling liquid films. *Phys. Fluids* **13**, 1918–1925.

Gjevik, B. 1971 Spatially varying finite-amplitude wave trains on falling liquid films. *Acta Polytech. Scand. Me.* **61**, 1–16.

Glendinning, P. & Sparrow, C. 1984 Local and global behaviour near homoclinic orbits. *J. Statist. Phys.* **35**, 645–696.

Herbert, T. 1988 Secondary instability of boundary layers. *Annu. Rev. Fluid Mech.* **20**, 487.

Joo, S. & Davis, S. 1992 Instabilities of three-dimensional theory viscous falling films. *J. Fluid Mech.* **242**, 529.

Kapitza, P. L. 1948 Wave flow of thin layers of a viscous fluid. In *Collected Papers of P.L. Kapitza* (ed. D. T. Haar), pp. 662–689. Pergamon, original paper: *Zh. Ekper. Teor. Fiz.* **18**, 3–28 (in Russian).

Kapitza, P. L. & Kapitza, S. P. 1949 Wave flow of thin layers of a viscous fluid. In *Collected Papers of P.L. Kapitza* (ed. D. T. Haar), pp. 690–709. Pergamon, original paper: *Zh. Ekper. Teor. Fiz.* **19**, 105–120 (in Russian).

Lin, S. P. 1974 Finite amplitude side-band stability of a viscous fluid. *J. Fluid Mech.* **63**, 417–429.

Liu, J. & Gollub, J. P. 1993 Onset of spatially chaotic waves on flowing films. *Phys. Rev. Lett.* **70**, 2289–2292.

Liu, J. & Gollub, J. P. 1994 Solitary wave dynamics of film flows. *Phys. Fluids* **6**, 1702–1712.

Liu, J., Paul, J. D. & Gollub, J. P. 1993 Measurements of the primary instabilities of film flows. *J. Fluid Mech.* **250**, 69–101.

Liu, J., Schneider, J. B. & Gollub, J. P. 1995 Three-dimensional instabilites of film flows. *Phys. Fluids* **7**, 55–67.

Malamataris, N. A., Vlachogiannis, M. & Bontozoglou, V. 2002 Solitary waves on inclined films: Flow structure and binary interactions. *Phys. Fluids* **14**, 1082–1094.

Nakaya, C. 1975 Long waves on a thin fluid layer flowing down an inclined plane. *Phys. Fluids* **18**, 1407–1412.

Nosoko, T. & Miyara, A. 2004 The evolution and subsequent dynamics of waves on a vertically falling liquid film. *Phys. Fluids* **16**, 1118–1126.

Nosoko, T., Yoshimura, P. N., Nagata, T. & Okawa, K. 1996 Characteristics of two-dimensional waves on a falling liquid film. *Chem. Engng Sci.* **51**, 725–732.

Ooshida, T. 1999 Surface equation of falling film flows with moderate Reynolds number and large but finite Weber number. *Phys. Fluids* **11**, 3247–3269.

Oron, A. & Gottlieb, O. 2004 Subcritical and supercritical bifurcations of the first- and second order Benney equations. *J. Engng Maths* **50**, 121–140.

Panga, M. K. R. & Balakotaiah, V. 2003 Low-dimensional models for vertically falling viscous films. *Phys. Rev. Lett.* **90**, 154501.

Panga, M. K. R., Mudunuri, R. R. & Balakotaiah, V. 2005 Long-wavelength equation for vertically falling films. *Phys. Rev.* E **71**, 036310.

Park, C. D. & Nosoko, T. 2003 Three-dimensional wave dynamics on a falling film and associated mass transfer. *AIChE J.* **49**, 2715–2727.

Press, W., Teukolsky, S., Vetterling, W. & Flannery, B. 1992 *Numerical Recipes in C–The Art of Scientific Computing*, 2nd edn. Cambridge University Press.

Pumir, A., Manneville, P. & Pomeau, Y. 1983 On solitary waves running down an inclined plane. *J. Fluid Mech.* **135**, 27–50.

Ramaswamy, B., Chippada, S. & Joo, S. W. 1996 A full-scale numerical study of interfacial instabilities in thin-film flows. *J. Fluid Mech.* **325**, 163–194.

Roberts, A. 1996 Low-dimensional models of thin film fluid dynamics. *Phys. Lett*. A **212**, 63–71.

Roskes, G. 1969 Three-dimensional long waves on a liquid film. *Phys. Fluids* **13**, 1440–1445.

Roy, R., Roberts, A. & Simpson, M. 2002 A lubrication model of coating flows over a curved substrate in space. *J. Fluid Mech.* **454**, 235–261.

Ruyer-Quil, C. 1999 Dynamique d'un film mince s'écoulant le long d'un plan incliné. PhD dissertation, École polytechnique.

Ruyer-Quil, C. & Manneville, P. 1998 Modeling film flows down inclined planes. *Eur. Phys. J.* B **6**, 277–292.

Ruyer-Quil, C. & Manneville, P. 2000 Improved modeling of flows down inclined planes. *Eur. Phys. J. B* **15**, 357–369.

Ruyer-Quil, C. & Manneville, P. 2004 Comment on "Low-dimensional models for vertically falling viscous films". *Phys. Rev. Lett* **93**, 199401.

Ruyer-Quil, C., Scheid, B., Kalliadasis, S., Velarde, M. G. & R. Kh. Zeytounian 2005 Thermocapillary long waves in a liquid film flow. Part 1. Low-dimensional formulation. *J. Fluid Mech.* **538**, 199–222.

Salamon, T., Armstrong, R. & Brown, R. 1994 Traveling waves on vertical films: Numerical analysis using the finite element method. *Phys. Fluids* **6**, 2202–2220.

Saprykin, S., Demekhin, E. A. & Kalliadasis, S. 2005 Self-organization of two-dimensional waves in an active-dispersive-dissipative nonlinear medium. *Phys. Rev. Lett*. **94**, 224101.

Scheid, B., Ruyer-Quil, C., Kalliadasis, S., Velarde, M. G. & R. Kh. Zeytounian 2005*a* Thermocapillary long waves in a liquid film flow. Part 2. Linear stability and nonlinear waves. *J. Fluid Mech.* **538**, 223–244.

Scheid, B., Ruyer-Quil, C., Thiele, U., Kabov, O., Legros, J. & Colinet, P. 2005*b* Validity domain of the Benney equation including Marangoni effect for closed and open flows. *J. Fluid Mech.* **527**, 303–335.

Schlichting, H. 1955 *Boundary-Layer Theory*. McGraw-Hill.

Schmid, P. J. & Henningson, D. S. 2001 *Stability and Transition in Shear Flows*. Springer.

Shkadov, V. 1967 Wave flow regimes of a thin layer of viscous fluid subject to gravity. *Izv. Ak. Nauk SSSR, Mekh. Zhi. Gaz* **2**, 43–51 (English transl. *Fluid Dynamics* **2**, Faraday Press, NY, 1970, pp. 29–34).

Shkadov, V. 1977 Solitary waves in a layer of viscous liquid. *Izv. Ak. Nauk SSSR, Mekh. Zhi. Gaz* **1**, 63–66.

Tihon, J., Tovchigrechko, V., Sobol'ik, V. & Wein, O. 2003 Electrodiffusion detection of the near-wall flow reversal in liquid films at the regime of solitary waves. *J. Appl. Electrochem.* **33** (7), 577–587.

Trifonov, Y. Y. 1989 Bifurcations of two-dimensional into three-dimensional wave regimes for a vertically flowing liquid film. *Izv. Ak. Nauk SSR, Mekh. Zh. Gaza* **5**, 109–114.

Vlachogiannis, M. & Bontozoglou, V. 2001 Observations of solitary wave dynamics of film flows. *J. Fluid Mech.* **435**, 191.

Whitham, G. B. 1974 *Linear and Nonlinear Waves*. Wiley-Interscience.

Heated falling films

3

In this chapter I quickly summarize the work I have done in the period 2003–2008 in collaboration with Serafim Kalliadasis (University of Leeds, now at Imperial college London), Philip Treveleyan (University of Leeds, now at University of Glamorgan, Cardiff), Benoit Scheid (Université Libre de Bruxelles), Manuel Garcia Velarde (Universidad Complutense, Madrid) and Radhyadour Kh. Zeytounian (Université des Sciences et Technologies de Lille). This work was initiated by Manuel G. Velarde who kindly invited me for the summertime in Madrid.

The question that was raised by Manuel G. Velarde at that time was the coupling between the Kapitza instability of a falling film (see previous chapter 2) and the Marangoni instability of a free surface heated from below. It is well known since the works by Pearson (1958), Scriven and Sterling (1964), Smith (1966) that a fluid layer bounded by a deformable upper surface and heated from below may develop a long-wave instability mode, referred hereinafter as the S-mode following the terminology adopted by Goussis and Kelly (1991). This long-wave instability is triggered by the deformability of the free surface and by the dependence of the surface tension on the temperature, the Marangoni effect. [1] As the elevation of the free surface varies, the heat transfer across the film promotes gradients of temperature, the surface of thick film being cooler than the surface of thin film. As a result, gradients of surface tension build up promoting stresses from spots of low surface energy towards spots of high surface energy. Whenever surface tension decreases with temperature (which is the general case), an unstable situation is reached. The fluid is dragged from the troughs to the crests and perturbations are promoted by the Marangoni effect.

In our study of this problem, we have assumed some simplifications. We assumed a dynamically and thermally *passive gas*. The ambient atmosphere is at rest and no tangential shear stresses are exerted on the liquid film by the gas flow (zero gas viscosity). Besides the heat transfer from the liquid to the gas is modeled by a Robin mixed condition on the temperature using a single Biot number (that is a constant heat transfer coefficient). Our study of this instability is therefore one-sided: the dynamics of the flow being entirely piloted by the liquid phase. Real problems are much more difficult: the heat transfer at the liquid-gas interface involves evaporation processes —considered e.g. in Joo et al. (1991)— so that a constant heat transfer coefficient is a rather crude assumption.

[1] A modern account of this instability mechanism can be found for instance in the monographs by Colinet et al. (2001), Velarde and Zeytounian (2002).

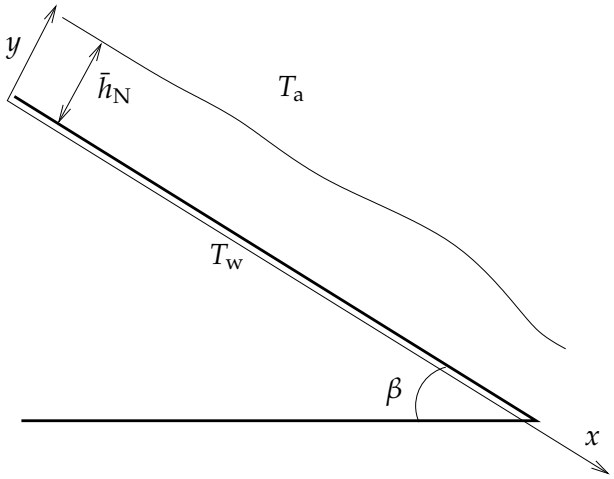

(a) *specified temperature : ST case*

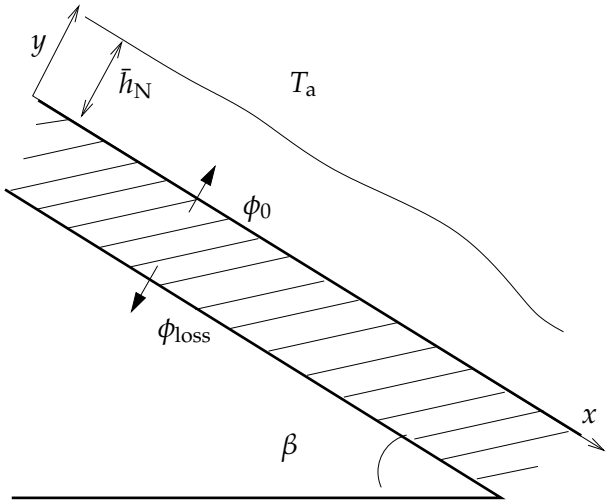

(b) *specified flux : HF case*

Figure 3.1 – *Sketches of a film falling down a uniformly heated plane. $\bar{h}_N$ is the Nusselt flat film thickness. (a) ST case; (b) HF case.*

Yet, this problem is a very rich one. Its interest stems mainly in the coupling between a first instability that is oriented in the direction of the flow and a second instability that is isotropic in nature. Indeed, the Kapitza mode —K mode— of instability results from the inertia of the flow and is thus oriented by the gravity acceleration which triggers the flow, whereas the Marangoni S mode has no preferential direction in the (x,z) plane of the wall.

Two cases have been considered. In the first once, christened ST case, a constant temperature is specified at the wall. Yet, in practice, the temperature at the wall is not controlled by the operator who instead specify the amount of heat that is dissipated by means of a heater. This leads to the second HF case where the heat generated in the wall is specified. Both cases are sketched in figure 3.1

In the HF case, at the lower boundary of he wall a heat transfer coefficient specify the heat flux ϕ_{loss} that is lost to a surrounding fluid. It is important to note that the presence of such a loss of heat is paramount

for the S-Marangoni instability mode. Indeed, without this heat loss, the temperature at the free surface of a uniform film is independent of the film thickness, and the Marangoni effect would be lost in the long-wave limit (Scheid 2004).

Because the ST case is simpler than the HF case, we have studied it much more thoroughly (Ruyer-Quil et al. 2005, Scheid et al. 2005a, Trevelyan et al. 2007, Scheid et al. 2008a;b) than the HF case which is first considered in Benoit Scheid's PhD thesis (Scheid 2004) and later on in Trevelyan et al. (2007) (to which I only slightly contributed). An extended review of our findings in the case of the ST case can be found in the ninth chapter of the recent monograph by Kalliadasis et al. (2012). I will give a short account of my contribution to this problem and I limit myself to sketch the simpler ST case in the remainder of this chapter.

3.1 Notations and parameters

Geometry and notations are introduced in figure 3.1(a). A film falling down a uniformly heated inclined plane with inclination angle β with respect to the horizontal direction. The ambient gas phase is air at temperature T_a . The wall is maintained at a constant and uniform temperature T_w ($> T_a$). Density ρ, viscosity μ, thermal conductivity K of the liquid, thermal diffusivity χ, heat transfer coefficient q_0 at the liquid-gas interface are all assumed constant. The reference Nusselt thickness of the film is denoted by $\bar{h}_N$ and the inlet flow rate per unit length is referred to as $\bar{q}_N$. Taking for reference the temperature T_a of ambient air, the surface tension varies linearly with temperature, i.e. $\sigma = \sigma(T_a) + d\sigma/dT|_{T_a}(T - T_a)$. Surface tension is supposed to decrease with temperature $d\sigma/dT|_{T_a} < 0$ (this last assumption ensures that the Marangoni instability can be observed).

By contrast with the isothermal problem (see chapter 2), the set of dimensionless groups, inclination angle β, Reynolds number $Re = \bar{q}_N/\nu = h_N^3/3$ and Kapitza number $\Gamma = \sigma(T_a)/[\rho\nu^{4/3}(g\sin\beta)^{1/3}]$ is completed by a Marangoni number, a Biot number and a Prandtl number defined as

$$Ma = \frac{-d\sigma/dT|_{T_a}(T_w - T_a)}{\rho\nu^{4/3}(g\sin\beta)^{1/3}}, \quad Bi = \frac{q_0\,\nu^{2/3}}{K(g\sin\beta)^{1/3}}, \quad Pr = \frac{\nu}{\kappa},$$

The Prandtl number compares viscous and thermal diffusivities, whereas the Biot number is a dimensionless heat transfer and pilots the exchange of heat at the free surface. The Marangoni number reckons the intensity of the coupling at the free surface between the momentum balance and the thermal diffusion. Finally, the product $Pe = PrRe$ defines the Péclet number which compares thermal conduction to the convection of heat by the flow.

Similarly to the isothermal case (cf. § 2.2) the set of six independent parameters (β, Re, Γ, Ma, Bi, Pr) can be reduced by one in the limit of high Kapitza number by neglecting he viscous damping of the waves —elongational Trouton viscosity. Following Shkadov (1977), let us use a scale $\kappa\bar{h}_N$ in the x and z directions and the Nusselt thickness $\bar{h}_N$ in the cross-stream direction y. The aspect ratio κ is adjusted by balancing streamwise gravity acceleration and capillary pressure gradient. A set of

'reduced' parameters now appears

$$\begin{aligned} \delta &= \frac{\bar{h}_N^3}{\kappa} = \frac{(3Re)^{11/9}}{\Gamma^{1/3}}, \quad \zeta = \frac{\cot\beta}{\kappa} = \frac{\cot\beta (3Re)^{2/9}}{\Gamma^{1/3}}, \quad B = Bi\,(3Re)^{1/3} \\ \eta &= \frac{1}{\kappa^2} = \frac{(3Re)^{4/9}}{\Gamma^{2/3}} \quad \text{and} \quad M = \frac{Ma}{\kappa \bar{h}_N^2} = \frac{Ma}{\Gamma^{1/3}(3Re)^{4/9}}, \end{aligned} \tag{3.1}$$

The number of parameters is thus reduced by one in the limit $\eta \to 0$ (equivalent to $\Gamma \gg 1$).

3.2 Low-dimensional modeling

As for isothermal falling films (cf. chapter 2), low-dimensional models are based on the long-wave asymptotics with the introduction of a formal film parameter $\epsilon \sim \partial_{x,z,t}$. Each low-dimensional strategy thus aim at the elimination of the 'fast' cross-stream variable y, the flow being governed by the 'slow' variables x, z and t. We have applied the weighted residual method that has been successful to treat the isothermal problem. The strategy and a hierarchy of models, consistent at first and second order is developed in the ninth chapter of the recent monograph Kalliadasis et al. (2012). I thus only give a short account (limited to two-dimensional flows and mostly to first-order models) of the peculiarities of the application of the method to the non-isothermal case.

Obviously, the difference with the isothermal case originates from the treatment of the energy balance and its coupling to the momentum equation through the interfacial Marangoni effect. The first degree of freedom associated to the temperature field should be the temperature at the free surface $T(y = h) \equiv \theta(x, t)$ which explicitly appears in the tangential stress boundary condition (here truncated at second order) :

$$\partial_y u\big|_h = \eta \left(4\partial_x h \partial_x u\big|_h - \partial_x v|_h \right) - M\partial_x \left[T\big|_h \right] + O(\epsilon^3) \tag{3.2}$$

Gradient expansion

Following Kalliadasis et al. (2003b), let us assume a linear temperature distribution at $O(\epsilon^0)$ and decompose the velocity field into a zeroth order part and a $O(\epsilon)$ correction

$$T = T^{(0)} + T^{(1)} \quad \text{with} \quad T^{(0)} = 1 + (\theta - 1)\bar{y} \quad \text{where} \quad \bar{y} = y/h \tag{3.3a}$$

As for the isothermal case, a similar ansatz is introduced for the velocity field

$$u = u^{(0)} + u^{(1)} \quad \text{with} \quad u^{(0)} \equiv \frac{3q}{h}\left(\bar{y} - \frac{1}{2}\bar{y}^2 \right) \tag{3.3b}$$

The unicity of the decomposition (3.3) is made unique by the gauge conditions

$$\int_0^h u^{(1)} dy = 0 \qquad \text{and} \qquad T^{(1)}(y = h) = 0\,. \tag{3.4}$$

which are consequences of the definitions of the adopted degrees of freedom. Substitution (3.3) into the energy balance truncated at first order

$$\partial_{yy} T = Pr\delta \left(\partial_t T + u\partial_x T + v\partial_y T \right) \tag{3.5}$$

followed by a double integration with the help of the boundary conditions

$$T|_{y=0} = 1 \qquad \text{and} \qquad \partial_y T|_{y=h} = -BT|_{y=h} \tag{3.6}$$

finally yields

$$\begin{aligned} T^{(1)} &= \bar{y} - (\bar{y} + Bh\bar{y})\theta + \delta Pr \left[\frac{1}{6}\bar{y}(-3+\bar{y}^2)h^2\partial_t\theta \right. \\ &\quad + \frac{1}{120}\bar{y}\{-15+\bar{y}^2[20+3(-5+\bar{y})\bar{y}]\}(\theta-1)\partial_x q \\ &\quad \left. - \frac{1}{40}\bar{y}[25+\bar{y}^3(-10+3\bar{y})]hq\partial_x\theta \right] + O(\epsilon^2)\,. \end{aligned} \tag{3.7}$$

The gauge condition $T^{(1)}(\bar{y}=1) = 0$ then leads to an evolution equation for the free surface temperature

$$Pr\delta\partial_t\theta = 3\frac{[1-(1+Bh)\theta]}{h^2} + Pr\delta\left[\frac{7}{40}\frac{(1-\theta)}{h}\partial_x q - \frac{27}{20}\frac{q}{h}\partial_x\theta\right] \tag{3.8a}$$

which is consistent at $O(\epsilon)$ (Ruyer-Quil et al. 2005). From the above derivation it is obvious that the averaged energy balance (3.8a) is a direct consequence of the specific choice of variables and the ansatz (3.3).

Proceeding similarly for the velocity profile (a computation that is similar to the one discussed in § 2.3.1 and that is not repeated here), one obtains

$$\delta\partial_t q = \frac{5}{6}h - \frac{5}{2}\frac{q}{h^2} + \delta\left(\frac{9}{7}\frac{q^2}{h^2}\partial_x h - \frac{17}{7}\frac{q}{h}\partial_x q\right) - \frac{5}{4}M\partial_x\theta - \frac{5}{6}\zeta h\partial_x h$$

which is coupled to (3.8a) by the thermocapillary term $-\frac{5}{4}M\partial_x\theta$. The system of equations to be solved is completed by the mass balance

$$\partial_t h = -\partial_x q\,. \tag{3.8b}$$

The system (3.8) is a tree-equation consistent model.

Weighted residual method

The weighted residual method provides again a shortcut to the derivation of equation (3.8a): Multiplying the energy balance (3.5) by a weight function $w(\bar{y})$ and integrating across the film layer to obtain a residual that is set to zero, the only place where the correction $T^{(1)}$ to the linear temperature distribution may enter the computation is the integral $\int_0^h w\partial_{yy}T$ which can be written

$$\begin{aligned} \int_0^h w\partial_{yy}T\,dy &= -Bw(1)T\big|_h - w(0)\partial_y T\Big|_0 + \frac{1}{h}\left[w_j{}'(0) - w_j{}'(1)T\Big|_h\right] \\ &\quad + \frac{1}{h^2}\int_0^h w''\left(\frac{y}{h}\right)T\,dy\,, \end{aligned} \tag{3.9}$$

once the boundary conditions (3.6) have been invoked. Following exactly the same approach as before, the weight is chosen in view of the gauge conditions (3.4) which leads to the choice $w(0) = 0$, $w'' = 0$ so that $w \propto \bar{y}$

(Kalliadasis et al. 2003a). As in the isothermal case, the Galerkin method is the most efficient one bringing the result with the minimum of algebra.

In Ruyer-Quil et al. (2005) a second order model has been constructed using the weighted residual method and introducing three supplementary variables to represent the first-order deviations of the velocity field from the Nusselt profile and three others for the $O(\epsilon)$ deviations of the temperature field from the linear distribution. Tests functions have been chosen so that to match the $O(\epsilon)$ distribution of velocity and temperature (3.7). The result is a (cumbersome) nine equation model. As for the isothermal case, the added $O(\epsilon)$ fields can be consistently eliminated yielding a consistent three-equation model. A regularization procedure is also necessary to avoid the finite-time blow-up behaviors, which leads to a three-equation model consistent at $O(\epsilon^2)$:

$$\partial_t h = -\partial_x q \,, \tag{3.10a}$$

$$\begin{aligned}\delta\partial_t q = {} & \delta\left[\frac{9}{7}\frac{q^2}{h^2}\partial_x h - \frac{17}{7}\frac{q}{h}\partial_x q\right] + \left[1 - \frac{\delta}{70}q\partial_x h + M\frac{5}{56}\frac{\partial_x\theta}{h}\right]^{-1} \\ & \times\left\{\frac{5}{6}h - \frac{5}{2}\frac{q}{h^2} + \eta\left[4\frac{q}{h^2}(\partial_x h)^2 - \frac{9}{2h}\partial_x q\partial_x h - 6\frac{q}{h}\partial_{xx}h + \frac{9}{2}\partial_{xx}q\right]\right. \\ & \left. -\frac{5}{6}\zeta h\partial_x h + \frac{5}{6}h\partial_{xxx}h - M\left[\frac{5}{4}\partial_x\theta - \frac{\delta}{224}hq\partial_{xx}\theta\right]\right\} \,,\end{aligned} \tag{3.10b}$$

$$\begin{aligned}Pr\delta\partial_t\theta = {} & 3\frac{(1-\theta-Bh\theta)}{h^2} + Pr\delta\left[\frac{7}{40}\frac{(1-\theta)}{h}\partial_x q - \frac{27}{20}\frac{q}{h}\partial_x\theta\right] \\ & +\eta\left[\left(1-\theta-\frac{3}{2}Bh\theta\right)\left(\frac{\partial_x h}{h}\right)^2 + \frac{\partial_x h\partial_x\theta}{h} + \right. \\ & \left.(1-\theta)\frac{\partial_{xx}h}{h} + \partial_{xx}\theta\right] \,.\end{aligned} \tag{3.10c}$$

Noteworthy is that the momentum equation (3.10b) with $M = 0$ reduces to its isothermal version (2.12).

Some further modeling attempts

Noteworthy is that, contrary to the zeroth-order parabolic distribution $u^{(0)} \propto \bar{y} - \frac{1}{2}\bar{y}^2$ of the velocity, the zeroth-order linear distribution $T^{(0)}$ fulfills the boundary conditions (3.6) only with the specific value $\theta = 1/(1+Bh)$ corresponding to the base flow of uniform thickness. In fact, in the weighted residual approach followed in Ruyer-Quil et al. (2005), none of the test functions does fulfill the boundary condition for the temperature at the free surface. This choice does not bring inconsistencies, though, as the boundary conditions are used in the integration by parts [in weighted residual terminology, this is equivalent to the 'tau' method (Gottlieb and Orszag 1977)]

This discrepancy with the classical Galerkin method motivate *Trevelyan et al. (2007)* to introduce polynomial test functions that do fulfill the boundary conditions irrespectively of the values of the associated variables. The starting point of the study is the primitive equations truncated at first order of the film parameter, or the boundary-layer equations (the naming 'boundary-layer' originates from the similitude between the

Prandtl equation in boundary-layer theory and the obtained set of equations (Chang et al. 1994, Schlichting 1979)). The Galerkin method is applied, i.e. the weights ware chosen to be the test functions themselves, without taking into account the ordering of the variables with respect to the film parameter. A sequence of models, christened GSST[m], is obtained, m being the number of variables used. Owing to the good convergence properties of spectral methods, the solution to the models then converge to the solutions of the energy equation (3.5) as m is increased.

Truncated at $m = 1$, the approach by Trevelyan et al. (2007) introduces a zeroth order temperature distribution than can be written

$$\begin{aligned} T^{(0)} &= 1 + \left(\frac{1}{1+Bh} - 1\right)\bar{y} + \left(\theta - \frac{1}{1+Bh}\right)\phi_1(\bar{y}) \\ \text{with} \quad \phi_1 &= \frac{3}{2}\bar{y} - \frac{\bar{y}^3}{2} + Bh(1-\bar{y}^2)\frac{\bar{y}}{2}\,. \end{aligned} \tag{3.11}$$

As announced, $\phi_1(0) = 0$ and $\phi_1'(1) + B\phi(1) = 0$ ensures that the boundary conditions (3.6) are fulfilled irrespectively of the value of θ. It is important to note that the ansatz (3.11) is asymptotically equivalent to the linear distribution $T^{(0)} = 1 + (\theta - 1)\bar{y}$ introduced by Ruyer-Quil et al. (2005), the difference between the two being an $O(\epsilon)$ small term. Indeed, one can play with the zeroth order equivalence $\theta = 1/(1+Bh) + O(\epsilon)$ provided by the solution to the base flow. There is thus an infinity of possible consistent ansatz !

As an exercise, the reader can plug the decomposition (3.3) of the velocity and temperature fields into the energy balance (3.5), where $T^{(0)}$ and $u^{(0)}$ are given by (3.11) and (3.3b), take a linear weight $w = \bar{y}$ and integrate across the layer. The result is

$$Pr\delta\partial_t\theta = \mathcal{A}\frac{[1-(1+Bh)\theta]}{h^2} + Pr\delta\left[\frac{(\mathcal{B}-\mathcal{C}\theta)}{h}\partial_x q - \mathcal{D}\frac{q}{h}\partial_x\theta - \mathcal{E}\frac{q\theta}{h^2}\partial_x h\right] \tag{3.12a}$$

where the coefficients $\mathcal{A}$ to $\mathcal{E}$ are functions of Bh and thus vary with the free surface geometry

$$\begin{aligned} \mathcal{A} &= \frac{15}{6+Bh}\,, \quad \mathcal{B} = \frac{93}{112(6+Bh)}\,, \quad \mathcal{C} = \frac{3(39Bh-31)}{112(6+Bh)}\,, \\ \mathcal{D} &= \frac{3(149+23Bh)}{56(6+Bh)} \quad \text{and} \quad \mathcal{E} = \frac{69Bh}{(6+Bh)} \end{aligned} \tag{3.12b}$$

Equation (3.12) is consistent at $O(\epsilon)$ and provides a possible alternative to (3.8a). The evolution equation (3.12) is a direct consequence of the ansatz (3.11) irrespectively of the form of the corrections $T^{(1)}$. This equation is however more complex than (3.8a) since the coefficients are now functions of the product $Bh(x,t)$ which varies with space and time. The reader is invited to contrast (3.12) with GST[1], equation (B1b) in Trevelyan et al. (2007), that has been derived using the Galerkin method and yet is inconsistent at $O(\epsilon)$.

Turning from weighted residual method to Roberts center manifold analysis (CMA), that is described at length in § 1.3, the fluctuations of the temperature field around the base flow equilibrium are assumed to be

governed by the linearized problem in the long-wave limit $\partial_x \to 0$. Considering a constant and uniform thickness h, Linearisation of the energy balance around the conductive equilibrium $T = 1 + [Bh/(1+Bh)]\bar{y} + \tilde{T}$, $\tilde{T} \ll 1$ leads to

$$Pr\delta h^2 \partial_t \tilde{T} = \partial_{\bar{y}\bar{y}} \tilde{T} \equiv \mathcal{L}\tilde{T} \quad \text{with} \quad \tilde{T}|_{\bar{y}=0} = 0 \quad \text{and} \quad \partial_{\bar{y}} \tilde{T}|_1 + Bh\tilde{T}|_1 = 0 \tag{3.13}$$

where again $\bar{y} = y/h$. The discrete spectrum of $\mathcal{L}$, eigenfunctions $v^n(\bar{y})$ and eigenvalues λ^n are given by

$$v^n = \sin(l^n \bar{y}) / \sin(l^n)\,, \quad \lambda^n = -(l^n)^2 \tag{3.14}$$

and where l^n are solutions to

$$l \cot l + Bh = 0\,. \tag{3.15}$$

All eigenvalues l^n are real and negative. Roberts CMA is based on the idea that all eigenmodes but the first one λ^0 corresponding to the largest eigenvalue are effectively damped. The looked-after invariant manifold is thus tangent to the linear subspace spanned by $v^0(\bar{y})$. In fact, nonlinearities being $O(\epsilon)$ terms in (3.5), the invariant manifold again coincides with the linear subspace at leading order. Adopting a parametrization based on the temperature θ at the free surface, the invariant manifold $T(x,y,t) = \mathcal{T}(\theta(x,t),y)$, is given at $O(1)$ by

$$\mathcal{T}(\theta(x,t),y) = 1 + \left(\frac{1}{1+Bh} - 1\right)\bar{y} + \left(\theta - \frac{1}{1+Bh}\right) v^0(\bar{y}) + O(\epsilon)\,, \tag{3.16}$$

the evolution on the manifold being governed by

$$Pr\delta \partial_t \theta = -\frac{\lambda^0}{1+Bh}\frac{[1-(1+Bh)\theta]}{h^2} + O(\epsilon)\,. \tag{3.17}$$

Equation (3.16) is another consistent ansatz for $T^{(0)}$ that must be contrasted with the linear distribution $T^{(0)} = 1 + (\theta - 1)\bar{y}$ and (3.11) proposed by Treveleyan *et al.* As a matter of fact, (3.16) and (3.11) differs only by the choice of the functions $\phi_1(\bar{y})$ and $v^0(\bar{y})$ that are graphically compared in figure 3.2a. As it turns out that $\phi_1(\bar{y})$ and $v^0(\bar{y})$ are close, one thus expects that Roberts CMA would yied a $O(\epsilon)$ consistent evolution equation for θ very similar to (3.12). Indeed, figure 3.2b compares the first coefficients appearing in (3.8a), (3.12) and (3.17). The rate at which heat conduction relaxes θ to its equilibrium state $\theta = 1/(1+Bh)$ is similar for Roberts CMA and (3.12) whereas the linear temperature distribution adopted in Ruyer-Quil et al. (2005) overestimates it.

3.3 Discussion

3.3.1 Two-dimensional flows

Interestingly, at a given value of the heat transfer coefficient and for a given fluid (Bi, Ma and Γ constant) all the reduced parameters (3.1) vanish as the Reynolds number tends to zero except for the reduced Marangoni number which tends to infinity. At small flow rates, the Marangoni S mode

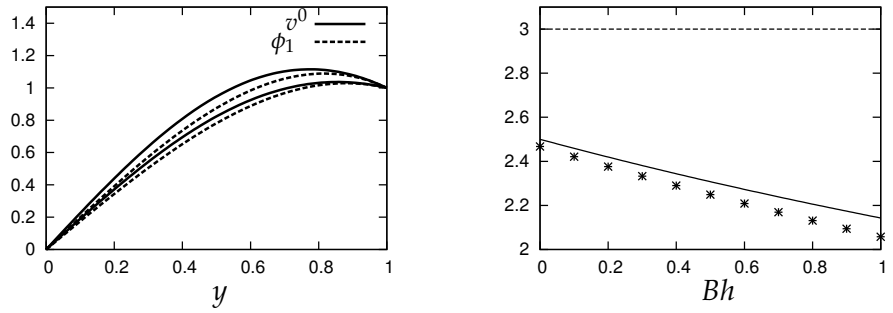

(a) *test functions* (b) *first coefficient*

Figure 3.2 – *(a) Test function ϕ_1 and eigenfunction v^0 computed for $Bh = 0.5$ and $Bh = 1$; (b) coefficient $-\lambda^0/(1+Bh)$ (crosses) compared to $\mathcal{A}(Bh)$ (solid line) and $-3(1+Bh)$ from (3.8a) (dashed line).*

dominates over the Kapitza K instability mode. The Reynolds number being small, the dynamics of the film is slaved to the kinematics of the film. Considering a 2D flow, Benney long-wave expansion yields the following surface equation *(Kalliadasis et al. 2003a)*

$$\partial_t h + \partial_x \left[\frac{h^3}{3} \left(1 + \partial_{xxx} h\right) + \frac{MB}{2} h^2 \partial_x h \right] = 0 \tag{3.18}$$

where the leading order term involving B has been retained as $MB \propto (3Re)^{-1/9}$ becomes large at $Re \ll 1$. Equation (3.18) must be contrasted with the Frenkel equation (4.12) which models the Rayleigh-Plateau instability of a axisymmetrical film coating a fiber. In this region of small flow rates and hence small film thicknesses, the amplitude of the waves is expected to be large as compared to the film thickness. However because the order of the nonlinearity associated to the thermocapillary effect is not large (cubic term), solitary-wave solutions can be found for all values of the parameter $M \cot\beta$ (cf. figure 2.6 and the associated discussion in § 2.3.1): the flow advection is sufficient to arrest the growth of the waves and 2D dry patches do not form. Yet, this argument is true only for a spanwise-independent 2D flow. No mechanism can arrest the thermocapillary S mode in the transverse directions and film ruptures are indeed observed between rivulets (Krishnamoorthy and Ramaswamy 1995, Ramaswamy et al. 1997), in which case van der Waals forces become important. Such forces of non-hydrodynamic origin are expected to arrest the singularity formation.

Inversely, if Re tends to infinity, both M and $M \cot\beta$ tend to zero and the velocity and temperature fields are decoupled in this limit. Therefore, at large Reynolds numbers, the shape of the waves should be unaffected by the Marangoni effects and the Kapitza K mode predominates.

This situation is illustrated in the stability diagram presented in figure 3.3. The regions of linear stability (and instability) of the uniform film are given in the plane Reynolds number Re versus wavenumber k. The inclination of the plane is moderate ($\beta = 15°$) and the fluid properties are constant (and thus Γ and Bi). The movement of the neutral stability curves is indicated as a result of the variation of the Marangoni number

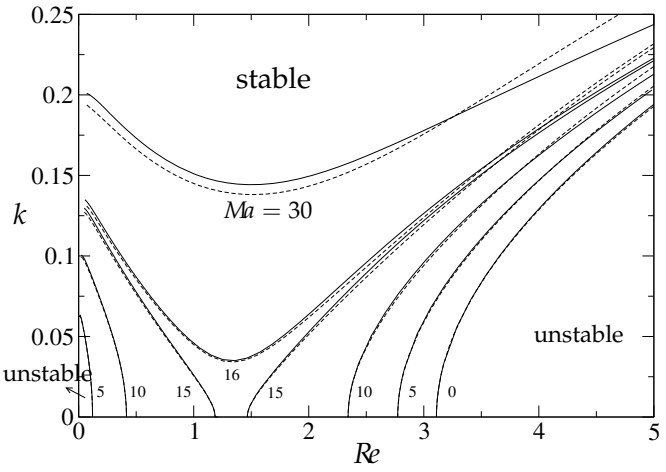

Figure 3.3 – *Influence of the Marangoni number on the neutral stability for an inclined plate forming an angle $\beta = 15^\circ$ with the horizontal direction with $\Gamma = 250$, $Pr = 7$ and $Bi = 1$, and computed with the Orr–Sommerfeld eigenvalue problem (solid lines) and the regularized model (3.10) (dashed lines). After figure 9.3 in Kalliadasis et al. (2012).*

(which is monitored in the experiments by varying the temperature difference $T_w - T_a$). At values of Ma lower than ≈ 16, two unstable regions are found corresponding to the predominance of the thermocapillary S-mode (at low Reynolds numbers) and of the hydrodynamic K mode (at large Reynolds numbers). Note that the critical Reynolds number of the K mode decreases with Ma which indicates that the Marangoni effect amplifies the hydrodynamic instability (in fact the reverse is also true).

The neutral stability curves solutions to the Orr-Sommerfeld eigenvalue problem of the full Navier-Stokes linearized equations are compared to the results from the three-equation model (3.10). An excellent agreement is achieved which illustrates the good behavior of the WRM model in the linear regime.

As emphasized in chapter 2, an important test of reliability of low-dimensional models is the construction of solitary-wave branches of solutions. We focus on positive-hump waves. In fact, much like the isothermal falling film negative-hump waves are unstable in time-dependent computations. In figure 3.4 are presented the maximum amplitude and speed of the single-hump solitary wave family of the regularized model (3.10) as function of Re for two different values of Prandtl and Marangoni numbers. The single-hump solitary wave solution branch obtained from seems to exist for all Reynolds numbers, i.e. it does not present any turning points with branch multiplicity connected to finite-time blow-up behavior.

Increasing the Marangoni number leads to larger amplitudes and speeds showing that the thermocapillary S-mode reinforces the hydrodynamic K-mode. This effect is more pronounced at low Reynolds numbers ($\mathcal{M}$ being proportional to $Re^{-4/9}$). By similitude to the isothermal case, we shall refer to this regime as the drag-gravity regime (see § 2.4). On the other hand, in the region of large Re, the different curves merge with the isothermal one. In this region, the destabilizing interfacial Marangoni forces are weaker compared to the dominant inertia forces and we shall

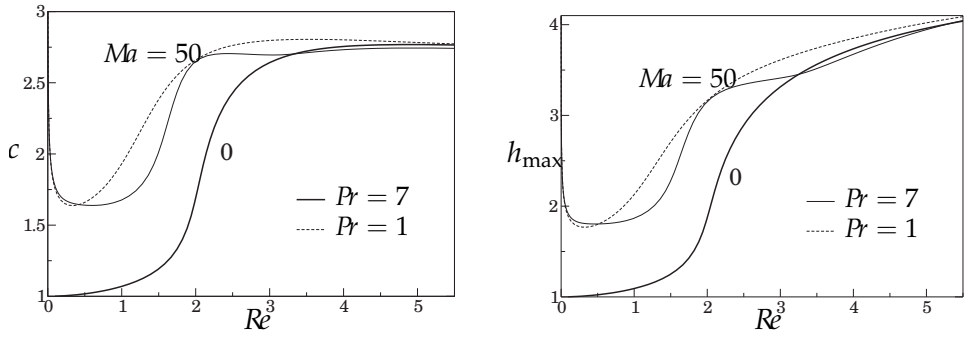

(a) *speed* (b) *maximum height*

Figure 3.4 – *Characteristics of single-hump solitary wave solutions of the three-equation regularized model (3.10) with* $\cot\beta = 0$, $Bi = 0.1$ *and* $\Gamma = 250$. *After figure 9.5 in Kalliadasis et al. (2012)*

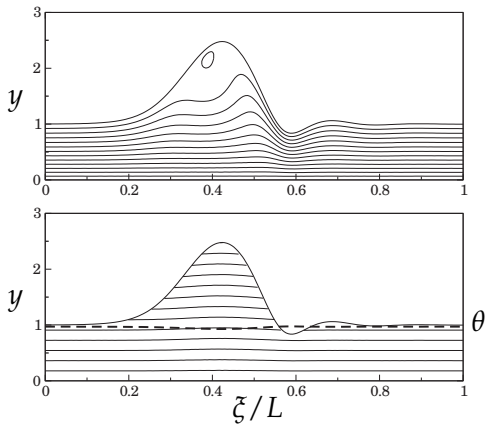

Figure 3.5 – *Streamlines (above) and isotherms (below) of a solitary wave in its moving frame, The wave is computed for the point* $(Re, Ma) = (0.01, 50)$ *in figure 3.4 and for* $Pr = 7$. *Interfacial temperature is denoted by a dashed line. After figure 9.6 in Kalliadasis et al. (2012)*

refer here to the drag-inertia regime. The speed of the waves saturates similarly to what is observed in the isothermal case.

The effect of Prandtl number is more subtle. At low Reynolds numbers, $Re \lesssim 0.5$, larger values of Pr seem to slightly favor instability, whereas for any larger Re, we have the opposite effect. This intricate effect can be understood by plotting the streamlines and isotherms under the waves.

Figure 3.5 shows the streamlines and isotherms for $Re = 0.01$ of a solitary-wave solution in its moving frame. The film flow evolution is well approximated by the evolution equation for the free surface (3.18). The Péclet number being small, the temperature field is nearly linear and the isotherms are practically aligned with the wall. The wave presents a recirculation zone in its hump which creates a downward movement below it. As a consequence, raising the Pr number (and thus the Péclet number) promotes a cooling of the wave crest by downward convective heat flux which enhances the Marangoni effect and promotes the instability.

At somewhat larger values of the Reynolds number, say $Re = 1$, the Marangoni instability is less strong as $BM \propto (3Re)^{-1/9}$ and solitary waves

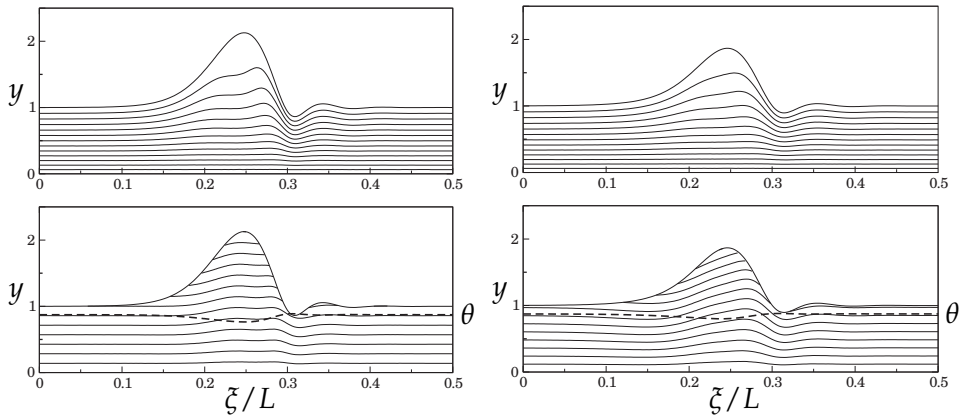

(a) $Pr = 1$ (b) $Pr = 7$

Figure 3.6 – *Streamlines (above) and isotherms (below) for* $(Re, Ma) = (1, 50)$ *and for two different value of Pr. (a)* $T_{\min} = 0.765$*; (b)* $T_{\min} = 0.8$*. After figure 9.7 in Kalliadasis et al. (2012)*

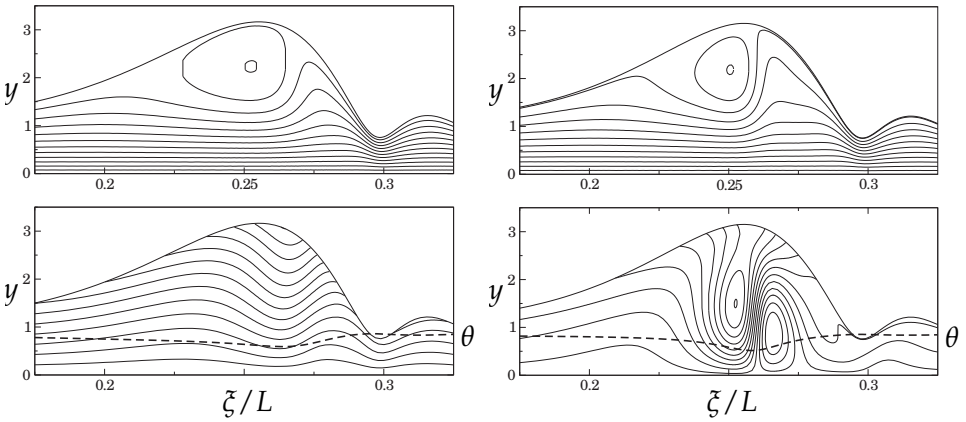

(a) $Pr = 1$ (b) $Pr = 7$

Figure 3.7 – *Streamlines (above) and isotherms (below) for the point* $(Re, Ma) = (2, 50)$ *in Fig. 3.4. (a)* $T_{\min} = 0.591$*; (b)* $T_{\min} = 0.429$ *and* $T_{\max} = 1.26$*. After figure 9.8 in Kalliadasis et al. (2012).*

do not present recirculation zone (see figure 3.6). In the absence of a recirculation zone, the effect of convection is reversed. Isotherms are deflected upwards by the movement of the fluid in the crest. Convection warms up the fluid and the minimum of temperature is reduced which weakens the Marangoni effect. The transport of heat by the motion of the fluid has a stabilizing effect in this case.

For larger Reynolds numbers, e.g. $Re = 2$, corresponding to the drag-inertia regime, inertia becomes increasingly dominant, and the speed and amplitude of solitary waves increase substantially, as shown in Fig. 3.4. As a consequence, a recirculation zone can now be present inside the main solitary hump, much like at $Re \lessapprox 0.5$, but there the large amplitude and speed of the solitary wave and hence recirculation zone in the main hump were due to the action of the Marangoni effect (see figure 3.7). One of the stagnation points (in the frame moving with the wave) is shifted from

the front of the wave to its crest. This is evinced in figure 3.8b where the streamlines at $Re = 3$ when the thermocapillary effect is switched off ($Ma = 0$) are compared to the flow pattern with $Ma \neq 0$. Thus, the Marangoni effect enhances the recirculation in the crest and promotes a strong downward flow there. As a consequence, the transport of heat by the flow contributes to cooling down the crest and amplifying the Marangoni effect. Nevertheless, this strong circulation and downward flow create a strong shear and therefore increases the effect of viscous dissipation which in turn reduces the amplitude and speed of the waves if the Prandtl number is raised. These observations indicate that the interaction of the hydrodynamic K-mode and the Marangoni S-mode is non-trivial especially in the region of large-amplitude solitary waves.

Unfortunately, at some larger values of the Reynolds number, negative values of the dimensionless temperature appear in the fluid. Turning back to dimensional quantities, this would lead to a temperature in the fluid that can be locally higher than the temperature of the wall or lower than the temperature of the air. This is physically unacceptable as the temperature everywhere in the fluid should be bounded between the wall and air temperatures.

To understand the appearance of this unphysical behavior when a recirculation zone is present, i.e. for large amplitude waves, let us consider the influence of the heat transport convective effects in the high-Péclet number limit, $Pe = RePr \gg 1$. Cross-stream convection associated with the recirculation zone dominates over diffusion, the temperature field in the recirculation zone is simply transported by the flow and the streamlines are identical to the temperature contours (see *e.g.* Shraiman (1987), Trevelyan et al. (2002)). This means that the temperature along each streamline is constant due to the strong advection mixing. The temperature field becomes a passive scalar and is simply transported by the flow. Hence, within the recirculation zone the isotherms are closed curves, as start to be visible in Fig. 3.7(b) Because of the inward orientation of the streamline at the stagnation point located at the front of the wave, the transport of heat tends to increase the gradient of temperature around this stagnation point and to promote the formation of a thermal boundary layer which develops from the front stagnation point around the recirculation zone (Trevelyan et al. 2007). In this case, transport of heat via conduction can be neglected except in the (fully developed) boundary layer of thickness $(\delta Pr)^{-1/2}$. Consequently, the hypothesis $\partial_y T \gg \partial_x T$ necessary for the derivation of the models would be violated in these regions.

There are different possibilities to cure the limitation of the WRM models. One such possibility is to relax the assumption $\partial_y T \gg \partial_x T$ and use instead the original energy equation without any approximations. In this case the original energy equation should be solved numerically to obtain the temperature distribution within the film. Another possibility explored in Trevelyan et al. (2007) consists in the introduction of appropriately modified weight functions for the energy equation prior to averaging.

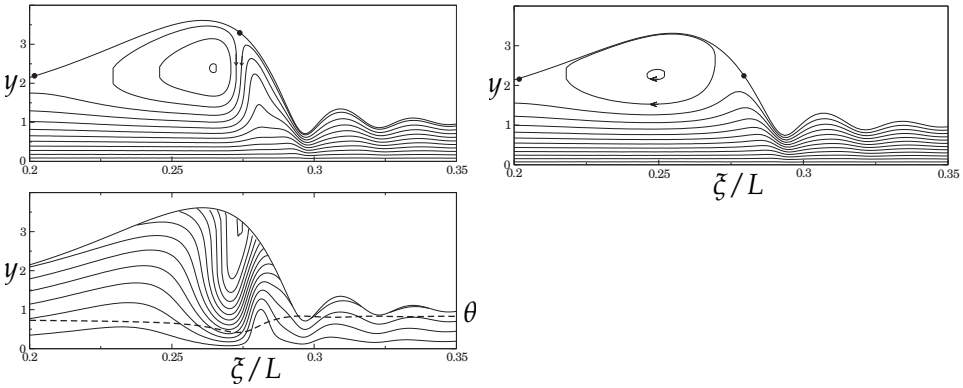

(a) $Ma = 50 - Pr = 1$ (b) $Ma = 0$

Figure 3.8 – *(a) Streamlines (above) and isotherms (below) for the point* $Re = 3$*. The reduced parameter values are* $\delta = 2.33$*,* $\eta = 0.067$*,* $M = 2.99$ *and* $B = 0.21$ *with* $T_{\min} = 0.414$*. Black dots represent stagnation points; (b) same parameters values for* δ, η *as in (a) but for the isothermal case. After figure 9.9 in Kalliadasis et al. (2012).*

3.3.2 Three-dimensional flows

The study of 2D spanwise-independent flows was followed by numerical simulations of 3D flows over extended domains using periodic boundary conditions in both directions. This study revealed a very intricate interplay between the hydrodynamic K-mode whose action is oriented by the direction of the flow, and the thermocapillary S-mode which is isotropic in the plane of the film. A detailed phase portrait detailing the different observed regimes can be found in *Scheid et al. (2008a;b)*.

A typical example of the spatio-temporal evolution of the film is presented in figure 3.9. After the development of a parallel wave train (a), drop-like accumulation breaks the two-dimensional wave structure into a fully-developed three-dimensional pattern (b,c), prior to rivulet-like patterns aligned with the flow (d,e). The liquid then accumulates into rivulets which increases the local Reynolds number and fosters two-dimensional solitary-like waves of larger amplitude and phase speed than in isothermal conditions (f).

This spontaneous channeling process of the flow into localized structures in the spanwise direction —the rivulets— is a particularly nontrivial effect. It is observed in a range of parameters for which neither the K-mode or the S-mode are dominant, otherwise the Marangoni effect would be ineffective to orientate the flow pattern or the development of spanwise rivulets would overcome the growth of traveling waves. This interplay is illustrated by the variety of observable patterns, some being reported in figure 3.10. In the drag-gravity regime, quasi-regularly spaced rivulets arise and grow up until rupture (a). Meanwhile, the rivulets confine the flow in such a way that waves riding them behave like two-dimensional solitary waves, but of higher flow rate because of the local increase of the Reynolds number. On the contrary, no qualitative influence of the Marangoni effect has been observed in the drag-inertia regime, at least during the time of the computer simulations, showing that inertia fully dominates the dynamics of the film (c). The transition between these two

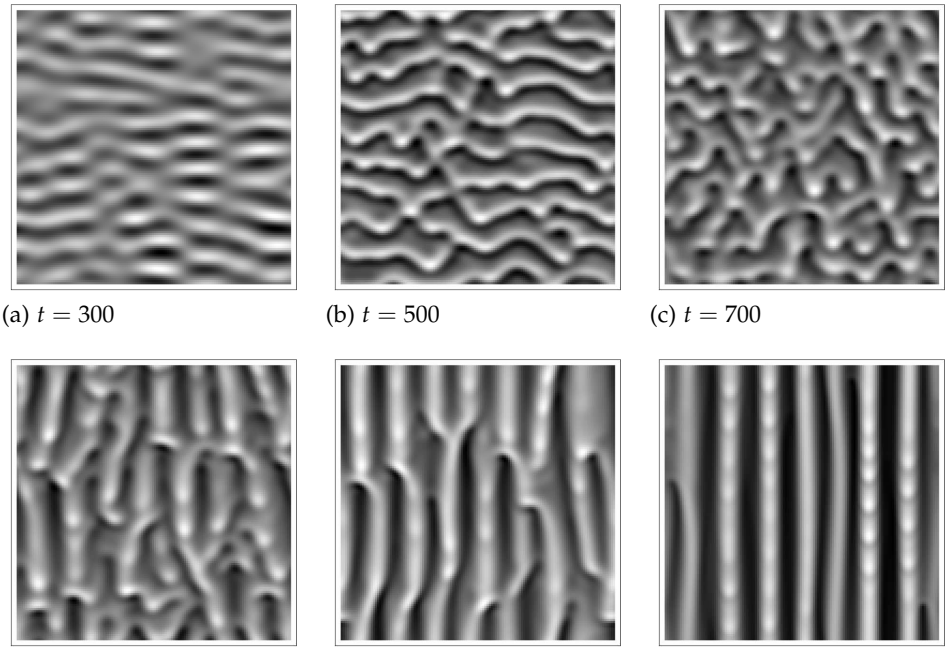

(a) $t = 300$ (b) $t = 500$ (c) $t = 700$

(d) $t = 900$ (e) $t = 1100$ (f) $t = 1500$

Figure 3.9 – *Water film free surface at different times. Parameter values are* $Re = 2$ *for* $Ma = 50$, $Bi = 0.1$, $Pr = 7$, $\cot\beta = 0$ *and* $\Gamma = 3375$. *The domain size is* $2\pi/k_x \times 2\pi/k_z$ *where* $k_x = k_z = 0.05$. *Bright/dark zones correspond to elevations/depressions, respectively. After figure 9.12 in Kalliadasis et al. (2012).*

regimes for $4 < Re < 6$ shows a complex cooperative behavior between both hydrodynamic K- and thermocapillary S-modes, as illustrated for $Re = 5$ in figure 3.10b

To end this section, let us emphasize that the spontaneous channeling phenomenon should be particularly attractive from the experimental point of view, especially as fluid flow settings where 2D waves can be stabilized are quite rare. This patterning might be generic for systems exhibiting a competition between monotonic and oscillatory (or wave) instabilities with anisotropy (here, due to the direction of the basic flow).

Some perspectives

If the thermocapillary S-mode and the hydrodynamic K-mode are found to always reinforce each other in the linear regime, the nonlinear regime is far more intricate, especially when large-amplitude solitary waves are considered. For instance, the coupling between the hydrodynamic K-mode and the thermocapillary S-mode are far from being fully understood, in particular when three-dimensional flows are considered. Indeed, this chapter constitutes only a preliminary study, the "tip of the iceberg" that underlines the richness of the problem. In fact, in most problems involving heat transfer, phase changes through either evaporation or condensation or both have also to be taken into account. As far as mass transport is concerned there is a large class of problems that involve transport of a species from a gas to a falling film. An important question in these

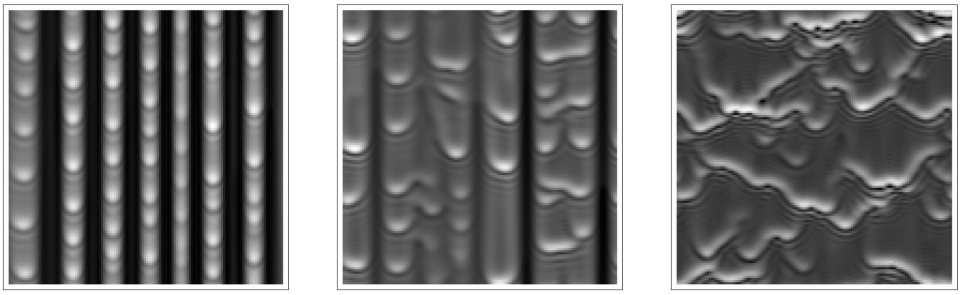

(a) $Re = 2$ - $t = 1795$ (b) $Re = 5$ -$t = 2650$ (c) $Re = 10$ - $t = 442$

Figure 3.10 – *Wave patterns for* $Ma = 50$, $Bi = 0.1$, $Pr = 7$ *and* $\Gamma = 3375$ *for different Re. Times given for (a, b) are close to rupture. After figure 9.13 in Kalliadasis et al. (2012).*

problems is the development of systematic ways for obtaining effective heat/mass transport coefficients.

There is no doubt that falling films in presence of heat and mass transfer will continue to attract a considerable interest in the coming years. In addition to the purely theoretical interest, falling liquid films play a central role in the development of efficient means for interfacial heat and mass transfer in a wide variety of engineering and technological applications, such as evaporators, heat exchangers, absorbers, scrubbers, rectification columns, crystallizers, and falling film reactors. This is mostly due to the large surface-to-volume ratio and to the small heat and mass transfer resistance of a thin liquid film at relatively small flow rates. This resistance is further decreased by the presence of wavy patterns at the interface of the film which typically leads to a significant enhancement of heat and mass transfer (Frisk and Davis 1972, Goren and Mani 1968). Yet, the precise mechanisms that leads to a considerable enhancement of the transfer of heat by the wavy motion of the film is still beyond our comprehension.

3.4 B. Scheid *et al.* J. Fluid Mech. (2005)

J. Fluid Mech. (2005), *vol.* 538, *pp.* 223–244.
doi:10.1017/S0022112005005446 Printed in the United Kingdom

Thermocapillary long waves in a liquid film flow. Part 2. Linear stability and nonlinear waves

By B. SCHEID[1,2], C. RUYER-QUIL[2], S. KALLIADASIS[3]†, M. G. VELARDE[4] AND R. Kh. ZEYTOUNIAN[5]

[1]Chimie-Physique E.P., Université Libre de Bruxelles, C.P. 165/62, 1050 Brussels, Belgium

[2]Laboratoire FAST, UMR 7608, CNRS, Universités P. et M. Curie et Paris Sud, Bât. 502, Campus Universitaire, 91405 Orsay Cedex, France

[3]Department of Chemical Engineering, University of Leeds, Leeds LS2 9JT, UK

[4]Insituto Pluridisciplinar, Universidad Complutense de Madrid, Paseo Juan XXIII, n. 1, E-28040 Madrid, Spain

[5]Université des Sciences et Technologies de Lille, 59655 Villeneuve d'Asq cédex, France

bscheid@ulb.ac.be; ruyer@fast.u-psud.fr; s.kalliadasis@imperial.ac.uk; velarde@fluidos.pluri.ucm.es; zeytounian@aol.com

(Received 16 February 2004 and in revised form 23 March 2005)

We analyse the regularized reduced model derived in Part 1 (Ruyer-Quil *et al.* 2005). Our investigation is two-fold: (i) we demonstrate that the linear stability properties of the model are in good agreement with the Orr–Sommerfeld analysis of the linearized Navier–Stokes/energy equations; (ii) we show the existence of nonlinear solutions, namely single-hump solitary pulses, for the widest possible range of parameters. We also scrutinize the influence of Reynolds, Prandtl and Marangoni numbers on the shape, speed, flow patterns and temperature distributions for the solitary waves obtained from the regularized model. The hydrodynamic and Marangoni instabilities are seen to reinforce each other in a non-trivial manner. The transport of heat by the flow has a stabilizing effect for small-amplitude waves but promotes the instability for large-amplitude waves when a recirculating zone is present. Nevertheless, in this last case, by increasing the shear in the bulk and thus the viscous dissipation, increasing the Prandtl number decreases the amplitude and speed of the waves.

1. Introduction

The present study is devoted to the problem of long-wave instabilities – namely hydrodynamic H- and thermocapillary S-modes (Goussis & Kelly 1991) – and concomitant formation of solitary waves on the surface of a film falling down a uniformly heated plane. In Part 1 (Ruyer-Quil *et al.* 2005), we developed a low-dimensional model capable of capturing these phenomena in a wide range of Reynolds numbers, i.e. in both drag–gravity and drag–inertia regimes (Ooshida 1999). The model, which also takes into account the second-order dissipative effects that can play an important role in the drag–inertia regime (Ruyer-Quil & Manneville 2000), was referred to as the 'second-order regularized reduced model'. It is rewritten here

† Present address: Department of Chemical Engineering, Imperial College, London SW7 2AZ, UK.

for ease of presentation:

$$\partial_t h = -\partial_x q, \tag{1.1a}$$

$$\begin{aligned}\partial_t q = {} & \frac{9}{7}\frac{q^2}{h^2}\partial_x h - \frac{17}{7}\frac{q}{h}\partial_x q \\ & + \left\{\frac{5}{6}h - \frac{5}{2}\frac{q}{h^2} + 4\frac{q}{h^2}(\partial_x h)^2 - \frac{9}{2h}\partial_x q\,\partial_x h - 6\frac{q}{h}\partial_{xx}h + \frac{9}{2}\partial_{xx}q\right. \\ & \left. - \frac{5}{6}\cot\beta\, h\partial_x h + \frac{5}{6}\Gamma h\partial_{xxx}h - Ma\left(\frac{5}{4}\partial_x\theta - \frac{1}{224}hq\partial_{xx}\theta\right)\right\} \\ & \times\left(1 - \frac{1}{70}q\partial_x h + Ma\frac{5}{56h}\partial_x\theta\right)^{-1},\end{aligned} \tag{1.1b}$$

$$\begin{aligned}Pr\partial_t\theta = {} & 3\frac{(1-\theta-Bi\,h\theta)}{h^2} + Pr\left[\frac{7}{40}\frac{(1-\theta)}{h}\partial_x q - \frac{27}{20}\frac{q}{h}\partial_x\theta\right] \\ & + \left(1-\theta-\frac{3}{2}Bih\theta\right)\left(\frac{\partial_x h}{h}\right)^2 + \frac{\partial_x h\partial_x\theta}{h} + (1-\theta)\frac{\partial_{x^2}h}{h} + \partial_{xx}\theta,\end{aligned} \tag{1.1c}$$

where the Kapitza, Marangoni, Biot and Prandtl numbers are defined as

$$\Gamma = \frac{\sigma(T_0)}{\rho\nu^{4/3}(g\sin\beta)^{1/3}}, \quad Ma = \frac{-\mathrm{d}\sigma/\mathrm{d}T|_{T_0}(T_\mathrm{w}-T_0)}{\rho\nu^{4/3}(g\sin\beta)^{1/3}}, \quad Bi = \frac{q_0\,\nu^{2/3}}{K(g\sin\beta)^{1/3}}, \quad Pr = \frac{\nu}{\kappa},$$

and where σ is the surface tension, ρ the density, ν the viscosity, $g\sin\beta$ the streamwise gravity component, q_0 the heat transfer coefficient of the liquid–gas interface, K the thermal conductivity of the liquid, κ the thermal diffusivity, T_w the wall temperature and T_0 a reference temperature, taken here as the ambient temperature T_a. This set of parameters is completed by the flat-film thickness h_N or equivalently the Reynolds number

$$Re = \frac{g\sin\beta h_\mathrm{N}^3}{3\nu^2} = \frac{\bar{h}_\mathrm{N}^3}{3} \tag{1.2}$$

while the product $Pe = Pr\,Re$ defines the Péclet number. A bar in (1.2) has been introduced to distinguish between dimensional and dimensionless quantities.

In § 2, the linear stability properties of (1.1) are examined and compared to results from Orr–Sommerfeld analysis of the full Navier–Stokes/energy equations, the Benney expansion, as well as the full-size model of reduced dimensionality (see Part 1), from which (1.1) was derived through a regularization procedure. In § 3 we scrutinize the effect of the Reynolds, Prandtl and Marangoni numbers on the shape, speed, temperature distribution and flow patterns for the single-hump solitary waves obtained from (1.1). We also explore the interaction between the S- and H-modes in the nonlinear regime. Finally, a conclusion and discussion is offered in § 4.

2. Linear stability results

We now examine the linear stability of the basic Nusselt flow and we compare the results obtained from the regularized reduced model to those obtained from the Orr–Sommerfeld eigenvalue problem of the full Navier–Stokes/energy equations. This eigenvalue problem was first formulated and solved by Goussis & Kelly (1991) and the reader is referred to this study for details. It is also instructive here to include the linear stability analysis obtained from the first-order model (§ 4.1 in Part 1), boundary-layer equation (§ 3 in Part 1) and full-size second-order model

(Appendix A in Part 1). The dispersion relation corresponding to (1.1) can be obtained by introducing perturbations to the flat-film solution in the form of normal modes with wavenumber $\tilde{k}$ and frequency $\tilde{\omega}$ (here we focus on temporal stability so that the wavenumber is real and the frequency complex)

$$\begin{pmatrix} h \\ q \\ \theta \end{pmatrix} = \begin{pmatrix} \bar{h}_{\mathrm{N}} \\ \bar{h}_{\mathrm{N}}^3/3 \\ 1/(1+Bi\,\bar{h}_{\mathrm{N}}) \end{pmatrix} + \varepsilon \begin{pmatrix} 1 \\ A_q \\ A_\theta \end{pmatrix} \exp\{\mathrm{i}(\tilde{k}x - \tilde{\omega}t)\} \tag{2.1}$$

in (1.1) and then linearize for $\varepsilon \ll 1$. For the resulting system of linear algebraic equations to have non-trivial solutions, it is necessary and sufficient that its principal determinant be equal to zero. Similarly, substituting (2.1), $s_i = \varepsilon A_{s_i} \exp\{\mathrm{i}(\tilde{k}x - \tilde{\omega}t)\}$ and $t_i = \varepsilon A_{t_i} \exp\{\mathrm{i}(\tilde{k}x - \tilde{\omega}t)\}$ in the full-size model (see Appendix A of Part 1) gives its dispersion relation.

To compare our linear stability analysis with the one performed by Kalliadasis *et al.* (2003), we must non-dimensionalize the length scales with the Nusselt film thickness h_{N}. Still utilizing bars to distinguish dimensional and dimensionless quantities when needed, we are thus led to the transformation $\tilde{k} = k/\bar{h}_{\mathrm{N}}$ and $\tilde{\omega} = \bar{h}_{\mathrm{N}}\omega$, where $\bar{h}_{\mathrm{N}} = (3Re)^{1/3}$ from (1.2). The phase speed $\tilde{c} = \tilde{\omega}/\tilde{k}$ is transformed to $\tilde{c} = \bar{h}_{\mathrm{N}}^2 c$. The averaged velocity of the flat-film solution is then 1/3 with this scaling. A different set of parameters based on the Nusselt flat-film solution therefore appears:

$$Ma_{\Delta T} = \frac{-\mathrm{d}\sigma/\mathrm{d}T|_{T_0}\,\Delta T}{\rho h_{\mathrm{N}}^2 g \sin\beta}, \quad We = \frac{\sigma(T_{\mathrm{a}})}{\rho g h_{\mathrm{N}}^2 \sin\beta}, \quad B = \frac{q_0 h_{\mathrm{N}}}{K}, \tag{2.2}$$

where ΔT is the temperature difference across the uniform fluid layer of thickness h_{N}. This set is completed by the definition of the Reynolds number given in (1.2). These are effectively the parameters adopted by Kalliadasis *et al.* (2003) except that these authors expressed the Weber number as the ratio of surface tension over inertia forces instead of surface tension over gravitational forces as in (2.2).

Performing a small-wavenumber expansion of the dispersion relation $D(k, \omega; Re, \cot\beta, We, Pr, Ma_{\Delta T}, B)$, similar to the one performed by Kalliadasis *et al.* (2003), leads to the following expression for the complex phase velocity:

$$c = 1 + \mathrm{i}k\left(\frac{2}{5}Re - \frac{1}{3}\cot\beta + \frac{Ma_{\Delta T}}{2(1+B)}\right) - \mathrm{i}k^3\frac{We}{3} + O(k^2) \tag{2.3}$$

where We is considered to be large such that $We\,k^2 = O(1)$. Note that the above expansion only gives the root of the dispersion relation that can become unstable. As was pointed out by Kalliadasis *et al.* (2003), the other two roots are always stable. The neutral stability condition is now easily found to be

$$c = 1, \quad k = \sqrt{\frac{1}{We}\left(\frac{6}{5}Re - \cot\beta + \frac{3Ma_{\Delta T}}{2(1+B)}\right)}. \tag{2.4}$$

Therefore, linear waves propagate with a velocity three times the averaged velocity or twice the interfacial velocity of the flat film. From (2.4) we also notice that increasing the Reynolds number or Marangoni number enlarges the range of unstable wavenumbers while decreasing β or increasing the Weber number has a stabilizing effect.

The onset of instability is obtained by considering the zero critical wavenumber as given by (2.4). This yields the critical condition

$$\frac{6}{5}Re + \frac{3Ma_{\Delta T}}{2(1+B)} = \cot\beta, \tag{2.5}$$

which is identical to the one obtained by Goussis & Kelly (1991) by performing a small wavenumber expansion of the Orr–Sommerfeld eigenvalue problem of the full Navier–Stokes/energy equations. The expression (2.5) has the same functional form as the one derived by Kalliadasis *et al.* (2003) for two-dimensional waves at criticality, but some of the coefficients are different: 6/5 instead of 1 in front of the Reynolds number, i.e. a 20% error, and 3/2 in front of the Marangoni number instead of 1/2 due to a factor of 3 introduced in the definition of the Marangoni number by Kalliadasis *et al.* (2003). Notice that here we try as much as possible to avoid numerical factors in the definitions of the dimensionless groups – with an exception to this rule being the definition of the Reynolds number – so that numerical factors in the equations do not change with different scalings. The discrepancy now for the coefficient in front of the Reynolds number corresponds exactly to the one observed using the Shkadov model (Shkadov 1967) in the case of an isothermal flow ($Ma_{\Delta T} = 0$). This inaccuracy has been eliminated by using a more complete description of the velocity field (Ruyer-Quil & Manneville 2000), which fully corrects the critical Reynolds number. Notice also that the Benney expansion for the heated falling film yields the correct critical Reynolds number (see Joo, Davis & Bankoff 1991). This is not surprising since this expansion is exact close to criticality (see our discussion in Part 1, § 1).

Let us now consider a falling film whose inclination angle, temperatures at the wall and air side and all physical quantities are fixed such that the sole control parameter is the liquid flux at the inlet or equivalently the Reynolds number $Re \propto \bar{h}_N^3$. From (2.2), one has $Ma_{\Delta T} \propto 1/\bar{h}_N \propto Re^{-1/3}$, $We \propto 1/\bar{h}_N^2 \propto Re^{-2/3}$ and $B \propto Re^{1/3}$. Therefore, if the flow rate is large, inertia effects are large and the interfacial forces due to the Marangoni effects are not important compared to the dominant inertia forces, so that the H-mode dominates in this regime. Conversely, in the limit of vanishing Reynolds number, inertia effects are negligible and the Marangoni effect is very strong. This corresponds to the S-mode described by Scriven & Sternling (1964). In this region of small film thicknesses, the destabilizing forces are interfacial forces due to the Marangoni effect (capillary forces are always stabilizing). Since now $Ma_{\Delta T}/We \propto Re^{1/3}$, the critical wavenumber tends to zero as the Reynolds number tends to zero. This seems to contradict the results obtained by Goussis & Kelly (1991) which predict that the wavenumber approaches infinity in this limit. This inconsistency is due to the fact that Goussis & Kelly based the definition of their Marangoni number on the temperature difference across the basic flat film instead of the temperature difference between the wall and the ambient gas phase. As a consequence their Marangoni number should also depend on B (which in turn depends on Re) but this dependence was not taken into account in their study.

The Orr–Sommerfeld problem is a set of two complex ordinary differential equations of degree four and two, for the amplitudes of the perturbed cross-stream velocity and perturbed temperature, respectively, and subject to six boundary conditions. As these differential equations are linear, an integral constraint must be added, e.g. $\int_0^1 \phi(y)\,dy = 1$ with $\phi(y)$ the amplitude of the perturbed cross-stream velocity. The Orr–Sommerfeld problem can then be recast in the form of a dynamical system of dimension six and subject to the above integral constraint. To solve numerically this

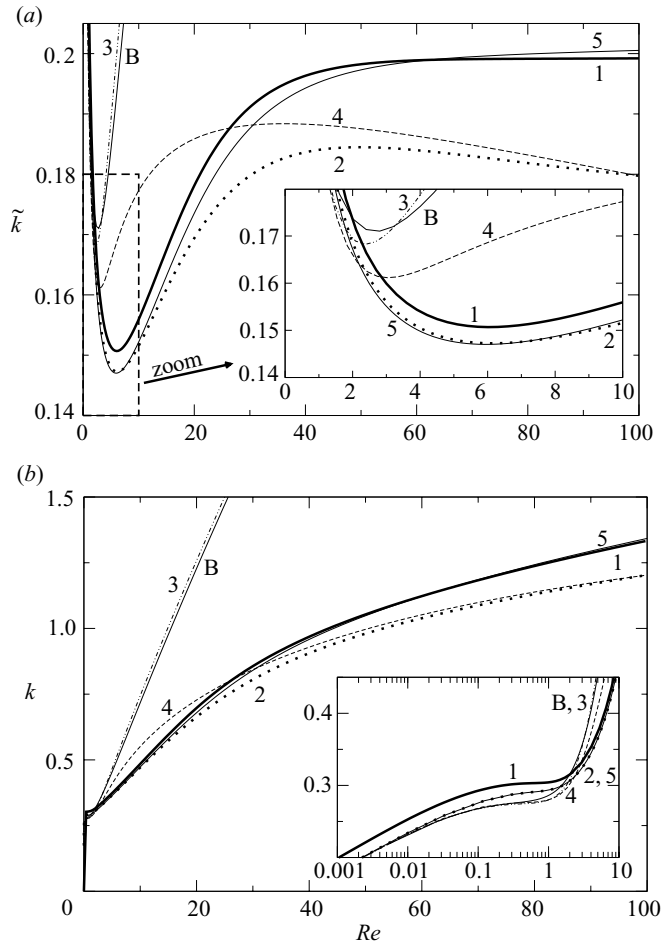

FIGURE 1. (*a*) Neutral stability curves in the $(\tilde{k}, Re)$-plane for $\Gamma = 250$, $\cot\beta = 0$, $Pr = 7$, $Ma = 50$ and $Bi = 1$ from the different models. (*b*) Neutral stability curves in the (k, Re)-plane; k is scaled with h_N. Thick solid curve 1: Orr–Sommerfeld; dotted curve 2: full-size second-order model; dot-dashed curve 3: first-order model; dashed curve 4: regularized reduced model (1.1); solid curve 5: boundary-layer equations. The solid curve B corresponds to the Benney long-wave expansion.

boundary-value problem, we utilized the long-wave nature of the instability. Indeed, the zero-wavenumber mode is neutral, i.e. $(\tilde{k},\ \tilde{\omega}) = (0,\ 0)$ is a solution of the eigenvalue problem. Therefore the solution branches were constructed by continuation starting from the trivial zero-wavenumber solution. For this purpose, we used the software AUTO97 developed by Doedel *et al.* (1997) and based on Keller's pseudo-arclength continuation method (Keller 1977). The same software was also used to obtain the dispersion relations of the other systems, namely, first-order, full-size second-order, boundary-layer and regularized reduced model.

In what follows, we fix the inclination angle β and all physical parameters – i.e. we fix the liquid–gas system or, equivalently, $\cot\beta$, Γ, Ma, Bi and Pr – as in a real experiment where the inlet flow rate is the actual control parameter. Therefore, we only vary the Nusselt film thickness h_N, or equivalently, the Reynolds number Re. Figure 1 depicts the neutral stability curves in the wavenumber–Reynolds number plane for $Pr = 7$, $\Gamma = 250$, $\cot\beta = 0$, $Ma = 50$ and $Bi = 1$ computed from the different models. The figure also shows the stability map obtained from the full Orr–Sommerfeld

stability analysis of the linearized Navier–Stokes/energy equations. The parameters are chosen so that the differences between the various systems of equations can be clearly identified. Hence the choice of an $O(1)$ and therefore unrealistically 'large' Biot number which would amplify the Marangoni effect. For the same reason, we choose to plot in figure 1(a) the critical wavenumber $\tilde{k}$ defined through the length-scale $\nu^{2/3}(g\sin\beta)^{-1/3}$ which only depends on the fluid parameters. Indeed as Re tends to zero, the prediction for the critical wavenumber k given in (2.4) tends to zero as $\sqrt{Ma_{\Delta T}/We}\propto\bar{h}_{\mathrm{N}}^{1/6}$. Thus $\tilde{k}=k/\bar{h}_{\mathrm{N}}\propto\bar{h}_{\mathrm{N}}^{-5/6}$ approaches infinity in that limit and the different curves are more easily separated.

The first-order model (curve 3) has already deviated from the other models at small Reynolds numbers. This is due to the relatively 'small' Kapitza number indicating that the second-order viscous effects are of primary importance in this regime. The full-size second-order model (curve 2) compares very well with the exact Orr–Sommerfeld solution (curve 1) even though at large Reynolds numbers it slightly underpredicts the neutral wavenumber. However, this small discrepancy at large Reynolds numbers cannot be attributed to the boundary-layer approximation (curve 5) since the trend is inverted in this latter case and it is most likely due to the limited radius of convergence of the perturbation scheme, as is the case with any approximate method. Nevertheless, we note the excellent agreement between the full-size model (curve 2) and the boundary layer equations (curve 5) for $Re<10$. Notice also the saturation of curves (1, 2, 5) for large Re: the critical wavelength $2\pi/\tilde{k}$ remains constant in this region and hence it is independent of the film thickness. On the other hand, at low Reynolds numbers all models are in agreement with the solution of the Orr–Sommerfeld eigenvalue problem. In this region, the dynamics of the flow is slaved to its kinematics, i.e. both flow rate and interfacial temperature are adiabatically slaved to the film thickness and they depend on time only through the dependence of the film thickness on time. This is the region where the Benney long-wave expansion applies.

Figure 1(b) depicts the marginal stability curves when the wavenumber is scaled with the base-state film thickness h_{N}. As expected, the curves approach the origin as Re decreases. Figure 3(a) in the study by Kalliadasis *et al.* (2003) on the other hand, indicates that for a vertically falling film with $Ma\neq0$ the neutral stability curves intersect the wavenumber axis at finite values. However, this was due to the relatively rough mesh in the computation of the neutral curves. A much smaller mesh shows that for Reynolds numbers smaller than $\sim10^{-4}$ (in terms of the scalings adopted by Kalliadasis *et al.* 2003) and for the parameter values used in the figure, the neutral curves turn sharply on themselves and approach the origin for very small Reynolds numbers as in figure 1(b). Finally, notice that all curves in figure 1(b) approach a plateau for $Re\sim1$.

By contrasting figures 1(a) and 1(b), it is evident that the principal advantage of the scaling based on the length scale constructed from the kinematic viscosity and gravitational acceleration, over the scaling based on the base-state film thickness, is to enable a clear distinction between the H- and S-modes of instability identified by Goussis & Kelly (1991). Indeed, the Orr–Sommerfeld neutral stability curve (curve 1) has a minimum at $R\approx5.6$ in figure 1(a). This minimum corresponds to the transition between the thermocapillary mode which predominates at low Reynolds numbers and the classical hydrodynamic mode which prevails at larger Reynolds numbers.

Figure 2 shows the growth rate $\mathrm{Im}\tilde{\omega}$ as function of $\tilde{k}$ for the long-wave instability of the basic flat-film solution. For the 'small' value $Re=1$, the growth rates predicted

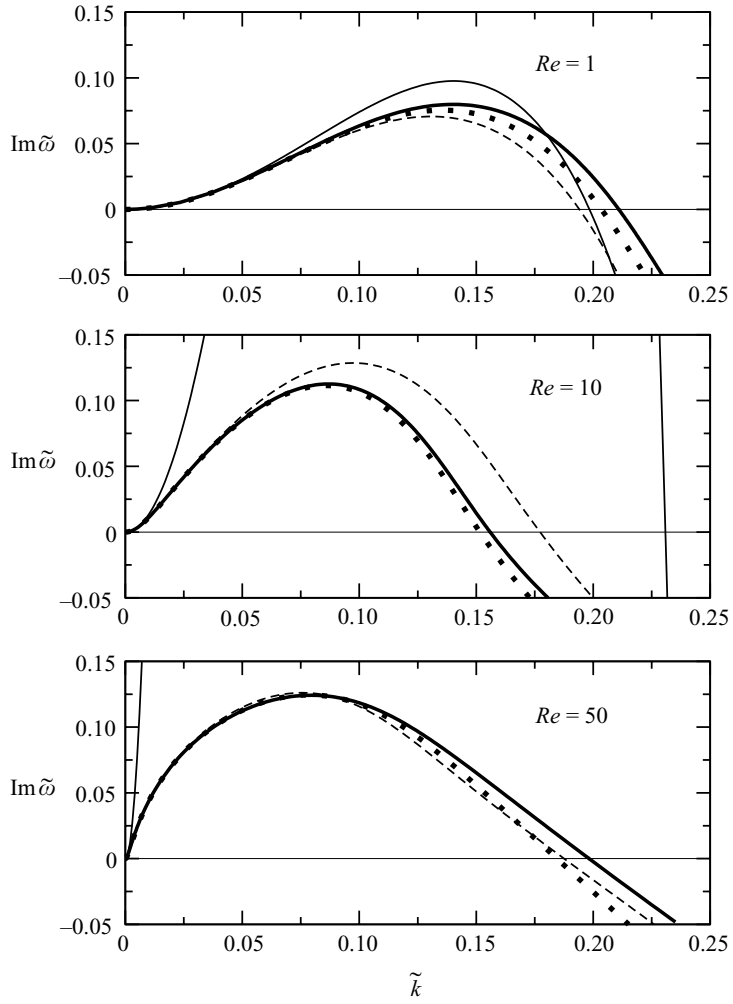

FIGURE 2. Growth rate $\mathrm{Im}\,\tilde{\omega}$ versus wavenumber $\tilde{k}$ for different Reynolds numbers obtained from the Orr–Sommerfeld analysis (solid lines), the full-size model (dotted lines), the regularized reduced model (dashed lines) and the Benney expansion (thin solid lines). Parameters are given in the caption of figure 1.

by the regularized reduced model (1.1), the full-size model and the second-order Benney expansion, are fairly close to the growth rate obtained by the exact Orr–Sommerfeld stability analysis. For larger Reynolds numbers, the Benney expansion no longer provides an accurate prediction for the growth rate, which increasingly deviates from the exact solution as the Reynolds number increases. This divergence is due to the fact that the Benney expansion assumes the dynamics of the flow to be slaved to its kinematics which is obviously not true at large Reynolds numbers. At $Re = 50$, where the H-mode is predominant, we note the good agreement of the full-size model and the regularized reduced model with the exact Orr–Sommerfeld analysis. At $Re = 10$, the full-size model is in good agreement with the exact Orr–Sommerfeld analysis while the regularized reduced model predicts a larger growth rate (still, the agreement with Orr–Sommerfeld is qualitative for all wavenumbers). This clearly shows the inability of the regularized reduced model to correctly take into account the second-order convective terms in the heat equation and to describe

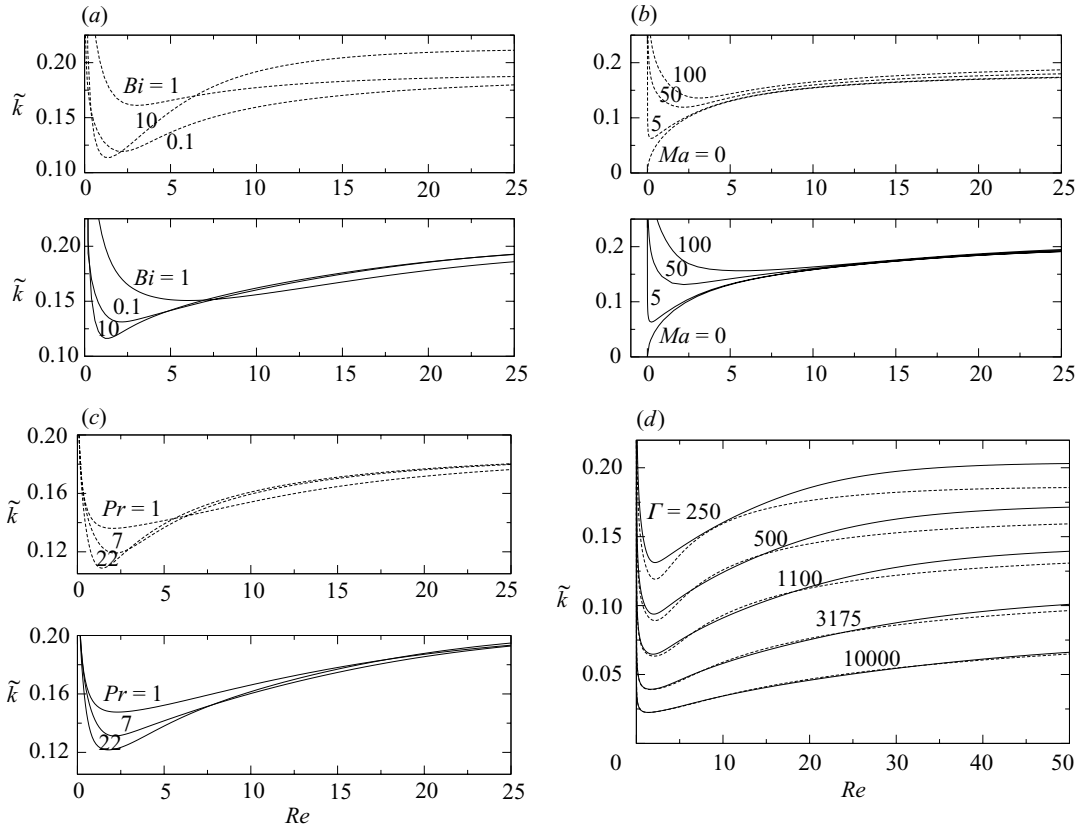

FIGURE 3. Influence of the Biot number (*a*), the Marangoni number (*b*), the Prandtl number (*c*) and the Kapitza number (*d*) on the marginal stability curves for a film falling down a vertical plane: (*a*) $Pr = 7$, $Ma = 50$ and $\Gamma = 250$; (*b*) $Bi = 0.1$, $Pr = 7$ and $\Gamma = 250$; (*c*) $Bi = 0.1$, $Ma = 50$ and $\Gamma = 250$; (*d*) $Bi = 0.1$, $Ma = 50$ and $Pr = 7$. The solid lines correspond to the Orr–Sommerfeld analysis and the dashed lines to the regularized reduced model (1.1).

the instability at large Péclet numbers where the S-mode is important. This issue will be discussed in the next section.

Figure 3(*a*) depicts the marginal stability curves obtained from the regularized reduced model (1.1) for a vertical plane and different Biot numbers. For $Bi = O(1)$ the influence of the Marangoni effect is large at small and moderate Reynolds numbers. Indeed, if *Bi* tends to zero or infinity, the free-surface temperature of the undisturbed solution, recalled in (2.1), becomes independent of h_N and the Marangoni effect is simply not an issue. For the other plots of figure 3, we choose a small Biot number, $Bi = 0.1$, which is motivated by experiments on the problem of a film heated by a local heat source (Kabov 1996; Kabov, Marchuk & Chupin 1996; Kabov *et al.* 2002) indicating that the Biot number in experiments is indeed small.

We have also investigated the influence of the Marangoni, Prandtl and Kapitza numbers and comparisons of the marginal stability curves obtained from Orr–Sommerfeld and the regularized reduced model are given in figure 3. As expected, for $Ma = 0$, we recover the classical hydrodynamic H-mode, with the corresponding curve starting from the origin of the plane ($\tilde{k}$, *Re*) – see figure 3(*b*). For $Pr = 7$, increasing the Marangoni number increases the range of unstable wavenumbers, especially at low Reynolds numbers where the Marangoni effect is predominant (S-mode). Again the results obtained using the regularized reduced model compare very well with the

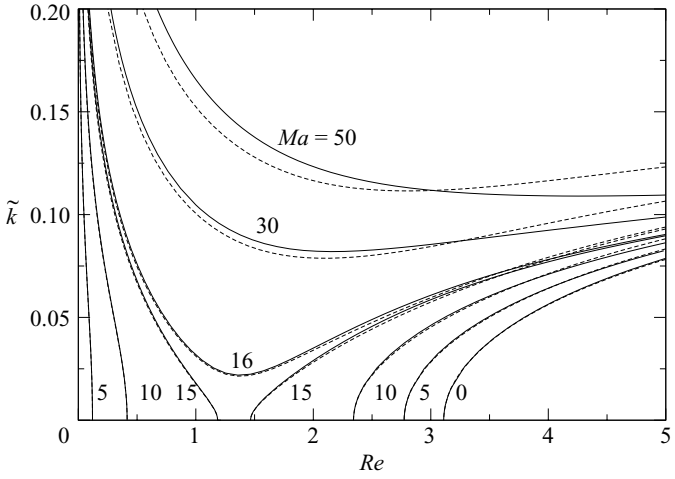

.

FIGURE 4. Influence of the Marangoni number on marginal stability for an inclined plane forming an angle $\beta = 15°$ with the horizontal direction with $\Gamma = 250$, $Pr = 7$ and $Bi = 1$. Solid lines are for the Orr–Sommerfeld analysis and dashed lines for the regularized reduced model.

Orr–Sommerfeld eigenvalue problem. Note, however, that at large Reynolds numbers, the marginal stability curves obtained from Orr–Sommerfeld merge into a single curve while the ones obtained from the regularized reduced model do not. Clearly, if Re is sufficiently large, the hydrodynamic H-mode predominates and the thermocapillary effects as measured by Ma do not modify significantly the critical wavenumber. The small disparity of the curves corresponding to the regularized reduced model is therefore a consequence of the increased inaccuracy of this model in the region of large Péclet numbers.

Figure 3(c) depicts the effect of Prandtl number on the marginal stability curves. The results now are less intuitive. Indeed, since the instability is primarily an inertia-driven instability, at least if the H-mode predominates, a larger value of Pr would imply a larger range of unstable wavenumbers since the Péclet number, $Pe = PrRe$, measuring the convective effects in the heat transport equation is also larger. Nevertheless, it is found that the Prandtl number has little influence for large Re (H-mode) whereas the curves are strongly affected by the Prandtl number for small Re (S-mode). If the S-mode predominates, the origin of the instability is the gradient of temperature at the interface. This gradient may be weakened by the transport of heat from the troughs to the crests due to the motion of the fluid, a process which is intensified with large Prandtl numbers. Note that the regularized reduced model agrees better with Orr–Sommerfeld for $Pr = 1$ than for larger values of Pr.

Finally, figure 3(d) shows the influence of Kapitza number on the marginal stability curves. Note the excellent agreement with the Orr–Sommerfeld eigenvalue problem for large values of Γ ($\Gamma = 3175$ corresponds to water at 18 °C). Now, decreasing the value of Γ increases the range of unstable wavenumbers and a discrepancy between the regularized reduced model and the Orr–Sommerfeld eigenvalue problem appears, which increases with decreasing Γ. It is precisely for this reason, i.e. to emphasize the differences between the different models, that we choose the worse case scenario in which the Kapitza number is relatively small, $\Gamma = 250$, throughout this study.

For non-vertical planes and Marangoni numbers Ma of $O(1)$, the critical condition (2.5) can lead to two different values for the onset of the instability corresponding to

the H- and S-modes, respectively. This is confirmed in figure 4 for a plane inclined at an angle $\beta = 15^\circ$ with respect to the horizontal direction. For moderate values of *Ma*, two distinct unstable regions are observed, each corresponding to a different instability mode as reported first by Goussis & Kelly (1991). Note the excellent agreement of the curves corresponding to the regularized reduced model (1.1) with Orr–Sommerfeld in the vicinity of the two thresholds. This agreement results from taking into account the second-order dissipative terms in our formulation and from a correct representation of the instability threshold. Noticeable discrepancies between the two sets of curves can be observed if the Marangoni number is increased or at larger Reynolds numbers. Finally, we have analysed the linear stability properties of different second-order reduced models, but in all cases, the system in (1.1) offers the best agreement with Orr–Sommerfeld.

3. Solitary waves

We now seek travelling wave solutions of (1.1). Here we restrict our attention to single-hump solitary waves. It is well known that for isothermal films, the long-time evolution is characterized by a train of soliton-like coherent structures each of which resembles the infinite-domain solitary pulses (see e.g. Alekseenko, Nakoryakov & Pokusaev 1994). Although time-dependent computations are beyond the scope of the present study, by analogy with the isothermal case, we anticipate that for the non-isothermal problem studied here, the long-time evolution is also dominated by solitary waves.

Comparisons of the different shapes of solitary waves is made easier by using a scaling based on the intrinsic length scales of the structures considered. For this purpose we adopt the scalings suggested by Shkadov (1977). These scalings are motivated by the observation that the largest slope of a solitary wave is at the front of the main solitary hump where the breaking of the wave is promoted by the stream wise gravity force $\rho g \sin\beta$ and balanced by the pressure gradient induced by the surface tension $\propto \sigma \partial_{xxx} h$. Therefore the characteristic slope $1/\kappa$ is given by $(\rho g h_N^2 \sin\beta/\sigma)^{1/3} = We^{-1/3}$. This analysis is valid at least close to the threshold of instability where the range of unstable wavenumbers is small. Thus introducing the transformation $x \to \kappa \bar{h}_N x$, $y \to \bar{h}_N y$, $u \to \bar{h}_N^2 u$, $t \to t\kappa/\bar{h}_N$ in the boundary-layer equations (see § 3 in Part 1) yields

$$\delta(\partial_t u + u\partial_x u + v\partial_y u) - (\partial_{yy} + 2\eta\partial_{xx})u - \eta\partial_x[\partial_x u|_h] - 1 + \zeta\partial_x h - \partial_{xxx} h = 0, \quad (3.1a)$$

$$Pr\delta\left(\partial_t T + u\partial_x T + v\partial_y T\right) - (\eta\partial_{xx} + \partial_{yy})T = 0, \quad (3.1b)$$

completed by the continuity equation $\partial_x u + \partial_y v = 0$, the boundary conditions

$$\partial_y u|_h = \eta(4\partial_x h\partial_x u|_h - \partial_x v|_h) - M\partial_x[T|_h], \quad (3.2a)$$

$$\partial_y T|_h = -B\left(1 + \frac{\eta}{2}(\partial_x h)^2\right)T|_h + \eta\partial_x h\partial_x T|_h, \quad (3.2b)$$

the kinematic condition at the free surface $\partial_t h + u|_h \partial_x h = 0$ and the Dirichlet conditions at the wall, $u|_0 = v|_0 = 0$ and $T|_0 = 1$. A set of 'reduced' parameters is now obtained:

$$\left.\begin{aligned} \delta &= \frac{\bar{h}_N^3}{\kappa} = \frac{(3Re)^{11/9}}{\Gamma^{1/3}}, \quad \zeta = \frac{\cot\beta}{\kappa} = \frac{\cot\beta\,(3Re)^{2/9}}{\Gamma^{1/3}}, \\ \eta &= \frac{1}{\kappa^2} = \frac{(3Re)^{4/9}}{\Gamma^{2/3}}, \quad M = \frac{Ma}{\kappa\bar{h}_N^2} = \frac{Ma}{\Gamma^{1/3}(3Re)^{4/9}}, \end{aligned}\right\} \quad (3.3)$$

along with $B = Bi\,(3Re)^{1/3}$ defined in (2.2); δ is the reduced Reynolds number† and ζ the reduced slope. The parameter η appears in all second-order streamwise dissipative terms in the momentum and heat transport equations. Similarly M is a reduced Marangoni number. Since the long-wave approximation requires the slope to be small, η must be small – or equivalently the Kapitza number large enough – so that in many studies dealing with vertical isothermal film flows ($\zeta = 0$, $M = 0$) η is set to zero and the set of parameters is reduced to δ only (see e.g. Chang 1994). Again, considering isothermal vertical flows, another advantage of the above set of parameters is that, using Shkadov's scalings, the speed and maximal height of the solitary waves depend strongly on the reduced Reynolds number δ and are not affected much by the strength of the streamwise viscous terms as measured by η, whereas the amplitude of the front-running capillary waves depends strongly on η (see e.g. the direct numerical computations by Salamon, Armstrong & Brown 1994). Still considering isothermal vertical flows, if the effect of inertia becomes dominant, the maximum slope of the waves ceases to correspond to the equilibrium of the streamwise gravity and surface tension but rather to the largest wavenumber triggered by the instability which corresponds to the critical wavenumber $k_c \propto \sqrt{Re/We}$ (see (2.4)). Therefore $\epsilon Re \sim k_c Re \sim \delta^{3/2}$ and the transition from the drag–gravity regime ($\epsilon Re \ll 1$) to the drag–inertia regime ($\epsilon Re = O(1)$) corresponds to δ of order unity. As already noticed by Ooshida (1999), this transition corresponds closely to the loss of solitary wave solutions observed for the Benney equation for $\delta \approx 0.986$. Finally, the reduced parameters (3.3) also give a good indication of the influence of the different physical effects on these waves. Therefore, since Shkadov's scalings are appropriate for the study of the strongly nonlinear solitary waves, in the next section we shall compare the main properties of the solutions obtained from the regularized reduced model – namely phase speed c, maximum height and shapes – using these scalings also.

Interestingly, all the reduced parameters (3.3) vanish as the Reynolds number tends to zero except for the reduced Marangoni number which tends to infinity. Hence, for small flow rates, $\delta \ll 1$, $\zeta \ll 1$ and $\eta \ll 1$ and the corresponding terms multiplied by these parameters can be neglected. Integrating (3.1) twice thus leads to

$$q = \frac{h^3}{3}(1 + \partial_{xxx} h) - \frac{M}{2} h^2 \partial_x \theta, \quad \theta = \frac{1}{1 + Bh} = 1 - Bh + O(B^2), \tag{3.4}$$

and the mass conservation equation $\partial_t h + \partial_x q = 0$ then gives

$$\partial_t h + \partial_x \left[\frac{h^3}{3}(1 + \partial_{xxx} h) + \frac{MB}{2} h^2 \partial_x h \right] = 0 \tag{3.5}$$

where the leading-order term involving B has been retained. Apart from numerical factors and different scalings, equation (3.5) is identical to the one obtained by Kalliadasis *et al.* (2003). The reduced parameter proposed by Kalliadasis *et al.* (2003) is $\propto 1/BM$. These authors observed that homoclinic solutions to (3.5) tend to infinity as their parameter tends to zero, that is when MB tends to infinity. Because we have $MB \propto (3Re)^{-1/9}$, this limit corresponds to the zero Reynolds number limit. As was pointed out by these authors, in this region of small flow rates and hence small film thicknesses, the film is expected to form isolated drops separated by very thin

† The reduced Reynolds number defined initially by Shkadov (1977) was $\delta_{\mathrm{Shk}} = \delta/45$. The numerical factor originates from a slightly different choice of variables.

layers of fluid for which van der Waals forces become important. Such forces of non-hydrodynamic origin are expected to arrest the singularity formation observed for the homoclinic orbits in the region of small Reynolds numbers. Inversely, if *Re* tends to infinity, both M and MB tend to zero and the velocity and temperature fields are decoupled in this limit. Therefore, at large Reynolds numbers, the shape of the wave should be unaffected by the Marangoni effects. These two limits will enable us to elucidate the influence of Reynolds number on the shape of the waves for given inclination angle and physical properties.

In what follows, we discuss in detail the properties of the solitary wave solutions of the system (1.1) as well as the influence of the different physical effects and different parameters, primarily *Re*, *Pr* and *Ma*, on these waves. In all cases the wall is taken to be vertical – for the isothermal case vertical apparatus is most frequently used in experiments (Alekseenko, Nakoryakov & Pokusaev 1994). Our main interest is to decipher the coupling between the hydrodynamic H-mode and thermocapillary S-mode in the nonlinear regime and particularly for large amplitude waves, that is in the drag–inertia regime where inertia plays a dominant role.

Consider now travelling wave solutions propagating at constant speed c and hence stationary in the moving frame $\xi = x - ct$. In this frame, the set of equations (1.1) can be written in dynamical system form as

$$\frac{\mathrm{d}\boldsymbol{U}}{\mathrm{d}\xi} = \boldsymbol{F}(\boldsymbol{U};\, \delta,\, \zeta,\, \eta,\, B,\, M,\, Q), \tag{3.6}$$

where $\boldsymbol{U} = (h,\, h',\, h'',\, \theta,\, \theta')^t$. The constant Q is the mass flux under the wave in the moving frame of reference and is obtained after one integration of the mass conservation equation $-c\,h' + q' = 0$, $Q = q - c\,h$. For solitary pulses, the Nusselt flat-film solution $h = 1$ should be approached far from the pulses which gives $Q = 1/3 - c$. Since the speed of the waves is larger than the maximum velocity in the liquid, Q is a negative constant. Note, however, that in experiments, the time-averaged film thickness can be smaller downstream than at the inlet (the presence of the waves usually accelerates the fluid motion). As a consequence, the local Reynolds number varying with the third power of the thickness can be significantly smaller than the Reynolds number based on the flow rate or the inlet Nusselt film thickness.

Singe-hump solitary wave solutions – also called 'principal homoclinic orbits' by Gelndinning & Sparrow (1984) – are computed using the continuation software AUTO97 with the HOMCONT option for tracing homoclinic orbits (Doedel *et al.* 1997). In figure 5 we present the maximum amplitude and speed of the single-hump solitary wave family of the regularized reduced model as a function of *Re* for different values of Prandtl and Marangoni numbers. For comparison purposes, we also show in the same figure the wave family corresponding to isothermal flows ($Ma = 0$). In all our computations in this section we take the values $\Gamma = 250$ and $Bi = 0.1$ for the Kapitza and Biot numbers, respectively. As already mentioned, the Kapitza number is chosen much smaller than its value for common liquids in order to clearly isolate the role of the second-order dissipative and inertia terms.

The single-hump solitary wave solution branch obtained from (1.1) seems to exist for all Reynolds numbers, i.e. it does not present any turning points with branch multiplicity connected to finite-time blow-up behaviour as for the Benney expansion (Pumir, Manneville & Pomeau 1983; Oron & Gottlieb 2002; Scheid *et al.* 2005). Different reduced second-order formulations – from the family of reduced models developed in Part 1 – were also tested (not shown) and their solitary-wave solution branches do exhibit turning points. This, along with the good agreement with the

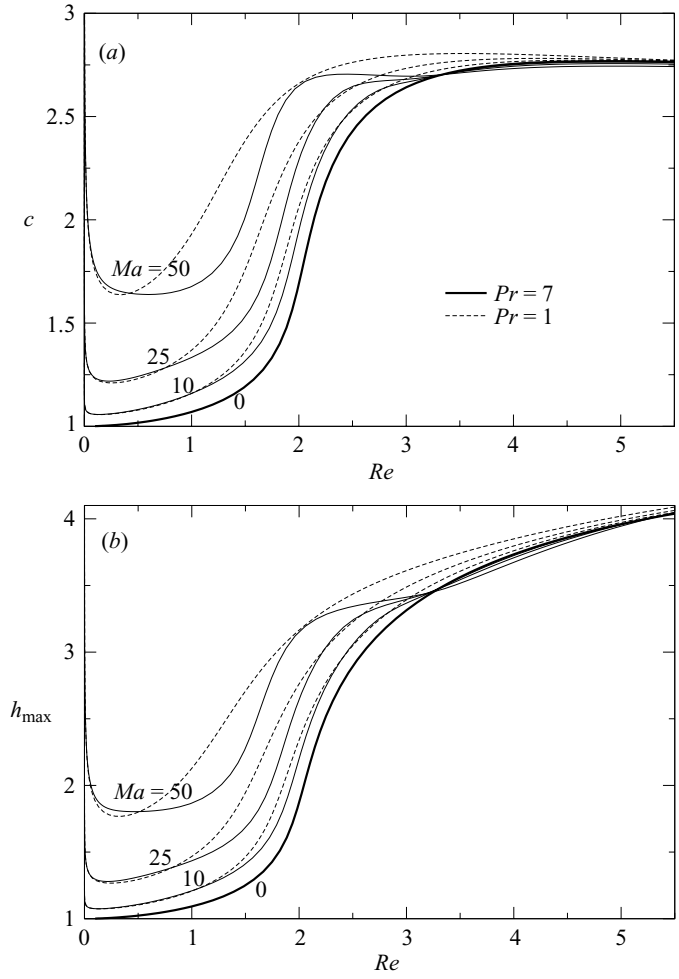

FIGURE 5. (*a*) Speed and (*b*) maximum height of single-hump solitary wave solutions computed with the regularized reduced model (1.1) for different values of Ma and Pr with $\cot\beta = 0$, $Bi = 0.1$ and $\Gamma = 250$.

Orr–Sommerfeld eigenvalue problem shown in the previous section, confirms that (1.1) is indeed a well-behaved low-dimensional model.

As expected, increasing the Marangoni number leads to larger amplitudes and speeds since the two instability modes reinforce each other. This effect is more pronounced at low Reynolds numbers (the reduced Marangoni number M defined in (3.3) is proportional to $Re^{-4/9}$). This is also consistent with our linear stability analysis in the previous section which suggests that the Marangoni effect is amplified in the region of small Reynolds numbers. On the other hand, in the region of large Re, the different curves merge with the isothermal one. In this region of large Reynolds numbers the destabilizing interfacial Marangoni forces are weaker than the dominant inertia forces.

The effect of Prandtl number is more subtle. At low Reynolds numbers, larger values of Pr seem to favour the instability, whereas at larger Re, we have the opposite effect. To elucidate the influence of Prandtl number, we compute the streamlines and isotherms in the moving frame by computing the velocity and temperature fields from the polynomial expansions and by utilizing the first-order approximation of the corrections s_i and t_i (see Part 1 for details). Note that the second-order corrections for

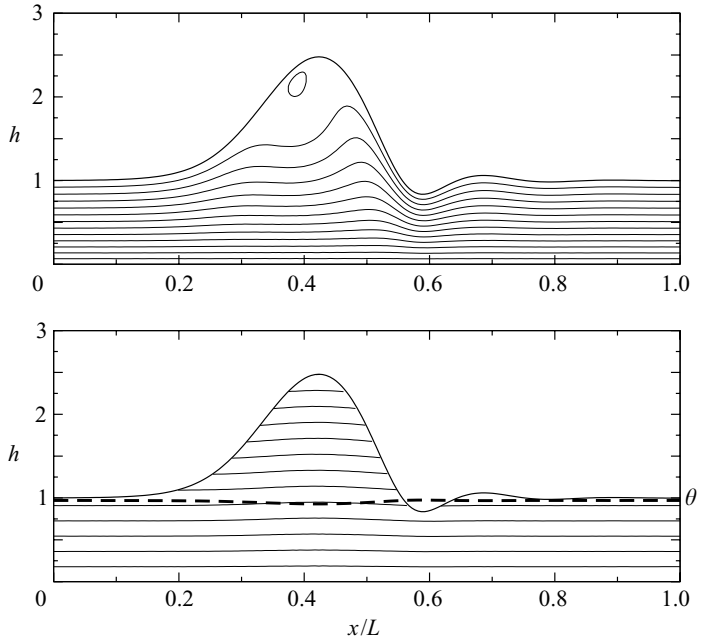

FIGURE 6. Streamlines (top) and isotherms (bottom) of a solitary wave in its moving frame obtained for $Pr = 7$, $Re = 0.01$, $\cot\beta = 0$, $\Gamma = 250$, $Ma = 50$ and $Bi = 0.1$. The dashed line represents the interfacial temperature θ. There are 12 isotherms separating 13 equally spaced intervals, ranging from $T = 1$ on the wall to $T_{\min} = 0.929$.

both fields can also be computed from the residuals associated with the corresponding test functions followed by an inversion of the resulting linear system. Nevertheless, due to the complexity of this procedure, we assume here that the velocity and temperature fields are described sufficiently accurately by their representation at first order, at least for the purpose of a qualitative discussion. In all computations of this section the Marangoni number is fixed at $Ma = 50$.

Figure 6 shows the streamlines and isotherms for $Re = 0.01$. The reduced parameters are $\delta = 0.0022$, $\eta = 0.0053$, $M = 37.6$ and $B = 0.031$. With the product $Pr\delta$, η and B being small, the film flow evolution is well approximated by the evolution equation for the free surface (3.5). We also have $\partial_{yy}T \approx 0$ so that the temperature field is nearly linear, $T \approx 1 - By$. Therefore, the isotherms are nearly aligned with the wall. Notice also from figure 6 that the interfacial temperature θ is nearly uniform since $B \ll 1$. For such a small Reynolds number, inertial effects are almost absent and the Marangoni effect is free to form large-amplitude humps. Consequently, the phase speed is sufficiently large – $c = 2.35$ for the wave shown in figure 6 – to create a recirculation zone at the crest of the wave along with the transport of fluid mass downstream. Interestingly, this behaviour triggered by the Marangoni effect is very similar to that triggered by inertia for larger Reynolds numbers (see below).

The streamlines and isotherms computed for $Re = 1$ and $Pr = 1$ and 7 are shown in figure 7. The reduced parameters are now $\delta = 0.61$, $\eta = 0.041$, $M = 4.86$ and $B = 0.14$. Again, at $Pr = 1$, the isotherms are nearly aligned (with both B and $Pr\delta$ being still relatively small). Conversely, at $Pr = 7$, the isotherms are deflected upwards by the movement of the fluid in the crest. Therefore, the minimum of temperature (which is achieved at the crest of the solitary wave) increases to $T_{\min} = 0.8$ – from 0.765 for $Pr = 1$ – and consequently the Marangoni effect is reduced, and therefore the amplitude and the phase speed of the wave are also reduced. The transport of heat

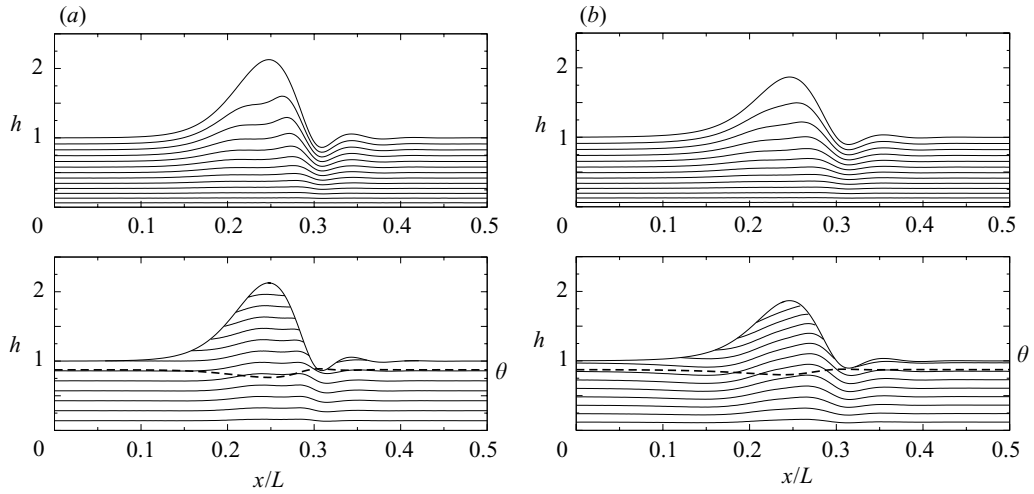

FIGURE 7. Streamlines (top) and isotherms (bottom). $Re = 1$ and all other parameters are given in the caption of figure 6. In (*a*) $Pr = 1$ and $T_{\min} = 0.765$ and in (*b*) $Pr = 7$ and $T_{\min} = 0.8$. In all cases, a total of 12 isotherms separating 13 equally spaced intervals between $T = 1$ and $T = T_{\min}$ is shown.

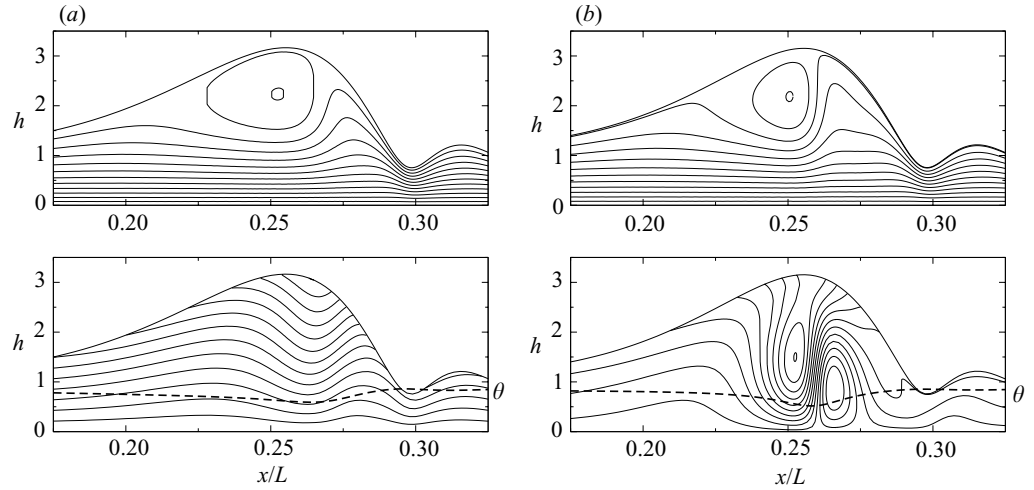

FIGURE 8. Streamlines (top) and isotherms (bottom) for $Re = 2$. All other parameters are given in the caption of figure 6. In (*a*), $Pr = 1$ and $T_{\min} = 0.591$ and in (*b*), $Pr = 7$, $T_{\min} = 0.429$ and $T_{\max} = 1.26$.

by the motion of the fluid has a stabilizing effect in this case. Nevertheless, at larger Reynolds numbers, inertia dominates, the solitary wave amplitude and speed increase dramatically and a recirculation zone appears inside the solitary wave. Streamlines computed for $Re = 2$ and $Re = 3$ ($\delta = 1.42$ and $\delta = 2.33$) shown in figures 8 and 9 do exhibit such recirculation zones, turning clockwise, and implying the existence of two stagnation points at the free surface at the back and the front of the primary solitary hump. In this case solitary waves transport the trapped fluid mass downstream.

Comparison with the streamlines at $Re = 3$ when the thermocapillary effect is switched off ($Ma = 0$) indicate that the Marangoni instability shifts one of the stagnation points from the front of the wave to its crest (see figure 10). Thus, because thermocapillary stresses push the fluid from the rear to the top of the crest,

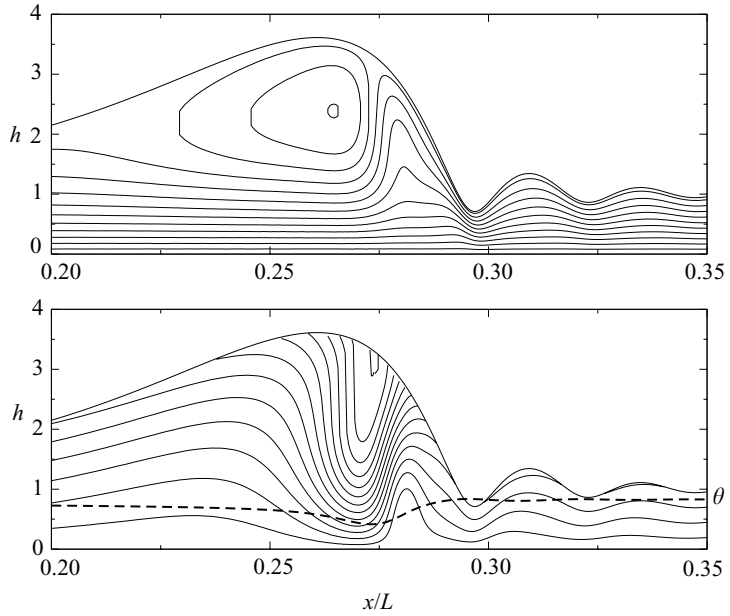

FIGURE 9. Streamlines (top) and isotherms (bottom) for $Re = 3$ and $Pr = 1$. Here $T_{\min} = 0.414$.

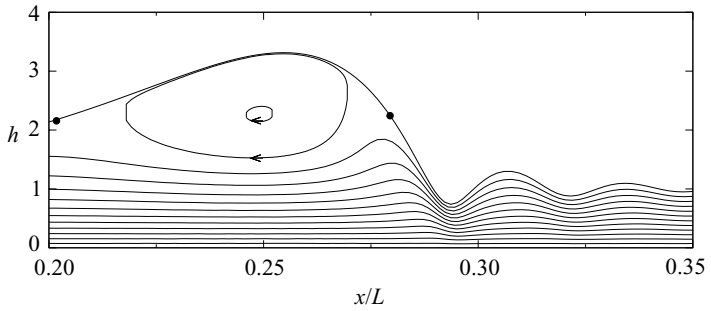

FIGURE 10. Streamlines for $Ma = 0$, $Re = 3$, $\cot\beta = 0$ and $\Gamma = 250$.

they reinforce the clockwise circulation in the crest. Meanwhile, the transport of heat by the downward fluid motion at the front of the recirculation zone cools down the surface at its crest and the minimum of interfacial temperature is now located close to the stagnation point at the front. Therefore the two mechanisms reinforce each other, promoting the speed and amplitude of the wave. This explains the formation of a recirculation zone at $Re = 2$ and $Ma = 50$ whereas it is not present if $Ma = 0$. Indeed, the abrupt increase of amplitude and speed of the solitary waves corresponding to the transition from the drag–gravity to the drag–inertia regime occurs for smaller values of the Reynolds number if the Marangoni effect is present (see figure 5).

Comparison of figures 8(a) and 8(b) indicates that increasing the Prandtl number from $Pr = 1$ to $Pr = 7$ at $Re = 2$ enhances the cooling process of the crest and reduces the temperature minimum from $T_{\min} \equiv \theta_{\min} = 0.591$ – which appears on the surface and very close to the stagnation point – to $T_{\min} = 0.429$ somewhere in the bulk of the wave, thus contributing to the Marangoni effect. Similarly, comparing figures 8(a) and 9, $T_{\min} \equiv \theta_{\min}$ drops from to 0.591 to 0.414 when Re increases from 2 to 3 at $Pr = 1$.

However, if the H- and S- instability modes reinforce each other for $Re = 2$ and $Re = 3$, the speed and amplitudes of the solitary waves do decrease as the Prandtl number increases as indicated in figure 5. This apparent paradox can be explained only by observing that on shifting one of the stagnation points to the crest, thermocapillarity tightens the streamlines and isotherms at the front of the recirculation zone. Moreover, the circulation in the hump is enhanced by the Marangoni stresses at the surface. Therefore, large temperature and velocity gradients appear in that region of the flow. As a consequence, the dissipation of heat and momentum is increased, which contributes to stabilizing the growth of the instability and to limiting the speed and amplitude of the solitary waves.

For $R = 2$ and $Pr = 7$, the maximum of temperature is $T_{\max} = 1.216$ and is no longer located at the wall. Notice also that at larger values of the Reynolds number, negative values of the dimensionless temperature appear in the fluid. Turning back to dimensional quantities, this would imply that the temperature in the fluid can be locally greater than the temperature of the wall or smaller than the temperature of the air. This obviously has no physical basis as the temperature everywhere in the fluid should be bounded between the wall and air temperatures. To understand the appearance of this unphysical behaviour when a recirculation zone is present, i.e. for large-amplitude waves, let us consider the high-Péclet-number limit $Pe = PrRe \gg 1$. In this case, transport of heat via molecular diffusion can be neglected except in a diffusive boundary layer of thickness $Pe^{-1/2}$ on the stagnation line and part of the interface associated with the recirculation zone (see e.g. discussion by Shraiman 1987). Hence, cross-stream convection associated with the recirculation zone dominates over diffusion, the temperature field in the recirculation zone is simply transported by the flow and the streamlines are identical to the temperature contours (see e.g. Trevelyan *et al.* 2002). This means that the temperature along each streamline is constant due to the strong advection mixing. The temperature field becomes a passive scalar and is simply transported by the flow. Hence, within the recirculation zone the isotherms are closed curves. Consequently, the temperature can vary locally in the horizontal direction only and the hypothesis $\partial_y T \gg \partial_x T$ necessary for the derivation of our models would be violated in these regions.†

At the same time we have neglected in the averaged heat balance (1.1*c*) the transport of heat due to the Marangoni flow, Mar_θ (see § 5 in Part 1). Though these terms are formally of second order, they could be quite significant due to the enhancement of the Marangoni flow by the hydrodynamics. This might also contribute to the appearance of negative temperatures. Different possibilities – not examined here – exist to cure this strong limitation on the applicability of the three-equation model (1.1). One such possibility would be to consider more unknowns, such as t_1, for the description of the heat transfer process in the flow. Another possibility would be to relax the assumption $\partial_y T \gg \partial_x T$ and use instead the full energy equation without any approximations. In this case the full energy equation would have to be solved numerically to obtain the temperature distribution within the film.

The basic question here is whether the observed limitations are truly due to a breakdown of the basic assumptions at large Péclet numbers and for large-amplitude waves for which recirculation zones could be observed, or are spuriously caused by the addition of the strongly nonlinear second-order terms appearing in the expansion

† Note however that the presence of recirculation zones does not invalidate the assumption $u \gg v$ necessary for any boundary-layer approach since the computed streamlines correspond to the envelopes of the velocity field in the moving frame $(u - c,\ v)^t$.

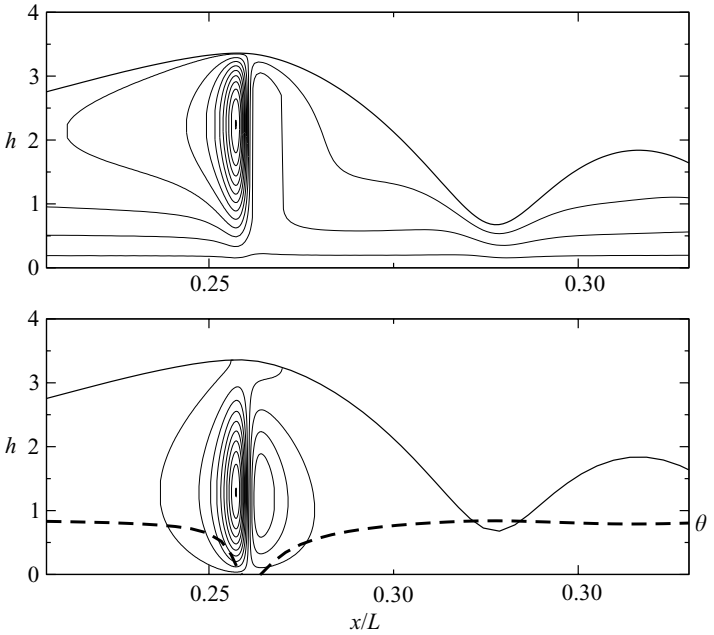

FIGURE 11. Streamlines (top) and isotherms (bottom) for $Re = 2.5$ and $Pr = 7$ obtained from the first-order model. Here $T_{\min} = -10$ and $T_{\max} = 4$.

procedure. To check these possibilities, we have computed the single-hump solitary wave solution branch corresponding to the first-order model (system (4.18) in Part 1) for $\Gamma = 250$, $\cot\beta = 0$, $Bi = 0.1$ and two values of the Prandtl number, $Pr = 1$ and $Pr = 7$. In both cases, a limit point, at which the branch of solutions terminates, appears (at $Re \approx 2.4$ for $Pr = 1$ and $Re \approx 2.7$ for $Pr = 7$). This loss of solutions follows the formation of steep temperature gradients in the bulk of the flow as is evident from the isotherms shown in figure 11 at $Re = 2.5$ and $Pr = 7$. In fact, the isothermal first-order model, an improved representation of the Shkadov model, has no limit points and so the limit points for the non-isothermal model must be due to the treatment of the energy equation. Notice that, quite surprisingly, the loss of solutions appears at smaller values of Re for $Pr = 1$ than for $Pr = 7$. This unusual result can be attributed to the fact that the transition between the drag–gravity and the drag–inertia regimes is delayed by the upward displacement of the isotherms by the flow as already observed in figure 7. Consequently, the second-order terms do contribute to the delay of the breakdown of our formulation and hence the limitations of our model are not caused by the added second-order terms. This effect is certainly due to the fact that the second-order diffusion terms reduce the range of unstable wavenumbers and smooth out temperature gradients (compare the amplitude of the front-running capillary wave preceding the main hump in figures 9 and 11).

It is important to emphasize that unlike the first-order model, the second-order regularized reduced model has no limit points at which the solution branches terminate. This is due to an improved treatment of the energy equation by taking into account the second-order dissipative terms in the streamwise direction as mentioned above. The first-order model on the other hand has not taken into account these terms – contrast (1.1c) with (4.18c) of Part 1. It is precisely the presence of diffusion of heat in the streamwise direction for the regularized reduced model that smooths out the large temperature gradients as was pointed out above and hence this model has no limit points. Nevertheless, for sufficiently large Péclet numbers and as we

have already pointed out, negative temperatures are observed somewhere in the bulk of the wave. The Re value at which this happens depends on Pr, with the larger Pr corresponding to smaller Re at which negative temperatures appear. After these points, the bifurcation diagrams for the speed of the solitary waves c as a function of Re can be continued to larger Re but the temperature will remain negative (in fact continuation of the curves in figure 5 will eventually lead to negative temperatures). The reason that this continuation is possible is that c is effectively determined by the momentum equation which is treated accurately; it is the treatment of the energy equation that needs to be improved and some suggestions for this have already been discussed above.

4. Concluding remarks

We have analysed the linear and nonlinear regimes of the two long-wave instability modes for a film falling down a uniformly heated plane by using the regularized reduced model derived in Part 1. The linear stability properties of the model are in good agreement with the Orr–Sommerfeld analysis for small and moderate Reynolds numbers and for all Marangoni numbers (§ 2) while its single-hump solitary wave solution branches do not exhibit the non-physical turning points encountered with the Benney equation (§ 3). Therefore, time-dependent integrations of the regularized reduced model (1.1) (not done here) should not lead to the finite-time blow-up behaviour observed with the Benney expansion in the region of the parameter space where solitary waves do not exist.

We also examined in detail the shape, streamlines and isotherms of single-hump solitary waves obtained from the regularized reduced model and for different Reynolds, Prandtl and Marangoni numbers. In the drag–gravity regime, the transport of energy by the flow contributes to heating the crest of the solitary waves. In this region, the inertial terms in the averaged heat transport equation have a stabilizing effect. For $Re \ll 1$, inertial effects are nearly absent and the Marangoni effect is free to form large-amplitude humps and hence large phase speed so that a recirculation zone at the crest of the wave appears. As far as we are aware, a recirculation zone has never been obtained before for such small Reynolds numbers and is usually known to exist only in the drag–inertia regime for large Reynolds numbers. In this regime, the amplitudes and speeds of the solitary waves are also large. However, the effect of the transport of heat by the flow is reversed. One of the stagnation points (in the frame moving with the wave) is shifted from the front of the wave to its crest. Thus, the Marangoni effect enhances the recirculation in the crest and promotes a strong downward flow there. As a consequence, the transport of heat by the flow contributes to cooling the crest and amplifying the Marangoni effect. Nevertheless, this strong circulation and downward flow create a strong shear and therefore increase the effect of viscous dissipation which in turn reduces the amplitude and speed of the waves if the Prandtl number increases. These observations indicate that the interaction of the hydrodynamic H-mode and the Marangoni S-mode is non-trivial especially in the region of large-amplitude solitary waves.

With regard to experiments, comparisons with the theory developed here should be facilitated by the fact that most fluids used in applications have high Kapitza numbers. Note also that the heat transfer coefficient is generally small so that the Biot number is also small. Thus considering the limit $Bi \ll 1$, the basic-state temperature gradient $b_\perp = (T|_{y=0} - T|_{y=h_N})/h_N = Bi/(1 + Bih_N)$ can be assumed to be independent of the film thickness h, $b_\perp \approx Bi$. This basic-state temperature gradient is then uniquely

defined by the heat transfer coefficient q_0 and the diffusivity κ and not by the flow rate. As a consequence, many studies on Marangoni instabilities have used explicitly the gradient $b_\perp$ to scale the temperature field (Takashima 1981; Davis 1987; Goussis & Kelly 1991). Following this approach, one can define a reference temperature T_{s0} corresponding to the surface temperature of a flat film of thickness equal to the length scale $\nu^{2/3}(g\sin\beta)^{-1/3}$. A new dimensionless temperature $T^\star$ is thus introduced using the difference $T_w - T_{s0}$ such that $T^\star = 1$ at the wall and $T^\star = 0$ at the surface of the film of thickness l_0. T and $T^\star$ are then related by

$$T = \frac{1 + BiT^\star}{1 + Bi}, \tag{4.1}$$

and the heat transfer condition at the interface becomes

$$-\nabla T^\star \cdot \boldsymbol{n} = BiT^\star + 1. \tag{4.2}$$

The linear stability analysis of a thin film in the limit of a vanishing Biot number was considered by Takashima (1981). Obviously, taking this limit is not consistent with the problem in hand as $Bi = 0$ implies that the transfer of heat through the fluid layer vanishes and therefore the temperature at the free surface is constant. Nevertheless, the product $Ma\,Bi$ can be $O(1)$ even if Bi is small and so the Marangoni effect can be strong. Thus, Takashima's limit corresponds in fact to a constant temperature gradient $q_0(T_w - T_a)/\kappa$, that is simply obtained by neglecting the term $BiT^\star$ in (4.2) which gives

$$\nabla T^\star \cdot \boldsymbol{n} = -1. \tag{4.3}$$

In this limit, the change of variables from the dimensionless temperature T to $T^\star$ given by (4.1) is translated to the definition of the temperature at the free surface as $\theta = (1 + Bi\theta^\star)/(1 + Bi)$. The approximation of the heat transfer at the interface leading from (4.2) to (4.3) can be readily applied in our formulation by expanding $\theta \approx 1 + Bi(\theta^\star - 1)$. A modified system of equations is then obtained simply by substituting $\theta^\star$ for θ in (1.1) and keeping the leading-order terms in Bi:

$$\partial_t h = -\partial_x q, \tag{4.4a}$$

$$\begin{aligned}\partial_t q = {} & \frac{9}{7}\frac{q^2}{h^2}\partial_x h - \frac{17}{7}\frac{q}{h}\partial_x q \\ & + \left\{\frac{5}{6}h - \frac{5}{2}\frac{q}{h^2} + 4\frac{q}{h^2}(\partial_x h)^2 - \frac{9}{2h}\partial_x q\,\partial_x h - 6\frac{q}{h}\partial_{xx}h + \frac{9}{2}\partial_{xx}q \right. \\ & \left. - \frac{5}{6}Bh\partial_x h + \frac{5}{6}\Gamma h\partial_{xxx}h - MaBi\left(\frac{5}{4}\partial_x\theta^\star - \frac{1}{224}hq\partial_{xx}\theta^\star\right)\right\} \\ & \times \left(1 - \frac{1}{70}q\partial_x h + MaBi\frac{5}{56h}\partial_x\theta^\star\right)^{-1},\end{aligned} \tag{4.4b}$$

$$\begin{aligned}Pr\partial_t\theta^\star = {} & 3\frac{(1-\theta^\star - h)}{h^2} + Pr\left[\frac{7}{40}\frac{(1-\theta^\star)}{h}\partial_x q - \frac{27}{20}\frac{q}{h}\partial_x\theta^\star\right] \\ & + \left(1 - \theta^\star - \frac{3}{2}h\right)\left(\frac{\partial_x h}{h}\right)^2 + \frac{\partial_x h\,\partial_x\theta^\star}{h} + (1-\theta^\star)\frac{\partial_{x^2}h}{h} + \partial_{xx}\theta^\star.\end{aligned} \tag{4.4c}$$

Now the Marangoni and Biot numbers appear through their product only, which reduces the number of relevant parameters by one and simplifies the parametric study of the nonlinear waves.

Another open question concerns large Péclet number flows. In this case the assumption of a small temperature gradient in the cross-stream direction is violated such that our three-variable model is no longer capable of describing accurately the wave dynamics. Nevertheless, a suggestion can be made. Indeed, our linear stability analysis and computations of solitary waves have suggested that more fields in addition to θ are necessary to correctly represent the heat transport process. In particular, we wish to overcome the spurious appearance of temperatures lower than the temperature of air that we observed for large-amplitude waves for sufficiently large Reynolds and Prandtl numbers. Hence, the aim would be to obtain reliable models, e.g. in terms of h, q, θ and t_1, compatible with the long-wave expansion up to second order, and which would also enable us to extend the present study to larger Péclet numbers. This and related issues will be addressed in a future study.

Despite the limitations of the regularized reduced model for large Péclet numbers, the model has substantially extended the region of validity of the Benney long-wave expansion which exhibits a turning point with branch multiplicity at an $O(1)$ value of Re, and for all Péclet numbers (see Kalliadasis *et al.* 2003), while in these regions our model has no turning points and predicts the continuing existence of solitary waves for all Reynolds numbers. Moreover, the appearance of unphysical negative temperatures at large Prandtl numbers is connected to the formation of recirculation zones in the solitary waves. Therefore, the regularized reduced model (1.1) should give results in reasonable agreement with experiments for waves of smaller amplitude for which no recirculation zones are observed.

C. R.-Q. and B. S. gratefully acknowledge fruitful discussions with Professor Paul Manneville. C. R.-Q. thanks Laurent Martin-Witkowski and Anne Sergent for their helpful comments. B. S. acknowledges support from European Union (Marie Curie contract HPMT-CT-2000-00207). This work has been facilitated by a CNRS/CGRI-FNRS cooperation. S. K. acknowledges financial support from EPSRC through an Advanced Research Fellowship, grant no. GR/S49520/01. The authors thank the Instituto Pluridisciplinar for hospitality.

REFERENCES

Alekseenko, S., Nakoryakov, V. & Pokusaev, B. 1994 *Wave Flow in Liquid Films*, 3rd Edn. Begell House.

Chang, H.-C. 1994 Wave evolution on a falling film. *Annu. Rev. Fluid Mech.* **26**, 103–136.

Davis, S. H. 1987 Thermocapillary instabilities. *Annu. Rev. Fluid Mech.* **19**, 403–435.

Doedel, E. J., Champneys, A. R., Fairgrieve, T. F., Kuznetsov, Y. A., Sandstede, B. & Wang, X.-J. 1997 Auto97: Continuation and bifurcation software for ordinary differential equations. *Tech. Rep.* Department of Computer Science, Concordia University, Montreal, Canada (available by FTP from `ftp.cs.concordia.ca` in directory `pub/doedel/auto`).

Gelndinning, P. & Sparrow, C. 1984 Local and global behavior near homoclinic orbits. *J. Statist. Phys.* **35**, 645–696.

Goussis, D. & Kelly, R. 1991 Surface wave and thermocapillary instabilities in a liquid film flow. *J. Fluid Mech.* **223**, 25–45, and corrigendum *J. Fluid Mech.* **226**, 663.

Joo, S. W., Davis, S. H. & Bankoff, S. G. 1991 Long-wave instabilities of treated falling films: two-dimensional theory of uniform layers. *J. Fluid Mech.* **230**, 117–146.

Kabov, O. A. 1996 Heat transfer from a small heater to a falling liquid film. *Heat Transfer Res.* **27**, 221–226.

Kabov, O. A., Marchuk, I. & Chupin, V. 1996 Thermal imaging study of the liquid film flowing on vertical surface with local heat source. *Russ. J. Engng Thermophys.* **6**, 105–138.

KABOV, O. A., SCHEID, B., SHARINA, I. & LEGROS, J. C. 2002 Heat transfer and rivulet structures formation in a falling thin liquid film locally heated. *Intl J. Thermal Sci.* **41**, 664–672.

KALLIADASIS, S., DEMEKHIN, E. A., RUYER-QUIL, C. & VELARDE, M. G. 2003 Thermocapillary instability and wave formation on a film flowing down a uniformly heated plane. *J. Fluid Mech.* **492**, 303–338.

KELLER, H. B. 1977 Numerical solution of bifurcation and nonlinear eigenvalue problems. In *Applications of Bifurcation Theory* (ed. P. H. Rabinowitz), pp. 359–384. Academic.

OOSHIDA, T. 1999 Surface equation of falling film flows which is valid even far beyond the criticality. *Phys. Fluids* **11**, 3247–3269.

ORON, A. & GOTTLIEB, O. 2002 Nonlinear dynamics of temporally excited falling liquid films. *Phys. Fluids* **14**, 2622–2636.

PUMIR, A., MANNEVILLE, P. & POMEAU, Y. 1983 On solitary waves running down an inclined plane. *J. Fluid Mech.* **135**, 27–50.

RUYER-QUIL, C. & MANNEVILLE, P. 2000 Improved modeling of flows down inclined planes. *Eur. Phys. J.* B **15**, 357–369.

RUYER-QUIL, C., SCHEID, B., KALLIADASIS, S., VELARDE, M. G. & ZEYTOUNIAN, R. Kh. 2005 Thermocapillary long waves in a liquid film flow. Part 1. Low-dimensional formulation. *J. Fluid Mech.* **538**, 199–222.

SALAMON, T., ARMSTRONG, R. & BROWN, R. 1994 Traveling waves on vertical films: Numerical analysis using the finite element method. *Phys. Fluids* **6**, 2202–2220.

SCHEID, B., RUYER-QUIL, C., THIELE, U., KABOV, O., LEGROS, J. & COLINET, P. 2005 Validity domain of the Benney equation including Marangoni effect for closed and open flows.

SCRIVEN, L. E. & STERNLING, C. 1964 On cellular convection driven by surface-tension gradients: effects of mean surface tension and surface viscosity. *J. Fluid Mech.* **19**, 321–340.

SHKADOV, V. Ya. 1967 Wave flow regimes of a thin layer of viscous fluid subject to gravity. *Izv. Ak. Nauk SSSR, Mekh. Zhi. Gaz* **2**, 43–51; English transl. *Fluid Dyn.* **2**, 29–34.

SHKADOV, V. Ya. 1977 Solitary waves in a layer of viscous liquid. *Izv. Ak. Nauk SSSR, Mekh. Zhi. Gaz* **12**, 63–66; English transl. *Fluid Dyn.* **12**, 52–55.

SHRAIMAN, B. I. 1987 Diffusive transport in a Rayleigh-Bénard convection cell. *Phys. Rev.* A **36**, 261–267.

TAKASHIMA, M. 1981 Surface driven instability in a horizontal liquid layer with a deformable free surface. *J. Phys. Soc. Japan* **50**, 2745–2756.

TREVELYAN, P. M. J., KALLIADASIS, S., MERKIN, J. H. & SCOTT, S. K. 2002 Mass transport enhancement in regions bounded by rigid walls. *J. Engng Maths* **42**, 45–64.

Film flows down a fiber 4

In this chapter, I summarize a study of the linear and non-linear dynamics of an axisymmetrical Newtonian film falling down a vertical fiber that I conducted between 2006 and 2011 (Duprat et al. 2007, Ruyer-Quil et al. 2008, Duprat et al. 2009b, Ruyer-Quil and Kalliadasis 2012). I present here my personal contribution to this problem along with a collaborative work with S. Kalliadasis (Imperial College, London).

The problem of the dynamics of a falling film don a fiber has attracted a considerable interest since the experiments by Kliakhandler et al. (2001) (see figure 4.1). Such a flow is interesting from a fundamental point of view for at least two reasons: (i) the beads sliding down the fiber stay axisymmetrical for a very large range of parameters and therefore the flow is truly two-dimensional, independent from the azimuthal coordinate ; (ii) the base flow (uniform film solution) is a parallel flow. As a consequence, a film down a fiber is a prototype of an open-flow system exhibiting an instability from a 2D parallel base flow, a situation that is very rarely achieved in experiments. Besides the instability is of long-wave nature and is observable even at very low Reynolds numbers for very viscous fluids such as castor oil or silicon oils. These features considerably simplify the analytical treatment of this problem.

Furthermore, as we shall see, this flow exhibits an easily tractable transition from an absolute instability to a convective one. This transition, which is not observed in a falling film on an inclined plane (Brevdo et al. 1999), is a result of the curvature of the fiber which promotes another instability mechanism besides the Kapitza one: *the Rayleigh-Plateau instability.*

A liquid layer coating uniformly a thin wire is known to be unstable under the action of surface tension. The mechanism of this instability was identified in the seminal work of Lord Rayleigh (1878). When the wire is horizontal, the deformation of the film thickness rapidly leads to rupture and to the formation of a regular array of standing droplets, whereas in the vertical case, the flow induced by the gravity can prevent the film rupture (Quéré 1990). Contrary to the Kapitza instability mode, the Rayleigh-Plateau is not promoted by the flow but has a capillary origin. As a result, the convection by the flow may then competes with the growth of the instability with the possible occurrence of both absolute and convective instabilities in that geometry. The occurrence of an absolute–convective transition has been verified experimentally by Duprat and Giorgiutti-Dauphiné based on theoretical predictions that are detailed below (Duprat et al. 2007).

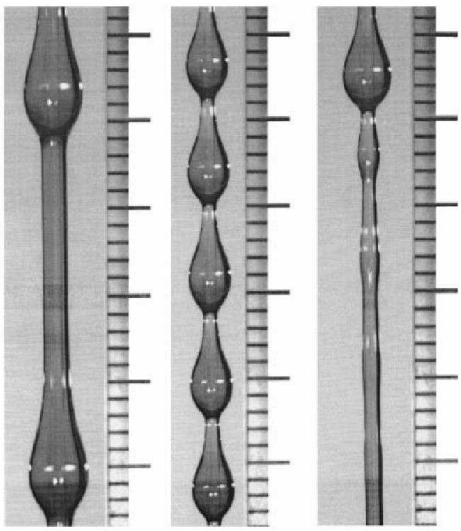

Figure 4.1 – *Experiments by Kliakhandler et al. (2001) with castor oil ($q = 21$ mg/s, $R = 0.25$ mm, $\nu = 44010^{-6}\,\mathrm{m^2 s^{-1}}$, $\rho = 961\,\mathrm{kgm^{-3}}$ and $\sigma = 3110^{-3}\,\mathrm{N^2 m^{-1}}$).*

In this chapter, I will first present the determination of the threshold of the transition form convective to absolute instabilities based on an inertialess approximation (§ 4.2). I then turn to the low-dimensional modeling of the film dynamics when inertia effects are included (§ 4.3). Finally, the competition of the Kapitza and Rayleigh-Plateau instability are discussed in § 4.4. The material presented here is taken from some (upublished) lecture notes and two published articles: Ruyer-Quil et al. (2008) and Ruyer-Quil and Kalliadasis (2012), one of which being appended to this chapter.

4.1 Geometry, governing equations and parameters

The geometry and notations of the annular falling film is described in figure 4.2. The fluid properties, viscosity μ, density ρ and surface tension

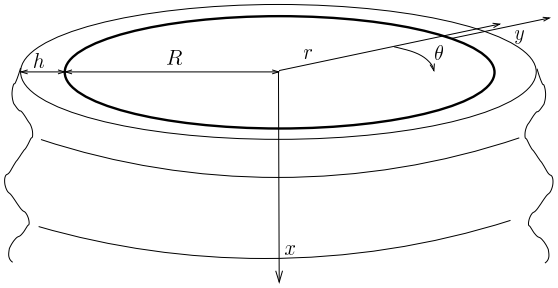

Figure 4.2 – *Geometry and notations.*

σ are all assumed to remain constant. Here x will denote the axial — or stream-wise— coordinate, r the radial coordinate and θ the azimuthal angle. The fiber radius is noted R whereas p_a is the atmospheric pressure.

In what follows a bar decoration is introduced in order to distinguish dimensional and dimensionless quantities unless the distinction is useless.

From simple physical considerations and without prior knowledge of the specific details of the system, the following scales can be readily identified: The fiber radius $\bar{R}$, the Nusselt thickness $\bar{h}_{\mathrm{N}}$ of the uniformly coated film, the length and time scales, $l_\nu = \nu^{2/3} g^{-1/3}$ and $t_\nu = \nu^{1/3} g^{-1/3}$, based

on gravity and viscosity (making explicit the balance between gravity and viscous forces giving rise to the Nusselt flat-film solution) and the capillary length $l_c = \sqrt{\sigma/(\rho g)}$.

4.1.1 Natural set of parameters

A first set of pertinent dimensionless groups arises from these scales. The aspect ratio

$$\tilde{\alpha} \equiv \bar{h}_{\mathrm{N}}/\bar{R} \tag{4.1a}$$

which assesses azimuthal curvature effects at the scale of the film, the Goucher number (Quéré 1999),

$$Go \equiv \bar{R}/l_c\,, \tag{4.1b}$$

that compares azimuthal and axial surface tension effects and the Kapitza number,

$$\Gamma \equiv \sigma/(\rho\nu^{4/3}g^{1/3}) = (l_c/l_\nu)^2\,, \tag{4.1c}$$

comparing surface tension and viscosity. Useful combinations of these parameters are $h_{\mathrm{N}} \equiv \bar{h}_{\mathrm{N}}/l_\nu$ and $\bar{h}_{\mathrm{N}}/l_c$. The former compares the film thickness to the gravity-viscous length scale and, indirectly, inertia and viscosity since the Nusselt base flow is the result of the balance of gravity and viscosity. The latter, $\bar{h}_{\mathrm{N}}/l_c$ is related to the Bond number $Bo = \rho g\bar{h}_{\mathrm{N}}^2/\sigma = (\bar{h}_{\mathrm{N}}/l_c)^2$ comparing surface tension and gravity at the scale of the film.

The advantage of the set of parameters $\tilde{\alpha}$, Go and Γ is that when the geometry and the working fluid are fixed, the Goucher and the Kapitza numbers Go and Γ are constant and the only free parameter is $\tilde{\alpha}$. From an experimental point of view, $\tilde{\alpha}$ can be varied independently by varying the inlet flow rate. The Kapitza number Γ is entirely defined by the fluid properties independently of the flow characteristics, whereas the Goucher number Go can be easily varied by replacing the fiber. Hence, the parameters $\tilde{\alpha}$, Go and Γ can therefore be viewed as 'natural' for the fiber problem.

Typical values of the the capillary length l_c, viscous-gravity length l_ν and Kapitza number are provided in table 4.1 showing the wide available range of Kapitza numbers for the typical fluids used in experiments.

4.1.2 Reduced parameters

We now adapt Shkadov's scaling (Shkadov 1977) and introduce different length scales for the streamwise (axial) and radial directions. The length scale in the radial direction is the Nusselt thickness $\bar{h}_{\mathrm{N}}$, whereas the length scale in the streamwise direction is chosen as $\kappa\bar{h}_{\mathrm{N}}$ defined by the balance of the streamwise pressure gradient induced by capillarity, $\propto \sigma\partial_{xxx}h$, and gravity acceleration, ρg, which gives $\kappa = [\sigma/(\rho g\bar{h}_{\mathrm{N}}^2)]^{1/3} = (l_c/\bar{h}_{\mathrm{N}})^{2/3}$. The time scale is defined with reference to the Nusselt solution of uniform thickness (a result of the balance of gravity and viscosity). The volumetric flow rate per unit length of circumference, $q_{\mathrm{N}} = R^{-1}\int_R^{R+h_{\mathrm{N}}} u\,r dr$, of a film of constant thickness $\bar{h}_{\mathrm{N}}$ is given by

$$\bar{q}_{\mathrm{N}} \equiv \frac{g\bar{h}_{\mathrm{N}}^3}{3\nu}\phi(\tilde{\alpha})\,, \tag{4.2}$$

	ν (mm^2s^{-1})	ρ (kgm^{-3})	σ (mNm^{-1})
water	1	998	72.5
silicon oil v50	50	963	20.8
castor oil	440	961	31
silicon oil v1000	1000	980	21.1
	l_c (mm)	l_ν (mm)	Γ
water	2.7	0.047	3376
silicon oil v50	1.5	0.63	5.48
castor oil	1.8	2.7	0.45
silicon oil v1000	1.5	4.7	0.10

Table 4.1 – *Fluid properties, capillary length l_c, gravity-viscous length l_ν and Kapitza number used in the present study. The data for silicon oil v50 and castor oil have been taken from Duprat et al. (2007), Kliakhandler et al. (2001). This table is taken from Ruyer-Quil and Kalliadasis (2012).*

where ϕ is a geometric factor defined by

$$\phi(\alpha) \equiv \frac{3\left(4(\alpha+1)^4\ln(\alpha+1) - \alpha(\alpha+2)(3\alpha(\alpha+2)+2)\right)}{16\alpha^3}. \tag{4.3}$$

which measures the deviation of the flow-rate-to-thickness relation from the cubic dependency corresponding to the planar geometry ($\phi(0) = 1$). Similarly to the streamwise length scale, the time scale is stretched by a factor κ and thus defined as $3\kappa\bar{h}_N^2/\bar{q}_N = \nu\kappa/[g\bar{h}_N\phi(\tilde{\alpha})]$.

Shkadov's scales introduce three new dimensionless groups besides the aspect ratio $\tilde{\alpha} = h_N/R$, a 'reduced Reynolds number',

$$\delta \equiv 3\bar{q}_N/(\nu\kappa) = (\tilde{\alpha}Go)^{11/3}\,\phi(\tilde{\alpha})\Gamma^{3/2}, \tag{4.4a}$$

which compares inertia and the viscous drag at the scale $\kappa\bar{h}_N$ introduced by the balance of gravity and capillarity, a streamwise 'viscous dispersion parameter',

$$\eta \equiv 1/\kappa^2 = (\bar{h}_N/l_c)^{4/3} = (\tilde{\alpha}Go)^{4/3}, \tag{4.4b}$$

and the dimensionless group,

$$\beta \equiv \tilde{\alpha}^2/\eta = \tilde{\alpha}^{2/3}Go^{-4/3}, \tag{4.4c}$$

which is a combination of $\tilde{\alpha}$ and η and compares azimuthal to axial surface tension effects. We have made explicit in (4.4) the relations of δ, η and β to the 'natural' parameters $\tilde{\alpha}$, Go and Γ. Finally, I recall the usual definition of the Reynolds number based on the flow rate, $Re = \bar{q}_N/\nu = h_N^3\phi(\tilde{\alpha})/3$ where again $h_N = \bar{h}_N/l_\nu$.

The advantage of Shkadov's scaling stems from (i) the direct reference to the Nusselt uniform film flow that simplifies the comparisons between solutions, with the Nusselt solution corresponding to constant values of the film thickness and flow rates $h = 1$ and $q = 1/3$; (ii) the association of a single parameter to each physical effect affecting the balance of the different forces: Inertia (δ), azimuthal surface tension (β), extensional "Trouton" viscosity or viscous dispersion (η) and geometry ($\tilde{\alpha}$).

4.1.3 Governing equations

Assuming axisymmetrical flows without any variation in the azimuthal θ-direction, the equations of motion are:

$$\begin{aligned}
\partial_t u_x + u_x\partial_x u_x + u_r\partial_r u_x &= -\frac{1}{\rho}\partial_x p + g + \nu\left[\partial_{rr} + \frac{1}{r}\partial_r + \partial_{xx}\right] u_x & (4.5a)\\
\partial_t u_r + u_x\partial_x u_r + u_r\partial_r u_r &= -\frac{1}{\rho}\partial_r p + \nu\left[\partial_{rr} + \frac{1}{r}\partial_r + \partial_{xx}\right] u_r \\
&\quad -\frac{\nu}{r^2}u_r\,, & (4.5b)\\
\partial_r u_r + \frac{u_r}{r} + \partial_x u_x &= 0\,. & (4.5c)
\end{aligned}$$

They are completed by the no-slip condition at the wall namely

$$u_r = u_x = 0\,, \quad \text{at} \quad r = R\,, \tag{4.5d}$$

the continuity of the stress at the free surface $r = R + h(x,t)$

$$\begin{aligned}
p - p_a &= \frac{2\mu}{1+(\partial_x h)^2}\left[-\partial_x h(\partial_r u_x + \partial_x u_r) + \partial_x u_x(\partial_x h)^2 + \partial_r u_r\right] \\
&\quad -\sigma\left[K_{\rm ax}(h) + K_{\rm az}(h)\right]\,, & (4.5e)\\
0 &= -(1-(\partial_x h)^2)(\partial_r u_x + \partial_x u_r) + 2\partial_x h(-\partial_r u_r + \partial_x u_x)\,, & (4.5f)
\end{aligned}$$

where

$$K_{\rm ax}(h) = \frac{\partial_{xx} h}{[1+(\partial_x h)^2]^{3/2}} \quad \text{and} \quad K_{\rm az}(h) = -\frac{1}{[1+(\partial_x h)^2]^{1/2}}\frac{1}{R+h} \tag{4.5g}$$

denote the axial and azimuthal curvatures, and the kinematic condition expressing the fact that the free surface is a material surface

$$\partial_t h + u_x\partial_x h - u_r = 0\,. \tag{4.5h}$$

4.2 Spatial stability analysis

This section presents my contribution to a published article (Duprat et al. 2007), along with some material from (unpublished) lecture notes that I have written at the occasion of a summer school organized during the summer 2007 at the Indian Statistical Institute in Calcutta.

4.2.1 No inertia models

Two assumptions greatly simplify the analysis of this instability: (i) inertial effects are negligible, (ii) the typical length of the free surface modulations are much longer than the film thickness. As we shall see, the latter, *long-wave*, assumption is supported by the fact that the instability onset occurs at a zero wavenumber.

In the no inertia limit, the basic axisymmetrical equations equations (4.5) simplify to

$$\begin{aligned}
-\partial_x p + \rho g + \mu\left[\partial_{rr} + \frac{1}{r}\partial_r + \partial_{xx}\right] u_x &= 0\,, & (4.6a)\\
-\partial_r p + \mu\left[\left(\partial_{rr} + \frac{1}{r}\partial_r + \partial_{xx}\right) u_r - \frac{u_r}{r^2}\right] &= 0\,, & (4.6b)
\end{aligned}$$

The continuity equation (4.5c) and the boundary conditions (4.5d)–(4.5h) remain unchanged. Integrating the continuity equation (4.5c) across the film, one obtains

$$\begin{aligned} 0 &= \int_R^{R+h} \left([\partial_r(ru_r)]/r + \partial_x u_x\right) r\, dr \\ &= (R+h)u_r\big|_{R+h} - Ru_r\big|_R + \partial_x \left[\int_R^{R+h} u_x r\, dr\right] - u_x\big|_h \partial_x h(R+h)\,, \end{aligned}$$

where evaluations at the wall $r = R$ or at the free surface $r = R + h(x,t)$ are denoted by $\cdot\big|_R$ and $\cdot\big|_h$ respectively. Making use of the no-slip condition (4.5d) and the kinematic condition (4.5h), we get

$$(R+h)\partial_t h + \partial_x \left[\int_R^{R+h} u_x r\, dr\right] = 0\,. \tag{4.7}$$

It is easy to recognize in (4.7) the mass conservation equation of the film.

Let us now make use of the long-wave assumption and introduce formal *film parameter* $\epsilon \sim |\nabla h|/h$. Stream-wise modulations are thus assumed to remain slow in space and time $\partial_{x,t} \sim \epsilon$. Integrating the continuity equation (4.5c) yields $u_r = -(\int_R^r \partial_x u_x \xi\, d\xi)/r$ so that the radial component of the velocity is formally of order ϵ. Therefore the radial momentum balance reads at first order $-\partial_r p = O(\epsilon)$. The pressure distribution is therefore uniform across the film, a usual assumption in lubrication theory, and therefore imposed by the Laplace law at the free surface (4.5e). The streamwise momentum equation then reads

$$\frac{\mu}{r}\partial_r(r\partial_r u_x) = -\rho g + \frac{d}{dx}\left(p\big|_h\right) + O(\epsilon^2)\,,$$

The no-slip condition at the wall (4.5d) and the continuity of the stress at the free surface (4.5f) yield $u_x|_R = 0$ and $\partial_r u_x|_h = O(\epsilon^2)$. After integration one then obtains

$$u_x = \frac{1}{\mu}\left[\rho g - \frac{d}{dx}\left(p\big|_h\right)\right]\left[\frac{1}{2}(R+h)^2 \ln\left(\frac{r}{R}\right) - \frac{1}{4}(r^2 - R^2)\right] + O(\epsilon^2)\,, \tag{4.8}$$

which gives the flow rate per unit length of the fiber perimeter

$$q \equiv \frac{1}{R}\int_R^{R+h} u_x r\, dr = \left[\rho g - \frac{d}{dx}\left(p\big|_h\right)\right]\frac{h^3\phi(h/R)}{3\mu} + O(\epsilon^2) \tag{4.9}$$

where ϕ, defined (4.3), measures the departure of the flow rate dependence to the film thickness from the planar case ($q = \frac{1}{3}h^3$). Viscous dissipation terms in the normal stress balance at the free surface (4.5f) are second order terms so that $p|_h = -\sigma[K_{\rm ax}(h) + K_{\rm az}(h)]$.

After substitution of (4.9) for the flow rate in the mass balance (4.7), a single evolution equation for the film thickness is finally obtained (Kliakhandler et al. 2001):

$$\partial_t\left(h + \frac{h^2}{2R}\right) + \partial_x\left\{\frac{h^3\phi(h/R)}{3\mu}\left[\rho g + \sigma\partial_x(K_{\rm ax}(h) + K_{\rm az}(h))\right]\right\} = O(\epsilon^2)\,, \tag{4.10}$$

Equation (4.10) is referred to as the Kliakhandler, Davis and Bankoff (KDB) equation. Craster and Matar derived an evolution equation analogous to (4.10) but retain only the main contributions to the axial and azimuthal curvatures, $K_{\mathrm{ax}} \approx \partial_{xx} h$ and $K_{\mathrm{az}} \approx (R+h)^{-1}$ (Craster and Matar 2006).

Equations can be made dimensionless with reference to a film of constant thickness h_{N} by setting $h = h_{\mathrm{N}}\tilde{h}$, $x = \kappa h_{\mathrm{N}}\tilde{x}$, and $t = T\tilde{t}$. The ratio κ of the length scales in the cross-stream and streamwise coordinates is adjusted such that the gravity acceleration ρg equilibrates the pressure gradient induced by the main contribution to the axial curvature gradient $\sigma\partial_{x^3} h$. Thus $\kappa = \left[\gamma/(\rho g h_{\mathrm{N}}^2)\right]^3 = (l_c/h_{\mathrm{N}})^{2/3}$ where $l_c = \sqrt{\sigma/(\rho g)}$ is the capillary length. The time scale $T = \kappa h_{\mathrm{N}}^2/(3q_{\mathrm{N}})$ is one third of the advection time where $q_{\mathrm{N}} = g h_{\mathrm{N}}^3 \phi(h_{\mathrm{N}}/R)/(3\nu)$ is the flow rate of a film of constant thickness h_{N}. Dropping the tildes, the Craster–Matar (CM) equation reads

$$\partial_t \left(h + \frac{\tilde{\alpha}}{2} h^2 \right) + \partial_x \left\{ \frac{h^3}{3} \frac{\phi(\tilde{\alpha} h)}{\phi(\tilde{\alpha})} \left[1 + \frac{\beta}{(1+\tilde{\alpha}h)^2} \partial_x h + \partial_{xxx} h \right] \right\} = 0\,, \quad (4.11)$$

with two dimensionless parameters: an aspect ratio $\tilde{\alpha} = h_{\mathrm{N}}/R$ of the film thickness to the fiber radius and a parameter $\beta = (\kappa h_{\mathrm{N}}/R)^2$ that expresses the relative importance of azimuthal and axial curvatures (Kalliadasis and Chang 1994).

In the limit of small aspect ratio h/R, i.e. $\tilde{\alpha} \to 0$, the KDB and the CM equations reduces to

$$\partial_t h + \partial_x \left[\frac{h^3}{3} \left(1 + \beta \partial_x h + \partial_{x^3} h \right) \right] = 0\,. \quad (4.12)$$

derived initially by Frenkel (1992). The Frenkel equation can also be obtained in another context: the Rayleigh-Taylor instability of a film flowing down an inverted plane (Lin and Kondic 2010). This equation must also be contrasted with (3.18) which governs a falling film flow in the presence of a long-wave thermocapillary instability (see chapter 3).

4.2.2 Analysis in the complex planes

A normal mode decomposition of infinitesimal perturbations around the uniform film $h = 1$ in the KDB or the CM equations leads to the same dispersion relation

$$k\, c_k(\tilde{\alpha}) - \omega + \frac{i k^2}{3(1+\tilde{\alpha})} \left(\frac{\beta}{(1+\tilde{\alpha})^2} - k^2 \right) = 0\,, \quad (4.13)$$

where

$$c_k = \frac{1}{1+\tilde{\alpha}} \left[1 + \frac{\tilde{\alpha}\phi'(\tilde{\alpha})}{3\phi(\tilde{\alpha})} \right] = \frac{8(b-1)\left(2\ln(b) b^2 - b^2 + 1\right)}{3\left(4\ln(b) b^4 - 3b^4 + 4b^2 - 1\right)}\,, \quad (4.14)$$

with $b = 1 + \tilde{\alpha}$, is the speed of the linear kinematic waves of (4.13) for $k \to 0$.

In the limit of small film thicknesses as compared to the fiber radius, the dispersion relation corresponding to the Frenkel equation reads

$$k - \omega + \frac{i k^2}{3} \left(\beta - k^2 \right) = 0\,, \quad (4.15)$$

Equation (4.15) can be recovered from (4.13) through the transformation $k \to k\,[c_k(1+\tilde{\alpha})]^{1/3}$, $\omega \to \omega c_k^{4/3}(1+\tilde{\alpha})^{1/3}$ and $\beta \to \beta\, c_k^{2/3}(1+\tilde{\alpha})^{8/3}$. Consequently, the linear stability analysis of the three KDB, CM and Frenkel equations reduces to a single problem.

Neutral stability ($k \in \mathbb{R}$ and $\omega \in \mathbb{R}$) is achieved when $\omega = k$ and $\beta - k^2 = 0$, i.e. for perturbations traveling at the speed of the kinematic waves at a wave length for which the stabilizing axial capillary pressure gradient $\propto k^4$ equilibrates the destabilizing azimuthal one $\propto \beta k^2$, which defines the cut-off wavenumber $k_c = \sqrt{\beta}$. The instability onset corresponds to $\beta = 0$ hence a uniform film is always unstable.

Let me recall the basics of the linear spatio-temporal analysis of an open flow (Huerre and Monkewitz 1990, Huerre and Rossi 1998). Writing formally

$$D(k,\omega) = 0 \tag{4.16}$$

the dispersion relation (4.15) which relates the wavenumber to the angular frequency ω of a given normal mode, the stability of the basic state is determined by the *temporal modes*, $\omega_j(k)$, defined as the zeroes of the dispersion relation for k real. In general, there is a countable number of temporal modes and the index j may take several integer values. Conversely, one can define *spatial modes*, $k_j(\omega)$ as the solutions to (4.16) for real angular frequencies ω. For complex wavenumber and complex angular frequencies, the concept of temporal and spatial modes can be extended with the introduction of *generalized* temporal $\omega_{j,F_k}(k)$ and spatial $k_{j,L_\omega}(\omega)$ modes defined by the integration paths L_ω and F_k in the ω and k-planes.

$$D(k_{j,L_\omega}(\omega),\omega) = 0\,, \quad \text{and} \quad \omega \in L_\omega\,, \tag{4.17a}$$

$$D(k,\omega_{j,F_k}(k)) = 0\,, \quad \text{and} \quad k \in F_k\,. \tag{4.17b}$$

The long-time response of the flow to a localized perturbations can be found using Briggs collision criterion. The process starts with a L_ω path in the complex ω-plane that lies above all temporal modes. This path defines generalized spatial modes in the complex k-plane. The integration path is then lowered until generalized spatial modes originating from different half planes of the k-space collide and pinch. The obtained *saddle* point gives the complex absolute angular frequency ω_0 which governs the long-time response of the flow. If the imaginary part $\omega_{0i} < 0$, then the flow is convective and behaves as a noise amplifier, otherwise the flow is absolute and admits a *global mode*.

The simplicity of (4.15) enables to illustrate all this. Dispersion relation (4.15) admits one temporal mode and four spatial modes (see figures 4.3a and 4.4d for $\beta = 2$). Following Briggs collision criterion, the generalized temporal and spatial modes have been searched for starting from an integration path in the complex ω-plane located above the maximum $\omega_{i,\max}$ of the temporal growth rate. The result of this process is displayed in figures 4.3 and 4.4 for $\beta = 2$.

The temporal mode is shown if figure 4.3a. The maximum growth rate is $\omega_{i,\max} = 0.331$ so that $L_{\omega,0}$ is chosen to lay at the level $\omega_i = 0.5$. A first non relevant pinching of two $k^+(\omega)$ modes is observed in figure 4.3d. The pinching of two $k^+(\omega)$ and $k^-(\omega)$ branches occur at $k_0 = \pm 1.12 + 0.29\mathrm{i}$ defining the absolute angular frequency $\omega_0 = \pm 1.05 + 0.17\mathrm{i}$ (figures 4.4a

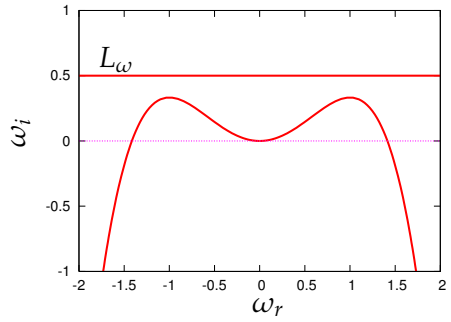

(a) $k_i = 0$

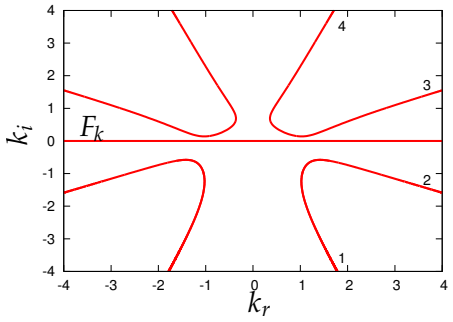

(b) $\omega_i = 0.5$

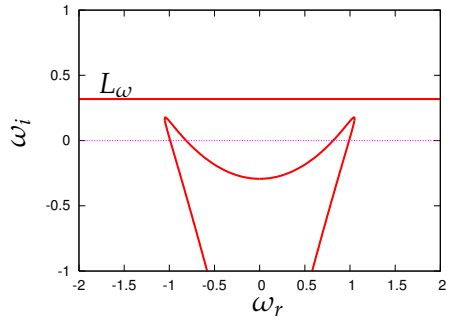

(c) $k_i = -0.25$

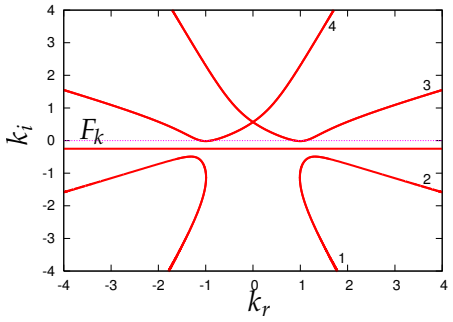

(d) $\omega_i = 0.3182$

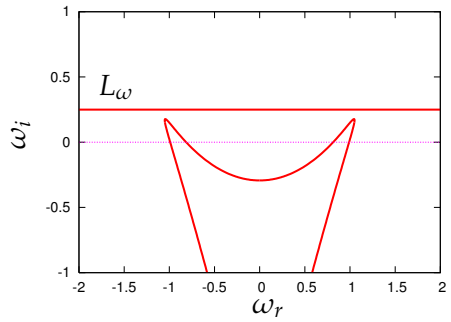

(e) $k_i = -0.25$

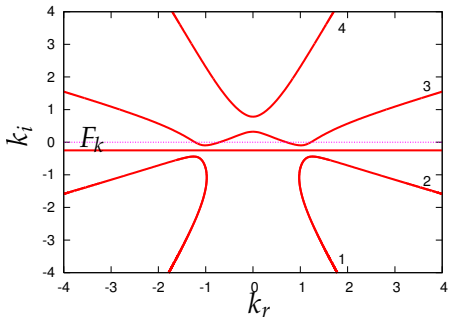

(f) $\omega_i = 0.5$

Figure 4.3 – *Generalized temporal and spatial modes solutions to the dispersion relation (4.15) with* $\beta = 2$.

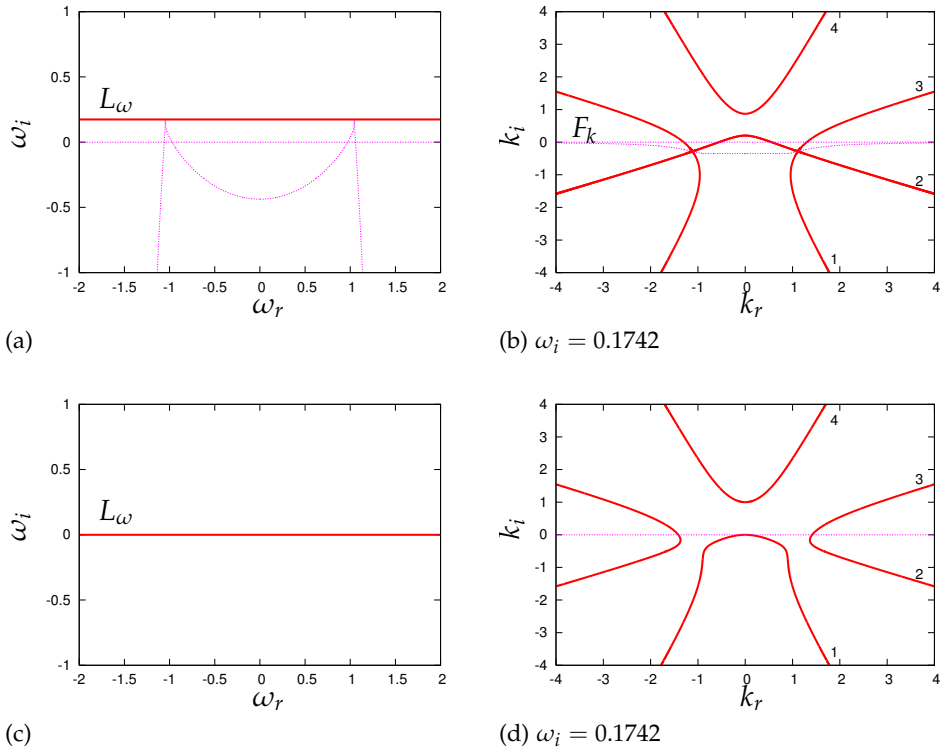

(a) (b) $\omega_i = 0.1742$

(c) (d) $\omega_i = 0.1742$

Figure 4.4 – *Generalized temporal and spatial modes solutions to the dispersion relation (4.15) with* $\beta = 2$.

and 4.4b). Since $\omega_{i,0} > 0$, the instability is absolute in that case. Notice that the extension to $k_r \pm \infty$ of F_k by the steepest descent path was possible in that case so that the corresponding generalized temporal mode present a very sharp drop in the ω-plane.

4.2.3 C/A transition

The nature of the linear response of open flows to inlet perturbations is determined by the convective or absolute nature of the instability. An important problem is therefore the determination of this nature and of possible transitions between absolutely unstable and convectively unstable situations. The transition from absolute to convective instabilities (C/A transition) corresponds to $\omega_{i,0} = 0$. A necessary condition is to show that

$$\omega \in \mathbb{R} \quad \text{verifying} \quad D(k,\omega) = 0 \quad \text{and} \quad \partial_k D(k,\omega) = 0 \tag{4.18}$$

admits solutions (Huerre and Monkewitz 1990). For simple relation dispersions, solving (4.18) can be done analytically.

Differentiating the dispersion relation (4.15) with respect to k gives

$$\frac{d\omega}{dk} = 1 + \frac{ik}{3}(2\beta - 4k^2) \tag{4.19}$$

Setting $d\omega/dk$ to zero and eliminating k from (4.19) and (4.15) yields a polynomial of degree three in $\xi = i\omega$

$$\frac{81}{256} + \frac{\beta^3}{192} + \left(\frac{9\beta}{16} + \frac{\beta^4}{144}\right)\xi + \frac{\beta^2}{16}\xi^2 + \xi^3 = 0$$

This polynomial can be reduced to the classical form $P(y) = y^3 + py + q = 0$ by the change of variables $\xi = y - \beta^2/18$, where

$$p = \frac{9\beta}{16} - \frac{\beta^4}{432} \quad \text{and} \quad q = \frac{81}{256} - \frac{5\beta^3}{192} - \frac{\beta^4}{23328}$$

The number of real roots depends on the sign of $4p^3 + 27q^2 = (\beta^3 + 243/8)^3$ which is always positive. One root is therefore real, λ_1 say, and the other two $\lambda_r \pm \mathrm{i}\lambda_i$ are complex conjugate. Since the sum of the roots is zero, $\lambda_r = -\lambda_1/2$. $P(\beta^2/18) > 0$ and then $\lambda_1 < \beta^2/18$ so that the corresponding value of ω, $\mathrm{i}(\beta^2/18 - \lambda_1)$, is an imaginary number. The other two roots give $\omega = \pm\lambda_i + \mathrm{i}(\lambda_1 + \beta^2/9)/2$. A sufficient and necessary condition for the existence of a real root ω solution to (4.19) and (4.15) is then $\lambda_1 = -\beta^2/9$ or equivalently

$$0 = P\left(-\frac{\beta^2}{9}\right) = \frac{81}{256} - \frac{17}{192}\beta^3 - \frac{1}{864}\beta^6$$

which admits only one positive root

$$\beta = \beta_{ca} \equiv \left[(9/4)\left(-17 + 7\sqrt{7}\right)\right]^{1/3} \approx 1.507 \tag{4.20}$$

When $\beta > \beta_{ca}$, $P(-\beta^2/9) < 0$, then $\lambda_1 > -\beta^2/9$ and the corresponding growth rate is positive. The instability is absolute when $\beta > \beta_{ca}$ and conversely convective for $\beta < \beta_{ca}$.

With $\beta = \tilde{\alpha}^{2/3}(l_c/R)^{4/3}$, where $\tilde{\alpha} = h_\mathrm{N}/R$, the inequality $\beta > \beta_{ca}$ reads

$$\tilde{\alpha} > \beta_{ca}^{3/2}\,(R/l_c)^2\ . \tag{4.21}$$

A localized disturbance may therefore invade the spatial domain whenever the Rayleigh-Plateau instability is stronger than the advection of the main flow, as reflected by the threshold β_{ca}. The threshold has been checked independently by Lin and Kondic (2010) whose numerical observations yields a value of the A/C threshold $\beta_{ca} \approx 1.51$.

It is quite remarkable that the threshold β_{ca} of the C/A transition from a convective to an absolute instability (C/A transition) is close to the value $\beta_c \approx 1.413$ above which a catastrophic growth of the speed and amplitude of the nonlinear solitary-wave solutions to (4.12) occurs as shown by Kalliadasis and Chang (1994).

The threshold above which the instability governed by the dispersion relation (4.13) becomes absolute can be readily obtained from the analysis of (4.15). The C/A transition then occurs at

$$\frac{\tilde{\alpha}}{c_k(\tilde{\alpha})(1+\tilde{\alpha})^4} > \beta_{ca}^{3/2}\left(\frac{R}{l_c}\right)^2. \tag{4.22}$$

The C/A boundaries (4.21) and (4.22) are compared to the experimental observations by Duprat and Giorgiutti-Dauphiné in figure 4.5. Primary sinusoidal wavetrains of constant frequencies and healing lengths are reported as crosses. Wavetrains displaying significant fluctuations of the frequency or the healing length are indicated by dots. The limit of small film thicknesses compared to the fiber radius, $\tilde{\alpha} \to 0$, corresponds to the

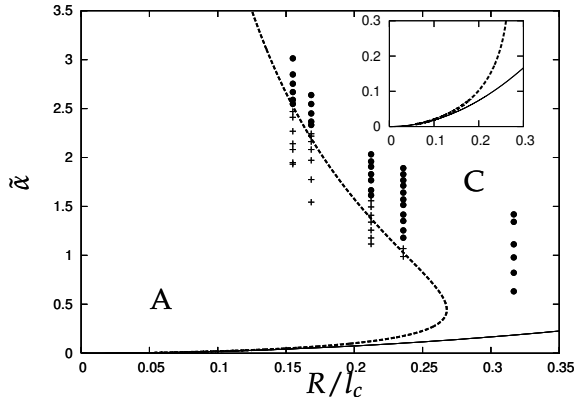

Figure 4.5 – *Absolute (AI) and convective (CI) instability regions in the parameter plane* $\tilde{\alpha} = h_N/R$ *versus* R/l_c. *Dashed and thin solid lines correspond to Eqs. (4.22) and (4.21), respectively. Regular and irregular primary wavetrains reported in the experiment by Duprat and Giorgiutti-Dauphiné are indicated by crosses and dots respectively. The insert is a blow-up of the diagram for small values of* $\tilde{\alpha}$.

case of a film flowing down a vertical wall for which the instability is always convective (Brevdo et al. 1999). In the case of thick films, i.e. $\tilde{\alpha}$ large, the Rayleigh-Plateau instability is weakened by the decrease of the free-surface azimuthal curvature, $1/(R + h_N)$. This effect is not compensated by the lower speed of the kinematic waves relative to the mean flow as $\tilde{\alpha}$ increases, and the instability is again convective. As a consequence, at a given value of the radius R, there exists an intermediate range of $\tilde{\alpha}$ values for which the Rayleigh-Plateau mechanism dominates over the advection of the waves, the instability being therefore absolute. On the other hand, the instability is always convective for fibers of larger radii, i.e. $R > 0.28 l_c$. For highly viscous liquids, such as silicon oils, the locus of the C/A transition (thick line labeled 1 in figure 4.5) is close to the zero-inertia limit (4.22).

It is possible to interpret the onset of transition from convective to absolute instabilities through the definition of the advection time τ_a of an interfacial structure over its length and the definition of a typical time of growth of the structure τ_g as the inverse of the maximum temporal growth rate.

Based on (4.15) the ratio τ_a/τ_g reads:

$$\tau_a/\tau_g = \omega_i/\omega_r|_{k=\sqrt{\beta/2}} = \frac{\beta^2}{12}\sqrt{\frac{2}{\beta}} = \frac{\sqrt{2}}{12}\beta^{3/2} \tag{4.23}$$

the maximum temporal growth rate being obtained at $k_{\max} = \sqrt{\beta/2}$ (see Ruyer-Quil et al. (2008) for details). Therefore, β compares τ_a to τ_g. For, $\beta < \beta_c$, the instability growth is slower and thwarted than the advection by the flow. The same mechanism is also in play in the saturation of the drops though it is then strongly nonlinear. For these reasons, we refer to β as a *saturation number*, a term that was first coined by Duprat et al. (2009a).

From the CM equation (4.11), we get

$$\tau_a/\tau_g = \omega_i/\omega_r|_{k=k_{RP}/\sqrt{2}} = \frac{\beta^2}{12(1+\tilde{\alpha})^5}\frac{\sqrt{2}(1+\tilde{\alpha})}{c_k\sqrt{\beta}} = \frac{\sqrt{2}}{12}(\beta^\star)^{3/2} \tag{4.24}$$

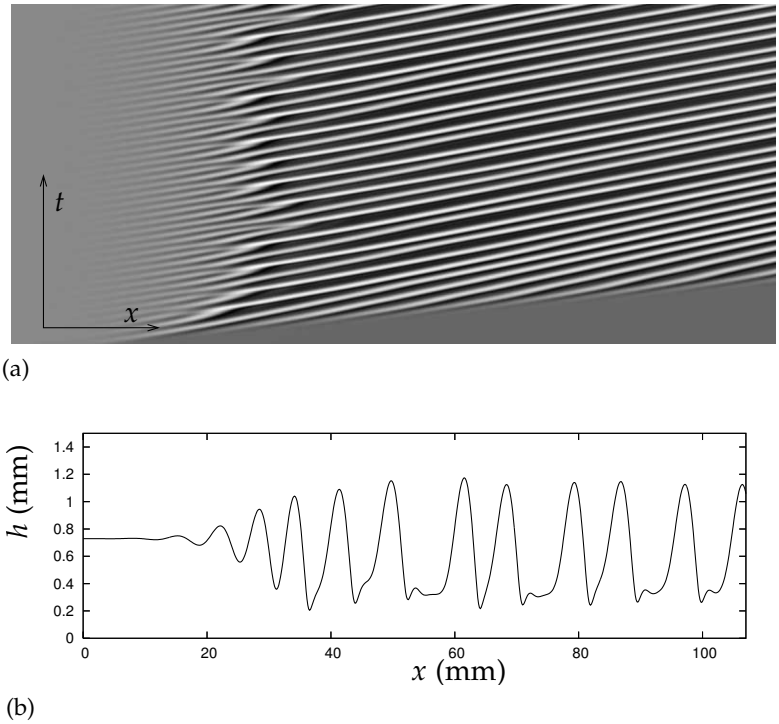

Figure 4.6 – *Simulation of the film dynamics corresponding to an experiment by Kliakhandler et al. (2001) with castor oil ($q = 21$ mg/s, $R = 0.25$ mm, $\nu = 44010^{-6}\,\mathrm{m^2 s^{-1}}$, $\rho = 961\,\mathrm{kgm^{-3}}$ and $\sigma = 3110^{-3}\,\mathrm{N^2 m^{-1}}$). Parameters are $\tilde{\alpha} = 2.92$, $\beta = 28.7$. (a) space-time diagram; (b) film thickness at the end of the simulation.*

where $k_{\mathrm{RP}} \equiv \sqrt{\beta}/(1+\tilde{\alpha})$ corresponds to the marginal stability condition and the composite parameter $\beta^\star$ is defined as (Duprat et al. 2007, Ruyer-Quil et al. 2008):

$$\beta^\star = \beta c_k^{-2/3}(1+\tilde{\alpha})^{-8/3}\,. \tag{4.25}$$

To conclude this section, it may be useful to stress that a linear stability analysis may not be sufficient to account for the development of global modes that follows an absolute instability [see for instance Chomaz (2005)]. As an example, I present in figure 4.6a the simulation of an experiment by Kliakhandler et al. (2001) based on the nonlinear KDB equation (4.11). The wavepacket initially created by a small hydraulic jump rapidly invade the whole numerical domain. However, only the waves close to inlet have a frequency in agreement with the linear analysis as a secondary instability rapidly destabilizes the flow by period doubling so that the global mode that sets in has a lower frequency.

4.3 Low-dimensional modeling

In this section, I sketch the derivation of a weighted-residual boundary-layer low-dimensional model made of two evolution equations for the film thickness h and the local flow rate q. The derivation and study of this model have been presented in a published article appended to this chapter (Ruyer-Quil et al. 2008).

4.3.1 Boundary layer approximation

Assuming slow space and time modulations of the flow allows to introduce the film parameter ϵ and to perform a 'gradient expansion' of the governing equations (4.5) in ϵ. The smallness of ϵ means that the ratio between the film thickness and the characteristic length-scale of the free-surface modulations is assumed to be small which then implies a separation of scales between x and r which in turn dictates a different treatment of the streamwise and cross-stream momentum equations as in boundary-layer theory in aerodynamics.

The formulation of the boundary-layer equations starts by determining the order of magnitude of the inertia terms in the left-hand side of the cross-stream momentum equation (4.5b). The continuity equation (4.5c) indicates that the radial component of the velocity is formally of $O(\epsilon)$. As a consequence the inertia terms in the left-hand side of the cross-stream momentum equation (4.5b) are of $O(\epsilon^2)$. Neglecting these terms, utilizing the relation obtained by differentiating the continuity equation (4.5c) once with respect to r,

$$\partial_{rr}u_r + \frac{1}{r}\partial_r u_r - \frac{u_r}{r^2} = -\partial_{xr}u_x \,,$$

and dropping the stream-wise viscous term $\partial_{xx}u_r = O(\epsilon^3)$, yields the simplified cross-stream momentum equation, $\partial_r p = -\partial_{xr}u_x$, which can be integrated once with respect to r to give:

$$p = p\big|_h + \mu\left(-\partial_x u_x + \partial_x u_x\big|_h\right) \,, \tag{4.26}$$

where terms of $O(\epsilon^2)$ have been neglected.

The first term $p\big|_h$ in the approximation for the pressure in (4.26) must be evaluated from the normal stress balance in (4.5e) that gives the pressure drop across the free surface. The contribution of the streamwise curvature due to surface tension must be kept in our formulation as it is well known from the planar case that this is the principal physical effect that prevents the waves from breaking. However, this term is formally of $O(\epsilon^2)$ and should be neglected. One thus obtains:

$$p = p_a + \mu\left(-\partial_x u_x + \partial_x u_x\big|_h + 2\partial_r u_r\big|_h\right) - \sigma\left[\partial_{xx}h + \tilde{K}_{\rm az}\right] \,, \tag{4.27}$$

where terms of $O(\epsilon^2)$ are neglected, and where

$$\tilde{K}_{\rm az} = -\frac{1}{R+h}\left(1 - \frac{1}{2}(\partial_x h)^2\right) \tag{4.28}$$

is the approximation of the azimuthal curvature of the free surface.

Substituting now (4.27) into the stream-wise momentum equation (4.5a) then leads to $O(\epsilon^2)$,

$$\begin{aligned}\rho\left(\partial_t u_x + u_x\partial_x u_x + u_r\partial_r u_x\right) &= g + \mu\left[\partial_{rr} + \frac{1}{r}\partial_r + 2\partial_{xx}\right]u_x \\ -\mu\partial_x\left[\partial_x u_x\big|_h + 2\partial_r u_r\big|_h\right] &+ \sigma\left\{\partial_{xxx}h + \partial_x\tilde{K}_{\rm az}\right\} \,,\end{aligned} \tag{4.29a}$$

where terms of $O(\epsilon^3)$ and higher have been neglected. (4.29a) is completed by the no-slip boundary condition (4.5d), the kinematic condition (4.5h) and the continuity of tangential stress at the interface truncated at $O(\epsilon^2)$

$$\partial_r u_x\big|_h = 2\partial_x h \left(\partial_x u_x\big|_h - \partial_r u_r\big|_h\right) - \partial_x u_r\big|_h \,. \tag{4.29b}$$

The system of equations (4.29) is consistent ar $O(\epsilon^2)$ and will be referred to as the *second-order boundary-layer equations* because of its similitude with the Prandtl equations in boundary-layer theory (Schlichting 1979).

4.3.2 Averaging

This section details the derivation of a two-equation model based on the weighted residual method introduced in § 1.2 and § 2.3.2.

Let us first consider the case of the Nusselt uniform layer: assuming no modulations of the free surface, $\partial_x = \partial_t = 0$, the basic Nusselt flow satisfies

$$\nu\mathcal{L}(u_x) = -g \qquad \text{with} \qquad u_x\big|_R = 0, \quad \partial_r u_x\big|_h = 0 \,, \tag{4.30}$$

where $\mathcal{L}$ denotes the (friction) linear differential operator, $\mathcal{L} \equiv \partial_{rr} + r^{-1}\partial_r$. The solution of (4.30) is simply

$$u_x = \frac{g}{\nu}\left[\frac{1}{2}(R+h)^2 \ln\left(\frac{r}{R}\right) - \frac{1}{4}(r^2 - R^2)\right] \equiv u_{x,0} \,, \tag{4.31}$$

which is also the inertia-less velocity profile obtained in (4.8).

I consider small departures of the streamwise velocity component u_x from the Nusselt uniform film solution (4.31) induced by the deformation of the free surface. Let us thus introduce the ansatz:

$$u_x = \frac{3q}{h^3\phi(h/R)} u_{x,0}(r; h(x,t)) + u_{x,1} \tag{4.32}$$

where $u_{x,1}$ stand for the $O(\epsilon)$ corrections to the velocity profile induced by the wavy interface. $\phi(h/R)$ is the geometric factor introduced in (4.3). The choice of the ansatz (4.32) stems form the fact that the mass balance (4.7) is *exact*. As a consequence, the film thickness (or more precisely $Rh + h^2/2$ which corresponds to the mass of fluid contained between two annular sections at coordinate x and $x + dx$) is naturally the first degree of freedom form the problem at hand, the mass balance (4.7) being an evolution equation for h. The second degree of freedom is the associated flux $q = \int_R^{R+h} u_x r dr$ (which can also be identified with the momentum of the mass of liquid in between the two sections separated by the distance dx).

The decomposition (4.32) is made unique after introducing a gauge condition which requires that the variable q truly stands for the local flow rate which reads

$$\int_R^{R+h} u_{x,1} r \, dr = 0 \,. \tag{4.33}$$

An evolution equation for q is necessary to obtain a closed system, or two-equation model mimicking the dynamics of the film. This evolution

equation will be provided by integrating the momentum balance (4.29a). Two remarks must be stated before proceeding: First, note that the Nusselt uniform film solution is retrieved when $q = (g/\nu)h^3\phi(h/R)/3$ and the Poiseuille velocity distribution in a film down an inclined plane is recovered in the limit $R \to \infty$ as $\lim_{R\to\infty} u_{x,0} = h(r-R) - (r-R)^2/2$.

Second, h and q can readily be identified with modes of zero-wavenumber perturbations to the Nusselt steady state. A uniform movement of the free surface from h to $h + \delta h$ is a first *kinematic mode*. A perturbation of the body force, or *dynamic mode*, from g to $g + \delta g$ leads back to the Nusselt solution (4.31) with $\delta q = (\delta g/\nu)h^3\phi(h/R)/3$ being proportional to the perturbation of the body force. A third mode can be thought of: it is the one that is triggered by a perturbation of the the tangential stress. However, this mode will be disregarded because of the passive gas approximation: the shear exerted by the gas on the film is neglected. However, in some applications it must be accounted for (Gruenig and Kraume 2009).

Monomials and powers of r and $\ln(r)$ constitute a closed set of functions with respect to differentiations, products and integrations involved in the momentum balance. Substituting (4.32) into (4.29a), where u_r is given by

$$u_r = -\frac{1}{r}\int_R^r \partial_x u_x(x,\zeta,t)\zeta\, d\zeta\,, \tag{4.34}$$

leads to an equation to be solved to obtain $u_{x,1}$. As a consequence the correction $u_{x,1}$ is necessarily a polynomial in r and $\ln(r)$ of the form

$$u_{x,1} = \sum_{m=1}^{m_{\max}}\sum_{n=0}^{n_{\max}} a_{m,n}(x,t)g_{m,n}(r)\,, \quad \text{with} \quad g_{m,n} \equiv [(r-R)^m]\,[\ln(r/R)]^n\,. \tag{4.35}$$

$u_{x,1}$ can thus be determined by identification. Multiplying the momentum balance ((4.29a) by r^2 gives a polynomial in r and $\ln r$, say $\mathcal{P}(r,\ln(r))$ that is uniformly equal to zero. Canceling all its monomials in r and $\ln(r)$ thus yields a number of independent relations equal to the number of unknowns $a_{m,n}$ if $m_{\max}$ and $n_{\max}$ are chosen sufficiently large. The gauge condition (4.33) then provides a compatibility condition which can be recast as an evolution equation for q, or equivalently, an averaged momentum balance which formally reads

$$\begin{aligned}
\partial_t q \;=\; & -F(h/R)\,\frac{q}{h}\partial_x q + G(h/R)\,\frac{q^2}{h^2}\partial_x h \\
& + I(h/R)\left[gh - \frac{3\nu}{\phi(h/R)}\frac{q}{h^2} + \frac{\sigma}{\rho}h\left\{\partial_{xxx}h + \partial_x \tilde{K}_{\mathrm{az}}\right\}\right] \\
& + \nu\left[J(h/R)\frac{q}{h^2}(\partial_x h)^2 - K(h/R)\frac{\partial_x q\partial_x h}{h} - L(h/R)\frac{q}{h}\partial_{xx}h\right. \\
& \left. + M(h/R)\partial_{xx}q\right] + \mathcal{K}(h,q,R)\,.
\end{aligned} \tag{4.36}$$

First order inertial terms are gathered in the first row of (4.36). The second row contains the gravity acceleration, the wall friction and the gradient of capillary pressure. The second-order elongational viscosity terms, or Trouton viscosity terms are found. These terms are referred here as the

viscous dispersion terms because of their role in the dispersion of the linear waves. $\mathcal{K}(h,q,R)$ stand for the second-order terms arising from the deviations $u_{x,1}$ from the Nusselt velocity profile.

In practice the determination of $u_{x,1}$ (and thus of $\mathcal{K}$) is a hardly tractable task requiring tedious algebra. Although the inclusion of the inertial terms $\mathcal{K}$ ensures that (4.9, 4.36) is consistent at $O(\epsilon^2)$, the nonlinearities involved in $\mathcal{K}$ may drastically restrict the range of parameters for which solutions to (4.9, 4.36) exist and can be favorably compared to experimental data. Indeed, in the planar case (cf. § 2.3.2), a 'regularization' procedure was necessary to avoid the presence of non-physical blow-ups of the time-dependent solutions due to second-order inertial terms even at moderate Reynolds numbers (Scheid et al. 2006). In fact, in the planar case dropping out the second-order inertial corrections leads to a simplified formulation which satisfactorily captures all physical mechanisms (Ruyer-Quil and Manneville 2000). For these reasons and to reduce the complexity of our second-order model, it is preferable to neglect second-order inertial effects and set $\mathcal{K}=0$.

Since it is advisable to disregard the second-order terms arising from $u_{x,1}$, one can think of the weighted residual technique as a useful shortcut for the derivation of (4.36). Let us introduce the inner product $\langle\cdot|\cdot\rangle = \int_R^{R+h} \cdot\cdot\, r\, dr$. Such a choice is suggested by the definition of q and the gauge condition (4.33) which then reads $\langle u_{x,1}|1\rangle = 0$. Weighted residuals are constructed by choosing weight functions $w_{m,n}(r)$ and averaging the momentum balance across the fluid layer, i.e. $\mathcal{R}_{m,n} = \langle w_{m,n}|\mathcal{P}\rangle$. Setting the residuals $\mathcal{R}_{m,n}$ equal to zero thus yields a system to be solved for the amplitudes $a_{m,n}$. Let me show that the choice of only one weight function, say w, is sufficient to yield (4.36).

Dropping out second-order inertial terms in $\mathcal{P}$, the only term where $u_{x,1}$ is involved in the residual $\mathcal{R} = \langle w|\mathcal{P}\rangle$ arises from the evaluation of the friction terms

$$\langle \mathcal{L}(u_{x,1})|w\rangle = \left[r\left(w\partial_r u_{x,1} - u_{x,1}w'\right)\right]_R^{R+h} + \langle u_{x,1}|\mathcal{L}(w)\rangle \tag{4.37}$$

$u_{x,1}$ verifies $u_{x,1}|_R = 0$ and $\partial_r u_{x,1}|_{R+h} = 0$. Demanding that w fulfills the same boundary conditions, i.e. $w(r=R)=0$ and $w'(r=R+h)=0$, one gets

$$\langle \mathcal{L}(u_{x,1})|w\rangle = \langle u_{x,1}|\mathcal{L}(w)\rangle \tag{4.38}$$

which shows that the operator $\mathcal{L}$ is self-adjoint. On can then make use of the gauge condition $\langle u_{x,1}|1\rangle = 0$ to cancel out the friction terms involving $u_{x,1}$ by demanding that w satisfies

$$\mathcal{L}(w) = A \qquad \text{with} \qquad w(R)=0\,, \quad w'(R+h)=0\,, \tag{4.39}$$

where A is a constant, so that the integral $\int_R^{R+h} u_x\, \mathcal{L}(w)\, rdr$ is proportional to the flow rate q. The system (4.39) is similar to (4.30) when $A=-1$, which reflects the fact that the operator $\mathcal{L}$ is self-adjoint with respect to the chosen inner product. Consequently, $w \equiv u_0$ which corresponds precisely to the Galerkin method (as for the planar case, see Ruyer-Quil and Manneville (2000)).

The expressions of the coefficients F to M are provided in the Appendix A of Ruyer-Quil and Kalliadasis (2012) (Note that a misprint error can be found in Appendix B of Ruyer-Quil et al. (2008)).

4.4 Wavy regimes

In that section we will consider the different wavy regimes that can be expected on the film and generated by the competition between the Kapitza and Rayleigh instability and the viscous dispersion of the waves. These findings are detailed in Ruyer-Quil and Kalliadasis (2012).

Les me now introduce the Shkadov's scaling Using the transformation $\mathcal{T} : [x \mapsto \kappa\bar{h}_{\rm N}x,\ (y,h) \mapsto (\bar{h}_{\rm N}y, \bar{h}_{\rm N}h),\ t \mapsto t\kappa\bar{h}_{\rm N}/(3\bar{q}_{\rm N}),,\ q \mapsto (3\bar{q}_{\rm N})q]$, the mass conservation equation (4.9) and the averaged momentum balance (4.36) read:

$$\partial_t h = -\frac{1}{1+\tilde{\alpha}h}\partial_x q\,, \tag{4.40a}$$

$$\begin{aligned}\delta\partial_t q = \delta\left[-F(\tilde{\alpha}h)\,\frac{q}{h}\partial_x q + G(\tilde{\alpha}h)\,\frac{q^2}{h^2}\partial_x h\right] + \frac{I(\tilde{\alpha}h)}{\phi(\tilde{\alpha})}\left[-\frac{3\phi(\tilde{\alpha})}{\phi(\tilde{\alpha}h)}\frac{q}{h^2}\right.\\ \left.+h\left\{1+\partial_{xxx}h+\frac{\beta}{(1+\tilde{\alpha}h)^2}\partial_x h-\frac{1}{2}\partial_x\left(\frac{\tilde{\alpha}}{1+\tilde{\alpha}h}(\partial_x h)^2\right)\right\}\right]\\ +\eta\left[J(\tilde{\alpha}h)\frac{q}{h^2}(\partial_x h)^2 - K(\tilde{\alpha}h)\frac{\partial_x q\partial_x h}{h} - L(\tilde{\alpha}h)\frac{q}{h}\partial_{xx}h + M(\tilde{\alpha}h)\partial_{xx}q\right],\end{aligned} \tag{4.40b}$$

Note that the viscous dispersion parameter η appears along with streamwise dissipative terms which contribute to the dispersion of the waves.

Contrary to the model obtained by Trifonov (1992) – see also Sisoev et al. (2006) – and to the model by Novbari and Oron (2009), (4.40) is consistent up to $O(\epsilon)$ for the inertia terms and up to $O(\epsilon^2)$ for the remaining contributions (and accounts for viscous dispersion). Indeed, both Trifonov's and Novbari and Oron's approaches assume a self-similar velocity distribution and do not account for the deviations of the velocity profile induced by the free-surface deformations. For this reason, their two-equation formulations lack consistency even at first order in the film parameter. Furthermore, the energy-integral approach employed by Novbari and Oron (2009) is not consistent with the kinetic energy balance of the flow. Indeed, writing formally the axial momentum equation as $\mathcal{M}(u_x) = 0$, Novbari and Oron's averaged momentum equation reads $\int_R^{R+h}\mathcal{M}(u_x)u_x\,dr = 0$ whereas the kinetic energy balance of a section of the liquid corresponds to $\int_R^{R+h}\mathcal{M}(u)u\,d(r^2) = 0$. Truncating then $\mathcal{M}(u)$ at $O(\epsilon^2)$ is tantamount to the Galerkin approach that can be used to reduce the algebra leading to (4.40b) (Ruyer-Quil et al. 2008). Noteworthy is that the two-equation model (4.40) is not limited to small aspect ratios unlike, e.g. the model by Roberts and Li (2006).

4.4.1 Validation

Model (4.40) has been validated in Ruyer-Quil et al. (2008), Duprat et al. (2009a) through direct comparisons to the experiments in Kliakhandler et al. (2001), Duprat et al. (2007; 2009a) [for both very viscous and less viscous liquids (castor oil and silicon oil) and a wide range of the parameters ($0.15 \leq Go \leq 1$, $0.5 \leq \tilde{\alpha} \leq 4.5$ and $0.05 \leq \delta \leq 4$)].

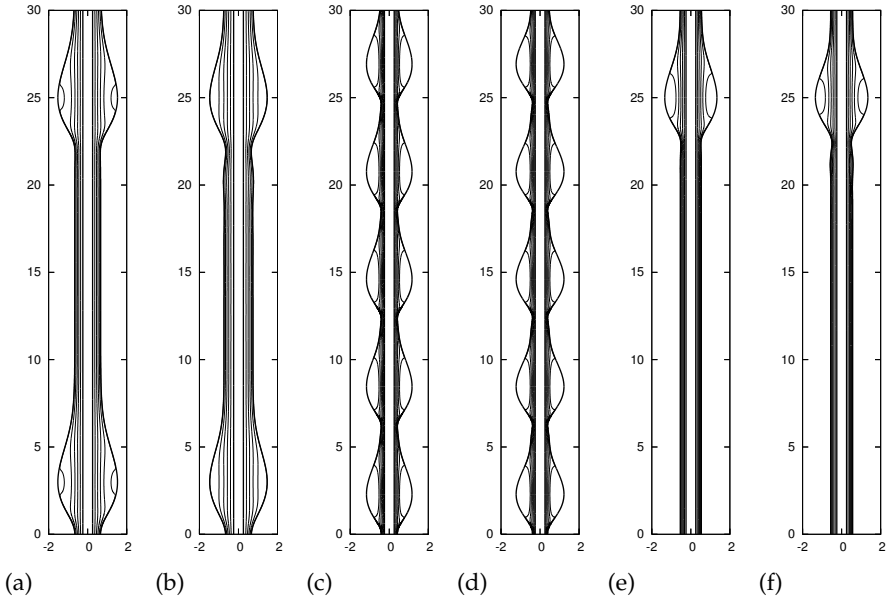

Figure 4.7 – *Profiles and streamlines in the moving frame of the TW solutions of model (4.40) (panels (a), (c) and (e)) and of the CM equation (4.11) (panels (b), (d) and (f)). (a-b), (c-d) and (e-f) correspond to the regimes 'a', 'b' and 'c' reported by Kliakhandler et al. (2001). (Compare with figure 4.1). Distances are given in dimensional units (mm). After Ruyer-Quil et al. (2008).*

The characteristics of the traveling-wave solutions of(4.40) are compared to the solutions to the CM equation in table 4.2 for the three regimes reported by Kliakhandler et al. (2001) and illustrated in figure 4.1.

At high flow rate corresponding to regime 'a' , these authors, they observed long and isolated waves moving rapidly and irregularly on a relatively thick substrate. At lower flow rate (termed regime 'b' by these authors), the wave pattern is highly organized with drops of smaller size moving at constant speed and periodicity. At even lower flow rate (regime 'c'), the regularity of the wave pattern is again lost with larger waves separated by long and irregular substrates. Comparisons of the results from the CM equation and model (4.40) show an excellent agreement.

Table 4.2 presents a comparison of the wave characteristics (ampli-

Model	q_N (mg/s)	λ (mm)	c_{expt} (mm/s)	c (mm/s)	h_{max}^{expt} (mm)	h_{max} (mm)	h_{min}^{expt} (mm)	h_{min} (mm)
(4.40)	21	30	25	22.4	1.47	1.34	0.50	0.44
(4.11)				24.7		1.26		0.45
(4.40)	11	6.2	5.4	7.22	1.02	0.92	0.20	0.17
(4.11)				6.98		0.97		0.14
(4.40)	5.3	36	12.0	12.1	1.20	1.09	0.25	0.26
(4.11)				12.6		1.10		0.25

Table 4.2 – *Comparisons of the characteristics of TW solutions at a given wavelength λ with the experimental values reported by Kliakhandler et al. (2001). From Ruyer-Quil et al. (2008).*

fluid	R (mm)	f_{for} (Hz)	h_N (mm)	h_s (mm)		h_{max} (mm)	
			exp	exp	num	exp	num
			± 0.01	± 0.05		± 0.05	
v100	0.2	9	0.84	0.414	0.410	1.12	1.21
–	–	8	–	0.42	0.435	1.16	1.27
–	–	6	–	0.47	0.49	1.28	1.40
–	–	sol	sol	0.54	0.54	**1.54**	**1.54**
v50	0.475	7	0.62	0.4	0.41	0.925	0.91
–	–	–	0.76	0.54	0.51	1.325	1.30
–	–	–	0.86	0.61	0.56	1.7	1.64
v50	1.5	10	0.87	0.66	0.63	1.17	1.18
–	–	4	0.87	0.7	0.69	1.7	1.68
–	–	sol	sol	0.95	0.78	**2.66**	**2.66**

Table 4.3 – *Comparisons of the experimental measurements of the substrate thickness h_s, maximum thickness h_{max} to the data obtained by integration of the model (4.40. In the case of the two solitary waves labeled 'sol', the numerical solution has been selected by adjusting the maximum height (boldface in the table). After (Duprat et al. 2009b).*

tude and speed) obtained from the models with the experimental data by Duprat et al. (2009b). Fluid are less viscous silicon oils than the castor oil employed by Kliakhandler et al. (2001) (cf. table 4.1). The Reynolds number is thus non-negligible. Again, an excellent agremment between experimental data and the solutions of model (4.40) is evidenced.

Experimental studies Kliakhandler et al. (2001), Craster and Matar (2006), Duprat et al. (2007; 2009a) reported the formation of axisymmetrical traveling waves (TWs) propagating without deformations and at constant speed over long distances. Solitary waves, that is, TWs separated by constant-thickness layers of fluid, or substrates, much longer than the characteristic length of the waves, were commonly observed sufficiently far downstream. Theoretically, solitary waves can be viewed as periodic TWs with an infinitely long wavelength. It is possible to distinguish three different regimes by examining the properties of the solitary-wave solutions.

Drop-like regime

This regime is observed on thin fibers for which the Rayleigh-Plateau (RP) instability is dominant, i.e. at small Goucher numbers ($Go \ll 1$), of more exactly when the saturation number $\beta^\star$ is large. In that case, the RP instability mechanism predominates over the advection by the flow.

The drop-like regime is characterized by the presence of very large bead-like nearly front-to-back symmetrical structures separated by regions of very thin films. Large recirculation regions can be found in the cores of these waves (see for instance figure 4.7) which contain and transport most of the fluid. These structures thus resemble axisymmetrical drops sliding down a coated fiber. The instability being promoted by the curvature if the fiber and the velocity of the beads resulting from the balance of viscosity and gravity acceleration, it is advisable to adopt then a scaling based on the radius $\bar{R}$ of the fiber, which gives the time scale $\nu/(g\bar{R})$. This scaling

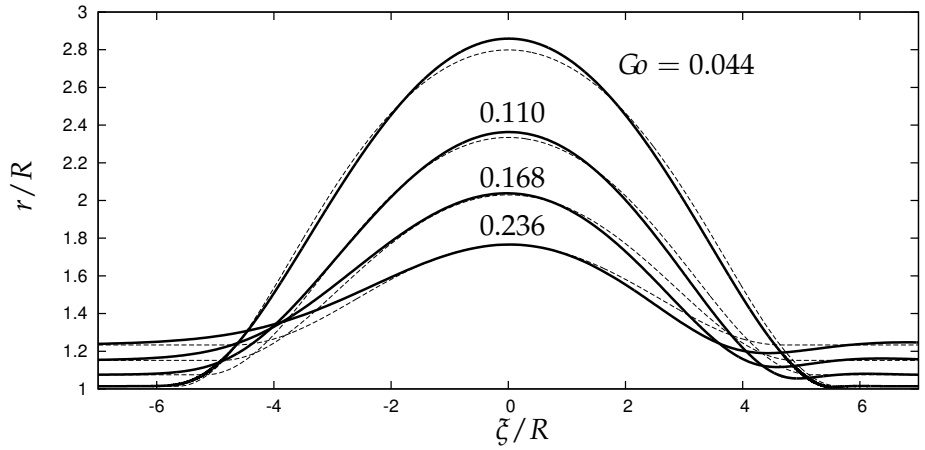

Figure 4.8 – *Wave profiles corresponding to the solutions to the CM equation (solid lines) and static drop shape (thin dashed lines). Labels correspond to the Goucher number. After Ruyer-Quil and Kalliadasis (2012).*

introduces a Galilei number, $Ga \equiv g\bar{R}^3/\nu^2 = Go^3\Gamma^{3/2}$, which is thus small and inertia effect are negligible.

Wave profiles are contrasted in Fig. 4.8. Their front-to-back symmetry shows that gravity does not affect the wave profile, as expected, since the typical size of the wave $\bar{R}$ is much smaller than the capillary length l_c. Therefore, solitary waves in this regime resemble isolated drops sliding under the action of gravity on a wettable fiber, which is precisely why one refers to this regime as the drop-like regime. It corresponds to the observation by Quéré Quéré (1990), Quéré (1999) in the coating of wires or thin fibers drawn out of a bath of viscous liquids that the thin annular film deposited on the wires/fibers breaks up into drops.

This analogy is checked by computing the shape of static drops with zero contact angles sitting on a fiber coated with a base liquid film ,or substrate film, of the same liquid (details of the calculation are given in the appendix B of Ruyer-Quil and Kalliadasis (2012)). The agreement is remarkable. The adopted modeling approach is accurate in the drop-like regime even if the long-wave approximation does not hold any more. This underlines the robustness of the long-wave approximation of the curvature terms $K_{\rm ax} \approx \partial_{xx}h$ and $K_{\rm az} \approx (R+h)^{-1}$. Following Kalliadasis and Chang (1994), an analytical estimate of the amplitude and speed of the drop-like waves in the limit $Go \to 0$ may be obtained via matched asymptotic expansions. The appropriate small parameter is the dimensionless speed of the drops. By balancing viscous and capillary forces at the back of the waves, one can easily extend to sliding drops the Landau-Levich-Derjaguin law obtained by Quéré Quéré (1999) in the case of fibers drawn out of a bath. The result compares favorably to the results from the CM equation.

The drop-like regime is also characterized by the possibility to find traveling-wave solutions when the Nusselt uniform film is still linearly stable (Novbari and Oron 2011). This subcritical situation must be contrasted with the planar case for which the onset of TWs is always supercritical. This phenomenon arises from capillary effects and depends

only on the geometry and thus on the aspect ratio $\tilde{\alpha}$ for sufficiently small Goucher numbers. It can be understood using thermodynamical arguments as slowly moving beads are slightly out-of-equilibrium drops. Subcritical onset of the TW solutions are thus associated with a energetically favorable reduction of the interfacial area.

Drag-inertia regime

The drag-inertia regime corresponds to the predominance of the Kapitza instability mode. This regime corresponds to thick fibers and large reduce Reynolds numbers δ for which the wave dynamics is not different from what is observed on a falling film down a vertical plane. It is characterized by highly non-symmetrical solitary waves with a steep front and a gentle back tail, whose speed and amplitude are close to the ones of 'roll-waves', i.e. shocks, or hydraulic jumps, periodically connected by laminar flows. This regime can also be referred to as a "capillary roll wave" regime, the formation of shock at the fronts being arrested by surface tension. The speed of the waves in the asymptotic limit $\delta \to \infty$ can be determined using Thomas condition (Thomas 1939) and the convergence to the asymptotic result is governed by $\eta/\delta^2 \propto Re^{-2}$ as in the planar case.

Drag-gravity regime

The 'drag-gravity' regime corresponds to the predominance of the flow advection over the instability mechanisms, either when inertia effects are weak, i.e. for $\delta \lessapprox 1$ or when the azimuthal curvature effects are non-dominant, $\beta^\star \lessapprox 1$. In both cases it is possible to interpret the 'drag-gravity' regime as one where the instability growth is arrested by the flow. The amplitude of the waves can be thus assumed small which enables a weakly nonlinear analysis. The flow is governed in that limit by the Kuramoto-Sivashinky equation and one is thus led to the following power laws fro the speed and amplitude of the waves:

$$c/c_k \approx 1 + 0.405\,\mathrm{Y}^{3/2} \qquad h_{\max} \approx 1 + 0.523\,\mathrm{Y}^{3/2}, \tag{4.41}$$

where $\mathrm{Y} = \frac{2}{5}\delta + \beta$ From (4.41) a linear relation between the speed and amplitude can be derived:

$$h_{\max} - 1 \approx 1.29\left(\frac{c}{c_k} - 1\right) \tag{4.42}$$

A linear dependence of the speed as a function of amplitude was initially found by Chang (1986) by utilizing a normal form analysis of the TW solutions of the Kuramoto-Sivashinsky equation. This linear dependence is a characteristic of the drag-gravity regime and must be contrasted with the experimental relation

$$h_{\max} - 1 \approx 1.67\left(\frac{c}{c_k} - 1\right) \tag{4.43}$$

obtained by Tihon *et al.* Tihon et al. (2006) for solitary waves running down a plane inclined at an angle 5°. A linear dependence of $h_{\max}$ with respect to c/c_k has also been found experimentally Duprat et al. (2009a) for solitary waves on a relatively thick fiber with a slope closer to 1.5.

Soliton-like regime

A fourth regime may be found for very viscous fluids and thick films $\tilde{\alpha} = O(1)$), for which both K and RP instability mechanisms are weak ($\delta \lessapprox 1$ and $\beta^\star \lessapprox 1$) and viscous dispersion is significant ($\eta = O(1)$). This 'soliton-like' regime corresponds to the balance of the nonlinearities with the dispersion induced by second-order viscous effects, with the speed and amplitude of the solitary waves being functions of the logarithm of the aspect ratio $\tilde{\alpha}$. This regime (only predicted in numerical experiments) is similar to the dynamics of the solitons governed by the Korteweg-de-Vries equation.

However, even in the drag-gravity regime, the influence of the second-order viscous terms (the Trouton viscous terms) is noticeable. By lowering the speed of kinematic waves, the advection time τ_a is increased. The saturation of the instability by the flow is therefore attenuated by viscous dispersion which thus raises the time of advection of the structures. The waves having more time to grow before reaching saturation, their amplitude becomes larger.

Regime map

The onset of the 'drop-like' regime and the 'drag-inertia' regime corresponds roughly to $\beta^\star \approx 1$ and $\delta \approx 1$. The 'soliton-like' regime arises when the instability mechanisms are weak ($\delta \lessapprox 1$ and $\beta^\star \lessapprox 1$), the film is thick, $\tilde{\alpha} = O(1)$, and viscous dispersion is strong, $\eta = O(1)$. Finally, the 'drag-gravity' regime is observed when all other effects are weak ($\delta \lessapprox 1$ and $\beta^\star \lessapprox 1$ and $\eta \ll 1$). Therefore, a phase diagram can be obtained for a given fluid, thus a given Kapitza number Γ, by drawing the curves $\delta = 1$, $\eta = 1$ and $\beta^\star = 1$ in the plane ($\tilde{\alpha}$, Go). Since $\eta = (\tilde{\alpha} Go)^{4/3}$ and $\beta^\star = \{\tilde{\alpha} c_k(\tilde{\alpha})/[Go^2(1+\tilde{\alpha})^4]\}^{2/3}$ are functions of $\tilde{\alpha}$ and the Goucher number only, the corresponding curves $\beta^\star = 1$ and $\eta = 1$ are independent of the working fluid considered. Thus, $\delta = 1$ is the only boundary that moves in the plane ($\tilde{\alpha}$, Go) when Γ is varied. Figure 4.9 is a tentative representation of the phase diagrams for the four working fluids considered in this study, from weakly viscous fluids like water with a high Kapitza number, $\Gamma = 3376$, to highly viscous fluids like silicon oil v1000 corresponding to a small Kapitza number, $\Gamma = 0.10$.

Some perspectives

A film flowing down a vertical fiber is probably one of the most simple and intriguing open flow. It is the archetype of a long-wave one-dimensional, dispersive, dissipative, active nonlinear medium. The 'activity' of this flow, that is its ability to generate structures, is sustained by two long-wave competing instability mechanisms, the Kapitza and the Rayleigh-Plateau instability. The 'dissipation' of the system originates not from viscosity but rather from surface tension and the axial curvature. 'Dispersion' has a viscous origin being triggered by the second-order viscous terms, or extensional 'Trouton' viscosity. The principal nonlinearity of this system is the flow-to-thickness third-order relation (4.2).

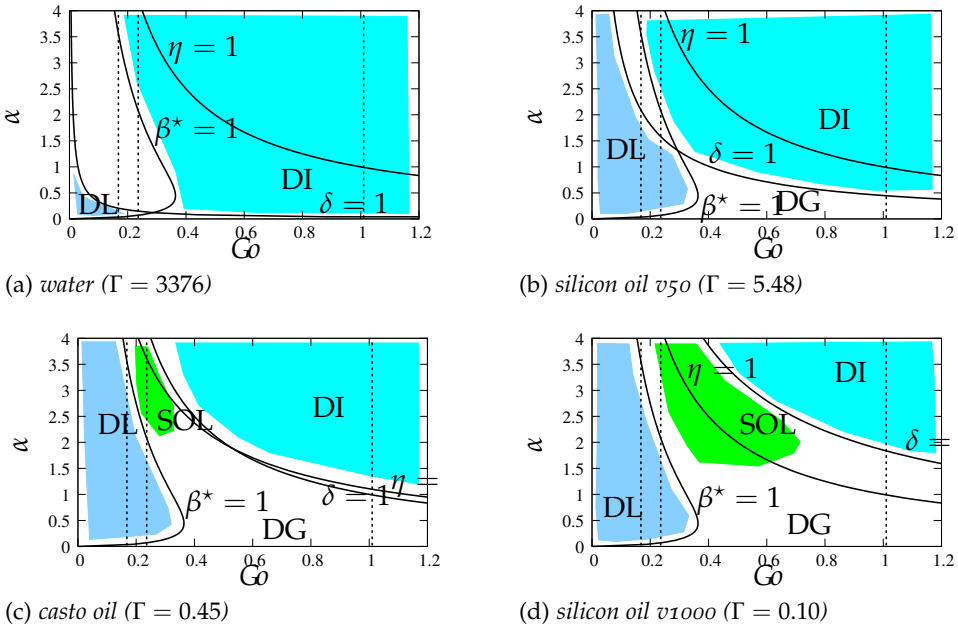

(a) *water* ($\Gamma = 3376$) (b) *silicon oil v50* ($\Gamma = 5.48$)

(c) *casto oil* ($\Gamma = 0.45$) (d) *silicon oil v1000* ($\Gamma = 0.10$)

Figure 4.9 – *Maps of the different regimes in the $Go - \tilde{\alpha}$ parameter space for fluids of increasing viscosity. The different curves are the loci of $\delta = 1$, $\eta = 1$ and $\beta^\star = 1$. 'DI' refers to the 'drag-inertia' regime, 'DL' to the Rayleigh-Plateau regime, 'SOL' to the 'soliton-like' regime and 'DG' to the 'drag-gravity' regime.*

Since the Rayleigh-Plateau mode can be triggered even in the absence of flow, the instability is observable at very low Reynolds number and for very viscous fluids which makes its study particularly easy both experimentally and numerically. Moreover, contrary to the Kapitza K mode which is triggered by the flow itself, the RP instability mode can compete with the flow advection and a convective–absolute transition is easily observable.

The most simple equation that presents all these features is the Kawaharah equation (Kawahara 1983, Kawahara and Toh 1988, Elphick et al. 1988),

$$\partial_t h + h\partial_x h + \partial_{xx} h + \delta_K \partial_{xxx} h + \partial_{xxxx} h \,, \tag{4.44}$$

also called 'generalized Kuramoto-Sivashinsky' equation since the Kuramoto-Sivashinsky equation is retrieved when the dispersive terms are dropped out, i.e. for $\delta_K = 0$. This equation has been extensively studied as a prototype of the development of spatio-temporal chaos (Chang et al. 1998, Chang and Demekhin 2002). In particular, a great deal of work has recently been devoted to the construction of coherent-structure theory based on wave-to-wave interaction of solitary pulses based on the Kawaharah equation (Tseluiko et al. 2010b). Kalliadasis and coworkers have noticed the strong analogy between the dynamics of beads down a fiber and the spatio-temporal chaos modeled by (4.44). Duprat and Giorgiutti-Dauphiné have reported the formation of bound states, made of several solitary waves moving as a whole and separated with constant distances, as predicted by the theory based on (4.44) (Duprat et al. 2009a, Tseluiko et al. 2010a).

However, a systematic and statistical analysis of the spatio-temporal

evolution of the flow along the fiber is still lacking. Hitherto, an open question remains: does the disordered dynamics of the wavy flow reaches a permanent state, characterized by a number of structures per unit of time (or 'density') independent of the spatial location, or is the coarsening process, that is the emergence of fewer and larger beads as a result of coalescence events, goes on for ever ?

This question can be answered only by constructing a coherent-structure theory in qualitative and quantitative agreement with the experiments. The two-equation model (4.40) is a good candidate for the construction of such a theory. This model has been checked to satisfactorily capture the linear and nonlinear dynamics of the film. The different wave regimes have been deciphered underlining the competitions between the two instability mechanisms, viscous dispersion and the advection by the flow. FollowingPradas et al. (2011), a straightforward extension of the coherent-structure theory for a film on a vertical plane based on two-equation model is a first step to answer that question.

The absolute instability of the film triggered a well-defined global mode (observable in the middle panel of figure 4.1), it would be interesting to see how such a global mode respond to a spatial perturbation at a wavelength that does not correspond to its selected wavelength. One may expect to generate phase soliton as in the Thorpe experiment of a tilting tube filled with two immiscible fluids of different density (Pouliquen et al. 1992; 1995).

In many industrial applications, the fluid is non-Newtonian. The presence of shear-thinning and normal forces may modify significantly the instability of the film and its dynamics. Some preliminary experimental reports can be found in the recent work by Boulogne et al. (2012). However, a consistent theory is still lacking for this flow. Liquid film down wires are also encountered in the design of new structure packings to optimize distillation and absorption columns in chemical engineering. The idea is that the liquid will be more easily distributed over bundles of wires (Hattori et al. 1994, Gruenig and Kraume 2009, Gruenig et al. 2012). To tackle this industrial problem, the model (4.40) can be extended by taking into account the shear exerted by the surrounding gas flow.

4.5 C. Ruyer-Quil *et al.*, J. Fluid Mech (2008)

J. Fluid Mech. (2008), *vol.* 603, *pp.* 431–462.
doi:10.1017/S0022112008001225 Printed in the United Kingdom

Modelling film flows down a fibre

C. RUYER-QUIL[1], P. TREVELEYAN[2], F. GIORGIUTTI-DAUPHINÉ[1], C. DUPRAT[1] AND S. KALLIADASIS[2]

[1]Laboratoire FAST – UMR CNRS 7608, Campus universitaire, 91405 Orsay, France
[2]Department of Chemical Engineering, Imperial College London, London SW7 2AZ, UK

(Received 9 October 2007 and in revised form 21 February 2008)

Consider the gravity-driven flow of a thin liquid film down a vertical fibre. A model of two coupled evolution equations for the local film thickness h and the local flow rate q is formulated within the framework of the long-wave and boundary-layer approximations. The model accounts for inertia and streamwise viscous diffusion. Evolution equations obtained by previous authors are recovered in the appropriate limit. Comparisons to experimental results show good agreement in both linear and nonlinear regimes. Viscous diffusion effects are found to have a stabilizing dispersive effect on the linear waves. Time-dependent computations of the spatial evolution of the film reveal a strong influence of streamwise viscous diffusion on the dynamics of the flow and the wave selection process.

1. Introduction

A liquid film flowing down a vertical fibre is an unstable open-flow hydrodynamic system that exhibits a rich variety of wave phenomena and transitions, ranging from the classical spatio-temporal disorder prompted by the Kapitza instability mode of films falling down vertical planes – hereinafter referred to as 'K mode'– and characterized by the presence of continuously interacting solitary waves, to the emergence of very regular drop-like wave patterns resulting from the Rayleigh–Plateau instability mode of a liquid layer coating a cylinder – hereinafter referred to as 'RP mode' (Kliakhandler, Davis & Bankoff 2001; Duprat *et al.* 2007).

The experimental investigation of flows down fibres was initiated by the studies of Quéré in the context of drawing of wires from liquid baths (Quéré 1990, 1999). Quéré observed the formation of axisymmetric drops, and showed that this break-up process may be arrested by mean flow. Kliakhandler *et al.* (2001) examined experimentally the dynamics of a film flowing down a fibre and reported several wavy regimes, consisting of isolated large-amplitude drops moving at constant speed and shape on a nearly flat substrate, regular periodic wavetrains or interaction events between large drops with smaller ones on the residual film separating the large drops.

The arrest by the mean flow of the drop formation process observed by Quéré was analysed in detail by Kalliadasis & Chang (1994). They computed the solutions to a lubrication-type evolution equation for the film thickness h derived by Frenkel (1992) assuming it to be much smaller than the radius R of the fibre and neglecting inertia. They observed a catastrophic growth of the speed and amplitude of the solitary-wave solutions that closely corresponds to the onset of drops in Quéré's experiments.

Roy, Roberts & Simpson (2002) extended Frenkel's equation by including higher-order terms in the small aspect ratio h/R (e.g. in Frenkel's equation only the

leading contribution of the azimuthal curvature to the capillary pressure is retained). Kliakhandler *et al.* (2001) examined the case of film thicknesses of the order of the fibre radii corresponding to their experiments. Their derivation is based on the lubrication approximation but contains an *ad-hoc* step within the framework of this approximation, namely the retention of the full curvature term. Craster & Matar (2006) derived a film-thickness evolution equation very similar to that obtained by Kliakhandler *et al.* (2001) based on the assumption that the total radius of the fluid ring $R + h$ is small compared to the capillary length. However, unlike the Kliakhandler *et al.* (2001) equation, the Craster–Matar equation retains the lower-order approximation of the curvature and is consistent at its level of truncation. Moreover, the time-dependent computations of the Craster–Matar equation show reasonable agreement to the experiments performed by these authors as well as to the study by Kliakhandler *et al.*

All modelling attempts described above assumed negligible inertia effects. Therefore they cannot account for the K hydrodynamic instability mechanism. A decisive first step towards accounting for inertia effects for moderate Reynolds numbers was undertaken by Trifonov (1992) who applied the Kàrmàn–Polhausen averaging technique for a film falling down a planar substrate, introduced first by Shkadov (1967), to formulate a system of two evolution equations for the film thickness h and the flow rate q. Trifonov demonstrated the presence of at least two families of travelling-wave solutions leading to 'negative' or 'positive' solitary waves in the limit of small wavenumbers. Sisoev *et al.* (2006) carried out transient numerical simulations of Trifonov's model with periodic forcing at the inlet. The spatial evolution of the waves is then characterized by the selection of the fastest travelling wave having the same frequency with the forcing at the inlet. However, the Kármán–Pohlhausen averaging technique is known to lead to an erroneous estimate of the instability threshold for a film falling down a planar inclined substrate, a direct consequence of neglecting the contribution of the streamwise viscous dissipation (Ruyer-Quil & Manneville 2000). More recently, Roberts & Li (2006) obtained a two-equation model based on a centre-manifold approach by taking into account both inertia and streamwise viscous diffusion, but assumed a small aspect ratio h/R, whereas the reported experimental conditions correspond to $h/R \sim 1$ (Kliakhandler *et al.* 2001; Duprat *et al.* 2007).

In this study we develop a generic modelling approach based on first principles to formulate a two-equation model for the film thickness h and flow rate q. The model overcomes the limitations of the Trifonov and the Roberts & Li models, i.e. it accounts for inertia, streamwise viscous diffusion, both small and $O(1)$ aspect ratios h/R as well as small and large surface tension fluids and is consistent with the above cited lubrication equations in the appropriate limit. In addition, we investigate the role of viscous streamwise effects in the experimental conditions of the Kliakhandler *et al.* and Duprat *et al.* studies and we demonstrate good agreement with these experiments. We also clearly demarcate regions in the parameter space where previous models are valid.

The different tests used for the validation of our model are as follows. (i) The linear stability characteristics of the base flow and their comparison with an Orr–Sommerfeld analysis of the full Navier–Stokes equations and wall and free-surface boundary conditions. A related test here is the analysis of the response of the base flow to a localized perturbation and the ability of the model to capture the absolute/convective instability transition as predicted by Orr–Sommerfeld. (ii) Direct comparisons with experiments of different features of the flow such as travelling-wave characteristics (speed, maximum amplitude).

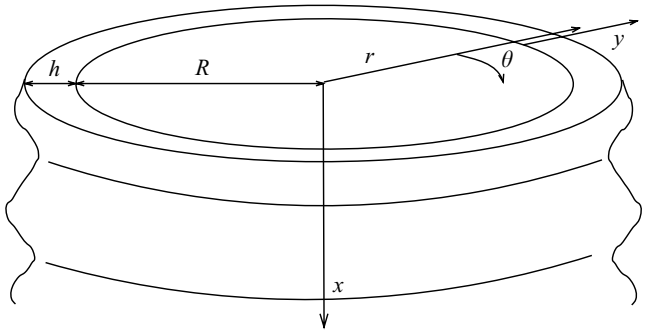

FIGURE 1. Sketch of the profile geometry for a thin liquid film falling down a vertical fibre. A cylindrical coordinate system (r, θ) is chosen at the fibre centreline $r = 0$. R is the fibre radius and h is the local film thickness. (x, y) is a Cartesian coordinate system with x the axial/streamwise coordinate along the fibre centreline and $y = r - R$ an outward pointing coordinate normal to the fibre surface and such that $y = 0$ corresponds to the fibre surface and $y = h$ to the film surface.

The paper is organized as follows. The governing equations for a film flowing down a vertical fibre and their non-dimensionalization are given in § 2. The boundary-layer approximation is outlined in § 3. A two-equation model is next formulated using a weighted residuals procedure in § 4 which is validated and compared to available experimental data in the linear and nonlinear regimes in § 5 and § 6, respectively. Time-dependent simulations of the spatial evolution of the flow along the fibre are presented in § 7 followed by concluding remarks in § 8.

2. Governing equations

Consider a film falling down a vertical fibre as illustrated in figure 1. The fluid properties, namely viscosity μ, density ρ and surface tension σ, are all assumed to remain constant. Our non-dimensionalization is based on the viscous–gravity time and space scales, $t_\nu = \nu^{1/3} g^{-2/3}$, $l_\nu = \nu^{2/3} g^{-1/3}$, built from the kinematic viscosity $\nu = \mu/\rho$ and the acceleration due to gravity g. Assuming axisymmetric flows without any variation in the azimuthal θ-direction, the equations of motion are:

$$\partial_t u_x + u_x \partial_x u_x + u_r \partial_r u_x = -\partial_x p + 1 + \left[\partial_{rr} + \frac{1}{r}\partial_r + \partial_{xx}\right] u_x, \tag{2.1a}$$

$$\partial_t u_r + u_x \partial_x u_r + u_r \partial_r u_r = -\partial_r p + \left[\partial_{rr} + \frac{1}{r}\partial_r + \partial_{xx}\right] u_r - \frac{1}{r^2} u_r, \tag{2.1b}$$

$$\partial_r u_r + \frac{u_r}{r} + \partial_x u_x = 0\,. \tag{2.1c}$$

They are subject to the no-slip/no-penetration boundary condition at the wall

$$u_r = u_x = 0 \quad \text{at} \quad r = R, \tag{2.1d}$$

the normal and tangential stress balances at the free surface, $r = R + h(x, t)$

$$p = \frac{2}{1 + (\partial_x h)^2}\left[-\partial_x h(\partial_r u_x + \partial_x u_r) + \partial_x u_x (\partial_x h)^2 + \partial_r u_r\right] \tag{2.1e}$$

$$-\frac{\Gamma}{[1 + (\partial_x h)^2]^{3/2}}\left[\partial_{xx} h - \frac{1}{R + h}(1 + (\partial_x h)^2)\right],$$

$$0 = (1 - (\partial_x h)^2)(\partial_r u_x + \partial_x u_r) + 2\partial_x h(\partial_r u_r - \partial_x u_x), \tag{2.1f}$$

where without loss of generality the pressure of the ambient gas phase has been set equal to zero and the kinematic boundary condition:

$$\partial_t h + u_x \partial_x h - u_r = 0\,. \tag{2.1g}$$

The Kapitza number $\Gamma = \sigma/(\rho\nu^{4/3}g^{1/3}) = (l_c/l_\nu)^2$ compares the surface stress σ/l_ν to the viscous stress μ/t_ν, or equivalently the capillary length $l_c = \sqrt{\sigma/(\rho g)}$ to l_ν. By integrating the continuity equation (2.1*c*) across the film and using the no-slip condition (2.1*d*), the kinematic condition (2.1*g*) can be written as a mass conservation equation,

$$(1 + \alpha h)\partial_t h + \partial_x q = 0, \tag{2.2}$$

where $q \equiv R^{-1}\int_R^{R+h} u_x r\,\mathrm{d}r$ is the flow rate per unit circumference length and $\alpha \equiv 1/R$ is the dimensionless curvature of the cylinder.

Therefore the flow is characterized by the dimensionless Nusselt uniform film thickness h_N, the dimensionless radius R and the Kapitza number Γ, or equivalently the Reynolds number $Re = q_\mathrm{N}$ which appears implicitly through h_N with q_N the dimensionless flow rate of the Nusselt uniform film solution (q_N and Re will be defined in § 4), the dimensionless fibre curvature α and the Weber number $We = \Gamma/h_\mathrm{N}^2 = \sigma/(\rho g \bar{h}_\mathrm{N}^2) = (l_c/\bar{h}_\mathrm{N})^2$ where $\bar{h}_\mathrm{N}$ is the dimensional Nusselt uniform film thickness (hereinafter bars are introduced to distinguish dimensional from dimensionless quantities when necessary).

Note that the classical planar case can be recovered when $\alpha = 0$. This can easily be seen by performing the change of variables $(x, r) \to (x, y)$ and thus measuring the cross-stream variation from the wall, and by defining $(u, v) \equiv (u_x, u_r)$, corresponding to the usual notations for the streamwise/cross-stream velocity components in the planar case. The dimensionless fibre curvature α then appears in the equations of motion (2.1*a–c*) and the normal stress balance (2.1*e*). The transformed equations simplify the comparison between the annular geometry and the planar one: the effect of the annular geometry appears through the terms containing the fibre curvature α and it is easy to verify that setting $\alpha = 0$ gives the governing equations for the planar case.

3. Boundary-layer equations for thin-film flow down a fibre

3.1. *Orders of magnitude assignments*

Assuming slow space and time modulations of the flow allows us to define a formal parameter $\epsilon \sim \partial_{x,t} \ll 1$ and to perform a 'gradient expansion' of the governing equations (2.1*a*–2.1*g*) in ϵ. The smallness of ϵ implies a separation of scales between x and r which in turn dictates a different treatment of the streamwise and cross-stream momentum equations as in boundary-layer theory in aerodynamics. Further we assume that $\alpha h \sim \alpha h_\mathrm{N}$ is at most $O(1)$ or h_N is at most $O(R)$ (in the experiments by Kliakhandler *et al.* (2001) and Duprat *et al.* (2007), $\alpha h_\mathrm{N} = O(1)$). We thus exclude the possibility of large αh_N, in which case the film does not really 'see' the fibre and resembles more a vertical falling free jet (and it is quite likely that the flow will be non-axisymmetric in this case).

The formulation of the boundary-layer equations starts by determining the order of magnitude of the inertia terms in the left-hand side of the cross-stream momentum equation (2.1*b*). Since $\bar{h} \sim \bar{h}_\mathrm{N}$, $u_x \sim \bar{u}_\mathrm{N}/(l_\nu/t_\nu)$ with $\bar{u}_\mathrm{N}$ the dimensional Nusselt uniform film velocity whose scaling can be easily obtained by balancing viscous diffusion in the r-direction with gravity, $\bar{u}_\mathrm{N} \sim g\bar{h}_\mathrm{N}^2/\nu$. We then have $u_x \sim h_\mathrm{N}^2$. The

continuity equation (2.1*c*) now indicates that the radial component of the velocity is formally of $O(\epsilon h_N^2)$. Since $x, y \sim h_N$, from $u_x \sim h_N^2 \sim h_N/t$, $t \sim 1/h_N$ and the inertia terms in the left-hand side of the cross-stream momentum equation (2.1*b*) are of $O(\epsilon^2 h_N^3)$. Neglecting these terms, using the relation obtained by differentiating the continuity equation (2.1*c*) once with respect to r, and dropping the streamwise viscous term $\partial_{xx} u_r = O(\epsilon^2 \epsilon h_N^2/h_N^2) \equiv O(\epsilon^3)$, yields the simplified cross-stream momentum equation, $\partial_r p = -\partial_{xr} u_x$, which can be integrated once with respect to r to give

$$p = p|_h - \partial_x u_x + \partial_x u_x|_h, \tag{3.1}$$

where terms of $O(\epsilon^3 h_N, \epsilon^2 h_N^4)$ have been neglected. This is indeed the case provided that $\epsilon^{3/2} \ll h_N \ll \epsilon^{-1/4}$ and $\alpha \gg \epsilon^{9/4}$, from a detailed examination of the orders of magnitude of the retained over the neglected terms.

The first term $p|_h$ in the approximation for the pressure in (3.1) must be evaluated from the normal stress balance in (2.1*e*) that gives the pressure drop across the free surface. The contribution of the streamwise curvature $\Gamma \partial_{xx} h$ due to surface tension must be kept in our formulation as it is well known from the planar case that this is the principal physical effect that prevents the waves from breaking. However, this term is formally of $O(\Gamma h_N \epsilon^2/h_N^2) \equiv \Gamma \epsilon^2/h_N$ and should be neglected, if for example Γ is at most of $O(1)$ and $h_N = O(1)$, as in this case terms of $O(\epsilon^2)$ and higher are neglected in our approximation for the pressure in (3.1). Unless the streamwise curvature is sufficiently large in certain regions/boundary layers of a free-surface deformation such as the steep front edge of a solitary hump: it contains the highest derivative of h multiplied by ϵ^2 and in these boundary layers this derivative is sufficiently large and cannot be neglected. However, proceeding via inner/outer asymptotic expansions is cumbersome if not impossible. It is more convenient to avoid any boundary layers and to stipulate that the streamwise curvature is important throughout a solitary hump and not just in certain regions.

The contribution of the streamwise curvature in (2.1*a*) is $\Gamma \partial_{xxx} h$ with formal order:

$$\Gamma \partial_{xxx} h \sim \Gamma \frac{h_N}{h_N^3} \epsilon^3 \equiv \frac{\Gamma}{h_N^2} \epsilon^3. \tag{3.2}$$

To proceed further we need to assign a relative order between Γ and ϵ. Two cases of particular interest here are large Γ and $\Gamma = O(1)$. The case of large Γ is representative of liquids with high surface tension and small kinematic viscosity such as water ($\Gamma \sim 3000$ at 25°C) while the second case corresponds to liquids with surface tension smaller than that of water and kinematic viscosity much larger than that of water such as silicone oils.

(i) Γ large, 'the strong surface tension limit'. This is quite frequently the case in inertia-driven films on planar substrates where water is used as the working fluid. A convenient order-of-magnitude assignment is $\Gamma = O(\epsilon^{-2})$. For simplicity let us also assume that $h_N = O(1)$ (a sufficiently large Γ/surface tension is required for 'thick' films in order to prevent the waves from breaking). From (3.2), $\Gamma \partial_{xxx} h$ is formally of $O(\epsilon)$ and must be retained since terms of $O(\epsilon^3)$ and higher are neglected. However, at the steep front edge of a solitary pulse and by analogy with the planar case, the pressure gradient $\Gamma \partial_{xxx} h$ due to surface tension and the gravitational acceleration equal to unity in (2.1*a*) balance. Hence, $\Gamma \partial_{xxx} h$ has its formal order, $O(\epsilon)$, throughout except at the front where it increases to $O(1)$. Let us introduce in this region the transformation $x = \kappa h_N x_S$ due to Shkadov (1977) – we shall return to it in §4. We

then have:

$$\Gamma\partial_{xxx}h = \Gamma\partial_{x_Sx_Sx_S}h\frac{1}{\kappa^3 h_N^3} \sim \frac{\Gamma h_N}{\kappa^3 h_N^3} \equiv \frac{\Gamma}{\kappa^3 h_N^2} \sim 1 \Rightarrow \kappa = \left(\frac{\Gamma}{h_N^2}\right)^{1/3} \equiv We^{1/3}. \qquad (3.3)$$

In terms of dimensional variables, (3.3) corresponds to the balance $\rho g \sim \sigma\partial_{\bar{x}\bar{x}\bar{x}}\bar{h}$ or $\rho g \sim \sigma\bar{h}_N/l_S^3$ where l_S is the length scale over which the pressure gradient due to streamwise surface tension and gravitational acceleration balance – it corresponds effectively to the characteristic length of the steep front of a solitary wave. We then have $\bar{h}_N/l_S \sim We^{-1/3} = 1/\kappa \sim \epsilon^{2/3}$ so that l_S is much larger than the film thickness $\bar{h}_N$ and the long-wave assumption is not violated. Equivalently, the long-wave assumption is sustained at the front of a solitary wave if $\partial_x h \ll 1$ there. Indeed,

$$\partial_x h = \partial_{x_S} h\frac{1}{\kappa h_N} \sim \frac{h_N}{\kappa h_N} \equiv \frac{1}{\kappa} \sim \epsilon^{2/3}. \qquad (3.4)$$

This estimate also shows that $\partial_x h$ at the front of a solitary wave is much larger than its formal order, $O(h_N\epsilon/h_N) \equiv O(\epsilon)$. However, $\partial_x h$ is never larger than unity at the front consistent with our stipulation that we do not have a singular perturbation problem since $\Gamma\partial_{xxx}h$ is important throughout a solitary wave.

(ii) $\Gamma = O(1)$. It is now clear that the order of magnitude of h_N with respect to ϵ is crucial for the validity of the boundary-layer approximation. For example, if $h_N = O(1)$, from, (3.2), $\Gamma\partial_{xxx}h \sim \epsilon^3$ and must be neglected. On the other hand if $h_N \sim \epsilon^{-1/5}$, which satisfies the requirement $h_N \ll \epsilon^{-1/4}$ given earlier, then $\Gamma\partial_{xxx}h \sim \epsilon^{17/5} \ll \epsilon^3 h_N^4 \sim \epsilon^{11/5}$ and the contribution of the streamwise curvature must be neglected. Hence h_N must be small ('thin' films do not require large Γ/surface tension to prevent the waves from breaking): in order to maintain $\Gamma\partial_{xxx}h$ in our perturbation expansion, it must be much larger than the neglected terms, i.e. $(\Gamma/h_N^2)\epsilon^3 \gg \epsilon^4 h_N, \epsilon^3 h_N^4$ or $h_N \ll \epsilon^{-1/3}, 1$ which are satisfied simultaneously if $h_N \ll 1$.

Again, $\Gamma\partial_{xxx}h$ has its formal order throughout except at the front of a solitary pulse where it must be increased to $\Gamma\partial_{xxx}h \sim 1$. As in case (i), in order to sustain the long-wave approximation we require $\kappa \gg 1$ which is indeed the case since $\kappa = (\Gamma/h_N^2)^{1/3} \gg 1$ for $h_N \ll 1$ but now κ can be much smaller than that in equation (3.4) for case (i) if a tighter lower bound is imposed on h_N, e.g. $h_N \gg \epsilon$ instead of $h_N \gg \epsilon^{3/2}$ we obtained earlier: with $\Gamma = O(1)$ and $h_N \gg \epsilon$, $\kappa \ll \epsilon^{-2/3}$ which then implies that in case (ii) the front of a solitary pulse must have a larger slope than in case (i) (and $\Gamma\partial_{xxx}h$ is formally $\ll \epsilon$, the formal order of this term in case (i)). On the other hand this is always the case when the condition $h_N \sim 1$ in case (i) is relaxed: $\kappa_i^{-1} \sim \epsilon^{2/3}h_N^{2/3}$ and $\kappa_{ii}^{-1} \sim h_N^{2/3}$. Physically, in case (ii) surface tension is not strong enough to prevent the slope from increasing but again the slope $\partial_x h$ is never larger than unity, which is consistent with our stipulation that we do not have a singular perturbation problem. Equivalently, for a given h_N, increasing Γ decreases the slope at the front.

3.2. *Boundary-layer approximation for large Γ*

We now return to the evaluation of the term $p|_h$ in the approximation for the pressure in (3.1) in case (i) with $\Gamma = O(\epsilon^{-2})$ and $h_N = O(1)$. In the first instance let us neglect terms of $O(\epsilon^3)$ and higher associated with the viscous part of the pressure in the normal stress balance (2.1*e*). Note that independently of the order of h_N, $1/(R+h) \equiv \alpha/(1+\alpha h) = O(\alpha)$: $\alpha/(1+\alpha h) \sim \alpha$ for $\alpha h \ll 1$ and $\sim \alpha$ for $\alpha h = O(1)$. Hence by neglecting terms $O(\epsilon^2, \epsilon^2\alpha) = O(\epsilon^2)$, since in the particular case we are considering $h_N = O(1)$ which with αh_N at most of $O(1)$ implies that α is at most of

$O(1)$, the pressure on the free surface is given by:

$$p|_h = -2\partial_x h \partial_r u_x|_h + 2\partial_r u_r|_h - \Gamma\left[\partial_{xx} h - \frac{1}{R+h}\left(1 - \frac{1}{2}(\partial_x h)^2\right)\right]. \tag{3.5}$$

This expression can be further simplified by considering the tangential stress boundary condition (2.1*f*) where terms of $O(\epsilon^3)$ and higher are neglected:

$$\partial_r u_x|_h = 2\partial_x h\left(\partial_x u_x|_h - \partial_r u_r|_h\right) - \partial_x u_r|_h + (\partial_x h)^2 \partial_r u_x|_h. \tag{3.6}$$

All terms in the right-hand side of this equation are of $O(\epsilon^2)$ and hence the contribution of the term $\partial_x h \partial_r u_x|_h$ in (3.5) is of $O(\epsilon^3)$ and can be neglected so that the pressure field is

$$p = -\partial_x u_x + \partial_x u_x|_h + 2\partial_r u_r|_h - \Gamma\left[\partial_{xx} h + K_{\mathrm{az}}\right], \tag{3.7}$$

where terms of $O(\epsilon^2, \epsilon^2\alpha) = O(\epsilon^2)$ are neglected, which is indeed the case provided that $\epsilon^2 \ll \alpha$ and α at most of $O(1)$ (again from a detailed examination of the orders of magnitude of the retained over the neglected terms), and where

$$K_{\mathrm{az}} = -\frac{1}{R+h}\left(1 - \frac{1}{2}(\partial_x h)^2\right) \equiv -\frac{\alpha}{1+\alpha h}\left(1 - \frac{1}{2}(\partial_x h)^2\right) \tag{3.8}$$

is the approximation of the azimuthal curvature of the free surface obtained by neglecting terms of $O(\epsilon^4\alpha) = O(\epsilon^4)$ and higher. Note that with $\alpha \to 0$, $\alpha/(1+\alpha h) \to 0$ and $K_{\mathrm{az}} \to 0$ corresponding to the planar limit. Also, since $h_{\mathrm{N}} = O(1)$, $\alpha \to 0$ is equivalent to $\alpha h \to 0$. In the general case, however, when $\alpha h \to 0$, $\alpha/(1+\alpha h) \to \alpha$ corresponding to a very thin film compared to the fibre radius but we still have the azimuthal curvature effect: $\alpha h \to 0$ does not necessarily imply the planar limit when the condition $h_{\mathrm{N}} = O(1)$ is relaxed – see also our discussion at the end of § 2.

Substituting (3.7) into the streamwise momentum equation (2.1*a*) then leads to the following consistent equation up to $O(\epsilon^2)$,

$$\begin{aligned}\partial_t u_x + u_x\partial_x u_x + u_r\partial_r u_x - \left[\partial_{rr} + \frac{1}{r}\partial_r + 2\partial_{xx}\right] u_x \\ = 1 - \partial_x\left[\partial_x u_x|_h + 2\partial_r u_r|_h\right] + \Gamma\left\{\partial_{xxx} h + \partial_x K_{\mathrm{az}}\right\},\end{aligned} \tag{3.9}$$

where terms of $O(\epsilon^3)$ and higher have been neglected.

Case (ii) is treated in Appendix A. By analogy now with the planar case where quite frequently $\Gamma = O(\epsilon^{-2})$ as noted earlier, equation (3.9) where terms of $O(\epsilon^3)$ and higher are neglected will be referred to as the 'second-order boundary-layer equation' for the problem of film flow down a fibre and for simplicity our analysis in § 4 is based on case (i). The set of equations to be solved at $O(\epsilon^2)$ (this refers to the truncation of the ϵ-expansion if for example case (ii) is considered), the 'second-order boundary-layer equations', consists of the streamwise momentum equation in the boundary-layer approximation (3.9), the continuity equation (2.1*c*), the no-slip/no-penetration condition at the wall (2.1*d*), the tangential stress balance at the free surface (3.6) and the mass conservation (2.2) or equivalently (2.1*g*). Notice that, when truncated at $O(\epsilon)$ as in the approach followed by Trifonov (1992) and Sisoev *et al.* (2006), the boundary-layer equations do not account for the streamwise viscous diffusion terms $-\partial_x[\partial_x u_x|_h + 2\partial_r u_r|_h]$ in (3.9) and $2\partial_x h(\partial_x u_x|_h - \partial_r u_r|_h) - \partial_x u_r|_h + (\partial_x h)^2\partial_r u_x|_h$ at the right-hand side of the tangential stress boundary condition in (3.6).

4. Formulation of a low-dimensional model

We now develop a low-dimensional model with a systematic reduction procedure based on a combination of the long-wave approximation and a projection of the velocity field on an appropriately chosen set of test functions. Our approach is not limited to a small ratio of the film thickness to the fibre radius and does not require precise and overly restrictive stipulations on the order of magnitude for this ratio – recall for example from our analysis in § 2 that in case (i) with $h_N = O(1)$, $\epsilon^2 \ll \alpha$ and α at most of $O(1)$ so that αh_N could be small or $O(1)$. As pointed out earlier, for simplicity we present in this section the formulation of the model for case (i). Case (ii) can be treated similarly; the final equations are the same for both cases.

4.1. *First-order model*

Let us first consider the case of the Nusselt uniform layer: assuming no modulations of the free surface, $\partial_x = \partial_t = 0$, the basic/Nusselt flow satisfies

$$\mathscr{L}(u_x) = -1 \qquad \text{with} \qquad u_x|_R = 0, \quad \partial_r u_x|_h = 0, \tag{4.1}$$

where $\mathscr{L}$ denotes the (friction) linear differential operator, $\mathscr{L} \equiv \partial_{rr} + r^{-1}\partial_r$. The solution of (4.1) is simply

$$u_x = \frac{1}{2}(R+h)^2 \ln\left(\frac{r}{R}\right) - \frac{1}{4}(r^2 - R^2) \equiv u_{x,0}, \tag{4.2}$$

which can also be written as

$$u_x = h^2 f_{\alpha h}(\hat{y}), \quad f_{\alpha h}(\hat{y}) \equiv -\frac{1}{4}\hat{y}^2 - \frac{1}{2\alpha h}\hat{y} + \frac{1}{\alpha h}\left[1 + \frac{1}{2}\alpha h + \frac{1}{2\alpha h}\right]\ln(1 + \alpha h\,\hat{y}), \tag{4.3}$$

where $\hat{y} = y/h \equiv (r-R)/h$ is a reduced cross-stream coordinate. Therefore, the effect of the curvature of the cylinder on the velocity profile of the uniform film solution is measured by the local aspect ratio $\alpha h = h/R$. Notice that in the limit $\alpha h \to 0$, which without specifying the order of h_N corresponds either to the planar limit or to a very thin film compared to the fibre radius (recall, however, from § 3 that due to the condition $h_N = O(1)$ in case (i), the limits $\alpha \to 0$ and $\alpha h \to 0$ are equivalent), the velocity profile is parabolic,

$$f_0 \equiv \lim_{\alpha h \to 0} f_{\alpha h} = \hat{y} - \frac{1}{2}\hat{y}^2,$$

as expected.

Let us now use for the x-velocity a projection of the form,

$$u_x = a_{0,0}(x,t)g_{0,0}(r; h(x,t)) + \sum_{m=1}^{m_{\max}}\sum_{n=0}^{n_{\max}} a_{m,n}(x,t)g_{m,n}(r) \tag{4.4}$$

while the radial component is obtained by integrating the continuity equation (2.1c):

$$u_r = -\frac{1}{r}\int_R^r \partial_x u_x(x,\zeta,t)\zeta\,\mathrm{d}\zeta. \tag{4.5}$$

$g_{0,0} \equiv u_{x,0}$ is precisely the Nusselt velocity profile so that (4.4) simply reduces to $u_{x,0}(r; h(x,t))$ and $a_{0,0} = 1$ if the film remains uniform. Consequently, the test functions $g_{m,n}$ account for the deviations of the velocity field from the Nusselt profile and their amplitudes are at most $O(\epsilon)$ quantities. Concerning the particular choice of test functions, we notice that monomials/powers of r and $\ln(r)$ constitute a closed set of functions with respect to differentiations and products involved in the momentum balance (3.9) and the linear operator $\mathscr{L}$. A plausible choice therefore is $g_{m,n} \equiv [(r-R)^m]\,[\ln(r/R)]^n$ which satisfy the no-slip/no-penetration condition on

the wall, (2.1*d*). Note that it can easily be shown that the above expressions for u_x, u_r are consistent with their order-of-magnitude assignments in § 3 obtained from simple scaling arguments.

After multiplication now of the momentum balance (3.9) by r^2, truncation at $O(\epsilon)$ and substitution of the projection (4.4) for the streamwise component of the velocity u_x, we are led to a polynomial in r and $\ln(r)$, say $\mathscr{P}(r, \ln(r))$, that is uniformly equal to zero. Cancelling all its monomials in r and $\ln(r)$ thus yields a number of independent relations equal to the number of unknowns $a_{m,n}$ if $m_{\max}$ and $n_{\max}$ are chosen sufficiently large. Further, since $a_{m,n}$, $m+n \geqslant 1$ are $O(\epsilon)$ corrections to the Nusselt velocity profile, their derivatives can be neglected at that order, and a linear system is obtained. Inversion of this linear system gives the amplitudes $a_{m,n}$, $m+n \geqslant 1$, as functions of $a_{0,0}$ and h, and an evolution equation for $a_{0,0}$ coupled to the evolution of the film thickness h through the mass conservation equation (2.2). The number of non-zero coefficients $a_{m,n}$, i.e. of amplitudes that are of $O(\epsilon)$, can be estimated from the degrees in r and $\ln(r)$ of the advection terms and by parity arguments. Finally, the corrections to the Nusselt velocity profile induced by the deformations of the film surface can be accounted for at $O(\epsilon)$ with seven test functions $g_{m,n}$.

The actual determination of the amplitudes $a_{m,n}$ requires some cumbersome algebraic manipulations that can be substantially simplified with the use of a weighted residuals approach such as the Galerkin or collocation method. With these methods, appropriate weights $w_{m,n}(r)$ are chosen and residuals $\mathscr{R}_{m,n} = \langle w_{m,n} | \mathscr{P} \rangle$ are evaluated where $\langle \cdot | \cdot \rangle$ is an inner product defined over the depth of the film $R \leqslant r \leqslant R + h(x,t)$. Setting the residuals $\mathscr{R}_{m,n}$ equal to zero, or equivalently projecting the polynomial $\mathscr{P}(r, \ln(r))$ onto zero, thus yields a system to be solved for the amplitudes $a_{m,n}$. If the number of test functions is chosen sufficiently large, the number of residuals is equal to the number of independent relationships obtained by setting $\mathscr{P}(r, \ln(r))$ uniformly to zero, so that equivalent systems of equations are found leading to the same system of evolution equations for h and $a_{0,0}$. We look for the best choice for the scalar product and the weighting functions $w_{m,n}$ that leads to the final result with a minimum of algebra.

The mass conservation equation (2.2) is exact and can be kept in a straightforward manner if the flow rate q is substituted with the amplitude of the Nusselt profile $a_{0,0}$ which can easily be done through the definition $q = R^{-1} \int_R^{R+h} u_x r \, \mathrm{d}r$ given in § 2,

$$a_{0,0} = \frac{q}{R^{-1} \displaystyle\int_R^{R+h} g_{0,0}(r\,;h) r \, \mathrm{d}r} - \sum_{m>1,n>1} a_{m,n} \frac{\displaystyle\int_R^{R+h} g_{m,n}(r) r \, \mathrm{d}r}{\displaystyle\int_R^{R+h} g_{0,0}(r\,;h) r \, \mathrm{d}r} \equiv \frac{3q}{h^3 \phi(\alpha h)} + O(\epsilon), \tag{4.6}$$

where ϕ is a measure of the departure of the flow-rate dependence on the film thickness from the planar case $q \equiv \frac{1}{3}h^3$, $\phi(\alpha) \equiv \int_0^1 f_{\alpha h}(\xi)(1+\alpha\xi)\,\mathrm{d}\xi / \int_0^1 f_0(\xi)\,\mathrm{d}\xi$ (the explicit functional dependence on α can be obtained from (B 1) in Appendix B with $b \to 1+\alpha$). The derivation of (2.2) through integration of the continuity equation (2.1*c*), suggests the use of the inner product $\langle \cdot | \cdot \rangle = \int_R^{R+h} \cdot \cdot \, r \, \mathrm{d}r$.

Considering next the streamwise momentum balance truncated at first order, the residual corresponding to a given weight function $w(r)$ is

$$\int_R^{R+h} \left(\partial_t u_x + u_x \partial_x u_x + u_r \partial_r u_x - \mathscr{L}(u_x) - 1 - \Gamma \left\{ \partial_{xxx} h + \partial_x K_{\mathrm{az}} \right\} \right) r w(r) \, \mathrm{d}r = 0 \,. \tag{4.7}$$

Substituting for u_x the projection (4.4) and truncating (4.7) at order ϵ, the fields $a_{m,n}$, $m, n \geqslant 1$, corresponding to the corrections to the uniform-film profile $f_{\alpha h}$, may enter into the calculation only through the evaluation of the zeroth order terms:

$$\int_R^{R+h} [\mathscr{L}(u_x) + 1]\, r w\,(r)\, \mathrm{d}r = [r(w\partial_r u_x - u_x w')]_R^{R+h} + \int_R^{R+h} [u_x\, \mathscr{L}(w) + w]\, r\, \mathrm{d}r. \quad (4.8)$$

The evaluation of these terms can be drastically simplified by demanding that the weight function satisfies

$$\mathscr{L}(w) = A \qquad \text{with} \qquad w(R) = 0, \quad w'(R+h) = 0, \quad (4.9)$$

where A is a constant, so that the integral $\int_R^{R+h} u_x\, \mathscr{L}(w)\, r \mathrm{d}r$ is proportional to the flow rate q. The system (4.9) is similar to (4.1) when $A = -1$, which reflects the fact that the operator $\mathscr{L}$ is self-adjoint with respect to the chosen inner product. Consequently, the choice $w \equiv u_{x,0}$ is the most appropriate, which corresponds precisely to the Galerkin method.

After truncation at $O(\epsilon)$ and use of the mass balance (2.2), which enables the substitution of $-\partial_x q/(1+\alpha h)$ for $\partial_t h$, equation (4.7) becomes:

$$\partial_t q = -F(\alpha h)\, \frac{q}{h}\, \partial_x q + G(\alpha h)\, \frac{q^2}{h^2}\, \partial_x h + I(\alpha h) \times \left[h - \frac{3}{\phi(\alpha h)}\, \frac{q}{h^2} + \Gamma h\, \{\partial_{xxx} h + \partial_x K_{\mathrm{az}}(\alpha h, \alpha)\} \right]. \quad (4.10)$$

Coefficients F, G and I are positive functions of αh defined in Appendix B, equation (B 1). The Nusselt solution is recovered in the uniform thickness limit, $\partial_t \to 0$, $\partial_x \to 0$, where

$$q = \frac{h^3}{3}\phi(\alpha h). \quad (4.11)$$

Notice the dependence of the azimuthal curvature K_{az} on both the aspect ratio αh and α. Nevertheless, the product $h\partial_x K_{\mathrm{az}}$ depends on αh only, a consequence of the averaging procedure across the film and the elimination of the pressure from the cross-stream component of the momentum equation. Hence, the planar geometry now corresponds to both limits $\alpha \to 0$ and $\alpha h \to 0$, when the condition $h_{\mathrm{N}} = O(1)$ is relaxed (in both cases the azimuthal curvature vanishes), unlike the full Navier–Stokes equations in (2.1).

The integral momentum balance (4.10) is similar to that obtained by Trifonov (1992) by averaging the first-order boundary-layer equation with a uniform weight and assuming a self-similar velocity distribution, $u_x = a_{0,0} u_{x,0}$. The coefficients F, G and I obtained by Trifonov are given in Appendix B, equation (B 2). However, the Trifonov model is not consistent at $O(\epsilon)$ since it does not account for the deviations of the velocity profile from the Nusselt profile $u_{x,0}$.

4.2. *Second-order model*

Although the first-order model (2.2), (4.10) is consistent at $O(\epsilon)$, it does not take into account important physical features such as the dispersion induced by the streamwise second-order viscous dissipative terms. These effects can be taken into account by extending the derivation process to $O(\epsilon^2)$. Starting from the second-order momentum balance (3.9), averaging with the weight $u_{x,0}$ and replacing $-\partial_x q/(1+\alpha h)$ with $\partial_t h$,

we obtain

$$\begin{aligned}\partial_t q = &-F(\alpha h)\,\frac{q}{h}\partial_x q + G(\alpha h)\,\frac{q^2}{h^2}\partial_x h \\ &+ I(\alpha h)\left[h - \frac{3}{\phi(\alpha h)}\frac{q}{h^2} + \Gamma h\left\{\partial_{xxx}h + \partial_x K_{\mathrm{az}}(\alpha h,\alpha)\right\}\right] \\ &+ J(\alpha h)\frac{q}{h^2}(\partial_x h)^2 - K(\alpha h)\frac{\partial_x q\,\partial_x h}{h} - L(\alpha h)\frac{q}{h}\partial_{xx}h \\ &+ M(\alpha h)\partial_{xx}q + \mathscr{K}(h,q,\alpha)\,. \end{aligned} \tag{4.12}$$

Comparing (4.12) to (4.10) shows that the additional terms taking into account the second-order effects have been collected in the last line row of (4.12). The first four terms in this line arise from the streamwise viscous dissipation, whereas $\mathscr{K}$ contains second-order inertial terms corresponding to the first-order corrections to the Nusselt velocity profile and is a rather complex function of q, h and their derivatives. Although the inclusion of these inertial terms ensures that the system (2.2), (4.12) is consistent at $O(\epsilon^2)$, the nonlinearities involved in $\mathscr{K}$ may drastically restrict the range of parameters for which solutions to (2.2), (4.12) exist and can be favourably compared to experimental data. Indeed, in the planar case, a 'regularization' procedure was necessary to avoid the presence of non-physical blow-ups of the time-dependent solutions due to second-order inertial terms even at moderate Reynolds numbers (Scheid, Ruyer-Quil & Manneville 2006). In fact, in the planar case, dropping the second-order inertial corrections leads to a simplified formulation which satisfactorily captures all physical mechanisms (Ruyer-Quil & Manneville 2000). For these reasons and to reduce the complexity of our second-order model, we neglect hereinafter the second-order inertial effects and set $\mathscr{K}=0$.

The expressions of the (positive) functions J, K, L and M accounting for the second-order streamwise viscous effects are given in Appendix B, equation (B 3). For $\alpha \ll 1$ (which as pointed out earlier in our average model is equivalent to $\alpha h \ll 1$), (B 1) and (B 3) give at $O(\alpha^2)$:

$$F(\alpha h) \approx \frac{17}{7} - \frac{1873}{1344}\alpha h + \frac{425623}{564480}\alpha^2 h^2 \approx 2.43 - 1.39\,\alpha h + 0.75\,\alpha^2 h^2, \tag{4.13a}$$

$$G(\alpha h) \approx \frac{9}{7} - \frac{9}{448}\alpha h - \frac{27423}{62720}\alpha^2 h^2 \approx 1.29\ - 0.02\,\alpha h - 0.44\,\alpha^2 h^2, \tag{4.13b}$$

$$\frac{3I(\alpha h)}{\phi(\alpha h)} \approx \frac{5}{2} - \frac{25}{24}\alpha h + \frac{1391}{2016}\alpha^2 h^2 \approx 2.5 - 1.04\,\alpha h + 0.69\,\alpha^2 h^2 \tag{4.13c}$$

$$I(\alpha h) \approx \frac{5}{6} + \frac{35}{72}\alpha h + \frac{47}{6048}\alpha^2 h^2 \approx 0.83 + 0.49\,\alpha h + 0.0078\,\alpha^2 h^2, \tag{4.13d}$$

$$J(\alpha h) \approx 4 + \frac{7}{12}\alpha h - \frac{1679}{1008}\alpha^2 h^2 \approx 4 + 0.58\,\alpha h - 1.67\,\alpha^2 h^2, \tag{4.13e}$$

$$K(\alpha h) \approx = \frac{9}{2} + \frac{21}{8}\alpha h - \frac{5641}{1120}\alpha^2 h^2 \approx 4.5 + 2.62\,\alpha h - 5.04\,\alpha^2 h^2, \tag{4.13f}$$

$$L(\alpha h) \approx 6 - \frac{1}{4}\alpha h + \frac{259}{240}\alpha^2 h^2 \approx 6 - 0.25\,\alpha h + 1.08\,\alpha^2 h^2, \tag{4.13g}$$

$$M(\alpha h) \approx \frac{9}{2} - \frac{15}{8}\alpha h + \frac{559}{224}\alpha^2 h^2 \approx 4.5 - 1.87\,\alpha h + 2.50\,\alpha^2 h^2, \tag{4.13h}$$

which can be contrasted with the result obtained by Roberts & Li (2006). These authors also eliminated the cross-stream variable dependence through a 'centre manifold' approach that led to a system of two evolution equations for the film thickness h and an averaged axial velocity $\langle u\rangle = q/h$. However, the procedure is cumbersome and was limited to $\alpha h_{\rm N} = O(\epsilon)$ (unlike the experiments by Kliakhandler *et al.* (2001) and Duprat *et al.* (2007) where $\alpha h_{\rm N} = O(1)$). Recasting this model (referred to hereinafter as the 'RL model') in terms of the film thickness h and flow rate q leads to a set of equations similar to (4.12) with

$$\left.\begin{array}{l} F = 2.504, \quad G = 1.356, \quad 3I/\phi = \pi^2/4 - \alpha h + 0.647\,\alpha^2 h^2 \\ I = \pi^2/12 + 0.4891\,\alpha h, \quad J = 3.459, \quad K = 3.353, \\ L = 4.676, \quad M = 4.093. \end{array}\right\} \tag{4.14}$$

The coefficients of the expansion (4.13) are close to those of the RL model (4.14) in spite of the differences between the two approaches.

Finally, in the planar limit, $\alpha = 0$, the second-order simplified model derived by Ruyer-Quil & Manneville (2000) is recovered from (4.12) with coefficients given by:

$$F = \tfrac{17}{7}, \quad G = \tfrac{9}{7}, \quad I = \tfrac{5}{6}, \quad 3I/\phi = \tfrac{5}{2}, \quad J = 4, \quad K = \tfrac{9}{2}, \quad L = 6, \quad M = \tfrac{9}{2}. \tag{4.15}$$

4.3. *Shkadov scaling*

Comparisons of the waves appearing on the surface of the film can be greatly simplified by introducing a scaling based on the uniform film thickness $h_{\rm N}$ and the average velocity of the uniform flow $u_{\rm N} = q_{\rm N}/h_{\rm N} = h_{\rm N}^2\phi(\alpha h_{\rm N})/3$. However, to avoid the introduction of a numerical coefficient 3, we shall use $3u_{\rm N} = h_{\rm N}^2\phi(\alpha h_{\rm N})$ instead. Our analysis is further simplified with the scaling first introduced by Shkadov for a film falling down a vertical plane (Shkadov 1977) which was used in § 3.1 (with this scaling, the number of parameters reduces to only one in the case of our first-order model as for the Trifonov model (Sisoev *et al.* 2006)): we introduce different length scales for the streamwise and cross-stream direction, $\kappa h_{\rm N}$ (or in terms of dimensional variables $l_S \sim \kappa \bar{h}_{\rm N}$ introduced in § 3.1) and $h_{\rm N}$, respectively. The parameter κ was defined in § 3.1.

Using the transformation $\mathscr{T} : [x \mapsto \kappa h_{\rm N} x, (y, h) \mapsto (h_{\rm N} y, h_{\rm N} h), t \mapsto t\kappa/[h_{\rm N}\phi(\alpha h_{\rm N})], (u, v) \mapsto (h_{\rm N}^2\phi(\alpha h_{\rm N})u, h_{\rm N}^2\phi(\alpha h_{\rm N})v/\kappa), q \mapsto (h_{\rm N}^3\phi(\alpha h_{\rm N})q]$, the mass conservation equation (2.2) and the averaged momentum balance (4.12) are

$$\partial_t h = -\frac{1}{1+\tilde{\alpha}h}\partial_x q, \tag{4.16a}$$

$$\begin{aligned} \delta\partial_t q = {} & \delta\left[-F(\tilde{\alpha}h)\,\frac{q}{h}\partial_x q + G(\tilde{\alpha}h)\,\frac{q^2}{h^2}\partial_x h\right] + \frac{I(\tilde{\alpha}h)}{\phi(\tilde{\alpha})}\left[-\frac{3\phi(\tilde{\alpha})}{\phi(\tilde{\alpha}h)}\frac{q}{h^2}\right. \\ & \left. + h\left\{1 + \partial_{xxx}h + \frac{\beta}{(1+\tilde{\alpha}h)^2}\partial_x h - \frac{1}{2}\partial_x\left(\frac{\tilde{\alpha}}{1+\tilde{\alpha}h}(\partial_x h)^2\right)\right\}\right] \\ & + \eta\left[J(\tilde{\alpha}h)\frac{q}{h^2}(\partial_x h)^2 - K(\tilde{\alpha}h)\frac{\partial_x q\,\partial_x h}{h} - L(\tilde{\alpha}h)\frac{q}{h}\partial_{xx}h + M(\tilde{\alpha}h)\partial_{xx}q\right], \end{aligned} \tag{4.16b}$$

where the parameter set $(h_{\rm N}, \Gamma, \alpha)$ has been replaced by $(\delta, \eta, \tilde{\alpha})$ corresponding to a reduced Reynolds number,

$$\delta \equiv \frac{h_{\rm N}^3\phi(\alpha h_{\rm N})}{\kappa} = \frac{3Re}{\kappa}, \tag{4.17}$$

a viscous dispersion parameter (this term will be clarified in § 5.3),

$$\eta \equiv 1/\kappa^2 = We^{-2/3} = (\bar{h}_{\rm N}/l_c)^{4/3}, \tag{4.18}$$

and the aspect ratio,

$$\tilde{\alpha} \equiv \alpha h_{\rm N} = h_{\rm N}/R\,. \tag{4.19}$$

The parameter η appears along with streamwise dissipative terms which contribute to the dispersion of the waves as discussed later on.

Besides the introduction of the parameters δ, $\tilde{\alpha}$ and η in equation (4.16*b*), the transformation $\mathscr{T}$ modifies the coefficient I to $I/\phi(\tilde{\alpha})$, which results from our choice of the time scale $h_{\rm N}^2\phi(\alpha h_{\rm N})$. Similarly, the expression (4.11) of the flow rate at $O(1)$ becomes

$$q = \frac{h^3}{3}\frac{\phi(\tilde{\alpha}h)}{\phi(\tilde{\alpha})}, \tag{4.20}$$

so that $h=1$ corresponds to $q=1/3$ with this scaling. Finally, we have isolated the main contribution from the azimuthal curvature gradient, where the parameter

$$\beta = \tilde{\alpha}^2/\eta = (\bar{h}_{\rm N}/\bar{R})^{2/3}(l_c/\bar{R})^{4/3} \tag{4.21}$$

defined by Kalliadasis & Chang (1994) appears. This parameter expresses the relative importance of axial and azimuthal curvature effects. Note that the planar geometry is recovered from the rescaled boundary-layer equations (4.16) in the limit $\tilde{\alpha} \to 0$ which also makes $\beta \to 0$ (the azimuthal curvature term vanishes in this limit).

4.4. *Inertialess limit*

For highly viscous fluids or very thin films and since $\tilde{\alpha}$ is at most $O(1)$ (for very thin films $\tilde{\alpha} = O(1)$ implies that the fibre is very thin also) so that $\phi(\tilde{\alpha})$ is at most of $O(1)$, $Re \to 0$ or equivalently $\delta \to 0$. Further, by neglecting the viscous second-order terms, $\eta = 0$, (4.16*b*) gives an expression for q in terms of h which when substituted into (4.16*a*) leads to a single evolution equation for h written in conservative form:

$$\partial_t\left(h + \frac{\tilde{\alpha}}{2}h^2\right) + \partial_x\left[\frac{h^3}{3}\frac{\phi(\tilde{\alpha}h)}{\phi(\tilde{\alpha})}\left(1 + \frac{\beta}{(1+\tilde{\alpha}h)^2}\partial_x h + \partial_{xxx}h\right)\right] = 0\,. \tag{4.22}$$

$h + (\tilde{\alpha}/2)h^2$ corresponds to the volume of fluid contained in a sector of angle $\mathrm{d}\theta$ and axial length $\mathrm{d}x$, that is the ratio of the surface of a planar section to the perimeter of the fibre. Equation (4.22) is very close to the evolution equation derived by Kliakhandler *et al.* (2001) and was studied numerically by Craster & Matar (2006). However, the derivation of Kliakhandler *et al.* (2001) contains an *ad-hoc* step, i.e. the retention of the full curvature term, $[1+(\partial_x h)^2]^{-3/2}[\partial_{xx}h - \{\tilde{\alpha}/[\eta(1+\tilde{\alpha}h)]\}(1+\eta(\partial_x h)^2)]$, instead of its lower-order expression, $\partial_{xx}h - \tilde{\alpha}/[\eta(1+\tilde{\alpha}h)]$. Hereinafter we refer to equation (4.22) as the 'CM equation' ((4.22) differs from the Craster–Matar equation only in the choice of scalings) and to (4.22) with the full curvature term as the 'KDB equation'.

For thick enough fibres, that is $\tilde{\alpha} \to 0$, equation (4.22) reduces to

$$\partial_t h + \partial_x\left[\frac{h^3}{3}(1 + \beta\partial_x h + \partial_{xxx}h)\right] = 0, \tag{4.23}$$

which is the equation derived initially by Frenkel (1992) and used by Kalliadasis & Chang (1994).

5. Linear stability analysis

5.1. *Dispersion relations*

We now examine the linear stability of the Nusselt flow. We first present the simplest dispersion relations obtained in the inertialess limit and studied by Kliakhandler *et al.* (2001) and Duprat *et al.* (2007).

The normal mode decomposition $h = 1 + \varepsilon h_1 \exp[\mathrm{i}(kx - \omega t)]$, $\varepsilon \ll 1$, of both the KDB equation and CM equation (4.22) where k and ω the wavenumber and wave frequency, respectively, leads to the dispersion relation,

$$\omega = k\, c_k(\tilde{\alpha}) + \frac{\mathrm{i}\,\mathrm{k}^2}{3(1+\tilde{\alpha})}\left(\frac{\beta}{(1+\tilde{\alpha})^2} - k^2\right), \tag{5.1}$$

where c_k is the speed of the linear kinematic wave solutions of (4.22) for small wavenumbers, i.e. in the limit $k \to 0$,

$$c_k = \frac{1}{1+\tilde{\alpha}}\left[1 + \frac{\tilde{\alpha}\phi'(\tilde{\alpha})}{3\phi(\tilde{\alpha})}\right] = \frac{8(b-1)\left(2\log(b)b^2 - b^2 + 1\right)}{3\left(4\log(b)b^4 - 3b^4 + 4b^2 - 1\right)}, \tag{5.2}$$

with $b = 1 + \tilde{\alpha}$.

For $\tilde{\alpha} \ll 1$, in which case the Frenkel evolution equation (4.23) applies, we obtain

$$\omega = k + \frac{\mathrm{i}\,\mathrm{k}^2}{3}\left(\beta - k^2\right). \tag{5.3}$$

Notice that the dispersion relation (5.3) can be recovered from (5.1) through the transformation (Duprat *et al.* 2007)

$$k \to k\,[c_k(1+\tilde{\alpha})]^{1/3}, \quad \omega \to \omega c_k^{4/3}(1+\tilde{\alpha})^{1/3}, \quad \beta \to \beta\, c_k^{2/3}(1+\tilde{\alpha})^{8/3}, \tag{5.4}$$

which leads to the definition of the composite parameter $\beta^\star = \beta\, c_k^{-2/3}(1+\tilde{\alpha})^{-8/3}$.

The parameters β and $\beta^\star$ can be related to the ratio of the characteristic time of advection of a structure over its length and the characteristic time of growth of this structure. Considering the dispersion relation (5.3), the RP instability selects structures whose length closely corresponds to the wavenumber with the maximum temporal growth rate, i.e. $k = \sqrt{\beta/2}$. The ratio of the characteristic time of advection of these structures τ_a to their characteristic time of growth τ_g is

$$\tau_a/\tau_g = \omega_i/\omega_r|_{k=\sqrt{\beta/2}} = \frac{\beta^2}{12}\sqrt{\frac{2}{\beta}} \propto \beta^{3/2}. \tag{5.5}$$

Similarly, in the case of dispersion relation (5.1), the maximum of the temporal growth rate corresponds to $k = \sqrt{\beta}/[\sqrt{2}(1+\tilde{\alpha})]$ and we have

$$\tau_a/\tau_g = \omega_i/\omega_r|_{k=\sqrt{\beta}/[\sqrt{2}(1+\tilde{\alpha})]} = \frac{\beta^2}{12(1+\tilde{\alpha})^5}\frac{\sqrt{2}(1+\tilde{\alpha})}{c_k\sqrt{\beta}} \propto (\beta^\star)^{3/2}, \tag{5.6}$$

and therefore β and $\beta^\star$ compare the advection process at the speed of the kinematic waves to the growth of the RP instability.

The dispersion relations (5.1) and (5.3) cannot account for the K-instability mechanism prompted by inertia. Turning back to the two-equation model (4.16), close to the Nusselt solution we set $h = 1 + \tilde{h}$ and $q = 1/3 + \tilde{q}$ where $\tilde{h} \ll 1$ and $\tilde{q} \ll 1$ and we obtain a single equation for $\tilde{h}$ after elimination of $\tilde{q}$ that we purposely split

into two parts by separating odd and even derivatives,

$$3(1+\tilde{\alpha})\frac{I}{\phi}\left[\partial_t + c_k\partial_x\right]\tilde{h} - \eta\left[\frac{L}{3}\partial_{xxx} + (1+\tilde{\alpha})M\partial_{txx}\right]\tilde{h} = \lambda, \qquad (5.7a)$$

$$\left\{\delta(1+\tilde{\alpha})\left[\partial_{tt} + \frac{F}{3}\partial_{tx}\right] + \left[\delta\frac{G}{9} + \frac{\beta}{(1+\tilde{\alpha})^2}\frac{I}{\phi}\right]\partial_{xx}\right\}\tilde{h} + \frac{I}{\phi}\partial_{xxxx}\tilde{h} = -\lambda, \qquad (5.7b)$$

where the coefficients F, G, I, L, M and ϕ are evaluated at $\tilde{\alpha}$. The symbol c_k again denotes the speed (5.2) of the kinematic waves in the limit $k \to 0$. The normal mode decomposition $\tilde{h} = h_1 \exp[\mathrm{i}[k\,x - \omega\,t]$ in (5.7), leads to the dispersion relation:

$$D(k,\omega) \equiv \mathrm{i}\left\{3(1+\tilde{\alpha})\frac{I}{\phi}\left[c_k k - \omega\right] + \eta k^2\left[k\frac{L}{3} - \omega(1+\tilde{\alpha})M\right]\right\}$$
$$+\delta(1+\tilde{\alpha})\left[-\omega^2 + \frac{F}{3}\omega k\right] - k^2\left[\delta\frac{G}{9} + \frac{\beta}{(1+\tilde{\alpha})^2}\frac{I}{\phi}\right] + k^4\frac{I}{\phi} = 0\,. \qquad (5.8)$$

The reason now for splitting (5.7) into two parts becomes clear: the split corresponds to a phase shift of $\pi/2$ in (5.8) between two parts of this equation. The marginal stability of the film is then achieved when the two parts are set to zero independently.

5.2. *Influence of viscous dissipation on the RP-instability*

The instability mechanism of a liquid layer coating a cylinder is similar to the instability of a liquid jet as explained by Rayleigh (1878) in his seminal work. Considering the inertialess limit $\delta \to 0$, (5.8) reduces to the dispersion relation (5.1) of both the KDB and CM evolution equations augmented with the second-order viscous effects $\propto \eta k^2$. Since in the absence of these effects, linear wave solutions to (5.1) travel at the speed c_k of the kinematic waves, the effect of second-order viscous terms can be estimated by substituting kc_k for ω except for the 'critical term' $c_k k - \omega$ (Whitham 1974). We obtain

$$\omega = k\,c_k(\tilde{\alpha}) - \eta\Upsilon_\eta(\tilde{\alpha})k^3 + \frac{\mathrm{i}\,\mathrm{k}^2}{3(1+\tilde{\alpha})}\left(\frac{\beta}{(1+\tilde{\alpha})^2} - k^2\right), \qquad (5.9)$$

where $\Upsilon_\eta = \phi[(1+\tilde{\alpha})Mc_k - L/3]/[3(1+\tilde{\alpha})I]$ is a positive function of $\tilde{\alpha}$.

The marginal stability of the film is therefore still given by $k_{\mathrm{RP}} = \sqrt{\beta}/(1+\tilde{\alpha})$ which corresponds to the classical result for the RP instability that the neutral dimensional wavelength $2\pi(R + \bar{h}_N)$ is proportional to the maximum diameter of the liquid layer. However, second-order viscous terms have a dispersive effect on the waves by decreasing the speed of the linear waves from c_k to $c_k - \eta\Upsilon_\eta(\tilde{\alpha})k^2$.

5.3. *Mechanism of the K instability mode*

We now consider the limit of non-dominant RP instability mode (β/δ and $\tilde{\alpha}$ sufficiently small). In this case the instability results from the K hydrodynamic mechanism.

First, let us extend to our problem the arguments given by Ooshida (1999) in the framework of Whitham wave-hierarchy theory (Whitham 1974) for the planar geometry, and let us consider small wavenumbers, $k \to 0$, for which both surface tension and second-order viscous effects can be neglected. The linear operator of (5.7*b*) can be thus factorized corresponding to waves propagating at speeds $c_{d\pm}$:

$$c_{d\pm} = \frac{F}{6} \pm \sqrt{\Delta} \qquad \text{with} \qquad \Delta = \frac{F^2}{36} - \frac{1}{9}\frac{G}{1+\tilde{\alpha}} - \frac{\beta}{\delta(1+\tilde{\alpha})^3}\frac{I}{\phi}\,. \qquad (5.10)$$

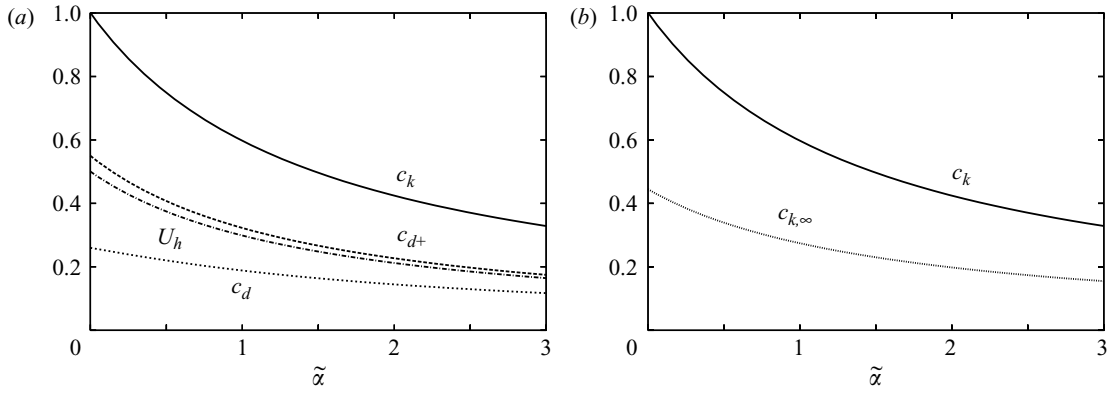

FIGURE 2. (*a*) Speeds c_k of kinematic and $c_{d\pm}$ of dynamic waves as functions of the aspect ratio $\tilde{\alpha} = h_N/R$ in the limit of negligible viscous dispersion and large Reynolds number ($\eta \to 0$ and $\beta/\delta \to 0$). The interfacial velocity $U_h = f_{\tilde{\alpha}}(1)/\phi(\tilde{\alpha})$ of the uniform thickness base flow is also displayed. (*b*) Comparison of the speeds of the kinematic waves in the limit $\eta \to 0$ and $\eta \to \infty$.

In this limit, system (5.7) has a two-wave structure that can be recast into a second-order wave equation,

$$3\frac{I}{\phi}\left[\partial_t + c_k\partial_x\right]\tilde{h} + \delta\left[\partial_t + c_{d-}\partial_x\right]\left[\partial_t + c_{d+}\partial_x\right]\tilde{h} = 0, \tag{5.11}$$

a situation that corresponds precisely to the wave hierarchy considered by Whitham. The lower-order waves propagating at speed c_k are kinematic waves whose origin is the response to a deformation of the interface to satisfy the kinematic condition (2.1*g*), or equivalently the mass balance (2.2), when the velocity distribution is governed by the balance of the acceleration due to gravity and the wall friction, which in turn leads to the explicit dependence (4.20) of the flow rate q on the film thickness h. Propagating at speed $c_{d\pm}$, the higher-order waves are dynamic waves corresponding to the response of the film to the variation of momentum induced by a deformation of the free surface. Alekseenko, Nakoryakov & Pokusaev (1985) and Ooshida (1999) have similarly derived equations presenting a 'two-wave' structure for the vertical-planar wall geometry. However, these authors did not consider the influence of the streamwise viscous diffusion that is taken into account in (5.7).

Whitham has shown that when a multi-speed equation such as (5.11) holds, an instability occurs whenever the constraint,

$$c_{d-} \leqslant c_k \leqslant c_{d+}, \tag{5.12}$$

is violated, in other words, whenever the speed of the kinematic waves is outside the speed interval allowed to dynamic waves. Figure 2(*a*) compares the speed of the kinematic and dynamics waves given by (5.2) and (5.10) as a function of the aspect ratio $\tilde{\alpha}$ in the limit of dominating inertia ($\beta/\delta \to 0$). Kinematic waves always travel faster than dynamic waves and the stability criterion (5.12) is never satisfied in that case. Small but finite values of β/δ lower the speed of the faster dynamic waves, c_{d+}. Therefore, azimuthal surface-tension effects are destabilizing and the Nusselt constant-thickness solution is always unstable in the limit $k \to 0$. The speeds of kinematic and dynamic waves are compared to the interfacial velocity of the base flow $U_h = f_{\tilde{\alpha}}(1)/\phi(\tilde{\alpha})$ in figure 2(*a*). The fastest dynamic waves travel at a speed which is close to the maximum velocity of the base flow, which indicates that perturbations

of the momentum are basically advected by the flow. Consequently, as in the planar case, the K mode of instability results from the ability of the kinematic waves to move much faster than any fluid particle (Smith 1990).

For finite wavenumbers, second-order viscous terms must be accounted for and the speed of kinematic waves is modified into:

$$c_{k,\eta} = \frac{c_k + \eta k^2 \dfrac{\phi}{9(1+\tilde{\alpha})}\dfrac{L}{I}}{1 + \eta k^2 \dfrac{\phi}{3}\dfrac{M}{I}}. \tag{5.13}$$

The dispersive effect of second-order viscous effects on kinematic waves is evident as $c_{k,\eta}$ is a function of ηk^2 (contained in two terms, one in the numerator due to transport of momentum and one in the denominator due to transport of mass). This justifies the term 'viscous dispersion parameter' introduced for η in § 4.3 and we shall also refer to second-order viscous effects as 'viscous dispersion effects'. Considering real wavenumbers, the limit $\eta \to \infty$ gives

$$c_{k,\infty} \equiv \lim_{\eta\to\infty} c_{k,\eta} = \frac{L}{3(1+\tilde{\alpha})M}, \tag{5.14}$$

which is compared to the small-wavenumber limit c_k in figure 2(*b*). Since $c_{k,\infty} < c_{k,\eta} < c_k$, viscous dispersion lowers the speed of the kinematic waves, as observed when the RP mode is dominant (cf. § 5.2), and is therefore stabilizing.

Similarly, axial surface tension modifies the speed of dynamic waves into

$$c_{d\pm ST} = \frac{F}{6} \pm \sqrt{\Delta_{ST}} \qquad \text{with} \qquad \Delta_{ST} = \frac{F^2}{36} - \frac{1}{9}\frac{G}{1+\tilde{\alpha}} + \frac{1}{\delta(1+\tilde{\alpha})}\frac{I}{\phi}\left[k^2 - \frac{\beta}{(1+\tilde{\alpha})^2}\right]. \tag{5.15}$$

Hence, axial surface tension effects accelerate the fastest dynamic waves and tend to stabilise the constant-thickness Nusselt flow.

5.4. *Marginal stability*

Having considered the two limiting cases of dominant RP and K instability modes, let us turn to the marginal stability of the Nusselt flow (ω and k real) as a test of the validity of our modelling approach in comparison with the solutions to the linearized primitive equations. Linearization of the Navier–Stokes equations (2.1) leads to the Orr–Sommerfeld (OS) equation, i.e. a fourth-order ordinary differential equation for the complex streamfunction $\psi(r)$ completed with the linearized stress balances and the no-slip/no-penetration condition at the fibre. The OS equation was solved numerically by using the continuation software AUTO97 (Doedel *et al.* 1997). The starting points for the continuation are the analytical expressions of the solutions in the limit $k \to 0$.

In figure 3, the marginal stability curves corresponding to model (4.16) (upper dashed lines) are compared to those obtained from the Trifonov model (upper thin solid lines) and the OS equation (upper thick solid lines) in the (k_r, δ)-plane. The fluids are Rhodorsil silicon oil v50 ($\rho = 963\,\mathrm{kg\,m^{-3}}$, $\nu = 50 \times 10^{-6}\,\mathrm{m^2\,s^{-1}}$ and $\sigma = 20.8 \times 10^{-3}\,\mathrm{N\,m^{-1}}$; water: $\rho = 998\,\mathrm{kg\,m^{-3}}$, $\nu = 10^{-6}\,\mathrm{m^2\,s^{-1}}$ and $\sigma = 72.5 \times 10^{-3}\,\mathrm{N\,m^{-1}}$), corresponding to Kapitza numbers $\Gamma = 5.48$ and 3376, respectively. Two radii R have been chosen so that they correspond to the same ratio $R/l_c = 0.24$ (for water, $l_c = 2.7$ mm, and for silicon oil v50, $l_c = 1.5$ mm).

As surface tension damps short waves, the regions of stability (labelled 'S') are located above the marginal stability curves. At small values of δ, the RP instability

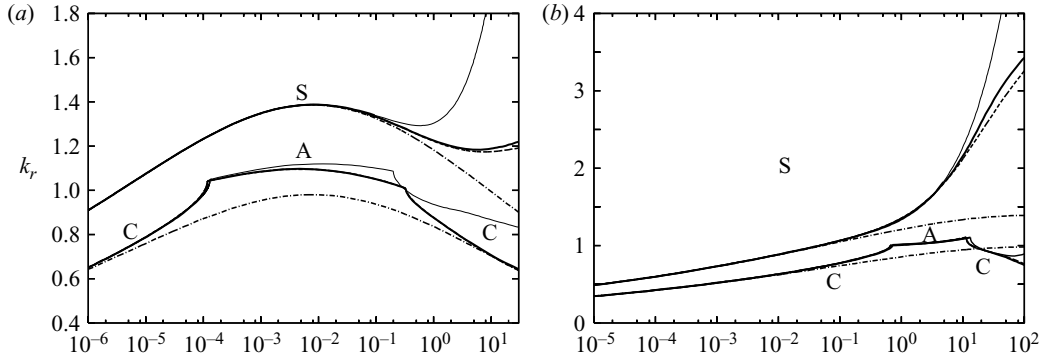

FIGURE 3. Neutral stability curves (upper lines) and loci of the spatially most amplified harmonic perturbations (for convectively unstable flows, C) and of the absolute wavenumber (in the absolutely unstable case, A). The real part of the wavenumber k_r is shown as a function of the reduced Reynolds number δ. Linear stable regions are labelled S. Fluid parameters correspond to (*a*) Rhodorsil silicon oil v50 ($\Gamma = 5.48$) and $R = 0.35$ mm, (*b*) water ($\Gamma = 3376$) and $R = 0.64$ mm. Thick solid and dashed lines refer to OS analysis and to dispersion relation (5.8), respectively (nearly superimposed except for the largest values of δ). Thin solid lines refer to the linear stability analysis of the Trifonov model. The neutral wavenumber k_{RP} and the temporally most amplified wavenumber $k_{\mathrm{RP}}/\sqrt{2}$ of the RP instability (see text) are indicated by dashed-dotted lines.

dominates and all marginal stability curves collapse with $k_r = k_{\mathrm{RP}}$ (dashed-dotted lines). Noticeable differences are observed only at δ above 0.1 for which the hydrodynamic K mode starts to take over. At large values of δ, the marginal curve corresponding to (4.16) remains remarkably close to the OS results, whereas the Trifonov model overestimates the range of unstable wavenumbers. This large discrepancy is mainly a consequence of neglecting the streamwise dissipation terms. As the Kapitza number increases, hence the viscous dispersion parameter η decreases, the marginal stability curve predicted by the Trifonov model is closer to the OS results (compare figures 3*a* and 3*b*). The same trend can be observed with the speed of neutral infinitesimal waves displayed in figure 4(*a*). Neutral wave solutions to the Trifonov model and to (4.16) are kinematic waves travelling at speeds c_k and $c_{k,\eta}$ defined in (5.2) and (5.13), respectively. The agreement of $c_{k,\eta}$ with the speeds of neutral waves solutions of the OS equations is again remarkable.

5.5. *Spatial stability analysis*

Another test of the accuracy of model (4.16) consists of the analysis of the response of the base flow to a localized perturbation. If the resulting wavepacket is advected by the flow, the instability is said to be convective and the flow behaves much like a signal amplifier: at a fixed point in the laboratory frame of reference, the signal eventually dies out if it is not sustained continuously. When the wavepacket is able to move upstream, a self-sustained intrinsic dynamics or 'global mode' can be observed and the flow behaves like an 'oscillator' (Huerre & Rossi 1998). At a given location, the long-time evolution of the wavepacket is dominated by the part of the signal whose energy remains stationary, hence by the wave corresponding to a zero group velocity, $v_g = \partial\omega/\partial k = 0$, which defines the absolute wavenumber k_0 and frequency ω_0. In the complex k-plane, the condition $v_g = 0$ occurs at a saddle point that must result from the collision of two spatial branches coming from opposite sides of the real axis in order to fulfil the causality condition (Huerre & Rossi 1998).

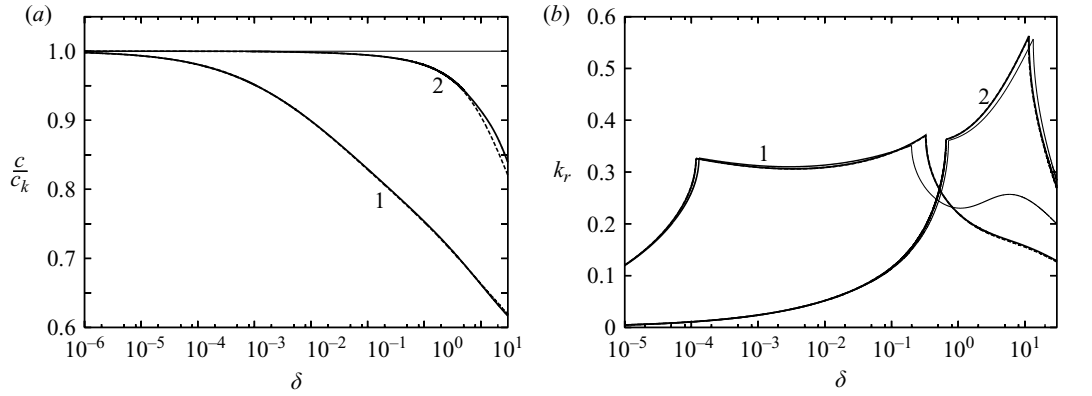

FIGURE 4. (*a*) Wave speed c of linear neutral waves normalized with the speed of the kinematic waves c_k and (*b*) spatial growth rate of the most amplified perturbations (convective case, C) and of the absolute wavenumber (absolutely unstable region, A) as function of δ. Thick solid and dashed lines refer to the OS analysis and to dispersion relation (5.8) whereas thin solid lines are obtained from the Trifonov model. Labels 1 and 2 correspond to Rhodorsil silicon oil v50 ($\Gamma = 5.48$ and $R = 0.35$ mm) and to water ($\Gamma = 3376$ and $R = 0.64$ mm), respectively. See also the caption of figure 3. The increased deviation of the wave speed in (*a*) from unity is a dispersive effect.

The wavenumber k_r of the most spatially amplified perturbation in the convective case and the absolute wavenumber k_{0r} are shown in figure 3(*a*) and are compared to $k_{\mathrm{RP}}/\sqrt{2}$ which corresponds to the most temporally amplified perturbation for dispersion relation (5.1). The corresponding growth rates $-k_i$ and $-k_{0i}$ are shown in figure 4(*b*). In the limit $\delta \to 0$, all curves converge to $k_r = k_{\mathrm{RP}}/\sqrt{2}$, which is unexpected since the latter corresponds to a temporal stability analysis instead of a spatial one. This limit corresponds to a vanishingly small film thickness, for which both the group velocity v_g and the phase velocity c_k are nearly equal to one and dispersion effects from inertia and viscosity are negligible since $\eta \propto \Gamma h_{\mathrm{N}}^{4/3}$. As $h_{\mathrm{N}} \ll R$, the growth rate is also small and the Gaster transformation, $v_g \approx -\omega_i/k_i$, between temporally and spatially increasing disturbances applies (Gaster 1962). Surprisingly, the wavenumbers k_r of the most amplified spatial perturbations stay close to $k_{\mathrm{RP}}/\sqrt{2}$ even at large values of δ. A remarkable agreement is again observed between results from the model (4.16) and the OS analysis, whereas the Trifonov model, which neglects the stabilizing second-order viscous effects, overestimates the spatial growth rate at large δ for silicon oil.

The RP instability mechanism results from the competition of axial and azimuthal surface-tension effects, irrespective of the presence of a flow. Instead, the K mode results from the competition of dynamic and kinematic waves whose existence is strongly linked to the flow. This explains the fact that the RP mode may trigger an absolute instability (Duprat *et al.* 2007), whereas a film falling down an inclined planar wall can only be convectively unstable (Brevdo *et al.* 1999). The C/A transition from a convective to an absolute instability corresponds to a real absolute frequency. In the inertialess limit, the C/A transition occurs at $\beta = \beta_{ca} \approx 1.507$ for the dispersion relation (5.3) to the Frenkel equation (4.23). Based on the transformation (5.4) from dispersion relation (5.1) to (5.3), we can infer that the C/A transition predicted by the CM equation (4.22) occurs at $\beta^\star = \beta_{ca}$. At a given value of R/l_c, $\beta^\star$ which compares axial and azimuthal curvatures to the advection by the kinematic waves, reaches a maximum at $\tilde{\alpha} \approx 0.44$ and tends to zero as $\tilde{\alpha} \to \infty$. Figure 5(*a*) shows the contour line

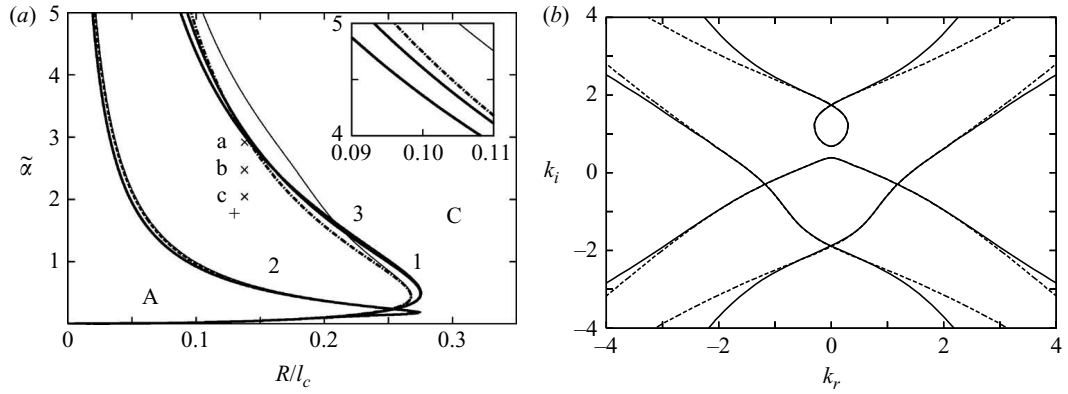

FIGURE 5. (*a*) Absolute A and convective C instability regions in the $(\tilde{\alpha}, \bar{R}/l_c)$ parameter plane for silicon oil v50 ($\Gamma = 5.48$, labelled 1), water ($\Gamma = 3376$, labelled 2) and castor oil ($\Gamma = 0.45$, labelled 3). The dashed-dotted line corresponds to the C/A boundary $\beta^\star = \beta_{ca} \approx 1.507$ for the CM equation (4.22). It is not affected by changing the fluid properties and hence it is the same for the three fluids. The inset is an enlargement of the upper end of the curves. (*b*) Spatial branches in the complex k-plane for silicon oil v50, $q_N = 0.01$ g s^{-1}, $\bar{R} = 0.2$ mm and $\omega_{0i} = 0.126$ (indicated by a + in (*a*): $\delta = 0.1874$, $\tilde{\alpha} = 1.72$, $\eta = 0.143$). Thick solid, thick dashed and thin solid lines refer to the OS analysis, to the dispersion relation (5.8) and to the dispersion relation of the Trifonov model respectively. Values of $\tilde{\alpha}$ and $\bar{R}/l_c$ corresponding to the experiments by Kliakhandler *et al.* (2001) are indicated by crosses. All three experiments and the example shown in (*b*) and indicated by a + in (*a*) are absolutely unstable flows.

$\beta^\star = \beta_{ca}$ in the $(R/l_c, \tilde{\alpha})$-plane along with the C/A transition loci obtained from OS and the dispersion relation (5.8). For $R > 0.28 l_c$, the instability is always convective, whereas for $R < 0.28 l_c$, there is an intermediate range of aspect ratios $\tilde{\alpha}$, or film thicknesses, for which an absolute instability can be observed. As we pointed out in §4, for our low-dimensional models the limit of very small thicknesses $h_N \ll R$ corresponds to the planar case (the same is not true for full Navier–Stokes, however, the linear stability characteristics for $h_N \ll R$ obtained from OS are the same to those of the planar limit) for which it is well known that the instability is always convective, and the RP instability is weakened at large thicknesses $h_N \gg R$ by the decrease of the total curvature $(R + h_N)^{-1}$. C/A boundaries predicted by the dispersion relation (5.8) nearly coincide with the OS results, discrepancies being noticeable only for water and for large thicknesses ($\tilde{\alpha} \gg 1$).

For less viscous fluids and higher Kapitza numbers, for example water ($\Gamma = 3376$), the C/A boundaries are shifted significantly downwards, a direct consequence of the higher influence of the hydrodynamic K mode since large values of the aspect ratio $\tilde{\alpha}$ correspond also to large values of the reduced Reynolds number δ. However, the C/A boundary $\beta^\star = \beta_{ca}$ given by the CM equation remains unchanged as this equation does not account for the hydrodynamic K mode and hence it is the same when the working fluid changes, for example from a highly viscous liquid, such as silicone oil, to a relatively inviscid liquid, such as water. The influence of the K mode on the absolute instability can also be noted in figure 3(*b*) where the wavenumber k_r corresponding to the maximum growth rate $-k_i$ of spatially amplified perturbations (real ω) in the convective case and to k_{0r} in the absolute case are depicted. The Nusselt flow is absolutely unstable for relatively high values of δ for which a significant discrepancy between the OS marginal curve and the inertialess limit $k = k_{RP}$ is observed, thus indicating the influence of the K mode.

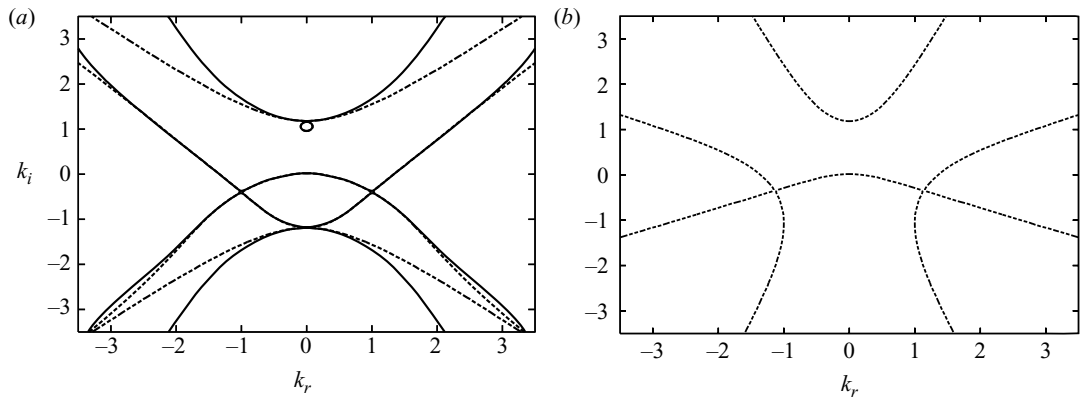

FIGURE 6. Spatial branches in the complex k-plane for castor oil $q_N = 0.021\ \mathrm{g\,s^{-1}}$, $\bar{R} = 0.25$ mm and $\omega_i = 0.006$ ($\delta = 0.052$, $\tilde{\alpha} = 2.91$ and $\eta = 0.30$). (*a*) Model (2.2), (4.12); (*b*) CM equation (4.22). Solid lines refer to the OS analysis. Dashed lines in (*a*) and (*b*) refer to the dispersion relations (5.8) and (5.1), respectively.

Let us now focus on the details of the branches of solutions in the complex k-plane. Figure 5(*b*) shows an example of pinching of branches of solutions for the model dispersion relation (5.8) compared to the OS result for a moderately viscous fluid. Chosen parameters correspond to a flow of silicon oil v50 ($\Gamma = 5.48$) on a fibre of radius $R = 0.2$ mm. At small values of $|k|$ the curves are practically indistinguishable. Solutions to (5.8) start to deviate from OS as $|k|$ increases. This remarkable agreement can be understood by considering the derivation of the momentum balance (4.12). Since the neglected second-order inertial corrections $\mathscr{K}(h, q, \alpha)$ are all nonlinear terms, the corresponding dispersion relation (5.8) is exact up to $O(|k|^2)$. For highly viscous fluids and small Kapitza numbers, such as the castor oil used by Kliakhandler *et al.* (2001) ($\nu = 440 \times 10^{-6}\ \mathrm{m^2\,s^{-1}}$, $\rho = 961\ \mathrm{kg\,m^{-3}}$ and $\sigma = 31 \times 10^{-3}\ \mathrm{N\,m^{-1}}$ hence $\Gamma = 0.45$), an excellent agreement between the results of the OS analysis and the dispersion relation (5.8) is again achieved (see figure 6(*a*) where an example of pinching of k-branches is given). This could have been expected since in that case the inertialess limit $\delta \to 0$ is perfectly admissible. However, the spatial branches of solutions to the dispersion relation (5.1) corresponding to the CM evolution equation (4.22) show large discrepancies with the results to the OS analysis (compare figure 6*b* to figure 6*a*). These topological differences must be attributed to the second-order viscous dispersion terms that are also neglected in the derivation of the CM equation ($\eta \to 0$).

6. Travelling waves

The experimental response of the flow to a periodic inlet perturbation remains periodic in time at each location in space. Consequently, the integration in time of the mass balance (2.2) gives $\partial_x \langle q \rangle = 0$ where the brackets denote averaging over a temporal period. $\langle q \rangle$ is thus conserved all along the fibre and is equal to its value at the inlet which gives the condition $\langle q \rangle = 1/3$. Travelling waves (TW) of (4.16) are computed with the continuation software AUTO97 (Doedel *et al.* 1997) enforcing the above integral condition on the flow rate at each step of the continuation. The bifurcation diagrams of TW solutions to the two-equation model (4.16) and to the CM equation (4.22) are compared in figure 7(*a*). The parameters in the figure correspond to 'regime b' reported by Kliakhandler *et al.* (see table 1). Figure 7(*b*)

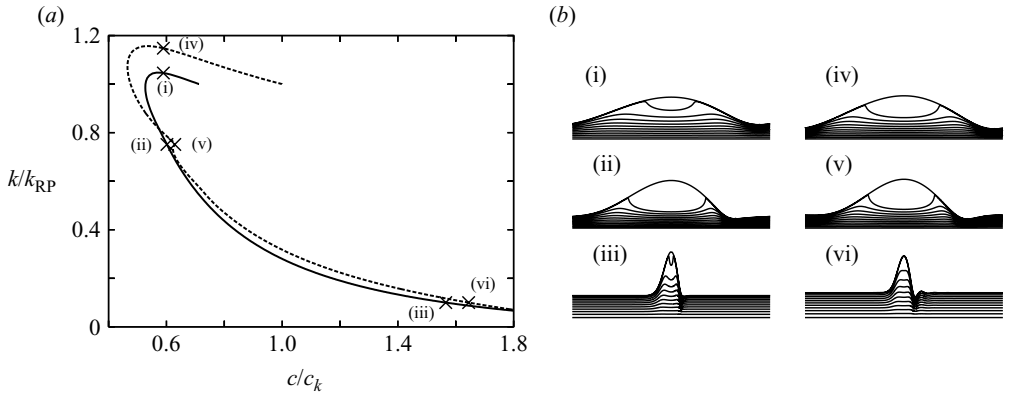

FIGURE 7. (*a*) Speed c of TW solutions as function of their wavenumber k. Parameters correspond to the experimental conditions of Kliakhandler *et al.* (2001) (regime 'b' in table 1, $\delta = 0.024$, $\eta = 0.24$, $\tilde{\alpha} = 2.47$). Solid and dashed lines refer to (4.16) and to the CM equation (4.22), respectively. (*b*) Wave profiles and streamlines in the moving frame for solutions indicated by crosses in (*a*); left: solutions to (4.16); right: solutions to (4.22).

Model	Regime	q_{N} (mg s^{-1})	h_{N} (mm)	λ (mm)	c_{expt} (mm s^{-1})	c (mm s^{-1})	$h_{\mathrm{max}}^{\mathrm{expt}}$ (mm)	h_{max} (mm)	$h_{\mathrm{min}}^{\mathrm{expt}}$ (mm)	h_{min} (mm)
(4.16)	a	21	0.73	30	25	22.4	1.47	1.34	0.50	0.44
(4.22)						24.7		1.26		0.45
(4.16)	b	11	0.62	6.2	5.4	7.22	1.02	0.92	0.20	0.17
(4.22)						6.98		0.97		0.14
(4.16)	c	5.3	0.51	36	12.0	12.1	1.20	1.09	0.25	0.26
(4.22)						12.6		1.10		0.25

TABLE 1. Comparisons of the characteristics of TW solutions at a given wavelength λ with the experimental values reported by Kliakhandler *et al.* (2001).

shows corresponding wave profiles with regularly spaced streamlines in the moving frame. Only one branch of TW solutions has been found emerging from the marginal linear stability conditions (it does so through a Hopf bifurcation). Since inertia is small here ($\delta = 0.024$) and the RP mode is dominant ($\beta = 25.7$), the TW branch of solutions of (4.16) bifurcates at $k \approx k_{\mathrm{RP}}$. However, weakly nonlinear TW solutions of (4.16) travel at a lower speed than the TW solutions of the CM equation (4.22) since the speed of linear kinematic waves is significantly affected by the streamwise viscous terms ($c_{k,\eta} < c_k$). At small wavenumbers, TW accelerate, become more and more localized and terminate in single-humped solitary waves. The speed, amplitude and shape of the solutions (4.16) and (4.22) are comparable in this limit, though our model predicts solitary waves of larger amplitude and speed than the CM equation.

The characteristics of the TW solutions of model (4.16) are compared to the solutions to the CM equation in table 1 for the three regimes reported by Kliakhandler *et al.* (2001). At high flow rate, corresponding to 'regime a' reported by these authors, they observed long and isolated waves moving rapidly and irregularly on a relatively thick substrate. At lower flow rate (termed 'regime b' by these authors), the wave pattern is highly organised with drops of smaller size moving at constant speed and periodicity. At even lower flow rate ('regime c'), the regularity of the wave pattern is again lost with larger waves separated by long and irregular substrates.

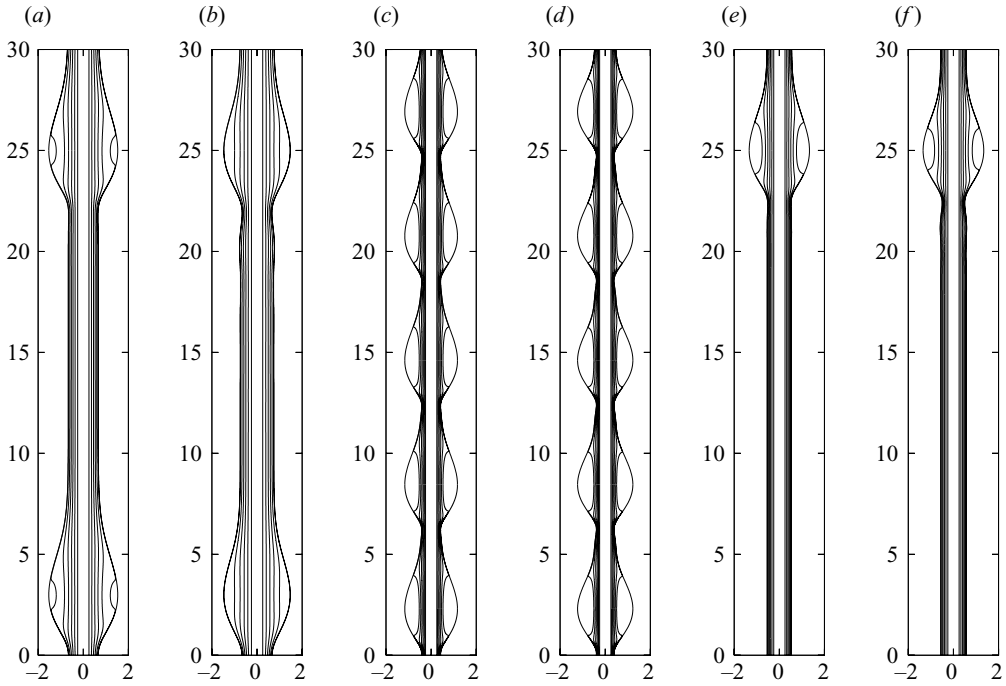

FIGURE 8. Profiles and streamlines in the moving frame of the TW solutions of model (4.16) (*a*, *c*, *e*) and of the CM equation (4.22) (*b*, *d*, *f*). (*a*, *b*), (*c*,*d*) and (*e*, *f*) correspond to the regimes a, b and c reported by Kliakhandler *et al.* (2001). Distances are given in dimensional units (mm).

The wavelength λ has been adjusted to its experimental value. Model (4.16) and CM equation (4.22) give comparable results, in good agreement with the experimental observations. Wave profiles and streamlines in the moving frame of reference are shown in figure 8. Dimensions have been chosen to enable a direct comparison with the experimental snapshots (Kliakhandler *et al.* 2001, figure 1). The agreement between both models is again very good. The sole noticeable difference is the presence of capillary ripples in front of the beads observed with the CM equation. Capillary ripples are almost absent from the solutions of model (4.16), in agreement with experimental observations. We note that the streamlines in the moving frame reveal large recirculation zones inside the beads in regime b and c. As in the moving frame the fluid moves upwards underneath the waves, the presence of recirculation zones proves that the beads carry mass. In fact, in regime b, the beads carry nearly all the fluid and the waves resemble drops sliding on a liquid substrate.

7. Time-dependent computations and wave selection

We now examine the spatio-temporal dynamics of a flow down a fibre. For this purpose we employed a second-order finite-differencing quasi-linearized Crank–Nicolson scheme. We impose simple soft boundary conditions at the outlet: the integral momentum balance (4.16*b*) is replaced at the last two nodes of the discretized domain with a simple linear hyperbolic (wave) equation $\partial_t q + v_f \partial_x q = 0$ where v_f is set to unity in most simulations. A similar methodology is followed for the Trifonov and RL models. In the case of the CM equation, the high-order spatial derivatives

were set equal to zero at the last two nodes while the parameter β was artificially set to zero in a 'damping layer' of typically 100 nodes. This simple procedure turns out to be sufficient and without any spurious backwards reflections of the waves. Following Chang, Demekhin & Kalaidin (1996), we have chosen a random-phase formulation of the noise applied at the inlet. The Fourier spectrum of the zero-mean perturbation $F(t)$ of the inlet flow rate contain frequencies of equal Fourier coefficients but with different phases obtained through a random-number generator. The coefficients of frequencies higher than a few times the linear critical frequency are set to zero to avoid instabilities of our numerical scheme.

We first present time-dependent simulations for the three regimes reported by Kliakhandler *et al.* (see table 1). All of them correspond to linearly absolutely unstable flows (indicated by crosses in figure 5*a*). The initial condition – a small hydraulic jump connecting two regions of different uniform thicknesses – therefore gives way to a regular wavetrain invading the whole computational domain. Snapshots of the film thickness at the end of the simulations for regimes a and b are displayed in figures 9 and 10. In regime a, model (4.16) shows that the regular global mode is disorganized downstream by a secondary instability. Intermittent coalescence events (one such event can be seen occurring at $x \approx 210$ mm) widen the spacing between the waves: the waves become more and more localized. At the final stage, we observe a train of solitary-like coherent structures (that resemble the infinite-domain solitary pulses computed in the previous section). These pulses are separated by portions of flat films of small but irregular thicknesses. The amplitudes and distances between the solitary pulses are in reasonable agreement with the experimental observations ($h_{\max}^{\text{expt}} = 1.47$ mm and approximately 30 mm between pulses). In regime b, a stable regular global mode invades the entire computational domain. The wave characteristics compare well to the experimental observations (wavelength $\lambda = 5.84$ mm, speed $c = 7.2\ \text{mm}\,\text{s}^{-1}$, maximum and minimum heights 0.90 mm and 0.17 mm) and correspond to a frequency, 1.23 Hz, close to the linear absolute frequency, 1.34 Hz. However, we have been unable to reproduce the irregular regime c reported in the experiments by Kliakhandler *et al.* (2001). In our simulations, a stable global mode (not shown) is again observed in the entire domain.

Time-dependent computations of the CM equation (4.22) show a radically different dynamics. In regime a, a slowly modulated wavetrain rapidly invades the entire computational domain whereas intermittent coalescence events are not observed. The average separation between neighbouring pulses, around 10 mm, is three times smaller than reported in experiments. The waves tend to group themselves in 'bound states' of two or three pulses as observed by Craster & Matar (2006).

In regime b, the global mode that sets in has a frequency 0.9 Hz which is approximately half the linear absolute frequency, 1.81 Hz. The wave length, $\approx$14 mm, is therefore approximately twice the experimental one, 6.2 mm. This selection of wave patterns different to that observed in the experiments might explain why Craster & Matar were unable to find TW solutions corresponding to the experimental wavelength for regime b. A growing modulation of the wave amplitude can be observed in figure 9(*b*) leading eventually to a disorganization of the wave pattern. As noted by Craster & Matar, it turns out that the periodic wavetrain solutions to the CM equation are unstable in regime b. In regime c (not shown) the resulting wave patterns are similar to those in regime b but more irregular.

Let us now present some time-dependent computations for the experimental conditions reported in the recent study by Duprat *et al.* (2007). Figure 11 shows the corresponding spatio-temporal diagrams. Duprat *et al.* used a fluid less viscous than Kliakhandler *et al.* (2001) and Craster & Matar (2006) so that inertia plays

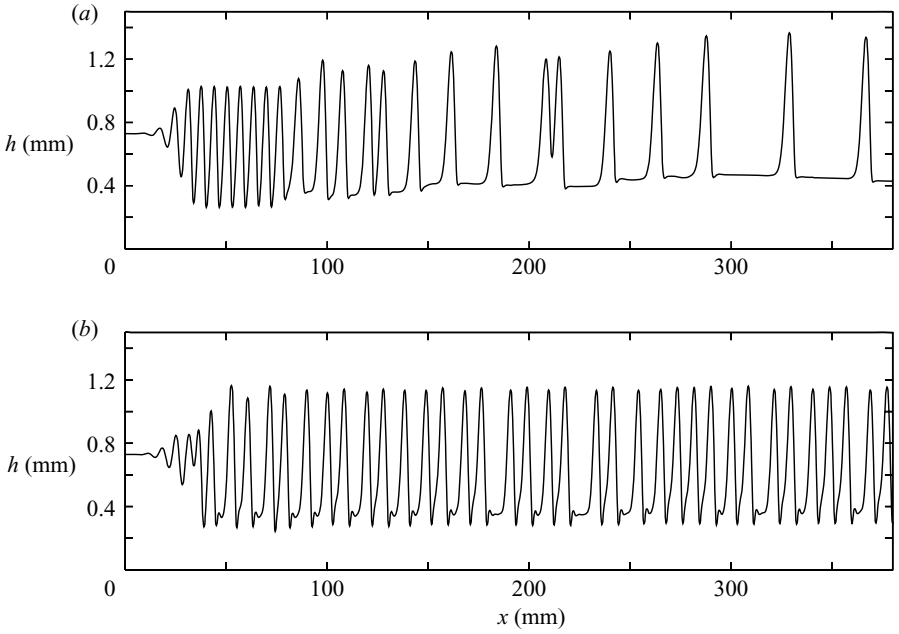

FIGURE 9. Computed film thickness as a function of the distance from the inlet. Parameters correspond to regime a in table 1. (*a*) Solution of model (4.16). (*b*) Solution of CM equation (4.22).

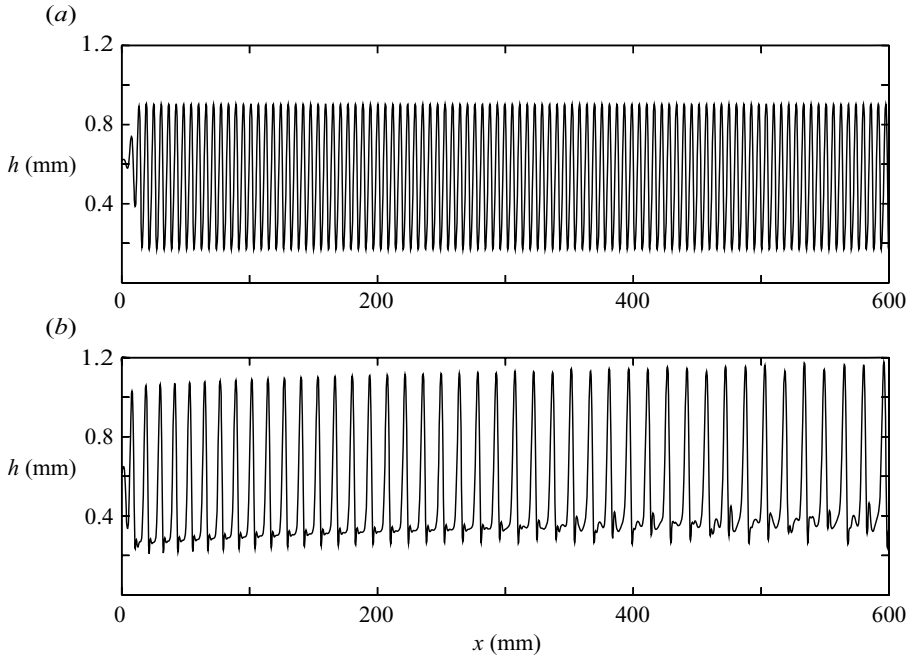

FIGURE 10. Computed film thickness as function of the distance from the inlet. Parameters correspond to regime b in table 1. (*a*) Solution of model (4.16). (*b*) Solution of CM equation (4.22).

a non-negligible role. We therefore compare simulations of model (4.16) and the Trifonov model.

The spatio-temporal diagrams depicted in figure 11 correspond to the 'permanent' wave regimes obtained at the end of the simulations to be contrasted with the

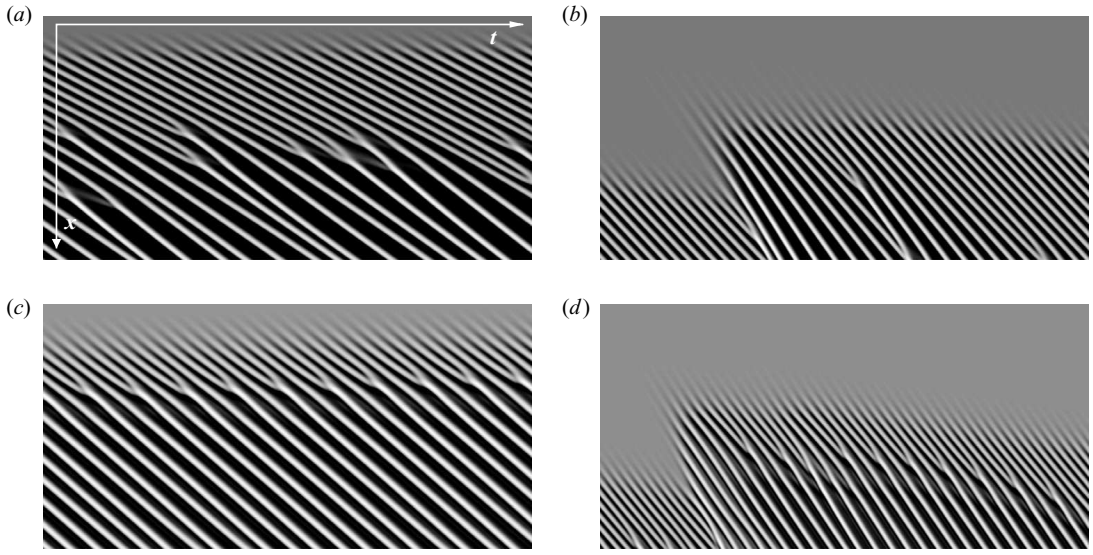

FIGURE 11. Spatio-temporal diagrams showing the response of the film to a coloured noise (see text). (a, b) Solutions of the second-order model (4.16). (c, d) Solutions to the Trifonov model. Parameters correspond to the experimental conditions (Duprat *et al.* 2007, figure 2, silicon oil v50 and $R = 0.32$ mm): $(a$–$c)$ $q_N = 24$ mgs^{-1} ($\delta = 0.3$, $\tilde{\alpha} = 1.32$, $\eta = 0.19$), $(b$–$d)$ $q_N = 77$ mgs^{-1} ($\delta = 1.3$, $\tilde{\alpha} = 1.80$, $\eta = 0.28$). Dark (light) regions correspond to small (large) elevations. Vertical and horizontal ranges are 4 s and 10 cm, respectively.

spatio-temporal diagrams reported in Duprat *et al.* An absolutely unstable flow (figures 11*a* and 11*c*) and a convectively unstable one (figures 11*b* and 11*d*) are shown. A small-amplitude coloured noise been has again been applied at the inlet, therefore sustaining the structures observed in the convectively unstable regime.

For the absolutely unstable flow, model (4.16) gives results in reasonable agreement with experimental observations (cf. figure 11*a*). A very regular wavetrain develops from the inlet but it is quickly destroyed. As in the experiment, this disorganization process looks irregular and is probably promoted by a secondary sideband instability. Waves of larger amplitudes and travelling at greater speeds emerge through intermittent coalescence events in a fashion that is comparable to the noise-driven transitions observed in the case of film falling down a planar vertical wall (Chang, Demekhin & Saprikin 2002). The simulation of the Trifonov model shows a different scenario. The wavetrain that emerges from the primary instability undergoes a subharmonic instability that doubles its frequency (cf. figure 11*c*). No further bifurcations are observable downstream.

The differences between the two spatio-temporal evolutions illustrated in figures 11(*a*) and 11(*c*) may be better understood by looking at the snapshots of the film thickness at the end of the simulations (cf. figure 12). In the case of model (4.16), solitary-like coherent structures emerging from the secondary instability of the primary regular wavetrain are again separated by portions of nearly flat films. The capillary oscillations/ripples preceding the solitary humps are small. In contrast, the snapshot of the film at the end of the simulation for the Trifonov model is quite different. The waves are not localized and the main humps are separated by secondary ones resembling the capillary oscillations/ripples preceding the γ_2 solitary waves. This observation suggests that the selection of either a subharmonic or a sideband secondary instability is responsible for the localisation of the waves, which in turn is strongly dependent on the streamwise viscous terms.

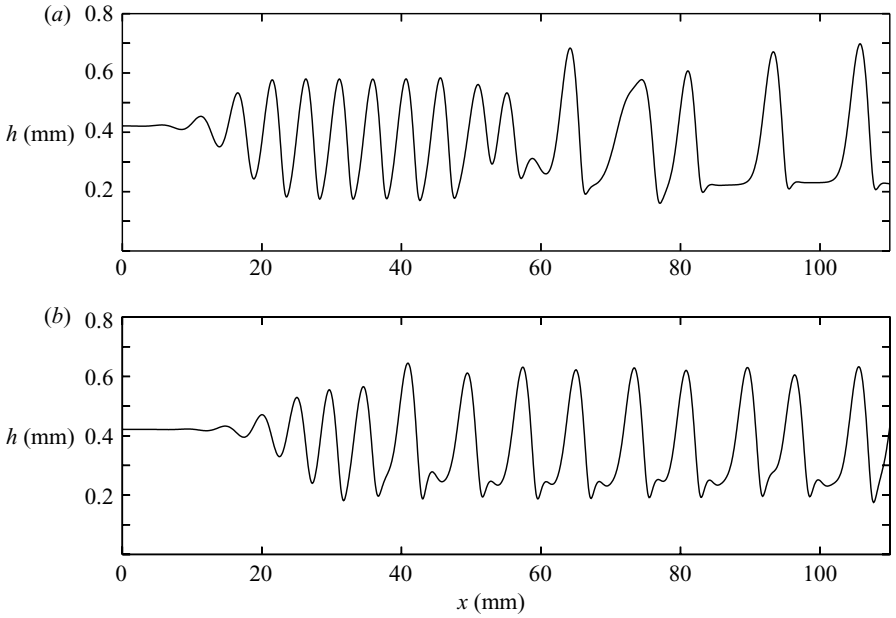

FIGURE 12. Film thickness as function of the distance from the inlet at the end of the simulations presented in figures 11(*a*) and 11(*c*); (*a*) Solution of model (4.16). (*b*) Solution of Trifonov model.

For the convectively unstable flow, the irregular motion of the 'healing length', i.e. the distance from the inlet at which the waves are first noticeable, resembles the experimental observations. The time-dependent computations of model (4.16) show some coalescence events as observed in the experimental spatio-temporal diagram (cf. figure 11*b*). It is, however, difficult to conclude that this is always the case since the number of coalescence events strongly depends on the amplitude and spectrum of the inlet experimental perturbation which is unknown. Simulations with the Trifonov model show again a tendency to period doubling not observed in the experiments but also a series of coalescence events are observed as in the experiment (cf. figure 11*d*). We note that in general the Trifonov model gives a larger number of coalescence events compared to (4.16) owing to the larger band of unstable wavenumbers, a consequence of neglecting streamwise viscous dissipation, which in turn leads to a larger susceptibility to noise.

Finally, we note that we have attempted to simplify our second-order model (4.16) by using polynomial expansions of the coefficients in the form of (4.13). Non-physical blow-ups in time-dependent computations were generally observed even at quite low values of the aspect ratio $\tilde{\alpha}$. This drawback is probably a manifestation of the poor convergence properties of the coefficients of our model due to the presence of the logarithmic function $\log(\tilde{\alpha})$ in these coefficients. This poor convergence is illustrated in figure 13(*a*) where we display the speed of linear kinematic and dynamic waves in the limit of negligible viscous dispersion ($\eta \to 0$) and large Reynolds numbers ($\beta/\delta \to 0$) corresponding to the $O(\tilde{\alpha}^2)$ expansion (4.13). For aspect ratios $\tilde{\alpha}$ above 1.2, the speed c_k of the kinematic waves lies in the interval $[c_{d-},\ c_{d+}]$ which implies linear stability, in contradiction with the results from model (4.16) (compare figure 13(*a*) to figure 2(*a*)).

A similar drawback is observed with the RL model (see figure 13*b*). The spatial dynamics of the film predicted by this model is shown in figure 14 for the flow

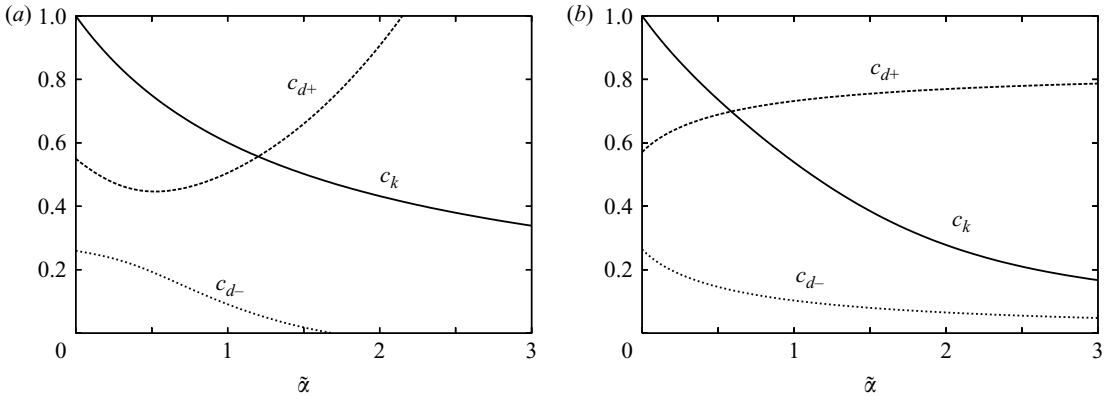

FIGURE 13. Speeds c_k (5.2) of kinematic waves and $c_{d\pm}$ (5.10) of dynamic waves as functions of the aspect ratio $\tilde{\alpha} = h_N/R$ in the limit of negligible viscous dispersion ($\eta \to 0$) and large Reynolds numbers ($\beta/\delta \to 0$). (*a*) Expansion (4.13); (*b*) RL model (4.14).

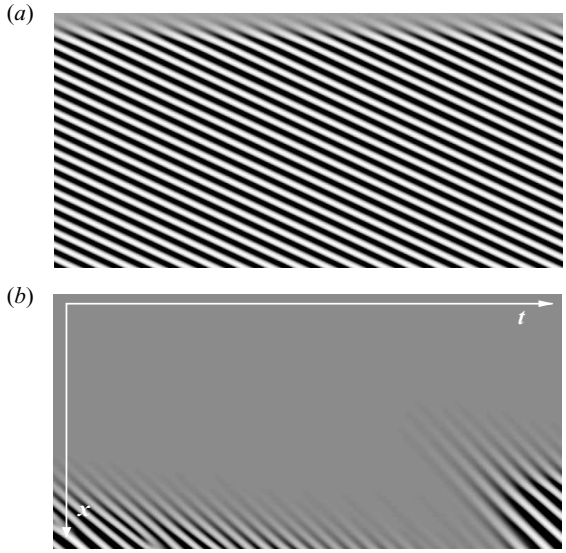

FIGURE 14. Spatio-temporal diagrams showing the response of the film to a coloured noise simulated with RL model (4.14). Parameters are $\delta = 0.3$, $\tilde{\alpha} = 1.32$ and $\eta = 0.19$ (*a*), and $\delta = 1.3$, $\tilde{\alpha} = 1.80$ and $\eta = 0.28$ (*b*). Vertical and horizontal ranges are 4 s and 10 cm, respectively. See also the caption of figure 11.

conditions corresponding to the experiments by Duprat *et al.* (2007). For the two simulations shown in the figure, the aspect ratio $\tilde{\alpha}$ is $O(1)$ as in the experiments and the RL model unphysically stabilises the hydrodynamic K mode (the RL model always suppresses the K mode for $\tilde{\alpha} \gtrsim 0.6$). As a consequence, the base flow is less unstable, and for similar inlet noise, the spatial development of the waves is delayed in the convective case (compare figures 14*b* and 11*b*). In the absolute case, a very regular wavetrain is observed in disagreement with the experimental observations.

8. Summary and conclusions

We have formulated, within the framework of the boundary-layer approximation, a low-dimensional model that consists of two coupled evolution equations for the film

thickness h and the flow rate q. The model is rather general: it accounts for both inertial and streamwise viscous effects, it is not limited to small aspect ratios h/R and is applicable even if $\Gamma = O(1)$. Previous one-equation models are recovered in the appropriate limit. The key steps of our approach are: (i) elimination of the pressure by integrating the cross-stream momentum balance; (ii) projection of the velocity field onto an appropriately chosen set of test functions assuming small departures from the Nusselt uniform film velocity distribution. As in the planar case (Ruyer-Quil & Manneville 2002), we have shown that the use of the Galerkin weighted residual method is the optimum one leading to the desired formulation with a minimum of algebra.

In the linear regime, an excellent agreement with the Orr–Sommerfeld analysis of the primitive equations is attained. Streamwise viscous diffusion was shown to have a dispersive effect. The role of the K instability has been understood within the Whitham wave hierarchy framework (Whitham 1974). Streamwise viscous diffusion was shown to play a stabilising role by decreasing the speed of the kinematic waves.

In the nonlinear regime, TW branches of solutions have been obtained by continuation and have been favourably compared to the experiments by Kliakhandler *et al.* (2001). Time-dependent computations show that our second-order model recovers the regimes observed experimentally by Kliakhandler *et al.*, except for the irregular motion of large waves at very small flow rate ('regime c'). Good agreement has also been obtained with the recent experiments by Duprat *et al.* (2007) for which the wave dynamics in the absolute and convective regimes are recovered. In contrast, by neglecting streamwise viscous diffusion, the CM evolution equation (4.22) overestimates the speed of linear waves. Our simulations of the spatial evolution of the flow then reveal that the wave selection observed with the CM equation does not correspond to the experimental observations. Therefore, the CM equation should be used with caution and certainly not to describe the spatio-temporal dynamics. The Trifonov model suffers from similar limitations. In the linear regime, it overestimates the range of unstable wavenumbers. Time-dependent computations in the nonlinear regime reveal a subharmonic secondary instability that was not observed in the experiments by Duprat *et al.*

In conclusion, despite its apparent 'complexity', the model in equation (4.16) performs well in both linear and nonlinear regimes and captures the dynamics for the largest possible range of parameters.

C.R.-Q. would like to thank S. Ndoumbe and F. Lusseyran with whom a preliminary study was undertaken, and Y. Bardoux for a careful reading of the manuscript. We acknowledge financial support through a travel grant supported by the Franco-British Alliance Research Partnership Programme. S.K. thanks Laboratoire FAST for hospitality.

Appendix A. Boundary-layer approximation for $\Gamma = O(1)$

Here we consider the more involved case (ii) with $\Gamma = O(1)$ and $\epsilon^{3/2} \ll h_N \ll 1$. In the first instance we neglect terms $O(\epsilon^3 h_N)$ and higher associated with the viscous part of the pressure in the normal stress balance (2.1*e*) and approximate the pressure as,

$$p|_h = \{\text{right-hand-side of (3.5)}\} + O\left((\partial_x h)^2 \partial_{xx} h, \frac{\epsilon^4}{R+h}\right), \tag{A 1}$$

where the neglected terms are of $O(\epsilon^4/h_N, \epsilon^4\alpha)$. As a result $p|_h$ is identical to that in (3.5). The tangential-stress boundary condition (2.1*f*) up to of $O(\epsilon^2 h_N)$ yields equation (3.6). Hence the contribution of the term $\partial_x h \partial_r u_x$ in (A 1) is of $O(\epsilon^3 h_N)$ and must be neglected. As a result p is identical to that in (3.7) but now terms of $O(\epsilon^4/h_N, \epsilon^4\alpha, \epsilon^3 h_N, \epsilon^2 h_N^4)$ are neglected which is indeed the case provided that $\max\{\epsilon^3/h_N, \epsilon h_N, h_N^4, \epsilon^5/h_N^3, \epsilon^{9/4}\} \ll \alpha \ll \min\{1/(\epsilon^2 h_N), h_N/\epsilon^3, h_N^{3/2}/\epsilon^2, 1/\epsilon^{3/2}, h_N/\epsilon^5\}$ and $\epsilon^{4/5} \ll h_N \ll 1$ (once again through a detailed examination of the orders of magnitude of the retained over the neglected terms). As an example, with $h_N \sim \epsilon^{1/2}$, $\epsilon^{3/2} \ll \alpha \ll \epsilon^{-5/4}$ and α is allowed to take both small and large values, for example $\alpha \sim \epsilon^{\pm 1/2}$ which also satisfies the requirement αh_N at most of $O(1)$. K_{az} is also identical to (3.8) but now terms of $O(\epsilon^4\alpha)$ and higher are neglected (moreover, $\alpha h \to 0$ now does not imply the planar limit as in case (i)). Hence the final streamwise momentum equation for case (ii) is identical to (3.9) for case (i).

Finally, we note that the order-of-magnitude assignment $h_N \sim 1$ in case (i) can be relaxed, allowing α and h_N to be both small and large (and so that the requirement αh_N at most of $O(1)$ is still satisfied). For this purpose we would have to repeat the analysis for case (ii) to obtain lower/upper bounds on h_N and α but now with $\Gamma = O(\epsilon^{-2})$ instead of $\Gamma = O(1)$.

Appendix B. Coefficients of models (4.10) and (4.12)

The coefficients of the first-order momentum balance (4.10) consist of ratios of polynomials in b and $\log(b)$ where $b = 1 + \alpha h$:

$$\phi = \{3[(4\log(b) - 3)b^4 + 4b^2 - 1]\}/[16(b-1)^3], \tag{B 1a}$$

$$F = 3F_a/[16(b-1)^2\phi F_b], \tag{B 1b}$$

$$\begin{aligned} F_a = {} & -301b^8 + 622b^6 - 441b^4 + 4\log(b)\{197b^6 - 234b^4 + 6\log(b) \\ & \times[16\log(b)b^4 - 36b^4 + 22b^2 + 3]b^2 + 78b^2 + 4\}b^2 + 130b^2 - 10, \end{aligned} \tag{B 1c}$$

$$F_b = 17b^6 + 12\log(b)[2\log(b)b^2 - 3b^2 + 2]b^4 - 30b^4 + 15b^2 - 2, \tag{B 1d}$$

$$G = G_a/[64(b-1)^4\phi^2 F_b], \tag{B 1e}$$

$$\begin{aligned} G_a = {} & 9b\{4\log(b)[-220b^8 + 456b^6 - 303b^4 + 6\log(b)(61b^6 - 69b^4 \\ & +4\log(b)(4\log(b)b^4 - 12b^4 + 7b^2 + 2)b^2 + 9b^2 + 9)b^2 + 58b^2 + 9]b^2 \\ & +(b^2-1)^2(153b^6 - 145b^4 + 53b^2 - 1)\}, \end{aligned} \tag{B 1f}$$

$$I = 64(b-1)^5\phi^2/[3F_b]\,. \tag{B 1g}$$

Expressions (B 1) can be contrasted to the corresponding ones for the first-order averaged momentum balance obtained by Trifonov (1992) with a uniform weight:

$$F = \frac{6 - 45b^2 + 90b^4 - 51b^6 - 36b^4\log(b)[2 - 3b^2 + 2b^2\log(b)]}{32(b-1)^5\phi}, \tag{B 2a}$$

$$G = G_a/\{512(b-1)^7\phi^3\}, \tag{B 2b}$$

$$\begin{aligned} G_a = {} & 9b\{(b^2-1)^2(1 - 26b^2 + 37b^4) - 8b^2\log(b)[2 + 12b^2 - 36b^4 + 22b^6 \\ & +3b^2\log(b)(3 + 4b^2 - 9b^4 + 4b^4\log(b))]\}, \end{aligned} \tag{B 2c}$$

$$I = (b+1)/2\,. \tag{B 2d}$$

The coefficients of the second-order corrections in (4.12) are:

$$J = J_a/[128(b-1)^4\phi^2 F_b], \tag{B 3a}$$

$$J_a = 9\{(490b^8 - 205b^6 - 235b^4 + 73b^2 - 3)(b^2 - 1)^3 + 4b^2\log(b)[2b^4\log(b)(72\log(b)(2\log(b)b^4 - 6b^4 + b^2 + 6)b^4 + (b-1)(b+1)(533b^6 - 109b^4 - 451b^2 + 15)) - 3(b^2-1)^2(187b^8 - 43b^6 - 134b^4 + 17b^2 + 1)]\}, \quad \text{(B 3b)}$$

$$K = 3K_a/[16b^3(b-1)^2\phi F_b], \quad \text{(B 3c)}$$

$$K_a = 4b^4\log(b)(233b^8 - 360b^6 + 12\log(b)(12\log(b)b^4 - 25b^4 + 12b^2 + 9)b^4 + 54b^4 + 88b^2 - 15) - (b^2-1)^2(211b^8 - 134b^6 - 56b^4 + 30b^2 - 3), \quad \text{(B 3d)}$$

$$L = L_a/[8b(b-1)^2\phi F_b], \quad \text{(B 3e)}$$

$$L_a = 4b^2\log(b)\{6\log(b)(12\log(b)b^4 - 23b^4 + 18b^2 + 3)b^4 + (b-1)(b+1) \times (95b^6 - 79b^4 - 7b^2 + 3)\} - (b^2-1)^2(82b^6 - 77b^4 + 4b^2 + 3), \quad \text{(B 3f)}$$

$$M = 3 + [24\log(b)b^8 - 25b^8 + 48b^6 - 36b^4 + 16b^2 - 3]/[2b^2F_b]. \quad \text{(B 3g)}$$

REFERENCES

Alekseenko, S. V., Nakoryakov, V. Y. & Pokusaev, B. G. 1985 Wave formation on a vertical falling liquid film. *AIChE J.* **31**, 1446–1460.

Brevdo, L., Dias, F., Bridges, T. J. & Laure, P. 1999 Convective unstable wave packets in a film flow down an inclined plane. *J. Fluid Mech.* **396**, 37–71.

Chang, H.-C., Demekhin, E. A. & Kalaidin, E. 1996 Simulation of noise-driven wave dynamics on a falling film. *AIChE J.* **42**, 1553–1568.

Chang, H.-C., Demekhin, E. A. & Saprikin, S. 2002 Noise-driven wave transitions on a vertically falling film. *J. Fluid Mech.* **462**, 255–283.

Craster, R. V. & Matar, O. K. 2006 On viscous beads flowing down a vertical fibre. *J. Fluid Mech.* **553**, 85–105.

Doedel, E. J., Champneys, A. R., Fairgrieve, T. F., Kuznetsov, Y. A., Sandstede, B. & Wang, X.-J. 1997 Auto97: Continuation and bifurcation software for ordinary differential equations. *Tech. Rep*. Department of Computer Science, Concordia University, Montreal, Canada (available by FTP from ftp.cs.concordia.ca in directory pub/doedel/auto).

Duprat, C., Ruyer-Quil, C., Kalliadasis, S. & Giorgiutti-Dauphiné, F. 2007 Absolute and convective instabilities of a film flowing down a vertical fiber. *Phys. Rev. Lett.* **98**, 244502.

Frenkel, A. L. 1992 Nonlinear theory of strongly undulating thin films flowing down vertical cylinders. *Europhys. Lett.* **18**, 583–588.

Gaster, M. 1962 A note on the relation between temporally-increasing and spatially increasing disturbances in hydrodynamic stability. *J. Fluid Mech.* **14**, 222–224.

Huerre, P. & Rossi, M. 1998 Hydrodynamic instabilities in open flows. In *Hydrodynamic and Nonlinear Instabilities* (ed. C. Godréche & P. Manneville), pp. 81–294. Cambridge University Press.

Kalliadasis, S. & Chang, H.-C. 1994 Drop formation during coating of vertical fibres. *J. Fluid Mech.* **261**, 135–168.

Kliakhandler, I. L., Davis, S. H. & Bankoff, S. G. 2001 Viscous beads on vertical fibre. *J. Fluid Mech.* **429**, 381–390.

Ooshida, T. 1999 Surface equation of falling film flows with moderate Reynolds number and large but finite Weber number. *Phys. Fluids* **11**, 3247–3269.

Quéré, D. 1990 Thin films flowing on vertical fibers. *Europhys. Lett.* **13**, 721–726.

Quéré, D. 1999 Fluid coating on a fiber. *Annu. Rev. Fluid Mech.* **31**, 347–384.

Rayleigh, Lord 1878 On the stability of liquid jets. *Proc. Lond. Math. Soc.* **10**, 4.

Roberts, A. J. & Li, Z. 2006 An accurate and comprehensive model of thin fluid flows with inertia on curved substrates. *J. Fluid Mech.* **553**, 33–73.

Roy, R. V., Roberts, A. J. & Simpson, A. J. 2002 A lubrication model of coating flows over a curved substrate in space. *J. Fluid Mech.* **454**, 235–261.

Ruyer-Quil, C. & Manneville, P. 2000 Improved modeling of flows down inclined planes. *Eur. Phys. J.* B **15**, 357–369.

Ruyer-Quil, C. & Manneville, P. 2002 Further accuracy and convergence results on the modeling of flows down inclined planes by weighted-residual approximations. *Phys. Fluids* **14**, 170–183.

Scheid, B., Ruyer-Quil, C. & Manneville, P. 2006 Wave patterns in film flows: modelling and three-dimensional waves. *J. Fluid Mech.* **562**, 183–222.

Shkadov, V. Ya. 1967 Wave flow regimes of a thin layer of viscous fluid subject to gravity. *Izv. Akad. Nauk SSSR, Mekh. Zhidk Gaza* **1**, 43–51 (English translation in *Fluid Dyn.* **2**, 29–34, 1970, Faraday Press, NY).

Shkadov, V. Ya. 1977 Solitary waves in a layer of viscous liquid. *Izv. Ak. Nauk SSSR, Mekh. Zhid Gaza* **1**, 63–66.

Sisoev, G. M., Craster, R. V., Matar, O. K. & Gerasimov, S. V. 2006 Film flow down a fibre at moderate flow rates. *Chem. Eng. Sci.* **61**, 7279–7298.

Smith, M. K. 1990 The mechanism for the long-wave instability in thin liquid films. *J. Fluid Mech.* **217**, 469–485.

Trifonov, Yu. Ya 1992 Steady-state travelling waves on the surface of a viscous liquid film falling down vertucal wires and tubes. *AIChE J.* **38**, 821–834.

Whitham, G. B. 1974 *Linear and Nonlinear Waves*. Wiley-Interscience.

Recent works and perspectives

5

The first part of this chapter summarizes the work that has been achieved by Symphony Charaborty and Arghya Samanta during their PhDs theses from 2009 to 2012. I have participated to the supervision of these two PhDs along with Neil Ribe (CNRS, FAST) and Benoit Goyeau (École Centrale Paris). I shall also provide some perspectives for possible follow-ups based on their works and write a few words about Nicolas Kofman PhD thesis that has started in October 2011 under the guidance of Sophie Mergui (UPMC, FAST) and Béatrice Guerrier (CNRS, FAST). Finally, I will end this chapter with a few preliminary results obtained by Georg Dietze (initially DAAD PostDoc, now CNRS researcher at FAST).

Up to now, Arghya's and Symphony's works have led to two publications (Samanta et al. 2011, Ruyer-Quil et al. 2012). A third one is submitted (Samanta et al. 2012) and there is matter for at least a fourth manuscript. A manuscript has been submitted based on Georg's work (Dietze and Ruyer-Quil 2012).

5.1 Falling film on a porous medium

In many environmental problems involving falling films, the solid substrate is in fact permeable, for instance when erosion, surface water and soil systems are encountered. Leaving aside the difficult problem of erosion processes and transport of material by the flow, the porous nature of the substrate makes the study of the flow in the substrate and at the liquid-substrate boundary already a formidable difficulty by itself. The very complex geometry of even the simplest porous material makes impossible any attempt to solve the primitive equations in the porous medium. Our study is therefore based on a modeling of the porous medium. The *upscaling* process leading from the primitive *microscopic* problem to the *macroscopic* governing equations of the equivalent continuous porous medium is a difficult task by itself, requiring a high level of technicalities and applied mathematics.

5.1.1 Macroscopic modeling

The considered geometry is sketched in figure 5.1. A Newtonian and incompressible fluid flows on a planar substrate under the action of gravity. The above gas is passive. The porous medium is saturated and bounded from below by a solid planar wall. Notations are introduced in the sketch.

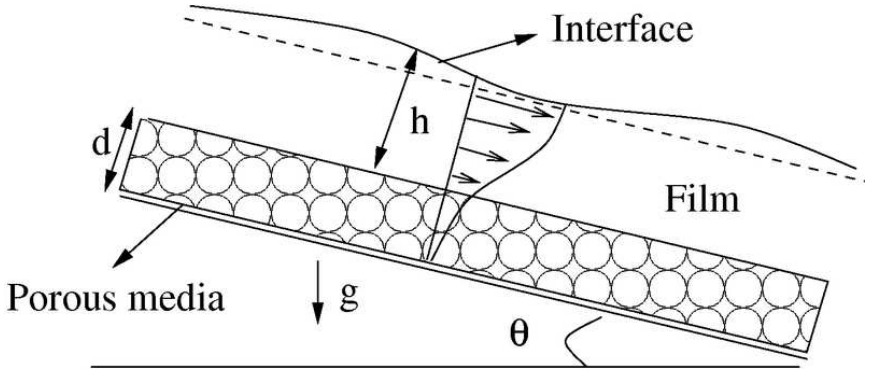

Figure 5.1 – *Sketch of a falling film on a saturated inclined porous medium*

Three approaches have been considered. They differ one from the other by the treatment of the liquid-substrate interface. In the first approach, the porous medium is assumed passive and its action on the liquid film is modeled by a liquid-substrate boundary condition. In the second one, the fluid and porous media are governed by different equations and coupled by macroscopic boundary conditions. In the third approach, the liquid and porous media are replaced by a single composite medium.

One-sided approach: the slip approximation

The porous medium can be assumed to play a passive role on the dynamics of the film when the characteristic superficial (or Darcian) velocity in the porous medium is small as compared to the characteristic velocity of the film, which is the velocity at the free interface.

Considering that a small momentum diffusion layer at the liquid-porous interface introduces a macroscopic discontinuity of tangential velocity Beavers and Joseph (1967) postulate a jump of the tangential velocity

$$u - \tilde{u} = l_s \partial_y u \tag{5.1}$$

where u is the velocity in the liquid layer, $\tilde{u}$ refers to the Darcian velocity in the porous region and l_s is a slip length.

Pascal (1999) first realized that whenever the Darcian velocity u_p is small in comparison to the typical velocity in the fluid region, i.e. $u_p \ll u$, then (5.1) reduces to a Navier slip boundary condition

$$u = l_s \partial_y u \,. \tag{5.2}$$

Similarly the normal velocity $\tilde{v}$ is neglected and an impermeable wall is substituted for the permeable porous region. With this slip approximation, the problem becomes one-sided and entirely piloted by the liquid medium.

Pascal's initial work has been followed by several ones (Sadiq and Usha 2008, Usha et al. 2011) which all have concluded to an amplification of the Kapitza instability mechanism by the slip at the liquid-porous interface with a lowering of the critical Reynolds number signaling the onset of the Kapitza long-wave instability. In *Samanta et al. (2011)* this problem has been revisited and reviewed.

It is important to give some figures to sustain the slip-approximation. Since the flow is driven by gravity and the Darcy equation applies in the bulk of the porous medium, $u_p \approx g \sin\beta \kappa_H / \nu$ where κ_H is the (homogeneous) permeability and $\nu = \mu/\rho$ is the apparent kinematic viscosity in the porous medium which is assumed to be equal to the fluid kinematic viscosity. The typical velocity of the fluid $\bar{U}_\mathrm{N}$ is the free surface velocity which is determined by the balance of viscosity and gravity $\bar{U}_\mathrm{N} \sim g\bar{h}_\mathrm{N}^2 \sin\beta/\nu$. The ratio $u_p/\bar{U}_\mathrm{N} \sim \kappa_H/\bar{h}_\mathrm{N}^2$ and Pascal's slip approximation holds whenever the permeability of the porous region is small compared to the square of the film thickness. Typical thicknesses of water films range from 0.1 to 1 mm, whereas permeabilities of porous media in geophysical applications range from 10^{-5} cm^2 (sand and gravel) to 10^{-11} cm^2 (layered clay) (Bear 1988). Therefore $\kappa_H/\bar{h}_\mathrm{N}^2$ ranges from 10^{-9} up to 0.1. There are therefore many geophysical problems for which the slip approximation does not hold.

Two-domain approach

Obviously, the slip approximation is a rather crude one as it does not allow to account for the transfer of mass at the liquid-porous interface, the porous medium being replaced by a solid impermeable one. This drawback motivates Thiele et al. (2009) to reconsider this problem and to adopt a modeling based on a two-sided approach The porous and liquid media are considered as two different homogeneous regions connected by an interface of negligible thickness. Thiele *et al.* macroscopic model of the porous medium relies on the Darcy-Brinkman equation and a stress jump condition at the fluid-porous interface (Ochoa-Tapia and Whitaker 1995, Goyeau et al. 2003). The difficulty of the two-domain approach stems from the modeling of the boundary conditions at the porous-liquid interface whose expressions are still a matter of active research. Besides, similarly to the slip length in the velocity jump (5.1), these boundary conditions involve coefficients that need to be computed by direct numerical simulations. Some discussions on the two-domain approach can be found in Samanta (2012).

One-domain approach

A third alternative approach is the following : the porous and liquid media are modeled by a single composite medium characterized by a continuous distribution of the permeability and porosity. In this one-domain macroscopic model (Beckermann et al. 1988), a mesoscopic thin layer accounts for the rapid variations of porosity and permeability in the porous-liquid interfacial region. This one-domain approach relaxes the main difficulties of the two-domain approach since interfacial boundary conditions do not need to be introduced. However, this approach introduces a large separation of scales between the film height and the thickness of the transitional layer, and numerical simulations require a sufficiently fine mesh or a mesh refinement at the porous-liquid interface. This approach has been adopted in *Samanta et al. (2012)*.

5.1.2 Salient features

In this section a short presentation of the findings of Samanta et al. (2011; 2012) are given. Interested readers are invited to read these two papers.

Film on a slippery plane

All previous studies devoted to the problem of a falling liquid film on a slippery wall have concluded to an amplification of the Kapitza mechanism due to an acceleration of the flow (Pascal 1999, Sadiq and Usha 2008, Usha et al. 2011). However, these studies suffer from several flaws: (i) they are generally based on $O(\epsilon)$ approximations and focus on the instability threshold, (ii) they generally adopt definitions of dimensionless parameters that do not take into account the effect of the slip on the base flow. For instance, the Reynolds number is defined as $Re = g \sin\beta \bar{h}_N^3/(3\nu^2)$ as in the no-slip case. Yet, the free surface velocity, which characterizes the flow, and the relation between the film thickness and the flow rate per unit length are both affected by the modifications of the base flow introduced by a slip at the wall.

We have therefore reviewed this problem by taking into account the second-order streamwise viscous terms —contributions from the elongational viscosity or Trouton viscosity, and by adopting a scaling based on the free surface velocity (which depends on the slip length).

Our study of the primary stability of the film is summed up in figure 5.2 where the marginal stability curves are displayed and separate the region of stability (above the curves) from the instability region (below the curves). The results are also presented using experimentally controlled parameters to avoid any bias from the choice of the scaling. We thus introduce the forcing frequency $f = kc/(2\pi)$ and the flow rate per unit channel width at inlet q_N. Figure 5.2 compares the cut-off frequency f_c corresponding to marginal stability conditions when plotted with respect to the Reynolds number Re (panel a) and with respect to the dimensionless flow rate per unit length q_N (panel b), which offers another definition of the Reynolds number based on the averaged velocity instead of the free surface velocity. The same qualitative behavior is observed in both panels of figure 5.2. In agreement with Pascal (1999), Sadiq and Usha (2008), the Navier slip condition lowers the critical Reynolds number (and the critical flow rate) and promotes the instability close to its onset. However, at large Reynolds number, the Navier slip conditions tends to reduce the range of unstable wavenumbers and is therefore stabilizing. This effect is observable whether the Kapitza number is large or not which suggests that it does not result from the competition of the capillary and viscous damping of the short waves.

Close to threshold, the stability of the film on a slippery inclined plane is nearly tantamount to the stability of a film on a non-slippery wall with a thickness augmented with the slip length l_s characterizing the Navier slip boundary condition (Samanta et al. 2012). A film falling on a slippery wall has an effective flow rate augmented by the flow in the porous region that is modeled by the Navier slip condition, which explains a lowering of the critical inlet flow rate at the threshold of instability.

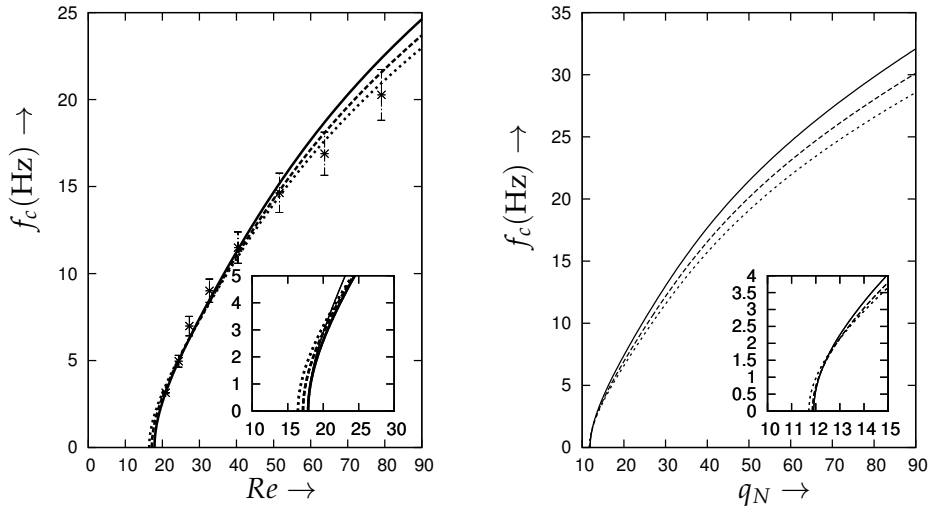

(a) *Frequency versus Reynolds number* (b) *Frequency versus inlet flow rate*

Figure 5.2 – *Marginal stability curves. The experimental results of Liu et al. (1995) are indicated by crosses. Solid, dashed and dotted lines stand for* $\alpha_1 = 0.0$, $\alpha_1 = 0.04$ *and* $\alpha_1 = 0.08$ *respectively. Parameters correspond to water-glycerin mixture (*$\Gamma = 2431.0$*). The inclination angle is* $\beta = 4^\circ$*. After figure 3 in Samanta et al. (2011).*

The unexpected attenuation of the primary instability far from its threshold can be explained as follows: In presence of a slip, the base flow accelerates, the film thickness decreases and consequently the surface tension damping becomes more effective.

Following the weighted residual approach detailed in § 1.2 and § 2.3.2, a closed set of coupled evolution equations has been obtained for the local flow rate $q(x,t)$ and the local film thickness $h(x,t)$. The model is consistent up to first-order with respect to the film parameter ϵ. This consistency holds at order ϵ^2 for the streamwise viscous diffusion effects. As for the problem of a film on a non-slippery wall (Ruyer-Quil and Manneville 2002), this level of consistency is sufficient to accurately capture the primary stability (both threshold and marginal stability curves).

In the nonlinear regime, a slippery substrate contributes to increase the amplitude of the waves. One-humped solitary waves, which structure the flow at the last stages of its evolution, are accelerated and amplified by a slip at the wall. Capillary separation of streamlines and backflow phenomena have been found to be intensified. This effect is quite large, even at relatively small values of the slip length, and an enhancement of the mass and heat transfer between the wall and the liquid is very likely.

Nonlinear solutions to the model have been compared to DNSs obtained with Gerris using VOF method (Popinet 2003; 2009) demonstrating a convincing agreement for all tested parameters.

Film on a saturated porous medium

A priori, this problem is a difficult one : the choice of a continuous distribution of permeability $\kappa(y)$ and porosity $\underline{\varepsilon}(y)$ implies that even the base flow has no analytical solutions. Worse, solving the primitive equations is

numerically costly because of the necessary refinement of the mesh at the transitional layer in order to capture the rapid variations of porosity and permeability in that region. I shall demonstrate that the weighted residual method provides a welcome simplification, the detail of the transitional layer geometry being embedded in the computations of the coefficients of the model. Because of the technical novelties brought to the treatment of this problem, I give a somewhat detailed account of them in what follows (More details can be found though in Samanta et al. (2012)).

Governing equations and parameters

The geometry of the flow is sketched in figure 5.1. The thicknesses of the porous layer and of the transitional layer are denoted by d and D respectively. The characteristic scales for velocity, length and pressure are denoted by $\bar{U}_\mathrm{N}$, $\bar{H}_\mathrm{N}$ and $\rho\bar{U}_\mathrm{N}^2$ respectively, where $\bar{H}_\mathrm{N}$ is the thickness of the entire layer. The velocity scale $\bar{U}_\mathrm{N}$ stands for the free surface velocity of the uniform film as it characterizes the wavy motion of the interface. (Again, this choice is different from the previous studies on the subject, e.g. Pascal (1999), where the velocity scale was based on the impermeable non-slippery problem, which biased their conclusions.) These scales introduce the following dimensionless groups: Reynolds number $Re = (\bar{U}_\mathrm{N}\bar{H}_\mathrm{N}/\nu)$, Froude number $Fr^2 = \bar{U}_\mathrm{N}^2/(g\sin\beta\bar{H}_\mathrm{N})$, Weber number $We = \sigma/(\rho\bar{U}_\mathrm{N}^2\bar{H}_\mathrm{N})$ and Darcy number $\mathrm{Da} = \kappa_H/\bar{H}_\mathrm{N}{}^2$. Two geometrical aspect ratios complete the set of parameters: $\underline{\delta} = d/\bar{H}_\mathrm{N}$ and $\underline{\Delta} = D/\bar{H}_\mathrm{N}$, namely the dimensionless thicknesses of the porous layer and the transitional layer at the porous-liquid interface.

As usual, length and time scales can also be defined with reference to viscosity and gravity acceleration as $l_\nu = \nu^{2/3}(g\sin\beta)^{-1/3}$ and $t_\nu = \nu^{1/3}(g\sin\beta)^{-2/3}$. These scales introduce the Kapitza number $\Gamma = (l_c/l_\nu)^2 = \sigma/[\rho\nu^{4/3}(g\sin\beta)^{1/3}]$, which compares l_ν to the capillary length $l_c = \sqrt{\sigma/(\rho g\sin\beta)}$, and a modified Darcy number $\mathrm{Da}_\nu = \kappa_H/l_\nu^2$. The interest of the dimensionless groups Γ and Da_ν stem from the fact that they are functions of the liquid and porous media physical and effective properties only. As a consequence, they remain constant once the fluid and porous medium are specified and for a given inclination angle.

The dimensionless 2D governing equations for the liquid and the porous medium under the basis of continuum approach can be written as (Beckermann et al. 1988, Whitaker 1996, Bousquet-Melou et al. 2002, Hirata et al. 2009)

$$\partial_x u + \partial_y v = 0, \tag{5.3a}$$

$$\underline{\varepsilon}^{-1}Re\left[\partial_t u + \underline{\varepsilon}^{-1}u\partial_x u + \underline{\varepsilon}^{-1}v\partial_y u + uv\partial_y\underline{\varepsilon}^{-1}\right] = -Re\partial_x p + \underline{\varepsilon}^{-1}(\partial_{xx}u + \partial_{yy}u) - \frac{u}{\kappa} + \frac{Re}{Fr^2}, \tag{5.3b}$$

$$\underline{\varepsilon}^{-1}Re\left[\partial_t v + \underline{\varepsilon}^{-1}u\partial_x v + \underline{\varepsilon}^{-1}v\partial_y v + v^2\partial_y\underline{\varepsilon}^{-1}\right] = -Re\partial_y p + \underline{\varepsilon}^{-1}(\partial_{xx}v + \partial_{yy}v) - \frac{v}{\kappa} - \cot\beta\frac{Re}{Fr^2}, \tag{5.3c}$$

where porosity $\underline{\varepsilon}(y)$, permeability $\kappa(y)$ are both continuous and differentiable functions of the transverse co-ordinate y. The distributions of $\underline{\varepsilon}(y)$ and $\kappa(y)$ follow a tangent hyperbolic profile across the transition layer of

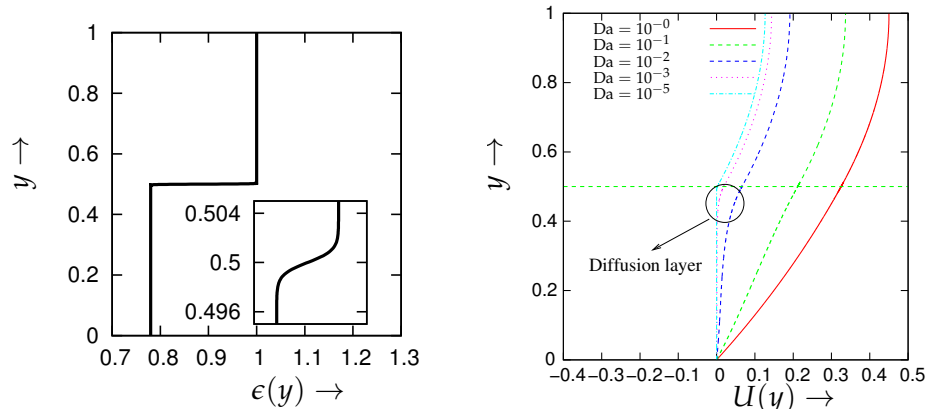

(a) *porosity* (b) *base flow*

Figure 5.3 – *One-domain approach: (a) porosity distribution ; (b) base flow.*

typical thickness $\underline{\Delta}$ such as

$$\underline{\varepsilon}(y) = \frac{(1+\underline{\varepsilon}_H)}{2} + \frac{(1-\underline{\varepsilon}_H)}{2}\tanh\left[(y-\underline{\delta})/\underline{\Delta}\right], \tag{5.4}$$

$$\frac{1}{\kappa(y)} = \frac{1}{\mathrm{Da}}\left(\frac{1}{2} - \frac{1}{2}\tanh\left[(y-\underline{\delta})/\underline{\Delta}\right]\right) \tag{5.5}$$

i.e. porosity and permeability change from their constant values $\underline{\varepsilon}_H$, κ_H in the homogeneous porous layer to the values 1 and ∞ in the liquid layer respectively. The conclusions of this study are not affected by the specific choice of a hyperbolic tangent profile. The distribution of porosity is illustrated in figure 5.3a.

In (5.3), u and v stand for the superficial Darcian velocities on the porous medium side and the true fluid velocities on the fluid side. The difference between the definitions of the Darcian and intrinsic velocities result in the introduction of the porosity in the inertial terms at the l.h.s. of the momentum balance (5.3b), (5.3c) and in the Brinkman momentum diffusion terms at their r.h.s. The reader can easily check that setting $\underline{\varepsilon} = 1$ and $\kappa^{-1} = 0$ in (5.3) leads back to the classical Navier-Stokes equations for an incompressible fluid flow. (5.3) contain the specific Darcy terms $-u/\kappa$ and $-v/\kappa$ that account for the viscous friction exerted by the solid phase on the liquid phase.

By combining the governing equations in the porous and fluid media, the boundary conditions at the porous–liquid interface are satisfied automatically. Boundary conditions at the lower boundary $y = 0$ and at the free surface $y = H$ are therefore sufficient to close the system of equations to be solved.

Base flow

Let us first consider the steady Nusselt solutions of (5.3) corresponding to a film of constant thickness $H = 1$. The streamwise velocity satisfies $U = (Re/F^2)f(y)$ where f is solution to

$$\mathcal{L}f = -\underline{\varepsilon}, \qquad f(0) = f'(1) = 0, \tag{5.6}$$

and $\mathcal{L} \equiv \partial_{yy} - \underline{\varepsilon}/\kappa$ is a linear differential operator which accounts for the viscous diffusion and the viscous drag at the solid phase in the porous

medium. Figure 5.3b presents the velocity profile $f(y)$ corresponding to the solutions of (5.6). The reference velocity scale $\bar{U}_{\mathrm{N}}$ being chosen so that $U(1) = 1$, the ratio Fr^2/Re is equal to $f(1)$ which varies with the properties of the porous medium and the geometry of the flow.

For intermediate values of Da, two boundary layers develop at the porous-liquid interface and lower boundary respectively. Apart from these boundary layers, the velocity in the porous medium is nearly constant and given by the Darcy law, i.e. $u_p = \mathrm{Da}Re/Fr^2 \ll 1$. The typical thickness d_B of the momentum boundary layer near the porous-liquid interface can be found by balancing the Darcy drag and the Brinkman diffusion terms which gives the dimensional value $d_B = \sqrt{\kappa_H/\underline{\varepsilon}_H}$. It is important to note that whenever u_p is small the flow is located in the film layer augmented with the upper momentum diffusion layer.

Low-dimensional modeling

Because of the absence of analytical expressions of the base flow velocity distribution, the weighted residual strategy has to be adapted. As usual, the streamwise velocity component is decompose as an $O(1)$ term and an $O(\epsilon)$ correction induced by the deformations of the free surface :

$$u(x,t) = \frac{q(x,t)}{\phi(H)} f(y;H) + u^{(1)}, \tag{5.7}$$

where $\phi(H) = \int_0^H f(y;H)dy$ and f corresponds to the base flow velocity profile, For any values of the total height H, f satisfies

$$\mathcal{L}f = -\underline{\varepsilon}\,, \qquad f(0;H) = \partial_y f(H;H) = 0\,, \tag{5.8}$$

$u^{(1)}$ stands for the $O(\epsilon)$ corrections to the velocity profile induced by the deformations of the free surface. The decomposition (5.7) is made unique by imposing the gauge condition $\int_0^H u^{(1)}dy = 0$ which ensures that q still corresponds to the local flow rate. Solutions to (5.8) for $H = 1$ are shown in figure 5.3b.

The flat-film solution is dependent on the film thickness and therefore on H and this dependence is underlined in the notation $f(y;H)$. Its variation with respect to the total height is denoted by $g = \partial_H f \equiv \lim_{\delta H\to 0} f(y;H+\delta H) - f(y;H)/\delta H$ which is a solution to

$$\mathcal{L}g = 0\,, \qquad g(0;H) = 0 \quad \text{and} \quad \partial_y g(H;H) = 1\,, \tag{5.9}$$

It is easy to show that $\partial_{HH} f = \partial_H g$ are solutions to $\mathcal{L}\partial_H g = 0$ with $\partial_H g(0;H) = 0$ and $\partial_y g(H;H) = 0$, and therefore that $\partial_H g = 0$.

We next proceed to the averaging of the momentum balance with the usual inner product $\langle u|v\rangle = \int_0^H uvdy$ and an appropriate weight $w(y)$. Leading order contribution of the corrections $u^{(1)}$ comes from the $O(\epsilon)$ friction terms. These terms can be eliminated by using the gauge condition $\langle u^{(1)}|1\rangle = 0$. and adjusting the weight w which is then defined by

$$\mathcal{L}w = -\frac{Re}{Fr^2}\,, \qquad w(0;H) = \partial_y w(H;H) = 0\,, \tag{5.10}$$

where the constant $-Re/Fr^2 = -1/f(1;1)$ has been chosen for convenience and ensures that w is positive.

Integration of the momentum balance with the weight $w(y;H)$ yields a residual, which set to zero and divided by H^2 is recast into a depth-averaged momentum balance written below as an evolution equation for the local flow rate q:

$$S(H)\partial_t q = -F(H)\frac{q}{H}\partial_x q + G(H)\frac{q^2}{H^2}\partial_x H + \frac{1}{Fr^2}\left[I(H)H\,b(H) - \frac{q}{H^2}\right] + \frac{1}{Re}\left[J(H)\frac{q}{H^2}(\partial_x H)^2 - K(H)\frac{\partial_x q\partial_x H}{H} - L(H)\frac{q}{H}\partial_{xx}H + M(H)\partial_{xx}q\right] \quad (5.11)$$

where $b(H) = 1 - \cot\beta\partial_x H + WeF^2\partial_{xxx}H$ is the body force corresponding to the gravity acceleration and the gradient of hydrostatic and capillary pressures. The coefficients $S(H)$ to $M(H)$ in (5.11) are integrals of the base flow profile f, the weight w and their derivatives (see the appendix, § 5.4). The averaged momentum equation (5.11) and the (exact) mass balance

$$\partial_t h + \partial_x q = 0 \quad (5.12)$$

form a two-equation model in terms of the flow rate $q(x,t)$ and the entire layer thickness $H(x,t)$ that is consistent at first order in the long-wave parameter ϵ. Consistency up to $O(\epsilon^2)$ is achieved for the streamwise viscous diffusion terms at the last row of (5.11). Again, this consistency requirement is sufficient to capture the primary stability correctly. In practice, the coefficients $S(H)$ and $M(H)$ are computed by solving simultaneously (5.8) and (5.10) and then tabulated. As a result, solving (5.12, 5.11) can be done very efficiently.

Interestingly, even though the linear operator $\mathcal{L}$ is self-adjoint, the peculiar weighted residual approach, that we made use of, does not reduce to the usual Galerkin method. The origin of this discrepancy lies in the non-homogeneous distribution of the porosity, which introduces a difference between the viscosity of the liquid and the effective viscosity in the porous medium.

Besides, in the usual WRMs detailed in (2.3.2), the reduced coordinate $\bar{y} = y/H(x,t)$ is introduced. This choice stems from the presence of a self-similar semi-parabolic uniform-film solution. In the present problem, such a self-similar solution is not found because of the introduction of two supplementary lengthes, namely the thicknesses $\underline{\delta}$ and $\underline{\Delta}$ of the porous and transitional layers. An ansatz in terms of the reduced coordinate $\bar{y}$ yields two local aspect ratios $\underline{\delta}/H$ and $\underline{\Delta}/H$ that are functions of the time and the spatial coordinate, which needlessly complicate the derivation process.

Whitham wave hierarchy

Let us linearise the two-equation system (5.12, 5.11) around the base state by writing $H = 1 + \tilde{H}$ and $q = I(1) + \tilde{q}$ where $\tilde{H} \ll 1$ and $\tilde{q} \ll 1$. After elimination of the flow rate, decomposition in normal modes, i.e. $\tilde{H} \propto \exp[\mathrm{i}k(x-ct)]$ where k and c are respectively the complex wavenumber and complex phase speed, we are led to a dispersion relation that can be written into the form:

$$\mathrm{i}[c - c_k(k)] + k\Omega(Re,k)[c - c_{d+}(k)][(c - c_{d-}(k)] = 0\,, \quad (5.13)$$

The dispersion relation (5.13) has a two-wave structure and was initially introduced by Whitham (1974). First-level kinematic waves propagate at

a speed c_k, whereas second-level dynamic waves travel at two possible speeds $c_{d\pm}$. Kinematic waves arise from the response of the velocity distribution to a free surface deformation. This response is driven by the kinematic condition at the free surface, or equivalently, by the mass balance (5.12). Dynamic waves correspond to the response of the momentum balance to a disturbance at the free surface, which is governed by the tangential and normal stress continuity conditions. Whitham (1974) studied the stability of hyperbolic two-equation systems that are described by a two-wave hierarchy of the kind given in (5.13) and obtained a simple stability condition

$$c_{d-} \leq c_k \leq c_{d+}\,, \tag{5.14}$$

The origin of the condition (5.14) stems from the evolution of a wavepacket originating from a localized initial perturbation. Since kinematic waves tend to emerge from the wavepacket at long times, whereas the short-term dynamics is dominated by dynamic waves, the only stable situation is one where the back and front of the wavepacket are made of dynamic waves, which implies the condition (5.14). In practice, the instability arises when $c_k = c_{d+}$

The instability mechanism can thus be reasoned in terms of the competitions of kinematic and dynamic waves. Kinematic waves travel at two times the velocity $\bar{U}_\mathrm{N}$ of the liquid at the free surface whereas dynamic waves propagate approximately at speed $\bar{U}_\mathrm{N}$ plus or minus the speed of gravity waves. The onset of the instability can then be rationalized as the balance between the propagation of gravity waves and the advection by the flow at the free surface velocity. The speed of gravity waves in the shallow-water limit is determined by the requirement that the normal velocity component must vanish at the wall (see for instance Guyon et al. (2001)). For a sufficiently deep porous substrate ($d > 2d_B$) and a sufficiently small permeability, so that the Darcy velocity u_p is small, the flow in the porous medium is localized in the momentum boundary layer close to the interface. Therefore, the bottom of the boundary-layer acts as an equivalent solid surface and gravity waves sit on an effective liquid layer made of the film augmented with the upper momentum diffusion layer in the porous medium. As a consequence, gravity waves travel at a speed that is close to $\sqrt{g(\bar{H}_\mathrm{N} - d + d_B)\cos\beta}$ and with a length that is scaled by the thickness $\bar{H}_\mathrm{N} - d + d_B$.

The above reasoning is supported by the fact that the difference $\bar{c}_{d+} - \bar{c}_{d-} \approx \sqrt{g(\bar{H}_\mathrm{N} - d + d_B)\cos\beta}$ and the sum $\bar{c}_{d+} + \bar{c}_{d-} \approx 1.6\bar{U}_\mathrm{N}$, so that dynamic waves are effectively gravity waves moving on a liquid film whose thickness is augmented by the thickness of the momentum diffusion layer d_B and advected by the flow. Kinematic waves moves at $c_k \approx 2\bar{U}_\mathrm{N}$. We thus introduce a modified Froude number

$$\tilde{\mathrm{Fr}}^2 = \frac{\bar{U}_\mathrm{N}^2}{g(\bar{H}_\mathrm{N} - d + d_B)\cos\beta} = \frac{Fr^2}{\cot\beta}(1 - \underline{\delta} + \underline{\delta}_B)^{-1} \tag{5.15}$$

which compares the velocity of the flow and the phase speed of gravity waves. Here $\underline{\delta}_B = d_B/\bar{H}_\mathrm{N}$ refers to the dimensionless thickness of the boundary layer.

Absence of significant effects

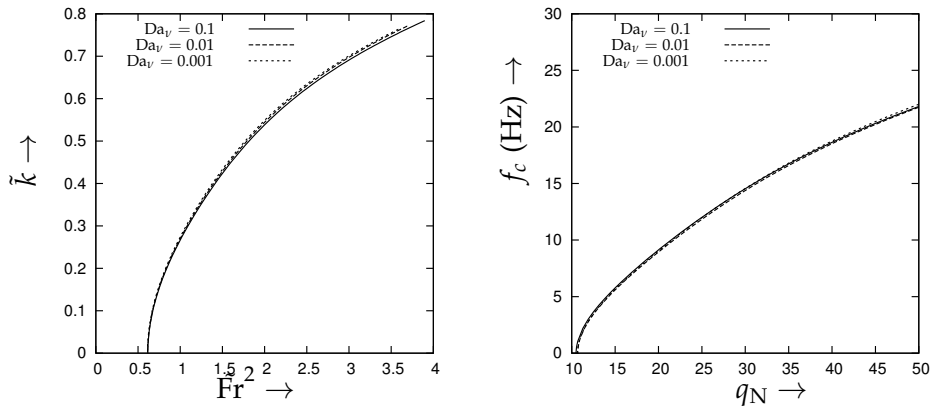

(a) (b)

Figure 5.4 – *Marginal stability curves for different values of the Darcy number. (a) modified dimensionless wavenumber $\tilde{k}$ versus modified Froude number $\tilde{\mathrm{Fr}}^2$; (b) dimensional cut-off frequency f_c versus flow rate q_N.* $\Gamma = 769.8$, $\beta = 4.6°$, $\underline{\delta} = 0.1$, $\underline{\Delta} = 0.001$ *and* $\underline{\varepsilon}_H = 0.78$.

The linear stability of the film based on the linearized governing equations (a Orr-Sommerfeld problem) has been compared to the solutions of the dispersion relation (5.13) showing a good agreement. Marginal stability curves are presented in figure 5.4 in the parameter plane consisting of the dimensional cut-off frequency f_c (Hz) versus the dimensionless flow rate q_N. The choice of such a parameter plane stems from experimental conditions where the forcing frequency and flow rate are both monitored at the inlet. A collapse of the different curves on a single master one is observed. An experimental study of the influence of the substrate permeability on the primary stability of the film would conclude to the absence of significant effects. This surprising absence can be understood by observing that the base-flow velocity profiles shown in figure 5.3b are not far from an equivalent Poiseuille flow in the flow region made of the liquid medium and the momentum boundary layer of the porous medium. Therefore, since at a given flow rate and inclination, that is a given gravitational acceleration, corresponds only one uniform film solution on an impermeable substrate, the free-surface velocity and effective thickness of a uniform film flowing on a porous medium does not vary significantly with the permeability of the porous medium, which explains the absence of effects observed in figure 5.4b.

Our investigation in the nonlinear regime concludes to the same absence of effects. As an example, figures 5.5 displays the wave profiles obtained at the end of the numerical experiments at three different locations taken at increasing distance from the inlet. These profiles can be contrasted to the experimental ones provided by Liu and Gollub (1994) in the case of an impermeable substrate (figure 7 in that reference).

The same qualitative responses of the film is observed for the two tested Darcy numbers. At the relatively high frequency $f = 4.5$ Hz, an inlet forcing generates a spatially modulated wavetrain. Waves are initially single-peaked with a hollow-like shape. Further downstream, they become multi-peaked as a result of the growth of secondary depres-

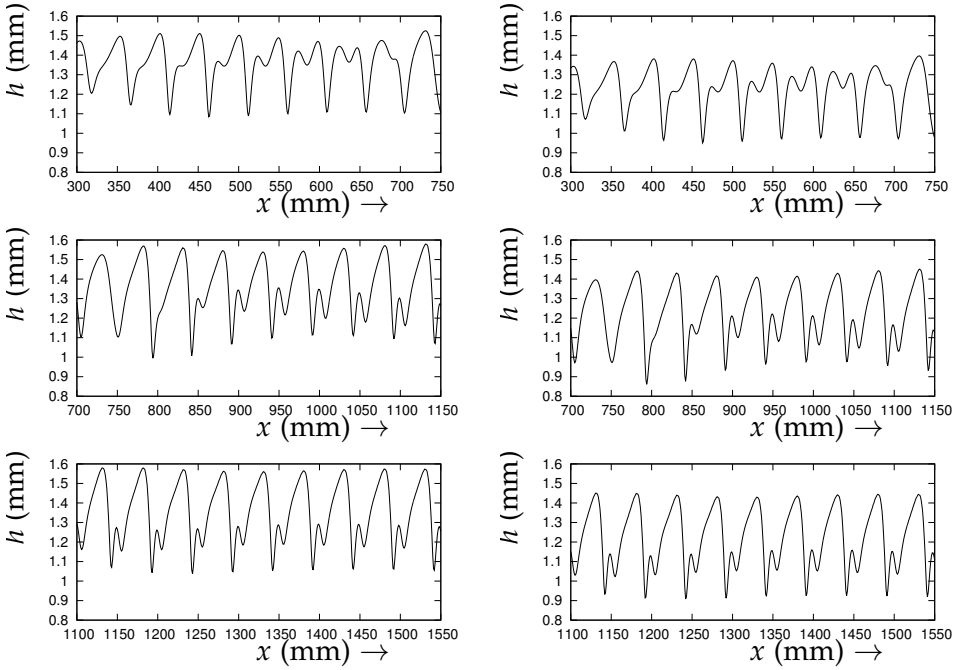

Figure 5.5 – *Simulations of the spatial response of the film to an inlet forcing in the experimental conditions of Liu and Gollub (1994). Left:* $\mathrm{Da} = 10^{-5}$ *($d_B = 0.037$ mm), $Re = 29$ and $A = 0.08$; right:* $\mathrm{Da} = 1$ *($d_B = 0.14$ mm), $Re = 26.2$ and $A = 0.06$. Glycerin-water mixture flowing on metal foam. $A = 0.03$, $\underline{\delta} = 0.1$, $\underline{\varepsilon}_H = 0.78$, $d = 0.14$ mm, $f = 4.5$ Hz, $\beta = 6.4°$, and $\Gamma = 526$. Snapshots of the film thickness at three different locations from upstream (top) to downstream (bottom).*

sions and a phase-locking process. These observed spatial evolutions are nearly identical to what was observed in the experiment by Liu and Gollub. At low permeability ($\mathrm{Da} = 10^{-5}$), the momentum boundary layer in the porous substrate is relatively thin in comparison to the film thickness ($d_B = 0.037$ mm as compared to $\bar{H}_\mathrm{N} - d = 1.2$ mm). The amount of liquid flowing in the porous substrate is not significant and the dynamics of the film is therefore not different to what is observed on an impermeable substrate ($\mathrm{Da} \to 0$).

At high permeability ($\mathrm{Da} = 1$), the effect of the porous medium remains quite limited on the waves, whose speed and wavelength are not affected. The main significant effect of the presence of the porous layer is a uniform displacement of the interface corresponding to the invasion of the porous medium by the flow. The wave profiles at $\mathrm{Da} = 10^{-5}$ and $\mathrm{Da} = 1$ are close when moved by a distance equal to the displacement of the lower end of the momentum boundary layer, i.e. $d - d_B(\mathrm{Da} = 10^{-5}) = 0.103$ mm. In the nonlinear regime as well as in the linear regime, the effect of a porous substrate onto the wave dynamics is not very significant. This is again related to the fact that, at a given flow rate and at the relatively large porosity $\underline{\varepsilon}_H = 0.78$ of a metal foam, the velocity distribution of the base flow remains close to the semi-Poiseuille Nusselt solution on an impermeable substrate. Consequently, varying the permeability does not change noticeably the free surface velocity and the effective thickness of the film, i.e. augmented with the thickness of the momentum boundary layer in the porous substrate. The length and velocity scales remaining

nearly unchanged, the nonlinear regime is not much affected by the presence of a permeable substrate.

5.2 non-Newtonian falling film

The second problem I have tackled during these last three years concerns the influence of rheology on the Kapitza instability of a falling film. This problem has been considered by Symphony Chakraborty in her PhD thesis (Chakraborty 2012). I am summarizing the key findings of her study in this section.

5.2.1 Power-law fluids

The most simple non-Newtonian fluids are generalized Newtonian fluids, for which an effective viscosity function of the rate of strain $\dot{\gamma}$ can be defined. Our study thus started with this simple —but not so simple as we shall see— fluids. In what follows, I focus mainly on shear-thinning fluids (power-law index $n < 1$), which is the most interesting case. However, shear-thickening fluids ($n > 1$) are also considered in Ruyer-Quil et al. (2012).

Because of the simplicity of the Ostwald-de-Waele power-law model

$$\mu_{\text{eff}}(\dot{\gamma}) = \mu_n \dot{\gamma}^{n-1}, \tag{5.16}$$

shear-thinning falling films have recently been the subject of a consequential interest (see e.g. Dandapat and Mukhopadhyay (2001; 2003), Sisoev et al. (2007), Amaouche et al. (2009), Fernández-Nieto et al. (2010)). These studies are based on the shallow-water averaging of the primitive equations (cf. § 2.3.4). Amaouche et al. (2009) and Fernández-Nieto et al. (2010) have corrected the Kármán-Polhausen averaged momentum equation derived by Hwang et al. (1994) and Ng and Mei (1994) and formulated two-equation models that are consistent up to order ϵ. This consistency enabled them to correctly capture the instability threshold obtained by Ng and Mei (1994), Miladinova et al. (2004). However, they do not account for $O(\epsilon^2)$ effects such as streamwise viscous diffusion (Trouton viscosity), which is known to affect wave-to-wave interaction processes and thus the wave dynamics for Newtonian film flows (Kawahara 1983, Kawahara and Toh 1988, Pradas et al. 2011).

As a consequence, we have attempted to develop a model including second-order viscous diffusion terms in a consistent way. To account for streamwise viscous diffusion, the effective viscosity $\mu_{\text{eff}}(\dot{\gamma})$ and its derivative $d\mu_{\text{eff}}/d\dot{\gamma}$ must be computed at the free surface, where the strain rate $\dot{\gamma}$ goes to zero for an unperturbed interface. In the case of the power law (5.16) either $\mu_{\text{eff}}(0)$ or $d\mu_{\text{eff}}/d\dot{\gamma}(0)$, or both, are undefined for $n < 3$ which corresponds to most shear-thinning and shear-thickening fluids. This calls for a regularization at zero strain rate of the power law (5.16) which is here accounted for by introducing a Newtonian plateau at low strain rates.

A regularization of the power-law Ostwald-de-Waele (5.16) is assumed at low shear rate to recover the Newtonian behavior in that limit. This is

Set	Concentration	μ_n (Pa.s^n)	n	μ_0 (Pa.s)	$\dot\gamma_c$ (s^{-1})	$\dot\gamma_c t_\nu$	Γ
1.	500 ppm	0.04062	0.607	0.08	0.18	1.8×10^{-3}	378
2.	1500 ppm	0.3592	0.40	1.43	0.1	1.7×10^{-3}	48.7
3.	2500 ppm	0.9913	0.34	7.16	0.05	1.2×10^{-3}	13.0

Table 5.1 – *Parameters of xanthan gum solutions in water. Surface tension and density are $\sigma = 65$ mN/m and $\rho = 995$ kg/m^3. Values of the Kapitza number are computed for a moderate inclination $\beta = 15°$.*

the spirit of a three-parameter Carreau law:

$$\mu_{\text{eff}}(\dot\gamma) = \mu_0 \left[1 + (\dot\gamma/\dot\gamma_c)^2\right]^{(n-1)/2} . \tag{5.17}$$

However, using (5.17) forbids to determine analytically the base flow and one can instead introduce a Newtonian plateau:

$$\mu_{\text{eff}}(\dot\gamma) = \mu_n \dot\gamma^{n-1} \quad \text{for} \quad \dot\gamma > \dot\gamma_c , \tag{5.18a}$$
$$\mu_{\text{eff}}(\dot\gamma) = \mu_0 \quad \text{for} \quad \dot\gamma \le \dot\gamma_c . \tag{5.18b}$$

The continuity of the shear stress at $\dot\gamma = \dot\gamma_c$ requires $\mu_n \dot\gamma_c^{n-1} = \mu_0$.

To set up the frame of this study, let us precise the fluid properties of some considered shear-thinning fluids, the scaling and set of dimensionless parameters.

Table 5.1 presents reasonable values of the zero strain viscosity μ_0 and the critical strain rate $\dot\gamma_c$ separating Newtonian and non-Newtonian behavior of shear-thinning xanthan dilute solutions. The surface tension of xanthan solutions is assumed here to remain close to that of pure water $\sigma = 65$ mN/m.

The length scale is the uniform film thickness $\bar h_{\text{N}}$. The velocity scale V is defined by balancing viscous friction $\propto \mu_n V^n \bar h_{\text{N}}^{-(n+1)}$ and streamwise gravity acceleration $\propto \rho g \sin\beta$ which gives

$$V = \left(\frac{\rho g \bar h_{\text{N}}^{n+1} \sin\beta}{\mu_n} \right)^{1/n} \tag{5.19}$$

such that the Froude number $Fr = V/\sqrt{g\bar h_{\text{N}} \cos\beta}$, which compares the characteristic speed of the flow to the speed of the gravity waves propagating at the interface, and the Reynolds number

$$Re = \frac{\rho V^{2-n} \bar h_{\text{N}}^n}{\mu_n} = \left[(\mu_n/\rho)^{-2} (g\sin\beta)^{2-n} \bar h_{\text{N}}^{n+2} \right]^{1/n} \tag{5.20}$$

are related by the relation $Re/\cot\beta = Fr^2$. As usual we introduce $l_\nu = (\mu_n/\rho)^{2/(n+2)} (g\sin\beta)^{(n-2)/(n+2)}$ and $t_\nu = \left(\frac{\mu_n}{\rho}\right)^{\frac{1}{n+2}} (g\sin\beta)^{-\frac{2}{n+2}}$, the length and time scales corresponding to the balance of gravity acceleration and viscous drag. Surface tension, gravity and viscous drag can be compared by the Kapitza number

$$\Gamma = (l_c/l_\nu)^2 = (\sigma/\rho)(\mu_n/\rho)^{-4/(n+2)} (g\sin\beta)^{(2-3n)/(n+2)} , \tag{5.21}$$

where $l_c = \sqrt{[\sigma/(\rho g \sin\beta)]}$ is the capillary length. The Weber and Kapitza numbers are related one to the other by the relation $We = \Gamma(l_v/\bar{h}_{\rm N})^2$. Finally, the Newtonian plateau introduces a last parameter, namely dimensionless threshold $s = \dot{\gamma}_c \bar{h}_{\rm N}/V$, or equivalently $r = s^{n-1}$, which can be interpreted as the ratio $r = \mu_0/\mu_w$ of the shear viscosities $\mu_0 = \mu_n(\dot{\gamma}_c)^{n-1}$ and $\mu_w = \mu_n(V/\bar{h}_{\rm N})^{n-1}$ at the free surface and at the wall.

Let us emphasize that the velocity scale V given by (5.19) is the dimensional speed of the linear kinematic waves in the long wavelength limit, which is the typical speed of the nonlinear waves running on the falling film and thus back up our choice of scales. The averaged velocity of the Nusselt flat film is $Vn/(2n+1)$ so that there is a factor $n/(2n+1)$ between the adopted definition of the Reynolds number and the usual one based on the averaged velocity.

We invoked again the weighted residual method to obtain a two-equation model based on the mass balance (5.12) and an averaged momentum balance. A lengthy procedure [detailed in § 3 of Ruyer-Quil et al. (2012) appended to this chapter] leads to

$$\begin{aligned}
&Re\partial_t q = Re\left[-F(n)\,\frac{q}{h}\partial_x q + G(n)\,\frac{q^2}{h^2}\partial_x h\right]\\
&+I(n)\left[h\left(1-\cot\beta\partial_x h + We\partial_{xxx}h\right) - \frac{q|q|^{n-1}}{(\phi_0 h^2)^n}\right]\\
&+r(h,q)\left[J_0(n)\frac{q}{h^2}\left(\partial_x h\right)^2 - K_0(n)\frac{\partial_x q\partial_x h}{h} - L_0(n)\frac{q}{h}\partial_{xx}h + M_0(n)\partial_{xx}q\right]\\
&+r_w(h)\left[J_w(n)\frac{q}{h^2}\left(\partial_x h\right)^2 - K_w(n)\frac{\partial_x q\partial_x h}{h} - L_w(n)\frac{q}{h}\partial_{xx}h + M_w(n)\partial_{xx}q\right]
\end{aligned} \tag{5.22}$$

where the coefficients are all explicit fractional functions of the power-law index n. Here $r_w(h) = h^{1-1/n}$ stands for the effective viscosity at the wall, whereas $r(h,q)$ denotes the effective viscosity at the free surface $\mu_{\rm eff}(y=h)$ approximated from the model variables h and q as :

$$r(h,q) \equiv \left[s^2 + \partial_x v_s^2 + 4(\partial_x u_s)^2\right]^{(n-1)/2}\Big|_{y=h} \tag{5.23a}$$

where

$$\begin{aligned}
\partial_x v_s^2 + 4(\partial_x u_s)^2\big|_{y=h} \;=\; &\left[\frac{2(2n+1)}{n+1}\partial_x\left(\frac{q}{h}\right)\right]^2 + \left\{\frac{2n+1}{n+1}\left[-2\frac{\partial_x h\partial_x q}{h}\right.\right.\\
&\left.\left.+q\left(2\frac{(\partial_x h)^2}{h^2} - \frac{\partial_{xx}h}{h}\right)\right] + \partial_{xx}q\right\}^2 .
\end{aligned} \tag{5.23b}$$

We have considered as equivalent the assumption (5.18) of a Newtonian-plateau and the Carreau law (5.17) to express the effective viscosity $r(h,q)$. Our computations show that this assumption is reasonable in the limit of a vanishing Newtonian layer. The averaged momentum equation (5.22) retains the contribution to streamwise viscous diffusion from the free surface (second row) and from the bulk (third row).

Results from the two-equation low-dimensional model have been validated by comparisons with DNSs using Gerris software (Popinet 2003; 2009). Figure 5.6 presents the distribution of the strain rate under the

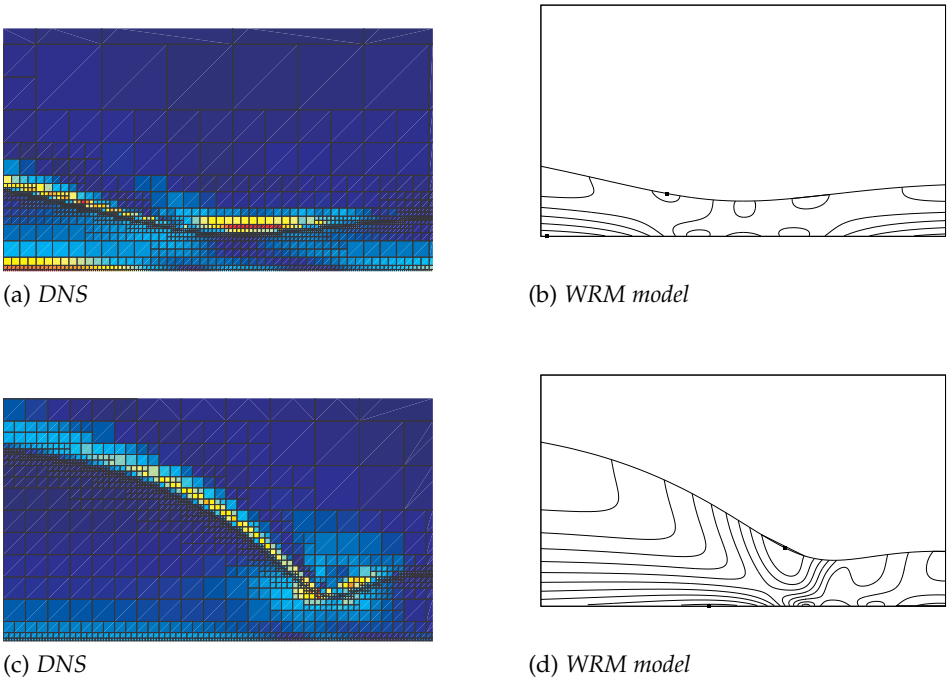

(a) *DNS* (b) *WRM model*

(c) *DNS* (d) *WRM model*

Figure 5.6 – *Distribution of the strain rate $\dot{\gamma}$ under the waves whose profiles are shown in figures 5.7a and 5.7c. Left: results from DNS. Dark blue (red) regions correspond to the minimum (maximum) of $\dot{\gamma}$. Right: isocontours of the strain rate corresponding to the WRM model. The location of the maxima of $\dot{\gamma}$ at the wall and at the free surface are depicted by squares.*

solitary-like waves whose profiles are shown in figures 5.7a and 5.7c for two different xanthan-gum solutions. From the results of the DNS simulations, the local maxima of the strain rate are located either at the wall or at the free surface.

This justifies the cumbersome expressions of the streamwise viscous terms [the last two rows in (5.22)] as both the effective viscosity of the fluid at the free surface and in the bulk act on the dispersion of the waves. In both cases, the model (left panels in figure 5.6) slightly underestimates the amplitude of the capillary ripples and predicts smaller values of the maxima of the strain rate. However, the locations of the local minima and maxima predicted with the model are in remarkable agreement with the strain rate distributions found by DNS.

The profiles of traveling waves obtained at the end of the DNS simulations are presented in figure 5.7 and contrasted to the solutions to the two-equation model. The waves systematically present capillary ripples preceding the main hump in spite of the very large ratio r of the free surface to wall effective viscosities. Their shapes are similar to the solitary waves observed experimentally for Newtonian fluids. A good agreement between DNSs and the results from the model is obtained. However, the model tends to overestimate the speed of the waves. We note that the nonlinear dependence of the effective viscosity (5.23) on the gradients of q and h is necessary to reproduce the capillary waves observed in the DNS simulations.

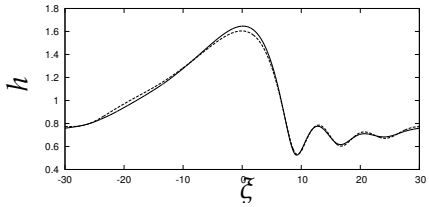

(a) *set 1*, $Re = 50$, $\lambda = 60$

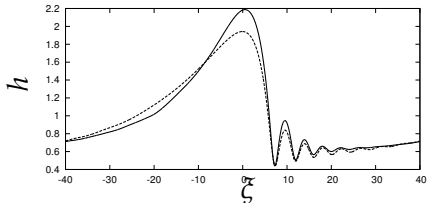

(b) *set 1*, $Re = 100$, $\lambda = 80$

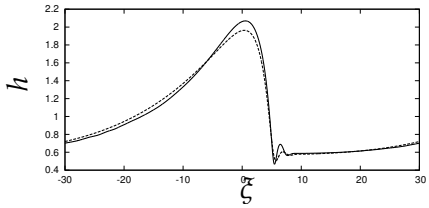

(c) *set 2*, $Re = 50$, $\lambda = 60$

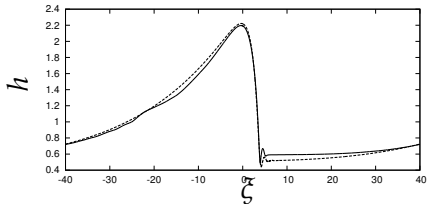

(d) *set 2*, $Re = 100$, $\lambda = 80$

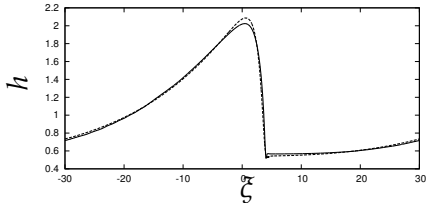

(e) *set 3*, $Re = 50$, $\lambda = 60$

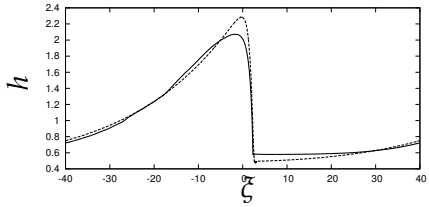

(f) *set 3*, $Re = 100$, $\lambda = 80$

Figure 5.7 – *Traveling wave profiles for shear-thinning xanthan-gum solutions in water. Solid lines refer to the DNS results from Gerris software, whereas dashed lines refer to the solutions to the two-equation model.*

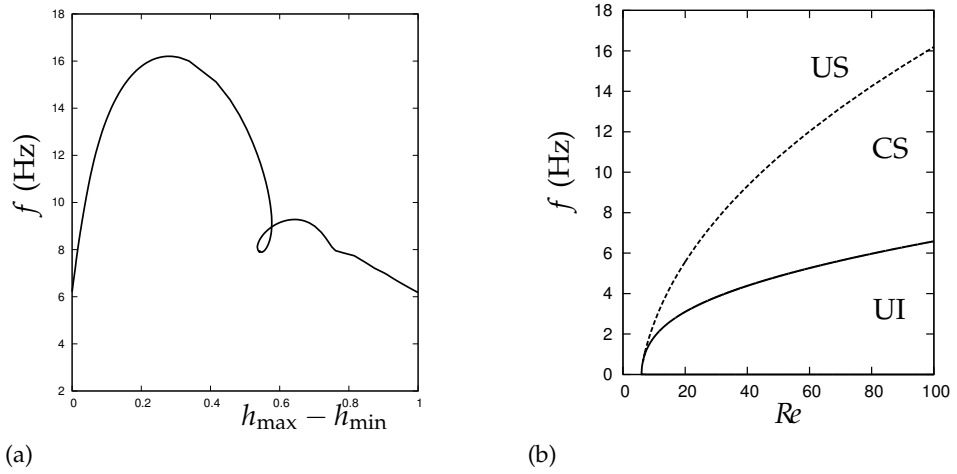

Figure 5.8 – *(a) Amplitude $h_{max} - h_{min}$ versus frequency at $Re = 100$ showing the subcritical onset of traveling waves when frequency is varied from the cut-off frequency f_c. (b) Stability diagram in the plane (Re, f). Solid and dashed lines refers to the marginal stability curve and to the locus of a saddle-node bifurcation f_{sub}. The unconditionally and conditionally stable regions are labeled 'US' and 'CS' respectively. The unconditional instability region is labeled 'UI'. Inclination angle is $\beta = 15°$, other parameters correspond to a shear-thinning xanthan-gum solution. Traveling wave solutions have been computed enforcing the integral constraint $\langle q \rangle = q_0$.*

An interesting phenomenon has been evidenced: shear-thinning promotes a subcritical onset of traveling waves at larger wavenumber than the linear cut-off wavenumber k_c. A conditional stability of the base flow is thus observed, the film being able to respond to a periodic forcing at inlet at $k > k_c$ if the amplitude of the perturbations is large enough. This phenomenon results from the removal of the Newtonian layer, the reduction of the effective viscosity at the free surface and therefore the attenuation of the damping of short waves. Comparisons to DNS show that this phenomenon is accurately captured by the weighted-residual model (5.12), (5.22).

Figure 5.8a presents the amplitude $h_{max} - h_{min}$ versus the frequency f of the principal branch of traveling-wave solutions for a xanthan gum solution (parameter set 2 in table 5.1), $Re = 100$ and a moderate inclination angle $\beta = 15°$. The integral constraint $\langle q \rangle = q_0$ has been enforced in order to enable comparisons with the wavetrains emerging from the time-dependent simulations of the spatial response of the film to a periodic excitation at frequency f. Traveling waves emerge at the cut-off frequency f_c from the Nusselt solution ($h_{max} - h_{min} = 0$). The control parameter being f, a saddle-node bifurcation is observed at the frequency f_{sub}. Monitoring f_c and f_{sub} in the plane (f, Re) gives the stability diagram displayed in figure 5.8b. Below the cut-off frequency f_c, the flat film is unconditionally unstable, whereas unconditional stability is expected above f_{sub}. Whenever f lies in the interval $[f_c, f_{sub}]$, a conditional stability is anticipated. The spatial response of the flat film to a periodic excitation at inlet then depends on the amplitude of the perturbation.

This intriguing phenomenon has not been reported yet in experiments.

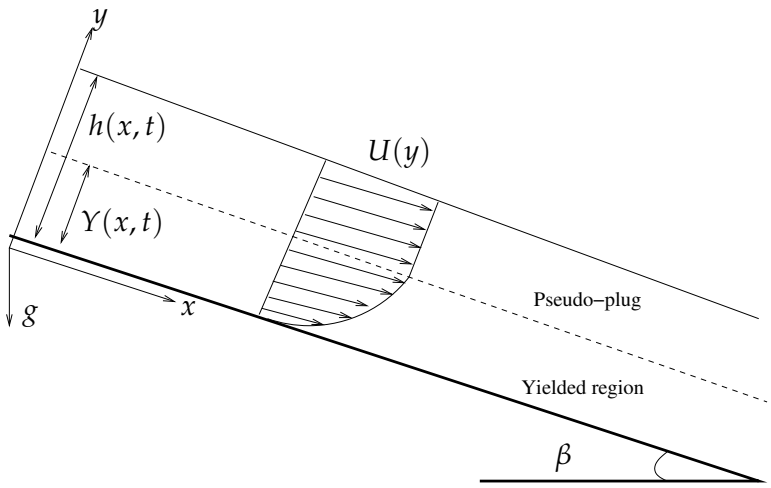

Figure 5.9 – *Geometry of a viscoplastic falling films.*

Indeed, our spatio-temporal simulations reveal that trains of short waves excited at larger frequencies than the cut-off one are quickly disrupted by secondary instabilities which lead to a disordered state organized around solitary waves in interaction. The conditional stability of the primary flow is thus likely to be difficult to observe in experiments.

5.2.2 Viscoplastic fluids

In this section I present some preliminary results detailed in S. Chakraborty's PhD thesis (Chakraborty 2012). A viscoplatic falling film is modeled by an elasto-viscoplatic constitutive relation introduced by Saramito (2008). The aim of this work is to extend the pseudo-plug theory formulated by Balmforth and Liu (2004) to deal with viscoplatic films at the moderate values of the Reynolds number.

(Balmforth and Liu 2004) considered the stability of a viscoplastic fluid layer flowing on an inclined plane under the action of gravity. Their concern was the onset of roll waves that are observable in mud surges. Their approach was truncated at first order in the film parameter. Balmforth and Liu showed that an unyielded plug region laying at the top of a uniform film forms a lid which forbids the instability to occur. The geometry of the base flow is sketched in figure 5.9.

However, as soon as the free surface is deformed, the plug starts to yield and the instability is possible which assumes that normal stresses appears instantly in the plug region so that the second invariant of the stress can exceed the yield stress. In other words, small but finite amplitude perturbations of the free surface are sufficient to trigger the instability and viscoplastic film flows should be conditionally unstable. Moreover, in order to describe the dynamics of a viscoplastic film, surface tension and streamwise viscous diffusion must be accounted for. Balmforth and Liu considered a viscoplastic fluid modeled by the Herschel and Buckley law

$$\tau = K|\sigma|^{n-1}\sigma + \tau_0 \frac{\sigma}{|\sigma|} \qquad \text{when} \qquad |\sigma| > 0 \tag{5.24a}$$

$$|\tau| < \tau_0 \qquad \text{when} \qquad |\sigma| = 0 \tag{5.24b}$$

where $\tau = (\tau_{ij})$ and $\sigma = (\sigma_{ij}) = [(\partial_i u_j + \partial_j u_i)/2]$ are the stress and rate of strain tensors, τ_0 is the yield stress, $|\tau| = \sqrt{2\tau_{kl}\tau_{kl}}$ and $|\sigma| = \sqrt{2\sigma_{kl}\sigma_{kl}}$ are the second invariants of the stress and rate of strain tensors. Equation (5.24) can be rewritten as (Saramito 2008)

$$\sigma = \max\left(0, \frac{|\tau| - \tau_0}{K|\tau|^n}\right)^{\frac{1}{n}} \tau \equiv \kappa_n(|\tau|)\tau \tag{5.25}$$

The viscosity of a viscoplastic fluid modeled by (5.24) is undefined in the unyielded region and diverges at zero strain rate. In order to take into account viscous effects at the interface and to capture the conditional stability of the film, one has to describe how the unyielded plug region is deformed which demands to include the elasticity of the solid-like behavior of the fluid into the constitutive equation. Recently, Saramito (2008) has proposed an extension of the Herschel-Bulkley law (5.24) including the viscoelastic properties of the fluid:

$$\frac{1}{G}\overset{\triangledown}{\tau} + \kappa_n(|\tau_d|)\tau - \sigma = 0 \tag{5.26}$$

where G is the elastic modulus, $\tau_d = \tau - \frac{1}{N}\mathrm{tr}(\tau)I$ denotes the deviatoric part of τ and

$$\overset{\triangledown}{\tau} = \partial_t \tau + \mathbf{v}\nabla\tau - \tau\nabla\mathbf{v}^T - \nabla\mathbf{v}\tau \tag{5.27}$$

is the upper convected time derivative of the stress tensor τ. We attempt to extend the pseudo-plug theory by Balmforth and Liu using the constitutive equation (5.26).

A Orr-Sommerfeld problem has been derived to study the linear stability analysis of this flow based on the linearized governing equations. Figure 5.10 shows the critical Reynolds number against the relative thickness of the pseudo-plug region h_{plug} for several values of the Deborah number (the Deborah number compares the characteristic time of elastic relaxation and the inertial time). The result of the Orr-Sommerfeld problem shows a good agreement with the result of a preliminary four-equation model. As expected, lowering the thickness of the pseudo-plug region has a stabilizing effect. Indeed, if $De = 0$ (no elastic effects) the plug is solid and cannot deform, as a consequence the instability threshold $Re_c \to \infty$. As expected, the stabilizing effect of the inelastic plug disappears along with the pseudo-plug region ($h_{\mathrm{plug}} \to 0$). Surprisingly enough, the same removal of this stabilizing effect also occurs when the plug starts to invade the whole domain.

A follow-up of this work is under way. Needless to say, a low-dimensional modeling of this problem requires a treatment of the divergence of the viscosity at the boundary of the pseudo-plug and the yielded region.

5.3 Current works and perspectives

I this section, I give a short account of the two different projects I am involved in at the present stage. For each project, I give some possible directions for follow-up and future studies.

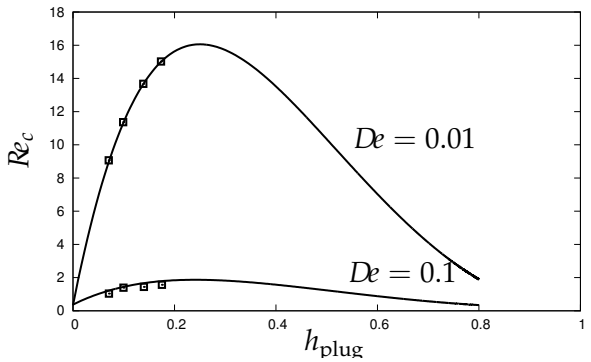

Figure 5.10 – *Critical Reynolds number Re_c as a function of the relative thickness h_{plug} of the pseudo-plug region. The solid line correspond to a four-equation low-dimensional model and squares refer to the numerical solutions to the Orr-Sommerfeld problem of the power-law index $n = 0.5$ and inclination angle $\beta = 45°$.*

5.3.1 Geophysical problems

A natural development of the study of non-Newtonian falling films concerns the study of rapid mass movements such as debris flows, lahars, snow avalanches.

The aspect ratio of these hazardous events justifies the use of shallow-water models. A good approximation concerning the material is to consider it as a yield-stress fluid. However, this poses challenging issues such as the account for elasticity and for the behavior of the (pseudo-)plug zone of the flow. Models that are currently in use rely indeed on simplified, empirical treatments of the fluid rheology (Laigle and Coussot 1997, Naaim et al. 2004). Accounting properly for the non-Newtonian rheology of mud and avalanches flows is presently a key issue for achieving realistic models. A current study consists in the derivation of an accurate model accounting for the elasto-viscoplastic constitutive law derived by Saramito (2008).

It is important to note that in many applications, a notable slip is observed at the wall region. In particular, flows of dense snow present a yield stress and a slip velocity at the wall as high as several meters per second (Dent and Lang 1983, Kern et al. 2004, Rougier and Kern 2010). An immediate extension of the derivation of low-dimensional models for elasto-viscoplastic fluids that is currently under way would be to account for a slip at the wall boundary.

An important aspect of real geophysical flows is the presence of a non-planar and rough geometry. Roberts and Li (2006) and Boutounet et al. (2008) have already proposed some models taking into account general topographies. The success of the weighted residual method for the different problems reviewed in this memoir offers a promising ground for future studies devoted to more realistic geophysical flows including complex rheologies, complex geometries and wall boundary conditions.

5.3.2 Industrial problems

Liquid falling films are encountered in a variety of industrial applications. For instance, the cooling of microelectronic equipment or the separation of

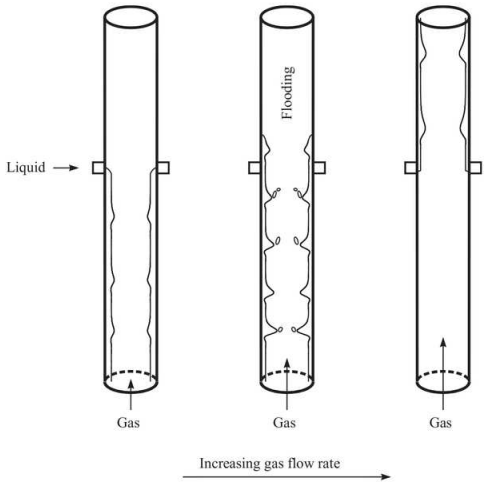

Figure 5.11 – *Sketch of gas stream shearing a liquid flow in a tube as gas flow rate is increased. After Tseluiko and Kalliadasis (2011).*

multi-component mixtures in the chemical and food industries are often ensured by means of falling films. They even represent the state-of-the-art technique in the sugar industry and constitute the basic components in sea-water desalination plants. As far as heat or mass transport applications are concerned, a drastic enhancement of heat/mass transport is observed (Colinet et al. 2001). For example, Frisk and Davis (1972) and Goren and Mani (1968) have reported that the waviness of the film can increase by as much as 10-100% the heat/mass transfer coefficients. Therefore liquid film flows play a central role in the development of efficient means for interfacial heat/mass transfer in engineering applications.

In most of the designs of the heat or mass exchangers involving falling films, a counter-current or a co-current gas flow is generated to enhance the transfer by shearing the liquid interface. An important technological limitation of such devices is the so-called flooding phenomenon: as the gas flow rate is increased, the initially downward-falling film starts to travel upwards. Also, just before the flow reversal, the amplitude of the interfacial waves grows very rapidly and at the same time the speed of the waves decreases. Eventually, as the flow reverses very rapidly, atomization of the liquid into the gas phase occurs. This phenomenon is sketched in figure 5.11. Yet, optimal operating conditions are generally close to the limit of flooding. As the flooding phenomenon is accompanied by an immediate deterioration of device efficiency, the prediction of its limit is thus an essential task. Turning to an example from the automotive industry, an improved prediction and control of water films developing on windscreens under rainy conditions is desirable in order to improve safety. This scenario differs from the above mentioned example in the sense that the gas flow shearing the liquid film is no longer geometrically confined, which brings up the question of interaction with a gaseous turbulent boundary layer.

At the experimental front, a large scattering of the experimental conditions at which the flooding phenomenon can be found is observed (Jeong and No 1996). This dispersion of the results is chiefly a consequence of the sensitivity of the flow to the inlet conditions of the gas and liquid

flows (Govan et al. 1991, Jeong and No 1994, Zapke and Kröger 1996) and also results from the interplay of several mechanisms. Three physical mechanisms are postulated: (i) wavy instability of the film promoted by the interfacial shear and leading to stationary waves of large amplitudes, or "wave levitation" (Deendarlianto et al. 2010) that could potentially evolve towards atomization; (ii) onset of liquid bridges in confined geometries, generally at liquid entrance or "liquid bridging" Vlachos et al. (2001), Mouza et al. (2002); (iii) standing wave trapped at the liquid exit, the growth of which ultimately seals the passage of the gas flow (Mouza et al. 2005).

As far as it is knowledgeable, no attention has been paid on the local geometry of the liquid outlet/gas inlet (shape of the edges, orientation) and it influence on the flooding phenomenon. If the enhancement of the liquid film instability in presence of a shear is a commonly accepted mechanism for flooding, I am not aware of any attempt to control the dynamics of the liquid film by applying a forcing at inlet. Yet, a significant progress in the understanding of a falling film dynamics has been achieved in this way (see for instance Liu and Gollub (1994) and § 2.1). The sequence of transitions, primary and secondary instabilities, leading from the Nusselt flat falling film solution to a disordered sate organized by 3D horseshoe waves is now quite well characterized and has helped to improved the different modeling attempts.

At the theoretical front, a first approach has been proposed by Miles (1957) and Benjamin (1959) who linearized the Navier-Stokes equations and modeled the effect of the turbulent gas flow with a generic mean velocity profile. However, this linearized description is by design limited to the case of small amplitude interfacial waves, which differs substantially from industrial conditions. Moreover, the representation of the turbulent velocity profile in the theory by Miles and Benjamin imposes further restrictions. Firstly, interfacial disturbances are to remain within the viscous sublayer of the undisturbed gas flow. Secondly, the theory cannot take into account the effect of confinement and thirdly, it cannot be applied when separation occurs and backflow regions develop in the gas flow. However, some substantial progress has been achieved along this line by Tseluiko and Kalliadasis (2011) who have revisited the theory by Miles and Benjamin and have adopted a one-sided approach: from the kinematics of the film flow, they have computed the shear induced by the gas. They thus have formulated hierarchies of models for which the action of the gas flow is modeled by a non-local operator. Trifonov (2010; 2011) has also invoked the Benjamin-Miles approach and has assumed the wavy liquid-gas interface to yield small linear disturbance to the turbulent gas flow. Both Tseluiko and Kalliadasis, and Trifonov have investigated the onset of flooding within the "wave levitation" mechanism and have pinpointed the flooding threshold at the divergence of the traveling-wave amplitude.

Hitherto, a systematic drawback of the theory stems from the one-sided approach for which the kinematics of the film is assumed to pilot the shear of the gas flow on the film. Indeed, little attention has been paid to the effect of gas flow itself.

Sophie Mergui (assistant professor UPMC) and myself have contrived a two-fold project on the experimental and theoretical axes. The first as-

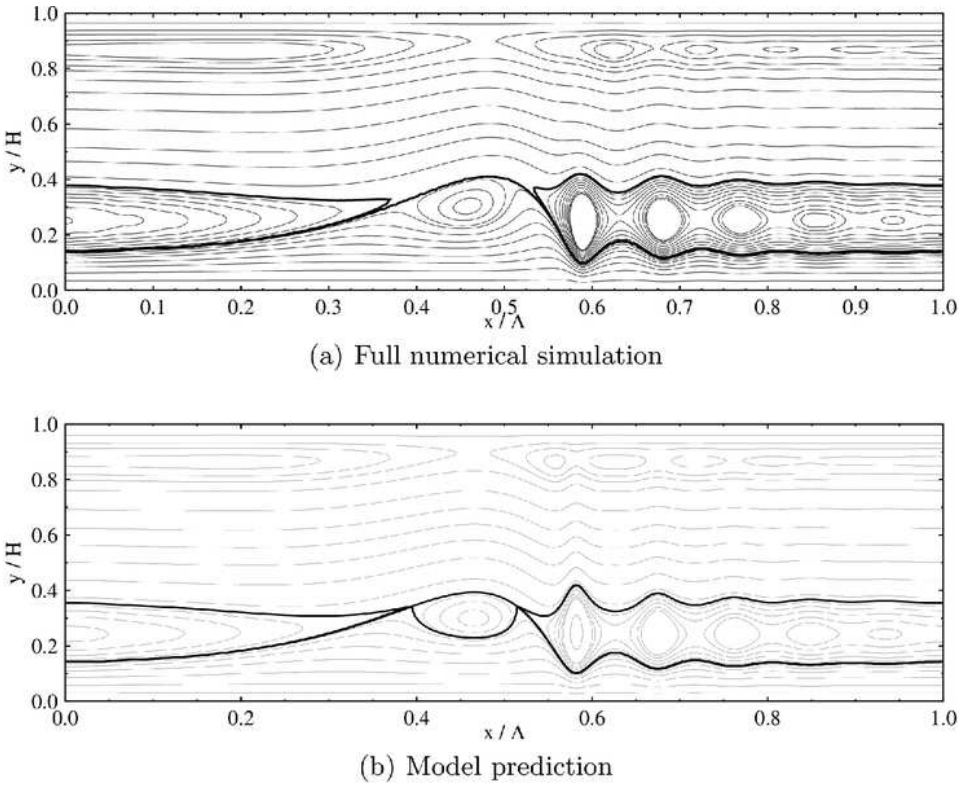

(a) Full numerical simulation

(b) Model prediction

Figure 5.12 – *Stream function contours (not equidistantly valued) in the wall-fixed reference frame for co-current gas flow:* $Re_l = 15.0$, $f = 16\,Hz$, $\Gamma = 509.5$, $H = 1.5\,mm$, $U_{GS} = 0.38\,m/s$.

pect of this project is under way with Nicolas Kofman's PhD thesis (from October 2011). An experimental set-up will be designed to study the onset of flooding. The inlet conditions both in the gas and in the liquid will be carefully designed in order to prevent the liquid to be sheared before the gas flow is steady. A forcing device will be also designed in order to monitor the excitation of the liquid inlet. Finally, the inclined plane geometry is adopted in order to study the effect of a shear on the threshold of the Kapitza instability.

The second part of this project benefited from Georg Dietze's postdoctoral fellowship (May 2011 until October 2012). Georg Dietze has now been recruited in CNRS. We have contrived a study of the coupling of the gas/liquid flows in a two-phase approach starting with the (simpler) problem of a falling film in presence of a laminar co- or counter-current gas flow. The approach is based on the long-wave theory and the weighted residual technique. A three-equation model has been derived which is consistent at $O(\epsilon)$ for inertial terms and $O(\epsilon^2)$ for the viscous terms. DNSs have been performed using two-phase flow solvers based on the VOF method, Gerris solver Popinet (2003; 2009) and OpenFOAM [1].

Some examples of non-linear traveling waves obtained with the model are compared to the DNSs in figures 5.12 and 5.13. Streamlines in the moving frame of the waves have been computed and evince intricate flow patterns in the gas flow with the formation of large eddies, the presence

[1] `http://www.openfoam.com/`

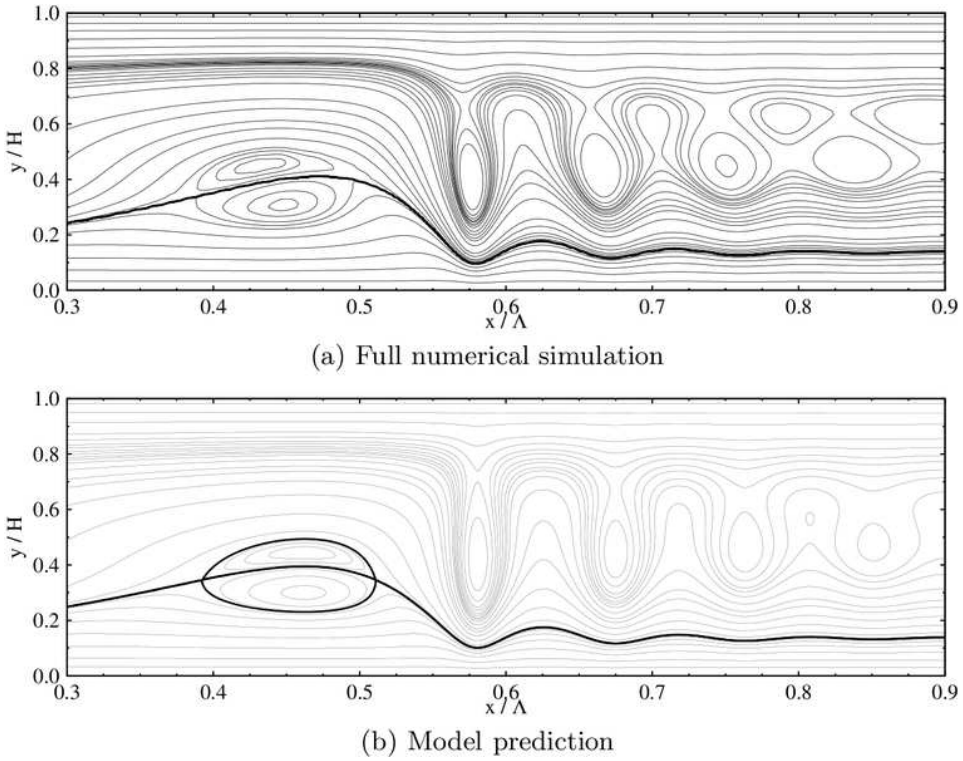

Figure 5.13 – *Idem figure 5.12 but for* $U_{GS} = 0.19$ *m/s.*

of which may strongly modify the heat and mas transfer at the liquid-gas interface.

A follow-up of this study will be devoted to the cylindrical geometry. Core-annular flows of two liquids inside a tube is a typical problem in oil extraction. The so called "bamboo waves" are typically observed when the viscosity of the outer liquid is smaller than the viscosity of the inner liquid. In horizontal pipes, the generation of waves at the interface separating core and outer flows is a necessary condition for the levitation from the wall of the core fluid, either lighter of heavier than the lubricating outer one. Experiments suggest that inertia plays a key role in the levitation process Joseph et al. (1997).

5.4 Appendix : Coefficients of the averaged momentum balance (5.11)

We give below the expressions of the coefficients $F(H)$ to $M(H)$ in terms of the base flow profile $f(y;H)$ solution to (5.6) and of the weight $w(y;H)$

defined by (5.10).

$$
\begin{aligned}
F(H) &= \frac{1}{\phi^2 H}\int_0^H \left[\underline{\varepsilon}' f\, l + \underline{\varepsilon}(f^2 - f' l) + \underline{\varepsilon}^2(\phi' f - \phi\, g)\right] w/\underline{\varepsilon}^2\, dy\,, && \text{(5.28a)}\\
G(H) &= \frac{1}{\phi^3}\int_0^H \left\{\underline{\varepsilon}' f(\phi' l - \phi m)\right.\\
&\quad \left. +\underline{\varepsilon}\left[\phi'(f^2 - f' l) + \phi(f' m - f g)\right]\right\} w/\underline{\varepsilon}^2\, dy, && \text{(5.28b)}\\
S(H) &= \frac{1}{\phi H^2}\int_0^H f\, w\, dy\,, \qquad I(H) = \Upsilon/H^2\,, && \text{(5.28c)}\\
J(H) &= \frac{1}{\phi^3}\left\{\Upsilon\left[\phi^2 + 4f|_H(\phi')^2 - 2\phi(f|_H + \phi')\phi''\right] + w|_H\phi(\phi\phi'' - 2f|_H\phi')\right.\\
&\quad + \int_0^H 2(\phi')^2 f - 2\phi\phi' g - \phi\phi'' f\\
&\quad \left. +\underline{\varepsilon}\left[[2(\phi')^2 - \phi\phi''](n - r) + 2\phi\phi'(s - o)\right] w\, dy\right\}\,, && \text{(5.28d)}\\
K(H) &= \frac{2}{H^3\phi^2}\left\{2f|_H\Upsilon\phi' - \Upsilon\phi\phi'' - f|_H w|_H\phi\right.\\
&\quad \left. + \int_0^H \left[\phi' f - \phi g + \underline{\varepsilon}\left(\phi'(n - r) + \phi(s - o)\right)\right] w\, dy\right\}\,, && \text{(5.28e)}\\
L(H) &= \frac{H^2}{2}K(H) + 2\frac{f|_H w|_H}{H\phi}\,, && \text{(5.28f)}\\
M(H) &= \frac{1}{H^2\phi}\left\{2f|_H\Upsilon + w|_H\phi + \int_0^H [f + \underline{\varepsilon}(n - r)]\, w\, dy\right\}\,, && \text{(5.28g)}
\end{aligned}
$$

where

$$
\begin{aligned}
g(y;H) &= \partial_H f\,, \qquad l(y;H) = \int_0^y f\, dy\,, && \text{(5.28h)}\\
m(y;H) &= \int_0^y g\, dy\,, \qquad n(y;H) = \int_H^y \underline{\varepsilon}^{-1}\partial_y f\, dy\,, && \text{(5.28i)}\\
o(y;H) &= \int_H^y \underline{\varepsilon}^{-1}\partial_y g\, dy\,, \qquad r(y;H) = \int_H^y l/\kappa\, dy\,, && \text{(5.28j)}\\
s(y;H) &= \int_H^y m/\kappa\, dy\,, \quad \phi(H) = \int_0^H f\, dy\,, && \text{(5.28k)}\\
\Upsilon(H) &= \int_0^H \underline{\varepsilon} w\, dy\,. && \text{(5.28l)}
\end{aligned}
$$

The expressions of the coefficients $F(H)$ to $K(H)$ have been condensed by using the relation $\phi'' = 2g(H;H)$ and by employing primes to refer to partial derivatives with respect to y, e.g. $f' = \partial_y f(y;H)$, and to total derivatives with respect to H whenever it is unambiguous, e.g. $\phi' = d\phi/dH$. $w|_H$ and $f|_H$ refer to $f(H;H)$ and $w(H;H)$ respectively.

5.5 C. Ruyer-Quil *et al.*, J. Fluid Mech (2012)

J. Fluid Mech., page 1 of 37.
doi:10.1017/jfm.2011.508

Wavy regime of a power-law film flow

C. Ruyer-Quil[1]†, S. Chakraborty[1] and B. S. Dandapat[2]

[1] Université Pierre et Marie Curie – Laboratoire FAST, campus universitaire, 91405 Orsay, France
[2] Sikkim Manipal Institute of Technology, Majitar, Rangpo, 737 132, East Sikkim, India

(Received 21 June 2011; revised 14 November 2011; accepted 15 November 2011)

We consider a power-law fluid flowing down an inclined plane under the action of gravity. The divergence of the viscosity at zero strain rate is taken care of by introducing a Newtonian plateau at small strain rate. Two-equation models are formulated within the framework of lubrication theory in terms of the exact mass balance and an averaged momentum equation, which form a set of evolution equations for the film thickness h, a local velocity amplitude or the flow rate q. The models account for the streamwise diffusion of momentum. Comparisons with Orr–Sommerfeld stability analysis and with direct numerical simulation (DNS) show convincing agreement in both linear and nonlinear regimes. The influence of shear-thinning or shear-thickening on the primary instability is shown to be non-trivial. A destabilization of the base flow close to threshold is promoted by the shear-thinning effect, whereas, further from threshold, it tends to stabilize the base flow when the viscous damping of short waves becomes dominant. A reverse situation is observed in the case of shear-thickening fluids. Shear-thinning accelerates solitary waves and promotes a subcritical onset of travelling waves at larger wavenumber than the linear cut-off wavenumber. A conditional stability of the base flow is thus observed. This phenomenon results from a reduction of the effective viscosity at the free surface. When compared with DNS, simulations of the temporal response of the film based on weighted residual models satisfactorily capture the conditional stability of the film.

Key words: complex fluids, shallow water flows, thin films

1. Introduction

Roll waves, i.e. hydraulic jumps connected by sections of gradually varying flows, are generally encountered in torrential regimes of river flows and in man-made conducts such as spillways (Dressler 1949; Julien & Hartley 1986; Chang & Demekhin 2000). The possible onset of roll waves was already accounted for in the design of aqueducts by Roman engineers (Fonder & Xanthoulis 2007). Roll waves can also be observed in overland flows, especially in rill flows, with a potential increase of the soil erosion (Liu *et al.* 2005). In estuaries, rivers may carry large amounts of clay and the resulting mud flows are frequently pulsating and resemble roll waves in turbulent flows of clear water (Liu & Mei 1994). For these two latter examples, interactions between clay particles create extensive microscopic structures that are

† Email address for correspondence: ruyer@fast.u-psud.fr

deformed and gradually broken down when a stress is applied. As a consequence the response of the fluid to a stress is nonlinear and mud presents a shear-thinning behaviour.

The onset of roll waves results from an instability mechanism that is similar to the formation of teardrop-like solitary waves on a laminar film falling down an inclined plane. In the latter case surface tension prevents the wave from breaking and arrests the formation of hydraulic jumps. These waves are sometimes referred to as 'capillary roll waves' (Balmforth & Liu 2004). In addition, at low flow rate, the observed wavy dynamics on a falling film remains spanwise independent (Alekseenko, Nakoryakov & Pokusaev 1994; Liu & Gollub 1994) which greatly simplifies their study. For these two reasons, film flows can be viewed as a toy system whose wavy dynamics is closely related to the torrential regime of rivers at larger flow rates.

The space–time evolution of a Newtonian liquid film flowing down an inclined plane exhibits a very rich phenomenology which has attracted a considerable number of studies since Kapitza's experiments in the 1940s (Kapitza & Kapitza 1949). This is a classical example of a convective primary instability (Brevdo *et al.* 1999) giving way to a sequence of secondary instabilities ending with teardrop-shape large-amplitude solitary waves (see e.g. Alekseenko *et al.* 1994; Chang & Demekhin 2002; Kalliadasis *et al.* 2011 for a review of this complex phenomenology). There is still a renewed interest for falling film wavy dynamics and, in particular, to its spatio-temporal disordered state of solitary waves in interaction, which is an example of weak turbulence organized by dissipative structures (Manneville 1990). The experiments by Liu & Gollub (1994) and Vlachogiannis & Bontozoglou (2001) have evidenced coalescence and repulsion events between waves resulting into a decrease of the number of solitary waves with the distance from inlet. This coarsening dynamics has been numerically investigated by Chang *et al.* (1996).

In comparison to the Newtonian case, far less studies have been devoted to generalized Newtonian film flows for which the effective viscosity $\mu_{eff}(\dot{\gamma})$ is a function of the strain rate $\dot{\gamma}$. Yet, because of the simplicity of the Ostwald–de Waele power-law model

$$\mu_{eff}(\dot{\gamma}) = \mu_n \dot{\gamma}^{n-1}, \tag{1.1}$$

shear-thinning falling films have recently been the subject of a consequential interest (see e.g. Dandapat & Mukhopadhyay 2001, 2003; Sisoev *et al.* 2007; Amaouche, Djema & Bourdache 2009; Fernández-Nieto, Noble & Vila 2010). These studies are based on the shallow-water averaging of the primitive equations, also often referred to as the integral boundary layer formulation in the context of falling films (Chang & Demekhin 2002). A scale separation is assumed in the streamwise and cross-stream directions, the free surface being deformed on a length scale that is much larger than the film thickness, which enables the introduction of a small film parameter ϵ. The continuity and momentum equations are integrated in depth and form a closed system of equations for the film thickness h and the local flow rate q once a closure hypothesis, generally a self-similar velocity distribution, is made. Amaouche *et al.* (2009) and Fernández-Nieto *et al.* (2010) have corrected the Kármán–Polhausen averaged momentum equation derived by Hwang *et al.* (1994) and Ng & Mei (1994) and formulated two-equation models that are consistent up to order ϵ. This consistency enabled them to correctly capture the instability threshold obtained by Ng & Mei (1994) and Miladinova, Lebonb & Toshev (2004).

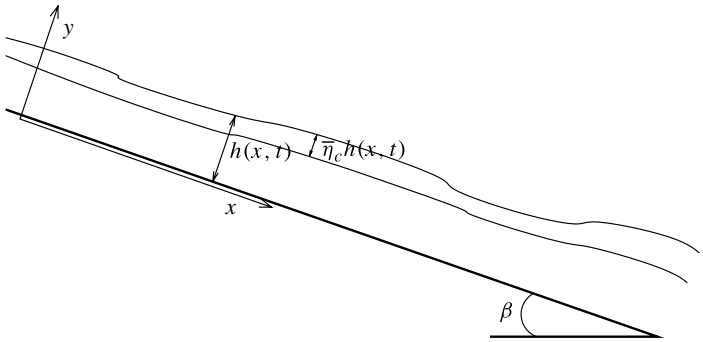

FIGURE 1. Geometry and notation.

The two-equation models derived by Amaouche *et al.* (2009) and Fernández-Nieto *et al.* (2010) are consistent at $O(\epsilon)$ but do not account for $O(\epsilon^2)$ effects such as streamwise viscous diffusion, which is known to affect wave-to-wave interaction processes and thus the wave dynamics for Newtonian film flows (Kawahara 1983; Kawahara & Toh 1988; Pradas, Tseluiko & Kalliadasis 2011). In this paper we shall present a modelling attempt of power-law falling film flows including second-order viscous diffusion terms in a consistent way. To account for streamwise viscous diffusion, the effective viscosity $\mu_{eff}(\dot\gamma)$ and its derivative $\mathrm{d}\mu_{eff}/\mathrm{d}\dot\gamma$ must be computed at the free surface, where the strain rate $\dot\gamma$ goes to zero for an unperturbed interface. In the case of the power law (1.1) either $\mu_{eff}(0)$ or $\mathrm{d}\mu_{eff}/\mathrm{d}\dot\gamma(0)$, or both, are undefined for $n < 3$ which corresponds to most shear-thinning and shear-thickening fluids. This calls for a regularization at zero strain rate of the power law (1.1) which is here accounted for by introducing a Newtonian plateau at low strain rates.

The paper is organized as follows. Section 2 presents the governing equations. The weighted-residual modelling approach is detailed in § 3. The linear stability of the base flow is discussed in § 4. Nonlinear travelling waves are obtained and compared with direct numerical simulations (DNSs) in § 5. The conditional stability of a shear-thinning film is considered in § 6. Section 7 concludes the present study.

2. Governing equations

We consider a power-law fluid flowing down an inclined plane under the action of gravity as sketched in figure 1. The flow is assumed to be incompressible and the fluid properties, density ρ and surface tension σ are constant. The angle of inclination β and the gravity acceleration g are also constant. The dimensional governing equations read

$$\partial_x u + \partial_y v = 0, \tag{2.1a}$$

$$\rho(\partial_t u + u\partial_x u + v\partial_y u) = -\partial_x p + \rho g \sin\beta + \partial_x \tau_{xx} + \partial_y \tau_{xy}, \tag{2.1b}$$

$$\rho(\partial_t v + u\partial_x v + v\partial_y v) = -\partial_y p - \rho g \cos\beta + \partial_x \tau_{yx} + \partial_y \tau_{yy}, \tag{2.1c}$$

$$\text{where} \quad \tau_{ij} = 2\mu_{eff}(\dot\gamma)\boldsymbol{D}_{ij}. \tag{2.1d}$$

Here $\boldsymbol{u} = u\boldsymbol{i} + v\boldsymbol{j}$ is the velocity field, $\boldsymbol{D}_{ij} = (\partial_i u_j + \partial_j u_i)/2$ is the rate of strain tensor, $\dot\gamma = \sqrt{2\boldsymbol{D}_{kl}\boldsymbol{D}_{kl}}$ is the strain rate and μ_{eff} is an effective viscosity which is a function of the strain rate $\dot\gamma$. The system of equations is completed by the boundary conditions at the free surface $y = h$

$$[1 - (\partial_x h)^2]\tau_{xy} + \partial_x h(\tau_{yy} - \tau_{xx}) = 0, \tag{2.2a}$$

Set number	Concentration	μ_n (Pa s^n)	n	μ_0 (Pa s)	$\dot{\gamma}_c$ (s^{-1})	$\dot{\gamma}_c t_v$	Γ
1	500 ppm	0.04062	0.607	0.08	0.18	1.8×10^{-3}	378
2	1500 ppm	0.3592	0.40	1.43	0.1	1.7×10^{-3}	48.7
3	2500 ppm	0.9913	0.34	7.16	0.05	1.2×10^{-3}	13.0

TABLE 1. Parameters from rheological measurements of xanthan gum solutions in water. Surface tension and density are $\sigma = 65$ mN m^{-1} and $\rho = 995$ kg m^{-3}. Values of the Kapitza number are computed for a moderate inclination $\beta = 15°$. Set 1 corresponds to data from Bewersdorff & Singh (1988) and Lindner *et al.* (2000). Sets 2 and 3 refer to the fluids studied by Seevaratnam *et al.* (2007).

$$p_a - p + \frac{\tau_{xx}\,(\partial_x h)^2 - 2\tau_{xy}\partial_x h + \tau_{yy}}{1 + (\partial_x h)^2} = \frac{\sigma\,\partial_{xx} h}{[1 + (\partial_x h)^2]^{3/2}}, \tag{2.2b}$$

$$\partial_t h + u\partial_x h = v, \tag{2.2c}$$

and at the wall $y = 0$

$$u = v = 0. \tag{2.2d}$$

A regularization of the Ostwald–de Waele power law model (1.1) is assumed at low shear rate to recover the Newtonian behaviour in that limit. This is the spirit of a three-parameter Carreau law:

$$\mu_{eff}(\dot{\gamma}) = \mu_0\,[1 + (\dot{\gamma}/\dot{\gamma}_c)^2]^{(n-1)/2}. \tag{2.3}$$

However, using (2.3) forbids the base flow from being determined analytically and one can instead introduce a Newtonian plateau:

$$\mu_{eff}(\dot{\gamma}) = \mu_n \dot{\gamma}^{n-1} \quad \text{for } \dot{\gamma} > \dot{\gamma}_c, \tag{2.4a}$$

$$\mu_{eff}(\dot{\gamma}) = \mu_0 \quad \text{for } \dot{\gamma} \leqslant \dot{\gamma}_c. \tag{2.4b}$$

The continuity of the shear stress at $\dot{\gamma} = \dot{\gamma}_c$ requires $\mu_n \dot{\gamma}_c^{n-1} = \mu_0$.

Table 1 presents reasonable values of the zero strain viscosity μ_0 and the critical strain rate $\dot{\gamma}_c$ separating Newtonian and non-Newtonian behaviour of shear-thinning xanthan dilute solutions. Those values are taken from Bewersdorff & Singh (1988), Lindner, Bonn & Meunier (2000) and Seevaratnam *et al.* (2007). Noteworthy is that dilute xanthan solutions do not present yield stresses (Choppe *et al.* 2010). The surface tension of xanthan solutions is assumed here to remain close to that of pure water $\sigma = 65$ mN m^{-1} (Seevaratnam *et al.* 2007). Conversely, table 2 presents the properties of three typical shear-thickening solutions of cornstarch in ethylene glycol. The dynamic viscosity μ_0 of the Newtonian plateau is assumed to correspond to the solvent viscosity.

The length scale is the uniform film thickness $\bar{h}_N$. The velocity scale V is defined by balancing viscous friction $\propto \mu_n V^n \bar{h}_N^{-(n+1)}$ and streamwise gravity acceleration $\propto \rho g \sin\beta$ which gives

$$V = \left(\frac{\rho g \bar{h}_N^{n+1} \sin\beta}{\mu_n} \right)^{1/n} \tag{2.5}$$

such that the Froude number $Fr = V/\sqrt{g\bar{h}_N \cos\beta}$, which compares the characteristic speed of the flow with the speed of the gravity waves propagating at the interface, and

Set number	Concentration	μ_n (Pa s^n)	n	μ_0 (Pa s)	$\dot{\gamma}_c$ (s^{-1})	$\dot{\gamma}_c t_\nu$	Γ
4	33 %	8	1.3	0.016	10^{-9}	1.3×10^{-10}	0.01
5	35 %	6	1.55	0.016	2.1×10^{-5}	2.8×10^{-6}	0.0077
6	38 %	1.8	2.4	0.016	0.034	5.2×10^{-3}	0.005

TABLE 2. Parameters from rheological measurements of cornstarch dispersions in ethylene glycol (Griskey *et al.* 1985). Surface tension and density are $\sigma = 48$ mN m^{-1} and $\rho = 1113$ kg m^{-3}. The viscosity μ_0 of the Newtonian plateau is assumed to correspond to the solvent viscosity. Values of the Kapitza number are computed for a moderate inclination $\beta = 15°$.

the Reynolds number

$$Re = \frac{\rho V^{2-n} \bar{h}_{\mathrm{N}}^n}{\mu_n} = \left[(\mu_n/\rho)^{-2} (g \sin\beta)^{2-n} \bar{h}_{\mathrm{N}}^{n+2}\right]^{1/n} \tag{2.6}$$

are related by the relation $Re/\cot\beta = Fr^2$. Finally, let us note that the Reynolds number can also be written as $Re = (\bar{h}_{\mathrm{N}}/l_\nu)^{(n+2)/n}$ where $l_\nu = (\mu_n/\rho)^{2/(n+2)} (g \sin\beta)^{(n-2)/(n+2)}$ is the length scale corresponding to the balance of gravity acceleration and viscous drag. We may also rewrite the velocity scale V as

$$V = \frac{l_\nu}{t_\nu} \left(\frac{\bar{h}_{\mathrm{N}}}{l_\nu}\right)^{(n+1)/n} \quad \text{where } t_\nu = \left(\frac{\mu_n}{\rho}\right)^{1/(n+2)} (g \sin\beta)^{-2/(n+2)} \tag{2.7}$$

t_ν is the time scale corresponding to the balance of viscosity and gravity acceleration.

With the above choice of scales, the dimensionless equations thus read

$$\partial_x u + \partial_y v = 0, \tag{2.8a}$$

$$Re(\partial_t u + u\partial_x u + v\partial_y u) = -\partial_x p + 1 + \partial_x \tau_{xx} + \partial_y \tau_{xy}, \tag{2.8b}$$

$$Re(\partial_t v + u\partial_x v + v\partial_y v) = -\partial_y p - \cot\beta + \partial_x \tau_{yx} + \partial_y \tau_{yy}, \tag{2.8c}$$

with boundary conditions

$$[1 - (\partial_x h)^2]\tau_{xy} + \partial_x h(\tau_{yy} - \tau_{xx}) = 0, \tag{2.8d}$$

$$-p + \frac{\tau_{xx} (\partial_x h)^2 - 2\tau_{xy}\partial_x h + \tau_{yy}}{1 + (\partial_x h)^2} = We \frac{\partial_{xx} h}{[1 + (\partial_x h)^2]^{3/2}}, \tag{2.8e}$$

the kinematic condition (2.2*c*) and the no-slip condition (2.2*d*) at the wall. The Weber number is defined by $We = \sigma/(\rho g \sin\beta \bar{h}_{\mathrm{N}}^2)$. Finally, surface tension, gravity and viscous drag can be compared by the Kapitza number

$$\Gamma = (l_c/l_\nu)^2 = (\sigma/\rho) (\mu_n/\rho)^{-4/(n+2)} (g \sin\beta)^{(2-3n)/(n+2)}, \tag{2.9}$$

where $l_c = \sqrt{[\sigma/(\rho g \sin\beta)]}$ is the capillary length. The Weber and Kapitza numbers are related to each other by the relation $We = \Gamma (l_\nu/\bar{h}_{\mathrm{N}})^2$.

The dimensionless Carreau law is given by

$$\mu_{eff}(\dot{\gamma}) = (s^2 + \dot{\gamma}^2)^{(n-1)/2} \tag{2.10}$$

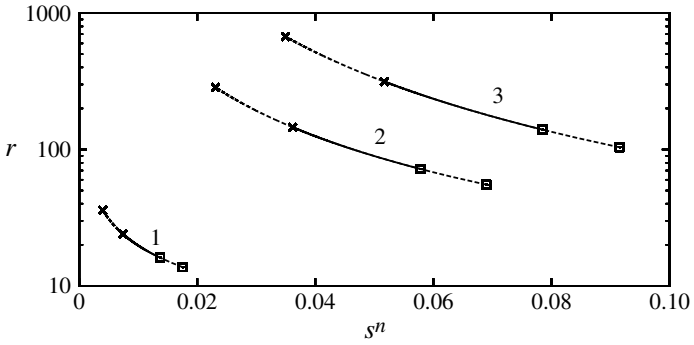

FIGURE 2. Ranges of dimensionless maximum viscosity $r = s^{n-1}$ and relative thickness s^n of the Newtonian surface layer attained for the Nusselt solution of uniform thickness (2.12) when the Reynolds number is varied between Re_c and 100. Solid (dashed) lines refer to $\beta = 15°$ ($\beta = 85°$). Labels refer to the shear-thinning dilute xanthan solutions whose properties are listed in table 1. Crosses (squares) correspond to $Re = 100$ ($Re = Re_c$).

where the dimensionless threshold s is defined by $s = \dot{\gamma}_c \bar{h}_N / V$. Similarly, the Newtonian plateau model reads

$$\mu_{eff}(\dot{\gamma}) = \dot{\gamma}^{n-1} \quad \text{for } \dot{\gamma} > s \quad \text{and} \quad \mu_{eff}(\dot{\gamma}) = r \text{ otherwise.} \tag{2.11}$$

The dimensionless maximum effective viscosity r is defined by $r = s^{n-1}$.

The advantage of the Newtonian plateau formulation (2.11) over the Carreau law (2.10) lies in the presence of an analytical solution for the base flow of constant film thickness h:

$$u_0 = h^{(n+1)/n} f_0(\bar{y}) \quad \text{for } \bar{y} < 1 - \bar{\eta}_c \tag{2.12a}$$

$$u_0 = h^{(n+1)/n} f_0(1 - \bar{\eta}_c) + s^{n+1}\, g_0[(\bar{y} + \bar{\eta}_c - 1)/\bar{\eta}_c] \quad \text{for } \bar{y} > 1 - \bar{\eta}_c, \tag{2.12b}$$

where $\bar{y} = y/h$ is a reduced coordinate, $f_0(\bar{y}) = n/(n+1)[1 - (1-\bar{y})^{(n+1)/n}]$, $g_0(\bar{y}) = \bar{y} - (1/2)\bar{y}^2$ and $\bar{\eta}_c = s^n/h$ is the fraction of the film thickness for which the fluid is Newtonian. From the uniform-thickness solution (2.12) we obtain $\partial_y u_0|_{y=0} = 1$ and the dimensional rate of strain at the wall is thus $V/\bar{h}_N$ for the base flow. Therefore, the dimensionless group r can be interpreted as the ratio $r = \mu_0/\mu_w$ of the shear viscosities $\mu_0 = \mu_n (\dot{\gamma}_c)^{n-1}$ and $\mu_w = \mu_n (V/\bar{h}_N)^{n-1}$ at the free surface and at the wall for the corresponding base flow Nusselt solution. The Newtonian plateau model (2.11) introduces a fake interface at $y = h(1 - \bar{\eta}_c)$ separating a power-law region and a Newtonian layer at the free surface. This is reminiscent of the pseudo-plug theory developed by Balmforth & Liu (2004) and Fernández-Nieto *et al.* (2010), although in that case the fake interface has a different physical meaning and separates a plastic upper layer from a fluid layer underneath.

In the case of the three shear-thinning xanthan solutions whose properties are listed in table 1, the approximation of a thin Newtonian layer ($\bar{\eta}_c \ll 1$) and a large viscosity ratio ($r \gg 1$) is well verified. Figure 2 presents the relative thickness s^n of the Newtonian layer and the viscosity ratio r for the Nusselt film solution (2.12) at two inclinations ($\beta = 15$ and $85°$) and for the three studied xanthan solutions when the Reynolds number is varied in the interval $[Re_c, 100]$. The instability threshold Re_c is here approximated by the formula (Ng & Mei 1994; Miladinova *et al.* 2004)

$$Re = Re_c = \frac{3n+2}{2} \cot\beta \quad \text{or} \quad Fr^2 = \frac{3n+2}{2} \tag{2.13}$$

which corresponds to the Ostwald–de Waele power-law model (1.1). In each case, the viscosity at the free surface is at least one order of magnitude larger than at the wall and the Newtonian layer at the free surface has a thickness that is at least one order of magnitude smaller than the total thickness of the film.

Turning to the cornstarch suspensions (see table 2) the Newtonian surface layer is very thin and the viscosity ratio is very small, s^n and r being less than 2×10^{-6} and 5×10^{-4}, respectively, for Re in the range $[Re_c, 100]$ and $\beta = 15$ or $85°$. We then conclude that a thin Newtonian layer at the free surface ($\bar{\eta}_c \ll 1$) can be assumed for typical shear-thinning and shear-thickening fluids, an assumption that will be useful to drastically simplify the derivation of the integral models that we detail below. Finally, let us note that, although not strictly equivalent, the two models (2.10) and (2.11) of generalized Newtonian fluids will be shown to lead to close results in the linear and nonlinear regimes whenever $s \ll 1$ and we consider them equivalent in our analysis in the limit $s \to 0$ (see § 3.1).

3. Low-dimensional formulation

Let us assume (i) slow space and time evolutions $\partial_{x,t} \sim \epsilon$ where $\epsilon \ll 1$ is a formal film parameter, (ii) surface deformations induce order-ϵ corrections of the velocity profile from the flat-film solution, (iii) the Newtonian plateau model (2.11) holds. Otherwise stated, assumption (ii) implies that viscosity is strong enough to ensure the cross-stream coherence of the flow which should be verified for small to moderate Reynolds numbers.

With the help of the continuity equation, assumption (i) implies that the cross-stream velocity $v = -\int_0^y \partial_x u \, \mathrm{d}y = O(\epsilon)$ so that inertia terms can be dropped from the cross-stream momentum equation, which yields the pressure distribution at order ϵ after integration:

$$\text{if } y > y_c, \quad p = \cot\beta(h-y) - We\partial_{xx}h - r[\partial_x u|_h + \partial_x u], \tag{3.1a}$$

$$\text{if } y \leqslant y_c, \quad p = \cot\beta(h-y) - We\partial_{xx}h - r[\partial_x u|_h + \partial_x u|_{y_c+}] + 2r\partial_x u|_{y_c-} - 2\partial_x u\dot{\gamma}_0^{n-1} - \int_y^{y_c} \partial_x[\partial_y u\dot{\gamma}_0^{n-1}]\,\mathrm{d}y, \tag{3.1b}$$

where $y_c = h(1-\bar{\eta}_c)$ defines the location of the fake interface separating the Newtonian and power-law layers and $\dot{\gamma}_0 = \sqrt{(\partial_y u)^2 + 4(\partial_x u)^2}$. Note that $\partial_y u$ and $\partial_x u$ must be taken of the same order of magnitude in the expression of the strain rate. Since $\partial_y u$ becomes small close to the free surface, the viscosity at the free surface is then governed by the value of the streamwise derivative $\partial_x u|_{y=h}$ for a thin or vanishing Newtonian layer.

Substitution of (3.1) into the streamwise momentum balance gives

$$Re(\partial_t u + u\partial_x u + v\partial_y u) = 1 + \partial_y \tau_{xy}^{(0)} + \mathscr{D}^{(2)} - \cot\beta\,\partial_x h + We\partial_{xxx}h \tag{3.2a}$$

where the definition of the lowest-order rate of strain $\tau_{xy}^{(0)}$ and of the second-order viscous terms $\mathscr{D}^{(2)}$ depend on whether the flow is Newtonian or non-Newtonian. For $y > y_c$ they read

$$\tau_{xy}^{(0)} = r\partial_y u \quad \text{and} \quad \mathscr{D}^{(2)} = 2r\partial_{xx}u + r\partial_x[\partial_x u|_h] \tag{3.2b}$$

whereas for $y \leqslant y_c$ we have

$$\tau_{xy}^{(0)} = \partial_y u \dot{\gamma}_0^{n-1}, \tag{3.2c}$$

$$\begin{aligned}\mathscr{D}^{(2)} = {} & \partial_y[\partial_x v(\dot{\gamma}_0^{n-1} + (n-1)\,(\partial_y u)^2\,\dot{\gamma}_0^{n-3})] + 4\partial_x[\partial_x u \dot{\gamma}_0^{n-1}] \\ & + \partial_x\left\{\int_y^{y_c} \partial_x[\partial_y u \dot{\gamma}_0^{n-1}]\,\mathrm{d}y\right\} - 2\partial_x[r\partial_x u|_{y_c-}] \\ & + r\partial_x[\partial_x u|_{y_c+} + \partial_x u|_h].\end{aligned} \tag{3.2d}$$

Equation (3.2*a*) is completed by the no-slip condition $u = v = 0$ at the wall and the tangential stress continuity at the free surface $y = h$ truncated at order ϵ^2:

$$\partial_y u = 4\partial_x h \partial_x u - \partial_x v. \tag{3.2e}$$

In spite of the elimination of the pressure, solving the boundary-layer equations (3.2) remains a formidable task. A further simplification can be achieved by taking advantage of the strong coherence of the velocity distribution across the fluid layer, in which case the velocity field can be assumed to be slaved to a limited number of unknowns and these are functions of time t and location x on the plane. The first of these effective degrees of freedom is necessarily the film thickness $h(x, t)$, for which an evolution equation is easily obtained after integration of the continuity equation

$$\partial_t h + \partial_x q = 0, \tag{3.3}$$

where $q = \int_0^h u\,\mathrm{d}y$ is the local flow rate. Equation (3.3) expresses the conservation of mass. In all cases found in the literature, surface equations are obtained using a closure assumption $q = Q(h)$ manifesting the complete slaving of the dynamics of the film to the evolution of the free surface. Integration of the base flow u_0 across the fluid layer leads to

$$q_0 = \int_0^h u_0\,\mathrm{d}y = \frac{n}{2n+1}h^{(2n+1)/n} + \frac{1-n}{6n+3}s \tag{3.4}$$

which relates the flow rate q to the film thickness h. Assuming that (3.4) still holds when the free surface is deformed, one is led after substitution into the mass balance equation (3.3) to a kinematic-wave equation (Whitham 1974):

$$\partial_t h + h^{(n+1)/n}\partial_x h = 0, \tag{3.5}$$

which governs the propagation of free surface deformations when the velocity field is slaved to the film thickness through the mass balance equation (3.3) or, equivalently, the kinematic boundary condition (2.2*c*). Infinitesimal waves $|h-1| \ll 1$ thus propagate at speed unity and the velocity scale V given by (2.5) is the dimensional speed of the linear kinematic waves in the long-wavelength limit.

The slaving of the velocity to the free surface evolution is verified only at small values of the Reynolds number Re. At moderate Reynolds number, some additional degrees of freedom must be added to capture the dynamics of the film, which can be done by projecting the velocity field on a set of chosen test functions. This closure assumption is generally reduced to the postulate of a self-similar profile (Hwang *et al.* 1994; Dandapat & Mukhopadhyay 2001; Sisoev *et al.* 2007). We avoid this restrictive closure which is known to lead to an incorrect prediction of the instability threshold (Ng & Mei 1994). However, since the mass conservation equation (3.3) is exact, we stick to the derivation of a low-dimensional model consisting of two evolution equations for the film thickness h and the local flow rate q. Considering that

assumption (ii) holds, i.e. that the velocity distribution across the fluid layer is never far from the flat-film solution, the velocity field is decomposed as

$$u = u_s + \tilde{u}^{(1)} \quad \text{where} \tag{3.6a}$$

$$u_s = \bar{u} f_0(\bar{y}) \quad \text{for } \bar{y} \leqslant 1 - \bar{\eta}_c, \tag{3.6b}$$

$$u_s = \bar{u}[f_0(1-\bar{\eta}_c) + \bar{\eta}_c^{(n+1)/n}\, g_0[(\bar{y}+\bar{\eta}_c-1)/\bar{\eta}_c]] \quad \text{for } \bar{y} \geqslant 1 - \bar{\eta}_c, \tag{3.6c}$$

and $\bar{\eta}_c$ is the local relative thickness of the Newtonian layer at the free surface. The definition of the velocity distribution u_s is based on the local film thickness $h(x,t)$ and a local velocity scale $\bar{u}(x,t)$ that can be related to the rate of strain at the wall $D_{xy}|_{y=0} = \bar{u}/h + O(\epsilon)$. Here $\tilde{u}^{(1)}$ accounts for the order-ϵ deviations of the velocity profile induced by the deformation of the free surface. We can also include in $\tilde{u}^{(1)}$ the $O(\epsilon)$ corrections of the relation between the flow rate $q = \int_0^h u\,\mathrm{d}y$, h and $\bar{u}$ provided by the flat-film profile

$$q = \frac{3n + (1-n)\bar{\eta}_c^{(2n+1)/n}}{6n+3} h\bar{u} \equiv \phi(\bar{\eta}_c) h\bar{u}, \tag{3.7}$$

so that $\int_0^h \tilde{u}^{(1)}\,\mathrm{d}y = 0$ is assumed without any restrictions.

The local thickness $\bar{\eta}_c$ of the Newtonian layer is defined by $\dot{\gamma}(\bar{y} = 1 - \bar{\eta}_c) = s$, which reads at order ϵ^2

$$s^2 = \{4\,(\partial_x u_s)^2 + [\partial_y u_s + \partial_x v_s]^2\}_{\bar{y}=1-\bar{\eta}_c}\,. \tag{3.8}$$

In the limit $\bar{\eta}_c \ll 1$, (3.8) can be further simplified to give

$$s^2 = \frac{4n^2}{(1+n)^2}\,(\partial_x \bar{u})^2 + \bar{\eta}_c^{2/n}\frac{\bar{u}^2}{h^2}. \tag{3.9}$$

Therefore, the Newtonian layer disappears locally if

$$|\partial_x \bar{u}| > \frac{n+1}{2n} s. \tag{3.10}$$

The formulation of an averaged momentum balance in terms of q and h is made difficult by the impossibility to invert (3.8) and (3.7) to express $\bar{u}$ as function of h and q. We thus aim at a three-equation model for the unknowns h, $\bar{\eta}_c$ and $\bar{u}$ made of the (exact) mass conservation equation (3.3) and (3.8) and an evolution equation for $\bar{u}$. We apply the weighted residual technique and average the boundary-layer equations (3.2) across the film. Let us introduce a weighting function $w(\bar{y})$ and the scalar product $\langle\cdot|\cdot\rangle = \int_0^h \cdot\,\mathrm{d}y$. Writing formally (3.2) as $BL(u) = 0$, we then set to zero the residual $\langle BL(u)|w\rangle$. To obtain an equation that is consistent at $O(\epsilon)$, the weight w must be chosen so that the viscous drag term

$$\int_0^{y_c} w(\bar{y})\partial_y[n|\partial_y u_s|^{n-1}\,\partial_y \tilde{u}^{(1)}]\,\mathrm{d}y + \int_{y_c}^h r w(\bar{y})\partial_{yy}\tilde{u}^{(1)}\,\mathrm{d}y$$
$$\equiv \frac{1}{h}\left|\frac{\bar{u}}{h}\right|^{n-1} \langle \mathscr{L}_{\bar{\eta}_c}\tilde{u}^{(1)}|w\rangle + O(\epsilon^2) \tag{3.11}$$

is $O(\epsilon^2)$. The linear operator $\mathscr{L}_{\bar{\eta}_c}$ is defined by

$$\mathscr{L}_{\bar{\eta}_c} = \partial_{\bar{y}}[n\,(f_0')^{n-1}\,\partial_{\bar{y}}\cdot] \quad \text{if } 0 \leqslant \bar{y} \leqslant \bar{\eta}_c \quad \text{and} \quad \mathscr{L}_{\bar{\eta}_c} = \bar{\eta}_c^{(n-1)/n}\partial_{\bar{y}\bar{y}}\cdot \text{ otherwise}, \tag{3.12}$$

where the thickness of the Newtonian layer is estimated by $\bar{\eta}_c = (sh/\bar{u})^n + O(\epsilon^2)$. The deviations $\tilde{u}^{(1)}$ of the velocity field verify the no-slip condition $\tilde{u}^{(1)}|_{\bar{y}=0} = 0$ at the wall, $\partial_{\bar{y}}\tilde{u}^{(1)}|_{\bar{y}=1} = 0$ at the interface and

$$n\partial_{\bar{y}}\tilde{u}^{(1)}|_{\bar{y}=\bar{y}_{c-}} = \bar{\eta}_c^{(n-1)/n}\partial_{\bar{y}}\tilde{u}^{(1)}|_{\bar{y}=\bar{y}_{c+}} \tag{3.13}$$

where $\bar{y}_c = 1 - \bar{\eta}_c$, which is a consequence of the continuity of the rate of stress at the fake interface:

$$|\partial_y u|^{n-1}\,\partial_y u|_{\bar{y}=\bar{y}_{c-}} + O(\epsilon^2) = r\partial_y u|_{\bar{y}=\bar{y}_{c+}}. \tag{3.14}$$

Two integrations by parts of (3.11) show that the linear operator $\mathscr{L}_{\bar{\eta}_c}$ is self-adjoint. To make use of the definition of the flow rate q, which implied the gauging condition $\int_0^h \tilde{u}^{(1)}\,\mathrm{d}y = 0$, the weight function w must be solution to $\mathscr{L}_{\bar{\eta}_c} w = cst$ which gives

$$\text{if } y < y_c, \quad w(\bar{y}) = f_0(\bar{y}), \tag{3.15a}$$

$$\text{if } y \geqslant y_c, \quad w(\bar{y}) = f_0(1-\bar{\eta}_c) + n\bar{\eta}_c^{(n+1)/n}\, g_0[(\bar{y}+\bar{\eta}_c-1)/\bar{\eta}_c]. \tag{3.15b}$$

Noteworthy is that the weight w is not proportional to the velocity profile u_s defined in (3.6). The adopted weighted residual method is therefore slightly different from the Galerkin method for which $w \propto u_s$. This discrepancy is an effect of the nonlinearity of the strain to stress relationship which introduces a factor n.

We next proceed to the averaging of the boundary-layer equations (3.2) with the appropriate weights (3.15). To compute the viscous terms appearing in the boundary-layer formulation (3.2*d*), we expand the nonlinear constitutive equation

$$\dot{\gamma}_0^{n-1} = |\partial_y u|^{n-1} + 2(n-1)\,(\partial_x u)^2\,|\partial_y u|^{n-3} + O(\epsilon^4), \tag{3.16}$$

and replace r with $\dot{\gamma}_0^{n-1}|_{y=h(1-\bar{\eta}_c)}$.

After some tedious algebra, the resulting averaged momentum equation (3.2) reads

$$\begin{aligned}\partial_t\bar{u} = -Re\left[\tilde{G}\frac{\bar{u}^2}{h}\partial_x h + \tilde{F}\bar{u}\partial_x\bar{u}\right] + \tilde{I}\left(1 - \cot\beta\,\partial_x h + We\,\partial_{xxx}h - \frac{\bar{u}|\bar{u}|^{n-1}}{h^{n+1}}\right)\\ + \tilde{J}\frac{\bar{u}}{h^2}(\partial_x h)^2 + \tilde{K}\frac{\partial_x\bar{u}\partial_x h}{h} + \tilde{L}\frac{\bar{u}}{h}\partial_{xx}h + \tilde{M}\partial_{xx}\bar{u} + \tilde{N}\frac{(\partial_x\bar{u})^2}{\bar{u}}.\end{aligned} \tag{3.17}$$

The coefficients $\tilde{F}$ to $\tilde{N}$ of the averaged momentum balance equation (3.17) are explicit, but cumbersome, functions of the power-law index n and of the relative thickness $\bar{\eta}_c$ of the Newtonian layer. We give in appendix A the full expressions of the coefficients $\tilde{F}$, $\tilde{G}$, $\tilde{I}$ of the terms of orders ϵ^0 and ϵ which will be needed to determine the value of the critical Reynolds number at onset. The system (3.3), (3.8) and (3.17) is consistent up to order ϵ and accurately accounts for second-order viscous terms. As stated in the introduction, the derivation of the (3.17) has required a regularization of the power law (1.1) for $n < 3$ in order to compute both $\mu_{eff}(0)$ and $\mathrm{d}\mu_{eff}/\mathrm{d}\dot{\gamma}(0)$ in the Taylor expansion (3.16).

3.1. *Shear-thinning film ($n < 1$) in the limit of vanishing Newtonian layer*

The system of equations (3.3), (3.8) and (3.17) is still formidable to solve, mainly because of the dependence of the coefficients (A1) on the relative thickness $\bar{\eta}_c$ of the Newtonian layer, which is in turn a nonlinear function of h, $\bar{u}$ and their derivatives. For this reason, we further simplify the formulation by retaining the asymptotic behaviour of the coefficients when the Newtonian layer is very thin ($\bar{\eta}_c \to 0$).

In this limit, $q \approx (n/(2n+1))h\bar{u}$ and q can be easily substituted for $\bar{u}$. After some algebra, we finally obtain

$$\begin{aligned} Re\partial_t q = Re\left[-F(n)\frac{q}{h}\partial_x q + G(n)\frac{q^2}{h^2}\partial_x h\right] \\ + I(n)\left[h\left(1 - \cot\beta\partial_x h + We\partial_{xxx}h\right) - \frac{q|q|^{n-1}}{(\phi_0 h^2)^n}\right] \\ + r\left[J_0(n)\frac{q}{h^2}(\partial_x h)^2 - K_0(n)\frac{\partial_x q\partial_x h}{h} - L_0(n)\frac{q}{h}\partial_{xx}h + M_0(n)\partial_{xx}q\right], \end{aligned} \quad (3.18)$$

where $\phi_0 = \phi(0) = n/(2n+1)$. The coefficients $F(n), \ldots, M_0(n)$ are also functions of the power-law index n whose expressions are given below:

$$F = \frac{11n+6}{4n+3}, \quad G = \frac{6n+3}{4n+3}, \quad I = \frac{3n+2}{2(2n+1)}, \quad (3.19a)$$

$$K_0 = J_0 = -\frac{(n-1)(2n+1)(3n+2)}{(n+1)^2}, \quad (3.19b)$$

$$L_0 = K_0/2, \quad M_0 = -\frac{(n-1)(3n+2)}{2(n+1)}. \quad (3.19c)$$

The derivation of (3.18) assumes the presence of the Newtonian layer at the interface and thus only retains its dominant contributions to the streamwise viscous effects (with the effective viscosity r). Yet, the limit of a very thin Newtonian layer implies that the strain-rate threshold s also goes to zero. The Newtonian layer is thus easily removed by $O(s)$ gradients $\partial_x h$ of the film thickness as can be deduced from (3.10), in which case the effective viscosity at the free surface $\mu_{eff}(y=h)$ is much lower than its maximum r. The streamwise viscous effects are therefore overestimated by (3.18) whenever the free surface is non-weakly deformed. To correctly account for these viscous effects, the regions of the film where the effective viscosity reaches its maximum must be considered.

In most cases, the effective viscosity is maximum at the free surface Yet, there is evidence that this maximum can sometimes be located at the wall. Indeed, Dietze, Leefken & Kneer (2008) and Dietze, AL-Sibai & Kneer (2009) have pointed out the onset of backflow phenomena at the minimum thickness of large-amplitude solitary waves running on Newtonian falling films. These backflow phenomena are accompanied by the occurrence of separation points at the wall where the strain rate necessarily goes to zero. In the case of shear-thinning fluids, the effective viscosity would be maximum at the wall close to the locations of the separation points.

The contributions of the effective viscosity at the free surface to the streamwise viscous diffusion terms of the averaged momentum balance can be easily accounted for by substituting $\mu_{eff}(y=h)$ for the effective viscosity r in (3.18). It is however more difficult to evaluate the leading contributions of the bulk and wall regions to the streamwise viscous diffusion terms in the averaged momentum balance. A simple but *ad hoc* way to proceed is to estimate the effective viscosity in the bulk region from its value at the wall $\mu_{eff}(y=0) \approx [|q|/((\phi_0 h^2)]^{n-1} = h^{(n-1)/n} + O(\epsilon)$, assume a constant viscosity within the layer and compute the $O(\epsilon^2)$ viscous contribution to the averaged momentum equation (see appendix B). We then obtain

$$Re\partial_t q = Re\left[-F(n)\frac{q}{h}\partial_x q + G(n)\frac{q^2}{h^2}\partial_x h\right] + I(n)\left[h\left(1 - \cot\beta\partial_x h + We\partial_{xxx}h\right) - \frac{q|q|^{n-1}}{(\phi_0 h^2)^n}\right]$$

$$+r(h,q)\left[J_0(n)\frac{q}{h^2}(\partial_x h)^2-K_0(n)\frac{\partial_x q\partial_x h}{h}-L_0(n)\frac{q}{h}\partial_{xx}h+M_0(n)\partial_{xx}q\right]$$
$$+h^{(n-1)/n}\left[J_w(n)\frac{q}{h^2}(\partial_x h)^2-K_w(n)\frac{\partial_x q\partial_x h}{h}-L_w(n)\frac{q}{h}\partial_{xx}h+M_w(n)\partial_{xx}q\right] \quad (3.20)$$

where J_w, K_w, L_w and M_w are defined by

$$J_w=\frac{3n^2+13n+8}{(n+2)(n+1)},\quad K_w=M_w=\frac{5n+4}{n+1}, \quad (3.21a)$$

$$L_w=\frac{17n^2+23n+8}{2\,(n+1)^2}, \quad (3.21b)$$

and $r(h,q)$ stands for the evaluation of the effective viscosity at the free surface $\mu_{eff}(y=h)$ from the model variables h and q:

$$r(h,q)\equiv\left[s^2+\partial_x v_s^2+4\,(\partial_x u_s)^2\right]^{(n-1)/2}\Big|_{y=h} \quad (3.22a)$$

where

$$\partial_x v_s^2+4\,(\partial_x u_s)^2\,|_{y=h}=\left[\frac{2(2n+1)}{n+1}\partial_x\left(\frac{q}{h}\right)\right]^2+\left\{\frac{2n+1}{n+1}\left[-2\frac{\partial_x h\partial_x q}{h}\right.\right.$$
$$\left.\left.+q\left(2\frac{(\partial_x h)^2}{h^2}-\frac{\partial_{xx}h}{h}\right)\right]+\partial_{xx}q\right\}^2. \quad (3.22b)$$

We have considered as equivalent the assumption (2.11) of a Newtonian plateau and the Carreau law (2.10) to express the effective viscosity $r(h,q)$. Our computations show that this assumption is reasonable in the limit of a vanishing Newtonian layer $\bar{\eta}_c\ll 1$ (see §§ 4.1 and 5.2). We note that the $O(\epsilon^2)$ term $\partial_x v_s$ has been kept in the expression of the strain rate at the free surface. Indeed, retaining only the dominant term $4\,(\partial_x u_s|_{y=h})^2\propto[\partial_x(q/h)]^2$ implies that the effective viscosity spuriously reaches local maxima at crests and troughs of travelling waves since q is a function of h in that case (cf. § 5).

The averaged momentum equation (3.20) retains the contribution to streamwise viscous diffusion from the free surface (second row) and from the bulk (third row). In the Newtonian limit $n\to 1$, the averaged momentum equation obtained by Ruyer-Quil & Manneville (2000) is recovered

$$Re\partial_t q=Re\left[-\frac{17}{7}\frac{q}{h}\partial_x q+\frac{9}{7}\frac{q^2}{h^2}\partial_x h\right]+\frac{5}{6}\left[h\,(1-\cot\beta\partial_x h+We\partial_{xxx}h)-3\frac{q}{h^2}\right]$$
$$+4\frac{q}{h^2}(\partial_x h)^2-\frac{9}{2}\frac{\partial_x q\partial_x h}{h}-6\frac{q}{h}\partial_{xx}h+\frac{9}{2}\partial_{xx}q. \quad (3.23)$$

The averaged momentum balance equation (3.3) accounts for the rapid decrease of the effective viscosity $\mu_{eff}(y=h)$ when the interface is disturbed. Consistency is achieved up to $O(\epsilon)$ for inertial terms and up to $O(\epsilon^2)$ for the contribution of the surface effective viscosity to the streamwise diffusion terms. The contribution of the bulk to the streamwise viscous diffusion terms is evaluated in an *ad hoc* way but ensures consistency with the Newtonian case in the limit $n\to 1$.

Truncated at order ϵ, i.e. when the second and third rows are omitted, (3.20) is identical to the momentum balance derived by Amaouche *et al.* (2009). Similarly to Ng & Mei (1994), Amaouche *et al.* used the power-law constitutive equation (1.1)

without regularization of the effective viscosity at zero strain rate. As a matter of fact, the divergence of the effective viscosity does not affect the boundary-layer momentum balance equation (3.3) when truncated at first order. Indeed at $O(\epsilon)$, the viscous contribution comes only through the tangential stress τ_{xy} which remains bounded. As a consequence, a regularization of the effective viscosity at low strain rate becomes necessary only when streamwise viscous effects are accounted for.

3.2. *Shear-thickening film ($n > 1$) in the limit of vanishing Newtonian layer*

Now, turning to the shear-thickening case, and retaining the leading-order terms in the limit $s \to 0$, the averaged momentum equation (3.17) reduces (for $1 < n < 3$) to

$$\begin{aligned} Re\partial_t q = Re &\left[-F(n)\,\frac{q}{h}\partial_x q + G(n)\,\frac{q^2}{h^2}\partial_x h\right] \\ &+ I(n)\left[h\,(1-\cot\beta\partial_x h + We\partial_{xxx}h) - \frac{q\,|q|^{n-1}}{(\phi_0 h^2)^n}\right] \\ &+ \left[\frac{|q|}{\phi_0 h^2}\right]^{n-1} \times \left[J_1(n)\frac{q}{h^2}\,(\partial_x h)^2 - K_1(n)\frac{\partial_x q\partial_x h}{h}\right. \\ &\left. - L_1(n)\frac{q}{h}\partial_{xx}h + M_1(n)\partial_{xx}q\right]. \end{aligned} \tag{3.24}$$

The set of coefficients is completed by

$$J_1 = -\frac{(2n+1)(2n+7)(3n+2)}{3(2n-1)(4n+1)}, \tag{3.25a}$$

$$K_1 = -\frac{(3n+2)(4n^4-12n^3-85n^2-23n+2)}{12n(2n-1)(4n+1)}, \tag{3.25b}$$

$$L_1 = \frac{(2n+1)(3n+2)(12n^3+36n^2+n-1)}{6n(2n-1)(3n+1)(4n+1)}, \tag{3.25c}$$

$$M_1 = \frac{(2n+1)(2n+7)(3n+2)}{6(4n+1)(2n-1)}. \tag{3.25d}$$

In the Newtonian limit $n \to 1$, the averaged momentum equation (3.23) derived by Ruyer-Quil & Manneville (2000) is recovered but for the coefficients of the streamwise viscous diffusion terms $q\,(\partial_x h)^2/h^2$ and $(\partial_x q\partial_x h)/h$ as $K_1(1) = 19/2$ and $J_1(1) = 9$. We note that these terms are nonlinear and do not contribute to the linear stability analysis of the Nusselt base flow so that the dispersion relations of the model (3.3), (3.24) and (3.3), (3.23) coincide when $n = 1$. The above discrepancy is a consequence of the Taylor expansion (3.16) of the effective viscosity $\dot{\gamma}_0^{n-1}$ which becomes invalid as $\partial_y u_s|_{y=h}$ goes to zero for $n = 1$. Yet, the assumption of a vanishing Newtonian layer, necessary to derive (3.24), is obviously not compatible with the Newtonian limit $n \to 1$ and a full agreement of (3.24) with (3.23) is therefore not expected.

4. Linear stability analysis

4.1. *Orr–Sommerfeld analysis*

In this section, we consider the linear stability of the Nusselt uniform film solution. We first linearize the governing equations (2.8) with a fluid modelled by a power law and a Newtonian behaviour at low rate of strain (2.4). We thus perturb the basic

state (2.12) with $h = 1$,

$$\text{if } y < 1 - s^n, \quad U(y) = f_0(y) \tag{4.1a}$$

$$\text{otherwise} \quad U(y) = f_0(1 - s^n) + s^{n+1} g_0[s^{-n}(y + s^n - 1)], \tag{4.1b}$$

$$P(y) = \cot\beta(1 - y). \tag{4.1c}$$

We introduce a stream function and proceed to a decomposition on normal modes:

$$u = U + Re\left(\psi'(y)\mathrm{e}^{\mathrm{i}k(x-ct)}\right), \quad v = Re\left(-\mathrm{i}k\psi(y)\mathrm{e}^{\mathrm{i}k(x-ct)}\right), \tag{4.2}$$

$$h_i = 1 - s^n + Re\left(f_i\mathrm{e}^{\mathrm{i}k(x-ct)}\right), \tag{4.3}$$

where k and c are the wavenumber and phase speed, respectively, and Re stands for the real part; h_i refers to the position of the fake interface separating the Newtonian and non-Newtonian regions of the flow. We thus obtain a Orr–Sommerfeld problem,

$$\text{if } y < 1 - s^n, \quad \mathrm{i}kRe[(U - c)(D^2 - k^2)\psi - \psi U''] = (D^2 + k^2)[n\,(U')^{n-1}(D^2 + k^2)\psi] - 4k^2 D[(U')^{n-1} D\psi], \tag{4.4a}$$

$$\text{otherwise}, \quad \mathrm{i}kRe[(U - c)(D^2 - k^2)\psi - \psi U''] = r\,(D^2 - k^2)^2\,\psi, \tag{4.4b}$$

where $D \equiv \mathrm{d}/\mathrm{d}y$ and again $r = s^{n-1}$ is the ratio of the viscosity at the free surface and at the wall. The system of equations (4.4) is completed by the boundary conditions at the wall and at the interface,

$$\psi(0) = \psi'(0) = 0, \tag{4.4c}$$

$$k^2\psi(1) + \psi''(1) + U''(1)\frac{\psi(1)}{c - U(1)} = 0, \tag{4.4d}$$

$$\frac{\psi(1)}{c - U(1)}(Wek^3 + \cot\beta k) + kRe[U(1) - c]\psi'(1) + \mathrm{i}r[\psi'''(1) - 3k^2\psi'(1)] = 0, \tag{4.4e}$$

The amplitude of the deformation of the fake interface is given by

$$f_i = ns^{n-1}(k^2\psi|_{y_c-} + \psi''|_{y_c-}), \tag{4.4f}$$

where $y_c = 1 - s^n$ refers to the location of the interface for the base flow. The continuity of the velocity implies the continuity of ψ and ψ' at $y = y_c$. Writing the continuity of stresses at the fake interface finally leads to

$$\psi''|_{y_c+} = [n\psi'' + (n - 1)k^2\psi]|_{y_c-}, \tag{4.4g}$$

$$s^n[\psi'''']|_{y_c+} = \left\{s^n[n\psi'''' + (n - 1)k^2\psi'] - (n - 1)[\psi'' + k^2\psi]\right\}|_{y_c-} \tag{4.4h}$$

at the fake interface $y_c = 1 - s^n$.

We solve systems equation (4.4) by continuation using AUTO07P software (Doedel 2008). We obtain the spatial long-wave mode (k complex and ω real) starting from its analytical solution at $k = 0$. We first present the result obtained for the three shear-thinning fluids whose properties are detailed in table 1. Figure 3(*a*) shows the behaviour of the spatial growth rate $-k_i = -\mathrm{Im}(k)$ as a function of the wavenumber $k_r = \mathrm{Re}(k)$. The Reynolds number is chosen large ($Re = 100$) and the inclination moderate ($\beta = 15°$). Similarly to the Newtonian case (Brevdo *et al.* 1999), the range of unstable wavenumbers extends from zero to the cut-off wavenumber k_c. Figure 3(*b*) presents the marginal stability curve, i.e. cut-off wavenumber k_c versus Reynolds number Re. As the concentration of xanthan gum increases from 500 ppm (set 1) to 2500 ppm (set 3), the instability threshold is displaced to lower values of the critical

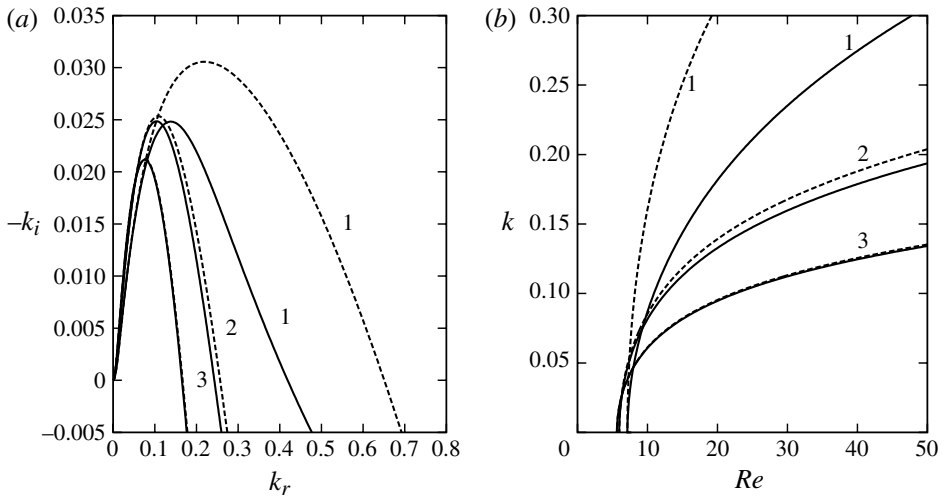

FIGURE 3. (*a*) Spatial growth rate $-k_i$ versus wavenumber k_r at $Re = 100$. (*b*) Marginal stability curves in the plane (Re, k). Inclination angle is $\beta = 15°$. Labels refer to shear-thinning xanthan gum solutions (cf. table 1). Solid lines refer to the solutions to the Orr–Sommerfeld problem (4.4). Dashed lines correspond to the solutions when surface tension is not taken into account ($We = 0$).

Reynolds number whereas the range of unstable wavenumbers is decreased. Shear-thinning effects therefore enhance the primary instability close to threshold (Millet *et al.* 2008), but also tend to stabilize the base flow far from threshold.

We have compared the Orr–Sommerfeld analyses with ($We \neq 0$) and without surface tension ($We = 0$). Differences are important for set 1 but hardly noticeable for the fluid sets 2 and 3, in which case the cut-off wavenumber is determined by the balance of inertia and viscous damping. For shear-thinning fluid, viscosity is maximal at the free surface and a competition of surface tension and viscous damping at the free surface can be evaluated by computing the Kapitza number Γ_0 based on the maximum viscosity μ_0 of the fluid:

$$\Gamma_0 = (l_c/l_{\mu_0})^2 = (\sigma/\rho)\,(\mu_0/\rho)^{-4/3}\,(g\sin\beta)^{-1/3}$$
$$\text{where } l_{\mu_0} = (\mu_0/\rho)^{2/3}\,(g\sin\beta)^{-1/3} \tag{4.5}$$

is the length at which viscosity μ_0 balances streamwise gravity acceleration. From the data in table 1, we get $\Gamma_0 = 8.8$ for a 500 ppm xanthan solution (set 1) and $\Gamma_0 = 0.19$ and 0.02, respectively, for the two more concentrated solutions corresponding to sets 2 and 3, which explains that for the concentrated xanthan solutions surface tension effects are rather weak in comparison with the wave damping by the viscosity of the fluid at the free surface.

Figure 4 compares the marginal stability conditions and spatial growth rate for given fluid properties, flow rate and inclination angle, when the threshold $\dot{\gamma}_c$, separating the shear-thinning and the Newtonian behaviours of the fluid, is varied. As expected, both the location of the marginal stability curve in the plane (Re, k_r) and the spatial growth rate $-k_i$ varies significantly with $\dot{\gamma}_c$ which underlines the damping role of the viscosity at the free surface on the linear stability of the Nusselt film. We therefore conclude that for a sufficiently small power-law index ($n = 0.4$ for set 2 and $n = 0.34$ for set 3), the marginal stability conditions and thus the range of unstable wavenumbers are governed by the viscous damping of short waves in the Newtonian layer below the

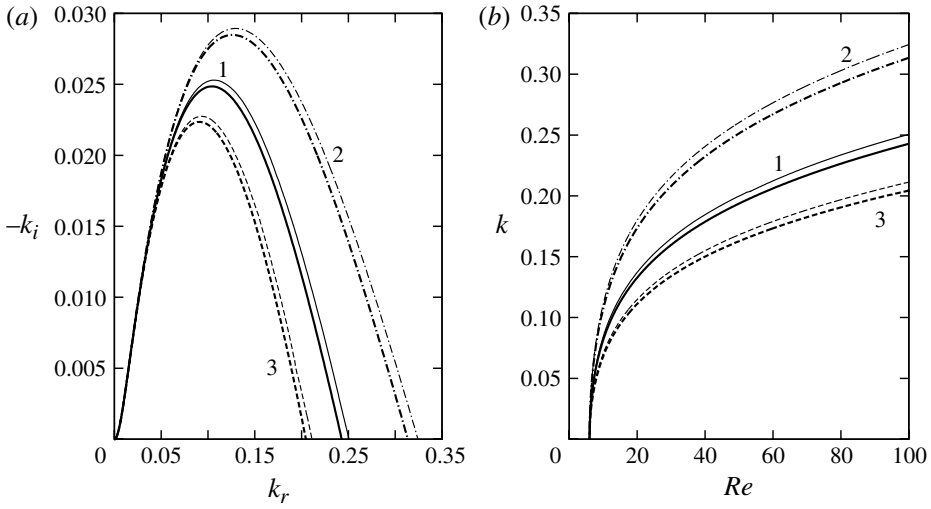

FIGURE 4. Spatial linear stability analysis based on the Orr–Sommerfeld problem (4.4) (thick lines) and based on the Orr–Sommerfeld analysis of Carreau-law fluids (C 2) (thin lines). (*a*) Spatial growth rate $-k_i$ versus wavenumber k_r at $Re = 100$. (*b*) Marginal stability curves in the plane (Re, k). Inclination angle is $\beta = 15°$. Fluid properties correspond to a shear-thinning xanthan gum solution of concentration 1500 ppm (set 2 in table 1). Labelled lines 1, 2 and 3 refer to $\dot{\gamma}_c = 0.1$, 1 and 0.02 s^{-1}, respectively.

interface, a mechanism which is more effective than surface tension and the viscous momentum diffusion in the bulk of the film.

We have compared the results of the spatial stability analysis obtained with the Newtonian plateau regularization equation (2.11) with those from the Carreau law (2.10) (see appendix C). The two analyses lead to close results as illustrated in figure 4. We have checked that it is also the case for the fluid properties listed in table 1 and the range of parameters $[Re_c, Re]$ for $\beta = 15$ and 85° for which the thickness of the Newtonian layer is small ($s^n \ll 1$). Therefore, the conclusions of our linear stability analysis do not depend on the peculiar choice of regularization of the power law (1.1) at low strain rate.

Turning to the shear-thickening cornstarch solutions, we present the spatial growth rate $-k_i$ versus wavenumber k_r at $Re = 100$ and the marginal stability curves in the plane (Re, k) in figure 5. Labels 4, 5 and 6 refers to the parameter sets given in table 2. As the concentration of the cornstarch solution is raised from 33 % (set 4) to 38 % (set 6), the instability threshold is displaced to larger values of the critical Reynolds number whereas the range of unstable wavenumber increases. Conversely to what is observed for shear-thinning fluids, shear-thickening effects stabilize the base flow close to the instability threshold but are destabilizing farther from threshold. The results presented in figure 5 are not noticeably modified whenever surface tension in neglected ($We = 0$) or the critical strain rate is raised up to $\dot{\gamma}_c = 1$ s^{-1}, which shows that the range of unstable wavenumbers is determined by the effective viscosity of the non-Newtonian bulk region and not by the significantly lower viscosity of the Newtonian layer at the free surface or surface tension effects.

4.2. *Whitham wave hierarchy*

Turning to the stability analysis of the low-dimensional model (3.3), (3.9), (3.17) and (3.7) leads to a dispersion relation written in canonical form as

$$c - c_k(k) - \mathrm{i}kRe[c - c_{d-}(k)][c - c_{d+}(k)] = 0, \tag{4.6}$$

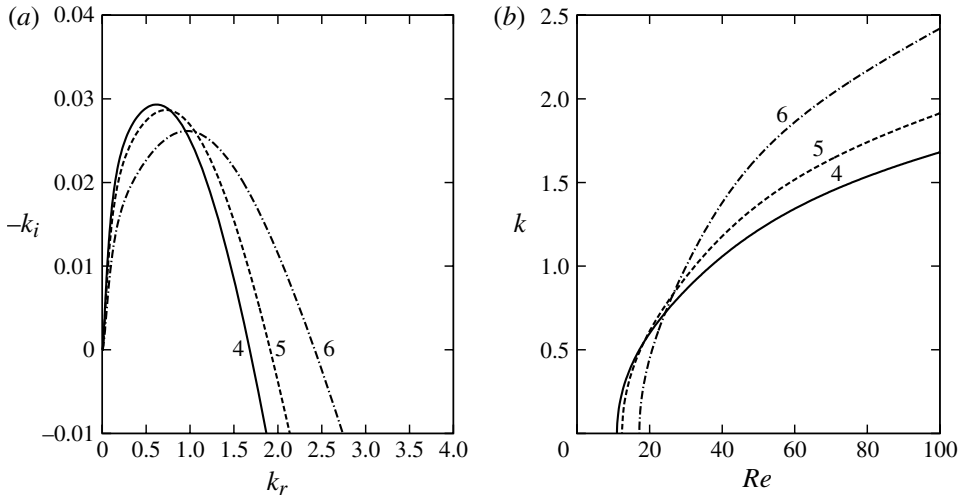

FIGURE 5. Spatial linear stability analysis based on the Orr–Sommerfeld problem (4.4). (*a*) Spatial growth rate $-k_i$ versus wavenumber k_r at $Re = 100$. (*b*) Marginal stability curves in the plane (Re, k). The inclination angle is $\beta = 15°$. Fluid properties correspond to the shear-thickening cornstarch solutions whose properties are listed in table 2.

which corresponds to the wave hierarchy situation considered by Whitham (1974). Each dispersion relation of the form (4.6) can be split into two parts with a $\pi/2$ phase shift, each part corresponding to a different kind of wave. The dispersion relation of the first kind of wave is obtained by taking the limit $Re \to 0$. In this limit, the velocity field and thus the flow rate q are utterly slaved to the evolution of the film thickness h and waves of the first kind are governed by the mass balance equation (3.3) or equivalently the kinematic boundary condition (2.2*c*). These kinematic waves result from the kinematic response of the free surface to a perturbation and propagate at speed

$$c_k = \frac{n\tilde{I} + rk^2\left\{n\tilde{L}(1-2\phi) + \tilde{M}\left[2(1+n)\phi - n\right]\right\}}{n\tilde{I} + rk^2\tilde{M}}, \tag{4.7}$$

where ϕ is a function of the relative thickness $\bar{\eta}_c$ of the Newtonian layer and is defined in (3.7). The coefficients $\tilde{I}, \tilde{L}, \tilde{M}$ and ϕ are computed for the base state relative thickness $\bar{\eta}_c = s^n$. In the limit $k \to 0$ we recover $c_k = 1$ which in dimensional units corresponds to the velocity scale V as already noticed in § 3. Let us stress that the dependence of c_k on the wavenumber k arises from the viscous diffusion of the momentum in the direction of the flow. This viscous dispersion effect was first noted in Ruyer-Quil *et al.* (2008).

In contrast, waves of the second kind correspond to the limit $Re \to \infty$. These dynamic waves are the responses of the film to the variation in momentum, hydrostatic pressure and surface tension (for bounded Froude number and ratios We/Re) which are induced by deformations of the free surface. They propagate at speeds

$$c_{d\pm} = \tfrac{1}{2}(\tilde{F} - n + 2(n+1)\phi \pm \sqrt{\Delta}), \tag{4.8}$$

$$\text{with} \quad \Delta = \left[\tilde{F} - n + 2(n+1)\phi\right]^2 + 4\{[n - 2(n+1)\phi]\tilde{F} + n(1-2\phi)\tilde{G}\} + 4n(1-2\phi)\tilde{I}\tilde{F}r^{-2}(k^2), \tag{4.9}$$

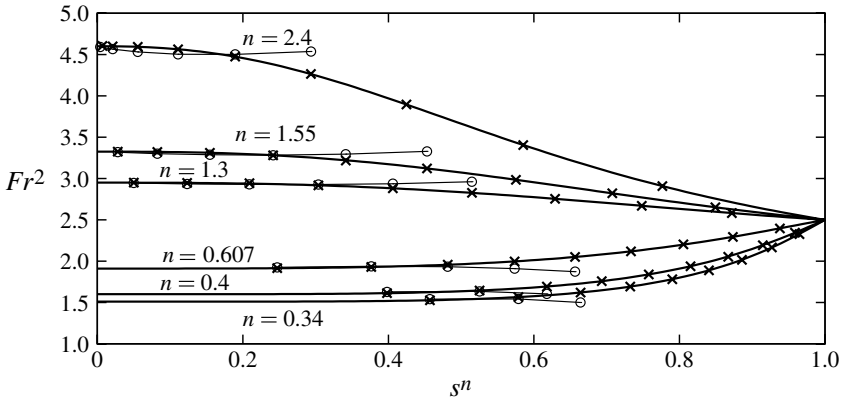

FIGURE 6. Critical Froude number $Fr^2 = Re/\cot\beta$ as a function of the relative thickness s^n of the Newtonian layer for the different values of the power-law index n. The solid lines correspond to (4.11). Crosses and circles refer to the numerical solutions to the Orr–Sommerfeld problem (4.4) and (C 2), respectively (the thin solid lines are guides to the eye).

where the coefficients are again computed at $\bar{\eta}_c = s^n$ and $\tilde{Fr}^{-2}(k^2) = (\cot\beta + Wek^2)/Re$. Dispersion of dynamic waves is induced by surface tension.

Considering real wavenumbers, the temporal stability condition of the base state can be written in terms of the speeds c_k and $c_{d\pm}$ of the kinematic and dynamic waves (Whitham 1974):

$$c_{d-} \leqslant c_k \leqslant c_{d+}. \tag{4.10}$$

The base state is marginally stable if $c_{d-} = c_k$ or $c_{d+} = c_k$. In our case, only the latter condition can be achieved. The instability threshold arises at $k = 0$ which reflects the long-wave nature of the instability and leads to

$$Fr^2 = \frac{Re}{\cot\beta} = \frac{n\tilde{I}}{(n+1)(1-\tilde{F}) - n\tilde{G}}. \tag{4.11}$$

We present in figure 6 the variations of the critical Froude number with respect to the relative thickness s^n of the Newtonian layer for the base flow for the shear-thinning and shear-thickening fluids reported in tables 1 and 2. The expression (4.11) is compared with the threshold obtained by solving the Orr–Sommerfeld problem (4.4) numerically. For all tested values of s^n and n a remarkable agreement is achieved. As for Newtonian film flows this agreement is related to the consistency of the modelling approach at order ϵ (Ruyer-Quil & Manneville 2000).

We have completed figure 6 with the values of the Froude number at the instability threshold given by the solution to the Orr–Sommerfeld problem (C 2) when the Carreau constitutive equation (2.10) is assumed. Whenever the relative thickness of the Newtonian layer s^n is less than 0.2, solving the Orr–Sommerfeld problem with the regularization given by (2.10) or (2.11) give close results.

The effect of the Ostwald–de Waele model on the stability of the uniform film Nusselt solution can be found by comparing kinematic and dynamic wave speeds. We have plotted in figure 7 the minimum of the fastest dynamic wave speed c_{d+} which is reached in the limit $\tilde{Fr}^{-2} \to 0$ corresponding to a vertical wall and a null wavenumber. The largest is the interval between the minimum of c_{d+} and c_k, the smallest is the threshold Fr^2 of the instability. Since the minimum of c_{d+} is always smaller than one,

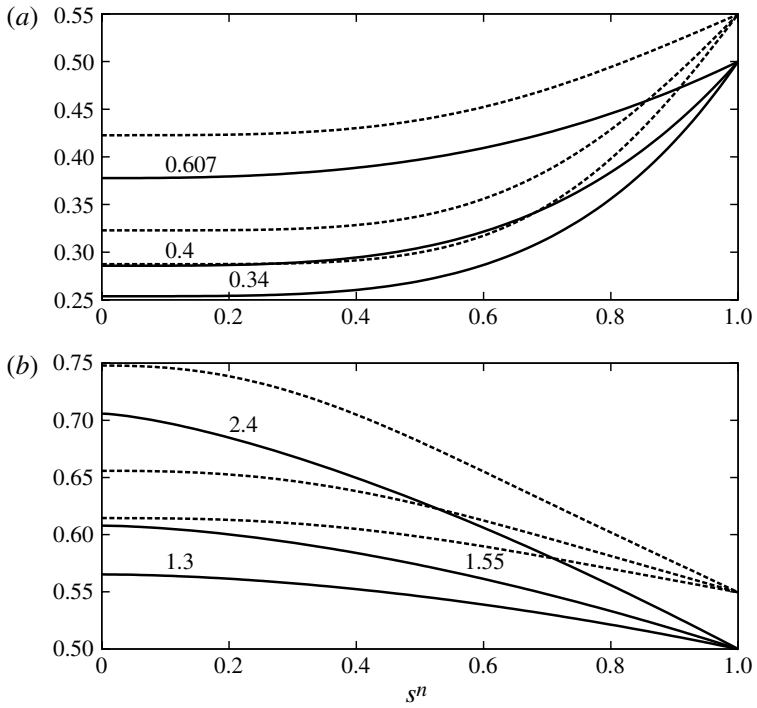

FIGURE 7. Velocity at the free surface u_i (solid lines) and dynamic wave speed c_{d+} in the limit $\tilde{Fr}^{-2} \to 0$ (dashed lines): (*a*) $n = 0.34$, 0.4 and 0.607; (*b*) $n = 1.3$, 1.55 and 2.4.

which is the dimensionless value of c_k for $k = 0$, lowering (increasing) the minimum of c_{d+} is destabilizing (stabilizing). The decrease of the instability threshold observed for a shear-thinning fluid ($n < 1$) in figure 6 is therefore made clear by the drop of the minimum of the fastest dynamic wave velocity observed in figure 7. The same analysis applies conversely for a shear-thickening fluid ($n > 1$). Figure 7 has been completed with the fluid velocity at the interface, i.e. $u_i = u|_{y=1}$ for the Nusselt base flow $h = 1$ (Equation (2.12)). Interestingly, u_i stays close to the minimum of c_{d+} whatever the values of n and s^n. Therefore, the variations of the interval between c_{d+} and c_k follow closely the variations of the interval between c_k and the velocity of the fluid at the interface (which is also the maximum velocity of the base flow). As noted by Smith (1990), the ability of kinematic waves to move faster than any fluid particles is the key ingredient of the instability mechanism of a falling liquid film. There is a direct correlation between the movement of the threshold Fr^2 in figure 6 and the variation of the velocity at the interface u_i depicted in figure 7. The smaller the power-law index n and the thinner the Newtonian layer, the smaller the minimum of c_{d+} and thus the instability threshold Fr^2 are (Rousset *et al.* 2007; Millet *et al.* 2008). The weak dependence of the maximum velocity of the base flow u_i and the speed c_{d+} of the fast dynamic waves on the thickness s^n of the Newtonian layer for s^n lower than 0.2 makes clear the similar trend observed for the critical Froude number.

4.3. *Limit of a vanishing Newtonian layer*

We now turn to the simplified models (3.3), (3.20) and (3.3), (3.24) obtained in § 3 in the limit of thin Newtonian layers at the free surface ($s^n \to 0$).

For a shear-thinning fluid the dispersion relation of model (3.3), (3.20) can be recast in the canonical form (4.6) where the kinematic wave speed now reads

$$c_k = \frac{n}{n+1} + \frac{1}{1+n+(1-n)rk^2} \tag{4.12}$$

so that $c_k = 1$ when the viscous dispersive effect vanishes ($r \to 0$). The dynamic wave speed reads

$$c_{d\pm} = \frac{1}{2}\phi_0(F \pm \sqrt{\Delta}), \quad \text{with } \Delta = F^2 - 4G + \frac{I}{\phi_0^2 \tilde{F} r^2}, \tag{4.13}$$

where again $\phi_0 = \phi(0) = n/(2n+1)$. Turning to a shear-thickening fluid, the dispersion relation of the two-equation model (3.3), (3.24) again admits the canonical form (4.6) where kinematic wave speed is given by

$$c_k = \frac{nI + \phi_0^2 L k^2}{nI + \phi_0 M k^2} \tag{4.14}$$

and dynamic wave speeds remain given by (4.13). For both models (3.3), (3.20) and (3.3), (3.24), the marginal stability condition $c_k = c_{d+}$ leads to the correct expression (2.13) of the instability threshold.

We compare in figures 8 and 9 the marginal stability curves obtained with the two-equation models (3.3), (3.20) and (3.3), (3.24) with the reference results from the Orr–Sommerfeld stability analysis. A good agreement is obtained for each shear-thinning and shear-thickening fluid properties listed in tables 1 and 2. More precisely, the instability threshold is very well captured for each tested set of parameters although we assume a negligible thickness of the Newtonian layer at the free surface ($s^n \to 0$). The very weak dependence of the instability threshold on the thickness s^n of the Newtonian layer for s^n lower than 0.2 observed in figure 6 does explain this agreement. Note that a better agreement between the models and the Orr–Sommerfeld analysis is achieved in the case of shear-thinning fluids than for shear-thickening fluids. Since the cut-off wavenumbers are smaller in the shear-thinning case, which reflects the stabilizing contribution of streamwise viscous diffusion at the free surface layer, the long-wave assumption is more easily verified in that case which explains the observed better agreement with the Orr–Sommerfeld analysis.

As for the Orr–Sommerfeld analysis, we note that the spatial stability analysis of the shear-thinning model (3.3), (3.20) is strongly dependent on the viscosity contrast r between the wall and the free surface. Indeed setting r to zero provides much larger values of the cut-off wavenumber and spatial growth rate. Conversely, we have not noticed significant differences for the stability of a uniform film of shear-thickening fluid based on the weighted-residual approach when the Newtonian layer viscosity is taken into account or not ($r = 0$).

5. Travelling waves

In this section we consider the nonlinear solutions to the simplified models (3.3), (3.20) and (3.3), (3.24) such as travelling waves propagating at constant speed c. In the frame of reference moving with the speed of the waves, $\xi = x - ct$, the flow is stationary and partial differential equations are converted into ordinary differential equations which we solved by continuation using AUTO07P software (Doedel 2008).

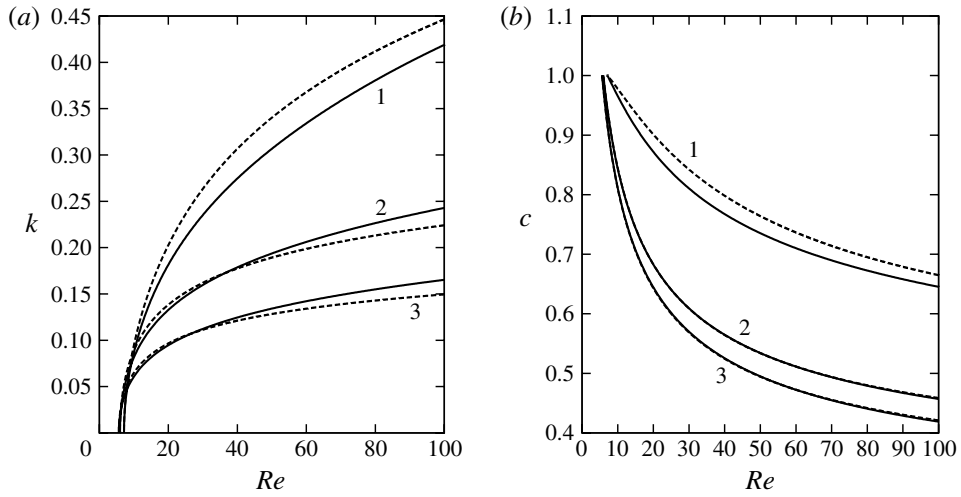

FIGURE 8. (*a*) Cut-off wavenumber k_c versus Reynolds number Re. (*b*) Phase speed c at marginal conditions versus Re. Inclination angle is $\beta = 15°$. Labels refer to the shear-thinning xanthan gum solutions whose properties are listed in table 1. Solid and dashed lines stand for the solutions to the Orr–Sommerfeld problem (4.4) and to the dispersion relation of (3.3) and (3.20), respectively.

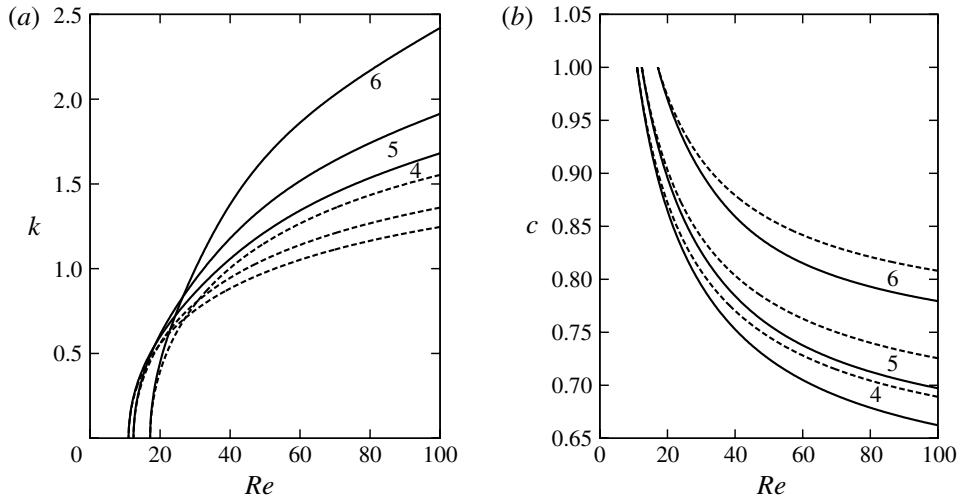

FIGURE 9. (*a*) Cut-off wavenumber k_c versus Reynolds number Re. (*b*) Phase speed c at marginal conditions versus Re. Inclination angle is $\beta = 15°$. Labels refer to the shear-thickening cornstarch solutions whose properties are given in table 2. Solid and dashed lines stand for the solutions to the Orr–Sommerfeld problem (4.4) and to the dispersion relation of (3.3) and (3.24), respectively.

5.1. *Bifurcation diagrams*

Considering first shear-thinning fluids, we have reported in figure 10 the bifurcation diagrams in the plane wavenumber versus speed of the travelling-wave branches of solutions to (3.3) and (3.20) for the fluid properties of the three xanthan gum aqueous solutions reported in table 1, at moderate inclination angle $\beta = 15°$ and $Re = 20$. The integral constraint $\langle h \rangle \equiv \lambda^{-1} \int_0^\lambda h \, \mathrm{d}\xi = 1$ has been enforced. Here $\lambda = 2\pi/k$ refers to the wavelength.

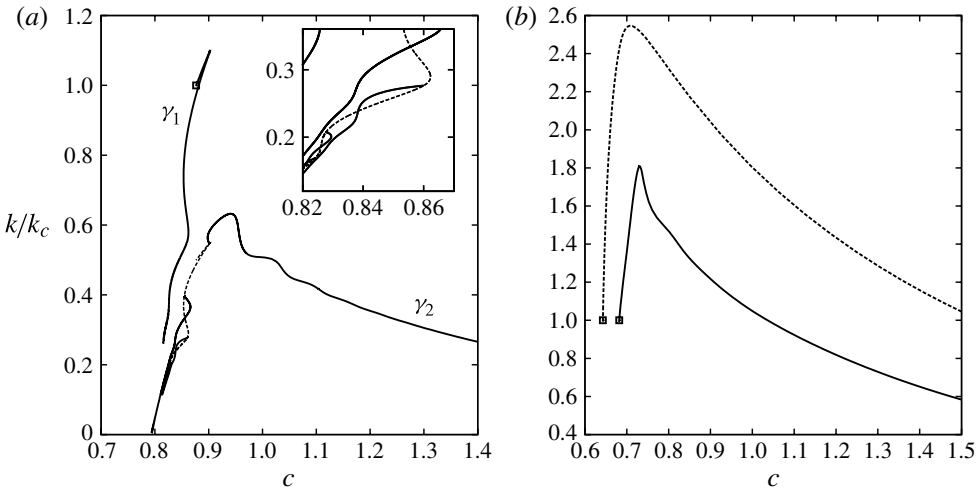

FIGURE 10. Speed c of travelling-wave solutions as a function of the wavenumber k/k_c normalized by the cut-off wavenumber k_c. Hopf bifurcation at k equal to the cut-off wavenumber k_c is indicated by squares. Here $Re = 20$, $\beta = 15°$. (a) A 500 ppm shear-thinning xanthan solution in water (set 1 in table 1). Dashed lines refer to the locus of solutions made of two γ_1 waves. (b) Solid and dashed lines refer to 1500 ppm and to 2500 ppm xanthan solutions: set 2 and 3 in table 1, respectively.

For the most dilute solution (a), a first branch of slow-wave solutions arises from the marginal stability condition $k = k_c$ through a Hopf bifurcation. Several secondary branches are found through period doubling of this first branch. One bifurcates at $k \approx 0.55k_c$ and terminates into fast waves. Following Chang, Demekhin & Kopelevitch (1993), we denote by γ_1 the principal branch of slow waves and by γ_2 the secondary branch of fast waves. The other secondary waves bifurcating from the principal γ_1 branch are slow.

Travelling waves correspond to limit cycles in the phase space that terminate into homoclinic trajectories as their lengthes are augmented. These trajectories correspond to small-wavenumber solitary-like wavetrains. Figure 11 presents the shapes of slow γ_1 and fast γ_2 waves at low wavenumbers. The γ_1 waves are made of a trough followed by capillary ripples (a) whereas γ_2 are one-humped waves preceded by capillary ripples (b).

The wrinkling of the solution branches in the k-versus-c diagram in figure 10(a) and the onset of numerous secondary branches are consequences of the interaction between the typical length of the capillary ripples preceding or following the waves and the wavelength. For the more condensed xanthan gum solutions in water (parameter sets 2 and 3), we observed a much simpler bifurcation diagram (see figure 10b). A unique branch of travelling-wave solutions bifurcate from the Nusselt solutions through a Hopf bifurcation. Secondary bifurcations through period doubling were not found. The number and amplitude of the capillary ripples preceding the main hump of the waves are considerably reduced because of the efficient damping of short waves by viscosity. This efficient damping of capillary waves is responsible for the drastic simplification of the bifurcation diagram in figure 10(b) when compared with figure 10(a).

For each bifurcation diagram displayed in figure 10, travelling-wave solutions are found at k larger than the cut-off wavenumber k_c which corresponds to a stable Nusselt uniform film flow. Travelling waves therefore bifurcate subcritically from the Nusselt solution. The range of subcritical wavenumbers $[k_{sub}, k_c]$ for which travelling waves

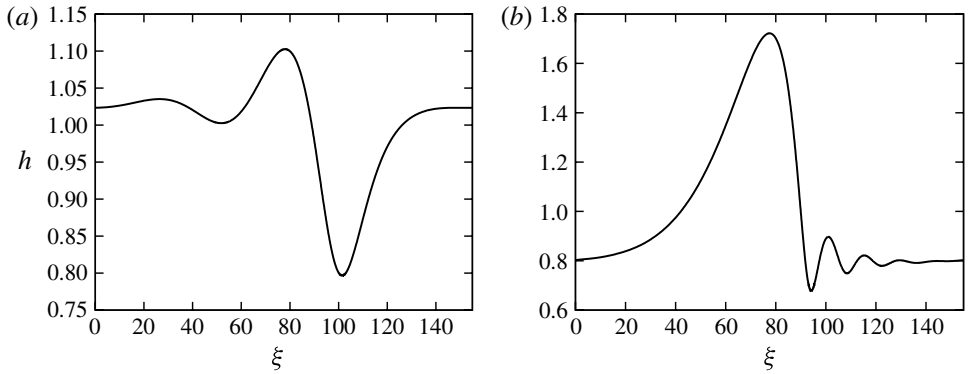

FIGURE 11. Travelling-wave profiles. A 500 ppm shear-thinning xanthan gum solution (set 1 in table 1), $Re = 20$, $\beta = 15°$, $k = k_c/3$ ($n = 0.607$): (*a*) γ_1 wave, $c = 0.819016$; (*b*) γ_2 wave, $c = 1.31315$.

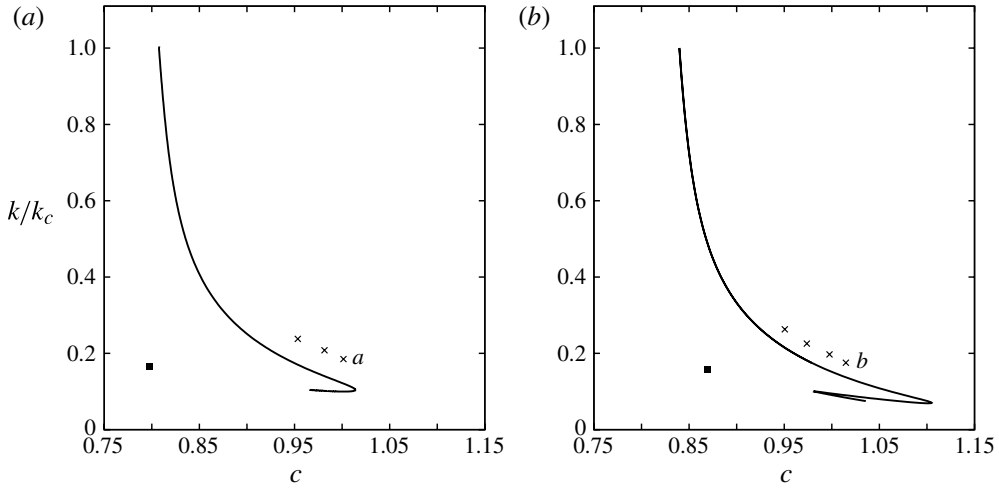

FIGURE 12. Speed c of travelling-wave solutions as a function of the wavenumber k. Solid line refers to model (3.3) and (3.24), crosses and square refers the phase speed of the wave before and after breaking, respectively, of the DNS result from Gerris software. Here $Re = 30$, $\beta = 15°$. The fluid properties of the shear-thickening cornstarch solutions are given in table 2. Labels *a* and *b* refer to the wave profiles displayed in figure 14: panel (*a*) set 4, $n = 1.3$; panel (*b*) set 5, $n = 1.55$.

coexist with a stable Nusselt solution tends to increase as the power-law index n is lowered. The onset of subcriticality is here related to the large viscosity ratio r between the wall and the free surface. Linear waves are efficiently damped by the free-surface viscosity and the cut-off wavenumber is determined by this effect. Finite-amplitude disturbances may survive to viscous damping by removing the Newtonian layer and thus significantly lower the viscosity at the free surface.

Turning to shear-thickening fluids ($n > 1$), figure 12 presents the bifurcation diagrams obtained with model (3.3), (3.24) for the cornstarch solutions whose properties are listed in table 2. The integral constraint $\langle h \rangle = 1$ is again enforced. For each set of fluid properties, the Kapitza number Γ is small and capillary waves are effectively damped by viscous effects so that (i) no capillary ripples are observable at the front of the nearly solitary waves at small wavenumber and (ii) no secondary

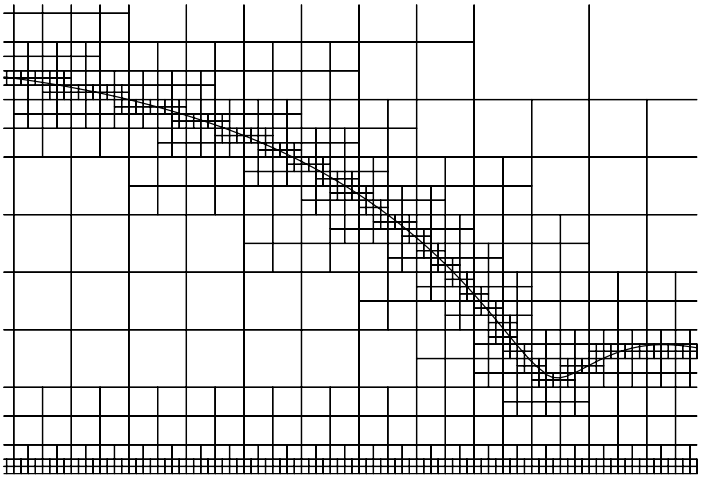

FIGURE 13. Detail of the mesh grid at the end of one Gerris run showing the dynamic refinement at the interface. The number of cells in the total grid is 15971. Here $Re = 100$, $\beta = 15^\circ$. The wavelength is $\lambda = 80$, fluid properties correspond to shear-thinning 1500 ppm xanthan gum solution (set 2 in table 1). The entire wave profile is displayed in figure 15(d).

branches have been found to emerge from the principal one through period-doubling bifurcations. In contrast to shear-thinning fluids, travelling-wave solutions are found only when the Nusselt base flow solution is unstable and the Hopf bifurcation corresponds to a supercritical situation.

5.2. *Comparisons with DNSs*

DNSs of the primitive set of equations (2.8) have been performed implementing periodic boundary conditions. Initial conditions correspond to the Nusselt flat-film solution to which a small disturbance has been added. At the final stage of the computation, nonlinear saturated travelling waves are observed that can be compared with the travelling-wave solutions to the models (3.3), (3.20) and (3.3), (3.24) with the integral constraint $\langle h \rangle = 1$.

Gerris software developed by Popinet (2003, 2009) enables us to implement the Ostwald–de Waele power-law model with a Newtonian plateau (2.4) and has been used extensively for this purpose. Gerris is a GPL licenced program that can be freely downloaded from http://gfs.sourceforge.net. Gerris uses a multilevel Poisson solver, an approximate projection method and a second-order accurate upwind scheme to discretize advection terms. Variable spatial resolution is enabled by a quadtree adaptive refinement method. Interfacial flow phenomena are captured by means of a generalized volume of fluid scheme which allows mesh refinement along the interface.

Refinement of the mesh to the deepest available level is imposed at the free surface in order to accurately capture the instability of the film. A typical mesh grid is presented in figure 13. Gerris automatically adapts the mesh in order to capture velocity variations as is observable at the liquid–solid interface.

Considering first shear-thickening cornstarch solutions (cf. table 2), the free surface elevations corresponding to the final time of our DNS simulations are displayed in figure 14. A striking agreement is obtained with the results to the weighted-residual model (3.3) and (3.24). The amplitude and speed of the waves are also faithfully captured (see table 3). However, for the largest tested numerical domains, either our

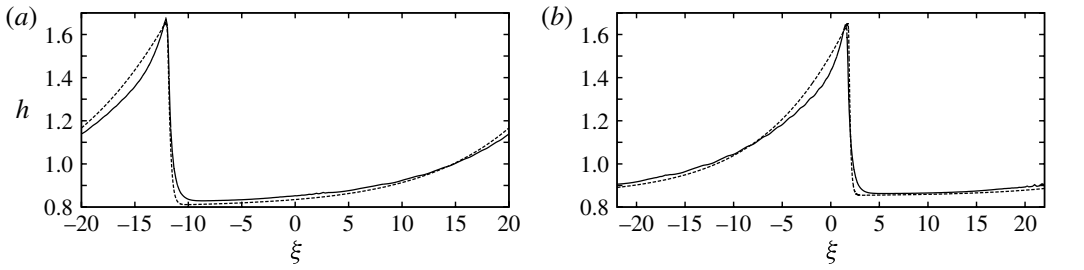

FIGURE 14. Travelling-wave profiles for the shear-thickening fluids ($n > 1$) whose properties are listed in table 2. Solid lines refer to the DNS results from Gerris software, whereas dashed lines refer to the solutions to model (3.3) and (3.24): (*a*) set 4, $Re = 30,\ \lambda = 40$; (*b*) set 5, $Re = 30,\ \lambda = 45$.

Fluid	Re	λ	c		h_m	
			DNS	model	DNS	model
Set 4	30	40	0.98	0.92	1.68	1.65
Set 5	30	45	1.01	1.00	1.65	1.65

TABLE 3. Phase speed c and maximum height h_m of travelling-wave solutions with $\langle h \rangle = 1$. Fluid properties correspond to a shear-thickening cornstarch dispersion in ethylene glycol and to a 15° inclination angle (table 2).

DNSs do not lead to permanent waves or wave breaking phenomena are observed. The speeds of the fronts, computed immediately before the breaking of the waves take place, are indicated by filled squares in figure 12(*a,b*). Curiously, the onset of the wave breaking phenomenon is accompanied by a reduction of the wave speed, a trend that is reproduced by the travelling-wave solutions to the weighted-residual model as the wavenumber k is lowered.

Turning to shear-thinning xanthan gum solutions in water (cf. table 1) the profiles of the travelling waves obtained at the end of the DNSs are presented in figure 15. The waves systematically present capillary ripples preceding the main hump in spite of the very large ratio r of the free surface to wall effective viscosities. Their shapes are similar to the solitary waves observed experimentally for Newtonian fluids (Liu & Gollub 1994; Chang & Demekhin 2002). If the amplitude of the waves are comparable for the three tested sets of fluid properties, the phase speed tends to be larger for the most concentrated xanthan solution (set 3) corresponding to the lowest value of the power-law index ($n = 0.34$).

Shapes, speeds and amplitudes are compared with the predictions of the weighted residual model (3.3) and (3.20) in figure 15 and table 4. Good agreement is obtained for the shape and amplitude. However, the model tends to overestimate the speed of the waves. We note that the nonlinear dependence of the effective viscosity (3.22) on the gradients of q and h is necessary to reproduce the capillary waves observed in the DNSs. Solutions to the two-equation model (3.3) and (3.18) with a constant effective free surface viscosity r do not present capillary ripples.

The DNSs presented in table 4 and figure 15 have been performed again using the smooth Carreau constitutive equation (2.10) instead of the continuous equation (2.11). The results of these simulations are labelled 'DNS(CL)' in table 4. Wave profiles are

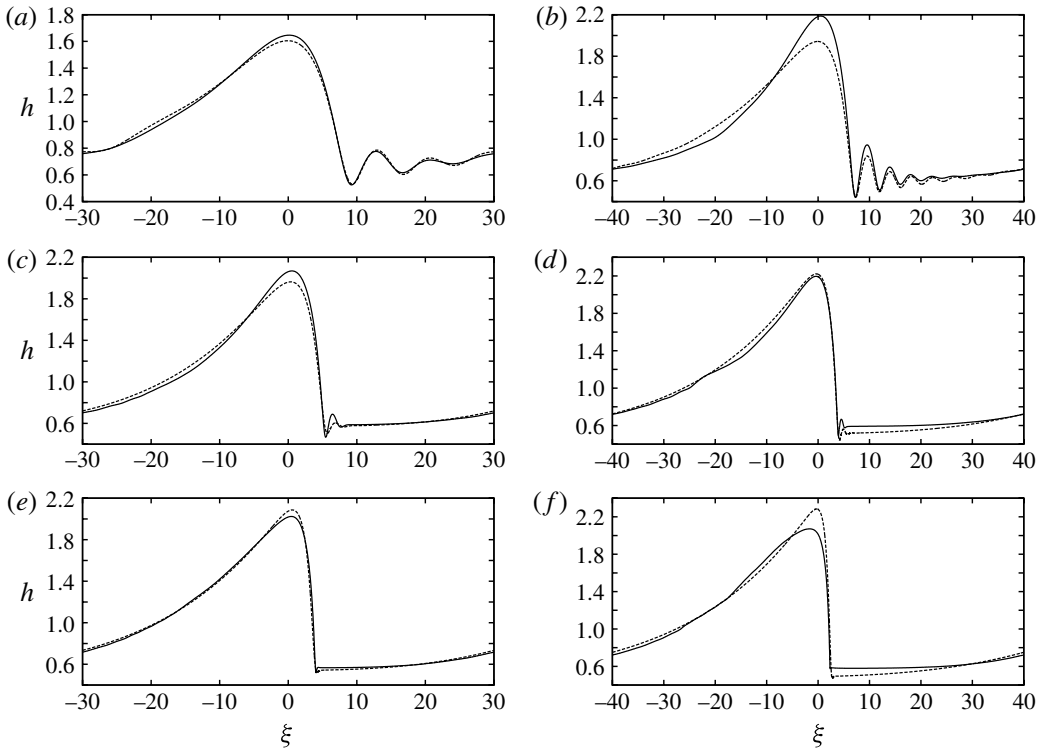

FIGURE 15. Travelling-wave profiles for shear-thinning xanthan gum solutions in water (see table 1). Solid lines refer to the DNS results from Gerris software, whereas dashed lines refer to the solutions to model (3.3) and (3.20): (*a*) set 1, $Re = 50, \lambda = 60$; (*b*) set 1, $Re = 100, \lambda = 80$; (*c*) set 2, $Re = 50, \lambda = 60$; (*d*) set 2, $Re = 100, \lambda = 80$; (*e*) set 3, $Re = 50, \lambda = 60$; (*f*) set 3, $Re = 100, \lambda = 80$.

Fluid	*Re*	λ	*c*			h_m		
			DNS	DNS(CL)	Model	DNS	DNS(CL)	Model
Set 1	50	60	0.86	0.86	0.88	1.65	1.65	1.60
	100	80	0.81	0.82	0.87	2.19	2.19	1.94
Set 2	50	60	0.92	0.92	1.03	2.07	2.07	1.96
	100	80	0.76	0.76	0.96	2.20	2.20	2.22
Set 3	50	60	0.93	0.92	1.14	2.02	2.01	2.09
	100	80	0.75	0.75	1.05	2.07	2.06	2.28

TABLE 4. Phase speed c and maximum height h_m of travelling-wave solutions with $\langle h \rangle = 1$. Fluid properties correspond to shear-thinning dilute solutions of xanthan gum and to a 15° inclination angle (see table 1). 'DNS' and 'DNS(CL)' refer to the results from Gerris using the Newtonian plateau constitutive equation (2.11) and the Carreau law (2.10), respectively.

nearly identical and no significant differences have been observed in the results of DNS using (2.10) or (2.11). We can therefore conclude that, at least for the fluids and parameters we have tested, travelling-wave solutions are not affected by the particular choice of regularization at low strain rates of the power-law model (1.1).

	Set 1 ($n = 0.607$)				Set 2 ($n = 0.4$)			
	$\dot{\gamma}_{max}$	$\max(\dot{\gamma}_{y=0})$	$\max(\dot{\gamma}_{y=h})$	$\Gamma_\star$	$\dot{\gamma}_{max}$	$\max(\dot{\gamma}_{y=0})$	$\max(\dot{\gamma}_{y=h})$	$\Gamma_\star$
DNS	1.6	1.6	0.8	470	4.5	1.8	4.5	380
Model	1.2	1.2	0.6		2.0	2.0	1.6	

TABLE 5. Maxima of the strain rate $\dot{\gamma}$, global, at the wall and at the free surface corresponding to figure 16. 'DNS' refers to the final stage of DNSs performed with Gerris software, whereas 'Model' denotes the travelling solutions to (3.3) and (3.20). Here $\beta = 15°$, $Re = 50$, $\lambda = 60$ and $\Gamma_\star$ is the Kapitza number corresponding to the viscosity minimum at the free surface, i.e. $\Gamma_\star = \Gamma_0\,(s/\max(\dot{\gamma}_{y=h}))^{4(n-1)/3}$.

Figure 16 presents the distribution of the strain rate under the solitary-like waves whose profiles are shown in figure 15(*a,c*). We limit ourselves to consider the capillary region at the front of the main hump where the free surface is the steepest. Parameters correspond to the same Reynolds number, inclination and wavelength but different xanthan-gum solutions. The more dilute one, set 1 in table 1 with $n = 0.607$ is less shear-thinning that the other one, set 2 with $n = 0.4$. From the results of the DNS simulations, the local maxima of the strain rate are located either at the wall or at the free surface. Global maxima of the strain rate, maxima along the wall and along the free surface are compared in table 5. For the most dilute xanthan-gum solution (set 1 with $n = 0.607$), the shear rate is maximum at the wall at a location that is close to the maximum elevation of the free surface as suggested by the leading order term of the gradient expansion $\dot{\gamma} = |\partial_y u_s| + O(\epsilon)$ whose maximum $|q/(\phi_0 h^2)| = h^{1/n} + O(\epsilon)$ is reached at the wall under the crest of the wave. Instead, for the less dilute solution (set 2 with $n = 0.4$), the global maximum of the strain rate is reached at the free surface at a point where the gradient of the thickness is the largest, which suggests that the long-wave approximation is not well verified at the front of the wave. Indeed, the front of the wave is quite steep and the assumption $\partial_x h \ll 1$ does not hold there. In that region, viscous diffusion and surface tension effects can be compared by computing the Kapitza number based on the minimum of viscosity at the free surface, i.e. $\Gamma_\star = \Gamma_0\,(s/\max(\dot{\gamma}_{y=h}))^{4(n-1)/3}$. In each case, $\Gamma_\star$ is found to be large which implies that the breaking of the wave is arrested by surface tension and shows that the observed ripples have indeed a capillary origin.

Figure 16 and table 5 have been completed with the corresponding results from the weighted-residual model (3.3) and (3.20). The strain rate distribution has been computed from the self-similar velocity profile (3.6*b*), (3.6*c*). In both cases, the model slightly underestimates the amplitude of the capillary ripples and predicts smaller values of the maxima of the strain rate. However, the locations of the local minima and maxima predicted with the model are in remarkable agreement with the strain rate distributions found by DNS. For the 500 ppm solution (set 1, $n = 0.607$), a convincing agreement is obtained, whereas for the more concentrated 1500 ppm solution (set 2, $n = 0.4$) the model fails to locate at the free surface the maximum of the strain rate. We note that in the latter situation the long-wave approximation starts to be violated.

6. Conditional stability of shear-thinning film flows

In § 5.1, we have seen that travelling waves may be found for shear-thinning fluids even if the Nusselt flat-film solution is linearly stable. Since infinitesimal perturbations are then damped, we conclude with a conditional stability of the Nusselt solution.

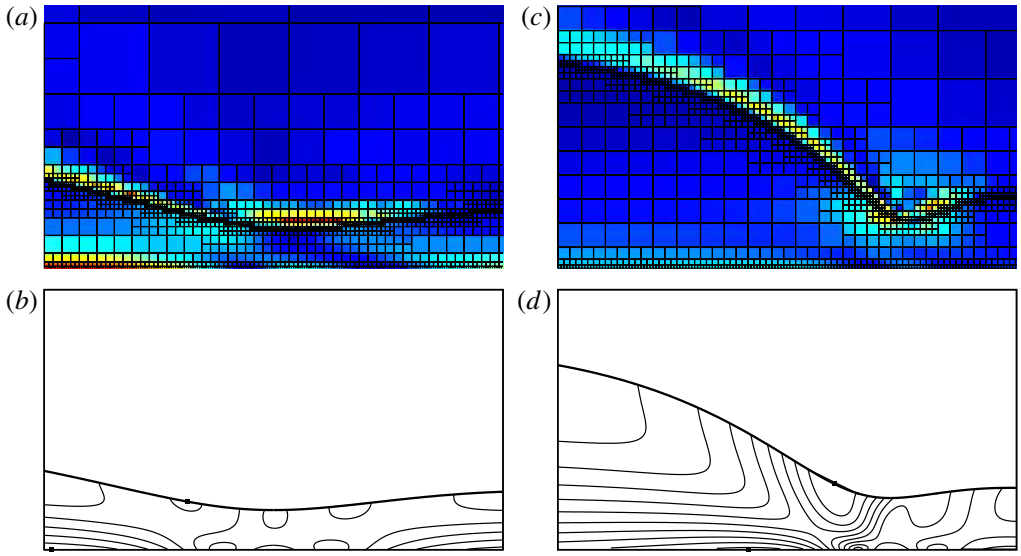

FIGURE 16. Distribution of the strain rate $\dot{\gamma}$ under the waves whose profiles are shown in figure 15(*a,c*). (*a,c*) Results from DNS. Dark blue (red) regions correspond to the minimum (maximum) of $\dot{\gamma}$. (*b,d*) Isocontours of the strain rate corresponding to the weighted-residual model (3.3) and (3.20). The location of the maxima of $\dot{\gamma}$ at the wall and at the free surface are depicted by squares.

DNSs of the temporal response of the film to an initial perturbation of the form $h(x, 0) = 1 + A\cos(kx)$ have been performed to test the conditional stability of the film. As in § 5.2, periodic boundary conditions have been implemented. Figure 17 reports the amplitude $h_{max} - h_{min}$ of the waves observed at the final stage of the simulations. DNS results are compared with the corresponding bifurcation diagrams of the travelling-wave solutions to the model (3.3) and (3.20) (the speed of these waves is already reported in figure 10*b*). At a given wavenumber, larger than the linear cut-off wavenumber k_c but smaller than a limiting values k_{sub}, we expect to find three solutions. For $k > k_{sub}$, only the Nusselt flat-film solution is found. In the range $[k_c, k_{sub}]$ the largest-amplitude travelling wave and the Nusselt flat-film solutions should be stable, whereas the smallest-amplitude travelling wave is presumed to be unstable. In most of our DNS simulations, travelling waves are found to emerge from a transient growth or decay. As expected, at small amplitude, the initial disturbance relaxes to the linearly stable flat-film solution, whereas at sufficiently large amplitude, travelling waves are found. Interestingly, the estimation of k_{sub} from DNS is in remarkable agreement with the bifurcation diagram from the weighted-residual model. We therefore conclude that the model (3.3) and (3.20) accurately captures the conditional stability of the Nusselt film solution. Some DNS simulations, indicated by double circles in figure 17, leads to temporally periodic waves whose amplitudes oscillate in time. This kind of wave is also observable in the DNSs of Newtonian falling films performed by Ramaswamy, Chippada & Joo (1996). They are observed only in few cases and within a quite narrow band of amplitudes A of the initial perturbation. We presume that these waves result from the instability of the low-amplitude travelling-wave solutions, which otherwise are not observable.

The use of periodic boundary conditions enables to limit the computational domain to the size of the waves and thus to drastically reduce the cost of DNSs. An immediate drawback is that we investigate the temporal response of the film whereas

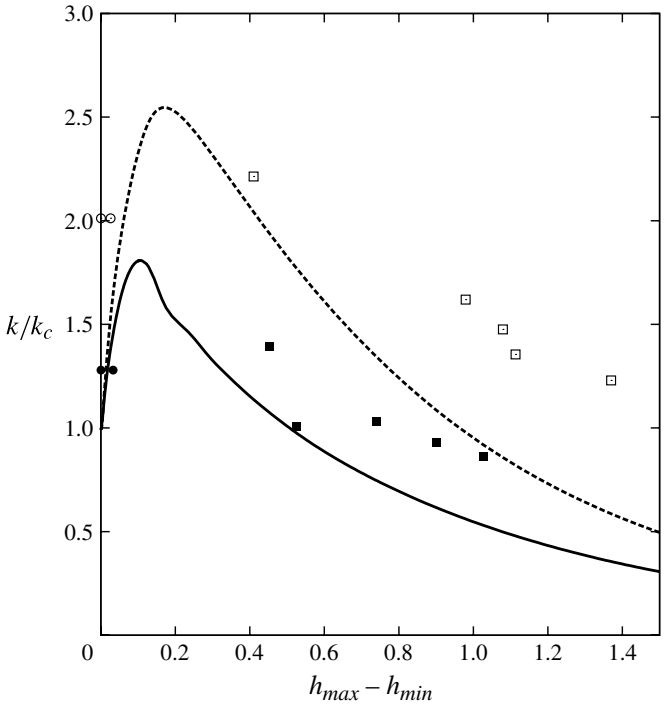

FIGURE 17. Amplitude of the waves obtained at the final stage of DNSs. Parameters correspond to shear-thinning xanthan gum, $Re = 20, \beta = 15°$. Black and white squares stand for the travelling-wave solutions for parameter sets 2 and 3, respectively. The range of amplitudes achieved for time-periodic solutions is indicated by double circles. Solid and dashed lines refer to the travelling-wave solutions to (3.3) and (3.20) for sets 2 and 3, respectively.

experimental conditions correspond to the spatial response of the film to periodic forcing at inlet. However, the weighted-residual model (3.3) and (3.20) accurately captures the conditional stability of the film and drastically reduces the cost of the simulations of extended spatial domains. We therefore investigate the spatial response of the film to a periodic excitation at frequency f within the frame of (3.3) and (3.20).

Figure 18(a) presents the amplitude $h_{max} - h_{min}$ versus the frequency f of the principal branch of travelling-wave solutions for a xanthan gum solution (parameter set 2 in table 1), $Re = 100$ and a moderate inclination angle $\beta = 15°$. The integral constraint $\langle q \rangle = \phi_0$ has been enforced in order to enable comparisons with the wavetrains emerging from the time-dependent simulations of the spatial response of the film to a periodic excitation at frequency f (Scheid *et al.* 2005).

Travelling waves emerge at the cut-off frequency f_c from the Nusselt solution ($h_{max} - h_{min} = 0$). The control parameter being f, a saddle-node bifurcation is observed at the frequency f_{sub}. Monitoring f_c and f_{sub} in the plane (f, Re) gives the stability diagram displayed in figure 18(b). Below the cut-off frequency f_c, the flat film is unconditionally unstable, whereas unconditional stability is expected above f_{sub}. Whenever f lies in the interval $[f_c, f_{sub}]$, a conditional stability is anticipated. The spatial response of the flat film to a periodic excitation at the inlet then depends on the amplitude of the perturbation.

We next simulate the response in space and time of the Nusselt flat-film solution to a periodic forcing at inlet. We have imposed a sinusoidal disturbance on the inlet flow

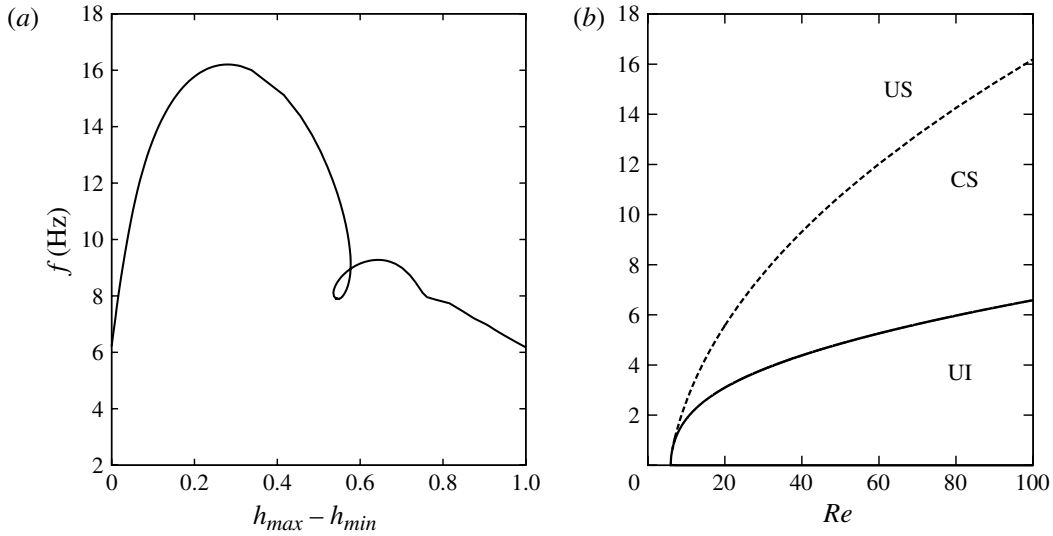

FIGURE 18. (*a*) Amplitude $h_{max} - h_{min}$ versus frequency at $Re = 100$ showing the subcritical onset of travelling waves when frequency is varied from the cut-off frequency f_c. (*b*) Stability diagram in the plane (Re, f). Solid and dashed lines refers to the marginal stability curve and to the locus of a saddle-node bifurcation f_{sub}. The unconditionally and conditionally stable regions are labelled 'US' and 'CS', respectively. The unconditional instability region is labelled 'UI'. The inclination angle is $\beta = 15°$, other parameters correspond to a shear-thinning xanthan gum solution (Set 2 in table 1). Travelling-wave solutions have been computed enforcing the integral constraint $\langle q \rangle = \phi_0$.

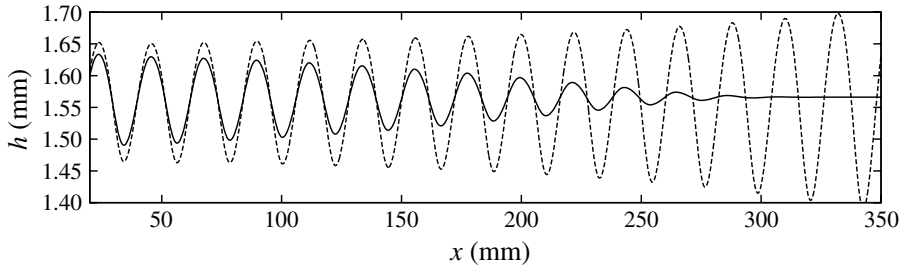

FIGURE 19. Snapshots of the free-surface elevation showing the response of the film to a forcing at inlet with two forcing amplitudes. The simulation is based on model (3.3) and (3.20). The fluid is a xanthan gum solution (set 2 in table 1 with $n = 0.4$). Here $Re = 100$, $\beta = 15°$ and the forcing frequency is $f = 14$ Hz. Solid and dashed lines refer to forcing amplitudes $A = 0.08$ and $A = 0.1$, respectively.

rate $q(0, t) = \phi_0[1 + A\cos(2\pi ft)]$. Chosen properties correspond to a 1500 ppm xanthan gum solution (parameter set 2 in table 1), $Re = 100$ and $\beta = 15°$ which corresponds to the travelling-wave branch drawn in figure 18(*a*). The chosen dimensional forcing frequency $f = 14$ Hz lies in the range [6.5, 16] bounded by f_c and f_{sub}. At low values of the forcing amplitude A, the inlet signal is attenuated as it travels downstream. After A reaches a certain threshold, inlet perturbations are amplified downstream and give way to regular trains of travelling waves whose temporal periodicity agrees with the inlet forcing frequency. Figure 19 presents snapshots of the film thickness at two amplitudes $A = 0.08$ and $A = 0.1$ chosen slightly below and above the threshold. The damping of the signal for $A = 0.08$ and its amplification for $A = 0.1$ are clearly visible.

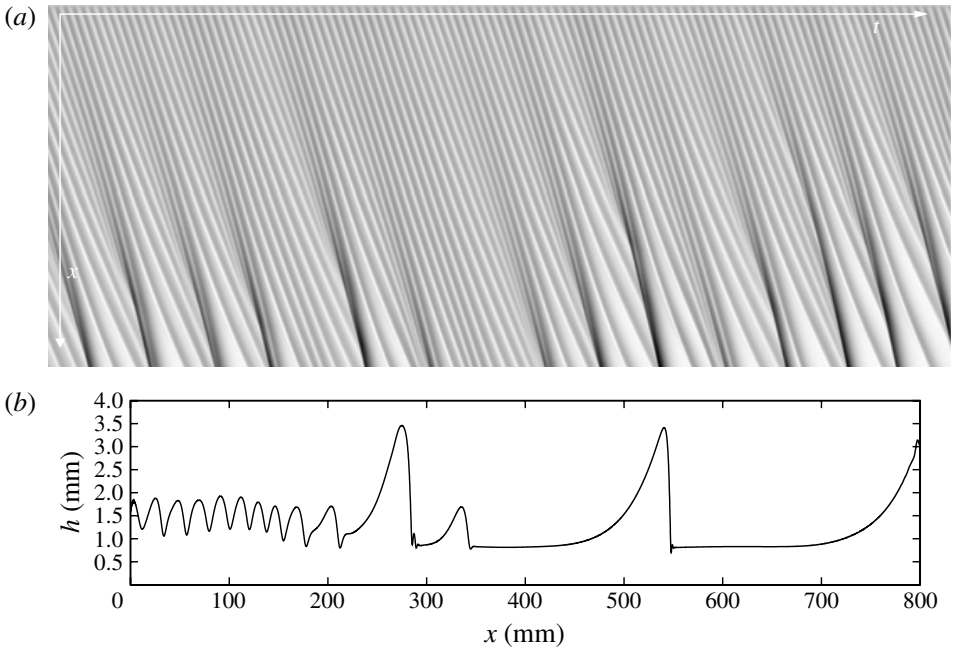

FIGURE 20. Simulation of the response of the film to a forcing at inlet with a small amount of noise. The simulation is based on model (3.3) and (3.20). The fluid is a xanthan gum solution (set 2 in table 1 with $n = 0.4$). Here $Re = 100$, $\beta = 15°$. The forcing frequency and amplitude are $f = 14$ Hz and $A = 0.4$. (*a*) Spatio-temporal diagram. Light (dark) regions correspond to small (large) elevations. Vertical and horizontal ranges are 7.5 s and 0.3 m, respectively. (*b*) Snapshot of the free-surface elevation at the end of the simulation.

We have rerun our simulations with the addition of a small amount of noise to the inlet periodic forcing. The spatio-temporal diagram displayed in figure 20(*a*) gives an illustration of the evolution of the wave pattern in time and space. The regular wavetrain that emerges at the forcing frequency close to inlet is quickly disorganized by secondary instabilities, even if the amplitude $A = 0.4$ of the forcing signal is already quite large. The primary wavetrain is disrupted by the onset of larger waves which accelerate and capture the smaller waves ahead of them. A series of coalescence events then occurs which drastically reduces the wave density. Figure 20(*b*) presents a snapshot of the film thickness at the end of the simulation showing the entire numerical domain. At the downstream end of the flow, large-amplitude solitary waves in interaction organize the disordered state of the flow. The resulting wave dynamics is qualitatively similar to the observation of noise-driven dynamics of a Newtonian falling film (Chang *et al.* 1993; Liu & Gollub 1994; Malamataris, Vlachogiannis & Bontozoglou 2002).

7. Summary and conclusions

The evolution of a power-law laminar film flow has been modelled within the frame of the lubrication approximation by means of the weighted residual approach. The derived models are made of the exact mass balance equation (3.3) and an averaged momentum equation, which form a set of two coupled evolution equations for the film thickness h and the flow rate q, or equivalently a local velocity amplitude $\bar{u}$. The

models consistently account for inertial terms up to $O(\epsilon)$ and to viscous diffusion terms up to $O(\epsilon^2)$. This choice has enabled us to limit the number of degrees of freedom to only two and to limit the complexity of the different averaged momentum equations. It is possible to extent the present analysis to account for second-order inertia terms but at the cost of an increased complexity (Ruyer-Quil & Manneville 2000; Scheid, Ruyer-Quil & Manneville 2006). We expect these terms to play an important role when three-dimensional wave dynamics are considered.

Consistency at first order of inertial terms is necessary to adequately capture the onset of the instability, whereas consistency at second order of the viscous terms enables us to accurately account for the damping of the short waves by streamwise viscous diffusion. Owing to the unphysical divergence of the effective viscosity of power-law fluids as the strain rate goes to zero, it is not possible to consistently account for the streamwise viscous diffusion. To avoid this difficulty, we introduce a bound to the effective viscosity and a Newtonian plateau at low strain rate and divide the flow into a Newtonian layer at the free surface and a non-Newtonian bulk separated by a fake interface. The relative thickness $\bar{\eta}_c$ of Newtonian layer and the local flow rate q are slaved to h and $\bar{u}$ by the implicit relations (3.8) and (3.7). Application of the weighted residual approach leads to the evolution (3.17) whose coefficients are functions of $\bar{\eta}_c$. The two-equation model (3.3) and (3.17) is thus formidable to solve. A drastic simplification is obtained in the limit $\bar{\eta}_c \to 0$ but at the cost of two different formulations (3.20) and (3.24) of the averaged momentum equation for shear-thinning fluids ($n < 1$) and shear-thickening fluids ($n > 1$), respectively. The momentum balance (3.20) accounts for the contributions of the free surface and wall regions to the viscous streamwise diffusion terms. It is consistent with the averaged momentum equation (3.23) previously derived in the Newtonian case in the limit $n \to 1$. In the case of (3.24), the averaged momentum balance (3.23) is not recovered as n goes to one. Yet, the dispersion relations corresponding to the linear stability of the Nusselt flow, and obtained from (3.24) and (3.23), coincide at $n = 1$. We note that a full agreement is not required as the limit of a vanishing Newtonian layer at the free surface is not compatible with the limit $n \to 1$.

The two-equation models (3.3), (3.20) and (3.3), (3.24) have been validated in the linear and nonlinear regimes by means of comparisons with the solutions of the primitive set of equations (2.1), (2.2) and (2.4). A remarkable agreement with the Orr–Sommerfeld stability analysis has been obtained. In particular, the instability threshold is accurately recovered. Comparisons to the DNSs of two-phase flows demonstrate that the models correctly predict the speed, amplitude and shape of large-amplitude nearly solitary waves. In particular, the details of the capillary ripples, the capillary shock region, preceding the main humps are captured correctly.

We have compared the results of our Orr–Sommerfeld analyses and DNSs with the only continuous Newtonian plateau constitutive law (2.11) and with the smooth Carreau law (2.10). Whenever the thickness of the Newtonian layer is small ($s^n \ll 1$), which is indeed the case for the fluids we have considered in our study, the two constitutive laws provide very similar results. This gives us confidence that the results of our study are not dependent on a particular regularization at low strain rate of the power law (1.1).

Our linear stability analysis shows that the threshold of the long-wave instability is weakly dependent on the relative thickness s^n of the Newtonian layer at the free

surface. The smaller the power-law index n and the thinner the Newtonian layer, the smaller the critical Froude number is. For shear-thinning fluids ($n < 1$) and low-power-law indices, the range of unstable wavenumbers is governed by the balance of inertia to streamwise viscous diffusion at the free surface, surface tension and the contribution of the bulk to viscous diffusion being negligible. Instead, in the case of shear-thickening fluids ($n > 1$), viscous diffusion at the free surface is negligible and the range of unstable wavenumbers is governed by the effective viscosity of the non-Newtonian bulk layer. The influence of shear-thinning and shear-thickening on the primary instability is shown to be nontrivial. Instead of the destabilization (stabilization) of the base flow close to threshold in the case of shear-thinning (shear-thickening) fluids, an unexpected reverse behaviour is observed further from threshold when the viscous damping of short waves becomes dominant.

Our study of nonlinear waves focuses on the one-humped large-amplitude solitary waves that are well known to organize the dynamics of a Newtonian film (Alekseenko *et al.* 1994). For shear-thickening fluids, surface tension is a weak effect as compared to viscous diffusion ($\Gamma \ll 1$) and travelling waves do not present the capillary ripples observed on shear-thinning and Newtonian films. Shear thinning accelerates solitary waves and promotes a subcritical onset of travelling waves at larger wavenumber than the linear cut-off wavenumber k_c. A conditional stability of the base flow is thus observed, the film being able to respond to a periodic forcing at the inlet at $k > k_c$ if the amplitude of the perturbations is large enough. This phenomenon results from the removal of the Newtonian layer, the reduction of the effective viscosity at the free surface and therefore the attenuation of the damping of short waves. Comparisons with DNSs show that this phenomenon is accurately captured by the weighted-residual model (3.3) and (3.20). Spatio-temporal simulations reveal that trains of short waves excited at larger frequencies than the cut-off frequency are quickly disrupted by secondary instabilities which lead to a disordered state organized around solitary waves in interaction. The spatio-temporal dynamics of this disordered state is then amenable to a coherent-structure theory in which the flow is discretized into particle-like solitary waves. Wave-to-wave interaction of solitary waves in Newtonian flows have been recently investigated by Pradas *et al.* (2011) who pointed out the role of viscous dispersion effects. An extension of the theory by Pradas *et al.* to shear-thinning film flows is currently under way.

A natural application of the present modelling effort is the study of roll waves in overland shallow flows which remain laminar and where clay suspensions present shear-thinning properties. For such flows, the onset of nonlinear waves in conditions for which the base flow is linearly stable have also been observed by Ng & Mei (1994) and Pascal & d'Alesio (2007). Yet, these studies do not correctly predict the instability threshold, a drawback which prevents quantitative comparisons with experimental data. The remarkable agreement of the solutions to the weighted-residual models with DNSs suggests that a quantitative representation of the roll wave dynamics might be achieved within the frame of shallow-water equations similar to (3.3) and (3.20).

Acknowledgements

The authors would like to thank S. Popinet and D. Chasseur for their help in performing the DNSs presented in § 5.2. We acknowledge financial support from the

Multiflow ITN Marie Curie network funded by the European Commission (GA-2008-214919). B.S. Dandapat is grateful to the University of Paris Sud for inviting him.

Appendix A. Coefficients of the Newtonian power-law model

The coefficients of the averaged momentum balance equation (3.3) are given in the following in a fraction form $\tilde{X} = \tilde{X}_a/\tilde{X}_b$:

$$\begin{aligned}\tilde{F}_a = {} & 630n((n+1)^2(7n+3)) + (n-1)\bar{\eta}_c^{2+1/n}\{105n(4n+3)[n(34n+35)+8] \\ & + 14(4n+3)\bar{\eta}_c^{1+1/n}[3(2n+1)(n(9n(n-4)-4)+6) \\ & + 10(n-1)\,(n+1)^2(3n+2)\bar{\eta}_c] \\ & + (2n+1)\bar{\eta}_c^{2+2/n}[-15(n-6)(2n+1)(3n+2)(4n-3) \\ & + 28(n-1)\,(n+1)^2(3n-7)(4n+3)\bar{\eta}_c\}],\end{aligned} \tag{A 1a}$$

$$\begin{aligned}\tilde{F}_b = {} & 42(n+1)(2n+1)(4n+3)[15(n+1) \\ & + (n-1)\bar{\eta}_c^{1+1/n}(30n+20+(2n+1)(3n-7)\bar{\eta}_c^{1+1/n})],\end{aligned} \tag{A 1b}$$

$$\begin{aligned}\tilde{G}_a = {} & 630n^3(n+1) + (n-1)\bar{\eta}_c^{2+1/n}\{105n^2(4n+3)(10n+7) + 14(4n+3)\bar{\eta}_c^{1+1/n} \\ & \times [3(2n+1)\{n[n(3n-25)+3)+6\} + 10(n-1)\,(n+1)^2(3n+2)\bar{\eta}_c] \\ & + (2n-1)\bar{\eta}_c^{2+2/n}[28\bar{\eta}_c(4n+3)(3n-7)\,(n+1)^2(n-1) \\ & - 15(4n-3)(3n+2)(2n+1)(n-6)]]\},\end{aligned} \tag{A 1c}$$

$$\tilde{G}_b = \frac{n}{n+1}\tilde{F}_b, \tag{A 1d}$$

$$\tilde{I}_a = 5(n+1)(3n+2)[3+2(n-1)\bar{\eta}_c^{2+1/n}], \tag{A 1e}$$

$$\tilde{I}_b = \frac{1}{21(2n+1)(4n+3)}\tilde{G}_b. \tag{A 1f}$$

Appendix B. Coefficients J_w, K_w, L_w and M_w

The contribution of the bulk region of the flow to the streamwise viscous diffusion terms are evaluated by assuming a constant viscosity μ_{eff}. The second-order boundary-layer equations then read (Ruyer-Quil & Manneville 2000):

$$\begin{aligned}Re(\partial_t u + u\partial_x u + v\partial_y u) = {} & \mu_{eff}[\partial_{yy}u + 2\partial_{xx}u + \partial_x(\partial_x u|_h)] \\ & + 1 - \cot\beta\,\partial_x h + We\,\partial_{xxx}h,\end{aligned} \tag{B 1a}$$

completed by the tangential stress balance at the free surface

$$\partial_y u|_h = 4\partial_x h\partial_x u|_h - \partial_x v|_h, \tag{B 1b}$$

the kinematic condition (2.2c) and the no-slip condition (2.2d) at the wall.

Considering the self-similar velocity profile (3.6b) and (3.6c) and averaging the momentum balance equation (B 1a) with the weight f_0 then leads to

$$\begin{aligned}Re\int_0^h f_0(\bar{y})(\partial_t u_s + u_s\partial_x u_s + v_s\partial_y u_s)\,\mathrm{d}y = {} & \mu_{eff}\left\{f_0(1)\,[4\partial_x h\partial_x u_s|_h - \partial_x v_s|_h]\right. \\ & \left. + \int_0^h f_0''(\bar{y})u_s + f_0(\bar{y})\,[2\partial_{xx}u_s + \partial_x(\partial_x u_s|_h)]\,\mathrm{d}y\right\}.\end{aligned} \tag{B 2}$$

We then obtain the following averaged momentum equation

$$\begin{aligned} Re\partial_t q = Re\left[-F(n)\,\frac{q}{h}\partial_x q + G(n)\,\frac{q^2}{h^2}\partial_x h\right] \\ + I(n)\left[h\,(1-\cot\beta\,\partial_x h + We\partial_{xxx}h) - \mu_{eff}\,\frac{I_w(n)}{\phi_0}\,\frac{q}{h^2}\right] \\ + \mu_{eff}\left[J_w(n)\frac{q}{h^2}\,(\partial_x h)^2 - K_w(n)\frac{\partial_x q\partial_x h}{h} - L_w(n)\frac{q}{h}\partial_{xx}h + M_w(n)\partial_{xx}q\right], \quad \text{(B 3)} \end{aligned}$$

where $I_w = (2n+1)/(n+2)$. Coefficients J_w, K_w, L_w and M_w are given in (3.21).

Appendix C. Orr–Sommerfeld analysis of Carreau-law films

In this section, we consider the primary stability of a uniform film flow when the rheological behaviour of the liquid is governed by the three-parameter Carreau law (2.3). The base flow is given by

$$1 - y = (s^2 + U'^2)^{(n-1)/2}\,U' \qquad \text{(C 1)}$$

with the no slip condition $U(0) = 0$.

Proceeding to a decomposition in normal modes of infinitesimal perturbations around the base state leads to the Orr–Sommerfeld equation

$$\begin{aligned} \mathrm{i}kRe[(U-c)(D^2-k^2)\psi - \psi U''] = (D^2+k^2)[(s^2+U'^2)^{(n-3)/2}(s^2+nU'^2)(D^2+k^2)\psi] \\ - k^2 D[(s^2+U'^2)^{(n-1)/2}\,D\psi], \qquad \text{(C 2)} \end{aligned}$$

where k and c refer again to the wavenumber and phase speed, respectively. The boundary conditions associated with (C 2) are (4.4*c*), (4.4*d*) and (4.4*e*). Rousset *et al.* (2007) and Usha *et al.* (2011) have considered the stability of a shear-thinning falling film using a four-parameter Carreau law accounting for Newtonian plateaus at high and low shear rates. The system (C 2), (4.4*c*), (4.4*d*) and (4.4*e*) corresponds to the Orr–Sommerfeld system of equations derived by Usha *et al.* (2011) when the influence of the Newtonian plateau at high shear rate is neglected, that is when the parameter I is set to zero in their formulation.

REFERENCES

ALEKSEENKO, S. V., NAKORYAKOV, V. E. & POKUSAEV, B. G. 1994 *Wave Flow in Liquid Films*, 3rd edn. Begell House.

AMAOUCHE, M., DJEMA, A. & BOURDACHE, L. 2009 A modified Shkadov's model for thin film flow of a power law fluid over an inclined surface. *C. R. Mécanique* **337** (1), 48–52.

BALMFORTH, N. J. & LIU, J. J. 2004 Roll waves in mud. *J. Fluid Mech.* **519**, 33–54.

BEWERSDORFF, H.-W. & SINGH, R. P. 1988 Rheological and drag reduction characteristics of xanthan gum solutions. *Rheol. Acta* **27**, 617–627.

BREVDO, L., LAURE, P., DIAS, F. & BRIDGES, T. J. 1999 Linear pulse structure and signaling in a film flow on an inclined plane. *J. Fluid Mech.* **396**, 37–71.

CHANG, H.-C. & DEMEKHIN, E. A. 2000 Coherent structures, self similarity, and universal roll-wave coarsening dynamics. *Phys. Fluids* **12** (9), 2268–2278.

CHANG, H.-C. & DEMEKHIN, E. A. 2002 *Complex Wave Dynamics on Thin Films*. Elsevier.

CHANG, H.-C., DEMEKHIN, E. A., KALAIDIN, E. & YE, Y. 1996 Coarsening dynamics of falling-film solitary waves. *Phys. Rev.* E **54**, 1467–1477.

CHANG, H.-C., DEMEKHIN, E. A. & KOPELEVITCH, D. I. 1993 Nonlinear evolution of waves on a vertically falling film. *J. Fluid Mech.* **250**, 433–480.

CHOPPE, E., PUAUD, F., NICOLAI, T. & BENYAHIA, L. 2010 Rheology of xanthan solutions as a function of temperature, concentration and ionic strength. *Carbohydrate Polymers* **82**, 1228–1235.

DANDAPAT, B. S. & MUKHOPADHYAY, A. 2001 Waves on a film of power-law fluid flowing down an inclined plane at moderate Reynolds number. *Fluid Dyn. Res.* **29**, 199–220.

DANDAPAT, B. S. & MUKHOPADHYAY, A. 2003 Waves on the surface of a falling power-law fuid. *Intl J. Non-Linear Mech.* **38**, 21–38.

DIETZE, G. F., AL-SIBAI, F. & KNEER, R. 2009 Experimental study of flow separation in laminar falling liquid films. *J. Fluid Mech.* **637**, 73–104.

DIETZE, G. F., LEEFKEN, A. & KNEER, R. 2008 Investigation of the backflow phenomenon in falling liquid films. *J. Fluid Mech.* **595**, 435–459.

DOEDEL, E. J. 2008 AUTO07P*: Continuation and Bifurcation Software for Ordinary Differential Equations*. Montreal Concordia University.

DRESSLER, R. F. 1949 Mathematical solution of the problem of roll-waves in inclined open channels. *Commun. Pure Appl. Maths* **2**, 149–194.

FERNÁNDEZ-NIETO, E. D., NOBLE, P. & VILA, J.-P. 2010 Shallow water equations for non-Newtonian fluids. *J. Non-Newtonian Fluid Mech.* **165** (13–14), 712–732.

FONDER, N. & XANTHOULIS, S. 2007 Roman aqueduct and hydraulic engineering: case of Nîmes aqueduct and its Pont du Gard bridge. *Water Sci. Technol. Water Supply* **7**, 121–129.

GRISKEY, R. G., NECHREBECKI, D. G., NOTHEIS, P. J. & BALMER, R. T. 1985 Rheological and pipeline flow behaviour of corn starch dispersion. *J. Rheol.* **29**, 349–360.

HWANG, C.-C., CHEN, J.-L., WANG, J.-S. & LIN, J.-S. 1994 Linear stability of power law liquid film flows down an inclined plane. *J. Phys. D: Appl. Phys.* **27**, 2297–2301.

JULIEN, P. Y. & HARTLEY, D. M. 1986 Formation of roll waves in laminar sheet flow. *J. Hydraul. Res.* **24**, 5–17.

KALLIADASIS, S., RUYER-QUIL, C., SCHEID, B. & VELARDE, M. G. 2011 Falling liquid films. In *Applied Mathematical Sciences*, 1st edn. 176. Springer.

KAPITZA, P. L. & KAPITZA, S. P. 1949 Wave flow of thin layers of a viscous fluid: III. experimental study of undulatory flow conditions. In *Collected papers of P. L. Kapitza (1965)* (ed. D. T. Haar), pp. 690–709. Pergamon, (Original paper in Russian: Zh. Ekper. Teor. Fiz. **19**, 105–120).

KAWAHARA, T. 1983 Formation of saturated solitons in a nonlinear dispersive system with instability and dissipation. *Phys. Rev. Lett.* **51**, 381–383.

KAWAHARA, T. & TOH, S. 1988 Pulse interactions in an unstable dissipative-dispersive nonlinear system. *Phys. Fluids* **31**, 2103–2111.

LINDNER, A., BONN, D. & MEUNIER, J. 2000 Viscous fingering in a shear-thinning fluid. *Phys. Fluids* **12**, 256–261.

LIU, J. & GOLLUB, J. P. 1994 Solitary wave dynamics of film flows. *Phys. Fluids* **6**, 1702–1712.

LIU, K. & MEI, C. C. 1994 Roll waves on a layer of a muddy fluid flowing down a gentle slope—a Bingham model. *Phys. Fluids* **6** (8), 2577–2589.

LIU, Q. Q., CHEN, L., LI, J. C. & SINGH, V. P. 2005 Roll waves in overland flow. *J. Hydrol. Engng* **10** (2), 110–117.

MALAMATARIS, N. A., VLACHOGIANNIS, M. & BONTOZOGLOU, V. 2002 Solitary waves on inclined films: flow structure and binary interactions. *Phys. Fluids* **14**, 1082–1094.

MANNEVILLE, P. 1990 *Dissipative Structures and Weak Turbulence*. Academic Press.

MILADINOVA, S., LEBONB, G. & TOSHEV, E. 2004 Thin-film flow of a power-law liquid falling down an inclined plate. *J. Non-Newtonian Fluid Mech.* **122**, 69–78.

MILLET, S., BOTTON, V., ROUSSET, F. & HADID, H. B. 2008 Wave celerity on a shear-thinning fluid film flowing down an incline. *Phys. Fluids* **20**, 031701.

NG, C.-O. & MEI, C. C. 1994 Roll waves on a shallow layer of mud modelled as a power-law fluid. *J. Fluid Mech.* **263**, 151–184.

PASCAL, J. P. & D'ALESIO, S. J. D. 2007 Instability of power-law fluid flows down an incline subjected to wind stress. *Appl. Math. Model.* **31**, 1229–1248.

POPINET, S. 2003 Gerris: a tree-based adaptive solver for the incompressible Euler equations in complex geometries. *J. Comput. Phys.* **190**, 572–600.

POPINET, S. 2009 An accurate adaptive solver for surface-tension-driven interfacial flows. *J. Comput. Phys.* **228**, 5838–5866.

PRADAS, M., TSELUIKO, D. & KALLIADASIS, S. 2011 Rigorous coherent-structure theory for falling liquid films: viscous dispersion effects on bound-state formation and self-organization. *Phys. Fluids* **23**, 044104.

RAMASWAMY, B., CHIPPADA, S. & JOO, S. W. 1996 A full-scale numerical study of interfacial instabilities in thin-film flows. *J. Fluid Mech.* **325**, 163–194.

ROUSSET, F., MILLET, S., BOTTON, V. & HADID, H. B. 2007 Temporal stability of Carreau fluid flow down an incline. *Trans. ASME: J. Fluids Engng* **129** (7), 913–920.

RUYER-QUIL, C. & MANNEVILLE, P. 2000 Improved modelling of flows down inclined planes. *Eur. Phys. J.* B **15**, 357–369.

RUYER-QUIL, C., TREVELEYAN, P., GIORGIUTTI-DAUPHINÉ, F., DUPRAT, C. & KALLIADASIS, S. 2008 Modelling film flows down a fibre. *J. Fluid Mech.* **603**, 431–462.

SCHEID, B., RUYER-QUIL, C. & MANNEVILLE, P. 2006 Wave patterns in film flows: modelling and three-dimensional waves. *J. Fluid Mech.* **562**, 183–222.

SCHEID, B., RUYER-QUIL, C., THIELE, U., KABOV, O. A., LEGROS, J. C. & COLINET, P. 2005 Validity domain of the Benney equation including the Marangoni effect for closed and open flows. *J. Fluid Mech.* **527**, 303–335.

SEEVARATNAM, G. K., SUO, Y., RAMÉ, E., WALKER, L. M. & GAROFF, S. 2007 Dynamic wetting of shear thinning fluids. *Phys. Fluids* **19**, 012103.

SISOEV, G. M., DANDAPAT, B. S., MATVEYEV, K. S. & MUKHOPADHYAY, A. 2007 Bifurcation analysis of the travelling waves on a falling power-law fluid film. *J. Non-Newtonian Fluid Mech.* **141**, 128–137.

SMITH, M. K. 1990 The mechanism for the long-wave instability in thin liquid films. *J. Fluid Mech.* **217**, 469–485.

USHA, R., MILLET, S., BENHADID, H. & ROUSSET, F. 2011 Shear-thinning film on a porous substrate: stability analysis of a one-sided model. *Chem. Engng Sci.* **66** (22), 5614–5627.

VLACHOGIANNIS, M. & BONTOZOGLOU, V. 2001 Observations of solitary wave dynamics of film flows. *J. Fluid Mech.* **435**, 191.

WHITHAM, G. B. 1974 *Linear and Nonlinear Waves*. Wiley-Interscience.

Bibliography

K. Alba, P. Laure, and R. E. Khayat. Transient two-layer thin-film flow inside a channel. *Phys. Rev. E*, 84:026320, Aug 2011. doi: 10.1103/PhysRevE.84.026320. URL `http://link.aps.org/doi/10.1103/PhysRevE.84.026320`. (Cited at page 18.)

S. V. Alekseenko, V. Y. Nakoryakov, and B. G. Pokusaev. Wave formation on a vertical falling liquid film. *AIChE J.*, 31:1446–1460, 1985. (Cited at page 19.)

S. V. Alekseenko, V. E. Nakoryakov, and B. G. Pokusaev. *Wave flow in liquid films*. Begell House (New York), third edition, 1994. (Cited at page 19.)

S. V. Alekseenko, V. A. Antipin, V. V. Guzanov, S. M. Kharlamov, and D. M. Markovitch. Three-dimensional solitary waves on falling liquid films at low reynolds number. *Phys. Fluids*, 121704:17, 2005. (Cited at page 19.)

M. Amaouche, N. Mehidi, and N. Amataousse. An accurate modeling of thin film flows down an incline for inertia dominated regimes. *Eur. J. Mech. B/Fluids*, 24:49–70, 2004. (Cited at page 18.)

M. Amaouche, A. Djema, and H. Ait Abderrahmane. Film flow for power-law fluids: Modeling and linear stability. *Eur. J. Mech. B/Fluids*, 34(0): 70–84, 2012. (Cited at page 18.)

Mustapha Amaouche, Amar Djema, and L. Bourdache. A modified Shkadov's model for thin film flow of a power law fluid over an inclined surface. *Comptes Rendus Mecanique*, 337(1):48–52, 2009. (Cited at pages 18, 30, and 209.)

N. J. Balmforth and J. J. Liu. Roll waves in mud. *J. Fluid Mech.*, 519:33–54, 2004. (Cited at page 215.)

J. Bear. *Dynamics of fluids in porous media*. Dover, New York, 1988. (Cited at page 199.)

G. S. Beavers and D. D. Joseph. Boundary conditions at a naturally permeable wall. *J. Fluid Mech.*, 30:197–207, 1967. (Cited at page 198.)

C. Beckermann, S. Ramadhyani, and R. Viskanta. Natural convection in vertical enclosures containing simultaneously fluid and porous layers. *J. Fluid Mech.*, 186:257–284, 1988. (Cited at pages 199 and 202.)

T. B. Benjamin. Shearing flow over a wavy boundary. *J. Fluid Mech.*, 6: 161–205, 1959. (Cited at page 219.)

T. B. Benjamin. The development of three-dimensional disturbances in an unstable film of liquid flowing down an inclined plane. *J. Fluid Mech.*, 10:401–419, 1961. (Cited at pages 19 and 25.)

D. J. Benney. Long waves on liquid films. *J. Math. and Phys.*, 45:150–155, 1966. (Cited at page 26.)

A. L. Bertozzi and M. Pugh. Long-wave instabilities and saturation in thin film equations. *Comm. Pure Appl. Math.*, 51:625–661, 1998. (Cited at page 27.)

F. Boulogne, L. Pauchard, and F. Giorgiutti-Dauphiné. Instability and morphology of polymer solutions coating a fibre. *J. Fluid Mech.*, 704:231–250, 2012. (Cited at page 163.)

P. Bousquet-Melou, B. Goyeau, M. Quintard, F. Fichot, and D. Gobin. Average momentum equation for interdendritic flow in a solidifying columnar mushy zone. *Int. J. Heat Mass Transfer*, 45:3651–3665, 2002. (Cited at page 202.)

M. Boutounet. *Modèles asymptotiques pour la dynamique d'un film liquide mince*. PhD thesis, Insitut Supérieur de l'Aéronautique et de l'Espace (ISAE), 2011. (Cited at page 35.)

M. Boutounet, L. Chupin, P. Noble, and J.-P. Vila. Shallow water equations for Newtonian fluids over arbitrary topographies. *Comm. Math. Sci.*, 6: 29–55, 2008. (Cited at pages 35 and 217.)

L. Brevdo, P. Laure, F. Dias, and T. J. Bridges. Linear pulse structure and signaling in a film flow on an inclined plane. *J. Fluid Mech.*, 396:37–71, 1999. (Cited at pages 22, 139, and 150.)

Richard R. Brock. Periodic permanent roll waves. *J. Hydr. Engng.*, 96(12): 2565–2580, 1970. (Cited at page 35.)

J. Carr. *Applications of centre manifold theory*. Springer-Verlag (New York), 1981. (Cited at pages 11 and 31.)

S. Chakraborty. *Dynamics and stability of a non-Newtonian falling film*. PhD thesis, Univerité Pierre et Marie Curie, Paris, France, 2012. (Cited at pages 209 and 215.)

H.-C. Chang. Traveling waves on fluid interfaces: Normal form analysis of the Kuramoto-Sivashinsky equation. *Phys. Fluids*, 29:3142–3147, 1986. (Cited at pages 43 and 160.)

H.-C. Chang. Wave evolution on a falling film. *Ann. Rev. Fluid Mech.*, 26: 103–136, 1994. (Cited at page 25.)

H.-C. Chang and E. A. Demekhin. Mechanism for drop formation on a coated vertical fibre. *J. Fluid Mech.*, 380:233–255, 1999. (Cited at page 27.)

H.-C. Chang and E. A. Demekhin. Coherent structures, self similarity, and universal roll-wave coarsening dynamics. *Phys. Fluids*, 12(9):2268–2278, 2000. (Cited at page 35.)

H.-C. Chang and E. A. Demekhin. *Complex Wave Dynamics on Thin Films*. D. Möbius and R. Miller, Elsevier, 2002. (Cited at pages 19, 44, and 162.)

H.-C. Chang, E. A. Demekhin, and D. I. Kopelevitch. Nonlinear evolution of waves on a vertically falling film. *J. Fluid Mech.*, 250:433–480, 1993a. (Cited at page 20.)

H.-C. Chang, E. A. Demekhin, and D. I. Kopelevitch. Laminarizing effects of dispersion in an active-dissipative nonlinear medium. *Physica D*, 63: 299–320, 1993b. (Cited at page 43.)

H.-C. Chang, M. Cheng, E. A. Demekhin, and D. I. Kopelevitch. Secondary and tertiary excitation of three-dimensional patterns on a falling film. *J. Fluid Mech.*, 270:251–275, 1994. (Cited at pages 19, 20, 34, 43, and 105.)

H.-C. Chang, E. A. Demekhin, and E. Kalaidin. Generation and suppression of radiation by solitary pulses. *SIAM J. Appl. Math.*, 58(4):1246–1277, 1998. (Cited at pages 43 and 162.)

D. Chasseur. *Écoulement de films liquides sur un plan incliné : analyse des phénomènes et optimisation d'un outil de calcul*. PhD thesis, Conservatoire National des Arts et Métiers, Paris, 2011. (Cited at page 37.)

J.-M. Chomaz. Global instabilities in spatially developping flows: Non-normality and nonlinearity. *Ann. Rev. Fluid Mech.*, 37:357–392, 2005. (Cited at page 151.)

P. Colinet, J. C. Legros, and M. G. Velarde. *Nonlinear Dynamics of Surface-Tension-Driven Instabilities*. Wiley-VCH (New York), 2001. (Cited at pages 99 and 218.)

R. V. Craster and O. K. Matar. On viscous beads flowing down a vertical fibre. *J. Fluid Mech.*, 553:85–105, 2006. (Cited at pages 145 and 158.)

R. V. Craster and O. K. Matar. Dynamics and stability of thin liquid films. *Rev. Mod. Phys.*, 81:1131–1198, 2009. (Cited at page 19.)

S. J. D. D'Alesio, J. P. Pascal, H. A. Jasmine, and K. A. Ogden. Film flow over heated wavy inclined surfaces. *J. Fluid Mech.*, 665:418–456, 2010. (Cited at page 18.)

B. S. Dandapat and A. Mukhopadhyay. Waves on a film of power-law fluid flowing down an inclined plane at moderate Reynolds number. *Fluid Dyn. Res.*, 29:199–220, 2001. (Cited at page 209.)

B. S. Dandapat and A. Mukhopadhyay. Waves on the surface of a falling power-law fuid. *Int. J. Non-Linear Mech.*, 38:21–38, 2003. (Cited at page 209.)

Henri Darcy. *Les fontaines publiques de la ville de Dijon*. Victor Dalmont, 1856. (Cited at page 7.)

Deendarlianto, A. Ousaka, Indarto, A. Kariyasaki, D. Lucas, K. Vierow, C. Vallee, and K. Hogan. The effects of surface tension on flooding in counter-current two-phase flow in an inclined tube. *Exp. Therm.*

Fluid Sci., 34(7):813 – 826, 2010. ISSN 0894-1777. doi: 10.1016/j.expthermflusci.2010.01.010. URL http://www.sciencedirect.com/science/article/pii/S0894177710000208. (Cited at page 219.)

E. A. Demekhin, E. N. Kalaidin, S. Kalliadasis, and S. Yu. Vlaskin. Three-dimensional localized coherent structures of surface turbulence: I. Scenarios of two-dimensional three-dimensional transitions. *Phys. Fluids*, 19:114103, 2007a. (Cited at pages 24, 34, and 44.)

E. A. Demekhin, E. N. Kalaidin, S. Kalliadasis, and S. Yu. Vlaskin. Three-dimensional localized coherent structures of surface turbulence: II. Λ solitons. *Phys. Fluids*, 19:114104, 2007b. (Cited at pages 24, 34, and 44.)

J. D. Dent and T. E. Lang. A biviscous modified Bingham model of snow avalanche motion. *Ann. Glaciology*, 4:42–46, 1983. (Cited at page 217.)

G. F. Dietze and C. Ruyer-Quil. Wavy liquid films interacting with a confined laminar gas flow. submitted to J. Fluid Mech., 2012. (Cited at page 197.)

G. F. Dietze, A. Leefken, and R. Kneer. Investigation of the backflow phenomenon in falling liquid films. *J. Fluid Mech.*, 595:435–459, 2008. (Cited at pages 40 and 42.)

G. F. Dietze, F. AL-Sibai, and R. Kneer. Experimental study of flow separation in laminar falling liquid films. *J. Fluid Mech.*, 637:73–104, 2009. (Cited at pages 40 and 42.)

E. J. Doedel. AUTO07P continuation and bifurcation software for ordinary differential equations. *Montreal Concordia University*, 2008. (Cited at page 14.)

R. F. Dressler. Mathematical solution of the problem of roll-waves in inclined open channels. *Comm. Pure Appl. Math.*, 2:149–194, 1949. (Cited at page 35.)

C. Duprat, C. Ruyer-Quil, S. Kalliadasis, and F. Giorgiutti-Dauphiné. Absolute and convective instabilities of a film flowing down a vertical fiber. *Phys. Rev. Lett.*, 98:244502, 2007. (Cited at pages 139, 142, 143, 151, 156, and 158.)

C. Duprat, F. Giorgiutti-Dauphiné, D. Tseluiko, S. Saprykin, and S. Kalliadasis. Liquid film coating a fiber as a model system for the formation of bound states in active dispersive-dissipative nonlinear media. *Phys. Rev. Lett.*, 103:234501, 2009a. (Cited at pages 150, 156, 158, 160, and 162.)

C. Duprat, C. Ruyer-Quil, and F. Giorgiutti-Dauphiné. Spatial evolution of a film flowing down a fiber. *Phys. Fluids*, 21:042109, 2009b. (Cited at pages 139 and 158.)

C. Elphick, E. Meron, and A. Spiegel. Spatiotemporal complexity in travelling patterns. *Phys. Rev. Lett.*, 61:496–499, 1988. (Cited at page 162.)

H. Émery and O. Brosse. *Écoulement d'un film le long d'un plan incliné: développement spatio-temporel des instabilités*. PhD thesis, École Polytechnique, rapport d'option X92, 1995. (Cited at page 45.)

E. D. Fernández-Nieto, P. Noble, and J.-P. Vila. Shallow water equations for Non-Newtonian fluids. *J. Non-Newtonian Fluid Mech.*, 165(13-14): 712 – 732, 2010. ISSN 0377-0257. doi: DOI:10.1016/j.jnnfm.2010.03.008. URL http://www.sciencedirect.com/science/article/B6TGV-4YT6D47-1/2/edfa1032c3593ae3880254702510bd37. (Cited at pages 35 and 209.)

B. A. Finlayson. *The Method of Weighted Residuals and Variational Principles, with Application in Fluid mechanics, Heat and Mass Transfer*. Academic Press, 1972. (Cited at page 9.)

A. L. Frenkel. Nonlinear theory of strongly undulating thin films flowing down vertical cylinders. *Europhys. Lett.*, 18:583–588, 1992. (Cited at pages 27 and 145.)

D. P. Frisk and E. J. Davis. The enhancement of heat transfer by waves in stratified gas-liquid flow. *Int. J. Heat Mass Transfer*, 15:1537–1552, 1972. (Cited at pages 114 and 218.)

B. Gjevik. Occurrence of finite-amplitude surface waves on falling liquid films. *Phys. Fluids*, 13:1918–1925, 1970. (Cited at page 26.)

B. Gjevik. Spatially varying finite-amplitude wave trains on falling liquid films. *Acta Polytech. Scand. Me.*, 61:1–16, 1971. (Cited at page 26.)

P. Gondret and M. Rabaud. Shear instability of two-fluid parallel flow in a Hele-Shaw cell. *Phys. Fluids*, 9(11):3267–3274, 1997. (Cited at pages 5 and 7.)

P. Gondret, P. Ern, L. Meignin, and M. Rabaud. Experimental evidence of a nonlinear transition from convective to absolute instability. *Phys. Rev. Lett.*, 82:1442–1445, Feb 1999. doi: 10.1103/PhysRevLett.82.1442. URL http://link.aps.org/doi/10.1103/PhysRevLett.82.1442. (Cited at page 6.)

S. L. Goren and P. V. S. Mani. Mass transfer through horizontal liquid films in wavy motion. *AIChE J.*, 14:57–61, 1968. (Cited at pages 114 and 218.)

B. Gottlieb and S. A. Orszag. Numerical analysis of spectral methods: Theory and applications. *SIAM J. Ind. and Appl. Math., Philadelphia*, 1977. (Cited at page 104.)

D. A. Goussis and R. E. Kelly. Surface wave and thermocapillary instabilities in a liquid film flow. *J. Fluid Mech.*, 223:25, 1991. corrigendum in J. Fluid Mech.226:663. (Cited at page 99.)

A. Govan, G. Hewitt, H. Richter, and A. Scott. Flooding and churn flow in vertical pipes. *Int. J. Multiphase Flow*, 17:27–44, 1991. (Cited at page 219.)

B. Goyeau, D. Lhuillier, D. Gobin, and M. G. Velarde. Momentum transport at a fluid-porous interface. *Int. J. Heat Mass Transfer*, 46:4071–4081, 2003. (Cited at page 199.)

J. Gruenig and M. Kraume. Annular liquid films on a vertical wire with counter current gas flow - eperimental investigations. *Chem. Eng. Trans.*, 17:621–626, 2009. (Cited at pages 154 and 163.)

J. Gruenig, E. Lyagin, S. Horn, T. Skale, and M. Kraume. Mass transfer characteristics of liquid films flowing down a vertical wire in a counter current gas flow. *Chem. Eng. Sci.*, 69:329–339, 2012. (Cited at page 163.)

J. Guckenheimer and P. Holmes. *Nonlinear oscillations, dynamical systems and bifurcations of vector fields*. Springer-Verlag (New York), 1983. (Cited at pages 11 and 31.)

E. Guyon, J.-P. Hulin, L. Petit, and C.D. Mitescu. *Physical Hydrodynamics*. Oxford University Press, New York, first edition, 2001. (Cited at page 206.)

T. Haecker and H. Uecker. An integral boundary layer equation for film flow over inclined wavy bottoms. *Phys. Fluids*, 21:092105, 2009. (Cited at page 18.)

K. Hattori, M. Ishikawa, and Y. H. Mori. Strings of liquid beads for gas-liquid contact operations. *AIChE J.*, 40:1983–1992, 1994. (Cited at page 163.)

S. C. Hirata, B. Goyeau, and D. Gobin. Stability of thermosolutal natural convection in superposed fluid and porous layers. *Transport in Porous Media*, 78:525–536, 2009. (Cited at page 202.)

P. Huerre and P. Monkewitz. Local and global instabilities in spatially developing flows. *Ann. Rev. Fluid Mech.*, 22:473–537, 1990. (Cited at pages 146 and 148.)

P. Huerre and M. Rossi. Hydrodynamic instabilities in open flows. In C. Godrèche and P. Manneville, editors, *Hydrodynamic and Nonlinear Instabilities*, pages 81–294. Cambridge University Press, 1998. Especially §8,9. (Cited at page 146.)

Chi-Chuan Hwang, Jun-Liang Chen, Jaw-Shi Wang, and Jenn-Sen Lin. Linear stability of power law liquid film flows down an inclined plane. *J. Phys. D: Appl. Phys.*, 27:2297–2301, 1994. (Cited at page 209.)

J. H. Jeong and H. C. No. Classification of flooding data according to type of tube-end geometry. *Nuclear Eng. Design*, 148:109–117, 1994. (Cited at page 219.)

J. H. Jeong and H. C. No. Experimental study of the effect of pipe length and pipe-end geometry on flooding. *Int. J. Multiphase Flow*, 22:499–514, 1996. (Cited at page 218.)

S. W. Joo, S. H. Davis, and S. G. Bankoff. Long-wave instabilities of heated falling films: two-dimensional theory of uniform layers. *J. Fluid Mech.*, 230:117–146, 1991. (Cited at page 99.)

D. D. Joseph, R. Bai, K. P. Chen, and Y. Y. Renardy. Core-annular flows. *Ann. Rev. Fluid Mech.*, 29:65–90, 1997. (Cited at page 221.)

S. Kalliadasis and H.-C. Chang. Drop formation during coating of vertical fibres. *J. Fluid Mech.*, 261:135–168, 1994. (Cited at pages 27, 145, 149, and 159.)

S. Kalliadasis, E. A. Demekhin, C. Ruyer-Quil, and M. G. Velarde. Thermocapillary instability and wave formation on a film flowing down a uniformly heated plane. *J. Fluid Mech.*, 492:303–338, 2003a. (Cited at pages 104 and 107.)

S. Kalliadasis, A. Kiyashko, and E. A. Demekhin. Marangoni instability of a thin liquid film heated from below by a local heat source. *J. Fluid Mech.*, 475:377–408, 2003b. (Cited at page 102.)

S. Kalliadasis, C. Ruyer-Quil, B. Scheid, and M. G. Velarde. *Falling liquid films*, volume 176 of *Applied Mathematical Sciences*. Springer, first edition, 2012. (Cited at pages 3, 17, 19, 20, 25, 44, 45, 101, 102, 108, 109, 110, 112, 113, and 114.)

P. L. Kapitza. Wave flow of thin layers of a viscous fluid: I. free flow - II. fluid flow in the presence of continuous gas flow and heat transfer. In D. Ter Haar, editor, *Collected papers of P. L. Kapitza (1965)*, pages 662–689. Pergamon (Oxford), 1948. (Original paper in Russian: Zh. Eksp. Teor. Fiz. **18**, I. 3–18, II. 19–28). (Cited at pages 19 and 34.)

P. L. Kapitza and S. P. Kapitza. Wave flow of thin layers of a viscous fluid: III. experimental study of undulatory flow conditions. In D. Ter Haar, editor, *Collected papers of P. L. Kapitza (1965)*, pages 690–709. Pergamon (Oxford), 1949. (Original paper in Russian: Zh. Eksp. Teor. Fiz. **19**, 105–120). (Cited at pages 19, 21, and 40.)

T. Kawahara. Formation of saturated solitons in a nonlinear dispersive system with instability and dissipation. *Phys. Rev. Lett.*, 51:381–383, 1983. (Cited at pages 43, 44, 162, and 209.)

T. Kawahara and S. Toh. Pulse interactions in an unstable dissipative-dispersive nonlinear system. *Phys. Fluids*, 31:2103–2111, 1988. (Cited at pages 43, 44, 162, and 209.)

M.A. Kern, F. Tiefenbacher, and J.N. McElwaine. The rheology of snow in large chute flows. *Cold. Reg. Sci. Technol.*, 39:181–192, 2004. (Cited at page 217.)

I. L. Kliakhandler, S. H. Davis, and S. G. Bankoff. Viscous beads on vertical fibre. *J. Fluid Mech.*, 429:381–390, 2001. (Cited at pages 139, 140, 142, 144, 151, 156, 157, and 158.)

S. Krishnamoorthy and B. Ramaswamy. Spontaneous rupture of thin liquid films due to thermocapillarity: A full-scale direct numerical simulation. *Phys. Fluids*, 7:2291, 1995. (Cited at page 107.)

D. Laigle and P. Coussot. Numerical modeling of mudflows. *J. Hydraul. Eng.*, 123:617–623, 1997. (Cited at page 217.)

S. P. Lin. Finite amplitude side-band stability of a viscous fluid. *J. Fluid Mech.*, 63:417–429, 1974. (Cited at page 26.)

T.-S. Lin and L. Kondic. Thin film flowing down inverted substrates: two dimensional flow. *Phys. Fluids*, 22:052105, 2010. (Cited at pages 145 and 149.)

J. Liu and J. P. Gollub. Onset of spatially chaotic waves on flowing films. *Phys. Rev. Lett.*, 70:2289–2292, 1993. (Cited at page 19.)

J. Liu and J. P. Gollub. Solitary wave dynamics of film flows. *Phys. Fluids*, 6:1702–1712, 1994. (Cited at pages 19, 40, 207, 208, and 219.)

J. Liu, J. D. Paul, and J. P. Gollub. Measurements of the primary instabilities of film flows. *J. Fluid Mech.*, 250:69–101, 1993. (Cited at page 19.)

J. Liu, J. B. Schneider, and J. P. Gollub. Three-dimensional instabilities of film flows. *Phys. Fluids*, 7:55–67, 1995. (Cited at pages 19, 20, 24, and 201.)

Q. Q. Liu, L. Chen, J. C. Li, and V. P. Singh. Roll waves in overland flow. *J. Hydrologic Engng.*, 10(2):110–117, 2005. (Cited at page 35.)

P. Luchini and F. Charru. Consistent section-averaged equations of quasi-one-dimensional laminar flow. *J. Fluid Mech.*, 656:337–341, 2010a. (Cited at pages 30 and 35.)

P. Luchini and F. Charru. The phase lead of shear stress in shallowwater flow overa perturbed bottom. *J. Fluid Mech.*, 665:516–539, 2010b. (Cited at page 30.)

N. A. Malamataris and V. Balakotaiah. Flow structure underneath the large amplitude waves of a vertically falling film. *AIChE J.*, 54(7):1725–1740, 2008. (Cited at page 40.)

N. A. Malamataris, M. Vlachogiannis, and V. Bontozoglou. Solitary waves on inclined films: Flow structure and binary interactions. *Phys. Fluids*, 14(3):1082–1094, 2002. (Cited at page 40.)

P. Manneville. *Dissipative Structures and Weak Turbulence*. Academic Press, New York, 1990. (Cited at page 22.)

Z. Mei, A. J. Roberts, and Zhenquan Li. Modelling the dynamics of turbulent floods. *SIAM J. Appl. Math.*, 63:423–458, 2002. (Cited at page 13.)

L. Meignin, P. Gondret, C. Ruyer-Quil, and M. Rabaud. Subcritical Kelvin-Helmholtz instability in a Hele-Shaw cell. *Phys. Rev. Lett.*, 90:234502, Jun 2003. doi: 10.1103/PhysRevLett.90.234502. URL `http://link.aps.org/doi/10.1103/PhysRevLett.90.234502`. (Cited at page 6.)

S. Miladinova, G. Lebonb, and E. Toshev. Thin-film flow of a power-law liquid falling down an inclined plate. *J. Non-Newtonian Fluid Mech.*, 122: 69–78, 2004. (Cited at page 209.)

J.W. Miles. On generation of surface waves by shear flows. *J. Fluid Mech.*, 3:183–204, 1957. (Cited at page 219.)

A. Miyara. Numerical simulation of wavy liquid film flowing down on a vertical wall and an inclined wall. *Int. J. Therm. Sci.*, 39:1015–1027, 2000. (Cited at pages 23, 40, and 42.)

A.A. Mouza, S.V. Paras, and A.J. Karabelas. The influence of small tube diameter on falling film and flooding phenomena. *Int. J. Multiphase Flow*, 28(8):1311–1331, 2002. ISSN 0301-9322. doi: 10.1016/S0301-9322(02)00033-2. URL `http://www.sciencedirect.com/science/article/pii/S0301932202000332`. (Cited at page 219.)

A.A. Mouza, M.N. Pantzali, and S.V. Paras. Falling film and flooding phenomena in small diameter vertical tubes: The influence of liquid properties. *Chem. Eng. Sci.*, 60(18):4981–4991, 2005. ISSN 0009-2509. doi: 10.1016/j.ces.2005.04.014. URL `http://www.sciencedirect.com/science/article/pii/S0009250905003088`. (Cited at page 219.)

M. Naaim, F. Naaim-Bouvet, T. Faug, and A. Bouchet. Dense snow avalanche modeling: flow, erosion, deposition and obstacle effects. *Cold. Reg. Sci. Technol.*, 39:193–204, 2004. (Cited at page 217.)

C. Nakaya. Long waves on a viscous fluid down a vertical wall. *Phys. FluidsA*, 18:1407–1412, 1975. (Cited at page 26.)

Ch.-O. Ng and C. C. Mei. Roll waves on a shallow layer of mud modelled as a power-law fluid. *J. Fluid Mech.*, 263:151–184, 1994. (Cited at page 209.)

L. T. Nguyen and V. Balakotaiah. Modeling and experimental studies of wave evolution on free falling viscous films. *Phys. Fluids*, 12:2236–2256, 2000. (Cited at page 34.)

T. Nosoko, P. N. Yoshimura, T. Nagata, and K. Okawa. Characteristics of two-dimensional waves on a falling liquid film. *Chem. Eng. Sci.*, 51: 725–732, 1996. (Cited at pages 23, 40, and 42.)

E. Novbari and A. Oron. Energy integral method model for the nonlinear dynamics of an axisymmetric thin liquid film falling on a vertical cylinder. *Phys. Fluids*, 21:062107, 2009. (Cited at pages 35 and 156.)

E. Novbari and A. Oron. Analysis of time-dependent nonlinear dynamics of the axisymmetric liquid film on a vertical circular cylinder: Energy integral model. *Phys. Fluids*, 23:012105, 2011. (Cited at page 159.)

J. A. Ochoa-Tapia and S. Whitaker. Momentum transfer at the boundary between a porous medium and a homogeneous fluid i: Theoretical development. *Int. J. Heat Mass Transfer*, 38:2635–2646, 1995. (Cited at page 199.)

T. Ooshida. Surface equation of falling film flows with moderate Reynolds number and large but finite Weber number. *Phys. Fluids*, 11:3247–3269, 1999. (Cited at pages 28 and 37.)

A. Oron and O. Gottlieb. Subcritical and supercritical bifurcations of the first- and second-order Benney equations. *J. Eng. Math.*, 50:121–140, 2004. (Cited at page 27.)

M. K. R. Panga and V. Balakotaiah. Low-dimensional models for vertically falling viscous films. *Phys. Rev. Lett.*, 90(15):1, 2003. (Cited at page 26.)

M. K. R. Panga and V. Balakotaiah. Long-wavelength equation for vertically falling films. *Phys. Rev. E*, 71:036310, 2005. (Cited at page 26.)

C. D. Park and T. Nosoko. Three-dimensional wave dynamics on a falling film and associated mass transfer. *AIChE J.*, 49:2715–2727, 2003. (Cited at page 21.)

J. P. Pascal. Linear stability of fluid flow down a porous inclined plane. *J. Phys. D: Appl. Phys.*, 32:417–422, 1999. (Cited at pages 198, 200, and 202.)

J. R. A. Pearson. On convection cells induced by surface tension. *J. Fluid Mech.*, 4:489–500, 1958. (Cited at page 99.)

S. Popinet. Gerris: a tree-based adaptive solver for the incompressible euler equations in complex geometries. *J. Comp. Phys.*, 190:572–600, 2003. (Cited at pages 37, 201, 211, and 220.)

S. Popinet. An accurate adaptive solver for surface-tension-driven interfacial flows. *J. Comp. Phys.*, 228:5838–5866, 2009. URL `http://gfs.sf.net/papers/tension.pdf`. (Cited at pages 37, 201, 211, and 220.)

S. Portalski. Eddy formation in film flow down a vertical plate. *Indust. Engng Chem. Fund.*, 3:49–53, 1964. (Cited at page 40.)

O. Pouliquen, J.M. Chomaz, and P. Huerre. Wave-number selection and phase solitons in spatially forced temporal mixing layers. *Phys. Rev. Lett.*, 68:2596–2599, 1992. (Cited at page 163.)

O. Pouliquen, P. Huerre, and J.M. Chomaz. Propagative sine-gordon solitons in the spatially forced Kelvin-Helmholtz instability. *Physica D*, 80: 333–355, 1995. (Cited at page 163.)

M. Pradas, D. Tseluiko, and S. Kalliadasis. Rigorous coherent-structure theory for falling liquid films: Viscous dispersion effects on bound-state formation and self-organization. *Phys. Fluids*, 23:044104, 2011. (Cited at pages 44, 163, and 209.)

T. Prokopiou, M. Cheng, and H.-C. Chang. Long waves on inclined films at high Reynolds number. *J. Fluid Mech.*, 222:665–691, 1991. (Cited at page 34.)

A. Pumir, P. Manneville, and Y. Pomeau. On solitary waves running down an inclined plane. *J. Fluid Mech.*, 135:27–50, 1983. (Cited at page 26.)

D. Quéré. Thin films flowing on vertical fibers. *Europhys. Lett.*, 13:721–726, 1990. (Cited at pages 139 and 159.)

D. Quéré. Fluid coating on a fiber. *Annu. Rev. Fluid Mech.*, 31:347–384, 1999. (Cited at pages 141 and 159.)

B. Ramaswamy, S. Krishnamoorthy, and S. W. Joo. Three-dimensional simulation of instabilities and rivulet formation in heated falling films. *J. Comp. Phys.*, 131:70–88, 1997. (Cited at page 107.)

Lord Rayleigh. On the stability of liquid jets. *Proc. Lond. Math. Soc.*, 10:4, 1878. (Cited at page 139.)

N.M. Ribe. Bending and stretching of thin viscous sheets. *J. Fluid Mech.*, 433:135–160, 2001. (Cited at page 36.)

A. J. Roberts. Low-dimensional models of thin film fluid dynamics. *Phys. Lett. A*, 212:63–71, 1996. (Cited at pages 13, 31, and 32.)

A. J. Roberts. Low-dimensional modelling of dynamics via computer algebra. *Comp. Phys. Commun.*, 100:215–230, 1997. (Cited at pages 6, 11, and 31.)

A. J. Roberts. A normal form of thin fluid film equations resolves the transient paradox. *Physica D*, 553:69–81, 2006. (Cited at page 13.)

A. J. Roberts and Z.-Q. Li. An accurate and comprehensive model of thin fluid flows with inertia on curved substrates. *J. Fluid Mech.*, 553:33–73, 2006. (Cited at pages 13, 39, 156, and 217.)

G. J. Roskes. Three-dimensional long waves on liquid film. *Phys. Fluids*, 13:1440–1445, 1970. (Cited at page 26.)

J. Rougier and M. Kern. Predicting snow velocity in large chute flows under different environmental conditions. *J. Roy. Stat. Soc.: Series C*, 59(5): 737–760, 2010. ISSN 1467-9876. doi: 10.1111/j.1467-9876.2010.00717.x. URL `http://dx.doi.org/10.1111/j.1467-9876.2010.00717.x`. (Cited at page 217.)

C. Ruyer-Quil. Inertial corrections to the Darcy law in a Hele-Shaw cell. *C. R. Acad. Sci. Série IIb*, 329:337–342, 2001. (Cited at pages 6, 8, and 10.)

C. Ruyer-Quil and S. Kalliadasis. Wavy regimes of film flow down a fiber. *Phys. Rev. E*, 85:046302, 2012. (Cited at pages 139, 140, 142, 155, 156, and 159.)

C. Ruyer-Quil and P. Manneville. Modeling film flows down inclined planes. *Eur. Phys. J. B*, 6:277–292, 1998. (Cited at pages 26 and 36.)

C. Ruyer-Quil and P. Manneville. Improved modeling of flows down inclined planes. *Eur. Phys. J. B*, 15:357–369, 2000. (Cited at pages 29, 37, and 155.)

C. Ruyer-Quil and P. Manneville. Further accuracy and convergence results on the modeling of flows down inclined planes by weighted-residual approximations. *Phys. Fluids*, 14:170–183, 2002. (Cited at pages 30, 36, 37, and 201.)

C. Ruyer-Quil and Paul Manneville. On the speed of solitary waves running down a vertical wall. *J. Fluid Mech.*, 531:181–190, 2005. (Cited at page 39.)

C. Ruyer-Quil, B. Scheid, S. Kalliadasis, M. G. Velarde, and R. Kh. Zeytounian. Thermocapillary long waves in a liquid film flow. Part 1. Low dimensional formulation. *J. Fluid Mech.*, 538:199–222, 2005. (Cited at pages 101, 103, 104, 105, and 106.)

C. Ruyer-Quil, P. M. J. Trevelyan, F. Giorgiutti-Dauphiné, C. Duprat, and S. Kalliadasis. Modelling film flows down a fiber. *J. Fluid Mech.*, 603: 431–462, 2008. (Cited at pages 44, 139, 140, 150, 151, 155, 156, and 157.)

C. Ruyer-Quil, S. Chakraborty, and B.S. Dandapat. Wavy regimes of a power-law film flow. *J. Fluid Mech.*, 692:220–256, 2012. (Cited at pages 37, 197, 209, and 211.)

I. M. R. Sadiq and R. Usha. Thin newtonian film flow down a porous inclined plane: stability analysis. *Phys. Fluids*, 20:022105.1–0.22105.22, 2008. (Cited at pages 198 and 200.)

A.-J.-C. Barré de Saint-Venant. Théorie du mouvement non-permanent des eaux, avec applications aux crues des rivières et à l'introduction des marées dans leur lit. *C. R. Acad. Sci. Paris*, 73:147–154, 1871. (Cited at page 34.)

A. Samanta. *Falling film over a porous medium*. PhD thesis, Univerité Pierre et Marie Curie, Paris, France, 2012. (Cited at page 199.)

A. Samanta, C. R. Ruyer-Quil, and B. Goyeau. Falling film down a slippery inclined plane. *J. Fluid Mech.*, 684:353–383, 2011. (Cited at pages 197, 198, 200, and 201.)

A. Samanta, B. Goyeau, and C. R. Ruyer-Quil. Falling film on a porous media. submitted to J. Fluid Mech., 2012. (Cited at pages 39, 197, 199, 200, and 202.)

P. Saramito. A new elastoviscoplastic model based on the Herschel-Bulkley viscoplastic model. *J. Non-Newtonian Fluid Mech.*, 158:154–161, 2008. (Cited at pages 215, 216, and 217.)

B. Scheid. *Evolution and stability of a falling liquid film with thermocapillary effects*. PhD thesis, Univerité Libre de Bruxelles, Chimie-Physique E.P., Belgium, 2004. (Cited at page 101.)

B. Scheid, C. Ruyer-Quil, S. Kalliadasis, M. G. Velarde, and R.Kh. Zeytounian. Thermocapillary long waves in a liquid film flow. Part 2. linear stability and nonlinear waves. *J. Fluid Mech.*, 538:223–244, 2005a. (Cited at page 101.)

B. Scheid, C. Ruyer-Quil, U. Thiele, O. A. Kabov, J. C. Legros, and P. Colinet. Validity domain of the Benney equation including the Marangoni effect for closed and open flows. *J. Fluid Mech.*, 527:303–335, 2005b. (Cited at page 26.)

B. Scheid, C. Ruyer-Quil, and P. Manneville. Wave patterns in film flows: modelling and three-dimensional waves. *J. Fluid Mech.*, 562:183–222, 2006. (Cited at pages 31, 40, 41, 44, and 155.)

B. Scheid, S. Kalliadasis, C. Ruyer-Quil, and P. Colinet. Spontaneous channeling of solitary pulses in heated film flows. *Europhys. Lett.*, 84:64002, 2008a. (Cited at pages 101 and 112.)

B. Scheid, S. Kalliadasis, C. Ruyer-Quil, and P. Colinet. Interaction of three-dimensional hydrodynamic and thermocapillary instabilities in film flows. *Phys. Rev. E*, 78:066311, 2008b. (Cited at pages 101 and 112.)

H. Schlichting. *Boundary-Layer Theory*. Mc Graw-Hill (New York), seventh edition, 1979. (Cited at pages 8, 9, 105, and 153.)

P. J. Schmid and D. S. Henningson. *Stability and Transition in Shear Flows*. Springer, Berlin, 2001. (Cited at page 20.)

L. E. Scriven and C. V. Sterling. On cellular convection driven surface tension gradients: effects of mean surface tension and surface viscosity. *J. Fluid Mech.*, 19:321–340, 1964. (Cited at page 99.)

V. Ya. Shkadov. Wave flow regimes of a thin layer of viscous fluid subject to gravity. *Izv. Akad. Nauk SSSR, Mekh. Zhidk Gaza*, 1:43–51, 1967. English translation in *Fluid Dynamics* **2**, 29–34, 1970 (Faraday Press, N.Y.). (Cited at page 34.)

V. Ya. Shkadov. Solitary waves in a layer of viscous liquid. *Izv. Akad. Nauk SSSR, Mekh. Zhidk Gaza*, 1:63–66, 1977. (Cited at pages 24, 101, and 141.)

V. Ya. Shkadov and G. M. Sisoev. Waves induced by instability in falling films of finite thickness. *Fluid Dyn. Res.*, 35:357–389, 2004. (Cited at page 34.)

B. I. Shraiman. Diffusive transport in a Rayleigh-Bénard convection cell. *Phys. Rev. A*, 36:261–267, 1987. (Cited at page 111.)

G. M. Sisoev and V. Ya. Shkadov. A two-parameter manifold of wave solutions to an equation for a falling film of viscous fluid. *Dokl. Phys.*, 44:454–459, 1999. (Cited at page 34.)

G. M. Sisoev, R. V. Craster, O. K. Matar, and S. V. Gerasimov. Film flow down a fibre at moderate flow rates. *Chem. Eng. Sci.*, 61:7279–7298, 2006. (Cited at pages 34 and 156.)

G. M. Sisoev, B. S. Dandapat, K. S. Matveyev, and A. Mukhopadhyay. Bifurcation analysis of the travelling waves on a falling power-law fluid film. *J. Non-Newtonian Fluid Mech.*, 141:128–137, 2007. (Cited at page 209.)

K. A. Smith. On convective instability induced by surface-tension gradients. *J. Fluid Mech.*, 24:401–414, 1966. (Cited at page 99.)

S. R. Tailby and S. Portalski. The hydrodynamics of liquid films flowing on vertical surfaces. *Trans. Instn. Chem. Engrs.*, 38:324–330, 1960. (Cited at page 24.)

U. Thiele, B. Goyeau, and M.G. Velarde. Stability analysis of thin film flow along a heated porous substrate. *Phys. Fluids*, 21:014103, 2009. (Cited at page 199.)

H. A. Thomas. The propagation of waves in steep prismatic conduits. In *Proc. Hydraulics Conf.*, pages 214–229. Univ. of Iowa, 1939. (Cited at pages 39 and 160.)

J. Tihon, K. Serifi, K. Argyiriadi, and V. Bontozoglou. Solitary waves on inclined films: their characteristics and the effects on wall shear stress. *Experiments in Fluids*, 41:79–89, 2006. (Cited at pages 37, 38, and 160.)

S. Toh, H. Iwasaki, and T. Kawahara. Two-dimensionally localized pulses of a nonlinear equation with dissipation and dispersion. *Phys. Rev. A*, 40:5472–5475, 1989. (Cited at page 43.)

P. M. J. Trevelyan, S. Kalliadasis, J. H. Merkin, and S. K. Scott. Mass transport enhancement in regions bounded by rigid walls. *J. Eng. Math.*, 42:45–64, 2002. (Cited at page 111.)

P. M. J. Trevelyan, B. Scheid, C. Ruyer-Quil, and S. Kalliadasis. Heated falling films. *J. Fluid Mech.*, 592:295–334, 2007. (Cited at pages 101, 104, 105, and 111.)

Y. Y. Trifonov. Steady-state travelling waves on the surface of a viscous liquid film falling down vertucal wires and tubes. *AIChE J.*, 38:821–834, 1992. (Cited at page 156.)

Y. Y. Trifonov. Counter-current gas-liquid wavy film flow between the vertical plates analyzed using the Naviee-Stokes equations. *AIChE J.*, 56:1975–1987, 2010. (Cited at page 219.)

Y. Y. Trifonov. Counter-current gas-liquid flow between vertical corrugated plates. *Chem. Eng. Sci.*, 66:4851–4866, 2011. (Cited at page 219.)

D. Tseluiko and S. Kalliadasis. Nonlinear waves in counter-current gas-liquid film flow. *J. Fluid Mech.*, 673:19–59, 2011. (Cited at pages 218 and 219.)

D. Tseluiko, S. Saprykin, C. Duprat, F. F. Giorgiutti-Dauphiné, and S. Kalliadasis. Pulse dynamics in low-reynolds-number interfacial hydrodynamics: Experiments and theory. *Physica D*, 239:2000–2010, 2010a. (Cited at page 162.)

D. Tseluiko, S. Saprykin, and S. Kalliadasis. Interaction of solitary pulses in active dispersive-dissipative media. *Proc. Est. Acad. Sci.*, 59:139–144, 2010b. (Cited at pages 43, 44, and 162.)

R. Usha and B. Uma. Modeling of stationary waves on a thin viscous film down an inclined plane at high Reynolds numbers and moderate Weber numbers using energy integral method. *Phys. Fluids*, 16(7):2679–2696, 2004. (Cited at page 35.)

R. Usha, S. Millet, H. BenHadid, and F. Rousset. Shear-thinning film on a porous substrate: Stability analysis of a one-sided model. *Chem. Eng. Sci.*, 66:5614–5627, 2011. (Cited at pages 198 and 200.)

M. G. Velarde and R. Kh. Zeytounian. *Interfacial Phenomena and the Marangoni Effect*. Springer-CISM (Wien), 2002. (Cited at page 99.)

J.-P. Vila. A two moments closure of shallow water type for gravity driven flows. in preparation. (Cited at pages 35 and 44.)

M. Vlachogiannis, A. Samandas, V. Leontidis, and V. Bontozoglou. Effect of channel width on the primary instability of inclined film flow. *Phys. Fluids*, 22:012106, 2010. (Cited at page 45.)

N.A. Vlachos, S.V. Paras, A.A. Mouza, and A.J. Karabelas. Visual observations of flooding in narrow rectangular channels. *Int. J. Multiphase Flow*, 27:1415–1430, 2001. (Cited at page 219.)

F.K. Wasden and A.E. Duckler. Insights into the hydrodynamics of free falling wavy films. *AIChE J.*, 187:35, 1989. (Cited at page 39.)

S. Whitaker. The forchheimer equation: A theoretical development. *Transport in Porous Media.*, 25:27–61, 1996. (Cited at page 202.)

G. B. Whitham. *Linear and Nonlinear Waves*. John Wiley & Sons (New York), 1974. (Cited at pages 26, 33, 205, and 206.)

C.-S. Yih. Stability of two-dimensional parallel flows for three dimensional disturbances. *Quart. Appl. Math.*, 12:434, 1955. (Cited at page 20.)

P. N. Yoshimura, T. Nosoko, and T. Nagata. Enhancement of mass transfer into a falling laminar liquid film by two-dimensional surface waves—some experimental observations and modeling. *Chem. Eng. Sci.*, 51(8): 1231–1240, 1996. (Cited at page 39.)

L.-Q. Yu, F. K. Wasden, A. E. Dukler, and V. Balakotaiah. Nonlinear evolution of waves on falling films at high Reynolds numbers. *Phys. Fluids*, 7:1886–902, 1995. (Cited at page 34.)

A. Zapke and D.G. Kröger. The influence of fluid properties and inlet geometry on flooding in vertical and inclined tubes. *Int. J. Multiphase Flow*, 22(3):461–472, 1996. ISSN 0301-9322. doi: 10.1016/0301-9322(95)00076-3. URL `http://www.sciencedirect.com/science/article/pii/0301932295000763`. (Cited at page 219.)

Titre De la modélisation et des instabilités des films liquides tombants

Résumé Ce mémoire présente une synthèse de travaux de recherche portant sur l'étude et la modélisation d'instabilités de grandes longueurs d'ondes en général et de films liquides tombants en particulier. Les différentes méthodes sont discutées au chapitre 1 et appliquées aux écoulements inertiels en cellule de Hele-Shaw. L'instabilité Kapitza d'un film tombant est étudiée au chapitre 2. Les couplages de l'instabilité Kapitza avec les instabilités Marangoni (films chauffés) et Rayleigh-Plateau (films sur fibres) font l'objet des chapitres 3 et 4. Le chapitre 5 présente mes derniers travaux sur les films non-Newtoniens, en présence d'une paroi poreuse ou encore cisaillés par un écoulement gazeux.

Mots-clés instabilités, modéliation, ondes longues, films liquides tombants, Rayleigh-Plateau, Marangoni, Kelvin-Helmholtz

Title Instabilities and modeling of falling film flows

Abstract This manuscript presents a synthesis of research activities devoted to the study and low-dimensional modeling of long-wave instabilities in general and to falling film flows in particular. The different methodologies are discussed in Chapter 1 and applied to the modeling of inertial flows in a Hele-Shaw cell. Chapter 2 is devoted to the Kapitza instability of a falling film. Chapter 3 and 4 investigate the coupling of the Kapitza instability with the Marangoni (heated films) and the Rayleigh-Plateau instabilities (films running down fibers). Chapter 5 presents recent works on non-Newtonian falling films, films running on porous media and some current works on films sheared by a gas stream.

Keywords instabilities, low-dimensional modeling, long waves, falling liquid films, Rayleigh-Plateau, Marangoni, Kelvin-Helmholtz